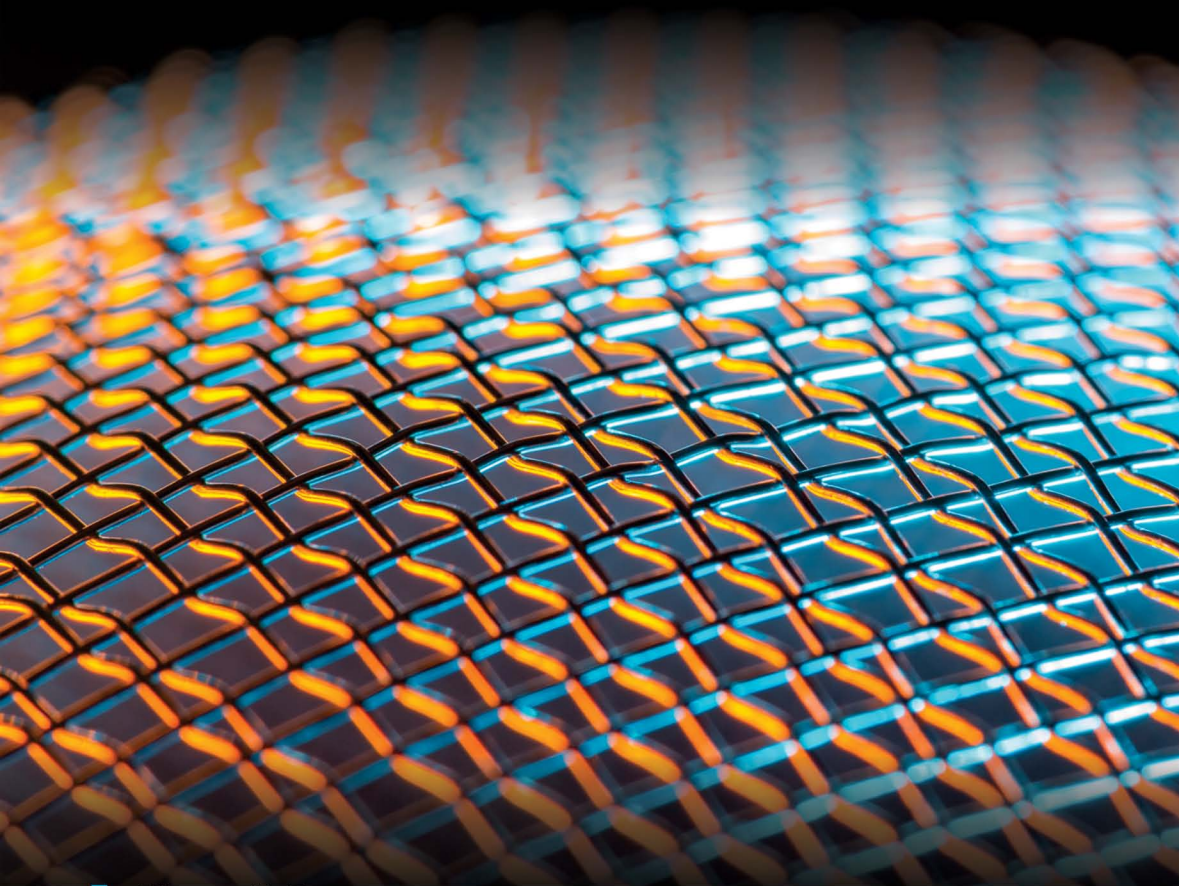


# FUNCTIONAL NANOCOMPOSITES AND THEIR APPLICATIONS



Dhanya K. R.  
Sanal P. S.  
Sabu Thomas  
Nandakumar Kalarikkal  
Editors

 **CRC Press**  
Taylor & Francis Group  
APPLE ACADEMIC PRESS

# **FUNCTIONAL NANOCOMPOSITES AND THEIR APPLICATIONS**

# **FUNCTIONAL NANOCOMPOSITES AND THEIR APPLICATIONS**

*Edited by*

**Dhanya K. R., PhD**

**Sanal P. S., PhD**

**Sabu Thomas, PhD**

**Nandakumar Kalarikkal, PhD**



First edition published 2025

**Apple Academic Press Inc.**

1265 Goldenrod Circle, NE,  
Palm Bay, FL 32905 USA

760 Laurentian Drive, Unit 19,  
Burlington, ON L7N 0A4, CANADA

**CRC Press**

2385 NW Executive Center Drive,  
Suite 320, Boca Raton FL 33431

4 Park Square, Milton Park,  
Abingdon, Oxon, OX14 4RN UK

© 2025 by Apple Academic Press, Inc.

*Apple Academic Press exclusively co-publishes with CRC Press, an imprint of Taylor & Francis Group, LLC*

Reasonable efforts have been made to publish reliable data and information, but the authors, editors, and publisher cannot assume responsibility for the validity of all materials or the consequences of their use. The authors are solely responsible for all the chapter content, figures, tables, data etc. provided by them. The authors, editors, and publishers have attempted to trace the copyright holders of all material reproduced in this publication and apologize to copyright holders if permission to publish in this form has not been obtained. If any copyright material has not been acknowledged, please write and let us know so we may rectify in any future reprint.

Except as permitted under U.S. Copyright Law, no part of this book may be reprinted, reproduced, transmitted, or utilized in any form by any electronic, mechanical, or other means, now known or hereafter invented, including photocopying, microfilming, and recording, or in any information storage or retrieval system, without written permission from the publishers.

For permission to photocopy or use material electronically from this work, access [www.copyright.com](http://www.copyright.com) or contact the Copyright Clearance Center, Inc. (CCC), 222 Rosewood Drive, Danvers, MA 01923, 978-750-8400. For works that are not available on CCC please contact [mpkbookspermissions@tandf.co.uk](mailto:mpkbookspermissions@tandf.co.uk)

Trademark notice: Product or corporate names may be trademarks or registered trademarks and are used only for identification and explanation without intent to infringe.

---

**Library and Archives Canada Cataloguing in Publication**

Title: Functional nanocomposites and their applications / edited by Dhanya K.R., PhD, Sanal P.S., PhD, Sabu Thomas, PhD, Nandakumar Kalarikkal, PhD.

Names: Dhanya, K. R., 1983- editor. | P. S., Sanal, editor. | Thomas, Sabu, editor. | Kalarikkal, Nandakumar, editor.

Description: First edition. | Includes bibliographical references and index.

Identifiers: Canadiana (print) 20240307267 | Canadiana (ebook) 20240307291 | ISBN 9781774914403 (hardcover) |

ISBN 9781774914410 (softcover) | ISBN 9781003412748 (ebook)

Subjects: LCSH: Nanocomposites (Materials)—Industrial applications.

Classification: LCC TA418.9.N35 F86 2024 | DDC 620.1/15—dc23

**Library of Congress Cataloging-in-Publication Data**

---

CIP data on file with US Library of Congress

---

---

ISBN: 978-1-77491-440-3 (hbk)

ISBN: 978-1-77491-441-0 (pbk)

ISBN: 978-1-00341-274-8 (ebk)



# About the Editors

---

## **Dhanya K. R., PhD**

*Postdoctoral Fellow, International and Inter University Center for Nanoscience and Nanotechnology, Mahatma Gandhi University, Kottayam, Kerala, India*

Dhanya K. R., PhD, is a postdoctoral fellow at the Inter University Center for Nanoscience and Nanotechnology, Mahatma Gandhi University, Kottayam, India. She has published many articles in international and national journals. She has authored and coauthored book chapters. She has published a book related to medicine. Her research interests include hydrogels, water purification studies, nanocomposites, biopolymers, and others. She has also presented her work at international conferences. She has coordinated several science-oriented programmes such as World Environmental Day, National Technology Day, Ozone Day, and so forth and has been a coordinator of several national conferences.

## **Sanal P. S., PhD**

*Patent Analyst and Technical Consultant*

Sanal P. S., PhD, is a Patent Analyst and Technical Consultant. He received his PhD in Polymer Engineering from the Indian Institute of Technology (IIT) Kharagpur, India, in 2015. During his PhD, he worked on block copolymers for biomedical applications. Thereafter, he worked as a postdoctoral researcher at Technion Israel Institute of Technology. He researched coaxial electrospinning of conducting polymers during his postdoctoral work. He worked as a postdoctoral researcher at the International and Interuniversity Centre for Nanoscience and Nanotechnology, Mahatma Gandhi University, India. There, he continued his research on the electrospinning of polymers. His main areas of research are polymer technology, electrospinning, and polymeric biomaterials.

**Sabu Thomas, PhD**

*Vice Chancellor, Mahatma Gandhi University, Professor of Polymer Science and Technology and Founding Director of International and Inter University Center for Nanoscience and Nanotechnology, Mahatma Gandhi University, Kottayam, Kerala, India*

Sabu Thomas, PhD, is the Vice Chancellor, Mahatma Gandhi University, and also Professor of Polymer Science and Technology and Founding Director of International and Inter University Center for Nanoscience and Nanotechnology, Mahatma Gandhi University, Kottayam, Kerala, India. He has supervised many PhD, MPhil, and master's theses. He has five patents to his credit. The research activities of Professor Thomas include surfaces and interfaces in multiphase polymer blend and composite systems; phase separation in polymer blends; compatibilization of immiscible polymer blends; thermoplastic elastomers; phase transitions in polymers; nanostructured polymer blends; macro-, micro- and nanocomposites; polymer rheology; recycling; reactive extrusion; processing–morphology–property relationships in multiphase polymer systems; double networking of elastomers; natural fibers and green composites; rubber vulcanization; interpenetrating polymer networks; diffusion and transport; and polymer scaffolds for tissue engineering. He received the coveted Sukumar Maithy Award for the best polymer researcher in the country for the year 2008. Recently, Professor Thomas received the MRSI and CRSI medals for his excellent work. He has more than 800 publications to his credit and over 35,765 citations, with an h-index of 87, and Dr. Thomas has been ranked fifth in India as one of the most productive scientists. He received his BSc degree (1980) in Chemistry from the University of Kerala, BTech (1983) in Polymer Science and Rubber Technology from the Cochin University of Science and Technology, and PhD (1987) in Polymer Engineering from the Indian Institute of Technology, Kharagpur.

**Nandakumar Kalarikkal, PhD**

*Senior Professor, School of Pure and Applied Physics, Mahatma Gandhi University, International and Inter University Centre for Nanoscience and Nanotechnology, School of Nanoscience and Nanotechnology, Mahatma Gandhi University, India*

Nandakumar Kalarikkal, PhD, is the Director of the International and Inter University Centre for Nanoscience and Nanotechnology as well as an

Associate Professor in the School of Pure and Applied Physics at Mahatma Gandhi University, Kerala, India. His current research interests include synthesis, characterization, and applications of various nanostructured materials, laser plasma, and phase transitions. He has published more than 260 research articles in peer-reviewed journals, six patents, and has edited 32 books. Dr. Kalarikkal obtained his master's degree in Physics with a specialization in industrial physics and his PhD in Semiconductor Physics from Cochin University of Science and Technology, Kerala, India. He was a postdoctoral fellow at NIIST, Trivandrum, and later joined Mahatma Gandhi University, Kerala, India. He has received several research grants and supervised more than 22 PhD students. Several international and national project works have been carried out under his guidance, and he has received many international fellowships as well as honors.

# Contents

---

<i>Contributors</i> .....	<i>xi</i>
<i>Abbreviations</i> .....	<i>xiii</i>
<i>Preface</i> .....	<i>xvii</i>
<b>1. Synthesis and Fabrication of Graphene and Reduced Graphene Oxide ....</b>	<b>1</b>
Sanal Sebastian Payyappilly, Mable Maria Baby, Simimol Sunny, and Ananta Kumar Mishra	
<b>2. Polythiophene Nanocomposites and their Applications .....</b>	<b>27</b>
Linda Maria Varghese, Om Prakash Bajpai, Dhanya K. R., and Sanal Sebastian Payyappilly	
<b>3. Polymer/Clay Nanocomposites for Tire Applications.....</b>	<b>49</b>
Asha Krishnan K.	
<b>4. Molecular Dynamics-Based Simulations to Study Structures and Properties of Graphene/Polyurethane Nanocomposites.....</b>	<b>75</b>
Animesh Talapatra, and Debasis Datta	
<b>5. Synthesis and Multifunctional Applications of Polymethyl Methacrylate-Based Nanocomposites: A Review .....</b>	<b>137</b>
K. B. Bhavitha, Srinivasarao Yarangalla, Kala M. S., Nandakumar Kalarikkal, and Sabu Thomas	
<b>6. MnO<sub>2</sub>-Based Nanostructure Synthesis, Properties, and Applications.....</b>	<b>165</b>
Sanal Sebastian Payyappilly, Vyshnavi Santosh, Sneha Sabu Mathew, and Ashina Muhammed	
<b>7. Dye Removal Using Nanocomposites .....</b>	<b>187</b>
Santra Santhosh and Dhanya K. R.	
<b>8. Bionanomaterials: Significance, Classification, and Application .....</b>	<b>217</b>
Neetha John, Abhijith Krishna, and Jeffy Joji	
<b>9. Luminescent Properties of Pure and Lanthanide Doped Rare Earth Sesquioxide Nanoparticles.....</b>	<b>241</b>
Morris Marieli Antoinette and Sujin P. Jose	
<b>10. Composites and their Applications in Light-Source-Enhanced Destruction of Organic Wastes .....</b>	<b>267</b>
I. Prabha	

<b>11. Recent Advances in the Biosynthesis of Noble Metal Nanoparticles Using Marine Macroalgae .....</b>	<b>289</b>
K. F. Princy, Sreeja E. S., and Anu Gopinath	
<b>12. Computer Simulation of Structure and Mechanical Behavior of Polymer Nanocomposites.....</b>	<b>325</b>
Shengwei Deng and Dhanya K. R.	
<b><i>Index</i>.....</b>	<b>347</b>

# Contributors

---

**Morris Marieli Antoinette**

Department of Physics, St. Joseph's College, Alappuzha, Kerala, India

**Mable Maria Baby**

Department of Chemistry, Nirmala College, Muvattupuzha, Kerala, India

**Om Prakash Bajpai**

Rubber Technology Centre, Indian Institute of Technology, Kharagpur, India

**K. B. Bhavitha**

International and Inter University Centre for Nanoscience and Nanotechnology,  
Mahatma Gandhi University, Kottayam, Kerala, India

**Debasis Datta**

Department of Mechanical Engineering, Indian Institute of Engineering Science and Technology,  
Shibpur, Howrah, West Bengal, India

**Shengwei Deng**

College of Chemical Engineering, Zhejiang University of Technology, Hangzhou, China

**Anu Gopinath**

Department of Aquatic Environment Management, Kerala University of Fisheries and Ocean Studies,  
Cochin, India

**Neetha John**

CIPET-Central Institute of Petrochemical Engineering and Technology, Udyogamandal, Kochi,  
Kerala, India

**Jeffy Joji**

CIPET-Central Institute of Petrochemical Engineering and Technology, Udyogamandal, Kochi,  
Kerala, India

**Sujin P. Jose**

School of Physics, Madurai Kamaraj University, Madurai, Tamil Nadu, India

**Asha Krishnan K.**

International and Interuniversity Centre for Nanoscience and Nano Technology,  
Mahatma Gandhi University, Kottayam, India

**Nandakumar Kalarikkal**

School of Pure and Applied Physics, Mahatma Gandhi University, Kottayam, Kerala, India

**Abhijith Krishna**

CIPET-Central Institute of Petrochemical Engineering and Technology, Udyogamandal, Kochi, Kerala

**Sneha Sabu Mathew**

School of Energy Materials, Mahatma Gandhi University, Kottayam, India

**Ananta Kumar Mishra**

Leibniz Institute of Polymer Research, Dresden e. V., Germany

**Ashina Muhammed**

International and Inter University Centre for Nanoscience and Nanotechnology,  
Mahatma Gandhi University, Kottayam, India

**Sanal Sebastian Payyappilly**

International and Inter University Centre for Nanoscience and Nanotechnology,  
Mahatma Gandhi University, Kottayam, Kerala, India

**I. Prabha**

Department of Chemistry, Bharathiar University, Coimbatore, Tamil Nadu, India

**K. F. Princy**

Government College Kattappana, Idukki, Kerala, India

**Dhanya K. R.**

International and Interuniversity center for Nanoscience and Nano Technology,  
Mahatma Gandhi University, Kottayam, India

**Sreeja E. S.**

Department of Marine Chemistry, Kerala University of Fisheries and Ocean Studies, Cochin, India

**Kala M. S.**

Department of Physics, St Teresa's College, Ernakulam, Kerala, India

**Santra Santhosh**

Indian Institute of Science Education and Research, Thiruvananthapuram, India

**Vyshnavi Santosh**

Department of Chemistry, Baselius College, Kottayam, India

**Simimol Sunny**

Department of Chemistry, Nirmala College, Muvattupuzha, Kerala, India

**Animesh Talapatra**

Department of Mechanical Engineering, Indian Institute of Engineering Science and Technology,  
Shibpur, Howrah, West Bengal, India

**Sabu Thomas**

School of Chemical Sciences, Mahatma Gandhi University, Kottayam, Kerala, India

**Linda Maria Varghese**

International and Interuniversity Center for Nanoscience and Nano Technology,  
Mahatma Gandhi University, Kottayam, India

**Srinivasarao Yaragalla**

Guru Nanak Institute of Technical Campus, Hyderabad, Telangana, India  
Smart materials Istituto Italiano di Tecnologia, Genova, Italy

# Abbreviations

---

AFM	atomic force microscopy
AOPs	advanced oxidation processes
APP	ammonium polyphosphate
AR	aspect ratio
BFO	bismuth ferrite
BNNSs	boron nitride nanosheets
BR	butadiene rubber
BUA	bottoms up approach
CF	crystal field
CFF	consistent force fields
CIE	Commission International del'Eclairage
CMC	carboxymethyl cellulose
CMD	chemical manganese dioxide
CMNC	ceramic matrix nanocomposites
CNT	carbon nanotube
COMPASS	condensed-phase optimized molecular potentials for atomistic simulation studies
CPN	clay-polymer nanocomposites
Cps	conducting polymers
CTAB	cetyltrimethylammonium bromide
CV	cyclic voltammetry
CVD	chemical vapor deposition
DGEBA	diglycidyl ether of bisphenol A
DMA	dynamic mechanical analyzer
DPD	dissipative particle dynamics
DPV	differential pulse voltammetry
DSC	differential scanning calorimetry
EAM	embedded atom method
ECM	extracellular matrix
EDS	energy-dispersive X-ray spectroscopic
EDTA	ethylenediaminetetraacetic acid
EF	enhancement factor
EG	ethylene glycol
EG	expandable graphite



EM	energy minimization
EMD	electrolytic manganese dioxide
EMD	equilibrium molecular dynamic
FE	finite element
FEM	finite element method
FESEM	field emission scanning electron microscopy
FET	field effect transistor
FF	flax fabric
fs	femtosecond
FTIR	Fourier-transformed infrared spectroscopy
GA	gum Arabic
GNP	graphene nanoplates
GO	graphene oxide
GFRP	glass fiber reinforced polymer
GrO	Gr oxide
HFMFs	high-frequency magnetic fields
HPHT	high-pressure high temperature
HPMR	hydrogen plasma-metal reaction
HRR	heat release rate
HTL	hole transporting layer
IE	interaction energy
IFNS	interfacial normal strength
i-PMMA	isotactic-poly(methyl methacrylate)
IR	isoprene rubber
LBL	layer-by-layer
LEDs	light emitting diodes
Ln	lanthanide
MMA	methyl methacrylate
MMCs	metal matrix composites
MB	methylene blue
MBE	molecular beam epitaxial
MD	molecular dynamics
MG	malachite green
MMNC	metal matrix nanocomposites
MNPs	magnetic nanoparticles
MnO <sub>x</sub>	manganese oxides
MO	methyl orange
MR	magnetorheological
MRGO	magnetite/reduced graphene oxide

MRI	magnetic resonance imaging
MSD	mean square displacement
MV	methyl violet
MW	microwave
MWCNT	multi-walled carbon nanotubes
NEMD	nonequilibrium molecular dynamic
NIR	near infrared
NIST	National Institute of Standards and Technology
NMD	natural manganese dioxide
NMR	nuclear magnetic resonance
NPs	nanoparticles
NR	natural rubber
n-UV	near-ultraviolet
ODA	octadecylamine
ODH	oxalylidihydrazine
OLS	organically modified layered silicate
OOFEM	object-oriented finite element
PAA	poly(acrylic acid)
PAH	poly(allylamine hydrochloride)
PBC	periodic boundary conditions
PCFF	polymer consistent force field
PDE	partial differential equations
PE	potential energy
PET	poly(ethylene terephthalate)
PINC	polymer inorganic nanocomposites
PL	photoluminescence
PMNC	polymer matrix nanocomposites
PNA	peptide nucleic acid
PNCs	polymer nanocomposites
POSS	polyhedral oligomeric silsesquioxanes
ps	pico second
PSCs	polymer solar cells
PtN	platinum nanoparticles
PVA	polyvinyl alcohol
PVDF	poly(vinylidene fluoride)
PVP	polyvinyl pyrrolidone
RB	rhodamine B
RDF	radial distribution function
RE	rare earth

REBO	reactive empirical bond order
ROS	reactive oxygen species
RSA	reverse saturable absorption
RVE	representative volume elements
SAXS	small angle X-ray scattering
SBR	styrene butadiene rubber
SEM	scanning electron microscopy
SLGR	single-layer Gr
SPM	scanning probe microscopy
STM	scanning tunneling microscopy
SWCNH	single-wall carbon nanohorn
TC	thermal conductivity
TDA	top-down approach
TEM	transmission electron microscopy
TGA	thermal gravimetric analyzer
TL	thermoluminescence
TOAB	tetraoctylammonium bromide
TOC	total organic carbon
TPU	thermoplastic polyurethane
TV	television
UC	unit cell
UC	upconversion
UFF	universal force field
UTS	ultimate tensile strength
UV	ultraviolet
Vis	visible
VOCs	volatile organic compounds
vdW	Van der Waals
WAXD	wide angle X-ray diffraction
WLED	white light emitting diode
XPS	X-ray photoelectron spectroscopy
XRD	X-ray diffraction
1-D	one-dimensional

# Preface

---

Functional nanocomposites are important materials with novel properties which can meet present and future demands. These composites show remarkable improvement in properties such as thermal conductivity, mechanical strength, toughness, and others. Carbon nanotubes, graphene, cellulose nanomaterials, titanium dioxide nanoparticles, and various other nanomaterials are generally used for enhancing their properties.

Functional nanocomposites have various applications such as biomedical, electronics, automobile, construction, etc. Polymer nanocomposites have hybrid as well as synergistic properties and show outstanding optical and mechanical properties. Nanocomposites have a high surface-to-volume ratio and hence have strong mechanical characteristics, making them suitable for application in the automotive and construction sectors. Other uses include power tool housing, electronic covers, and so forth.

Nanocomposites show better property enhancement over conventional composites, that is, properties such as electrical, thermal, mechanical, and barrier. They have good transparency and also reduce the property of flammability. Some of the most important nanocomposites used are in the aerospace sector, oil and gas pipelines, automobile, aircraft, films, food packaging, outdoor insulation applications, and environmental protection such as water treatment, and so forth.

This book, *Functional Nanocomposites and Their Applications*, explains innovative developments and the recent scope of nanocomposites. It covers novel findings and various applications of nanocomposites in different emerging fields. All the chapters use an elegant knowledge-sharing pattern and can be used as a reference book for students as well as research scholars. Chapters in this book cover several types of nanocomposites, as well as their synthesis, manufacturing, characteristics, and applications. Special emphasis is given to innovative works on functional nanocomposites and their relevant area of use. The authors depict the stability and functionality of nanocomposites and their applications in various sectors such as industrial, structural, biomedical, and others. Nanocomposites in wastewater treatment,  $\text{MnO}_2$  and graphene nanostructures, computer modeling of structure and mechanical behavior, polythiophene nanocomposites, and other topics are covered in the chapters.

Readers can easily understand the effective implementation of different types of nanocomposites-based research, such as environmental remediation, biomedical applications, lightweight designed goods with better mechanical, thermal, or chemical resistance qualities. This book also discusses the opportunities and challenges that beginners in the field of nanocomposites experience.

We hope that the information and knowledge presented in this book will be an added advantage to students, teachers, research scholars, and young scientists who aspire to follow the research of nanocomposites. We would like to thank all who kindly contributed chapters to this book and cooperated with us.

**—Dr. Dhanya K. R.**  
**Dr. Sanal Sebastian Payyappilly**  
**Prof. Nandakumar Kalarikkal**  
**Prof. Sabu Thomas**

## CHAPTER 1

---

# Synthesis and Fabrication of Graphene and Reduced Graphene Oxide

SANAL SEBASTIAN PAYYAPPILLY<sup>1</sup>, MABLE MARIA BABY<sup>2</sup>,  
SIMIMOL SUNNY<sup>2</sup>, and ANANTA KUMAR MISHRA<sup>3</sup>

*<sup>1</sup>International and Inter University Center for Nanoscience and Nanotechnology, Mahatma Gandhi University, Kottayam, Kerala, India*

*<sup>2</sup>Department of Chemistry, Nirmala College, Muvattupuzha, Kerala, India*

*<sup>3</sup>Leibniz Institute of Polymer Research, Dresden e. V., Germany*

---

### ABSTRACT

Graphene, a remarkable planar sheet of hexagonally arranged sp<sup>2</sup>-hybridized carbon atoms, has drawn substantial attention due to its extraordinary range of properties, including electronic, optical, magnetic, thermal, and mechanical attributes. This chapter provides a comprehensive overview of the synthesis and fabrication of graphene and reduced graphene oxide, shedding light on the cutting-edge methods and strategies employed in the field. The chapter delves into various techniques for synthesizing graphene, encompassing mechanical exfoliation, solvent-aided sonication, surfactant-assisted exfoliation, graphite intercalation-aided exfoliation, epitaxial growth, chemical vapor deposition, pyrolysis, sputtering, arc discharge, carbon implantation, and unzipping of single-walled carbon nanotubes into monolayer graphene. It explores the methods for producing reduced graphene oxide and sets criteria for assessing the effectiveness of reduction, such as visual characteristics, electrical conductivity, and the carbon-to-oxygen atomic ratio. The reduction strategies covered include chemical reagent reduction, thermal reduction (thermal annealing), photocatalyst reduction, and electrochemical reduction.

## **1.1 INTRODUCTION**

Graphene is a planar sheet of hexagonally arranged  $sp^2$ -hybridized carbon atoms and has captured enormous attention in the research field due to its extraordinary electronic, optical, magnetic, thermal, and mechanical properties.<sup>1</sup> It finds use in energy storage, polymer composites, and transparent electrodes. Graphene is often considered a zero-gap semiconductor due to its distinctive properties. Single-layer graphene behaves like a zero-gap semiconductor, whereas multilayer graphene behaves like a metal. This is due to the overlap of the carrier wave function in thick samples. Due to its excellent electrical conductivity and optical transparency, as well as its wide range of applications in liquid crystal displays, supercapacitors, organic light-emitting diodes, touch screens, and organic photovoltaic cells, graphene has sparked a lot of interest.<sup>2,3</sup>

Konstantin Novoselov and Andre Geim received Nobel Prize in 2010 for their research on graphene. They separated graphene from graphite by the micromechanical cleavage method for the first time.<sup>4</sup> Graphite is oxidized to generate graphene oxide. When graphite is oxidized, it loses its conductivity and transforms into a reddish-orange-tinted insulator that disperses quickly in water. To restore graphene's conductivity, graphene oxide is reduced to create reduced graphene oxide. Most of the attractive properties of graphene are a function of its low thickness. At the same time, the disadvantage of graphene is the difficulty of producing samples with the same thickness consistently. This limits its commercial-scale application in many areas.<sup>5</sup> Attempts are being made to prepare graphene, especially single-layered graphene, on a substrate, with a consistent thickness. This chapter provides a brief overview of current progress in graphene and reduced graphene oxide preparation methods.

## **1.2 SYNTHESIS AND FABRICATION OF GRAPHENE**

Methods of preparation of graphene consist of top-down and bottom-up approaches. In the top-down approach, stacked layers of graphite are broken down to yield single-layered graphene sheets, whereas in the bottom-up approach, graphene is synthesized from carbon-containing sources (small organic molecules).<sup>6</sup> The schematic depiction of both processes is shown in Figure 1.1. The different techniques for the synthesis of graphene are mentioned below.

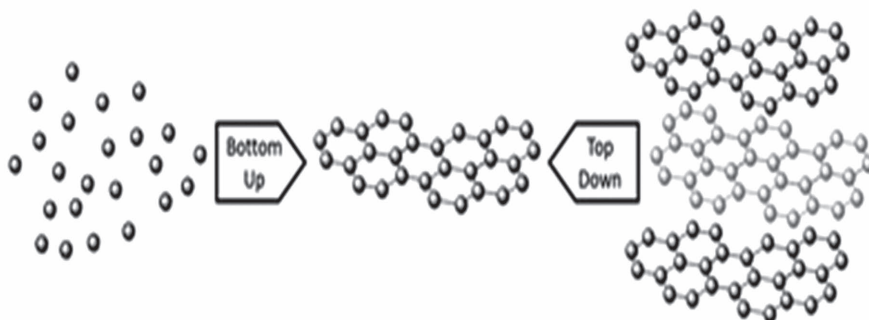


**FIGURE 1.1** A schematic illustration of “top-down” and “bottom-up” methods of graphene synthesis.

*Source:* Reprinted with permission from Ref. [6] © 2013 Royal Society of Chemistry.

### 1.2.1 MECHANICAL EXFOLIATION

A remarkable method for producing single-layer graphene on substrates is mechanical exfoliation. It belongs to the top-down approach. In this method, mechanical forces are applied to graphite to separate graphene sheets from each other. This does not affect the chemical properties of graphene. Mechanical methods yield high-quality graphene. The “Scotch tape method” or “Tape method” was the first method reported to synthesize graphene. This method is capable of producing a very small amount of high-quality graphene, but bulk production is not possible by this method.<sup>7</sup> In this method, graphite is placed between two strips of tape, and with the help of the tape, graphite is peeled into thinner layers. Then the tape is submerged in the acetone substrate, and graphene flakes get detached. Though this method is inefficient for bulk production, the formed graphene is perfect.

### 1.2.2 SOLVENT-AIDED SONICATION

In the liquid exfoliation technique, graphene is directly exfoliated into solvents or solutions. Graphene is insoluble in water or other polar solvents as it is hydrophobic in nature. Moreover, the tightly attached graphene sheets make them insoluble in any solvent. But by using ultrasonic treatment or sonication, small amounts of graphene ( $< 0.01$  mg/mL) can be dispersed in solvents.<sup>8</sup> In sonication, graphene is produced from graphite by dispersing it in a proper liquid medium. Solvent properties are important for graphene



exfoliation. Preferred solvents have a surface tension between 40 and 50 mJm<sup>-2</sup>. 1-methyl-2-pyrrolidinone,  $\gamma$ -butyrolactone, and benzyl benzoate are some of the successful solvents for graphene exfoliation.

Khan et al. utilized ultrasonic treatment for up to 460 h to produce a high concentration of graphene. A maximum concentration of 1.2 mg/mL is reached after 270 h of sonication.<sup>9</sup> Bourlinos et al. developed another method for increasing graphene concentration. Fluorinated aromatic solvents were used to produce graphene concentrations up to 0.1 mg/mL.<sup>10</sup> In the same manner, various aromatic and organic solvents were used to achieve graphene concentrations between 0.2 and 0.3 mg/mL. By using benzylamine, a concentration of graphene as high as 1 mg/mL could be achieved. The highest concentration of graphene achieved was 8 mg/mL in 3-glycidoxypyrroltrimethoxysilane.<sup>11</sup> This was done by just sonicating a graphite powder in an organic solvent. Recently, stable concentrations up to 27 mg/mL were achieved in N-methyl-pyrrolidine by concentrating 2 mg/mL of graphene dispersion by centrifugation and sonication.<sup>9</sup> Such high-concentration graphene finds use in conductive inks and composite fillers. Solvents with high boiling points are required for liquid exfoliation, and thus their feasibility is limited.<sup>12</sup>

Other than ultrasonic treatment, there are other forms of mechanical energy to prepare graphene. When a tube filled with graphite and N-methyl pyrrolidine is rotated at high speed, graphene is peeled off from graphite as a result of the generated mechanical force. Different kinds of liquid polymers are also used to prepare dispersions of graphene due to their high viscosity. Moreover, the long structure of polymers prevents the aggregation of graphene sheets.

### **1.2.3 SURFACTANT-ASSISTED EXFOLIATION**

Direct exfoliation of graphene in solvents can be done with the help of surfactant or adsorbate molecules. This is called surfactant-assisted exfoliation. Exfoliated graphene sheets are stabilized by adsorbate molecules. Graphene sheets are constantly exfoliated during sonication in solvents like water. But they reaggregate back to graphite due to unfavorable environments. This will not happen in the case of surfactant-assisted exfoliation because the momentarily formed graphene sheets attach to adsorbate molecules and are not allowed to reaggregate. Adsorbate molecules are usually aromatic, and they efficiently unite with graphene sheets. Organic molecules containing anthracene<sup>12</sup> or pyrene<sup>13</sup> moieties in their structures are commonly used as

adsorbates. These aromatic molecules exhibit the same pi-pi interactions with graphene as those present in graphene sheets. Sodium cholate<sup>14</sup> and its derivatives are also used as adsorbates, though they do not have an aromatic structure like other adsorbates. Sodium cholate can efficiently adsorb aromatic carbon structures and is used to solubilize graphene and carbon nanotubes (CNTs).<sup>15</sup> Adsorbate molecules should possess good solubility in the solvent used. Thus, side chains with highly polar groups like amines, sulfonic acids, and carboxylic acids are used to make them soluble in water or other polar solvents. Adsorbate molecules for nonpolar solvents include long alkyl chains or aromatic moieties.

The solvent layer on the top of the graphene surface should be replaced by adsorbate molecules. Polymeric adsorbates have also been used to attach graphene sheets. They are nonionic, unlike molecular adsorbates. Nonionic polymeric adsorbates give high graphene concentrations. Commonly used polymers are those with linear structures like polyvinylpyrrolidone or quinquethiophene-terminated poly(ethylene glycol) and branched structures like poly(ethyleneimine). Various organic solvents can be used to prepare such polymers. Polymers are firmly bonded to graphene, and changes in pH or the addition of salt have little effect on the dispersion's stability. By concentrating the dispersion or completely evaporating the solvent, the initial low concentration of graphene can be increased to a higher concentration, which results in graphene-polymer composites. Sonication power or time is an important factor in determining graphene concentration. The graphene concentration increases with an increase in sonication time. But intense sonication leads to detachment of the surface-bound molecules, which promotes aggregation instead of exfoliation. Molecular or polymeric interactions exist between adsorbate molecules and graphene sheets. Adsorbates also influence hole mobility and the minimum conductivity of graphene. Quenching of adsorbate luminescence gives evidence of close contact between graphene sheets and adsorbate molecules by indicating electron transfer between the two.<sup>15</sup>

#### **1.2.4 GRAPHITE INTERCALATION-AIDED EXFOLIATION**

Strong forces are required to remove graphene from graphite. The required shear rates of  $10^4 \text{ s}^{-1}$  can be achieved with powerful mixers or ultrasonicators.<sup>8</sup> Small vacancies, or intercalation sites, are found in the structure of graphite where small molecules or ions like Li can be placed. Less force is required to separate graphene sheets from intercalated graphite due to their larger interlayer distance. Such materials are known as graphite intercalation

compounds.<sup>16</sup> Expandable graphite (EG) is another kind of graphite that is intercalated with nitric acid or sulfuric acid. Such intercalated acids also increase the interlayer distance of graphite, making their separation easier. Graphene oxide synthesis or mechanical exfoliation can be done using EG. When EG is heated, its volume increases 100 times that of the original. This is due to the expansion of material as a result of acid vaporization. But heating may damage the graphene sheets.

Graphite intercalation compounds might even predate graphite oxide. Various kinds of chemical species can be included in the interplanar regions of graphite, and the properties thus obtained are greatly important. Alkali metals like lithium, potassium, and cesium are used in this method.

These metals easily enter into the crystal lattice. The metal donates electrons to the lattice, and the negatively charged graphene sheets thus formed are good reducing agents, and exfoliation follows rapidly. By increasing the space between graphene sheets, the alkali metal decreases van der Waals forces in the crystal lattice. The negatively charged sheets repel each other, making the separation process easier. When graphene is treated with proton donors, hydrogenated graphene is formed. The hydrogenated graphene can be restored to a quasi-pristine state by thermal annealing.<sup>17</sup>

According to Yoon et al., exfoliation energies vary substantially depending on the intercalant species, not only owing to intercalant size but also due to interactions with the host graphite.<sup>18</sup> While it is commonly assumed that increasing the interlayer distance weakens the bonding between graphene layers as the van der Waals forces decrease, analysis shows that intercalation of electronegative or electropositive intercalants (e.g., Li, K, F, Cl, and Br) results in a 1.5–5-fold higher exfoliation energy than pristine graphite due to an additional binding force. In contrast, the intercalation of neutral intercalants, such as benzene molecules or KCl, decreases the van der Waals forces between graphene layers without producing additional attraction forces. Also, the aid of sequential solvent intercalation markedly suppressed the charge transfer from intercalants to graphene layers, reducing the barrier to exfoliation.

### **1.2.5 FROM MOLTEN SALTS**

In molten salts, graphite particles can be corroded to produce graphene and a variety of carbon nanostructures.<sup>15</sup> In molten lithium chloride, hydrogen

cations are dissolved and discharged on cathodically polarized graphite rods. These hydrogen cations intercalate into graphite structures, which are then peeled to get graphene. Such graphene sheets have a single crystalline structure. They possess high thermal stability.<sup>19</sup>

### **1.2.6 EPITAXIAL GROWTH**

Heating and cooling a SiC crystal results in the formation of graphene.<sup>20</sup> On the Si face of the crystal, single or bilayer graphene is formed, and on the C face, few-layer graphene is formed.<sup>20</sup> The results depend on the parameters used, like temperature, pressure, or heating rate. The growth of nanotubes in place of graphene can occur if the temperature and pressure are high. Graphene and Ni (111) surfaces have almost the same lattice structure. But there is a difference in the lattice constant of 1.3%. A thin layer of Ni is evaporated onto a SiC crystal by using the evaporation method. On heating, carbon diffuses through the Ni layer, forming a graphene or graphite layer on the surface. Thus, formed graphene can be easily detached from the surface by using Ni.<sup>20</sup> On the crystal, graphene growth starts at different locations, and these islands grow together. The graphene formed by this process is not homogenous due to the presence of grain boundaries. The quality of this graphene is less than that of exfoliated graphene. The size of graphene formed depends on the size of the crystal used.

### **1.2.7 MOLECULAR BEAM EPITAXIAL METHOD (MBE)**

A high vacuum is required for this method. A furnace containing various components is heated, and the vapor so generated forms a single crystal layer on the substrate. This is achieved by spraying the vapor on the substrate directly through a small hole in the furnace. Molecules or atoms could be arranged layer by layer by controlling the molecular beam. Under ultrahigh vacuum conditions, the MBE growth method was used by Hernández-Rodríguez et al. to produce graphene on Pt and Au by evaporating carbon atoms from a carbon solid source.<sup>21</sup> Impurity contamination might occur in the evaporator due to the high vacuum. Moreover, this method is not cost-effective. The stability, smoothness, and purity of crystal growth parameters should be controlled in this process. Thus, controlling crystal growth parameters is a challenge for this method.

### 1.2.8 CHEMICAL VAPOR DEPOSITION (CVD)

CVD works by mixing gas molecules (frequently using carrier gases) in a reaction chamber that is generally kept at room temperature. A reaction happens when the mixed gases come into contact with the heated substrate within the reaction chamber, forming a material layer on the substrate surface.<sup>22</sup> Methane is generally used as a precursor gas with Ni or Cu films as the substrate. While cooling, the solubility of carbon decreases; therefore, carbon precipitates to form graphene sheets on the substrate. CVD and epitaxial methods are highly compatible. But it is difficult to control the film thickness, and secondary crystals will be formed.<sup>23</sup> Also, an expensive substrate material is required for graphene growth. However, CVD is an important method for producing graphene with fewer structural and electronic defects.<sup>24</sup>

The process of CVD of graphene grown on Ni is as follows: Polycrystalline Ni films deposited on Si/SiO<sub>2</sub> are annealed at 900–1000°C, under H<sub>2</sub> and Ar flow to generate smooth surfaces. Then, carbon atoms are allowed to dissolve into Ni films by exposing Ni films to an H<sub>2</sub> and CH<sub>4</sub> mixture. As a result, a solid solution is formed. Finally, in the Ar atmosphere, the substrate is cooled. As the temperature falls, the solubility of carbon atoms decreases. During cooling, carbon atoms diffuse out from the Ni-C solid solution and precipitate on the Ni surface to form graphene films.

A Pd metal surface can also be used to make graphene with the use of ethylene at 968 K. The size of the graphene formed lies between 200 and 2000 Å.<sup>25</sup> Figure 1.2a and b represents scanning tunneling microscope (STM) images of graphene grown on the Pd metal surface. Graphene's size lies between 200 and 2000 Å. Figure 1.2c shows the STM image of the honeycomb structure of graphene formed during the precipitation of carbon atoms. The surface height profile (Figure 1.2d) shows a periodicity of 20 Å. Figure 1.2e shows the orientation of graphene. Metal-semiconducting graphene structures and metal-doped graphene-based devices are prepared by this method.

Graphene films grown on Ni or Pd surfaces consist of both monolayers and a few layers due to the grain boundaries present on Ni or Pd surface.<sup>26</sup> Cu is also an excellent substrate for the synthesis of monolayer graphene due to the low solubility of carbon in Cu. At 1000°C, Cu foil is annealed in an H<sub>2</sub> atmosphere. Graphene growth on Cu foil is initiated by introducing H<sub>2</sub> and CH<sub>4</sub> mixtures into the system. After a complete graphene layer is formed, the system is cooled to room temperature.

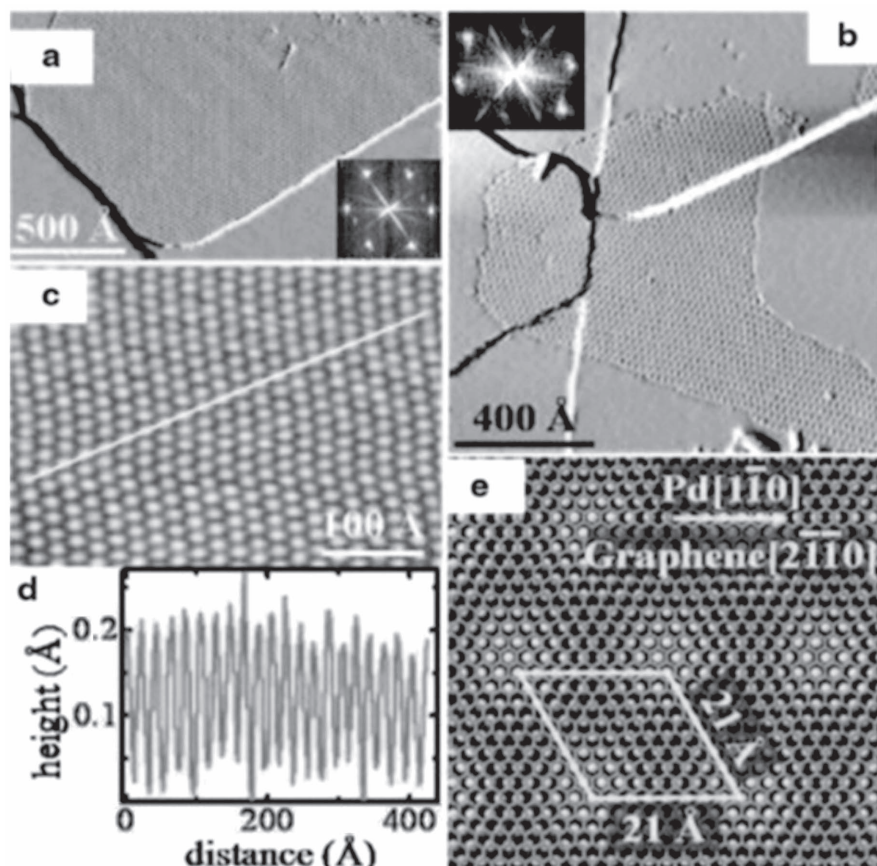


**FIGURE 1.2** (a–c) Scanning tunneling microscope (STM) images of graphene on Pd(111) acquired in situ during growth; (d) surface height profile along the white line shown in (c); and (e) atomic model showing the orientation of graphene.

*Source:* Reprinted with permission from Ref. [25] © 2009 American Chemical Society.

### 1.2.9 PYROLYSIS OF GRAPHENE

This is a bottom-up approach involving a solvothermal process for the synthesis of graphene. This method uses sodium and ethanol in a ratio of 1:1. Pyrolyzation of sodium ethoxide by sonication helps remove graphene sheets easily. Graphene sheets of dimensions up to 10  $\mu\text{m}$  could be synthesized by this method.<sup>27</sup> It is cost-effective, and high-purity graphene can be synthesized at low temperatures. But many defects are reported for this method. Cheng

et al. reported the synthesis of large sheets of multilayered graphene (graphene paper  $>10\text{ cm}^2$ ).<sup>28</sup> The condensation of fumes from the thermal breakdown of asphalt in a ceramic crucible onto a heated surface ( $650^\circ\text{C}$ ) creates carbon coatings with a metallic shine. The crucible was covered but exposed to the laboratory environment, and it was heated by a Fisher burner (natural gas or air) flame. A picture of the prepared graphene paper flake with a diameter of around 25 mm is shown in Figure 1.3A. The sample's flat form can be seen in the optical microscope (Figure 1.3B). Figure 1.3C and D show scanning electron micrographs of this substance. The SEM images show that the graphene paper sample is planar, with flatness down to around 10 nm or less. Because the material tends to fold back on itself, there are two layers, each with a thickness of about 1  $\mu\text{m}$ , which could be synthesized by this method, with the bottom layer on a silicon substrate (Figure 1.3C). In Figure 1.3D, the micron-level layered features are seen at an increased magnification. Layered features may be seen at the nanoscale level with the greater magnification of TEM (Figure 1.3E). It is also worth mentioning that the graphene paper in this study cleaved on flat planes, as seen by the micrographs. This method might be scaled up to make larger sheets. Furthermore, the procedure does not necessitate the use of metal substrates.

### **1.2.10 HIGH-TEMPERATURE AND HIGH-PRESSURE TECHNIQUE**

From a natural graphitic source, graphene can be synthesized by a high-pressure high-temperature (HPHT) growth process.<sup>29</sup> This is done by using molten Fe–Ni catalysts for the dissolution of carbon. This method of graphene synthesis is more reliable and easy to purify.

### **1.2.11 SPUTTERING**

Sputtering is the ejection of atoms from the surface of a solid or liquid following bombardment with ions, atoms, or molecules. This phenomenon is used to prepare a thin layer of material on an object. Due to the low solubility of C and Cu, demixing or segregation occurs during the cosputtering of C and Cu into a carbon matrix.<sup>30</sup> This results in a graphitic matrix homogeneously distributed by nanometric copper precipitates. These precipitates are elongated in shape. The formation of graphene layers parallel to the surface of copper precipitates occurs when the deposition is carried out at 273 K

with copper atomic concentrations greater than 55%. As a result, copper aggregates are encapsulated in carbon cages.

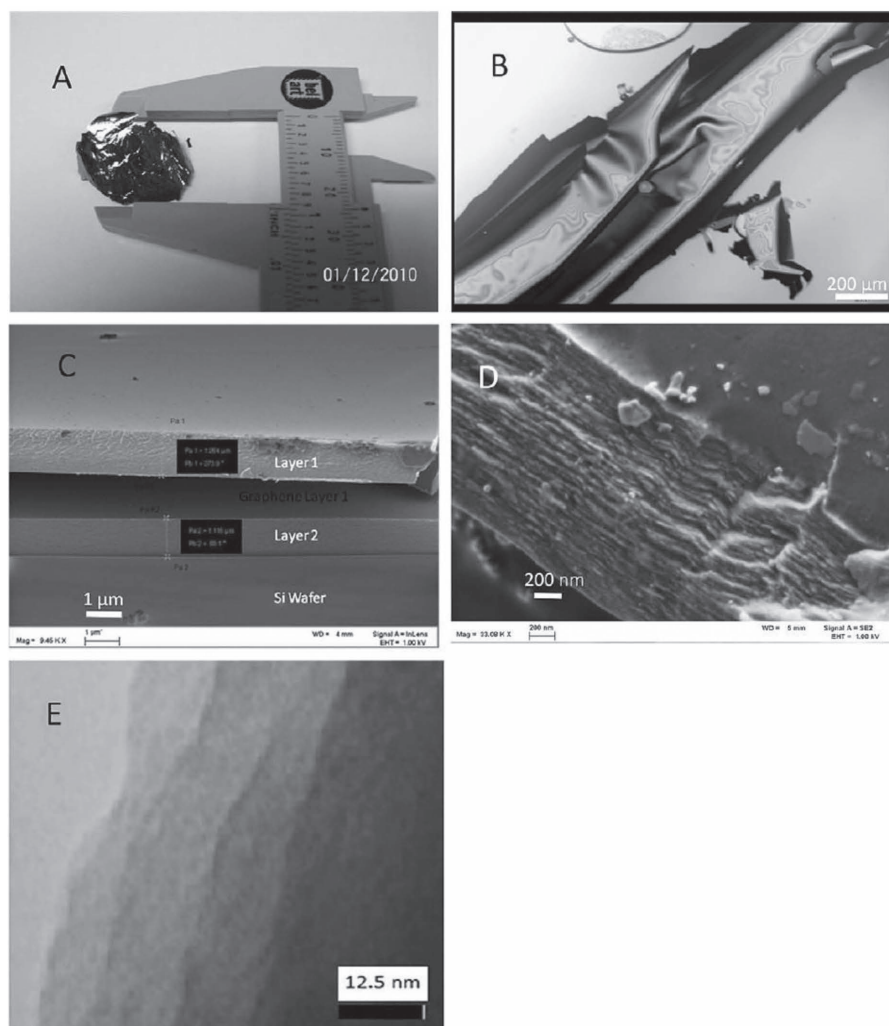


**FIGURE 1.3** (A) A picture of a graphene paper flake with a diameter of 25 mm; (B) an exfoliated graphene paper in water optical micrograph; (C) SEM cross sections of folded graphene paper layers on Si at 9.45 K; (D) SEM of the sample at 23.08 K, revealing the layered features (the distance between the two points is 200 nm); (E) a TEM image of the material's layered properties at the nanoscale level.

*Source:* Reprinted with permission from Ref. [28] © 2011 Elsevier.



### **1.2.12 ARC DISCHARGE METHOD**

In this method, graphite rods are used as electrodes. Electrodes are separated by small distances, and a high voltage is applied between the electrodes. Instantaneous sparks are produced, like in a welding process, as a result of the high electric field generated. The fallout during the discharge process consists of end products that are composed of graphene and CNTs. Simultaneous production and magnetic separation of graphene flakes and CNTs were reported by Volotskova et al.<sup>30</sup> Nanotubes and graphene in the arc discharge process are deposited in different areas by employing magnetic fields. This method is commercially viable, and bulk amounts of high-quality graphene can be produced in a single step. Double-layered graphene sheets were reported by Li et al. in their arc discharge debris.<sup>31</sup>

### **1.2.13 CARBON IMPLANTATION INTO CATALYST SUBSTRATES**

Large-scale and high-quality graphene with controllable thickness can be synthesized by the ion implantation method.<sup>23,32</sup> Carbon atoms implanted in thermally annealing polycrystalline nickel substrates lead to the surface growth of graphene films. Its thickness depends on the implantation dose. A variety of metallic substrates and growth temperatures can be used, as decomposition of chemical precursors or solvation of carbon into the substrate is not required in this process.

### **1.2.14 UNZIPPING OF SWCNT INTO MONOLAYER GRAPHENE**

Recently, the idea of unzipping single-walled carbon nanotubes (SWCNT) into graphene has been reported (Figure 1.4).<sup>33</sup> This is done by using harsh acids under the right thermodynamic conditions. CNT unzipping using a mixture of acids, such as sulfuric acid, and oxidants, like potassium permanganate, is an effective way to produce graphene nanoribbons.<sup>34</sup> Here, it is important to reduce strong van der Waals attractions between the walls of CNTs by the intercalation of  $\text{SO}_4^{2-}$  ions. The unzipping of CNT starts when oxidants attached to one of the internal C–C bond stretch and then break to form graphene nanoribbon structures. Another method of unzipping is by using an electric field. Using a tungsten electrode, an electric field is applied to a single MWNT, and it is seen that the noncontact end of the MWNT starts to unwrap, forming graphene nanoribbons.

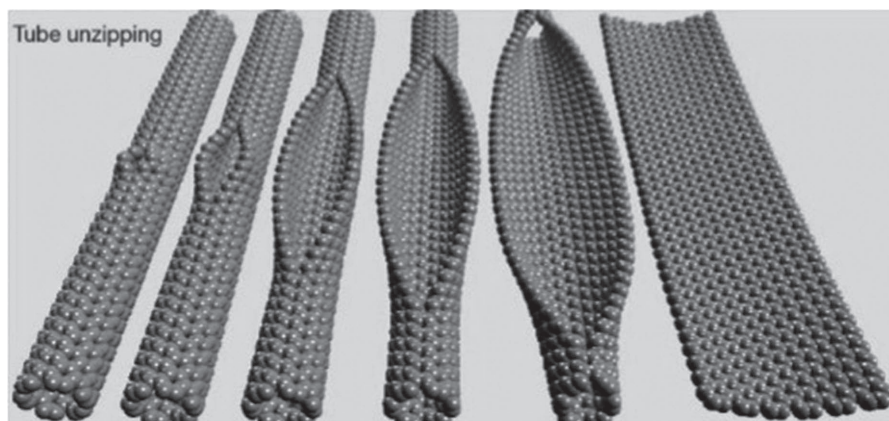


**FIGURE 1.4** Modeling illustration of the SWCNT unzipped into monolayer graphene.

*Source:* Reprinted with permission from Ref. [33] © 2009 Springer Nature.

### 1.3 SYNTHESIS AND FABRICATION OF REDUCED GRAPHENE OXIDE

Graphene oxide is produced by oxidizing graphite. Upon oxidation, graphite loses its conductivity and turns into a reddish-orange colored insulator, which gets dispersed in water very quickly. Reduced graphene oxide is created by reducing graphene oxide to restore graphene's conductivity. Synthesis and fabrication methods of reduced graphene oxide are mostly two-step processes. The first step involves the reduction of van der Waals forces between the interlayers present in graphite by oxidation to produce graphite oxide or graphene oxide. The second step involves the chemical reduction of the produced graphite oxide or graphene oxide to prepare graphene.<sup>35,36</sup>

Good quality graphene was produced from thermal exfoliation and reduction of graphite oxide. It is one of the known methods for making graphene. Alkali metals are often inserted within the graphite to assist in graphene layer separation. Graphene oxide flakes can be dispersed by sonication and then reduced to graphene. This process can be used for the large-scale preparation of graphene.<sup>37</sup> The older separation method consists of heating graphite oxide in an inert atmosphere to high temperatures, which results in the formation of large amounts of carbon dioxide and water in the interstitial space between the layers. The three known methods for graphene oxide synthesis are the Brodie method (1860), the Staudenmaier method (1898), and the Hummer and Offeman method (1958).<sup>37</sup> These methods involve the oxidation of graphite in the presence of strong acids and oxidants. The extent

of oxidation can be altered by varying reaction conditions on the basis of precursor graphite used initially.

Brodie et al. first prepared graphene oxide from a mixture of graphite, potassium chlorate, and nitric acid. A substance of yellow color was observed, comprising small transparent plates. It was called “graphic acid” which is presently known as “graphite oxide.”<sup>38</sup> But the process is tedious and unsafe. Hummer tried to overcome the problem by preparing GO from a mixture of graphite with sodium nitrite, sulfuric acid, and potassium permanganate. This method is still used in laboratories for the synthesis of graphite oxide.<sup>37</sup> Spacing between the layers increases two to three times in graphite oxide compared to graphite. The interlayer spacing of pristine graphite (3.34 Å) increased up to 5.62 Å when oxidation was done for 1 h, and it increased up to  $7 \pm 0.35$  Å upon continuation of oxidation for 24 h. When treated with hydrazine hydrate, graphene oxide is reduced to graphene. It is done by using dimethylhydrazine or hydrazine in the presence of polymer or surfactant in order to obtain uniform colloidal suspensions of graphene.

One of the prior needs for including a solution-based method for graphene for device manufacture is to get uniform and reproducible depositions. The deposition varies based on the design particulars. Chemically altered graphene suspensions are versatile and allow various kinds of deposition methods. They can produce films ranging from uniformly spaced single sheets to thickly packed, overlapping films. Huang’s group at Northwestern was able to manage overdepositions using Langmuir–Blodgett assembly<sup>39</sup> [honeycomb carbon] of graphite oxide. It was shown that electrostatic repulsion inhibits single layers from overlapping upon compression at an air or surface border.

The synthesis of reduced graphene oxide again came into attention in 2006, when Stankovich et al. developed monoatomic graphene chemically.<sup>40</sup> It was done by incorporating Hummer’s method and chemically altered graphene oxide to obtain a water-dispersible graphene oxide. The graphite oxide produced by the Hummers method was a layered stack of puckered sheets that could be separated by the application of mechanical energy.<sup>5</sup> It is because of the strong interactions between water and oxygen-containing functional groups that are present during oxidation. The hydrophilic nature of water helps scatter the sheets. Even though graphite oxide is nonconducting in nature, its network could be restored in the presence of chemical reducing agents or by other methods. Stankovich et al. used hydrazine hydrate to avoid oxidation by the formation and elimination of epoxide complexes.<sup>41</sup> To enable this, hydrazine was added directly into the graphite oxide solution.

The removal of oxygen groups from the initial solution of graphite oxide resulted in the cluster formation of sheets as the sheets became less hydrophilic. Later, it was shown that increasing the pH of the solution while reducing it resulted in charge-stabilized colloidal dispersions even in the case of deoxygenated sheets.<sup>42</sup>

When graphite undergoes oxidation and reduction, it develops various defects. The final product differs from pure graphene. There was confusion about what to call it as a result of this. Some scientists call it “graphene” while others call it “reduced graphene oxide” or “chemically converted graphene.” The oxidation of graphite is presently the most economical method to separate bulk graphite into single-layer compounds. Graphite as well as other reagents required for oxidation are easily available. One important disadvantage of using graphite oxide to synthesize graphene is that the electron mobility of graphene is affected. When reduced graphene oxide is prepared from graphite-intercalated compounds, it does not greatly affect the electronic structure but suffers from a restricted spatial extent of crystal. Reduced graphene oxide can be used in material composites whose mechanical strength and thermal properties can be tuned to manufacture very efficient materials. Another application of reduced graphene oxide is in water purification. Filters made from reduced graphene oxides are really good for water desalinization and purification.

## **1.4 CRITERIAS USED FOR DETERMINING THE EFFECT OF REDUCTION**

The reduction process brings about changes in the properties of graphene oxide, and the effects of various reduction processes can be noted from these observations.

### **1.4.1 VISUAL CHARACTERISTICS**

The variations in graphene oxide before and after reduction can be noted optically. When reduction is carried out chemically in the colloidal state, a black precipitate is formed from the initial yellow-brown suspension, which may be due to improved hydrophobicity of the material or a decrease in polar functionality on the surface of sheets.<sup>43</sup> There are some methods adopted to improve the processability of reduced graphene oxide, for example, the

addition of surfactants to the colloid state or controlling the solvent properties. The black color is a clear indicator of reduction. The images are shown in Figure 1.5. The color change can also be examined by optical microscopy of graphene oxide or reduced graphene oxide sheets lying on a substrate, like silicon dioxide or a silicon wafer.

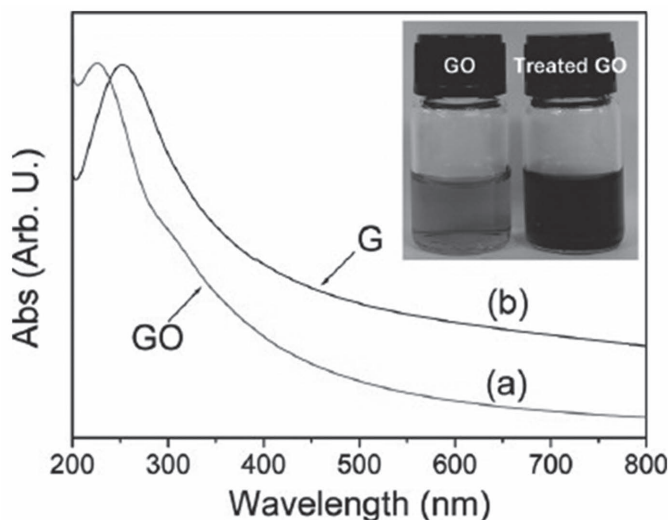


**FIGURE 1.5** UV–Vis absorption spectra of GO (a) before and (b) after 6 h of hydrothermal treatment at 180°C. The color changes, before and after hydrothermal treatment, are shown as an inset.

*Source:* Reprinted with permission from Ref. [43] © 2009 American Chemical Society.

### 1.4.2 ELECTRICAL CONDUCTIVITY

Graphene shows high electrical conductivity. The intention of reducing graphene oxide is to regain the conductivity of graphene. Hence, the electrical conductivity of reduced graphene oxide is a parameter to analyze the effect of various reduction methods. The electrical conductivity of reduced graphene oxide is determined in various ways. Two-probe and four-probe methods are commonly used to measure resistivity ( $R$ ). Sheet resistance ( $R_s$ ) measures the electrical resistance of a sheet and does not depend on thickness. The lowest “ $R_s$ ” known for graphene was about 14  $K\Omega$ .<sup>44</sup> The largest bulk conductivity of reduced graphene oxide was about 6300 S/cm.<sup>45</sup>

### 1.4.3 CARBON TO OXYGEN ATOMIC RATIO

Graphene oxide with a carbon-to-oxygen ratio ranging from 4:1 to 2:1 is typically produced. Once reduced, this ratio could be improved to approximately 12:1 in many cases. There are also recent reports of values as large as 246:1.<sup>46</sup> The carbon-to-oxygen ratio is determined by elemental analysis and X-ray photoelectron spectrometry. The difference is that elemental analysis gives bulk composition, whereas X-ray photoelectron spectrometry is based on a surface technique. It also gives more chemical information about graphene oxide and reduced graphene oxide. The extent of  $sp^2$  bonding provides more information about the properties of carbon-based materials because the  $\pi$  electrons from  $sp^2$  carbon determine their electrical and optical properties. There are also other useful techniques like Raman spectroscopy, solid-state FTNMR, TEM, and AFM. These techniques provide detailed information about the structure of graphene oxide and reduced graphene oxide and are useful in realizing their mechanisms. The XPS spectra of graphene oxide and reduced graphene oxide are shown in Figure 1.6. The graphitic carbon/C  $sp^2$  component becomes mainly dominant after reduction (Figure 1.6(B)). Although oxygen functional groups are still visible in the C1s XPS spectrum of reduced graphene oxide, their intensities are significantly lower than in graphite oxide (Figure 1.2). This demonstrates that during the reduction, the majority of oxygen-containing functional groups were eliminated.<sup>47</sup> In addition, a sharp increase in the C=C/C-C peak at 284.4 eV and the appearance of a  $\pi-\pi^*$  peak at 288.5 eV indicate the restoration of the  $sp^2$  carbon network. The C/O molar ratio calculated from the peak areas shows a very high content of oxygen species in GO (1:13.6), whereas in RGO, the molar ratio was found to be only 1:2.16, again confirming the successful reduction of GO.<sup>48</sup>

## 1.5 REDUCTION STRATEGIES

### 1.5.1 CHEMICAL REAGENT REDUCTION

Chemical reagent reduction can be carried out based on the chemical behavior of reagents with graphene oxide. It can be done at room temperature or with medium heating. Hence, there is no need for special apparatus or environmental conditions compared to those of thermal annealing. Therefore, these techniques are cost-effective and can be used for bulk production of graphene.

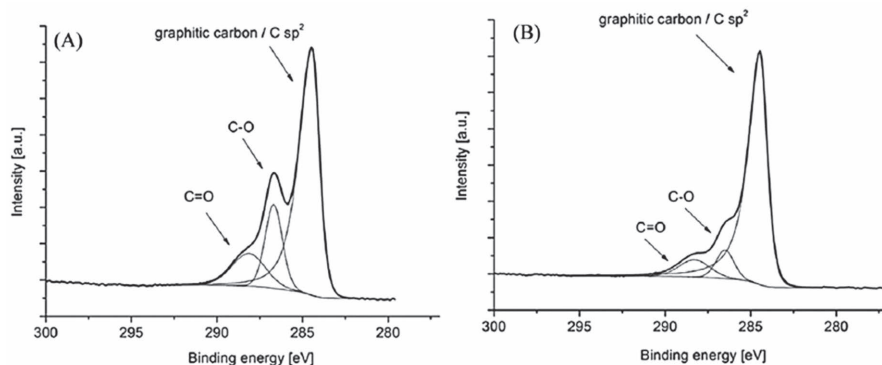


**FIGURE 1.6** XPS spectra of C1s. (A) Graphene oxide (B) Reduced graphene oxide (after UV reduction).

Source: Reprinted with permission from Ref. [47] © 2015 Elsevier.

Stankovich et al. reported that hydrazine can be used for the effective preparation of chemically derived graphene.<sup>41</sup> This paved an easy route for the bulk production of graphene.<sup>49</sup> The addition of hydrazine and its derivatives to a solution of graphene oxide creates clusters of nanosheets of graphene as a result of the increased hydrophobicity of the formed products. Upon drying, a black powder with a carbon-to-oxygen ratio of around 10 is formed and is found to be conductive in nature.<sup>41</sup> The known largest conductivity of reduced graphene oxide films by hydrazine reduction technique is 99.6 S/cm, and the carbon-to-oxygen ratio is 12.5.<sup>50</sup>

Metal hydrides like sodium borohydride, sodium hydride, and lithium aluminum hydride are known for their reducing properties. Recent reports showed that  $\text{NaBH}_4$  is more effective than hydrazine. Though it undergoes slow hydrolysis by water, it can reduce graphene oxide.  $\text{NaBH}_4$  is very effective at the reduction of the C=O group, but epoxy and carboxylic acid groups are not treated very efficiently, and the alcohol group remains as such.<sup>51</sup> As an improvement to this technique, Gao et al. proposed the treatment of reduced graphene oxide by  $\text{NaBH}_4$  followed by treatment with sulfuric acid at 180°C.<sup>52</sup> This alters the reduction effect. The carbon-to-oxygen ratio rises to 8.6, and the conductivity becomes about 16.6 S/cm.

A recently reported reducing agent is ascorbic acid. It is regarded as a suitable replacement for hydrazine.<sup>50</sup> Graphene oxide reduced by ascorbic acid is found to have a carbon-to-oxygen ratio of 12.5 and a conductivity of 77 S/cm. It is nontoxic and is more chemically stable with water than  $\text{NaBH}_4$ . It does not form aggregations of sheets when used in a colloidal state.

Hydroiodic acid is a recently known reducing agent. It can be used as a reducing agent for graphene oxide in colloid, powder, gas, or solution form.<sup>53</sup> The films produced by HI are flexible with good tensile strength, whereas the films produced by hydrazine and  $\text{NaBH}_4$  break into pieces. This indicates the high quality of graphene sheets produced by HI. Other known reducing agents are hydroquinone, pyrogallol, urea, thiourea, etc. Their efficiencies are less compared with  $\text{NaBH}_4$ , HI, and hydrazine. The reduction of graphene oxide with these reagents is shown in Figure 1.7.<sup>54</sup>

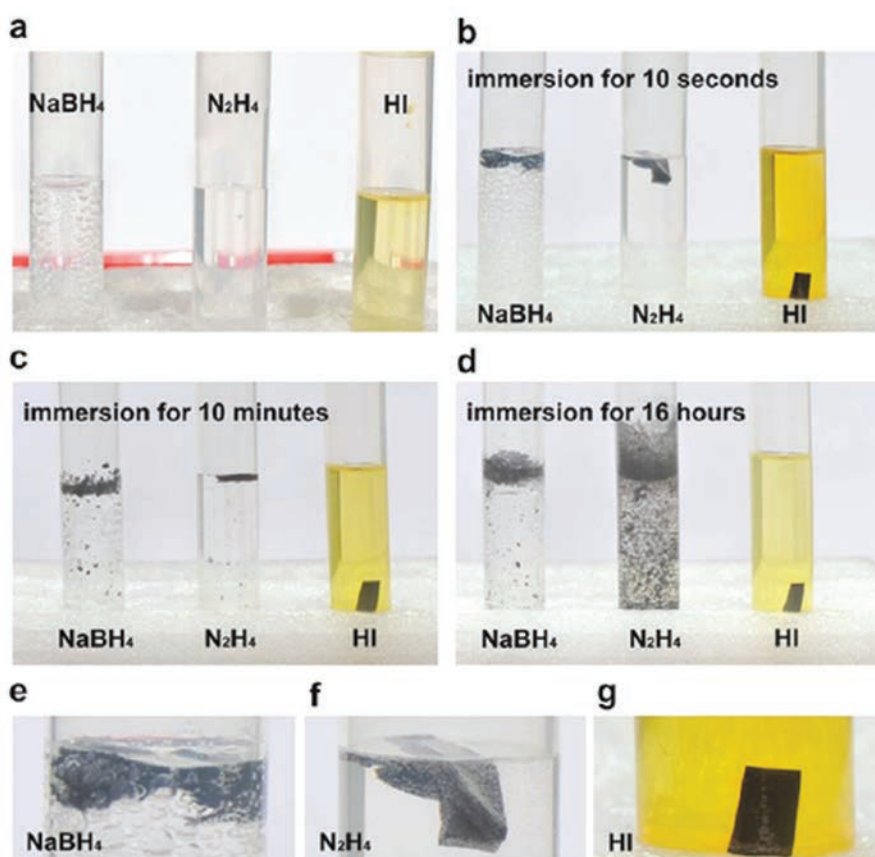


**FIGURE 1.7** Optical pictures of the reducing process taken by soaking a GO film in various reducing chemicals for varying periods at room temperature. (a) 50 mM  $\text{NaBH}_4$  aqueous solution ( $\text{NaBH}_4$ ), 85%  $\text{N}_2\text{H}_4\cdot\text{H}_2\text{O}$  solution ( $\text{N}_2\text{H}_4$ ), and 55% HI acid solution (HI); (b–d) The three agents decreased the GO films for 10 s, 10 min, and 16 h; (e–g) Enlarged views from (b), demonstrating that the event occurred after 10 s of immersion in the three liquid reducing agents.

Source: Reprinted with permission from Ref. [54] © 2010 Elsevier.



Optical images of the reducing process taken by immersing GO films in various reducing chemicals for various periods are shown in Figure 1.7. In the  $\text{NaBH}_4$  aqueous solution, as shown in Figure 1.7a, many  $\text{H}_2$  bubbles are detected before GO film immersion, but this is not the case in the  $\text{N}_2\text{H}_4\text{H}_2\text{O}$  and HI acid solutions. As a result, when a GO film is submerged in a  $\text{NaBH}_4$  aqueous solution, it begins to break apart. A GO film submerged in  $\text{N}_2\text{H}_4\text{H}_2\text{O}$  is covered by numerous fine bubbles (Figure 1.7f) after 10 s of reduction (Figure 1.7b), similar to the GO film immersed in a  $\text{NaBH}_4$  solution (Figure 1.7e), indicating that hydrazine may react with GO and generate gases. However, there were not too many bubbles surrounding the GO film imprint. As a result, as seen in Figure 1.7c, the GO film submerged in the  $\text{N}_2\text{H}_4\text{H}_2\text{O}$  solution begins to break apart. The films immersed in the  $\text{N}_2\text{H}_4\text{H}_2\text{O}$  and  $\text{NaBH}_4$  aqueous solutions are broken down to tiny graphene debris after 16 h of reaction, whereas the film in the HI acid solution retains its integrity extremely well (Figure 1.7d). Although 55% HI acid can effectively reduce GO films at room temperature, the reduction of GO films is enhanced at higher temperatures.

### 1.5.2 THERMAL REDUCTION (THERMAL ANNEALING)

Graphene oxide, when reduced by applying heat, is called thermal annealing. In the beginning stages of graphene research, graphene oxide was separated from graphene by rapid heating.<sup>55</sup> On heating, CO or  $\text{CO}_2$  gases entrapped between graphene sheets get expelled. As the temperature rises, the oxygen-bearing functional groups degrade into gases, creating large pressures within the stacked layers. A pressure of just 2.5 MPa is required to separate two stacked graphene oxide platelets. The separated sheets can be called graphene directly because of two reasons. The heating process separates graphene oxide, and the functionalized graphene sheets are reduced upon the decomposition of oxygen-bearing groups at high temperatures. This combined effect of thermal expansion of graphene oxide is a good technique for producing graphene in bulk amounts. But this process yields only small sheets of graphene. It is due to the removal of carbon from the carbon plane upon the degradation of oxygen-bearing groups. The graphene sheets get split into minute pieces and distort the carbon plane. The structural defects caused to graphene sheets upon removal of  $\text{CO}_2$  are to be noted in thermal exfoliation. Roughly 30% of the weight of graphene oxide is lost during this technique. This affects the electronic characteristics of the product. So the electrical conductivity of the graphene sheet by this method has a value in the range 10–23 S/cm, which is much lower than regular graphene.

### 1.5.3 PHOTOCATALYST REDUCTION

Graphene oxide is also reduced photochemically using catalysts like  $\text{TiO}_2$ .<sup>56</sup> The change in color confirms the reduction of graphene oxide. During UV irradiation, charges get separated on the surface of  $\text{TiO}_2$ . Ethoxy radicals are produced in the presence of ethanol, and the electrons settle on the  $\text{TiO}_2$  molecules. These electrons, upon interaction with graphene oxide sheets, reduce functional groups. The carboxyl group on graphene oxide sheets and the hydroxyl group on  $\text{TiO}_2$  undergo interaction before the reduction process through charge transfer. This produces a hybrid between  $\text{TiO}_2$  and graphene oxide. This structure remains as such after reduction. The reduced graphene oxide sheets can function as a current collector and are hence used in the dye-sensitized solar cell.<sup>56,57</sup>

### 1.5.4 ELECTROCHEMICAL REDUCTION

This involves the electrochemical removal of oxygen-bearing functional groups.<sup>58,59</sup> It can be achieved in a normal electrochemical cell at room temperature. There is no requirement for a special chemical reagent. It is facilitated by electron transfer between graphene oxide and electrodes. Hence, the use of hazardous reductants like hydrazine can be avoided. In this method, a thin film of reduced graphene oxide is deposited on a substrate placed opposite an inert electrode in the electrochemical cell. This method is an efficient reduction technique. The carbon-to-oxygen ratio of reduced graphene oxide is found to be 23.9 and the conductivity to be 85 S/cm. The pH of the buffer solution was also an important factor in the reaction. A low pH value is usually preferred for efficient electrochemical reduction.

### 1.5.5 GRAPHITE FLUORIDE

At higher temperatures, graphite could be fluorinated directly by fluoride gas. It finds application as a solid lubricant and as a promising cathode in lithium batteries. The inclusion of fluoride in the crystal raises the interlayer spacing from 0.35 nm to between 0.8 and 0.9 nm. Graphite fluoride is separated in DMF under sonication. With a laser pointer, the colloid exhibited a pale gray color and produced a strong Tyndall effect. The colloid formed is reduced by silane or a zinc-acid combination.<sup>60,61</sup>

## 1.6 CONCLUSIONS

We have discussed some of the advancements in the synthesis and fabrication of graphene and reduced graphene oxide in this chapter. Since its introduction, graphene has attracted a great deal of attention from the scientific community. This is largely due to its exceptional characteristics and the high-performance composite potential it offers. Sonication, surfactant-assisted exfoliation, graphite intercalation-aided exfoliation, epitaxial growth, chemical vapor deposition, pyrolysis, and sputtering are examples of graphene preparation techniques. Graphene made by various techniques is useful for a variety of applications. Chemical reagent reduction, thermal reduction, electrochemical reduction, and photocatalyst reduction are all examples of reduced graphene oxide preparation techniques. However, the challenge of scaling up graphene manufacturing with good quality and consistency remains unsolved. This is the objective to be achieved in the coming years.

## ACKNOWLEDGMENTS

Dr. Sanal Sebastian Payyappilly is grateful for the national postdoctoral fellowship from Science Engineering Research Board (SERB) (No. PDF/2016/004115/ES).

## KEYWORDS

- **graphene**
- **graphene oxide**
- **reduced graphene oxide**
- **graphene synthesis**
- **intercalation-aided exfoliation**
- **photocatalyst reduction**
- **thermal reduction**

## REFERENCES

1. Choi, W.; Lahiri, I.; Seelaboyina, R.; Kang, Y. S. Synthesis of Graphene and Its Applications: A Review. *Crit. Rev. Solid State Mater. Sci.* **2010**, *35* (1), 52–71.
2. H. Huang et al. The Chemistry and Promising Applications of Graphene and Porous Graphene Materials. *Adv. Funct. Mater.* **2020**, *30* (41), 1909035.
3. Korkmaz, S.; Kariper, İ. A. Graphene and Graphene Oxide Based Aerogels: Synthesis, Characteristics and Supercapacitor Applications. *J. Energy Storage* **2020**, *27*, 101038.
4. Geim, A. K.; Novoselov, K. S. The Rise of Graphene. In *Nanoscience and Technology: A Collection of Reviews from Nature Journals*; World Scientific, 2010; pp. 11–19.
5. Allen, M. J.; Tung, V. C.; Kaner, R. B. Honeycomb Carbon: A Review of Graphene. *Chem. Rev.* **2009**, *110* (1), 132–145.
6. Edwards, R. S.; Coleman, K. S. Graphene Synthesis: Relationship to Applications. *Nanoscale* **2013**, *5* (1), 38–51.
7. Novoselov, K. S. et al. Electric Field Effect in Atomically Thin Carbon Films. *Science* (80-.). **2004**, *306* (5696), 666–669.
8. Paton, K. R. et al. Scalable Production of Large Quantities of Defect-Free Few-Layer Graphene by Shear Exfoliation in Liquids. *Nat. Mater.* **2014**, *13* (6), 624.
9. Khan, U.; O'Neill, A.; Lotya, M.; De, S.; Coleman, J. N. High-Concentration Solvent Concentration Solvent Exfoliation of Graphene. *Small* **2010**, *6* (7), 864–871.
10. Bourlinos, A. B.; Georgakilas, V.; Zboril, R.; Steriotis, T. A.; Stubos, A. K. Liquid-Concentration Solvent Phase Exfoliation of Graphite Towards Solubilized Graphenes. *Small* **2009**, *5* (16), 1841–1845.
11. Nuvoli, D. et al. The Production of Concentrated Dispersions of Few-Layer Graphene by the Direct Exfoliation of Graphite in Organosilanes. *Nanoscale Res. Lett.* **2012**, *7* (1), 674.
12. O'Neill, A.; Khan, U.; Nirmalraj, P. N.; Boland, J.; Coleman, J. N. Graphene Dispersion And Exfoliation in Low Boiling Point Solvents. *J. Phys. Chem. C* **2011**, *115* (13), 5422–5428.
13. Parviz, D.; Das, S.; Ahmed, H. S. T.; Irin, F.; Bhattacharia, S.; Green, M. J. Dispersions of Non-Covalently Functionalized Graphene with Minimal Stabilizer. *ACS Nano* **2012**, *6* (10), 8857–8867.
14. Lotya, M.; King, P. J.; Khan, U.; De, S.; Coleman, J. N. High-Concentration, Surfactant-Stabilized Graphene Dispersions. *ACS Nano* **2010**, *4* (6), 3155–3162.
15. Paloniemi, H. et al. Water-Soluble Full-Length Single-Wall Carbon Nanotube Polyelectrolytes: Preparation and Characterization. *J. Phys. Chem. B* **2005**, *109* (18), 8634–8642.
16. Shih, C.-J. et al. Bi-and Trilayer Graphene Solutions. *Nat. Nanotechnol.* **2011**, *6* (7), 439.
17. Dresselhaus, M. S.; Dresselhaus, G. Intercalation Compounds of Graphite. *Adv. Phys.* **2002**, *51* (1), 1–186.
18. Yoon, G.; Seo, D.-H.; Ku, K.; Kim, J.; Jeon, S.; Kang, K. Factors Affecting the Exfoliation of Graphite Intercalation Compounds for Graphene Synthesis. *Chem. Mater.* **2015**, *27* (6), 2067–2073.
19. Kamali, A. R.; Fray, D. J. Large-Scale Preparation of Graphene by High Temperature Insertion of Hydrogen into Graphite. *Nanoscale* **2015**, *7* (26), 11310–11320.
20. Forbeaux, I.; Themlin, J.-M.; Debever, J.-M. Heteroepitaxial Graphite on 6 H– SiC (0001): Interface Formation Through Conduction-Band Electronic Structure. *Phys. Rev. B* **1998**, *58* (24), 16396.

21. Hernández-Rodríguez, I.; García, J. M.; Martín-Gago, J. A.; de Andrés, P. L.; Méndez, J. Graphene Growth on Pt (111) and Au (111) Using a MBE Carbon Solid-Source. *Diam. Relat. Mater.* **2015**, *57*, 58–62.
22. Cai, W. et al. Thermal Transport in Suspended and Supported Monolayer Graphene Grown By Chemical Vapor Deposition. *Nano Lett.* **2010**, *10* (5), 1645–1651.
23. Baraton, L. et al. Synthesis of Few-Layered Graphene by Ion Implantation of Carbon in Nickel Thin Films. *Nanotechnology* **2011**, *22* (8), 85601.
24. Zhang, Y. I.; Zhang, L.; Zhou, C. Review of Chemical Vapor Deposition of Graphene and Related Applications. *Acc. Chem. Res.* **2013**, *46* (10), 2329–2339.
25. Kwon, S.-Y. et al. Growth of Semiconducting Graphene on Palladium. *Nano Lett.* **2009**, *9* (12), 3985–3990.
26. Mwakikunga, B. W.; Hillie, K. T. Graphene Synthesis, Catalysis with Transition Metals and Their Interactions by Laser Photolysis. In *Graphene-Synthesis, Characterization, Properties and Applications*; InTech, 2011.
27. Choucair, M.; Thordarson, P.; Stride, J. A. Gram-Scale Production of Graphene Based on Solvothermal Synthesis and Sonication. *Nat. Nanotechnol.* **2009**, *4* (1), 30.
28. Cheng, I. F. et al. Synthesis of Graphene Paper from Pyrolyzed Asphalt. *Carbon NY* **2011**, *49* (8), 2852–2861.
29. Parvizi, F. et al. Properties of Graphene Produced by the High Pressure–High Temperature Growth Process. *Micro Nano Lett.* **2008**, *3* (1), 29–34.
30. Cabioch, T.; Naudon, A.; Jaouen, M.; Thiaudière, D.; Babonneau, D. Co-sputtering C–Cu Thin Film Synthesis: Microstructural Study of Copper Precipitates Encapsulated into a Carbon Matrix. *Philos. Mag. B* **1999**, *79* (3), 501–516.
31. Li, N.; Wang, Z.; Zhao, K.; Shi, Z.; Gu, Z.; Xu, S. Large Scale Synthesis of N-Doped Multi-Layered Graphene Sheets by Simple Arc-Discharge Method. *Carbon NY* **2010**, *48* (1), 255–259.
32. Garaj, S.; Hubbard, W.; Golovchenko, J. A. Graphene Synthesis by Ion Implantation. *Appl. Phys. Lett.* **2010**, *97* (18), 183103.
33. Kosynkin, D. V. et al. Longitudinal Unzipping of Carbon Nanotubes to Form Graphene Nanoribbons. *Nature* **2009**, *458* (7240), 872.
34. Rangel, N. L.; Sotelo, J. C.; Seminario, J. M. *Mechanism of Carbon Nanotubes Unzipping into Graphene Ribbons*; American Institute of Physics, 2009.
35. Wu, Y.; Wang, S.; Komvopoulos, K. A Review of Graphene Synthesis by Indirect and Direct Deposition Methods. *J. Mater. Res.* **2020**, *35* (1), 76–89.
36. Wu, Y. H.; Yu, T.; Shen, Z. X. Two-Dimensional Carbon Nanostructures: Fundamental Properties, Synthesis, Characterization, and Potential Applications. *J. Appl. Phys.* **2010**.
37. Hummers Jr, W. S.; Offeman, R. E. Preparation of Graphitic Oxide. *J. Am. Chem. Soc.* **1958**, *80* (6), 1339.
38. Brodie, B. C. Sur le poids atomique du graphite. *Ann. Chim. Phys.* **1860**, *59* (466), e472.
39. Cote, L. J.; Kim, F.; Huang, J. Langmuir–Blodgett Assembly of Graphite Oxide Single Layers. *J. Am. Chem. Soc.* **2009**, *131* (3), 1043–1049.
40. Stankovich, S. et al. Graphene-Based Composite Materials. *Nature* **2006**, *442* (7100), 282–286.
41. Stankovich, S. et al. Synthesis of Graphene-Based Nanosheets via Chemical Reduction of Exfoliated Graphite Oxide. *Carbon NY* **2007**, *45* (7), 1558–1565.
42. Li, D.; Müller, M. B.; Gilje, S.; Kaner, R. B.; Wallace, G. G. Processable Aqueous Dispersions of Graphene Nanosheets. *Nat. Nanotechnol.* **2008**, *3* (2), 101.

43. Zhou, Y.; Bao, Q.; Tang, L. A. L.; Zhong, Y.; Loh, K. P. Hydrothermal Dehydration for the ‘Green’ Reduction of Exfoliated Graphene Oxide to Graphene and Demonstration of Tunable Optical Limiting Properties. *Chem. Mater.* **2009**, *21* (13), 2950–2956.
44. López, V. et al. Chemical Vapor Deposition Repair of Graphene Oxide: A Route to Highly Conductive Graphene Monolayers. *Adv. Mater.* **2009**, *21* (46), 4683–4686.
45. Wang, Y. et al. Reduced Graphene Oxide Film with Record-High Conductivity and Mobility. *Mater. Today* **2018**, *21* (2), 186–192.
46. Thakur, K.; Kandasubramanian, B. Graphene and Graphene Oxide-Based Composites for Removal of Organic Pollutants: A Review. *J. Chem. Eng. Data* **2019**, *64* (3), 833–867.
47. Rella, S. et al. X-Ray Photoelectron Spectroscopy of Reduced Graphene Oxide Prepared by A Novel Green Method. *Vacuum* **2015**, *119*, 159–162.
48. Muthoosamy, K. et al. Exceedingly Biocompatible and Thin-Layered Reduced Graphene Oxide Nanosheets Using an Eco-Friendly Mushroom Extract Strategy. *Int. J. Nanomed.* **2015**, *10*, 1505.
49. Mattevi, C. et al. Evolution of Electrical, Chemical, and Structural Properties of Transparent And Conducting Chemically Derived Graphene Thin Films. *Adv. Funct. Mater.* **2009**, *19* (16), 2577–2583.
50. Fernández-Merino, M. J. et al. Vitamin C Is an Ideal Substitute for Hydrazine in the Reduction of Graphene Oxide Suspensions. *J. Phys. Chem. C* **2010**.
51. Periasamy, M.; Thirumalaikumar, M. Methods of Enhancement of Reactivity and Selectivity of Sodium Borohydride for Applications in Organic Synthesis. *J. Organomet. Chem.* **2000**, *609* (1–2), 137–151.
52. Gao, W.; Alemany, L. B.; Ci, L.; Ajayan, P. M. New Insights into the Structure and Reduction of Graphite Oxide. *Nat. Chem.* **2009**, *1* (5), 403.
53. Moon, I. K.; Lee, J.; Ruoff, R. S.; Lee, H. Reduced Graphene Oxide by Chemical Graphitization. *Nat. Commun.* **2010**, *1*, 73.
54. Pei, S.; Zhao, J.; Du, J.; Ren, W.; Cheng, H. M. Direct Reduction of Graphene Oxide Films into Highly Conductive and Flexible Graphene Films by Hydrohalic Acids. *Carbon NY* **2010**.
55. McAllister, M. J. et al. Single Sheet Functionalized Graphene by Oxidation and Thermal Expansion of Graphite. *Chem. Mater.* **2007**.
56. Williams, G.; Seger, B.; Kamt, P. V. TiO<sub>2</sub>-Graphene Nanocomposites. UV-Assisted Photocatalytic Reduction of Graphene Oxide. *ACS Nano* **2008**.
57. Shahid, M. U. et al. Solvent Exfoliated Graphene Incorporated Mixed Phase TiO<sub>2</sub> Transparent Photoelectrode for the Efficient and Color Transparent Dye-Sensitized Solar Cell. *Sol. Energy* **2020**, *206*, 317–329.
58. Zhou, M. et al. Controlled Synthesis of Large-Area and Patterned Electrochemically Reduced Graphene Oxide Films. *Chem. A Eur. J.* **2009**.
59. An, S. J. et al. Thin Film Fabrication and Simultaneous Anodic Reduction of Deposited Graphene Oxide Platelets by Electrophoretic Deposition. *J. Phys. Chem. Lett.* **2010**.
60. Bourlinos, A. B.; Safarova, K.; Siskova, K.; Zbořil, R. The Production of Chemically Converted Graphenes from Graphite Fluoride. *Carbon NY* **2012**, *50* (3), 1425–1428.
61. Bourlinos, A. B. et al. Water Dispersible Functionalized Graphene Fluoride with Significant Nonlinear Optical Response. *Chem. Phys. Lett.* **2012**, *543*, 101–105.



## CHAPTER 2

---

# Polythiophene Nanocomposites and their Applications

LINDA MARIA VARGHESE<sup>1</sup>, OM PRAKASH BAJPAI<sup>2</sup>, DHANYA K. R.<sup>1</sup>, and  
SANAL SEBASTIAN PAYYAPPILLY<sup>1</sup>

*<sup>1</sup>International and Inter University Centre for Nanoscience and  
Nanotechnology, Mahatma Gandhi University, Kottayam, Kerala, India*

*<sup>2</sup>Rubber Technology Centre, Indian Institute of Technology, Kharagpur,  
India*

---

### ABSTRACT

Polythiophene is a conductive polymer with high electrical conductivity. Polymer nanocomposites show excellent characteristics that have a significant role in modern life. This chapter describes the characteristics of polythiophene-based nanocomposites made with diverse materials such as carbon nanotubes, metal oxides, and fullerene, as well as their applications in many scientific fields. Polythiophene-based nanocomposites show excellent electrical, magnetic, optical, and mechanical properties. Polythiophene-based nanocomposites are found to be promising for applications such as solar cells, supercapacitors, electrochemical sensors, etc.

### 2.1 INTRODUCTION

The word nanotechnology is an umbrella term used to represent a broad category of different topics such as nanoscience and technology, organic chemistry, physics related to semiconductors, molecular biology, etc. Nanotechnology can provide new materials and technologies for a variety of uses,



including medicine, biomaterials, and energy generation. The focused topic elaborates on matter in a nanoscale unit. Recent interest in the development of nanomaterials is due to their superior material characteristics compared to conventional ones. When we started using polymers and their superior properties, such as electrical conductivity, carbon nanotubes (CNTs) and their nanocomposites opened a new world of discoveries.

Nanocomposites are categorized into different groups in accordance with the reinforcement materials and matrix materials utilized for their construction. There are three divisions for nanocomposites: a. metal matrix nanocomposites, b. ceramic matrix nanocomposites, and c. polymer matrix nanocomposites.<sup>1-3</sup> In the case of polymer nanocomposites, nanoadditives are reinforcement materials, and polymers act like matrix materials. These include one-dimensional additives, for example, nanotubes and fibers; two-dimensional additives, for example, layered materials like clay; and three-dimensional additives, for example, spherical particles with dissimilar sizes.

Reinforcement materials are chosen as per the applications. Normally, fillers and matrices are connected by weak intermolecular forces. Properties of nanocomposites depend on many factors, like the type of filler materials, nanoparticles' characteristics, degree of mixing of two phases, and type of adhesion between fillers and matrix. In industrial sectors, ceramic matrix nanocomposites are widely used and are considered novel engineering materials.

Metal matrix composites contain nanoparticle-filled metal or alloy matrix, and the chemical, mechanical, and physical characteristics are different from matrix material characteristics.

Two or more materials combined with various compositions or forms are known as composites. Nanocomposites are formed when constituents are mixed on a nanometer-length scale. They can be synthesized by simple and inexpensive methods, and they show superior properties over microscale composites. Some of them are metal carbide nanocomposites, metal oxide nanocomposites, and polymer-based nanocomposites.<sup>4</sup> Conducting nanocomposites have gained so much interest that they are used in drug delivery, conductive paints, and rechargeable batteries. Polymer nanocomposites are combinations of polymers and nanoparticles that show the properties of both polymers and nanoparticles. Materials with superior thermal, mechanical, and chemical properties can be fabricated by combining polymers and nanoparticles. Polymers have advantages such as being low-cost, flexible, and lightweight, but they have poor thermal, mechanical, and electrical properties. A common polymer composite combination is a combination of

filler (reinforcement) and polymer matrix. The advantage of using nanoparticles mainly results from their more reactive surface area. Nanocomposites embedded with polymers have significant characteristics when they are combined with complementary properties. Heat resistance, high gas barriers, better conductivity, recyclability, and remarkable mechanical resistance are some excellent characteristics shown by polymer nanocomposites.<sup>5</sup>

Recently, a significant development has been found in the synthesis of various types of polymer nanocomposites and in the recognition of basic theories or principles that determine their optical-electronic, electronic, and magnetic properties.<sup>6</sup> Polymers have importance due to their several unique properties, such as flexibility, lightweight, ease of processing, low cost, and the ability to form thin films. Adding inorganic nanomaterials into a polymer matrix will show the nature of inorganic nanoparticles as well as polymers. Consequently, an advanced novel function can be generated for the polymer inorganic nanocomposites (PINC).<sup>7</sup> The polymer “Au” nanocomposite was probably the first reported PINC in the literature. After “Au,” first used as an inorganic nanofiller in PINC for optical applications, other metals such as Ag, Pt, Cu, Fe, Si, and Hg were also used with natural polymers for similar optical applications. In many papers, it was found that polymer–clay nanocomposites have superior mechanical and thermal properties than those of pristine polymers. Therefore, these composites became very popular and have importance in a different category of PINC. The first polymer–clay nanocomposite used was clay/nylon-6 nanocomposite for a *Toyota car* to produce timing belt covers.<sup>8</sup> Commonly employed inorganic nanofillers include metals and metal alloys (Au, Ag, Cu, Ge, Pt, and Fe), semiconductors (PbS, CdS, CdSe, and ZnO), clay minerals (montmorillonite, vermiculite, and hectorite), and other oxides (TiO<sub>2</sub>, SiO<sub>2</sub>, and ferric oxide). But the choice of polymer matrix and inorganic nanofillers depends on their applications. Conducting polymers and metal oxide nanocomposites are considered important materials as they exhibit properties that are different from their pure forms. Polythiophene (PTh) nanocomposites are the most useful and significant PINC composites discovered.

## 2.2 POLYTHIOPHENE NANOCOMPOSITES

Earlier, polymers were known to be insulating, but the breakthrough came when the first iodine-doped polyacetylene showed conductivity ( $10^1$ – $10^3$  S.cm<sup>-1</sup>) in the mid-1970s.<sup>9</sup> A new era of conducting polymers started in 2000

when scientists Alan J. Heeger, Alan G. MacDiarmid, and Hideki Shirakawa received the chemistry Nobel Prize and discovered the remarkable properties of conducting polymers.<sup>10</sup> After that, rapidly many other conducting polymers have been recognized, for example, polyaniline, PTh,<sup>11</sup> polypyrrole, polycarbazole, etc. Since their discovery in the 1970s, conducting polymers have been extensively explored. It has been observed that polyacetylene (a noncyclic polyene) shows good conductivity after doping but has a considerable drawback in terms of processability and reactivity in an open environment (i.e., oxidation with air and moisture). Thus, there was a need to develop novel CPs. In this regard, scientists worked on cyclic conducting polymers like polypyrrole (PPy), PTh, polyaniline (PANI), poly(3,4-ethylenedioxythiophene) (PEDOT), etc.

PThs are polymerized thiophenes and contain a sulfur heterocycle. They become conducting when oxidized with a dopant. The most notable property of this material is its electrical conductivity, which results from the delocalization of electrons along the polymer backbone. When compared with polyacetylene-type polymers, doped PThs that are unsubstituted have very good conductivity and environmental stability. But these compounds are highly insoluble except for a mixture of arsenic pentafluoride and arsenic trifluoride. The most important one is that we can easily dope PThs with iodine and bromine. PThs also show excellent optical properties. Conducting polymers can be doped suitably to have either semiconducting or normal conductor behavior in them. Conducting polymer and metal oxide nanocomposites emerged as a new class of materials as they exhibit properties that are different from their pure forms. Among organic conductive polymers, PThs and their derivatives have been of special interest because of their ease of preparation and specific properties such as higher conductivity, environmental stability, and photoconduction. The structure of PTh is shown in Figure 2.1.

PTh-based nanocomposites exhibit good improvement in thermal stability and electrical conductivity. A large number of composites are synthesized for various purposes; among these, carbon-based nanocomposites are important.

### **2.2.1 NANOCOMPOSITES BASED ON POLY (3-ALKYLTHIOPHENES)**

It has been found that PThs are highly insoluble substances in most organic solvents. Because of their nature and properties, practical applications are limited. Moreover, PTh undergoes decomposition before it melts, which also restricts its applications in different fields. Substitution of the thiophenes

shows a large number of practically useful PThs. When it undergoes substitution, for example, poly (3-methyl thiophene), poly (3-hexylthiophene), etc., can be better soluble in common organic solvents. The chromic properties of substituted PThs offer great potential for applications such as light-emitting diodes, gas sensors, metal ion sensors, biosensors, biomedical applications, and other related applications.

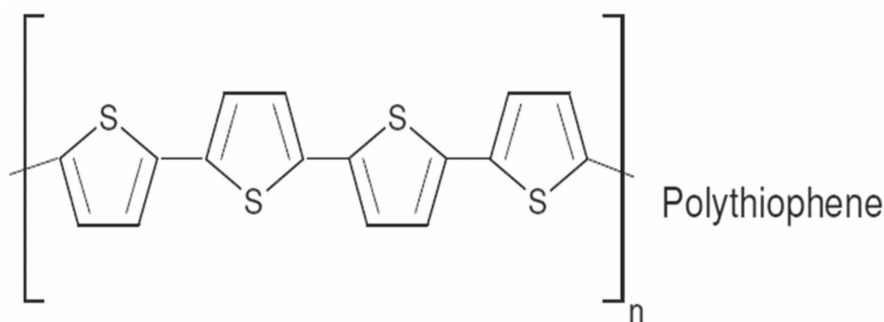


**FIGURE 2.1** Polythiophene's chemical structure.

Based on applications, PThs can be synthesized by different methods. If we need bulk product, usually a chemical method gives the undoped desired product. Electrochemical methods can yield very thin and better-ordered films. In the chemical method, the most common preparation is by “ $\text{FeCl}_3$  method.” Here,  $\text{FeCl}_3$  initiates oxidation of the alkylthiophenes to produce radical centers predominantly at the 2 and 5 positions of the thiophenes that can be generated to form the polymer. The obtained product is treated with chloroform and stirred for about 24 h under a gentle argon stream. The polymer is then precipitated with methanol and filtered. This method gives products that are highly crystalline in nature and have the same structure as the electrochemically synthesized product. Standard electrochemical synthesis is carried out using three electron modes. Here, dopant and monomer, both dissolve in some organic type of electrolyte. Generally, tetraalkyl ammonium tetrafluoroborate is the doping electrolyte used, and commonly used solvent media include acetonitrile ( $\text{CH}_3\text{CN}$ ), benzonitrile ( $\text{C}_7\text{H}_5\text{N}$ ), tetrahydrofuran, and dichloromethane ( $\text{CH}_2\text{Cl}_2$ ). In a standard electrochemical polymerization, Pt/Au is used as the working electrode, and the reference electrode is a saturated calomel electrode. The auxiliary electrode used is Ni or C, and the generated film is basically less homogeneous in nature as well as highly irregular due to its growth mechanism.<sup>2</sup>

Insoluble and infusible PThs can be converted to soluble ones by substitution. Substituted PThs exhibit good solubility in common organic solvents like chloroform. Substitution increases their stability, thermal stability, and conductivity. Substituted PThs are mainly used in display devices and secondary battery electrodes. They are also used for solar energy conversion, biosensors, and chemical sensors.

### **2.2.2 POLYTHIOPHENE/ZINC OXIDE NANOCOMPOSITES**

The most suitable composites for photoelectronic devices are structures based on conducting polymers or metal oxide. Especially metal oxides such as zinc oxide, tin oxide, and titanium dioxide are good choices for PThs/metal oxide nanocomposites. It can be prepared easily; hence, it is used as a versatile nanocomposite.

The PTh/zinc oxide nanocomposites (PTh/ZnO) were synthesized by chemical oxidative polymerization through the mixing of ZnO nanoparticles with the monomers before the polymerization reaction. In a typical procedure, thiophene, methanol, surfactant, and ZnO nanoparticles are mixed and stirred for 1 h. To this, a lithium perchlorate supporting electrolyte and ferric chloride oxidant are added for the initiation of the polymerization. The completed polymerization products of dark brown and black precipitates were collected in the reaction bath. These PTh/ZnO nanocomposites were purified by washing with acetonitrile.<sup>9</sup> The PTh/ZnO nanocomposites possess novel conducting properties that are suitable for the formation of electronic devices. They are used in display devices, lasers, FETs, and photovoltaic devices.

### **2.2.3 POLYTHIOPHENE/COO NANOCOMPOSITES**

Conjugated conducting polymers have wide applications due to their high optical, electrical, and thermal properties. In recent years, PThs have emerged as the best conducting polymers. Cobalt oxide is widely used as a supercapacitor electrode. The conductivity of PThs–CoO composites produced using the chemical oxidative method was found to be of the order of 4–10  $\Omega/\text{m}$ . The hydrothermal method is the most suitable method for the synthesis of nanocomposites of PThs–cobalt and their conductivity increases with increasing amounts of cobalt nanoparticles.<sup>12</sup> Nanoparticles of PThs–CoO (PThs–CO) composites can also be prepared by mechanical mixing of PThs and CoO in various weight percentages.

#### 2.2.4 POLYTHIOPHENE/ $V_2O_5$ NANOCOMPOSITES

PThs have significant electrical properties that can be enhanced by adding oxidizing agents like  $V_2O_5$ . Vanadium oxides are important metal oxides showing polyfunctional behavior and metal-semiconductor transitions. They are used in rechargeable lithium batteries as active electrodes, chromic devices, catalysts, etc. The PTh- $V_2O_5$  composite shows conductivity in a range of 103–104  $\Omega/m$ . PTh- $V_2O_5$  nanocomposites with attractive properties can be fabricated by mixing PTh and  $V_2O_5$  in various weight percentages.<sup>12</sup> The conductivity of the prepared nanocomposites is enhanced with the increase of both frequency and temperature.

Kaur et al. prepared and studied the characteristics of the PTh/ $V_2O_5$  nanocomposite.<sup>12</sup> They have observed that the increased concentration of  $V_2O_5$  is due to the higher current flow through the polymer matrix. The study focused on the oxidizing power and removal of a higher number of charge carriers from the backbone. These types of conducting PThs have a wide range of applications, such as metal ion detectors, molecular electronics, conductive adhesive, electrical displays, electromagnetic shields, chemical, biochemical, and thermal sensors, rechargeable batteries, etc.

Muruganet et al. worked on a PEDOT/ $V_2O_5$  nanocomposite.<sup>13</sup> They have prepared PEDOT/ $V_2O_5$  nanocomposite by inserting poly (3,4-ethylene dioxythiophene) PEDOT in  $V_2O_5$  layers by using oxidative polymerization or intercalation in air. Figure 2.2 shows SEM images of  $V_2O_5$  and PEDOT/ $V_2O_5$  composites. PEDOT/ $V_2O_5$  composites appear to develop a continuous, somewhat homogeneous matrix with a distinct lamellar morphology. The synthesis of the nanocomposites by direct *in situ* reaction of 3,4-ethylene dioxythiophene (EDOT) with  $V_2O_5$  fine powder shows that upon intercalation, the interlayer spacing of vanadium pentoxide expands. The interlayer separation is constant, with two phases in the PEDOT/ $V_2O_5$  system corresponding to the intercalation of one and two monolayers of PEDOT, respectively, in the whole framework. The applications as cathode materials in rechargeable lithium batteries are also confirmed by the electrochemical intercalation of lithium into the PEDOT/ $V_2O_5$  nanocomposites, where an enhancement in the discharge capacity (240 mAhg<sup>-1</sup>) is observed compared to that (140 mAhg<sup>-1</sup>) observed for vanadium pentoxide. The results also suggest that the polymer nanocomposites act as better cathode materials than the pristine  $V_2O_5$  oxide material by enhancing lithium diffusion.

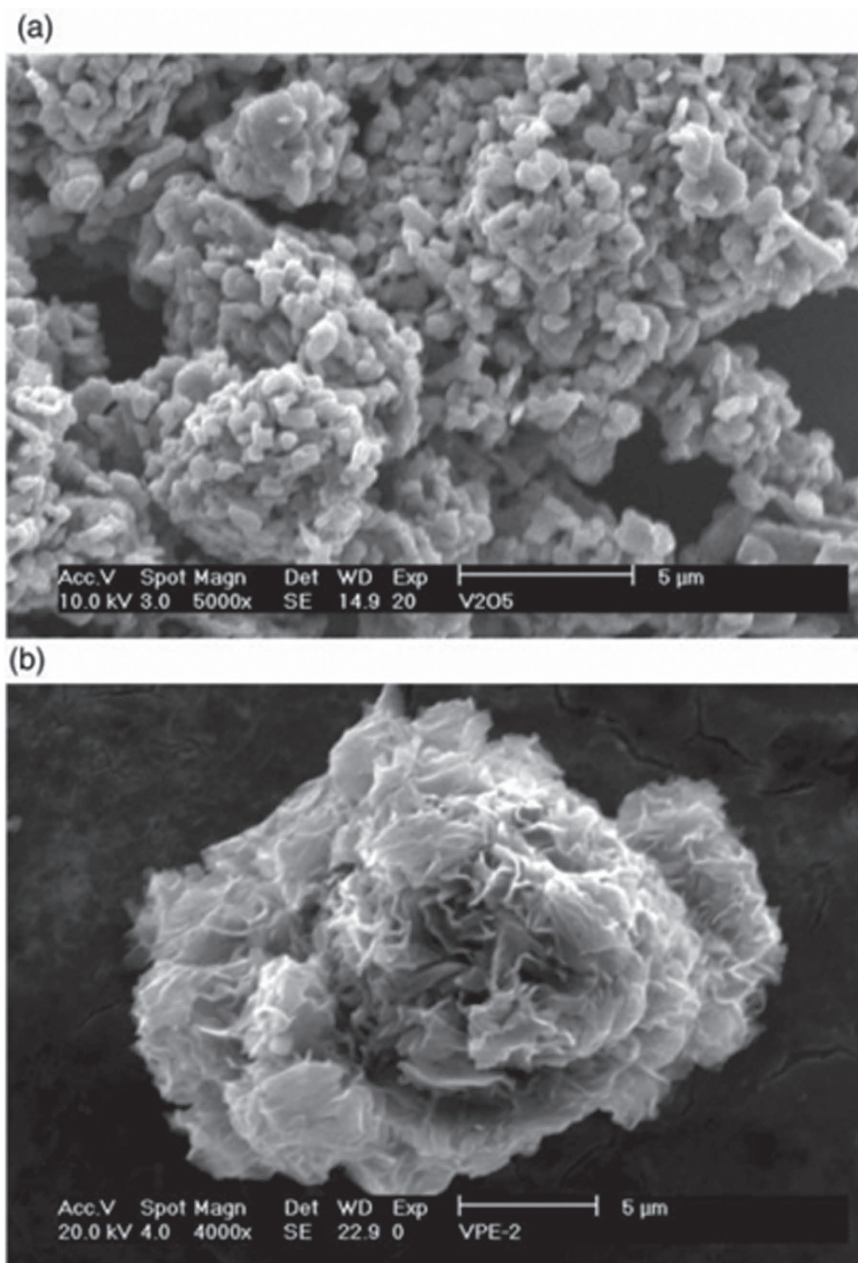


**FIGURE 2.2** SEM images of (a)  $V_2O_5$  and (b) PEDOT/ $V_2O_5$  nanocomposite.

Source: Reprinted with permission from Ref. [13], © 2001 Royal Society of Chemistry.

### 2.2.5 POLYTHIOPHENE/TiO<sub>2</sub> NANOCOMPOSITES

The electrochemical method is used for the preparation of PTh–TiO<sub>2</sub> nanocomposites. In the first step, TiO<sub>2</sub> is coated on a conducting glass surface and then calcinated at 450°C. PTh is prepared by electrochemical polymerization of thiophene, in which TiO<sub>2</sub> nanocrystalline film will be the working electrode, and Pt is considered the counter electrode. This nanocomposite showed high photovoltaic properties. Otsuka et al. prepared nanostructured PTh/TiO<sub>2</sub> novel heterojunction films using photoinduced polymerization of thiophene inside TiO<sub>2</sub> nanopores.<sup>14</sup> The resultant film possesses nanohybridization and electronic connections within the TiO<sub>2</sub> nanoporous domain. The photopolymerization process consisted of three steps: (i) Bithiophene is photoexcited and covalently attached to the TiO<sub>2</sub> surface; (ii) An electron injection reaction is carried out from the surface-attached thiophene to the TiO<sub>2</sub>; and (iii) An electron transfers from a thiophene reactant in an electrolyte to the surface-attached bithiophene. Photopolymerization reactions and thereby subsequent polymer growth were detected by various analyses; for example, we have to note down the light irradiation time, applied bias, nature of the electrolyte, type of thiophene reactant, their size and shape, etc. Electrochemical analysis showed that when bithiophene is adsorbed on TiO<sub>2</sub>, there is a larger circulation of redox potentials. This phenomenon was explained by the capacity of the local electric field on the TiO<sub>2</sub> surface, and on adding it, there is a strong interaction between the surface-bound bithiophene and the TiO<sub>2</sub>. The nanohybrid film was added to a photoelectrochemical solar cell, and the direct usage of the nanohybrid film in electronic devices was observed. The performance of the solar cell was closely associated with the interfacial arrangement as well as the behavior of the nanohybrid film and the photopolymerization process.

Kimura et al. explained that volatile organic compounds (VOCs) are detected by analyzing two output signals from integrated microcantilever sensor arrays that must be covered with organic and inorganic hybrid sensing layers.<sup>15</sup> TiO<sub>2</sub> porous film surface was modified using terthiophene monomers that are amphiphilic and polymerized at the surface of TiO<sub>2</sub> nanoparticles. PTh-filled TiO<sub>2</sub> shows high-sensitivity sensing interfaces and offers two output signals for weight and resistance changes upon exposure to VOC vapor. TiO<sub>2</sub> porous films were dyed with different amphiphilic monomers with different substituents; the films must give accurate information on VOC concentration.

Xu et al. studied the adsorption behavior as well as photocatalytic degradation of methyl orange (MO) under visible light illumination by using PTh/titanium



dioxide (PTh/TiO<sub>2</sub>) nanocomposite particles.<sup>16</sup> The results indicated that methyl orange dye molecules were degraded but not to a similar degree during the visible-light-induced photocatalysis reaction. The authors also proposed a new degradation mechanism for methyl orange dye by the photocatalytic reaction compared with the observed results. The data from the TOC analyzer explained that MO dye can be converted to CO<sub>2</sub> and H<sub>2</sub>O molecules, and intermediate products are eliminated in the photocatalytic degradation reaction.

Nanocomposites of poly (3-decylthiophene) and titanium dioxide, which is doped with N (P3DT/N/TiO<sub>2</sub>), are excellent organic–inorganic hybrid nanocomposites. P3DT/N/TiO<sub>2</sub> is a p-n semiconductor material with photoelectric properties and is studied for applications in solar cells. Poly (3-alkyl thiophene) has better solubility, processability, electrical conductivity, and chemical stability. Solar cells fabricated using this hybrid showed better performance than other conducting polymer-based nanocomposites.<sup>17</sup>

### 2.2.6 POLYTHIOPHENE/MnO<sub>2</sub> NANOCOMPOSITES

MnO<sub>2</sub> is extensively used for supercapacitor applications. It shows excellent properties such as high power delivery and long-term cycling stability. Currently, more studies are being conducted on MnO<sub>2</sub>-based nanocomposites due to their natural abundance and superior capacitance.<sup>18</sup> Xiao et al. proposed an approach to increasing the lithium storage capacities of metal oxide-based anodes for lithium-ion batteries through nanopainting with a thin layer of conducting PTh.<sup>19</sup> They developed a facile, single-step aqueous/organic interfacial synthesis to prepare PTh-coated ultrathin MnO<sub>2</sub> nanosheets (≈5 nm) with an identical mesoporous structure. The observed outcomes of the lithium storage capability test showed that MnO<sub>2</sub>/PTh nanocomposite exhibits superior retention capacity when we are applying high-rate charge/discharge cycling.

Liu et al. introduced a simple and single-step method to prepare MnO<sub>2</sub>/PEDOT nanocomposite by the coelectrodeposition reaction in a template of alumina.<sup>20</sup>

MnO<sub>2</sub> exhibits high energy density, low cost, environmental friendliness, natural abundance, etc., and is considered to be one of the most important electrochemical energy storage materials.

PEDOT has the merits of excellent values in conductivity, stability, and mechanical flexibility, but it shows a low electrochemical energy density. Electrodeposition is used in studies because of its easy and versatile nature in controlling shapes as well as structures and their composition by tuning applied potentials and electrolyte ingredients. Figure 2.3a shows the SEM

picture of free-standing coaxial nanowires produced at 0.75 V after removing the template. The transmission electron microscopy (TEM) picture of a single coaxial nanowire is shown in Figure 2.3b. Although the morphologies of the  $\text{MnO}_2$  and its shell PEDOT can be characterized and differentiated in TEM pictures, the coaxial nanostructure is clearly confirmed by energy-dispersive X-ray spectroscopic (EDS) elemental maps of sulfur and manganese (Fig. 2.3c and d) from the specified location in Figure 2.3b. The applied voltage can be used to regulate the thickness and length of the PEDOT as well as nanowires, respectively. Results showed that  $\text{MnO}_2$ /PEDOT coaxial nanowires have promising electrochemical energy storage capabilities.  $\text{MnO}_2$  shows excellent energy storage capacity, and the PEDOT shell shows a superior conductive, porous, and flexible nature. This provides easy electron transport and ion diffusion into  $\text{MnO}_2$  and protects it from collapsing and breaking behavior. Therefore, coaxial nanowires show high specific capacitances even at very high current densities.

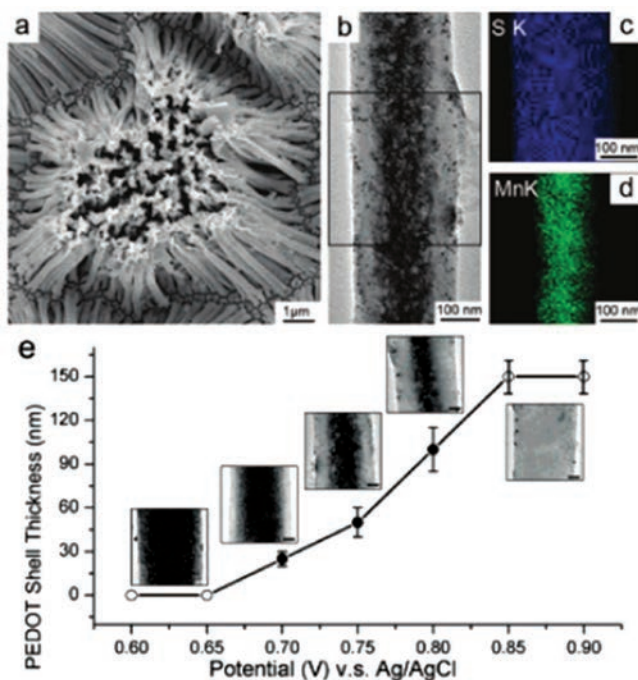


**FIGURE 2.3** (a) SEM micrograph of coaxial  $\text{MnO}_2$ /PEDOT nanowires, (b) a single coaxial nanowire (TEM), (c and d) EDS maps from the enclosed region in panel b, and (e) changes in PEDOT shell thickness as a function of applied voltage.

*Source:* Reprinted with permission from Ref. [20], © 2008 American Chemical Society.

### **2.2.7 POLYTHIOPHENE/MONTMORILLONITE NANOCOMPOSITES**

The in situ polymerization method can be used to prepare nanocomposites of PTh with natural and organophilic clay. These nanocomposites were studied by TEM, X-ray diffraction studies, and conductivity measurements. The morphology of the structure formed affects the conductivity of the prepared nanocomposites.<sup>21</sup> Çelik Meltem and Muşerref Onal prepared and characterized the PTh/Na-montmorillonite (Na-MMT) nanocomposites.<sup>22</sup> TEM images and XRD analysis showed that PTh was intercalated into the clay layers. The thermogravimetric analysis and the differential thermal analysis indicated that the introduction of Na-MMT improved the thermal stability of composites with respect to pure PTh. Furthermore, the adsorptive properties, moisture retention, and water uptake values of nanocomposites were lower after montmorillonite addition. The conductivity of the prepared nanocomposite was observed to be increasing with the increase in the percentage of PTh.

### **2.2.8 POLYTHIOPHENE/MULTIWALLED CARBON NANOTUBES (PTh/MWCNT) COMPOSITES**

CNTs are nanostructures of carbon and are large macromolecules that are unique in their properties such as size, shape, etc. It can be classified mainly into two types: multiwalled (MW) and single-walled (SW) CNTs. SWCNTs have one cylindrical tube, whereas MWCNTs consist of concentric tubes. CNTs have an important role in nanotechnology because of their unique chemical and physical properties. They also show very high mechanical properties. Moreover, CNTs are very good electrical conductors and are flexible along their axes. They act like semiconductors or metals. CNTs are good heat conductors, and they are one of the strongest materials known. CNTs have potential applications in a range of fields, such as nanoscale devices, field emissions, and scanning probe microscopy. Due to their unique electronic properties, high aspect ratio, high chemical stability, extraordinary mechanical properties, and the feasibility of attaching foreign species or chemical groups, CNTs have been widely studied for applications in many research areas. Their applications range from the field of microelectronic devices to hydrogen storage, field emission displays, catalyst supports for electrocatalysis, sensors, energy storage devices, hydrogen storage media, conductive materials, and nanosemiconductors. CNTs are synthesized by different methods, such as chemical vapor deposition (CVD), laser ablation

of a carbon target, electric arc discharge, pyrolysis of benzene, and electrochemical synthesis. CNTs are used as fillers for polymer nanocomposites for various applications because of their electrical, magnetic, and mechanical properties, which make them excellent fillers for fabricating polymer nanocomposites for advanced applications. MWCNTs have been widely studied as fillers in composite materials to improve electrical properties.

Recently, PThs/CNT composites have gained interest from various fields due to their distinct mechanical, surface, and functional features. The synthesis of PThs is usually carried out using anhydrous  $\text{FeCl}_3$ . In a typical synthesis,  $\text{FeCl}_3$  and chloroform ( $\text{CHCl}_3$ ) solutions are prepared. Thiophene monomers are added to this solution and stirred. The resultant polymer mixture is diluted with  $\text{CHCl}_3$ , filtered, and washed with methanol to remove the unreacted monomer and  $\text{FeCl}_3$ . PThs/MWCNT nanocomposite is synthesized in a similar way as PThs in the presence of MWCNTs. The preferred ratio of PThs:CNT is 10:2.

PThs/MWCNTs nanocomposite shows improvement in properties such as refractive index, impedance, dielectric constant, and permittivity. It is one of the most promising materials because of its environmental stability, ease of synthesis, and potential to be modified with different chemical groups. Advanced applications, like space exploration, require lightweight structural materials with high performance, which can be obtained by adding CNTs into the polymer matrix.

The great features of PThs/CNTs provide exciting opportunities for new nanocomposites. PThs/MWCNTs can also be used for solar cell applications.

The formation of MWCNT/poly (3-hexylthiophene) (MWCNT/P3HT) composite has been explained by Y. Du et al. by the oxidative polymerization of 3-hexylthiophene.<sup>23</sup> MWCNTs have a network structure in both their pure and composite states. A MWCNT-dispersed chloroform solution is used for the polymerization reaction. The composite sample containing 30% MWCNT showed a decrease in electrical conductivity from 0.13 to 0.11 S/cm and an enhancement in the Seebeck coefficient from 9.7 to 11.3  $\mu\text{V/K}$  within a temperature gradient of 293–493 K.

### **2.2.9 POLYTHIOPHENE/SINGLE-WALLED CARBON NANOTUBES NANOCOMPOSITES**

The in situ polymerization of doped conducting polymers along and around the SWCNTs beside the bulk polymer can enhance the electrical conductivity and thermal stability of the polymer nanocomposites. SWCNTs show

characteristic properties like thermal, mechanical, and electrical conductivity. They are found to be promising for the development of scanning probe microscopy, nanoelectronic devices, and field emitters. Similarly, nanocomposites based on SWCNTs and polymers can be used to fabricate advanced materials in a range of applications. They have extremely high mechanical and chemical stability, as well as excellent electrical properties. The main drawbacks of SWCNTs are that they are hard to incorporate into a polymer matrix and fabricate into thin films. Meanwhile, conducting polymers are highly transparent, flexible, and can be processed into thin films. The combination of these will produce high-performance SWCNTs/conducting polymer nanocomposite thin films.

PTh/SWCNT nanocomposites can be prepared by the in situ polymerization method.  $\text{FeCl}_3$  is used as the catalyst in this method, which is mixed with SWCNTs in chloroform. The nanocomposite was obtained by the addition of thiophene monomers, and in situ chemical oxidative polymerization onto SWCNTs can be seen. The prepared nanocomposites showed excellent conductivity and thermal properties compared to other similar compounds.

PEDOT is one of the important polymers that possess several attractive properties like high electrical conductivity, optical transparency, environmental stability, low density, good flexibility, low thermal conductivity, and excellent thermal stability. PEDOT is considered a promising candidate for thermoelectric material applications. But one major limitation observed was the dissolution of PEDOT in water. To rectify this issue, this polymer is emulsified with PSS in water. PEDOT:PSS is considered a highly efficient thermoelectric material.

To enhance the thermoelectric properties of PEDOT:PSS, CNT is used as a filler. CNT possesses high electrical conductivity when dispersed in a polymer matrix.<sup>24</sup> With the increase in filler concentration, the electrical conductivity of the composite increases considerably, and the thermal conductivity as well as the Seebeck coefficient remain intact. Kim et al. reported a CNT-filled PEDOT:PSS composite. Modified PTh like PEDOT doped with PSS (PEDOT:PSS) and poly(3-hexylthiophene) (P3HT) have been commonly used in the area of photovoltaics.<sup>25</sup> The schematics of CNTs distributed by gum Arabic (GA) and PEDOT:PSS are shown in Figure 2.4 panels a and b. Both dispersants exfoliate CNTs and alter their surfaces, resulting in hydrophilic CNTs that are water-stable. Figure 2.4c and d show the development of a segregated network after the inclusion of stabilized CNTs during the drying of water-based polymer emulsions.

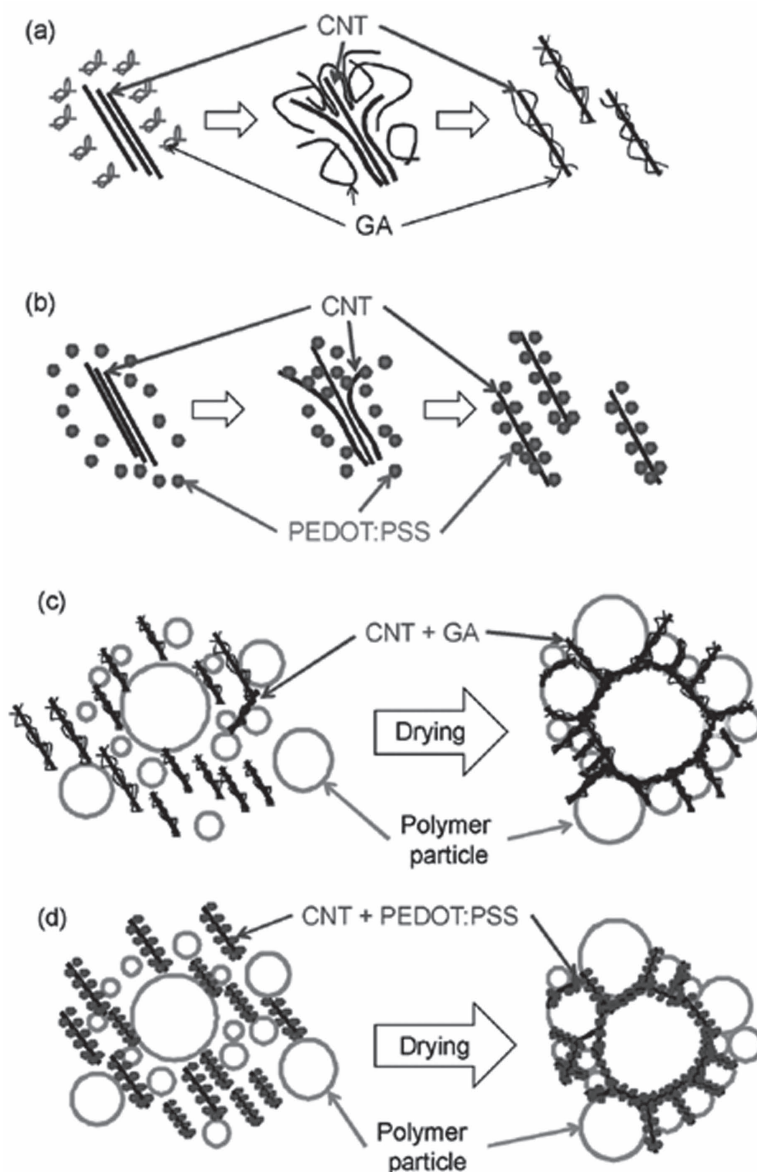


**FIGURE 2.4** Along the surface of spherical emulsion particles, CNTs create a three-dimensional network. Schematics of CNTs distributed by gum Arabic (GA) and PEDOT:PSS are shown in panels a and b, respectively. The schematic representations of segregated network development before (left) and after (right) drying of water-based polymer emulsions are shown in panels c and d.

**Source:** Reprinted with permission from Ref. [25], © 2009 American Chemical Society.

The nanotubes and polymer particles are distributed uniformly in water at first (left). The polymer particles force the nanotubes into interstitial areas during drying (water evaporation) to produce a segregated network (right). The PEDOT:PSS polymer matrix decorates the surface of CNT, making a bridge between tube–tube junctions and permitting electrons or holes to travel more easily through the polymer nanocomposite.<sup>25</sup> Thus, it generates a high electrical conductivity (approx. 40,000 S/m at 35% CNTs). On the other side, thermal conductivity along these tube–tube junctions was obstructed due to differences in vibration energy levels between PEDOT–PSS and CNT. The highest value of the figure of merit, that is, ZT, was achieved in the composite with a concentration of SWCNT of about 35%. This concept can be grasped by considering a network that is thermally disconnected but electrically connected. Along the surface of spherical emulsion particles, CNTs create a three-dimensional network.

### **2.2.10 POLYTHIOPHENE/GRAPHENE NANOCOMPOSITE**

CNTs have remarked properties that enhance the thermoelectric properties of PEDOT:PSS. Literature depicted that a 10-fold increase in its efficiency and its figure of merit was noted by the addition of 2–3 wt% graphene. The value mentioned is much larger than that of CNT-based composites. This is due to the strong  $\pi$ - $\pi$  interaction facilitated by superior dispersion. These interactions are supported by Raman spectroscopy. When graphene is distributed uniformly, it has an interfacial area of 2–10 times and that of CNT of the same weight.

Higher carrier mobility in graphene increases the electrical conductivity, but the thermal conductivity of PEDOT:PSS:graphene is comparatively smaller than that of PEDOT:PSS thin film containing 35 wt% of SWCNT.<sup>26</sup> This anomaly of the two properties was due to the following two reasons: firstly, a well-defined porous multilayer structure acts as a phonon scattering center, and secondly, the thermal conductivity of such materials is phonon dominated. Consequently, the effect of lattice thermal conductivity ( $k_l$ ) is higher than the influence of electronic thermal conductivity ( $k_e$ ). Maximum ZT (i.e.,  $2.1 \times 10^{-2}$ ) has been observed in PEDOT:PSS composite at 2 wt% of graphene at 300 K. This value was 10 times larger when compared to pure PEDOT:PSS. The formation of nanocomposite by the addition of graphene into PEDOT:PSS is considered an effective and novel method for enhancing thermoelectric performance.

### **2.2.11 POLYTHIOPHENE/FULLERENE NANOCOMPOSITE**

Fullerenes (also called buckyballs or buckminsterfullerenes) were discovered in 1985 by Buckminster Fuller.<sup>27</sup> At present, many fullerenes are known, like C<sub>60</sub>, C<sub>70</sub>, C<sub>76</sub>, C<sub>82</sub>, etc., in which carbon atoms are arranged in the form of a sphere or ellipsoid containing hexagonal and pentagonal rings of carbon (i.e., in C<sub>60</sub>, 20 hexagons and 12 pentagons). Among various fullerenes, C<sub>60</sub>, with its derivatives 6, 6-phenyl-C<sub>61</sub>-butyric acid methyl ester (PC<sub>61</sub>BM) and 6, 6-phenyl-C<sub>71</sub>-butyric acid methyl ester (PC<sub>71</sub>BM), has gained more attention in energy storage devices as acceptor materials.

PTh is used as a hole-transporting layer (HTL) and donor material in polymer solar cells. HTL in solar cell devices only allows holes to move toward the anode (i.e., block the flow of electrons toward the anode). Among many HTLs used in solar cell devices, PEDOT:PSS gained more attention because of its good conductivity, charge carrier concentration, suitable bandgap (i.e., the gap between HOMO and LUMO), and smoothening effect of the electrode surface. However, in the active layer, PTh works as a donor and HTL, together with acceptor metallofullerenes (PC<sub>61</sub>BM or PC<sub>71</sub>BM). Here, fullerene works as an electron acceptor. The combination of P3HT/PCBM was used as a standard active layer in polymer-based solar cell devices.<sup>28</sup> Power-conversion efficiencies are reported up to approximately 5%. Dang et al. explained that a detailed study of the literature that was available between 2002 and 2010 shows blends of P3HT and PCBM<sup>29</sup> that are solar cell-based.

### **2.2.12 POLYTHIOPHENE/CDSE NANOCOMPOSITES**

Solar energy is the most vital, inexhaustible, and pollution-free energy source. The common name of photovoltaic devices is solar cells, which convert solar energy to electrical energy, the most convenient form of energy. Photovoltaic devices contain crystalline silicon-based materials. It is an affordable approach to use cadmium nanocomposites as a photovoltaic device. CdSe nanoparticles have excellent properties that can be beneficial for the fabrication of optoelectronic devices, biomedical imaging, nanosensing, laser diodes, and high-efficiency solar cells. Sodium selenosulfate, thiophene, methanol, lithium perchlorate, ferric chloride, and cadmium nitrate solutions are often used for the synthesis of CdSe/PTh nanocomposites.

Zotti et al. prepared a series of terthiophenes and sexithiophenes that reacted with hexadecyl amine-capped CdSe nanoparticles (6 or 7.5 nm diameter) in CHCl<sub>3</sub> to form regular polymeric structures on ITO-glass surfaces



via layer-by-layer (LBL) alternation.<sup>30</sup> The LBL structures are constituted by quantum dots linked via hole-transporting conjugated chains. The formed structures displayed optical and electronic properties useful for photovoltaic devices. The most striking outcome of this investigation is that charge transport between dots is eased by the conjugated linker chains in electrochemical arrangements. However, in the solid state, transport of photogenerated carriers is dominated by interdot distance, with no help from conjugation. The photoluminescence (PL) quenching was observed in sexithiophene and not in terthiophene linkers, which could have suggested an enhanced photo-generation of carriers. This, in fact, proved of no relevance to the effective photoconductivity of the nanocomposites.

### **2.2.13 POLYTHIOPHENE/CADMIUM SULFIDE (CDS) NANOCOMPOSITES**

PTh/cadmium sulfide nanocomposites can be easily prepared. PThs/CdS nanocomposites are synthesized by the chemical oxidative polymerization of thiophene in the presence of cadmium sulfate. These composites will show low electrical conductivity compared to thermally annealed films because of their high grain size.<sup>31</sup> Prashant et al. prepared CdS and CdSe nanoparticles using a conducting poly(3-hexylthiophene) (P3HT) matrix, and the influence of nanoparticles on the polymer matrix was analyzed using electrochemical and spectroscopic techniques.<sup>32</sup> The spectroscopic results revealed that the electronic structure of the polymer greatly affects the added semiconducting nanoparticles. The ordered morphologies of the CdS and CdSe nanoparticles were observed in the presence of the polymer matrix. The conjugation in the polymer matrix has been analyzed using UV, and there must be an increased overlapping between electron-hole pair wave functions, while thermogravimetric analysis results show high thermal stability of the nanocomposites. Comparison of cyclic voltammograms for pure polymer, CdS/P3HT, and CdSe/P3HT nanocomposites in the presence and absence of light suggests the way quantum dots are immobilized in polymer and also the way of trapping the intermediate radical cation at a given potential.

## **2.3 APPLICATIONS OF POLYTHIOPHENE NANOCOMPOSITES**

The polymer conductivity depends upon the spatial arrangement of polymer chains, doping percentage, purity of the samples, and conjugation length.

Normally, undoped PTh shows poor electrical properties. The electrical properties of PThs can be increased by doping.  $\pi$  conjugation is the reason behind the improved conductivity after doping. PTh-based nanocomposites show excellent electrical, magnetic, optical, and mechanical properties.

PTh-based nanocomposites can be tailored for various charge storage applications. PTh-based nanocomposites are widely studied for supercapacitor applications. Supercapacitors are also known as electrochemical capacitors. The substances frequently used for supercapacitor electrode preparation are high surface carbons, transition metal oxide, and conducting polymers (Cps). PTh–CNT nanocomposites electrodes based on CNTs coated with CPs have been widely used in supercapacitor applications. The high conductivity and large surface area of CNT enhance the redox properties of CPs. The capacitance, conductivity, and structure of the nanocomposites predominantly depend on the mode of synthesis.<sup>33</sup>

Light-emitting diodes synthesized from PTh nanocomposites have far-reaching significance. Polymer solar cells (PSCs) have developed as a competent and industrial alternative to silicon-based solar cells. Some considerable merits of PSCs include low cost of production, mechanical flexibility, simple processing, and versatility of chemical structure. PTh-based nanocomposites also have utility in electronics as field-effect transistors and for charge storage due to their excellent characteristics. The superior sensitivity of CPs can be used for the fabrication of efficient field-effect transistors. PTh with modified structures forms excellent dispersions with a uniform size distribution of nanoparticles, which can be used for various applications in microelectronics and optoelectronics.

PTh nanocomposites-based electrodes are also used for modification of electrodes in sensors to increase sensitivity, suppress interference, impart selectivity, and serve as a support material for sensing compounds. The release of gaseous impurities like sulfur dioxide, hydrogen sulfide, ammonia, and other toxic gases from chemical industries has become a severe environmental concern. PTh nanocomposites-based sensors are found to be promising as gas sensors. They are also utilized as biosensors for food investigation, clinical detection, pharmaceutical, and agricultural industries. They are also found to be useful for batteries, electrochromic devices, radar, high-efficiency solar cells, scanning probe microscopy, field emitters, and field emission displays. PTh composites containing metal and magnetic nanoparticles have attracted researchers from many areas, especially in the electrical, magnetical, and optical fields. Nanocomposites of PTh have also been used for the analysis and removal of heavy metal ions, like lead and

cadmium. PTh nanocomposites exhibit excellent properties such as electrical, mechanical, optical, and thermal properties when we compared them with virgin PTh.<sup>34</sup> Recent research studies showed that PTh can be used as biosensors, for gene delivery, and for DNA detection.<sup>35</sup>

## KEYWORDS

- **polythiophene nanocomposites**
- **conducting polymers**
- **polythiophene applications**
- **nanotechnology**
- **nanoparticles**

## REFERENCES

1. Pradeep, T. *Nano: The Essentials: Understanding Nanoscience and Nanotechnology*; The McGraw-Hill Companies, Inc., 2007; p 432.
2. Sangoi, R. N. Nanocomposites Based on Carbon Nanotubes and Poly (3-alkylthiophenes) for Sensor and Charge Storage Applications, 2003.
3. Iqbal, T.; Ali, W. Synthesis and Characterization of Carbon Based Polymer Nanocomposites for Enhanced Conductivity. *J. Ovonic Res.* **2016**, *11* (6), 293–301, 2016.
4. Tiwari, D. C.; Sen, V.; Sharma, R. Temperature Dependent Studies of Electric and Dielectric Properties of Polythiophene Based Nano Composite. *Indian J. Pure Appl. Phys.* **2012**, *50* (1), 49–56.
5. Folarin, O. M.; Sadiku, E. R.; Maity, A. Polymer-Noble Metal Nanocomposites: Review. *Int. J. Phys. Sci.* **2011**, *6* (21), 4869–4882.
6. Cuentas-Gallegos, A. K.; Lira-Cantú, M.; Casañ-Pastor, N.; Gómez-Romero, P. Nanocomposite Hybrid Molecular Materials for Application in Solid-State Electrochemical Supercapacitors. *Adv. Funct. Mater.* **2005**, *15* (7), 1125–1133.
7. Li, S.; Meng Lin, M.; Toprak, M. S.; Kim, D. K.; Muhammed, M. Nanocomposites of Polymer and Inorganic Nanoparticles for Optical and Magnetic Applications. *Nano Rev.* **2010**, *1* (1), 5214.
8. Gao, F. Clay/Polymer Composites: The Story. *Mater. Today* **2004**, *7* (11), 50–55.
9. Shirakawa, H.; Louis, E. J.; MacDiarmid, A. G.; Chiang, C. K.; Heeger, A. J. Synthesis of Electrically Conducting Organic Polymers: Halogen Derivatives of Polyacetylene, (CH)<sub>x</sub>. *J. Chem. Soc. Chem. Commun.* **1977**, *16*, 578–580.
10. Bredas, J. L.; Marder, S. R.; Salaneck, W. R. Alan J. Heeger, Alan G. MacDiarmid, and Hideki Shirakawa-Tribute. *Macromolecules* **2002**, *35* (4).

11. Roncali, J. Conjugated Poly (Thiophenes): Synthesis, Functionalization, and Applications. *Chem. Rev.* **1992**, 92 (4), 711–738.
12. Kaur, V. Study of Electrical Properties of Polythiophene and Its Composites. *IOSR J. Appl. Chem.* **2013**, 5 (2), 07–10.
13. Murugan, A. V.; Kale, B. B.; Kwon, C. W.; Campet, G.; Vijayamohan, K. Synthesis and Characterization of a New Organo-Inorganic Poly(3,4-Ethylene Dioxathiophene) PEDOT/V2O5 Nanocomposite by Intercalation. *J. Mater. Chem.* **2001**, 11 (10), 2470–2475.
14. Otsuka, Y.; Okamoto, Y.; Akiyama, H. Y.; Umekita, K.; Tachibana, Y.; Kuwabata, S. Photoinduced Formation of Polythiophene/TiO<sub>2</sub> Nanohybrid Heterojunction Films for Solar Cell Applications. *J. Phys. Chem. C* **2008**, 112 (12), 4767–4775.
15. Kimura, M. et al. Sensing of Vaporous Organic Compounds by TiO<sub>2</sub> Porous Films Covered with Polythiophene Layers. *Adv. Funct. Mater.* **2012**, 22 (3), 469–476.
16. Xu, S.; Zhu, Y.; Jiang, L.; Dan, Y. Visible Light Induced Photocatalytic Degradation of Methyl Orange by Polythiophene/TiO<sub>2</sub> Composite Particles. *Water. Air. Soil Pollut.* **2010**, 213 (1–4), 151–159.
17. Zhang, J. C.; Zheng, X.; Chen, M.; Yang, X. Y.; Cao, W. L. Synthesis and Application of Solar Cells of Poly (3-Decylthiophene)/N/Titanium Dioxide Hybrid. *Express Polym. Lett.* **2011**, 5 (5), 401–408.
18. Wang, J.-G.; Kang, F.; Wei, B. Engineering of MnO<sub>2</sub>-Based Nanocomposites for High-Performance Supercapacitors. *Prog. Mater. Sci.* **2015**, 74, 51–124.
19. Xiao, W.; Chen, J. S.; Lu, Q.; Lou, X. W. Porous Spheres Assembled from Polythiophene (PTh)-Coated Ultrathin MnO<sub>2</sub> Nanosheets with Enhanced Lithium Storage Capabilities. *J. Phys. Chem. C* **2010**, 114 (27), 12048–12051.
20. Liu, R.; Duay, J.; Lee, S. B. Redox Exchange Induced MnO<sub>2</sub> Nanoparticle Enrichment in Poly(3,4-Ethylenedioxythiophene) Nanowires for Electrochemical Energy Storage. *ACS Nano* **2010**, 4 (7), 4299–4307.
21. Macêdo-Fonsêca, J. C.; Souto-Maior, R. M. Study of Electrical Conductivity of Polythiophene/Montmorillonite Nanocomposites.
22. Çelik, M.; Önal, M. Polythiophene/Na-Montmorillonite Composites via Intercalative Polymerization. *J. Thermoplast. Compos. Mater.* **2014**, 27 (2), 145–159.
23. Du, Y.; Shen, S. Z.; Yang, W. D.; Cai, K. F.; Casey, P. S. Preparation and Characterization of Multiwalled Carbon Nanotube/Poly (3-hexylthiophene) Thermoelectric Composite Materials. *Synth. Method* **2012**, 162 (3–4), 375–380.
24. Dey, A.; Bajpai, O. P.; Sikder, A. K.; Chattopadhyay, S.; Shafeeuulla Khan, M. A. Recent Advances in CNT/Graphene Based Thermoelectric Polymer Nanocomposite: A Proficient Move Towards Waste Energy Harvesting. *Renew. Sustain. Energy Rev.* **2016**, 53, 653–671.
25. Kim, D.; Kim, Y.; Choi, K.; Grunlan, J. C.; Yu, C. Improved Thermoelectric Behavior of Nanotube-Filled Polymer Composites with Poly(3,4-Ethylenedioxythiophene) Poly(Styrenesulfonate). *ACS Nano* **2010**, 4 (1), 513–523.
26. Dresselhaus, M. S. et al. New Directions for Low-Dimensional Thermoelectric Materials. *Adv. Mater.* **2007**, 19 (8), 1043–1053.
27. Prato, M. [60] Fullerene Chemistry for Materials Science Applications. *J. Mater. Chem.* **1997**, 7 (7), 1097–1109.
28. Fan, B.; Wang, P.; Wang, L.; Shi, G. Polythiophene/Fullerene Bulk Heterojunction Solar Cell Fabricated via Electrochemical Co-Deposition. *Sol. Energy Mater. Sol. Cells* **2006**, 90 (20), 3547–3556.

29. Dang, M. T.; Hirsch, L.; Wantz, G.; Wuest, J. D. Controlling the Morphology and Performance of Bulk Heterojunctions in Solar Cells. Lessons Learned from the Benchmark Poly(3-Hexylthiophene):[6,6]-Phenyl- C61-Butyric Acid Methyl Ester System. *Chem. Rev.* **2013**, *113* (5), 3734–3765.
30. Zotti, G. et al. Self-Assembled Structures of Semiconductor Nanocrystals and Polymers for Photovoltaics. 2. Multilayers of CdSe Nanocrystals and Oligo (poly) Thiophene-Based Molecules: Optical, Electrochemical, Photoelectrochemical, and Photoconductive Properties. *Chem. Mater.* **2010**, *22* (4), 1521–1532.
31. Sakil, M.; Singh, A. K.; Roy, G. S. Study of the Properties of Nanocomposite Cadmium Sulphide (CdS)\Polythiophene(PTh) by TGA/DTA, XRD, UV-VIS Spectroscopy, SEM-EDXA and FTIR. *Researcher* **2013**, *5* (1), 51–54.
32. Sonar, P.; Sreenivasan, K. P.; Maddanimath, T.; Vijayamohanan, K. Comparative Behavior of CdS and CdSe Quantum Dots in Poly(3-Hexylthiophene) Based Nanocomposites. *Mater. Res. Bull.* **2006**, *41* (1), 198–208.
33. Kumar, R.; Singh, S.; Yadav, B. C. Conducting Polymers: Synthesis, Properties and Applications. *Int. Adv. Res. J. Sci. Eng. Technol.* **2015**.
34. Husain, A.; Ahmad, S.; Mohammad, F. Preparation and Applications of Polythiophene Nanocomposites. **2020**, *01* (April), 36–53.
35. Mousavi, S. M. et al. Recent Advancements in Polythiophene-Based Materials and Their Biomedical, Geno Sensor and DNA Detection. *Int. J. Mol. Sci.* **2021**, *22* (13), 6850.

## CHAPTER 3

---

# Polymer/Clay Nanocomposites for Tire Applications

ASHA KRISHNAN K.

*International and Interuniversity Center for Nanoscience and Nano Technology, Mahatma Gandhi University, Kottayam, Kerala, India*

---

### ABSTRACT

Polymer nanocomposites have garnered a lot of interest from both academia and the manufacturing industry in the past two and a half decades and have become a stimulating part of current research. The dominance of polymer/clay nanocomposites in the automotive industry is attributed to the remarkable improvement in material properties compared to conventional micro- and macrocomposites. This chapter focuses on the scope of developing polymer/clay nanocomposites for various tire applications. The basic requirements of tires and introduction to organoclays are also discussed in this chapter.

### 3.1 INTRODUCTION

Polymer nanocomposites have a significant universal attraction in the automotive industry especially for tire applications because of their lesser rolling resistance, lightweight, product differentiation, environmental concerns, and better performance in terms of fuel savings. Nanoclay-reinforced elastomers are the most commonly used material in automotive tire applications. The use of nanocomposites as structural components could yield a 20–40% reduction in vehicle weight and a gain in fuel economy by up to 10–20%.<sup>1</sup> The concept of polymer nanocomposites was introduced in the late 1980s

and started to commercialize in 1991 when Toyota Motor Corporation first launched nylon-6/clay nanocomposites as timing belt covers, an engine part for their Toyota Camry cars, in collaboration with Ube Industries.<sup>2</sup> Nanoclays are the most frequently used additive for the preparation of nanocomposites amongst various nanoparticles such as carbon nanofibers, carbon nanotubes [mainly multi-walled carbon nanotubes (MWCNTs)], and polyhedral oligomeric silsesquioxanes (POSS). The large demand for clay in nanocomposites is due to the cost outlook and performance of end-use parts than other nanomaterials. The impetus key drivers for the growth of clay nanocomposites are the reduced weight, low emission, enhanced balance of stiffness and toughness, tremendous mechanical and barrier properties, better heat deflection temperature without loss in elongation, excellent flame retardancy, reduction in relative heat release improved color ability and improved scratch resistance.<sup>3</sup> Clay minerals belong to a most important set of silicates with a layered structure known as layered silicates. Organo-modified layered silicate (OLS) was found to be an efficient filler in polymer nanocomposites. The high aspect ratio of individual layers, abundance in nature, rich intercalation chemistry, high strength and stiffness, and low cost are some important characteristics of clays that make them apt for making polymer nanocomposites. Organoclays are also qualified as inorganic compatibilizers for immiscible polymer blends mainly due to two reasons. Surface-modified organoclays can form in situ grafts by absorbing numerous matrix polymer chains of both polymers. The interfacial tension among the immiscible polymers will lower and furthermore the plate-like organoclays, in a stacked structure, have narrow gaps among each plate. The absorption of polymer chains on the plate decreases the chain mobility and it retards phase growth by coalescence.

### **3.2 INTRODUCTION TO CLAYS**

Clay is a substance occurring in nature composed of fine-grained minerals, which show plasticity through a wide range of water content and can be hardened while dried or fired. Clay deposits are typically made of clay minerals (phyllosilicate minerals) and water is trapped in the mineral arrangement by polar attraction. Figure 3.1 shows the images for the comparison of various types of clays. Clay minerals consist of the following groups:

Kaolin group: the minerals kaolinite, dickite, halloysite, and nacrite with a general formula  $\text{Al}_2\text{Si}_2\text{O}_5(\text{OH})_4$  are included in this group. Kaolin clay has a 1:1 structure with one octahedral sheet and one tetrahedral per clay layer.

The smectite group includes dioctahedral smectites such as montmorillonite and nontronite and trioctahedral smectites, for example, saponite. The general formula for the chemical structure is  $(\text{Ca}, \text{Na}, \text{H})(\text{Al}, \text{Mg}, \text{Fe}, \text{Zn})_2(\text{Si}, \text{Al})_4\text{O}_{10}(\text{OH})_2\text{XH}_2\text{O}$ . Clay mineral contains two tetrahedral sheets and one octahedral sheet sandwiched in between these two tetrahedral sheets, and has a 2:1 phyllosilicate structure. Montmorillonite, vermiculite, talc, pyrophyllite, saponite, and nontronite are a few members of the larger smectite clay group.

Illite group: It includes the clay-micas. The general formula is  $(\text{K}, \text{H})\text{Al}_2(\text{Si}, \text{Al})_4\text{O}_{10}(\text{OH})_2\text{XH}_2\text{O}$ . Silicate layers are sandwiched in an aluminum oxide/hydroxide layer in the same stack sequence in this group.

Chlorites are 2:1:1 phyllosilicates with a T-O-T layer structure and a brucite-like octahedral interlayer. Amesite, chamosite, cookeite, and daphnite are some members of this group. The typical general formula is  $(\text{Mg}, \text{Fe})_3(\text{Si}, \text{Al})_4\text{O}_{10}(\text{OH})_2 \cdot (\text{Mg}, \text{Fe})_3(\text{OH})_6$ .<sup>4</sup>

Among all the different types of clays, smectites are the most usually used nanofillers in polymers because of their natural abundance and ease of organic modification to increase the dispersion within the polymer matrix.<sup>5</sup>

Clay minerals are characterized by the following characteristics: Two-dimensional sheets of corner-sharing  $\text{AlO}_4$  and  $\text{SiO}_4$  tetrahedra. The tetrahedral sheets have the chemical composition of  $(\text{AlSi})_3\text{O}_4$ . Each tetrahedron shares three of its vertex oxygen atoms with other tetrahedra forming a hexagonal array in two dimensions. The fourth vertex is not shared with other tetrahedrons, every tetrahedra “point” in the same direction. In clays, the tetrahedral sheets bonded to octahedral sheets form from small cations, such as aluminum or magnesium, coordinated by six oxygen atoms. The unshared vertex from the tetrahedral sheet also forms part of one side of the octahedral sheet but an extra oxygen atom is situated on top of the gap in the tetrahedral sheet at the center of the six tetrahedra, this oxygen atom is bonded to a hydrogen atom form an OH group in the clay structure. Clays are categorized depending on the way that both the tetrahedral and octahedral sheets are packaged into layers. If there is one tetrahedral and one octahedral group present in each layer; the clay is known as 1:1 clay. The two tetrahedral sheets with the unshared vertex of each sheet point towards each other and forms each side of the octahedral sheet is called 2:1 clay. 2:1:1 clay minerals are composed of an octahedral sheet near a 2:1 layer.

Depending upon the composition of both tetrahedral and octahedral sheets, the layer will have no charge or will have a net negative charge. If the layers are charged, then this charge is balanced by interlayer cations such as  $\text{Na}^+$  or  $\text{K}^+$  and in each case, the interlayer can also contain water. The crystal structure is produced from the pile of layers interspaced with the interlayer.<sup>6,7</sup>



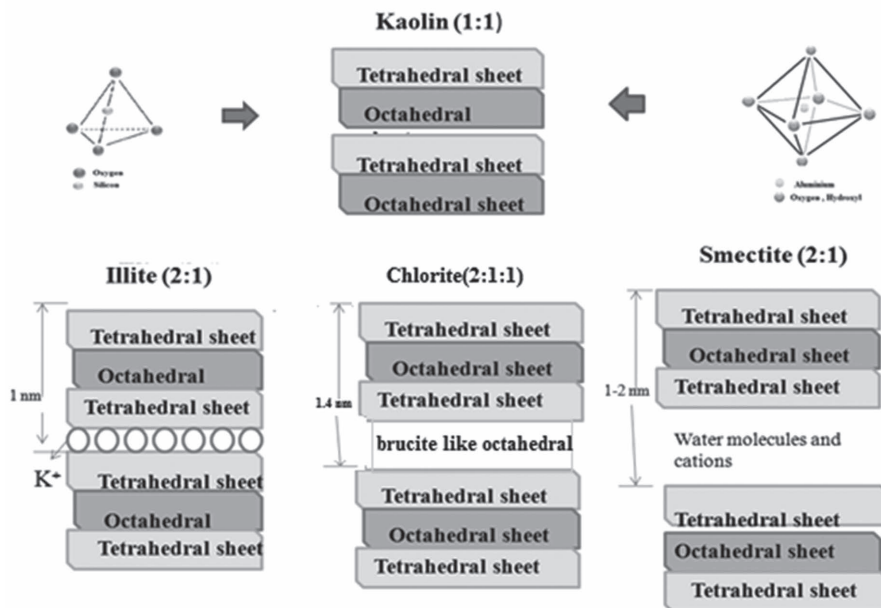


**FIGURE 3.1** Comparison of different types of clays.

### 3.2.1 PREPARATIVE METHODS OF CLAY NANOCOMPOSITES

#### 3.2.1.1 INTERCALATION OF POLYMER OR PREPOLYMER FROM SOLUTION

In this method a solvent system in which prepolymer or polymer is soluble and the silicate layers are swellable. At first, the layered silicate is swollen in a solvent, such as water, chloroform. The polymer and clay solutions are mixed together resulting in the intercalation of polymer chains and displacing the solvent molecule within the interlayer of the clay particles. Upon the removal of the solvent, the intercalated structure remains, resulting in polymer clay nanocomposites.

#### 3.2.1.2 IN SITU INTERCALATIVE POLYMERIZATION METHOD

In this, the organoclay is swollen in the liquid monomer or a monomer solution with the intention that the polymer formation can occur in between

the intercalated sheets. Polymerization can be initiated either by heat, radiation, or can be by the diffusion of a suitable initiator, or by an organic initiator or catalyst and is fixed through cation exchange in the interlayer before the swelling step by the monomer.

### **3.2.1.3 MELT INTERCALATION METHOD**

Melt intercalation involves annealing a mixture of the polymer and organoclay above the softening point of the polymer under shear or static. This method has enormous advantages compared to in situ intercalative polymerization or polymer solution intercalation. First, this method is environmentally gentle due to the lack of organic solvents and secondly is compatible with present industrial processes, such as extrusion molding and injection molding. This method involves the use of polymers which are previously not suitable for the other two methods.<sup>8</sup>

### **3.2.2 STRUCTURE OF POLYMER/CLAY NANOCOMPOSITES**

There are three probable arrangements of layered silicate clays that can be obtained while they are dispersed in a polymer matrix:

If the polymer cannot intercalate among the silicate sheets, a non-intercalated microcomposite is obtained. Ahead of this traditional class of polymer-filler composites, two other types of composites can also be obtained. An intercalated structure is obtained by the separation of clay layers by rising the interlayer spacing whereas an exfoliated or delaminated structure is formed by the complete separation of clay platelets into random arrangements. However, this ideal nanocomposite arrangement is difficult to attain during synthesis and/or processing.<sup>9</sup> Figure 3.2 shows the schematic representation of the arrangements of clay layers in the polymer matrix.

### **3.2.3 ADVANTAGES OF RUBBER/CLAY NANOCOMPOSITES**

Numerous properties like barrier properties, flammability, thermal properties, and mechanical strength, of polymer nanocomposites are enhanced when compared to neat polymer counterparts. The extent of the enhancement is dependent on the type of polymer and nanoclay used with the extent of

dispersion of the nanoparticle within the polymer matrix. Improvements in various properties have resulted in an increased interest in nanocomposite materials in several automotive and industrial applications. Some of the main advantages offered by nanocomposites are as follows:

1. Improvement in mechanical properties compared to conventional composites at low filler loading
2. High thermal stability and improved flame retardancy with low smoke emission
3. Improved impermeability to gases, vapors, and liquids
4. Good optical clarity
5. Tailor-made electrical conductivity
6. Better wear properties
7. Lightweight and low cost
8. In this section the various improved properties of nanocomposites are discussed.

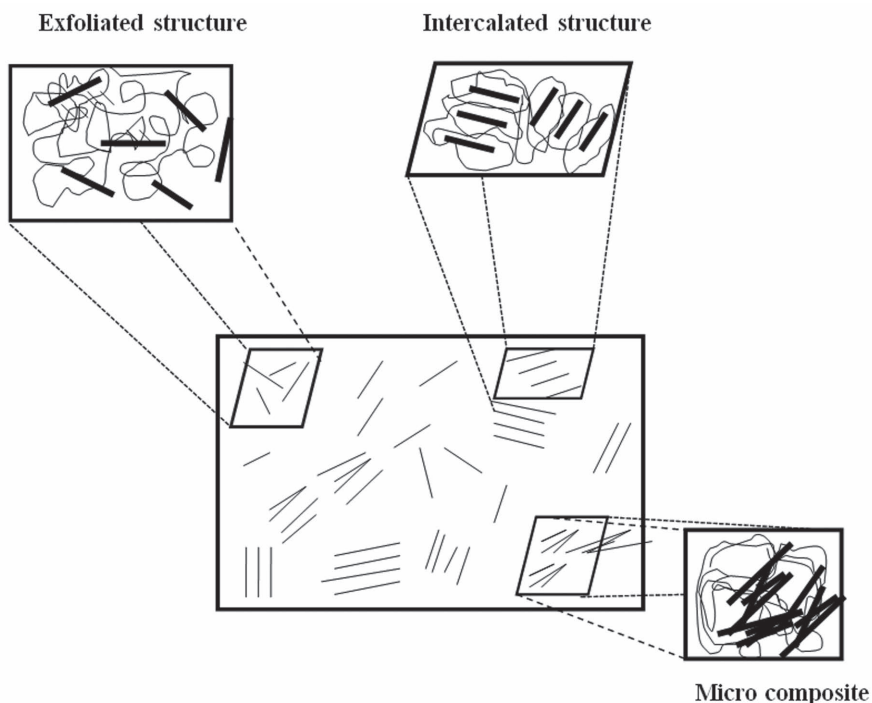


**FIGURE 3.2** Schematic representation for the arrangements of clay layers in the polymer matrix.

### *Mechanical Properties*

The modified organoclay (Closite 15 A) enhances the mechanical properties of the natural rubber (NR) nanocomposites with an increase in clay content up to 10 phr than the gum vulcanisate. A 50% increase in tensile strength, a 150% increase in modulus at 300% elongation is obtained for nanocomposites with 10 phr of clay. A further decrease observed at higher clay loading is observed due to the agglomeration of the clay. For composites with good interaction between filler and matrix, the mechanical properties tend to increase with increasing volume fraction and decreasing particle size.<sup>10</sup> Several authors have reported variations in the mechanical properties of rubber such as NBR<sup>11</sup> and EPDM<sup>12</sup> by choosing the type, the amount and the organic modification of the clay.

### *Flammability of Nanocomposites*

Flammability can be determined by measuring the heat release rate (HRR). The fire hazards of nanocomposites, such as fire size and fire growth, rate are found to be decreased than the matrix. This could be owing to the formation of highly charred carbonaceous silicate cumulating on the nanocomposite surface. The charred surface layer formed during decomposition may act as a barrier to prevent heat to the underlying composites and flammable gases into the flame zone. This may increase their thermal stability and may decrease releasing rate of heat.<sup>13</sup> The HRR of styrene butadiene rubber (SBR) is decreased by 27% in the presence of 20 phr of montmorillonites (MMT). The nanocomposite exhibits the longest time to ignite and time to burn out than the virgin polymer.<sup>14</sup>

### *Barrier Properties of the Nanocomposites*

A study conducted by Wang et al. observed that the dispersion of nanoscale-rectorite clay in SBR largely enhanced gas barrier property counter to results obtained in the N326 (carbon black)/SBR system. According to them, the incorporation of rectorite improves gas barrier property credited to the tortuous diffusional path and inferior fractional free volume.<sup>15</sup> Similarly, there was a reduction in the oxygen permeability of EPDM by the addition of 10 phr MMT.<sup>14</sup>

In addition to their enhanced properties, these nanocomposites can be extrudable easily or moldable to near final shape. The intercalation of clay particles inside the polymer matrix initiates to increase the solvent resistance of clay nanocomposite and as a result, the potential usage of

these materials in fuel line components for cars is also increased. The other properties that are strongly affected by the addition of clay particles are optical transparency and scratch resistance. The presence of nanoclay has been found to enhance transparency and reduce haze. At a lower filler loading, less than 1%, the wear rate of the matrix was reduced by thousands of times. The main reason for improved properties is due to the high aspect ratio of organoclays that results in better dispersion in polymer matrices ultimately leading to improvement in mechanical/physiochemical properties of polymers.

### 3.3 TIRE COMPONENTS

Tire is a toroidal high-performance composite that consists of a large number of rubber compounds along with fibers and metal wires. Different parts of the tire possess different functions. Tires are the only contact point between the vehicle and the ground, thus the various components in a tire are vital to road mobility.

Carcass, the most important structural element of the tire is made up of a number of layers of flexible cords encased in a matrix of rubber compounds. The cords are anchored around the beads made of steel wires and the beads supply the foundations for the carcass, providing adequate seating for the tire on the rim. Tire is made up of semi-finished products and the three main parts of the tire are casing, tread, and bead.<sup>16</sup> A schematic representation of the tire is shown in Figure 3.3.

The casing is made of a layer of textile cord fabric surrounded by rubber compounds. Following components structure a casing.

#### *a) Inner liner*

The inner liner forms an important internal membrane that holds the inflation medium at an elevated pressure inside the structure of the tire and has a rubber compound highly resistant to air migration to maintain air pressure devoid of leaking. The inner liner is also important to ensure safety, optimize fuel consumption and prevent oxidation of the interior components of the tire's inner liner plays an essential role in decreasing the diffusivity of the gas molecules and water vapor transmission through it. Air permeability is an important parameter in tubeless tires, as it influences the tire's durability and riding comfort. The finest air pressure in the tire has to be maintained for better fuel efficiency and longer tire life. High air permeability will lead

to pressure loss which adversely affects the rolling resistance of the tire which will further reduce its life and also thus increase fuel consumption. The rubber compound used for making the inner liner is a reclaimed butyl rubber which is a halogenated butyl rubber other than the reclaimed butyl rubber with at least one semi-reinforcing filler such as delicately ground talc, bituminous coal, hard clay–mica, and carbon black.<sup>17</sup>

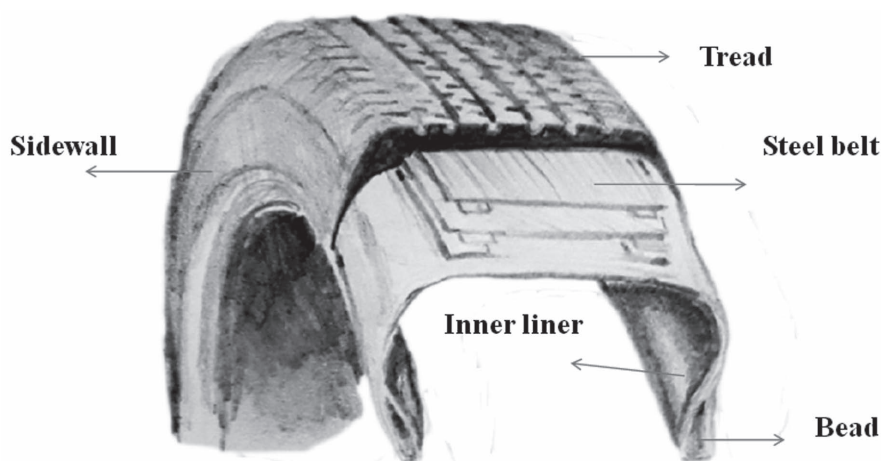


**FIGURE 3.3** Illustration of a tire component.

*b) Carcass or body ply*

The carcass or body ply of the tire is prepared of fabric cords such as nylon, rayon, or polyester or steel cords warped into parallel weftless cord layers also known as plies for the structural strength of the air chamber. These plies are covered with a NR-based compound that contains grip promoters to create a bond between the cord surface and other tire components. The function of the carcass is to allow the tire to adopt the desired shape and to stand the stresses as the tire is loaded and distorted carcass material chosen, the spacing between cords, and the plies number are the factors that will determine the tire's strength and stiffness.<sup>18</sup> The body plies also provide flexibility to the tire.

*c) Chafers*

Chafers are layers of textile fabric coated with rubber and they protect the casing from damage during mounting or demounting from the rim.

#### *d) Breakers*

Breakers are narrow bands of cord fabric coated with rubber. It is used to provide additional stiffness to tread and it absorbs high instantaneous shock loads.

#### *e) Insulation*

Insulations are layers of rubber compound fitted over the plies to provide extra reinforcement to the casing in critical regions.

### **3.3.1 SIDE WALL**

Sidewall rubber offers a shield for the body plies and covers the thinnest part of the tire where most of the flexing arises as the tire averts. It required a high degree of flex cracking resistance. The compound must be resistant to abrasion, tear, cracking, weathering, and heat aging.

### **3.3.2 TREAD**

Tire tread is the thickest component and the material is mislaid through an abrasion in the life of the tire. It will undergo cyclic energy losses and also a rise in the tire's running temperature and a rise in fuel consumption for the vehicle. To balance wear, rolling resistance, and wet grip and jointly with other performance requirements directs to a wide range of tread formulations including several rubbers (natural and synthetic) joints with alternative filler types. The tread must be cool running for durability.

### **3.3.3 BEAD**

Tire bead is an elevated-strength monofilament steel wire coated with rubber. The bead will give a safe fitment to the wheel rim so that it does not stir during the vehicle undergoes rigorous maneuvers. Bead components must be hard, bond well to the wire, and at the same time they give the finished bead the desired degree of rigidity and flexibility. The bead coil consists of a single wire wound numerous times around in a hoop to form a layered complex. Bead Chafer protects the bead area from rim chafing and mounting damage. The bead apex is extending up to the side wall to rise flexing around the bead cable and increasing stiffness of the lower sidewall

for better handling.<sup>19,20</sup> The beads guarantee the tire is properly seated on the rim and help to maintain an airtight fit.

### **3.4 BASIC REQUIREMENTS OF A TIRE**

Tire displays the characteristics of a flexible membrane pressure container which is either tube or tubeless, providing load-carrying capacity, cushioning, and damping; transmits driving and breaking force; provides traction and cornering force while running, dimensional stability, and resist abrasion; provides steering response; provides minimum noise; permits minimum road vibration; and provides durability and safety. Performance of a tire depends on the properties, interaction of the rubber and the fillers used and the conditions. The tire has to overcome obstacles like sharp objects or stones on the road to give traction, so that it is able to transmit the driving and breaking in dry and wet conditions. Various components of the tire are essential for mobility. The tread provides traction, grip, and rolling resistance. The body plies provide strength and flexibility and hold the tread flat on the road. The inner liner helps to keep the air inside the tire and provide safety and prevent oxidation of internal components of the tire. Beads help the tire to be seated properly seated on the rim and maintain an airtight fit. All desired properties required can be attained through the vigilant selection of one or more types of rubber, besides the type and amount of filler.<sup>21</sup> The ingredients of the rubber compounds have to be chosen wisely to provide the tire with specific properties. For example, rubber compounds for sidewalls require to be extremely resistant to fatigue and abrasion so styrene–butadiene compounds are widely used. Tubeless tires require a thin layer of rubber with high impermeability to air to be attached to the inner surface of the carcass; so, butyl rubber compounds are used. Lower rolling resistance, reliability, comfort, and esthetics are the crucial factors that need to be enhanced to meet the never-ending customer demands.<sup>22</sup>

The basic requirements of all types of pneumatic tires are the same irrespective of their differences and some of the basic features are discussed in the following.

#### **3.4.1 ROLLING RESISTANCE**

Rolling resistance is defined as the energy requisite to roll a tire along a road under an agreed vehicle load and is caused by the hysteresis in tire owing



to the deflection of the carcass while rolling. Studies have been reported to determine the contribution where each component causes energy loss and the tire tread is found to be responsible for a higher percentage of rolling resistance in a tire. Factors such as the structure of the tire (construction and materials) and its operating conditions (surface conditions, inflation pressure, speed, temperature, etc.) affect the rolling resistance of a pneumatic tire.<sup>23,24</sup> The rolling resistance can be enhanced devoid of affecting tractions and other properties of the tire by the proper choice of the tread compound. Another parameter related to rolling resistance is the weight of tire and the use of less material will guarantee there is a lowered level of heat build-up due to hysteric energy loss. Figure 3.4 depicts the basic mechanism of rolling resistance.

For a rolling tire:

$$\text{Torque, } T = F_{\text{driving}} \times R + N \times e$$

$$F_{\text{driving}} = (T/R) - (N \times e)/R$$

where  $e/R$  is the coefficient of rolling resistance.

These equations indicate that rolling resistance increases the torque output, hence reducing the driving force of a vehicle.

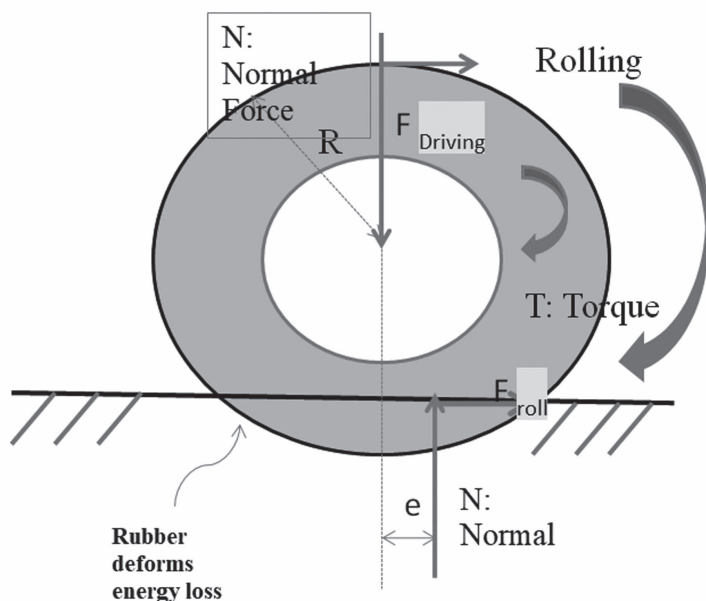


**FIGURE 3.4** Mechanism of rolling resistance.

Source: Inspired and redrawn from Ref. [24].

Tire's rolling resistance is starting to drive the focus of many tire manufacturers in recent years because it can be responsible for 20–30% of the total vehicle fuel consumption. Thus, lowering the rolling resistance will help in reducing fuel consumption. Tire hysteresis loss is the most important cause for tire rolling resistance which is greatly influenced by the nature and volume of filler present in the compound. A study conducted by Jineesh et al. observed that the addition of nanoclay into SBRENr illustrated a lower rolling resistance compared to conventional tire tread compound. According to the study, compounding with nanoclay facilitates reducing the filler content in tire tread compound because of the greater reinforcing power of nanoclay. Also, a decrease in filler content corresponds to a higher amount of elastic rubber in proportion to the damping filler phase in the compound is an effective way to reduce rolling resistance.<sup>25</sup>

### **3.4.2 TRACTION**

The frictional force linking the tire and the road surface which provides a grip is known as traction. A good tire should offer a balance of traction in wet, dry, and cold conditions. A tire's internal structure, tread pattern, and compound recipe all work together to offer the maximum lateral force and self-aligning torque for a known steering angle. The tire designers have to consider environmental conditions when developing tires for different territories.<sup>26</sup> According to Sandip et al., the addition of nanoclay into the NR system offers ice and wet grip in tires and it is evidenced by a higher tan value at 0°C. A higher than value is desirable to achieve the necessary wet traction and grip.<sup>27</sup>

### **3.4.3 CUSHIONING THE VEHICLE**

Recently, automotive engineers are benevolent attention to the enhancement of ride quality by ensuring comfort to driver and passengers as well as the long life of the vehicles. Tire is provided with cushioning effect which is imparted by the air. As a result of cushioning effect, a tire can absorb vibrations set up by road irregularities or obstacles. The right pressure within the tire gives optimum load-carrying capacity and high levels of comfort even as retaining good steering capability.<sup>28</sup>

### **3.4.4 LOAD CARRYING CAPACITY**

A tire should carry the load in a vehicle and also the stress during each revolution. Internal construction of a tire determines its ability to withstand pressure. Tires support the vehicle during both moving and static states and also resist load transfer during acceleration and braking. Good adhesion between the rubber compound and brass-plated steel cord plays a major role in absorbing the impact properly and bearing the load that comes on the tire. The consequence of NC loading on the adhesion of the NR/carbon black nanocomposites with brass-plated steel cord was analyzed by steel cord pull-out adhesion test in an experiment carried out by Tapas et al. The results showed an increment in pull-out force as well as rubber coverage after the addition of organoclay.<sup>29</sup>

### **3.4.5 WEAR AND DURABILITY**

Wear is the process in which the tire becomes unfit for use during a minimum service life. Wear of a tire depends on many factors counting the longitudinal and lateral movements of the tire while rolling, environment, tread pattern design, vehicle drive axle configurations harshness and condition of the road surface, and driving habits. The structural durability of a tire is affected by many factors such as compounding ingredients and techniques used in manufacture as well as the type and conditions of application. Gatos et Al. suggested that the wear resistance of rubber is affected by the organoclay modification (MMT, unmodified, and modified with various intercalants (i.e., octadecylamine, ODA; octadecyltrimethylammonium salt, ODTMA; and methyl-tallow-bis(2-hydroxyethyl) quaternary ammonium salt MTH), served as organoclays), intercalation/exfoliation of the clay layers. The author reported that the addition of nanoclays into hydrogenated acrylonitrile/butadiene rubber (BR) improved the wear resistance and it depended on the formation of intercalated/exfoliated clay layers.<sup>30</sup> A similar improvement in wear resistance was obtained in another study conducted by Dan Xu et Al; in their study, they used organoclay modified by quaternary amine with hydroxyl and double bonds.<sup>31</sup>

### **3.4.6 TRANSMITS STEERING RESISTANCE**

Tires have to transmit driving and breaking torque efficiently to the ground and they should steer the vehicle with accuracy irrespective of the weather

conditions and the surface states. In common, each vehicle has a meticulous inflation pressure for individual axles and the respective pressure variations among front and rear tires should ensure the ideal directional stability.

### **3.5 RUBBER CLAY NANOCOMPOSITES FOR TIRE APPLICATIONS**

Rubber nanocomposites have gained attention in tire manufacturing due to the significant enhancement in tire properties such as increased flexibility along with tensile strength, increased traction, lower rolling resistance, and low-cost-to-performance ratio.

The most important rubber matrices used in tire industry are SBR, BR, isoprene rubber (IR), NR, and halogenated butyl rubber. Also, NR possesses high molecular weight with excellent fatigue performance, low heat build-up from flexing, and resistance to tearing when hot than synthetic polymers. Truck tire treads and internal tire components are mainly NR-based compound. The synthetic side of NR, polyisoprene, is used in some cases and it offers some remuneration as a full or partial substitute due to its close resemblance to NR. Also, SBR is used as a synthetic elastomer in tires, as their apt properties meet performance requirements mostly in treads of passenger car tires. Furthermore, BR is a different elastomer that is used in tire applications. In tire tread, BR is blended at about 10–20% with SBR to gain a good balance of performance characteristics. BR is applied in higher loadings as a blend with NR in sidewall or truck tread. Butyl rubbers are important in tires because of their low gas permeability and good heat resistance. Due to their improved impermeability, butyls now fit in a low percentage of halogen atoms such as chlorine (ClIIR) or bromine (BrIIR) along the polymer backbone.<sup>32</sup>

The incorporation of clay nanocomposites in tire compounds will result in improved properties and performances such as reduced weight, heat build-up with consequent less tire failure and reduced dissipation of energy by the compounds, an addition of the equilibrium of the so-called magic triangle of tire tread performances: rolling resistance, traction, wear, enhanced air retention, electrical conductivity; and colorability. Rubber clay nanocomposites could be applied in tire parts such as tread, base, liner, and ply.

#### **3.5.1 RUBBER CLAY NANOCOMPOSITES IN TIRE TREAD**

Tire tread is the wearing surface and the mix must be resistant to abrasion, tear, cracking, weathering, and heat aging. Replacement of traditional fillers

such as silica with layered silicates (with or without an organic modifier) provides longer life and lower fuel consumption without upsetting the tread grip on the road at a small temperature. It also seems to provide properties like lower abrasion and lower hysteresis at medium-to-high temperatures. In a patent, Heinrich et al. reported the use dioctadecyldimethylammonium-Mt in a tire tread compound for racing. It provides high skid resistance (high friction coefficient; good grip) of the tires made therefrom, combined with a reduction in hardness at elevated temperatures. A rise in loss factor, at any temperature between 40 and 70°C is obtained in an organic clay content of about 40 phr.<sup>33</sup>

A study conducted by Lee et al. reported the use of organically modified MMT (fo-MMT) with alkyl-ammonium chains (octadecylamine) in SBR as tire tread compound, claiming high-grip performance, rolling resistance and superior wear resistance. Modified MMT-embedded SBR matrix showed a significant improvement in modulus and tensile strength even in the small loading. As we know tire tread offers traction and cornering grip and has the biggest effect of all components on rolling resistance. DMA is often used to predict both rolling resistance and wet traction properties and it is usually established that tan values at 600°C and 00°C are suitable to evaluate rolling resistance and wet traction of tire tread compounds for passenger cars. Results showed that tan values of fo-MMT modified SBR at 600°C are 30% advanced and value at 00°C is 13% inferior to that of unmodified clay added SBR indicating the great potential of pneumatic tire using fo-MMT modified SBR for improving wet grip and rolling resistant tire material.<sup>34</sup> This result was supported by another study conducted by Wook-Soo Kim et al. In the study *N,N*-dimethyldodecylamine (tertiary amine)-modified MMT is used as the filler in SBR prepared by using the latex method. Results showed that nanocomposite showed excellent dynamic viscoelasticity, wear resistance, and mechanical properties, which is considered to be an excellent tire tread compound for passenger cars.<sup>35</sup>

### **3.5.2 RUBBER CLAY NANOCOMPOSITES IN TIRE INNER LINER**

The inner liner is the component of a tubeless tire and its main purpose is to hold high pressure. Any drop in pressure causes more deflection, heat, and fall in performance and to achieve these goals, the inner liner should be manufactured with a material of low permeability. An improvement in air retention performance and tire casing durability is required for an inner liner. The usage of layered silicates in inner liner compounds will provide better

barrier properties, prevention of degradation of tire structure owing to air and moisture, superior flex fatigue, crack, and lasting aging resistance. Currently halogenated butyl rubber is used when low permeability is necessary. Nanoclays are used to enable permeability reduction. The plate-like structure of nanoclays makes them ideal as barriers to reduce air loss through the tire's inner liner. Permeation of a gas through a tire inner liner consists of three distinct processes.<sup>36,37</sup> First, the gas molecules dissolve in one side of the inner liner and then diffuse through to the opposite side of lower gas concentration. The rate of permeation dependent on the size of the diffusion gradient, and then evaporate or disperse in the adjacent tire component. In a well-exfoliated and dispersed state, individual clay platelets are supposed to increase the barrier properties by creating a maze or tortuous path' (Fig. 3.5) that lowers the progress of gas and vapor molecules throughout the polymer matrix. It has been established that moisture absorption and diffusion are reliant on the type of organoclay used.<sup>38</sup>

In a patent Gianluca Forte et.al reported the use of kaolin clay (60–80 phr) in halo butyl rubber along with a curing system to improve the impermeability of the inner liner without making it thicker. The improvement in impermeability would result in impairment of crack resistance even at low temperatures.<sup>39</sup> Hermenegildo et al. account for the use of chlorobutyl rubber (CIIR) and NR blend in the inner liner of tubeless tires, using organo-modified montmorillonite (Cloisite1 15A) and carbon black as fillers to increase the barrier properties. The maintenance of tensile properties along with acceptable barrier properties is obtained for (CIIR/NR: 60:40) and the clay content is about 5–10 phr.<sup>40</sup>

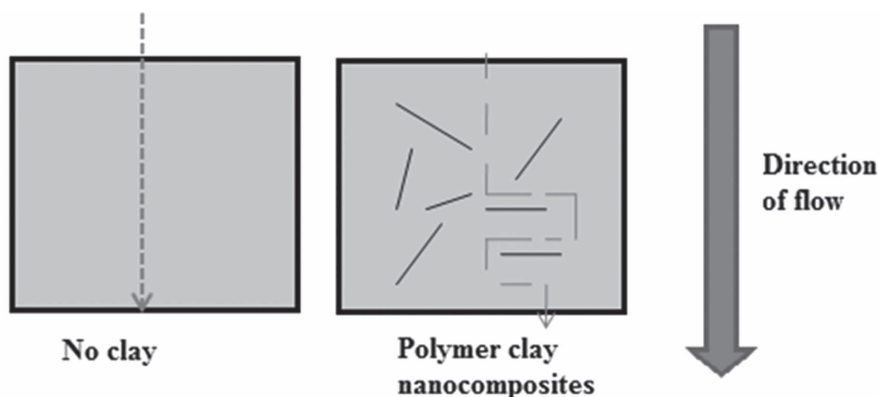


**FIGURE 3.5** Illustration of “tortuous path” in a polymer clay nanocomposite.

*Source:* Inspired and redrawn from Ref. [38].

Bridgestone Corporation developed a rubber compound made of a clay compound (60–100 phr) in halogenated butyl rubber for excellent air permeation resistance. It also showed good crack resistance and flexural fatigue resistance at low-temperature conditions. The inner liner was extremely thinner while maintaining the ability to retain the inner tire pressure.<sup>41</sup> Exxon chemicals prepared blends of general-purpose rubber and layered silicates for inner liners. The presence of layered silicates provides low air permeability without affecting flexibility.<sup>42</sup> Table 1 shows the comparison of air permeability improvement due to nanoclay available from the literature.

**TABLE 3.1** Comparison of reduction in gas permeability due to nanoclay obtained from literature

Polymer	Clay content	Gas used for testing	% of reduction	References
NR	70 phr	N <sub>2</sub>	40%	[43]
NR	0–15phr	O <sub>2</sub>	22–53%	[44]
NR/BR	20phr	O <sub>2</sub>	47–54%	[45]
IIR	7 phr	N <sub>2</sub>	33%	[46]
IIR	8%	N <sub>2</sub>	22%	[47]
SBR	16 phr	O <sub>2</sub>	46%	[48]
Polyurethane	8 wt%	He	~76%	[49]

*Notes:* IIR- isobutylene-isoprene rubber, SBR-Styrene Butadiene Rubber, phr: parts per hundred rubbers

### 3.5.3 RUBBER CLAY NANOCOMPOSITES IN BASE COMPOUNDS

The presence of layered silicates was reported to improve dynamic mechanical properties in base compounds. The utilizing a base compound containing organic clay in P zero tires was announced by Pirelli tire company in 2007 for high and ultrahigh performance. It was reported that the base compound possesses stiffness, better handling/comfort trade-off, no decay, and dynamic modulus stability with temperature.<sup>50,51</sup>

Benson et al. arranged NR/OMMT nanocomposites for reinforcement in tire ply. The plies provide flexibility to the tire and make sure that the tread is held flat on the road. OMMT is a big competitor of silica because of improved thermal, rheological, and mechanical characteristics. Tensile strength and percentage of elongation at break are found to be increased by 81 and 69%, respectively, by the addition of 7 phr of MMT. According to the authors, the increase is due to the increase in filler–filler interaction and

the Haloing effect. An age retention property is an important factor while evaluating the performance of a ply. OMMT reinforced NR showed 76% aged retention properties when compared to that of controlled samples.<sup>52</sup>

In addition to these, various types of clay nanocomposites discover their use in tire applications, and a few of them are discussed here.

#### *NR/SBR/Organoclay Nanocomposites*

NR and SBR are conservative rubbers with spacious usage in tire applications. NR shows excellent stress strength while SBR has higher abrasion resistance, but their deficiencies limit their usage in industrial applications. The incorporation of SBR into NR provides the products with higher abrasion resistance, wet skid resistance, oil resistance, and lower rolling resistance. It was observed that adding organoclay in NR/SBR composites decreased the score time, optimum cure time, and increased cure rate index, which would increase productivity and reduce the energy consumption in the production process. It could be distinguished that the addition of 3 phr of montmorillonite clay results in an improvement in abrasion resistance and mechanical properties.<sup>53</sup>

The exfoliated structure formation depends upon the curing time and clay concentration. The modulus of NR/SBR rubber has continuously increased when clay concentration increased in it and a maximum increase of 70% is observed in 3 wt.% nanoclay packed composites.<sup>54</sup>

#### *Butyl Rubber/Clay Nanocomposites*

Butyl rubber clay nanocomposites are made to get considerable dispersion of nanoclay in a polymer matrix that can be characterized by X-ray diffraction. It has been reported that at 3 phr montmorillonite organoclay strengthen butyl rubber to a large level affects its elastic and viscous behavior in dynamic conditions, and improves its barrier properties to CO<sub>2</sub> gas. The rate of enhancement in properties was reduced at organoclay contents superior to 3 phr.<sup>55</sup> It has been shown that both the chemical nature of the clay modifier and the physical effects such as limited by filler network, diffusion of vulcanizing agents in butyl rubber can vary vulcanization kinetics of butyl rubber. For less hydrophilic clays, dispersion is better; the development of filler network structure confines diffusion and ease of access of curing agents to vulcanization sites.<sup>56</sup>

Brominated isobutyleneisoprene rubber (BIIR) has good age and weather-resistant properties in addition to its excellent air impermeability because of its saturated backbone and also can be easily blended with unsaturated



rubbers such as NR, SBR, and BR and can impart better ply-to-ply adhesion. It has been reported that by composite made with BIIR/polyepichlorohydrin rubber (CO)/nanoclay shows a 64% reduction in air permeability and a 25% reduction in water vapor transmission rate.<sup>17</sup>

### *SBR/Clay Nanocomposites*

*N,N*-Dimethyldodecylamine (tertiary amine)-modified MMT has been used as OLS in SBR nanocomposites and it has been noted that by increasing the quantity of *N,N*-dimethyldodecylamine (DDA) up to 2.5 g, the utmost values of torque, tensile strength and wear resistance of the SBR nanocomposites have been enhanced. This might be owing to the improved dispersion of the silicate layers in the rubber matrix and the enhanced cross-linking of the SBR nanocomposites by DDA itself. In SBR/organoclay compound the usage of 35phr carbon black, 20 phr silica, and 5 phr of organoclay as its ternary filler system; 0.5 phr of calcium stearate was applied to manufacture the compound that showed the most excellent dynamic viscoelasticity, wear resistance and mechanical properties, which is measured to be the excellent tire tread compound for passenger cars.<sup>35</sup>

The effect of nanoclay in SBR is significantly influenced by the addition of carbon black. It has been observed that SBR-clay-carbon hybrids with 25 phr HAF and 6 phr nanoclay showed equivalent reinforcement to that of 40-phr carbon-loaded composites with lower heat generation and better dynamic properties.<sup>58</sup> S. J. He et al. prepared nanocomposite found on SBR latex and MMT is prepared by using the latex compounding method. The study exhibits that the nanocomposites acquire tremendous tensile strength, superior gas barrier properties, increased flame-retardant properties, and wonderful antifatigue properties. According to the author, the SBR-based clay nanocomposites can be useful in inner tubes of tires, tire, OTR tire, tread inner liner, and conveyor belts.<sup>59</sup>

### *EPDM/Clay Nanocomposites*

EPDM is a widely used rubber and has great commercial importance. EPDM does not have any polar groups in its strength of character and homogeneous distribution of the silicate layers in EPDM would be difficult. The types of surfactant used in clay particles also affect the properties of the nanocomposites. MMT modified with trimethyloctadecylamine or dimethylbenzyl-octadecylamine exists in the form of an intercalated layer structure and the MMT modified with methylybis(2-hydroxyethyl)cocoalkylamine was entirely exfoliated in the EPDM matrix is evidenced with the XRD and TEM.<sup>60</sup>

The properties of EPDM/clay nanocomposites are found to be increased by the presence of maleic anhydride. The organophilic modification is accompanied by increasing interlayer distances and also the energy gained through favorable interaction between the compatibilizer (MAH-g-EPDM) and the organo-silicate layer, while exerting a shearing force. This directs to the development of exfoliation structure. The coexistence of the three parameters, clay modification, use of a suitable compatibilizer, and exertion of shearing force are necessary for achieving a high degree of exfoliation structure in EPDM clay nanocomposites.<sup>61</sup>

### 3.6 CONCLUSIONS

Nanotechnology is one of the most competent approaches for future innovation in the tire industry, as they can improve properties without compromising the performance in other areas. Nanomaterials research has opened up new avenues in tire technology, with the potential to improve rolling resistance (fuel consumption) and wear resistance (tire lifetime) while maintaining wet grip (safety) drastically. This chapter summarizes the polymer clay nanocomposites for tire applications. The incorporation of nanoclays into tire components is ambitious by higher overall performance, especially focusing on fuel efficiency through reduced weight and energy dissipation. However, there exist some major challenges that include finding a suitable modification to attain homogeneous dispersion of nanoclays in the matrix and quantifying the extent of exfoliation/intercalation. Further investigation is required to clarify the important aspects of this area. Progress in overcoming the issues is likely to be hastened by enabling technologies that focus on improving fabrication tools, monitoring processes as well as utilizing recent advances in computer simulation.

### KEYWORDS

- **Nanoclays**
- **polymer nanocomposites**
- **nano materials**
- **rubber/clay nanocomposites**
- **organoclays**
- **tire components**

## REFERENCES

1. Patel, V.; Mahajan, Y. Polymer Nanocomposites: Emerging Growth Driver for the Global Automotive Industry. In: *Handbook of Polymer Nanocomposites, Processing, Performance and Application Volume A: Layered Silicates*; Pandey, K., Reddy, A., Mohanty, Misra, M., Eds.; Springer: Heidelberg, Berlin, 2014; p 512.
2. Sengupta, R.; Chakraborty, S.; Bandyopadhyay, S.; Dasgupta, S.; Mukhopadhyay, R.; Auddy, K.; Deuri, A.S. A Short Review on Rubber/Clay Nanocomposites with Emphasis on Mechanical Properties. *Polym. Eng. Sci.* **2007**, *47* (11), 1956–1974.
3. Olad, A. Polymer/Clay Nanocomposites. In *Advances in Diverse Industrial Applications of Nanocomposites*; Reddy, B., Eds.; Intech Open: London, 2011; pp 113–138.
4. Ehlmann; Bethany, L.; Mustard, J. F.; Swayze, G. A.; Clark, N. R.; Bishop, L.; Janice, F. P.; Des Marais, D. J.; Roach, L. H.; Milliken, R. E.; Wray, J. J.; Barnouin-Jha, O.; Murchie, S. L. Identification of Hydrated Silicate Minerals on Mars Using MRO-CRISM: Geologic Context Near Nili Fossae and Implications for Aqueous Alteration. *J. Geophys. Res.* **2009**, *114*, 1–33.
5. Uddin, F. Clays, Nanoclays, and Montmorillonite Minerals. *Metall. Mater. Trans. A.* **2008**, *39* (12), 2804–2814.
6. Okamoto, M. Polymer Layered Silicates. In: *Rapra Review Reports*. Humphreys, J., Ed.; iSmithersRapra Publishers: Shawbury, 2008; pp 3–7.
7. Utracki, L. A. Clay-Containing Polymeric Nanocomposites. In: *J. Rapra Technologies*, Eds.; iSmithersRapra Publishers: Shawbury, 2004; pp 74–80.
8. Okamoto, M. *Polymer/Clay Nanocomposites. Encyclopedia of Nanoscience and Nanotechnology*; Nalwa, H. S., Ed.; American Scientific Publishers, 2004; pp 791–843.
9. Nguyen, T. Q.; Baird, G. D. Preparation of Polymer Clay Nanocomposites and Their Properties. *Adv. Polym. Technol.* **2006**, *25* (4), 270–285.
10. Jacob, A.; Kurian, P.; Aprem, A. S. Cure Characteristics and Mechanical Properties of Natural Rubber–Layered Clay Nanocomposites. *Int. J. Polym. Mater.* **2007**, *56* (6), 593–604.
11. Fabiula, D. B.; de Sousa; Mantovani, G. L.; Scuracchio, C. H. Mechanical Properties and Morphology of NBR with Different Clays. *Polym. Test.* **2011**, *30* (8), 819–825.
12. Ahmadi, S. J.; Yudong, H.; Li, W. Synthesis of EPDM/Organoclay Nanocomposites: Effect of the Clay Exfoliation on Structure and Physical Properties. *Iran. Polym. J.* **2004**, *13* (5), 415–422.
13. Zhang, C.; Wang, J. Natural Rubber/Dendrimer Modified Montmorillonite Nanocomposites: Mechanical and Flame-Retardant Properties. *Materials* **2018**, *11* (1), 3–17.
14. Chang, Y-W.; Yang, Y.; Ryu, S.; Changwoon, N. Preparation and Properties of EPDM/Organomontmorillonite Hybrid Nanocomposites. *Polym. Int.* **2002**, *51* (4), 319–324.
15. Wang, Z. F.; Wang, B.; Qi, N.; Zhang, H. F.; Zhang, L. Q. Influence of Fillers on Free Volume and Gas Barrier Properties in Styrene-Butadiene Rubber Studied by Positrons. *Polymers* **2005**, *46* (3), 719–724.
16. Miyazaki, T. Inner Liner Rubber Composition and Pneumatic Tyre. U.S. patent, 20140116594 A1 October 25, 2014.
17. Kumar, S.; Chattopadhyay, S.; Sreejesh, A.; Nair, S.; Unnikrishnan, G.; Nando, G. B. Analysis of Air Permeability and WVTR Characteristics of Highly Impermeable Novel Rubber Nanocomposite. *Mater. Res. Express.* **2015**, *2* (2), 1–16.

18. Pacejka, H. *Tyre and Vehicle Dynamics*; Butterworth-Heinemann, Elsevier: New York, 2012; p 672.
19. Board of Consultants and Engineers. *The Complete Book on Processing and Compounding Technology*; NIIR Asia Pacific Business Press Inc.: New Delhi, India, 2006; p 712.
20. Willis, J. M. *Firestone Tyre & Rubber Co. Chafer for Tyre Bead Area Protection*; U.S. Patent, 2979101 A, April 10, 1961.
21. Karak, N. *Fundamentals of Polymers: Raw Materials to Finished Products*; New Delhi, 2009; p 290.
22. Evans, M. S. Tyre Compounding for Improved Performance. In: J. *Rapra Technologies*; Shawbury, Ed.; iSmithersRapra Publishers, 2001; pp 12–18.
23. Wong, J. Y. *Theory of Ground Vehicles*; Wiley: New York, 2008; p 320.
24. Chandra, A. K.; Bhandari, V. Nanocomposites for Tyre Applications: Advanced Structured Materials. In *Advances in Elastomers II*; Visakh, P., Thomas, S., Chandra, A., Mathew, A., Eds.; Springer: Berlin, Heidelberg, 2013; pp 183–203.
25. Gopi, J. A.; Patel, S. K.; Tripathy, D. K.; Chandra, A. K. Development of Cooler Running PCR Tyre Tread Using SBR–ENR–Nano Clay Composite. *Int. J. Plast. Technol.* **2016**, *20* (2), 345–363.
26. Pal, K.; Pal, S. K.; Das, C. K.; Kim, J. K. Elastomeric Nanocomposites for Tyre Applications: Recent Advances in Elastomeric Nanocomposites. In *Advanced Structured Materials*; Mittal, V.; Kim, J.; Pal, K., Eds.; Springer: Berlin, Heidelberg, 2011; pp 201–231.
27. Rooj, S.; Das, A.; Morozov, I. A.; Stöckelhuber, K. W.; Stoczek, R.; Heinrich, G. Influence of 'Expanded Clay' on the Microstructure and Fatigue Crack Growth Behavior of Carbon Black Filled NR Composites. *Compos. Sci. Technol.* **2013**, *76*, 61–68.
28. Kempshall, E. Cushioned Pneumatic Vehicle-Tyre. U.S. Patent, 639399 A, 19 Dec 1899.
29. Mohanty, T. R.; Chandra, A. K.; Bhandari, V.; Chattopadhyay, V. Steel Cord Skim Compound for Radial Tyre Based on Natural Rubber-Carbon Black-Organoclay Nanocomposites. *J. Mater. Sci. Eng. B* **2016**, *6* (11–12), 259–276.
30. Gatos, K. G.; Kameo, K.; Karger-Kocsis, J. On the Friction and Sliding Wear of Rubber/Layered Silicate Nanocomposites. *Express Polym. Lett.* **2007**, *1* (1), 27–31.
31. Xu, D.; Karger-Kocsis, J. Dry Rolling and Sliding Friction and Wear of Organophilic Layered Silicate/Hydrogenated Nitrile Rubber Nanocomposite. *J. Mater. Sci.* **2010**, *45* (5), 1293–1298.
32. Akshik, M.; Tjong, J.; Sain, M. *Lightweight and Sustainable Materials for Automotive Applications*; Faruk, O., Tjong, J., Sain, M., Eds.; Taylor and Francis, **2017**, p 497.
33. Heinrich, G.; Herrmann, W.; Kendziorra, N.; Pietag, T.; Recker, C. Rubber Compound for Tyre Tread Rubber. U.S. Patent. 6818693 B2, 19 Nov 2004.
34. Lee, S. P.; Kwon, O. S.; Kang, Y. G.; Song, S. H. Styrene Butadiene Rubber/Clay Nanocomposites for Tyre Tread Application. *Plast. Rubber Compos.* **2016**, *45* (9), 382–388.
35. Kim, W-S.; Lee, D-H.; Kim, I-J.; Son, M-J.; Kim, W. SBR/Organoclay Nanocomposites for the Application on Tyre Tread Compounds. *Macromol. Res.* **2009**, *17* (10), 776–784.
36. Bergaya, F.; Lagaly, *Hand Book of Clay Science: Fundamentals*; Elsevier, 2013; p 1246.
37. Jordan, J.; Jacob, K. I.; Tannenbaum, R.; Sharaf, M. A.; Jasiuk, I. Experimental Trends in Polymer Nanocomposites—A Review. *Mater. Sci. Eng. A.* **2005**, *393*, 1–11.
38. Weng, W.; Soisson, J.; Lohse, D.; Waddell, W.; Webb, R.; Rodgers, B. Permeability of Rubber Compositions Containing Clay. In: *Rubber-Clay Nanocomposites: Science,*

- Technology, and Applications*; Galimbert, M., Ed.; Wiley & Sons: New Jersey, 2012; pp 343–365.
39. Forte, G.; Rome. Tyre Inner Liner Compound. U.S. Patent, 0368451 A1, 15 Oct 2015.
  40. Hermenegildo, G.; Bischoff, E.; Mauler, R. S.; Giovanela, M.; Carli, L. N.; Crespo, J. S. Development of Chlorobutyl Rubber/Natural Rubber Nanocomposites Montmorillonite for Use in the Inner Liner of Tubeless Ride Tyres. *J. Elastomers Plast.* **2016**, 1–15.
  41. Wada, I.; Masashi, O.; Koura, U.; Kanoh, E.; Nakamura, K. Rubber Composition for Inner Liner. E.P 1195402 A1, 19 Aug 2002.
  42. Kresge, E. N.; Lohse, D. J. Composite Tyre Inner Liners and Inner Tubes. U.S. Patent. 5576372 A, 1996.
  43. Zhang, Y.; Liu, Q.; Zhang, Q. Y.; Lu, Y. Gas Barrier Properties of Natural Rubber/Kaolin Composites Prepared by Melt Blending. *Appl. Clay Sci.* **2010**, 50, 255–259.
  44. Suchiva, K.; Siririttikrai, N. Natural Rubber/Clay Nanocomposites, Rubber Centrefiles, Conference Presentation for the Web, Research and Development Centre for the Thai Rubber Industry, Mahidol University, 2013.
  45. Thomas, S.; Stephan, R. *Rubber Nanocomposites*; John Wiley and Sons Pte Ltd: Singapore, 2010; p 684.
  46. Liang, Y.; Cao, W.; Li, Z.; Wang, Y.; Wu, Y.; Zhang, L. A New Strategy to Improve the Gas Barrier Property of Isobutylene-Isoprene Rubber/Clay Nanocomposites. *Polym. Test.* **2008**, 27, 270–276.
  47. Liang, Y.; Wang, Y.; Wu, Y.; Lu, Y.; Zhang, H.; Zhang, L. Preparation and Properties of Isobutylene-Isoprenorubber (IIR)/Clay Nanocomposites. *Polym. Test.* **2005**, 24, 12–17.
  48. Bhattacharya; Biswas, M. S.; Bhowmick, A. K. Permeation Characteristics and Modeling of Barrier Properties of Multifunctional Rubber Nanocomposites. *Polymer* **2011**, 52, 1562–1576.
  49. Maji, P. K.; Das, N. K.; Bhowmick, A. K. Preparation and Properties of Polyurethane Nanocomposites of Novel Architecture as Advanced Barrier Materials. *Polymer* **2010**, 51, 1100–1110.
  50. Galimberti, M.; Fino, L.; Dessanti, F. Inventors, Tyre for Two-Wheeled Vehicles. EP1 597093 (WO 04/ 056586 A1).
  51. Galimberti, M.; Fino, L.; Verona, M. Tyre for Vehicle Wheels with Tread Band of Cap and Base Construction. WO. 05/002883, 2004.
  52. Benson, U. D.; Abdul Majeed, S. S. M.; Babu, R. Natural Rubber/OMMT Nanocomposites for Reinforcement in Tyre Ply. In *J. Nanosci. Nanotechnol.* **2016**, 7 (1), 41–55.
  53. Shan, C.; Gu, Z.; Wang, L.; Li, P.; Song, G. Gao, Z.; Yang, X. Preparation, Characterization, and Application of NR/SBR/Organoclay Nanocomposites in the Tyre Industry. *J. Appl. Polym. Sci.* **2011**, 119, 1185–1194.
  54. Mohan, T. P.; Kuriakose, J.; Kanny, K. Effect of Nanoclay Reinforcement on Structure, Thermal and Mechanical Properties of Natural Rubber–Styrene Butadiene Rubber (NR–SBR). *J. IndEngChem* **2011**, 17, 264–270.
  55. Razzaghi-Kashani, M.; Hasankhani, H.; Kokabi, M. Improvement in Physical and Mechanical Properties of Butyl Rubber with Montmorillonite Organo-Clay. *Iran. Polym. J.* **2007**, 16 (10), 671–679.
  56. Sepehri, A.; Razzaghi-Kashani, M.; Ghoreishy, M. H. R. Vulcanization Kinetics of Butyl Rubber–Clay Nanocomposites and Its Dependence on Clay Microstructure. *J. Appl. Polym. Sci.* **2012**, 125 (1), 204–213.

57. Kim, W.-S.; Lee, D.-H.; Kim, I.-J.; Son, M.-J.; Kim, W. SBR/Organoclay Nanocomposites for the Application on Tyre Tread Compounds. *Macromol. Res.* **2009**, *17* (10), 776–784.
58. Gopi, A.; Patel, J.; Chandra, S. K. SBR-Clay-Carbon Black Hybrid Nanocomposites for Tire Tread Application. *J. Polym. Res.* **2011**, *18*, 1625–1634.
59. He, S. J.; Wang, Y. Q.; Wu, Y. P.; Wu, X. H.; Lu, Y. L.; Zhang, L. Q Preparation, Structure, Performance, Industrialisation and Application of Advanced Rubber/Clay Nanocomposites Based on Latex Compounding Method. *Plast. Rubber & Compos. Macromol. Eng.* **2010**, *39* (1), 33–42.
60. Zheng, H.; Zhang, Peng, Z.; Zhang, Y. Influence of Clay Modification on the Structure and Mechanical Properties of EPDM/Montmorillonite Nanocomposites. *Poly Test.* **2004**, *23*(2), 217–223.
61. Ahmadi, S. J.; Huang, Y. D.; Li, W. Morphology and Characterization of Clay-Reinforced EPDM Nanocomposites. *J. Compos. Mater.* **2005**, *39* (8), 745–754.



## CHAPTER 4

---

# Molecular Dynamics-Based Simulations to Study Structures and Properties of Graphene/Polyurethane Nanocomposites

ANIMESH TALAPATRA<sup>1,2</sup> and DEBASIS DATTA<sup>3</sup>

<sup>1</sup>*Department of Mechanical Engineering, Indian Institute of Engineering Science and Technology, Shibpur, Howrah, West Bengal, India.*

<sup>2</sup>*MCKV Institute of Engineering (NAAC 'A' Grade), Liluah, Howrah, West Bengal, India*

<sup>3</sup>*Department of Mechanical Engineering, Indian Institute of Engineering Science and Technology, Shibpur, Howrah, West Bengal, India*

---

## ABSTRACT

Estimation of enhancement for mechanical properties of graphene-based thermoplastic polyurethane (Gr/TPU) is investigated by using molecular dynamics (MD)-based simulations approach. MD-based simulations are performed to develop different models of Gr/TPU nanocomposites. All the polymer nanocomposites (PNCs) periodic and non-periodic models undergo different ensembles like canonical ensemble (NVT), isobaric-isothermal ensemble (NPT) along with COMPASS force-field within the Forcite module in MS17 to characterize all models. All models are constructed in such a way so that the evaluated density (1.3 g/cc) in amorphous module is nearly to the experimental value. The simulation study shows that enhanced properties of three types of PNCs systems depend on the influences of Gr concentrations (wt.% of Gr), aspect ratio, orientation, clustering



effect (intercalated or exfoliated) and number of layers. The stress-strain responses are evaluated for three categories of Gr/TPU models to understand the effects of Gr concentrations, aspect ratio, and agglomeration on Young's modulus. From the pull-out force (normal and transverse) versus displacement data from interfacial model, it is noticed that enhancement of interfacial mechanical properties depends on higher Gr aspect ratios due to enlarged surface/interfacial area. Available experimental data in literature validate all the MD simulation-based obtained results.

#### 4.1 INTRODUCTION

The simulation methods for nanomaterial mainly have two classes, namely stochastic (i.e., Monte Carlo method) and deterministic (i.e., molecular dynamics [MD] method), respectively. The simulations carried out by MD method are based on the Newton's equations of motion-based solution for an  $N$  body system interacting through a potential function  $U(r_1, r_2, r_3, \dots, r_N)$ . The average values of properties can be determined from all these trajectories.

For a set of  $N$  atoms, Newton's equation of motion is presented by,

$$F_i = m_i a_i = m_i \frac{dv_i}{dt} = m_i \frac{d^2 r_i}{dt^2} \quad (4.1)$$

Where  $m_i$  is the  $i$  atom mass,  $a_i$  is the  $i$  atom acceleration and  $F_i$  is the resultant force acting on atom  $i$ . These forces should be balanced by the potential energy (PE) between atoms, which are usually presented as the gradient of a PE function.

Forces are obtained as a gradient of the PE function, which depend on the particle/atom coordinates.

$$F_i = -\frac{dU}{dr_i} \quad (4.2)$$

Where,  $r_i$  is the position vector of an atom  $i$ .  $U$  is the PE which is a function of the positions of the atoms. Combining these two equations,

$$-\frac{dU}{dr_i} = m_i \frac{d^2 r_i}{dt^2} \quad (4.3)$$

The acceleration is given the equation

$$a_i = -\frac{1}{m_i} \times \frac{dU}{dr_i} \quad (4.4)$$

The initial distribution of velocities is usually determined from the required temperature and corrected so there is no overall momentum, that is,

$$P = \sum_{i=1}^N m_i v_i = 0 \dots \quad (4.5)$$

The velocities,  $v_i$ , are chosen from a Maxwell–Boltzmann or Gaussian distribution.

$$p(v_{i,x}) = \left( \frac{m_i}{2\pi k_B T} \right)^{\frac{1}{2}} \exp \left[ -\frac{1}{2} \frac{m_i v_{i,x}^2}{k_B T} \right] \quad (4.6)$$

Where,  $m_i$  is the particle mass and  $k_B T$  is the product of Boltzmann's constant and thermodynamic temperature.  $P$  is the probability of particle  $i$  of mass  $m_i$  at temperature  $T$  to have velocity  $v_i$  in the  $x$ -direction. The temperature equation is given by

$$T = \frac{1}{(3N)} \sum_{i=1}^N \frac{|p_i|}{2m_i} \quad (4.7)$$

$$\text{or } T = \frac{2}{(3Nk_B)} \sum_{i=1}^N \frac{m_i v_i^2}{2} \quad (4.8)$$

Where,  $N$  is number of atoms in a system,  $m$  = mass of the  $i$ th atom,  $k_B$  = Boltzmann's constant. The PE of a system can be presented as a sum of bond and non-bond interactions, which together are commonly referred to as force fields as shown in Table 4.1. MD modeling and simulation use classical PE equations which consist of (a) bond interactions and (b) non-bonded interactions.

$$U_{\text{Total}} = U_{\text{bonded}} + U_{\text{non-bonded}} \quad (4.9)$$

$$U_{\text{Total}} = (U_{\text{valence}} + U_{\text{cross-term}}) + U_{\text{non-bonded}} \quad (4.10)$$

$$U_{\text{Total}} = (U_{\text{bond}} + U_{\text{angle}} + U_{\text{torsion}} + U_{\text{inversion}}) + U_{\text{cross-term}} + U_{\text{vdW}} + U_{\text{coulomb}} \quad (4.11)$$

$$U_{\text{cross-term}} = U_{\text{bond-bond}} + U_{\text{angle-angle}} + U_{\text{bond-angle}} + U_{\text{end-bond-torsion}} \\ + U_{\text{middle-bond-torsion}} + U_{\text{angle-torsion}} + U_{\text{angle-angle-torsion}} \quad (4.12)$$

The first four terms in eq 4.11 is bonded interactions between two planes which is formed by four neighboring atoms and also angle variation of two planes formed by four atoms where one atom is bonded to other three. Non-bonded terms usually include vdW and electrostatic interactions.

**TABLE 4.1** Details of Classical Potential Energy (PE) in MD Simulation.

Name of interaction		Energy equation
Bonded terms	Bond energy	$U_{bond} = \frac{1}{2} K_b (b - b_0)^2$ <p>Where, <math>k_b</math> is the stretching force constant, <math>b_0</math> is the equilibrium bond length, and <math>b</math> is the actual bond length</p>
	Angle energy	$U_{bend} = \frac{1}{2} K_\theta (\theta - \theta_0)^2$ <p>Where, <math>k_\theta</math> is the angle-bending force constant, <math>\theta_0</math> is the equilibrium bond angle, and <math>\theta</math> is the actual bond angle.</p>
	Torsional or dihedral Energy	$U_{torsion} = \frac{1}{2} K_\phi (1 + \cos(n\phi - \phi_0))$ <p>Where, <math>k_\phi</math> is the torsional barrier, <math>\phi</math> is the actual torsion angle, <math>n</math> is the periodicity, and <math>\phi_0</math> is the reference torsional angle</p>
	Out-of-plane or improper dihedral energy	$U_{inversion} = \frac{1}{2} K_\omega (\omega - \omega_0)^2$ <p>where <math>K_\omega</math> is the force constant and <math>\omega</math> is the angle between the axis and the plane</p>
	Cross-coupling terms	$U_{cross-term} = U_{bond-bond} + U_{angle-angle} + U_{bond-angle} + U_{end-bond-torsion} + U_{middle-bond-torsion} + U_{angle-torsion} + U_{angle-angle-torsion}$
Non-bonded terms	Coulombic interaction	$U_{coulomb} = \frac{1}{\epsilon} \frac{q_1 q_2}{r_{ij}}$ <p>Where, <math>q_1</math> and <math>q_2</math> are the charges on the interacting atoms, <math>\epsilon</math> is the dielectric constant, and <math>r_{ij}</math> is the interatomic distance</p>
	Van der Waals energy	$U_{vdw} = \sum \frac{A_{ij}}{r_{ij}^{12}} - \frac{B_{ij}}{r_{ij}^6}$ <p>Where, <math>A_{ij}</math> and <math>B_{ij}</math> are the repulsive and attractive term coefficients, respectively, and <math>r_{ij}</math> is the distance between the two atoms.</p>

**Bond stretching potential:** Generally, the interatomic forces are assumed to be harmonic and the bond-stretch (2 body) term is represented by a simple quadratic function:

$$U_{bond} = \frac{1}{2} K_b (b - b_0)^2 \quad (4.13)$$

Where,  $k_b$  is the stretching force constant,  $b_0$  is the equilibrium length of bond and  $b$  is the actual length of bond.



FIGURE 4.1 Bond stretching.

**Angle bending potential:** For angle bending (three body), a simple harmonic expression is used:

$$U_{bend} = \frac{1}{2} k_{\theta} (\theta - \theta_0)^2 \quad (4.14)$$

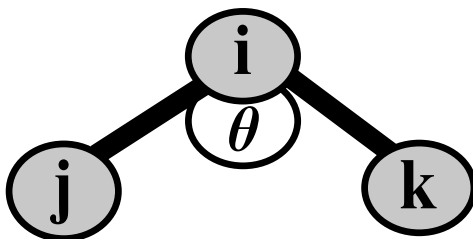


FIGURE 4.2 Bond bending.

Where, the angle-bending force constant is  $k_{\theta}$ , the equilibrium bond angle is  $\theta_0$ , and the actual bond angle is  $\theta$ .

**Torsional rotation potential:** A cosine expression is commonly used for the Torsions/dihedral (fourbody) PE, as represented,

$$U_{torsion} = \frac{1}{2} k_{\phi} (1 + \cos(n\phi - \phi_0)) \quad (4.15)$$

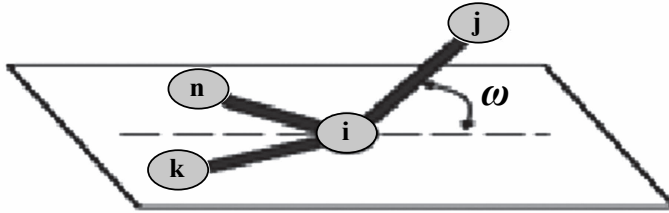


FIGURE 4.3 Dihedral angle torsion.

Where,  $k_{\phi}$  is the torsional barrier, the actual torsion angle is  $\phi$ , the periodicity is  $n$ , and  $\phi_0$  is the referencetorsional angle.

**Improper dihedral angle (four body) potential energy:** Improper dihedral angle (four body) potential energy, as represented,

$$U_{inversion} = \frac{1}{2} K_{\omega} (\omega - \omega_0)^2 \quad (4.16)$$



**FIGURE 4.4** Inversion.

Where  $K_{\omega}$  is the force constant and  $\omega$  is the angle between the axis and the plane. Some of the modern force fields also include cross-terms to account for bond or angle distortions caused by nearby atoms.

**Cross-terms** may include stretch–stretch, stretch–bend–stretch, bend–bend, torsion–stretch, torsion–bend–bend, bend–torsion–bend, and stretch–torsion–stretch terms.

**van der Waals interactions:** van der Waals (vdW) interactions between non-bonded atoms that are usually represented by Lennard–Jones potential,

$$U_{vdw} = \sum \frac{A_{ij}}{r_{ij}^{12}} - \frac{B_{ij}}{r_{ij}^6} \quad (4.17)$$

where  $A_{ij}$  and  $B_{ij}$  are the repulsive and attractive term coefficients, respectively, and  $r_{ij}$  is the distance between the two atoms.

**Electrostatic interactions:** Electrostatic interactions are described by a coulomb term

$$U_{coulomb} = \frac{1}{\epsilon} \frac{q_1 q_2}{r_{ij}} \quad (4.18)$$

where the charges on the interacting atoms are  $q_1$  and  $q_2$ ,  $\epsilon$  is the dielectric constant, and  $r_{ij}$  is the interatomic distance.

Nanocomposites are reinforced by one or more separate nanomaterials with nanometer dimensions ( $1 \text{ nm} = 10^{-9} \text{ m}$ ). Nanocomposites have higher physical and mechanical properties than conventional composite materials. The matrix materials are classified in three different categories as follows:

- a) Ceramic Matrix Nanocomposites (CMNC)
- b) Metal Matrix Nanocomposites (MMNC)
- c) Polymer Matrix Nanocomposites (PMNC).

But depending on the filler materials (reinforcement) geometry, it can be divided into three types

- a) Nanoparticle reinforced nanocomposite
- b) Nanotube reinforced nanocomposite
- c) Nano layer reinforced nanocomposite

There are different ways to characterize enhanced properties of nanocomposite

- a) **Analytical methods:** The analytical models include Voigt and Reuss bounds (V–R model), Hashin and Shtrikman bounds (H–S model), Halpin–Tsai model (H–T model), Hui-Shia model (H–S model), Cox model (Shear lag model), Mori and Tanaka models and Rule of mixture.
- b) **Experimental methods:** Dynamic mechanical analyzer (DMA), nano indentation, Scanning electron microscopy (SEM), transmission electron microscopy (TEM), atomic force microscopy (AFM), thermal gravimetric analyzer (TGA), and X-ray diffraction (XRD), etc.
- c) **Numerical methods:** There are two methods: first one is MD simulation or atomistic method, and the second one is finite element simulation or continuum method. Nano scale continuum methods are (i) unit cell (UC) method (ii) representative volume elements (RVE) method and (iii) image-based object-oriented finite element (OOFEM) method. OOFEM is public domain finite element analysis software created at the National Institute of Standards and Technology (NIST) to investigate nanocomposite material. In the year of 1990, object-oriented finite element analysis tools were developed in NIST. There are three versions of OOFEM available namely OOF1, OOF2, and OOF3D. Recently, Talapatra et al.<sup>47–50</sup> worked on Gr-based PNCs using MD simulation (MS 17 software) and OOFEM (OOF2 software). It has been found that OOFEM-based results are much similar to experimental results compare to MD simulation results. Because OOF2 has a capability to develop model from actual obtain microstructure.

## **4.2 CURRENT STATE-OF-THE-ART IN MD-BASED MODELING AND SIMULATION FOR NANOCOMPOSITES**

Alder and Wainwright introduced MD method in the year of 1950 for the study of interactions of hard spheres at Lawrence Radiation Laboratory in the USA. Next Gibson did MD calculations with potential based on a finite difference time integration method in 1961. Then in 1964, Rahman did MD simulation of liquid argon by using a realistic potential. Finally, Stillinger & Rahman conducted MD simulation of a realistic system in 1974. Since then, the MD modeling and simulation methods are being used from Physics to Materials Science and now to Mechanical Engineering and other disciplines. The discovery of Gr-based PNCs is one of the burning areas in ballistic protection technology. To develop transparent armor with higher impact strength as well as maintaining visibility after impact is a new area of research. Gr is a promising reinforcement material to replace carbon nanotubes (CNTs), carbon fibers and Kevlar presently used in ballistic protection technology. According to Singh et al.,<sup>49</sup> Gr is a new class of wonder nanomaterial having bulk ultimate strength of 130 GPa, Young's modulus of 1060 TPa, and fracture strength of 125 GPa. The carbon atoms with bond angle 120° and the neighboring layers are separated by the vdW distance (0.335 nm). Gr was discovered by Prof. A. K. Geim and Prof. K. S. Novoselov in 2004, leading to Nobel Prize in 2010. Lee et al.<sup>19</sup> gives that TPUs are linear block copolymers with good tribological properties, higher load bearing capacity, superior impact resistance, and better weight reduction.

Thermoplastic polyurethanes (TPUs) are widely used in different areas such as automobile application, structural application, construction, thermal insulation, and footwear. There are various problems to study the Gr-based PNCs at the molecular level with experimental techniques. According to Hadden et al.,<sup>15</sup> simulation approaches are valuable tools for design and development of this promising material's characterization. Out of various computational methods, MD simulation is a powerful tool in an atomic scale investigation. Inam et al. (2016) reviewed advances in the modeling and simulation of Gr-based PNCs. Various literature studies are available for numerical modeling and simulation of Gr-reinforced nanocomposites which are mainly divided into three types of modeling, such as (a) packing modeling (b) stacking modeling, and (c) interfacial modeling. Hao et al. (2009), Koratkar et al. (2009), Strachan et al. (2012), Haqueet al. (2013), Liu et al.<sup>26</sup>, Zaminpayma et al. (2016), Karatasos et al. (2016), Wang et al. (2017), and Shen et al. (2017) investigated the properties of Gr-based PNC

system by MD simulations using non-crystalline or packing model, and considered the effects of aspect ratio, orientation of reinforcement (orderly or randomly), volume fraction or weight fraction, number of reinforcement, reinforcement size, topographical effect, and functionalization of reinforcement during modeling. Rahman et al.<sup>36</sup> and Shiu et al.<sup>44</sup> carried out modeling and simulation on stacking or dispersion model changing different clustering morphologies (intercalated or exfoliated). Awasthi et al.<sup>4</sup>, Al-Ostaz et al. (2010), Hu et al. (2015), and Seifoori et al.<sup>40</sup> investigated on the most vital and burning research area which is interfacial modeling and simulation for calculation of interfacial shear force, stress, and interaction energy. Hao et al. (2009) determined the mechanical properties such as the stiffness of monolayer Gr under tensile testing by quantum MD technique. Koratkar et al. (2009) compared the mechanical properties of PNCs with Gr platelets, single-walled CNTs, and multi-walled CNTs additives. They found the superiority of Gr platelets over CNTs. This study clearly illustrates the superior enhancements produced by Gr compared to CNTs. Awasthi et al.<sup>4</sup> investigated the interfacial behavior between one layer of Gr and polymer using the MD. Al-Ostaz et al. (2010) studied the geometrical effects on the properties of Gr-VE nanocomposites and their constituents. Young's moduli of Gr layer and for graphite layers were found in the range of 1.3–1.16 TPa. Interfacial shear strength of Gr/VE and graphite/VE nanocomposite was found 256 and 126 MPa, respectively. Ebrahimi et al. (2012) examined the matter using a multi-scale modeling approach. Their results also displayed that Gr platelets work better than CNTs. Strachan et al. (2012) characterize multilayer Gr-reinforced epoxy nanocomposites using MD simulation. In the composites, Gr layers parallel and perpendicular to polymer/Gr interface. It was observed that the strengths of composites were close in both cases, while the damage mechanisms were different. Haque et al. (2013) measured the stiffness and strength of the Gr-based epoxy nanocomposites using MD simulation. A study performed on EPON 862/TETA reinforced by Gr platelets focused on the impact of aspect ratio and the number of platelets grouped together. Shiu et al. (2014) evaluated mechanical properties of Gr-reinforced nanocomposites with different morphologies such as Gr platelets intercalated Grand intercalated Gr oxide (GrO) using MD simulations. After the literature reviews, it is concluded that some vital parameters control to enhancement the properties of nanocomposites as seen in the simulation processes (MD simulation).

The parameters are mentioned below:

- a) Aspect ratio (AR),



- b) Reinforcement shape (crumpled or flat),
- c) Orientation of reinforcement (orderly or randomly),
- d) Clustering of reinforcement (intercalated or exfoliated),
- e) Volume fraction or weight fraction,
- f) Number of reinforcement,
- g) Reinforcement size,
- h) Functionalization of reinforcement,
- i) Defective reinforcement (stone-wales, vacancy, grain boundary, oxidation doping), etc.

These parameters control enhancement of properties of nanocomposites directly. These are mentioned below

- a) Stiffness: It totally depends on reinforcement, size, and orientation.
- b) Yield strength: Yield of the nanocomposites with rigid nanoparticles increases linearly with incorporation of more particles loading.
- c) Young's modulus: It is increased due to intercalated clustering and orderly reinforcement orientation.
- d) Toughness: Exfoliated clustering condition helps to increase toughness of PNCs. Because toughening mechanism is mainly occurred in process zone and bridge zone within PNCs.
- e) Interfacial strength: High aspect ratio increases the interfacial strength..

#### **4.3 DIFFERENT APPLICATION OF MD SIMULATION FOR NANOCOMPOSITES**

##### ***i) Enhancement of Mechanical Properties:***

MD simulation is a nano-level simulation tool which helps to investigate the enhanced mechanical properties like modulus of elasticity, strength, hardness, toughness, etc. Mechanical properties of the nanocomposites are evaluated by strain constant method. Atomic level simulations for fracture toughness are based on two methods (a) periodic crack method and (b) crack-tip displacement method. The two methods are used to determine the critical fracture toughness  $K_{IC}$ . Three-dimensional MD simulation is a very powerful tool to analyze the atomistic mechanism of nano indentation process for nanocomposites during hardness calculation. Enhancement of properties of Gr-based PNCs has been investigated by various researchers.

**ii) Enhancement of Thermal Properties:**

MD simulation helps to analyze heat transfer performance and is able to predict enhanced thermal properties. MD simulation is related to micro structural element which control thermal transport. Enhancement of thermal properties like thermal conductivity can be investigated by two methods, namely non-equilibrium molecular dynamic (NEMD) or equilibrium molecular dynamic (EMD) according to Sharma et al.<sup>42</sup>. In the direct method (introduced by Chantrenne and Barrat) or NEMD, it uses temperature gradient across the simulation box (Fourier's Law of conduction) to measure thermal conductivity. Other in-direct method (introduced by Green-Kub) or EMD, it uses the fluctuation-dissipation theorem to find out the thermal conductivity. Other important property is coefficient of thermal expansion which can be detected using MD simulation at atomic level in few femtosecond (fs).

**iii) Enhancement of Corrosion Properties:**

In the corrosion phenomena, the diffusion processes among atoms is the key factor. The MD simulation helps to find out surface interaction between corroded surfaces with corroding medium in different temperatures. According to Schmidt et al.<sup>39</sup>, molecular modeling and simulation are very much helpful to understand corrosion mechanisms with a view to develop more durable surface coatings in the future. MD simulations help to obtain full atomistic information in the corrosion mechanism. It can predict adsorption characteristics as well as interaction energy between inhibitors and surfaces.

**iv) Enhancement of Tribological Properties:**

Dynamic simulation provides better information of the mechanisms of the enhanced tribological (i.e., lower friction coefficients and abrasion rates) information at the atomic level. This is done by applying shear loading ( $\text{\AA}/\text{picoseconds}$  [ps]) for some time steps (ps) between upper and lower layers of the nanocomposite to determine the friction coefficient. However, some researchers worked on enhancement of various properties using MD modeling and simulation, for example, Sharma et al.<sup>41,42</sup>, Chawla and Sharma,<sup>9,10</sup> Li et al.<sup>22-24</sup> and Talapatra et al.<sup>49-53</sup> used MD to predict the different properties of PNCs.

#### 4.4 BASIC STEPS OF MD MODELING AND SIMULATION

Basic steps of MD simulation are

- i) Building the atomistic models or drawing the molecules
- ii) Geometric optimization
- iii) Assigning velocity
- iv) Calculating the potential energy using the adopted force field
- v) Finding the resultant force acting on each atom
- vi) Updating velocities, positions of each atom
- vii) Extracting properties.

Figure 4.5 illustrates details flow chart of MD simulation as shown below.

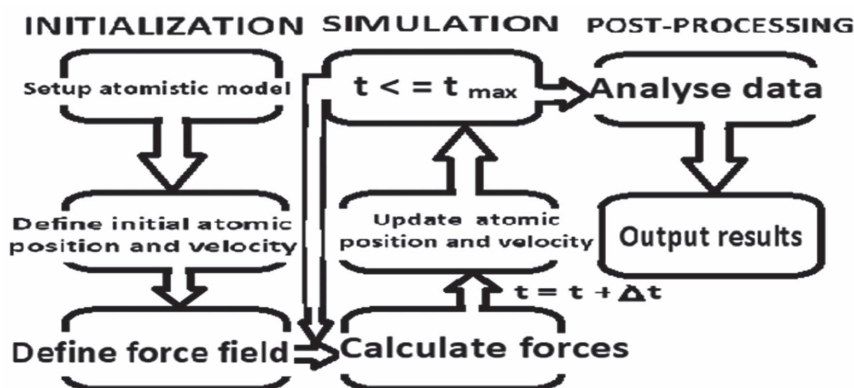


FIGURE 4.5 Flow chart of MD simulation.

##### i) Building the atomistic models or drawing molecules

To design atomistic model for crystalline and non-crystalline system, we have to follow any one out of two ways, namely (i) importing the structure and (ii) building the structure.

To build the crystalline model, import the model from the MS17 database, following the command (File > Import > Examples > Documents > 3D Model) from the menu bar to get the model required. Then select Build > Build Nanostructure > Nanocluster from the menu bar to set the shape and particle size. Then click the Build button to obtain nanocluster model.

To build the non-crystalline or amorphous model, draw a molecule in 3D atomistic document and set head atom and tail atom from the menu

bar following the command (Build>Build Polymers>Repeat unit) to get the repeated unit. To obtain the model of the polymer chain length and the tacticity, follow the command (Build>Build Polymers>Homopolymer). The Amorphous Cell module is used to develop the periodic structure model of complex amorphous materials.

The boundary of model may be periodic or non-periodic boundary. In periodic boundary conditions (PBCs), the simulation box is replicated throughout space to form an infinite lattice. PBC eliminates the effect of vacuum surface. The PBC is very important while calculating mechanical properties.

Unlike PBC, non-periodic boundary condition does not allow any replication of unit cell. It can be in all three-directions or it can be in any specific direction. Non-periodic BCs are important in evaluating thermal properties or interfacial properties.

### ***ii) Geometry optimization or energy minimization (volume reduction)***

Un-optimized structures may give erroneous results because un-optimized structures are made of sketching with high energy configuration. Therefore, the optimization or minimization of PE of the system is very essential before MD simulation. Energy minimization (EM) helps to get lowest energy with stable structure configurations molecular system. Some of the energy minimizing methods (algorithm) used in geometry minimization are steepest descents, conjugate gradient, Newton-Raphson, and simplex method.

### ***iii) Dynamic run (density adjustment)***

The optimized system is then equilibrated at room temperature in the constant temperature and volume canonical (NVT) ensemble over few time in the order of ps by using time step in the order of fs. The compressed system is equilibrated for another time ps in NPT ensemble to generate the correct density due to volume reduction.

### ***Ensembles***

The constant energy surface of a system in MD simulation is not constant due to external pressure and/or exchanges of heat with the environment. Hence, ensembles of MD simulation are required in dynamic run. Different

statistical ensembles are generated depending on state variables (energy,  $E$ ; enthalpy,  $H$ ; number of particles,  $N$ ; pressure,  $P$ ; stress,  $S$ ; temperature,  $T$ ; and volume,  $V$ , etc.). There are different ensembles with different characteristics like Isobaric–Isothermal Ensemble (NPT), Canonical Ensemble (NVT), Microcanonical Ensemble (NVE), NPH Ensemble and Grand Canonical Ensemble ( $\mu VT$ ).

### *Time Integration Algorithm*

Numerous numerical algorithms are available to solve the equations of motion. Accuracy of the simulation depends on the following factors: (i) the algorithm should conserve energy and momentum, (ii) it should be computationally efficient, and (iii) it should permit a long-time step for integration, etc. Some of the time integration methods are Verlet algorithm, Leapfrog algorithm, velocity Verlet algorithm, Beeman's algorithm, the fourth-order Runge–Kutta method, and Predictor–Corrector algorithm.

### *Prescribed potentials (the force-field)*

In MS software, different modules are available for different types of force field. The condensed-phase optimized molecular potentials for atomistic simulation studies (COMPASS), polymer consistent force field (PCFF), universal force field (UFF), and Dreiding are utilized independently in MD simulation for PNCs.

### *Empirical potentials*

These potentials consist of a summation of bonded forces and non-bonded forces which are associated with chemical bonds, bond angles, torsional forces, bond dihedrals, vdW forces, and electrostatic charge.

### *Semi-empirical potentials*

Empirical formulas are used to determine the energy contributions of the orbitals. Such potentials determine the occupancy of the different atomic orbitals.

### *Pair potentials*

The simplest atom–atom interaction is the pair potential, the PE of which only depends on the distance between two atoms. The system total energy is given by summing the energy of all atomic bonds over all  $N$  particles in the system.

*COMPASS force field*

COMPASS, as a member of the consistent force fields (CFF) family, has been widely used in describing the mechanical properties of Gr or CNTs and polymers. The COMPASS force field consists of terms for bonds as well as cross-terms, and two non-bonded functions.

$$E_{\text{total}} = E_b + E_{\theta} + E_{\varphi} + E_{\chi} + E_{b,b'} + E_{b,\theta} + E_{b,\varphi} + E_{\theta,\varphi} \\ + E_{\theta,\theta'} + E_{\theta,\theta',\varphi} + E_q + E_{\text{vdw}} \quad (4.19)$$

where,

$$E_b = \sum [k_2 (b - b_0)^2 + k_3 (b - b_0)^3 + k_4 (b - b_0)^4] \quad (4.20)$$

$$E_{\theta} = \sum [k_2 (\theta - \theta_0)^2 + k_3 (\theta - \theta_0)^3 + k_4 (\theta - \theta_0)^4] \quad (4.21)$$

$$E_{\varphi} = \sum [k_1 (1 - \cos\varphi) + k_2 (1 - \cos 2\varphi) + k_3 (1 - \cos 3\varphi)] \quad (4.22)$$

$$E_{\chi} = \sum k^2 \chi^2 \quad (4.23)$$

$$E_{b,b'} = \sum k (b - b_0) (b' - b_0') \quad (4.24)$$

$$E_{b,\theta} = \sum (b - b_0) (\theta - \theta_0) \quad (4.25)$$

$$E_{b,\varphi} = \sum (b - b_0) [k_1 \cos\varphi + k_2 \cos 2\varphi + k_3 \cos 3\varphi] \quad (4.26)$$

$$E_{\theta,\varphi} = \sum (\theta - \theta_0) [k_1 \cos\varphi + k_2 \cos 2\varphi + k_3 \cos 3\varphi] \quad (4.27)$$

$$E_{\theta,\theta'} = \sum k (\theta - \theta_0) (\theta' - \theta_0') \quad E_{\theta,\theta',\varphi} = \sum k (\theta - \theta_0) (\theta' - \theta_0') \cos\varphi \quad (4.28)$$

$$E_q = \sum \frac{q_i q_j}{ij} \quad (4.29)$$

$$E_{\text{vdw}} = \sum_{ij} \varepsilon_{ij} \left[ 2 \left( \frac{r_{ij}^0}{r_{ij}} \right)^9 - 3 \left( \frac{r_{ij}^0}{r_{ij}} \right)^6 \right] \quad (4.30)$$

where,

$k, k_1, k_2, k_3$  and  $k_4$  = force constants determined experimentally,  
 $b, \theta$  = bond length and bond angle after stretching and bending, respectively,  
 $b_0, \theta_0$  = equilibrium bond length and equilibrium bond angle, respectively,  
 $\varphi$  = bond torsion angle,  $\chi$  = out of plane inversion angle.

$E_{b,b'}, E_{\theta,\theta'}, E_{b,\theta}, E_{b,\varphi}, E_{\theta,\varphi}, E_{\theta,\theta',\varphi}$  = cross terms representing the energy due to interaction between bond stretch–bond stretch, bond bend–bond bend, bond stretch–bond bend, bond stretch–bond torsion, bond bend–bond torsion, and bond bend–bond bend–bond torsion, respectively.

$\varepsilon_{ij}$  = well depth or bond dissociation energy,

$r_{ij}^0$  = distance at which the interaction energy between the two atoms is zero;

$r_{ij}$  = separation between the atoms/molecules,  $q_i, q_j$  = atomic charges on the atoms/molecules,

$\varepsilon_0$  = permittivity of free space.

### *Multi-body potentials*

Multi-body potentials can capture possible edge or surface effects. One of the most popular multi-body potentials is embedded atom method (EAM) potential, which can describe the atomistic interactions in metallic materials. It was first developed by Daw and Baskes (1984) for studying the defects in the metals. EAMs are widely used in MD simulations. Tersoff potential is a three-body potential, which works well in the simulation of a variety of characteristics of C–C covalent bonds, for instance, bond length, bond angle, bond energy, lattice constant, and the dynamic behavior of bonds' cleavage and restructuring, and so on. Examples of multi-body potentials include EAM, Finnis/Sinclair EAM, modified EAM, etc.

### *Bond order and reactive potentials*

Based on the concept of bond orders, a new class of multi-body potentials is developed to describe the atomistic interactions in covalently bonded materials, such as carbon-based materials (fullerene, CNT, and Gr). The commonly used interaction potential functions include Tersoff, Tersoff–Brenner, reactive empirical bond order (REBO), and AIREBO potentials. Brenner developed an improved version of the Tersoff potential mainly in the aspect of the bond order function, resulting in the Tersoff–Brenner potential. It is mainly used to describe the chemical bond interaction potential between small molecules composed of hydrogen atoms or carbon atoms, for instance to simulate the mechanical properties of CNTs. REBO potential amends the Tersoff–Brenner potential and introduces multi-body potentials effects and local atomic environment effects. REBO potential can accurately reflect the chemical bonds energy between atoms, but lacks description of the long-range interaction potential, for example, the vdW forces between molecules is ignored in the potential. The AIREBO potential is actually the improved form of the REBO potential. It includes long-range interactions and torsion terms. There are other potential functions such as the polarizable potentials, potentials for polymers, etc. These are not discussed here as they have not been used in the present work.

### *Polarizable potentials*

During the 1990s, the first general polarizable force fields appeared. The PIPF (polarizable intermolecular potential function), DRF90, and AMOEBA force fields are good examples of such developments. For systems like water and protein, better simulation results obtained by introducing polarizability.

### *Potential for polymers*

The simulations of polymers depend on the force fields that describe the various chemical interactions based on a combination of energy terms. One of the most popular force fields for polymers is *ab initio* force field PCFF.

### *Cut-off distance*

Cut-off distance is a vital factor to obtain desirable degree of cross-linked structures. The cut-off distance for the vdW force is assigned in such a way that beyond this distance, there are no further vdW interactions take place. Therefore, cut-off radius ( $r_{\text{cut}}$ ) represents an effective maximum range for the vdW forces. The cut-off value should be adopted to avoid highly strained structures, that is, small cut-off values will lead to small degrees of cross linking. Cut-off radius is very important in non-bonded interaction calculation. The non-bonded interactions consist of short-range vdW interactions and long-range electrostatic interactions (Lennard–Jones (LJ) 9–6 and Coulombic functions). The atom-based summation method with cut-off radius is used to calculate vdW interactions whereas Ewald summation method is used to calculate electrostatic interactions. The possible shortest distance between two carbon atoms in atomic structure of Gr for the vdW interaction is 2.84 Å. Thus, the vdW calculation for carbon atoms with inter-atomic distance greater than 2.84 Å is considered.

The vdW interactions within 2.84 Å and the cut-off range are considered as the higher order vdW interaction. For example, increase in vdW interaction decreases the Young's modulus of material. Therefore, cut-off distance plays a vital rule for investigation for the enhancement of properties.

### *Temperature and pressure control methods*

Before the production run, the temperature and pressure are needed to be stabilized for the structure. The barostat and thermostat is used to control the pressure and temperature in MD simulation. The algorithms which are used to control the pressure of an NPH or NPT simulation (i) Andersen, (ii) Berendsen (default), (iii) Parrinello, and (iv) Souza-Martins, etc. The



Thermostat allows selecting the temperature control method to be used for a dynamics simulation. The algorithms are used to control the temperature of an NVT or NPT simulation (i) Velocity Scale, (ii) Nose (default in MS 17), (iii) thermostat (otherwise known as the Nosé-Hoover thermostat), (iv) Andersen, (v) Berendsen, and (vi) NHL, etc.

#### **iv) Determination of properties**

Selection of module is very important to calculate enhanced properties in material studio software. The stable structure calculations are based on the last 10 frames. Equilibrated system was subjected to uniaxial deformation to develop stress–strain diagram.

Three main approaches are available in MS 17,

- a) Static (constant–strain minimization) Theodorou and Suter et al.<sup>54</sup> and Raaska et al.<sup>34</sup>
- b) Dynamics (constant–stress MD)<sup>6,8</sup>
- c) Fluctuation formula (Parrinello et al.<sup>33</sup>, Ray et al.1988 and Gusev et al.<sup>14</sup>

Stress in MD simulations can be interpreted using either Cauchy stress or virial stress. Virial stresses relevant to a discrete particle system have equivalence to the continuum Cauchy stress. In fact, there are two schools of thought on this. One of them is based on Zhou et al.<sup>57</sup> where it is mentioned that the potential contribution (depending on interatomic forces and atomic positions) to the virial stress should be considered as the continuum Cauchy stress. The other one, however, assert that virial stress contain both the kinetic and potential parts together and is known as the Cauchy stress in continuum mechanics.<sup>58</sup> The second definition actually has been taken in the current work. The developed stress in the system due to applied unidirectional strain is written in terms of average hydrostatic stress. After every applied deformation, the running averaged hydrostatic stress  $\sigma$  is calculated in order to smooth the stress–strain response. The Young's modulus is also obtained from the slope of the linear regime of the stress–strain curve performing a regression analysis. The virial theorem was used due to its better accuracy over the energy approach. The stress components  $\sigma_{ij}$  (both tensile and compressive) can be calculated from virial expression,

$$\sigma_{ij} = -\frac{1}{Vol} \left[ \left( \sum_{i=1}^N m_i (v_i v_i^T) \right) + \left( \sum_{i < j} r_{ij} f_{ij}^T \right) \right] \quad (4.31)$$

Vol: Volume of the simulation box,

$m_i$ : Mass of  $i^{\text{th}}$  atom,  $v_i$ : Velocity of  $i^{\text{th}}$  atom,  
 $N$ : Total number of atoms,  $r_{ij}$ : Distance between  $i^{\text{th}}$  and  $j^{\text{th}}$  atoms,  
 $f_{ij}^T$ : Force exerted on  $j^{\text{th}}$  atom by  $i^{\text{th}}$  atom.

The above virial stress corresponds true stress. The first term is associated with the kinetic energy due to thermal vibrations, and the second term is associated with the PE due to the applied deformation. If the model is simulated at 1 K, the temperature effect was neglected in the stress computation as shown in the equation,

$$\sigma_{ij} = -\frac{1}{Vol} \left[ \left( \sum_{i < j} r_{ij} f_{ij}^T \right) \right] \quad (4.32)$$

Where  $r_{ij}$  and  $f_{ij}$  denote the atomic distance and the corresponding interaction force between any two atoms, respectively. Vol represents the total volume of the simulation cell.

Hence, for series of six uniaxial strains in the unit cell (simulation box) undergoes tensile and compressive deformations in all six directions.

$$\text{Six uniaxial strains } \epsilon = [\epsilon_{11} \ \epsilon_{22} \ \epsilon_{33} \ \epsilon_{12} \ \epsilon_{23} \ \epsilon_{31}]^T$$

The stress can be represented as an average of all the principle stresses or “hydrostatic stress.” So, for any small applied strain  $\epsilon$ , the average stress in the system is calculated using eq 4.24. Each stress component is calculated from the virial stress expression. The averaged hydrostatic stress,

$$\text{Hydrostatic stress} = \sigma_{\text{average hydrostatic}} = \left( \frac{\sigma_{11} + \sigma_{22} + \sigma_{33}}{3} \right) \quad (4.33)$$

$\sigma$  = Stresses in principle directions

In the case of linear elastic materials, the stress–strain behavior can be described by generalized Hooke’s law:

$$\sigma_{ij} = C_{ijkl} \epsilon_{kl} \quad (4.34)$$

where  $i, j, k, l = 1$  to 3.  $\sigma_{ij}$ ,  $C_{ijkl}$ , and  $\epsilon_{kl}$  are stress, stiffness, and strain tensors, respectively. The forth-order stiffness tensor has, in general, 81 components. The symmetry property of the stress and strain tensors ( $\sigma_{ij} = \sigma_{ji}$  and  $\epsilon_{kl} = \epsilon_{lk}$ ) leads to minor symmetries of the stiffness tensor, that is,  $C_{ijkl} = C_{jikl}$  and  $C_{ijkl} = C_{ijlk}$ , and consequently, results in reduction of independent components to 36. On the other hand, major symmetry of the stiffness tensor reduces the number of independent components to 21. Therefore, we can be written in a second-order form, using Voigt notation:

$$\sigma_i = C_{ij} \varepsilon_j \quad (4.35)$$

Where,  $\sigma_i$  and  $\varepsilon_i$  are the six-dimensional stress and strain vectors, and  $C_{ij}$  is the  $(6 \times 6)$  stiffness matrix. The full  $(6 \times 6)$  stiffness matrices were built up from the slopes  $\partial\sigma/\partial\varepsilon$  in tension and shear. By following the concept of continuum mechanics, the constitutive relation of nanocomposites in terms of the stiffness matrix  $[C]$  can be calculated as the derivative of the stress associated with the corresponding strain component.

$$\begin{bmatrix} C_{11} & C_{12} & C_{13} & C_{00} & C_{00} & C_{00} \\ C_{12} & C_{22} & C_{23} & C_{00} & C_{00} & C_{00} \\ C_{13} & C_{23} & C_{33} & C_{00} & C_{00} & C_{00} \\ C_{00} & C_{00} & C_{00} & C_{44} & C_{00} & C_{00} \\ C_{00} & C_{00} & C_{00} & C_{00} & C_{00} & C_{66} \end{bmatrix}$$

For an isotropic material, the stiffness matrix may be expressed by specifying only two independent coefficients, that is, the Lamé coefficients,  $\lambda$  and  $\mu$ , and the resulting stiffness matrix can be written as:

$$\begin{bmatrix} \lambda + 2\mu & \lambda & \lambda & 0 & 0 & 0 \\ \lambda & \lambda + 2\mu & \lambda & 0 & 0 & 0 \\ \lambda & \lambda & \lambda + 2\mu & 0 & 0 & 0 \\ 0 & 0 & 0 & \lambda + 2\mu & 0 & 0 \\ 0 & 0 & 0 & 0 & \lambda + 2\mu & 0 \\ 0 & 0 & 0 & 0 & 0 & \lambda + 2\mu \end{bmatrix}$$

The coefficients of the stiffness matrix ( $C_{ij}$ ) and can be related to the Lamé coefficients as:

$$C_{11} = C_{22} = C_{33} = (\lambda + 2\mu) \quad (4.36)$$

$$C_{44} = C_{55} = C_{66} = \mu \quad (4.37)$$

$$C_{11} - C_{12} = 2\mu \quad (4.38)$$

Bulk ( $K$ ) and shear modulus ( $G$ ) can be computed using Voigt definitions from the elastic stiffness matrix.

$$K_{Voigt} = \frac{1}{9} (C_{11} + C_{22} + C_{33} + 2(C_{11} + C_{13} + C_{23})) = \left( \lambda + \frac{2\mu}{3} \right) \quad (4.39)$$

$$G_{Voigt} = \frac{1}{15} (C_{11} + C_{22} + C_{33} + 3(C_{44} + C_{55} + C_{66}) - C_{12} - C_{13} - C_{23}) = \mu \quad (4.40)$$

Young's modulus (E) is can be computed from the following equation:

$$E = \frac{9KG}{3K + G} = \mu \frac{(3\lambda + 2\mu)}{(\lambda + \mu)} \quad (4.41)$$

Poisson's ratio ( $\nu$ ) which is the ratio of lateral to longitudinal strain can be computed from the following equation:

$$\nu = \frac{3K - 2G}{6K + 2G} = \frac{\lambda}{2(\lambda + \mu)} \quad (4.42)$$

#### *Calculation of modulus:*

One may apply a small amount of strain component to the simulation cell in one direction, while keeping the other strain components fixed. The negative sign pressure is used to express tensile stress whereas positive sign is used to express compression (default value). The simulation box is volumetrically strained by applying equal strains along all the three axes. The average shear modulus is determined by applying equal shear strains on the simulation box in xy, xz, and yz planes. Based on the calculated bulk and shear modulus, Young's modulus (E) and Poisson's ratio are determined.

#### *Calculations of hardness:*

The improvement of hardness of the nanocomposite is possible to be measured using MD modeling and simulations. The hardness of nanocomposite structures is given by depth of the indentations. The normal impact loading is used to measure the depths of the indentations.

#### *Calculation of toughness:*

Fracture phenomenon can be characterized through parameters such as strain energy release rate (G), stress intensity factor (K), and J-integral (J). The critical values of these parameters represent the fracture strength of a material. Stress intensity factor (K) and strain energy release rate (G) are applicable only in the linear and elastic range of the stress-strain response of the material. On the other end, J-integral is applicable in the non-linear case. The critical value of J-integral at crack initiation is directly related to fracture toughness of the material. The value of J is a function of crack length. The crack growth provides the resistance of the material or R-curve. MD simulation is used to compute atomistic J-integral which is essential to know the influence of nano-fillers (such as Gr) on fracture toughness of a polymer. In

MD simulation, the critical fracture toughness can be calculated by using two methods, namely periodic cracks method and the crack-tip displacement method. The fracture toughness for a given level of stress is described by Tada's equation.  $K_I$  is given by,

$$K_I = \sigma \sqrt{w \tan \frac{\pi a}{w}} \quad (4.43)$$

Where,  $a$  is the half-crack length and  $w$  is the width of the sample. MD approach can deliver detailed information on the deformation and damage mechanisms at the nanoscale. Interfacial debonding is the most likely source of damage nucleation and initiation. Cracks morphology in the unit cells can be detected for the effect of reinforced orientation (aligned and random). One can analyze fiber/matrix polymer interface effects, as well as the role of structural defects (weak interfaces, clustering, various orientations, etc.) on the damage initiation and fracture of the composites.

#### *Calculation of interaction energy*

The energy at the interface molecular cell is thus defined by

$$E_{A-B} = E_T - (E_A + E_B) \quad (4.44)$$

Where,  $E_T$  is the total energy of the entire layered cell, while  $E_A$  and  $E_B$  are the energies of the individual molecular models, and  $E_{A-B}$  defines the energy at the interface.

The interaction energy (IE) at the interface is given by,

$$\gamma = \frac{E_{A-B}}{NA} \quad (4.45)$$

Where,  $N$  is the number of moles and  $A$  is the interfacing lattice area in squared angstroms.

#### *Calculation of interfacial properties:*

MD simulations are carried out for fiber/polymer separation energies calculation. The separation energy (shear or normal) is defined as the energy difference. The interfacial shear stress can be calculated,  $\tau_s$  and  $\sigma_n$ , by the following:

$$E_{separation} = \int_0^{\Delta x} F_{separation} dx \quad (4.46)$$

$$\tau_{shear} = \frac{E_{shear}}{WL^2} \quad (4.47)$$

$$\sigma_{normal} = \frac{E_{normal}}{WL} \quad (4.48)$$

Where, W and L are the width and length, respectively, and x is the displacement of the fiber layer. Two separations, that is, normal separation and shear separation is conducted to evaluate the Gr/polymer interfacial normal strength (IFNS) and interfacial shear strength (IFSS), respectively.

*Special characterization of simulated molecular models:*

- **Mean square displacement (MSD):** MSD in uniaxial direction during quasi-static deformation process represent the diffusion of atoms into the newly elongated unit cell. The diffusion coefficients are calculated from the mean square displacement (MSD).
- **Radial distribution functions (RDF):** Radial distribution function (RDF) or pair correlation function (g(r)) gives insight into the structure and phase of material, that is, whether the material is in a solid, liquid, or gaseous state. Radial distribution function is measure of arrangement of atoms in material.
- **The free volume and Connolly surface:** A Connolly surface is the vdW surface of the model that is accessible to a solvent molecule having a non-zero radius. Free volume measurements have been carried out using atom volumes & surfaces tools in MS 17.
- **Atom density:** Atom density in a unit cell is changed with respect to different wt%. Mechanical properties improvement is totally dependent on the atom density in the unit cell.
- **Evolution in molecular energy:** The applied strain causes change in atom positions, velocities, and overall molecular structure which resulting an increase in overall PE, that is, the energy in each system gradually increases with increasing applied strain. PE consists of molecular energy and vdW energy. The PE has comparatively larger contribution in total molecular energy than vdW energy.
- **Molecular configuration:** Different packing configurations but all with same density were packed to accommodate for randomization due to cross linking and orientation.
- **The relative concentration:** The concentration profile in the direction of thickness for 3D periodic structure is calculated using MD

simulation. It is done by computing the profile of atom density within different planes of the periodic crystal.

#### **4.5 BASIC ASSUMPTIONS FOR MD MODELING AND SIMULATION**

- a) In MD modeling and simulation, all the molecules and atoms are considered as a system and the motion of that system is considered by using its own vector positions and velocities.
- b) The study of the system is done by integrating the classical equations of motion for a number of time steps or until some convergence criteria are met. For that, below-mentioned steps are to be followed during MD simulations.
  - i) The initial positions and velocities of every atom are to be described first.
  - ii) Interatomic potentials are used to calculate the forces between every atom.
  - iii) After small-time interval new positions and velocities are identified for the next step.
  - iv) Same procedures are repeated.
- (c) The system total energy is constant. There is no mass transfer or no atoms are leaving or entering within simulation box in the system during simulation.

#### **4.6 ADVANTAGE OF MD MODELING AND SIMULATION**

Experimental methods for prediction of the enhanced properties of nanocomposites are limited because measurements in the scale of nanometers are difficult and costly.

- Properties such as displacements, velocities, acceleration of all particles in the system are based on the equations of motion solution.
- Complete information of atomic trajectories is available within limited simulation time.
- It is possible to study non-equilibrium processes in atomic level (e.g., cluster impact, fracture and crack growth, ion bombardment, etc).
- Intermolecular interaction, that is, force field is the main input of MD simulation and modeling. This enables updation of atomic position and velocity for the next time step precisely.

## 4.7 LIMITATIONS OF THE MD MODELING AND SIMULATION

### *Time and size limitations*

MD simulations are required to analyze a system with thousands of atoms within a few fs that calls for highly efficient computers.

### *Realism of forces*

The interatomic forces are related to the gradient of PE function which is very essential for accurate simulation. Therefore, the realism of forces totally depends on the chosen potential.

### *Boundary conditions*

In MD simulation, rigid or PBCs are generally imposed to represent group of atoms of the system together due to the limitation in the computer power.

### *Time step*

Selection of time step should be such that the simulation takes minimum running time in realistic condition and the atoms motion are continuous. Time step is one of the important parameters in MD simulations, because the right choice of the time step value will lead to stable and accurate results. A time step of 1 fs has been employed in most of the MD analyses in the present study.

## 4.8 MD-BASED SIMULATIONS FOR MECHANICAL CHARACTERIZATION OF GR/PU NANOCOMPOSITES

Gr/TPU nanocomposites have been developed using build layer and packing option in MATERIAL STUDIO. Initially, both models of Gr and TPU unit cells were geometrically minimized separately before constructing the nanocomposite. After the construction of the nanocomposite, the equilibration procedure, similar to the pristine TPU model was applied to the nanocomposite. Final models of Gr/TPU nanocomposite are of three types, (a) Gr concentration models, (b) Stacked Gr/Gr dispersion model, and (c) Interfacial model. MD simulation is a nano level simulation tool which helps to investigate the enhanced mechanical properties like modulus, strength, hardness, toughness, etc. Atomic level simulations for fracture toughness are based on two methods (a) periodic crack method and (b) crack-tip displacement method. The two methods are used to determine the critical



fracture toughness  $K_{IC}$ . MD simulation is a very powerful tool to analyze the atomistic mechanism of nanoindentation process for nanocomposites during hardness calculation.

### *Modeling of single layer Gr (SLGR)*

To build the crystal model of Gr, the ball-and-stick model of Gr from the material database of Material Studio software is imported. Gr sheet is a 2D nano structure consisting of carbon atoms bonded by  $sp^2$  hybridized electrons. The shortest distance of carbon atoms is  $1.42 \text{ \AA}$  with a bond angle of  $120^\circ$ . The Gr ( $14.75 \text{ \AA} \times 17.03 \text{ \AA}$ ) structures considered for this work as shown in Figure 4.6. The unit cell dimension of ( $14.75 \text{ \AA} \times 17.03 \text{ \AA} \times 60 \text{ \AA}$ ) with lattice angles ( $\alpha = \beta = \gamma = 90^\circ$ ) is used in this study. The volume of the Gr sheet is obtained by assuming the thickness of Gr as  $3.4 \text{ \AA}$ . It is noted in the Gr sheet that the dimension of the simulation box in the thickness direction is set to be large enough that the vdW interaction between the neighboring layers cannot be attained.

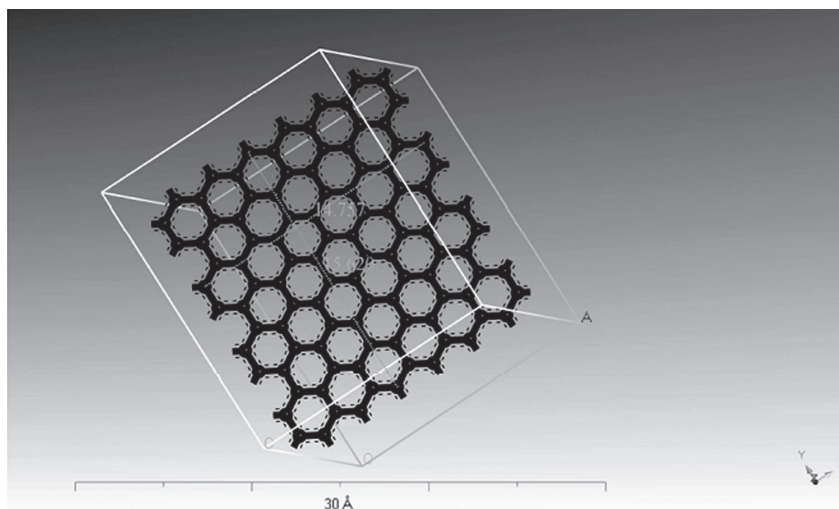


**FIGURE 4.6** Single layer Gr of unit cell dimension ( $14.75 \text{ \AA} \times 17.03 \text{ \AA} \times 60 \text{ \AA}$ ).

A structure energy minimization of geometry is done under dynamic equilibrium run under a dynamic step of  $0.1 \text{ fs}$  with COMPASS force-field.

The atomistic structure with stress-free configuration was obtained by performing an NPT ensemble at  $1 \text{ fs}$  for  $100 \text{ ps}$  (the total iteration steps are  $100,000$ ). The final structure obtained density of  $2.24 \text{ g/cc}$ .

To validate developed model, single layer Gr model with the dimensions of (14.75 Å × 17.03 Å) was analyzed through tensile loading to obtain its mechanical properties.

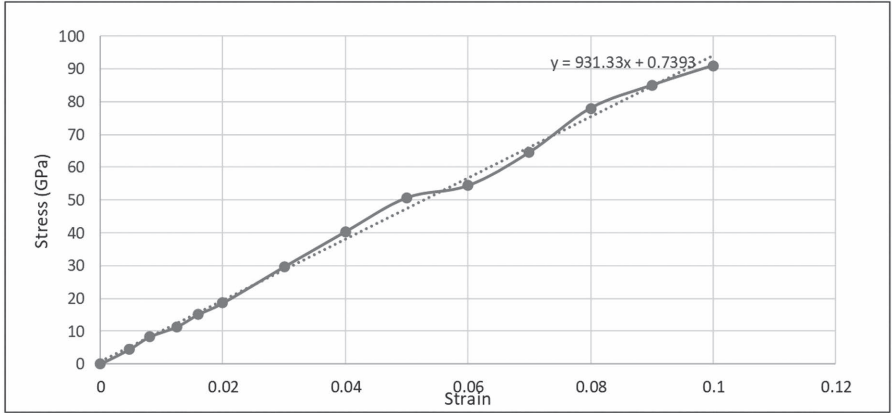


FIGURE 4.7 Stress–Strain diagram of single layer Gr (zigzag).

TABLE 4.2 Comparison of Young’s Modulus of Single Layer Gr with Available in the Literature.

Reference studies	Simulation approach	Elastic modulus (TPa)	Poisson’s ratio
Lu et al. (2009)	MD (REBO)	0.725	0.398
Zhao et al. (2009)	MD (AIREBO)	1.01 ± 0.03	0.21 ± 0.01
Jiang et al. (2012)	MD (COMPASS)	1.0322	–
Gupta et al. (2005)	MD (Brenner potential)	1.272	0.147
Sharma et al. (2016)		1.02	–
Present study	MD (COMPASS)	0.931	0.3
	MD (COMPASS)		

Modeling of thermoplastic polyurethane (TPU)

The elastomer “polyurethane” was discovered in 1937 by Otto Bayer<sup>5</sup> with containing three chemical components, namely di-isocyanate, polyol, and small diol (the chain extender). According to Zhu et al.,<sup>56</sup> TPUs are outstanding material with good resilience and ability to dissipate energy under large mechanical deformation. A segmented di-block TPU is modeled in this simulation study, following the procedure and the analysis described by Kim et al.<sup>18</sup> and Nguyen et al.<sup>31</sup>. The polyols model as shown in Figure 4.10

is related to the soft segment properties; other way, diisocyanate as shown in Figure 4.8 and chain extender model as shown in Figure 4.9 is related to soft segment properties. The TPU model can be represented by hard and soft segments as shown in Figure 4.11. The hard segments contain high amount of polar groups such as urethane and urea linkages, while the soft segments contain less polar structures such as methylene and ether groups. When developing any amorphous polymer molecular models, two issues have to be taken into considerations. First is the time factor, building of bulk polymers can be time consuming, therefore, it is important to choose a building scheme so that the final structure is as correct as possible and built within a reasonable time. Many approaches have been recently used to build cross-linked polymer network structures with more than 70% conversion rate for use in MD simulations. Many different configurations were constructed for randomization due to cross linking and orientation. MD simulation trajectories produced during the molecular modeling of the TPU provide a detailed description of the conformational behavior of the polyurethane chains.

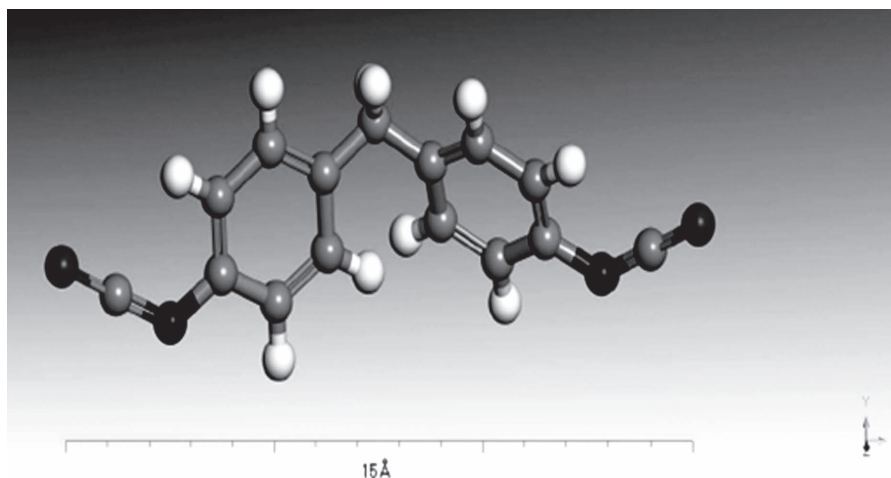


**FIGURE 4.8** 3D models of 4, 4' MDI (curing agent) in MS 17.

Few number of literature reports are available on MD simulation of TPU elastomer. Recently, Lempesis et al.<sup>20</sup> worked on atomistic simulation of TPU and micromechanical Modeling. The ball-and-stick model of cured PU repeat unit is built in the MS 17 as shown in Figure 4.12. The model has five chains in total whereas each chain consists of hard and soft segments. Different configurations of polyurethane chains are generated starting from

the repeat unit using the build polymer tool of the MS 17. Head-to-tail connectivity of the monomers is assumed for all polyurethane models. To estimate the density of the material for an infinite chain length, different amorphous polyurethane models were placed in a cubic periodic box using the Amorphous Cell module of the Material Studio suite of software with increasing chain lengths ( $[C_{12}H_{24}N_2O_4]_n$ ) with  $n = 5$ . For amorphous bulk polymers, it is necessary to build a model at low starting density, and then use energy minimization to obtain a target density.

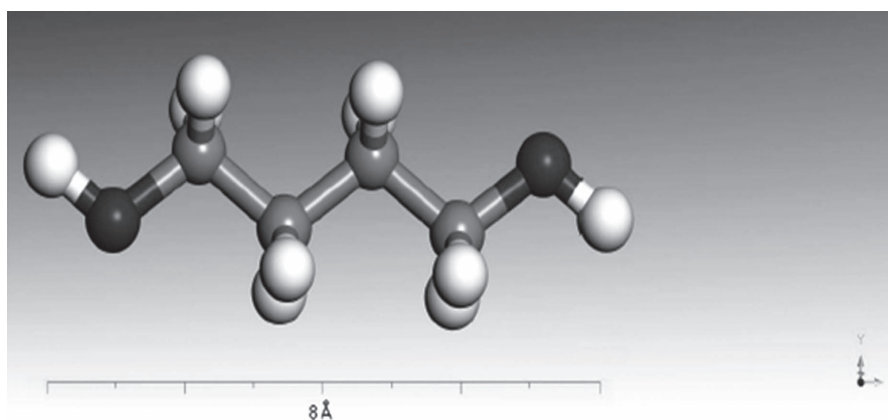


**FIGURE 4.9** 3D models of 1, 4 BDO (Butanediol) in MS 17.

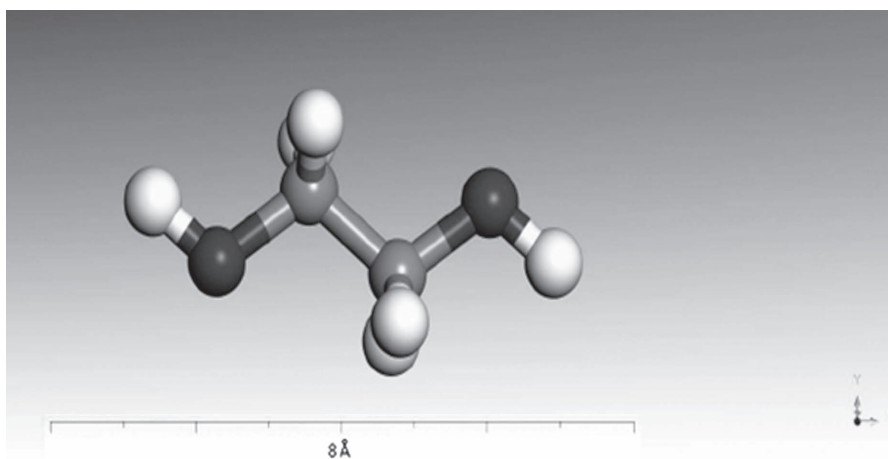


**FIGURE 4.10** 3D models of 1, 2 EDO in MS 17.

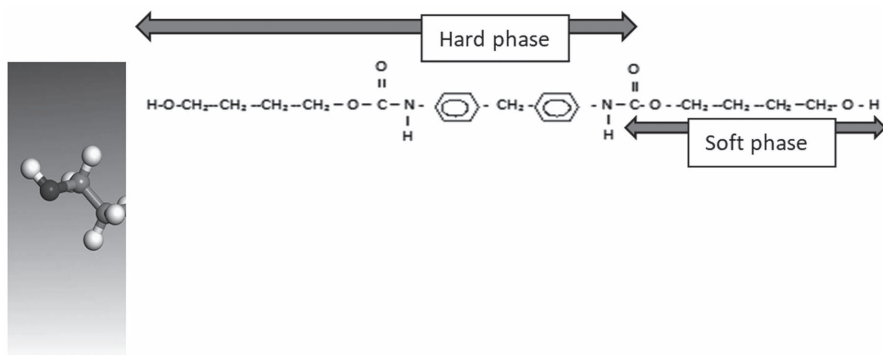


**FIGURE 4.11** 3D models of Cured structure of polyurethanein MS 17.

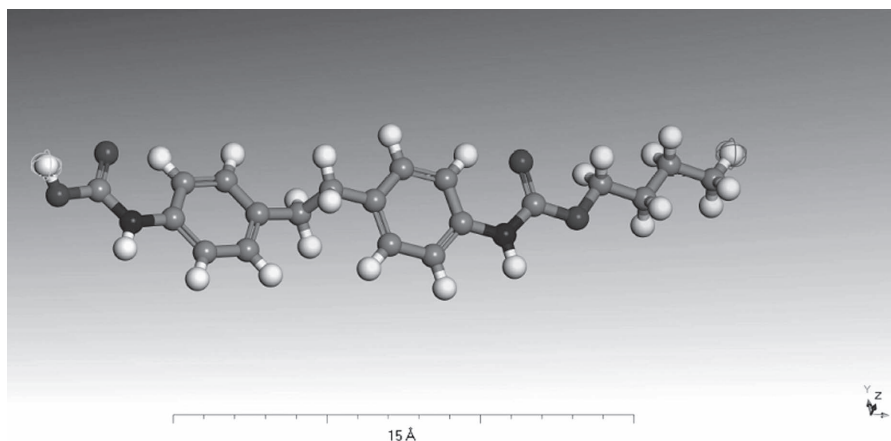


**FIGURE 4.12** 3D models of repeated unit of cured polyurethanein MS 17.

The amorphous polyurethane bulk models were generated at very low initial density of  $0.35 \text{ g/cm}^3$ . Ideally, the densities of the final structure should match the experimental values and be independent of their initial densities. At the end of the equilibrations, the density of the polyurethane is  $0.95 \text{ g/cc}$ . Constructed each TPU chain contains 20 repeating units because earlier studies showed that solubility parameter of TPU remains constant after the nine number of repeat units.

MD simulation contains two steps, namely equilibration and production. Equilibration step allows the molecular structure to obtain the suitable state, while the production step helps to calculate different properties parameters:

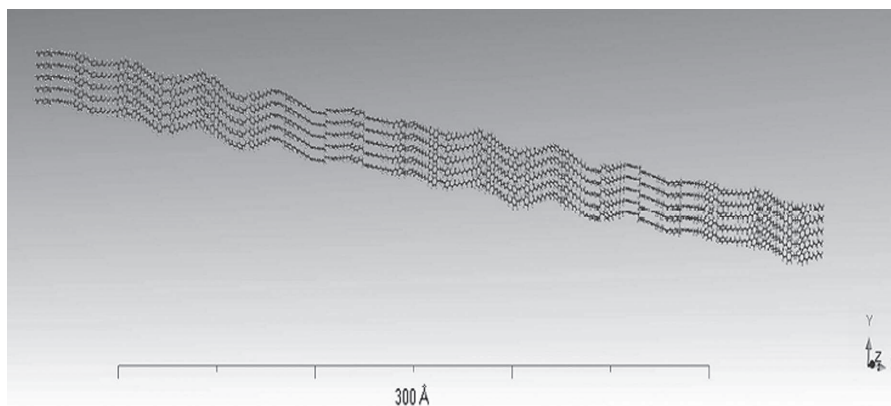


**FIGURE 4.13** 3D model of 5 chain length and 20 repeated unit of TPU in MS 17.

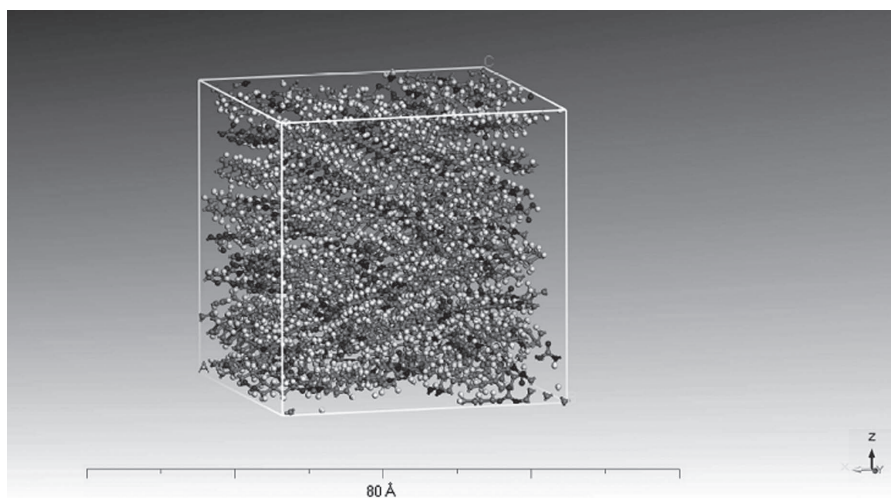


**FIGURE 4.14** Crystal polyurethane models of 20 repeated unit of 5 chain model in MS 17.

specific heat, thermal expansion, and elastic moduli over a specified period of time. In MD, attainment of the equilibrated state depends on the fulfillment of two major factors. The first target is to achieve energy equilibrium condition, and the next second target is to obtain the minimum initial stress state for the periodic boundary cell. MD simulation begins by geometry optimization with energy minimization so that the total energy of the structure is reduced to local minimum. The NVT ensemble helps to obtain homogeneous molecular structure within the simulation box. To find the global minimum, temperature

is periodically increased from an initial temperature (room temperature in this study) to a mid-cycle temperature, for example, 500 K, and then decreased again to the initial temperature. Anneal dynamics is used to capture a global minimum. To get an equilibrium molecular model, the PU full atomic model is heated to 600 K with a 25 K increment (100,000 fs run with a 0.1 fs time step for each 25 K), followed by cooling down to room temperature (glass temperature of TPU is  $-27^{\circ}\text{C}$  and melting temperature of TPU is  $194.8^{\circ}\text{C}$ ). The structure was allowed to relax at in an isobaric-isothermal (NPT) ensemble at temperature of 300 K under a pressure of 1.0 atm for duration of 500 ps with a time step used of 1 fs to achieve an accurate and stable stress-free structure before calculating the mechanical properties of the system. Subsequently, the NPT ensemble was run for 500 ps for all the amorphous polyurethane models to achieve a stress-free state. In the NPT dynamic run, the density increases gradually by reducing the lattice parameter of the unit cell but keeping the axes ( $\alpha = \beta = \gamma = 90^{\circ}$ ) orthogonal to each other. It is important to note that the density observed from the equilibration phase, may differ from experimental density of PU (1.00–1.12 g/cc). There are three methods for property calculation, namely static (constant-strain minimization), dynamics (constant-stress MD), and fluctuation. The static method was used in current study to estimate the mechanical properties of the cured polymer chain structure, via COMPASS force fields.

To compare with the results of with many articles the computational model, five chain length PU crystal ( $40 \text{ \AA} \times 40 \text{ \AA} \times 40 \text{ \AA}$ ) model was analyzed through tensile loading to obtain its mechanical properties.

### *Graphene Concentration Models*

Amorphous unit cells have been constructed with different Gr weight concentrations by using Gr sheets as individual system. PBCs have been applied on each unit cell during the equilibration and deformation process.

### *Model Development (Unit Cell Preparation)*

Rahman et al.<sup>36</sup> developed two different types of concentration models, namely (a) fixed Gr model (FGrM), and (b) varying Gr model (VGrM), and studied three different weight fractions of Gr (1, 3, and 5 wt%). In the FGrM, one Gr layer is fixed and the weight fraction of Gr was varied by changing the number of cured polymer molecules in the unit cell whereas in VGrM, the number of cured polymer molecules is kept constant and changing the weight fraction is by changing the number of Gr sheets in the unit cell. The total number of atoms in FGrMs is lower than in case of

VGrMs. It was observed that Young’s moduli as calculated by FGrMs were slightly lower than from VGrMs. The different weight % Gr-reinforced PU nanocomposites amorphous models were built using construction option in amorphous module within Material studio software. The initial amorphous nanocomposites models were built with a low density of 0.8 g/cm<sup>3</sup> (below the experimental density 1.3 g/c.c) at room temperature and under PBCs. The number of cured polyurethane monomers was determined in such a way which ensures expected wt% of Gr in the unit cell. Amorphous unit cells were constructed with 1, 2, 3, and 4% Gr weight concentrations by using one, two, three, and four Gr sheets in individual system. The number of the atoms within the computational bulk model was chosen according to Hofmann and co-workers suggestions.

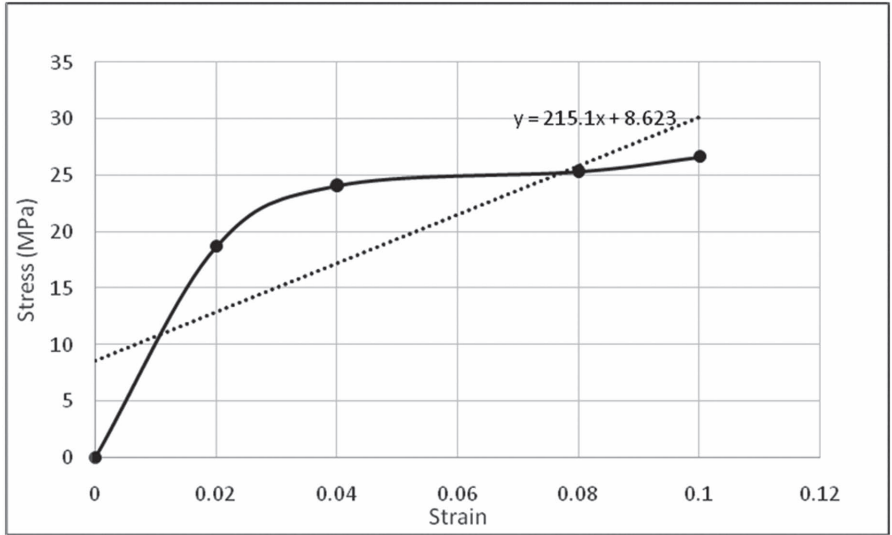


**FIGURE 4.15** Engineering stress–strain diagram of five chain polyurethane.

**TABLE 4.3** Comparison of Young’s modulus of PU with available in the literature.

Reference studies	Approach	Elastic modulus (MPa)	Poisson’s ratio
Uddin et al. (2015)	MD simulation (PCFF)	378	0.48
Njoroge et al.(2009)	MD simulation (Dreiding)	670	0.37
Bicerano et al. (2002)	Experimental	1000	0.43
Martienssen et al. (2005)	Experimental	700	0.43
Present study	MD simulation (COMPASS)	215	0.41



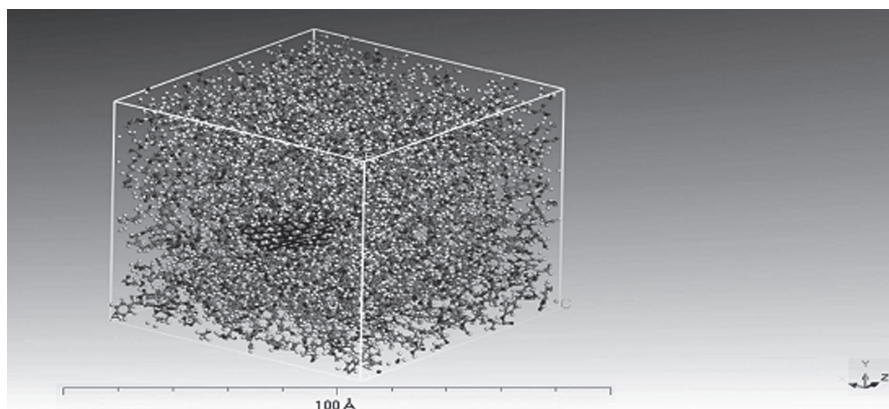


**FIGURE 4.16** Modeling of amorphous system with weight % of Gr as 1%.

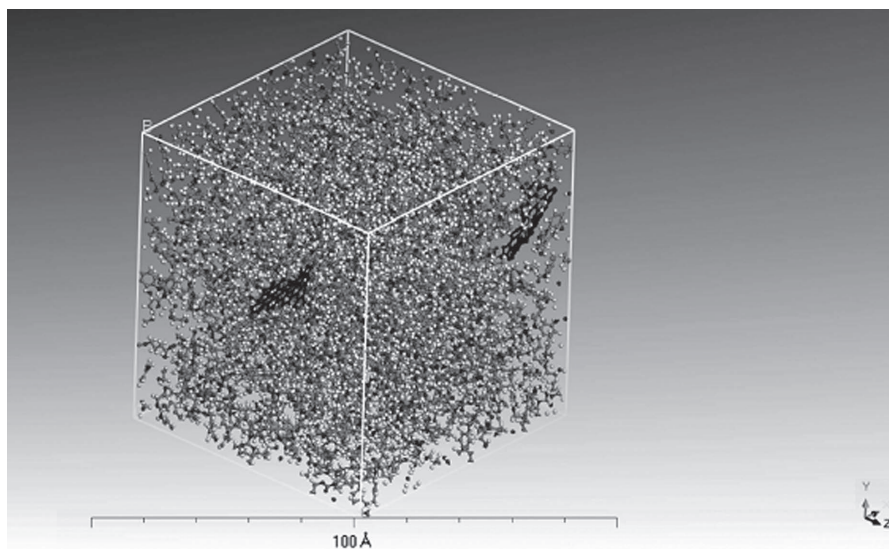


**FIGURE 4.17** Modeling of amorphous system with weight % of Gr as 2%.

*Boundary and constraint conditions:*

The PBC was applied on each simulation box during the dynamic equilibration and uniaxial deformation.

**Force field:** COMPASS force field is considered here which has two function categories, valence terms including the diagonal and off diagonal cross coupling terms, and non-bond interaction terms.

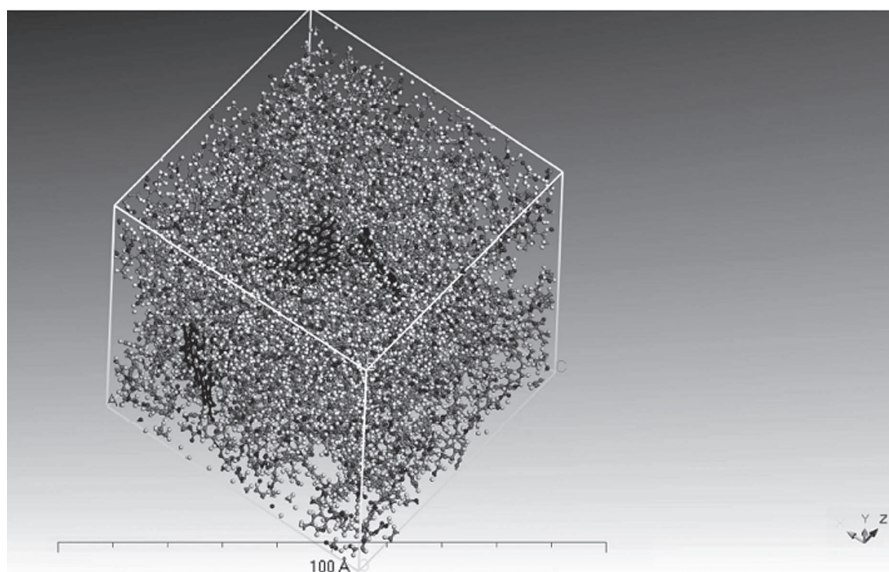


**FIGURE 4.18** Modeling of amorphous system with weight % of Gr as 3%.

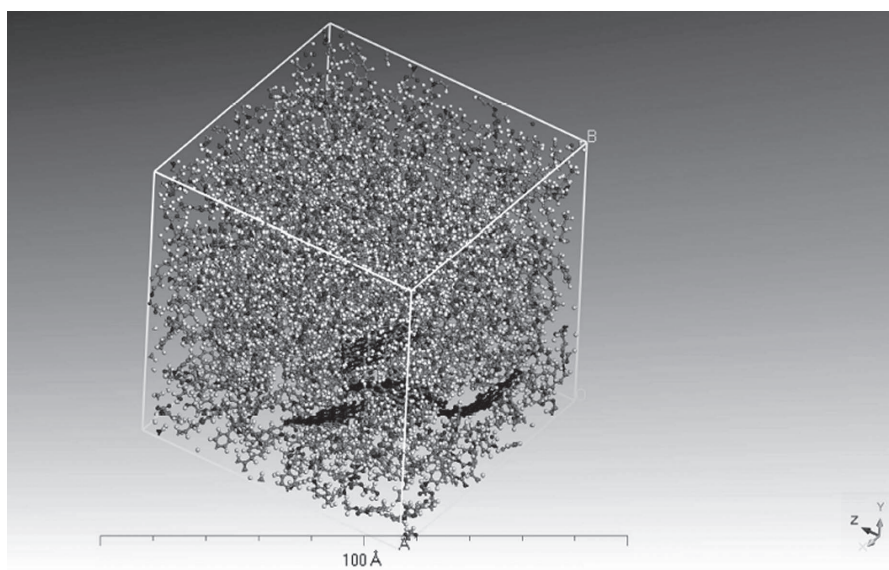


**FIGURE 4.19** Modeling of amorphous system with weight % of Gr as 4%.

*Simulations steps:*

Geometric optimization (energy convergence tolerance of  $1.0\text{e-}4$  kcal/mol and a force convergence tolerance of  $0.0001$  kcal/mol/Å) can be allowed along with the energy minimization in certain MD simulations. To find the global minimum, temperature is periodically increased from an initial temperature (room temperature in this study) to a mid-cycle temperature, for example, 500 K, and then decreased again to the initial temperature. Anneal dynamics help to capture a global minimum. Proper temperature and pressure controlling methods should be chosen after the choice of ensemble to generate the correct statistical ensemble. The Andersen thermostat and the Berendsen barostat were employed in the MD simulations. First, MD simulations were run with NVT ensemble at a temperature of 300 K for 50 ps by using a time step of 1 fs. A large number of iterations are usually needed to bring the system to an equilibrium configuration. Temperature annealing cycle involves a periodic increase in temperature from 100 to 700 K allowing the minimization of energy gradually without trapping the structure in a meta-stable, high-energy but “local” minimum. To further equilibrate the molecular systems, a five-cycle anneal process under NVT ensemble is carried out from 150 to 350 K for 200 ps. Afterward, the systems were equilibrated by NPT MD simulation for 3000 fs at 300 K temperature under 1.0 atm pressure to get accurate and stable structure. The atomistic structure with stress-free configuration was obtained under NPT ensemble with time increments at 1 fs for 20 ps. The profile of instantaneous values of energy was used to decide the cut-off between equilibration and production runs. Figure 4.20 shows equilibrated conditions of the total energy of the system by adjusting the bond energy, bond angle energy, torsional angle energy, and vdW energy after 20 ps run.

After NPT simulation run, the temperature of the system was allowed to attain the equilibrium condition temperature as shown in Figure 4.21. It was observed that the temperature fluctuated around 298 K in a small scale and the energy gradually converged until the system reached equilibrium condition with constant length of unit cell and density.

During NVT simulation run, the temperature of the system was changed to the required range but volume of system remains at constant with a little drop down in bit pressure. The pressure of the system was allowed to bring down to validate the equilibrium state with NPT ensemble. This was used over a period of approximately 50 ps to get the pressure around 1.0 atm as shown in Figure 4.22.

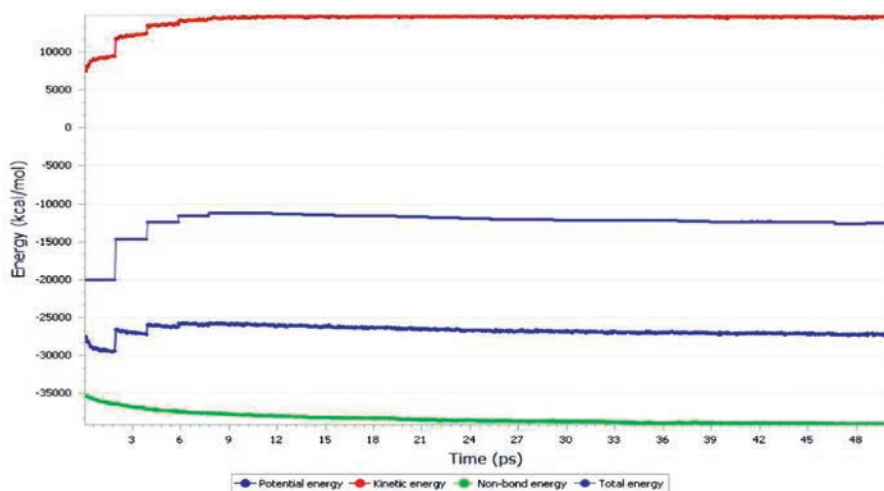


**FIGURE 4.20** Energy–time curve during MD simulation.

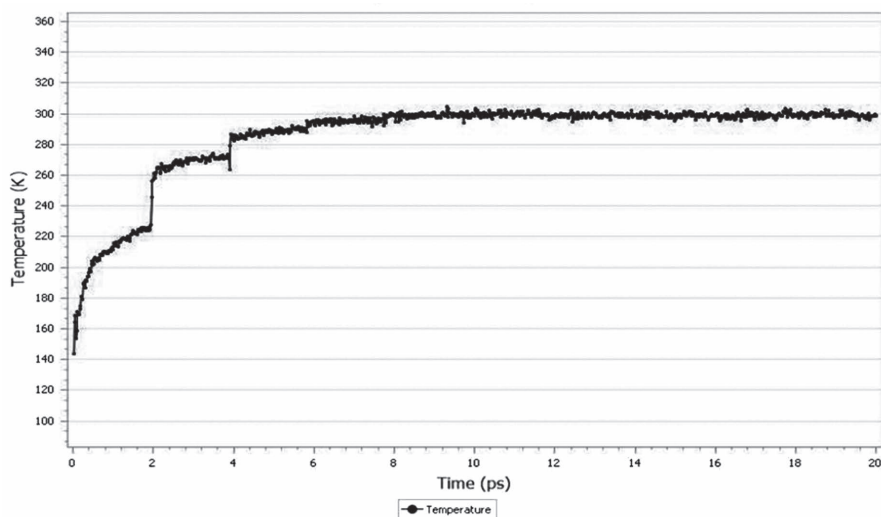


**FIGURE 4.21** Temperature–time curve during MD simulation.

During NPT simulation, volume reduction mechanism happened due to change of cell length as shown in Figure 4.23. Change of cell length dimension continued up to equilibrium condition, that is, after that no change of density of the system took place.

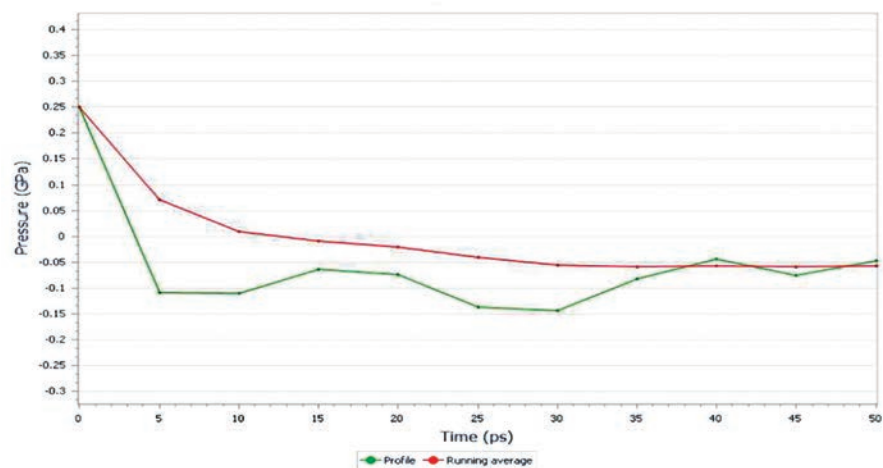


FIGURE 4.22 Pressure (GPa)-time (ps) curve for MD simulation.

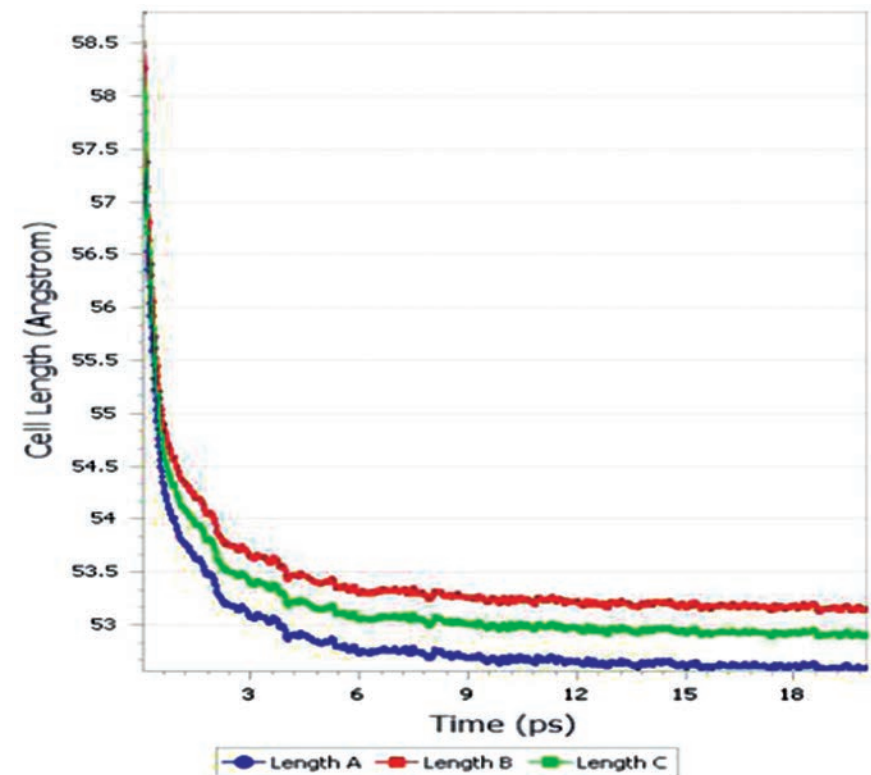
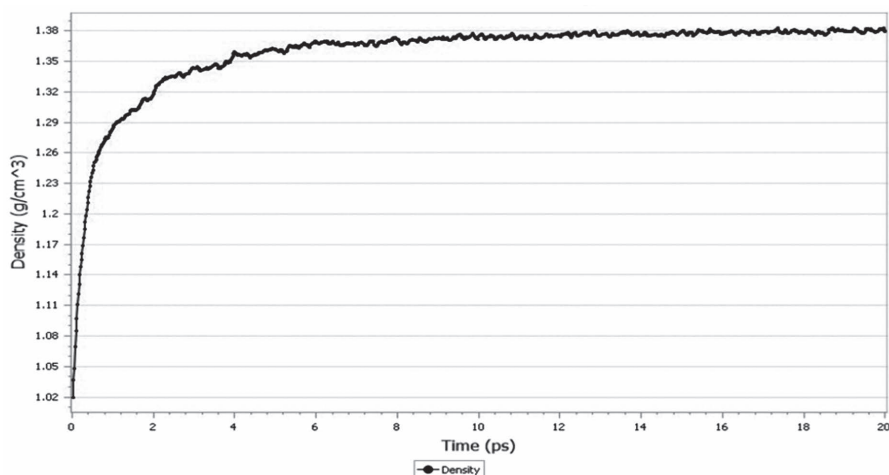


FIGURE 4.23 Cell length-time curve during MD simulation.

To attain an accurate and stable structure, NPT ensemble at temperature of 300 K and pressure of 1.0 atm for time duration of 20 ps with a time step 1 fs was applied. During NPT simulation, system was compressed to a somewhat higher density of 1.3 g/cc that the estimated experimental values as shown Figure 4.24.



**FIGURE 4.24** Density–time plots of Gr/TPU nanocomposites 4% (wt%).

### *Prediction of properties*

Gr nanosheets agglomeration was observed in the several configurations after the equilibration procedure. After the equilibration condition, the Young's modulus and shear modulus of the equilibrated models are calculated by the uniaxial normal and shear deformations, respectively. The Forcite module in MS 17 was used for mechanical properties calculations using the "Constant strain" approach. Elastic constants of the final atomic configuration were computed using the static approach [Theodorou and Suter (1986)]. Theodorou and Suter investigated atomic-level stresses of atomic structures in deformation. They found that the chain topology influences the atomic level stresses strongly. The packing module is used to develop the different weight % of Gr-reinforced nanocomposites unit cell (amorphous system) as shown in Figures 4.16–4.19. Forcite module calculation shows that increase in weight % of Gr lead to decrease in mechanical properties as shown in Table 4.4. Very high weight % (after 1% weight) of Gr decreases Connolly surface of the nanocomposites. High weight % of Gr decreases vdW energy due to polyurethane molecules between Grs. This energy can be analyzed using

mean square displacement (MSD) during deformation process. This lower increase of the Young's moduli displayed by the computational system with highest amount of Gr might be due to the Gr agglomeration. The improvement of the Young's moduli depends on uniform dispersion of Gr and better interfacial interaction between the Gr sheets and the polymer matrix.

**TABLE 4.4** Simulation Result of Amorphous System.

Weight. % of Gr	Total atoms	No of Gr atoms	No of Polymer atoms	Unit cell etails (Å) <sup>3</sup>	Model density (g/c.c)	E (GPa)	G (GPa)	K (GPa)	μ
1%	16220	104	16116	(62.8) <sup>3</sup>	1.3	1.007	1.084	4.553	0.321
2%	16324	208	16116	(63) <sup>3</sup>	1.3	1.046	1.074	4.245	0.270
3%	16428	312	16116	(63.2) <sup>3</sup>	1.3	1.313	1.054	3.840	0.289
4%	16532	416	16116	(63.4) <sup>3</sup>	1.3	0.139	1.925	7.128	0.255

#### *Effect of Gr weight concentration on stress–strain response*

The stress–strain response was calculated while deforming the unit cells under isothermal condition. Temperature was kept very low while deforming the unit cells. This was done in order to reduce the effect of kinetic energy on system's overall stress. Hence, the change in stress was mostly dependent on the topological deformation (i.e., change in bond, angle, or dihedral energy) of the amorphous polymer chains.

The MD simulation showed Young's moduli to have an increasing trend with respect to increasing wt% of Gr. It is observed from the slopes of stress–strain diagram that Gr enhances Young's modulus of Gr/PU nanocomposites compared to neat PU. This decrease of the Young's moduli of Gr/PU nanocomposites with highest amount of Gr might be due to the Gr agglomeration.

Gr agglomeration will lead to a highly inhomogeneous and anisotropic system with very poor mechanical properties. In simulation level, Park et al. (1996) first reported the aggregation of Gr sheets in Gr/water systems and Li et al. (1997) reported the self-assembly behavior of Grs in Gr/Polyethylene systems. The presence of Gr in higher concentration increased the possibility of void content due to inter Gr layer gap and Gr-polymer gap.

#### *Stacked Gr or Gr dispersion model*

This model of Gr/PU nanocomposite consists of a sandwiched structure of Gr-reinforced polyurethane matrix. The objective of the study to know the



stacking effects of single, dispersed and agglomerated Gr on the mechanical properties of the Gr/PU nanocomposite sandwiched structure.

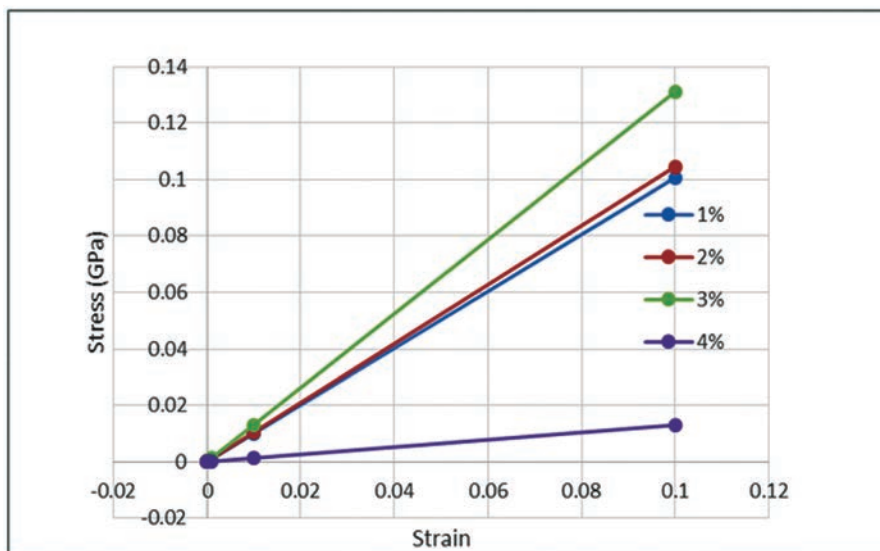


**FIGURE 4.25** Stress-strain diagram of different wt% of Gr/PU nanocomposite.

### *Model development (unit cell preparation)*

Three different dispersion models are constructed based on single, dispersed, and agglomerated Gr. The MATERIAL STUDIO Amorphous module packing option is used to develop the three types of Gr-reinforced polyurethane nanocomposites dispersion models unit cells. Each dispersion model, Gr/PU unit cell contains 3% (weight %) of Gr. The spacing between Gr and polyurethane matrix is less than 3 Å (average). Periodic boundary condition is applied in all the dispersion models unit cells as like as concentration model.

**Boundary and constraint conditions:** In the equilibrium stage, the Gr atoms were constrained (rigid structure) in such a way that the compression-energy minimization-anneal dynamic cycle applied in the  $z$  direction and had no effect on bulk Gr structure. We increased the density gradually by reducing the lattice parameter of the dispersion model unit cell (adjusting the cell dimension in the  $z$ -direction) but keeping the axis ( $\alpha = \beta = \gamma = 90^\circ$ ) orthogonal to each other. The non-constrained parts (the chains of the polymer structures) were compressed in such a way so that density increased nearly to



the estimated experimental values (1.3 g/cc). In the NVT ensemble, the Gr were fixed at their original position throughout the simulation. The reason behind this is to relax the chains of the polymer structure to an equilibrated structure without changing the Gr structure.

**Force field:** COMPASS force field is used in the MD-based simulations study. In the COMPASS force field the total PE is composed of diagonal (bond stretching, bond angle bending, torsion angle rotations, and Wilson out-of-plane angle potentials), off-diagonal cross-coupling (interactions between diagonal terms) terms and non-bonded energy (vdW, hydrogen bond Coulombic functions).

$$E_{\text{Total}} = E_b + E_\theta + E_\varphi + E_\chi + E_{b,b} + E_{b,\theta} + E_{b,\varphi} + E_{\theta,\varphi} + E_{\theta,\theta} + E_{\theta,\varphi} + E_q + E_{\text{vdW}} \quad (4.49)$$

Where,

$E_b$  = covalent bond-stretching energy,

$E_\theta$  = bond-angle bending energy,

$E_\varphi$  = torsion-angle rotation energy,

$E_\chi$  = out-of-plane energy,

$E_q$  = electrostatic energy,

$E_{\text{vdW}}$  = van der Walls energy and,

$E_{b,b}$ ,  $E_{b,\theta}$ ,  $E_{b,\varphi}$ ,  $E_{\theta,\varphi}$ ,  $E_{\theta,\theta}$ ,  $E_{\theta,\varphi}$  = cross terms representing the energy due to the interaction between bond stretch-bond stretch, bond stretch-bond bend, bond stretch-bond torsion, bond bend-bond torsion, bond bend-bond bend and bond bend-bond bend-bond torsion, respectively.

### Simulations steps

MD simulations involve two stages, namely (1) equilibration stage and (2) productions stage. Equilibration stage helps to obtain the desired thermodynamic condition, whereas the production stage enables one to calculated thermodynamic parameters: specific heat, thermal expansion, and elastic moduli over a specified period of time. It is also necessary to apply equilibrium condition prior to applying deformation in dispersion models as like as concentration models.

The purpose of the equilibrated state depends on two factors (i) prescribed temperature energy stabilized and (ii) minimum initial stress state for the periodic unit cell. The equilibrated molecular structure of Gr/PU nocomposites with minimized energy was accomplished by sequentially performing the NVT and NPT ensembles in the MD simulation, with a time

increment of 1 fs. To obtain energy, stabilized all unit cell models were subjected to an energy minimization and NVT dynamic simulations with temperature annealing cycle consecutively. This purpose of the step is to increase the density of the model by decreasing the simulation box size.

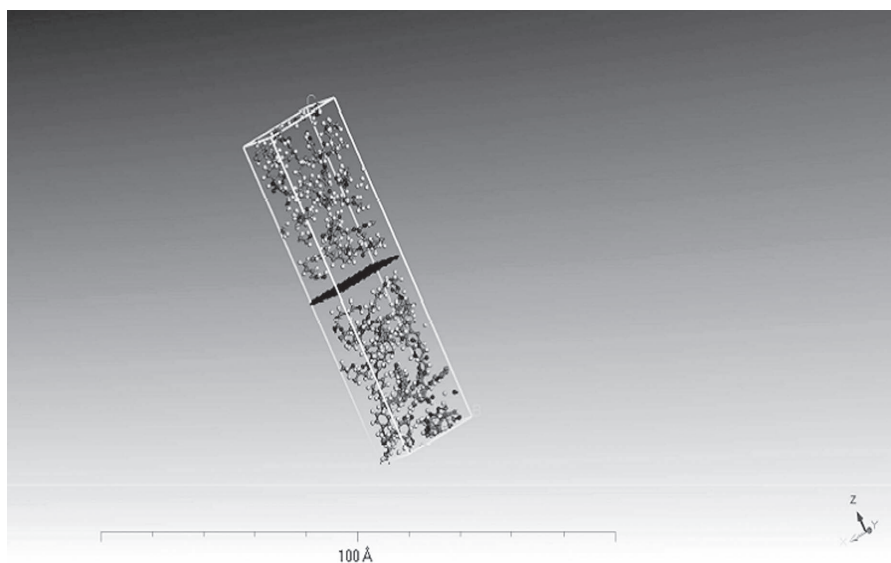


**FIGURE 4.26** Modeling of stacked system for single layer Gr reinforced.

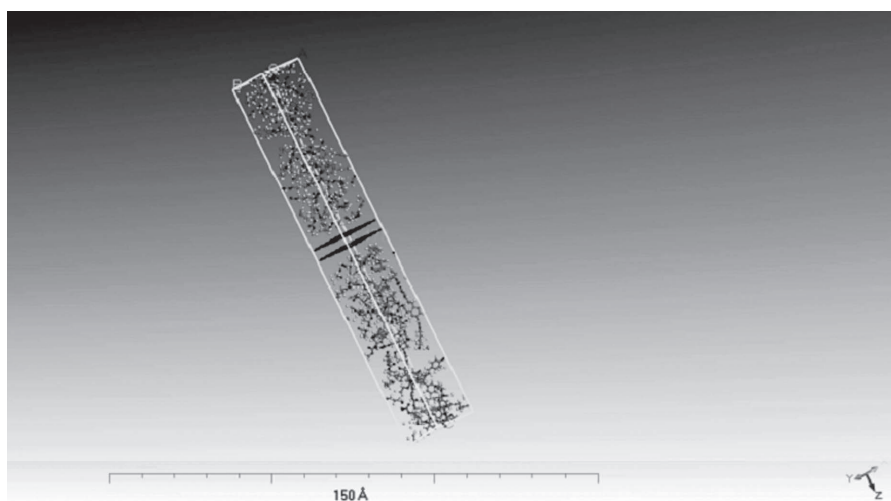


**FIGURE 4.27** Modeling of stacked system for double layer Gr reinforced (intercalated).

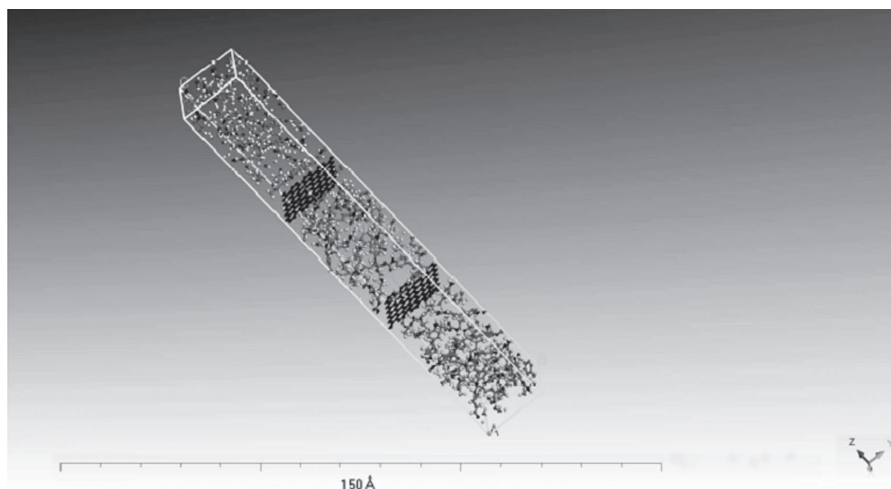


**FIGURE 4.28** Modeling of stacked system for double layer Gr reinforced (exfoliated).

These Gr-PU dispersion unit cells were first optimized geometrically using the “Smart algorithm” of MS 17 which is the combination of steepest descent, conjugate gradient, and Newton–Raphson method in order to achieve the stable initial structural configuration. Then, a geometry optimization with an energy convergence tolerance of  $1.0\text{e}^{-4}$  kcal/mol and a force convergence tolerance of  $0.0001$  kcal/mol/Å is applied for obtaining global minimum energy configuration for the three models.

The main objective of performing the NVT simulation was to bring the pressure of the system down to a minimum of approximately 1.0 atm. As NVT simulation was run on the model, the range of pressure drops down, but not considerably. Because of the nature of NVT ensemble, only the temperature of the system was changed to the mentioned range, keeping the volume constant. During NVT dynamics simulation, the system is allowed to exchange heat with the environment in order to control the temperature at a particular volume. The composite unit is first equilibrated at NVT ensemble for 100 ps under annealing, where the system is heated to 600 K, equilibrated at 600 K for 20 ps, and then cooled to 300 K. The NVT ensemble was conducted at 300 K for 100 ps to obtain homogeneous molecular structure of TPU.

The next step was to bring down the pressure to validate the equilibrium state. The objective was to equilibrate the system internal pressure as to obtain a stable volume. Prior to applying deformation, molecules in each unit cell were relaxed in order to attain minimum residual stress in the system.

Subsequently, the NPT ensemble was performed at 1 atm in order to achieve a stress-free state. The NPT dynamics allows for the relaxation of the cell parameters and angles to obtain a final reasonable equilibrated structure. In the equilibration stage, NPT-MD simulations were carried out for 100 ps. NPT ensemble, also called as isothermal–isobaric ensemble, as the name suggests, was used over a period of approximately 100 ps to get the pressure around 1.0 atm. This is the reason why a sudden drop in the pressure of the system after 100 ps is found. The structure was allowed to relax at NPT ensemble at temperature of 300 K and pressure of 1.0 atm for duration of 100 ps with a time step used of 1 fs to attain an accurate and stable structure before calculating the mechanical properties of the system. This stage generates a profile of density, volume, energy, pressure, and temperature, versus time after NPT-MD simulations at 300 K for final equilibrated structures are performed. These quantities should fluctuate around their average and remaining constant over time, thus confirming the most stable configuration with minimum initial stress of the molecular structure. The objective was to equilibrate the internal pressure of the system to obtain a stable volume. The volume and total energy profile w.r.t. time are used to decide the cut-off between equilibration and production runs. From the V–T curve, we can calculate the average volumetric coefficient of thermal expansion.

**Prediction of properties:** Once the system is equilibrated, it was subjected to uniaxial deformation. Stress in MD simulations can be interpreted using either the Cauchy stress or the virial stress. After every applied deformation, the running averaged hydrostatic stress  $\sigma$  is calculated in order to smooth the stress–strain response. The Young’s modulus is also obtained from the slope of the linear region by performing a regression analysis on the stress–strain data. In the case of linear elastic materials, the stress–strain behavior is described by generalized Hooke’s law:

$$\sigma_{ij} = C_{ijkl} \varepsilon_{kl} \quad (4.50)$$

Where,  $i, j, k, l = 1, 2, 3$ .  $\sigma_{ij}$ ,  $C_{ijkl}$ , and  $\varepsilon_{kl}$  are stress, stiffness, and strain tensors, respectively. The forth-order stiffness tensor has, in general, 81 components. The symmetry property of the stress and strain tensors ( $\sigma_{ij} = \sigma_{ji}$  and  $\varepsilon_{kl} = \varepsilon_{lk}$ ) leads to minor symmetries of the stiffness tensor, that is,  $C_{ijkl} = C_{jikl}$  and  $C_{ijkl} = C_{ijlk}$ , and consequently, results in reduction of independent components to 36. On the other hand, major symmetry of the stiffness tensor, resulted from strain energy, further reduces the number of independent components to 21. Therefore, we can be written in a second-order form, using Voigt notation:

$$\sigma_i = C_{ij} \varepsilon_j \quad (4.51)$$

Where,  $\sigma_i$  and  $\varepsilon_i$  are the six-dimensional stress and strain vectors, and  $C_{ij}$  is the 6\*6 stiffness matrix. The full 6\*6 stiffness matrices were built up from the slopes  $\partial\sigma/\partial\varepsilon$  in tension and shear.

Elastic modulus, Poisson's ratio, bulk modulus, and shear modulus were calculated based on the Voigt notations using the eq 4.38. Lamé coefficients,  $\lambda$  and  $\mu$ , can be used to calculate the other material properties as given in eqs 4.40 and 4.41.

**TABLE 4.5** Simulation Result of Stacked System.

Model configuration	Unit cell dimension ( $\text{\AA} \times \text{\AA} \times \text{\AA}$ )	No of Gr atoms	No of polymer atom	$E_{xx}$ (GPa)	$E_{yy}$ (GPa)	$E_{zz}$ (GPa)
One layer	$(14.75 \times 17.03 \times 60)$	96	976	41.24	32.14	1.623
Two layer (stacked)	$(14.75 \times 17.03 \times 120)$	192	2013	73.87	68.88	3.004
Two layer (separated)	$(14.75 \times 17.03 \times 120)$	192	2013	77.36	75.09	0.417

**Stress–strain response:** The Gr/TPU concentration model is isotropic in nature whereas the dispersion model is anisotropic nature. Results of clustering effect (intercalated or exfoliated) and changing number of layer in crystalline nanocomposite system are shown in Table 4.5. In the crystalline model, Gr sustains its stiffness along three directions and for that it is used to calculate the bulk elastic properties of the Gr-TPUPNCs. The in-plane Young's modulus,  $E_{xx}$  and  $E_{yy}$  are highly dependent on the effect of Gr vol% because Gr's in-plane property ( $E = 1$  TPa). As Grs are restacked and form graphite and for that in-plane Young's modulus ( $E_{xx}$  and  $E_{yy}$ ) drops whereas  $E_{zz}$  increases because Gr–Gr vdW interaction starts playing a significant role. It is seen that in-plane Young's modulus ( $E_{xx}$  and  $E_{yy}$ ) for the separated system is comparatively higher than the stacked system. Stress generated in  $z$  direction is significantly low compared to  $x$  and  $y$  direction for all three cases. It is seen that stresses in the  $z$ -direction is mostly depend on matrix whereas in  $x$  and  $y$  direction properties are controlled by stronger reinforcing Gr. The variations in stress–strain responses in  $x$  and  $y$  direction as seen in are due to different Gr aspect ratio and variable unit cell size used in different stacking models. This special design of the simulation box is intended to simulate the single layer of Gr sheets.

#### *Interfacial model of Gr/TPU nanocomposite*

When Gr pulled out in periodic environment from one periodic cell end, another Gr enters from its adjacent periodic cell and the total energy of the

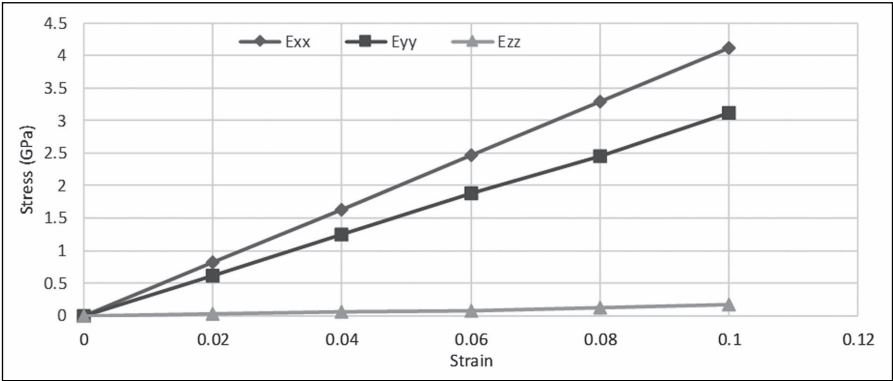


FIGURE 4.29 Stress-strain diagram for single layer Gr-reinforced TPU.

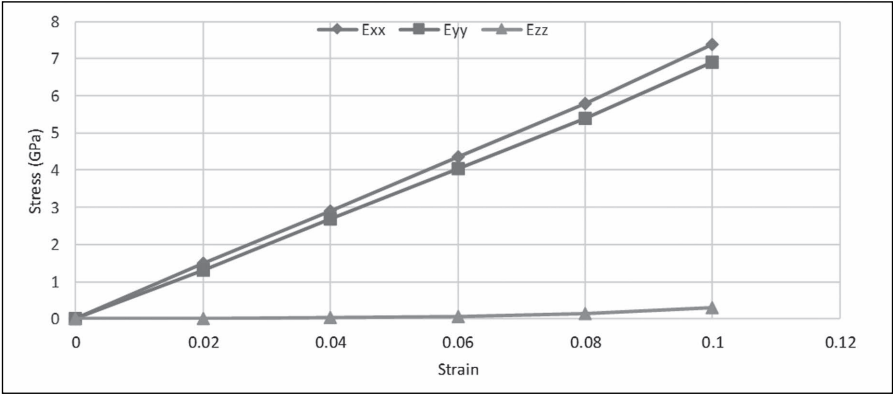


FIGURE 4.30 Stress-strain diagram for double layer (staked) Gr-reinforced TPU.

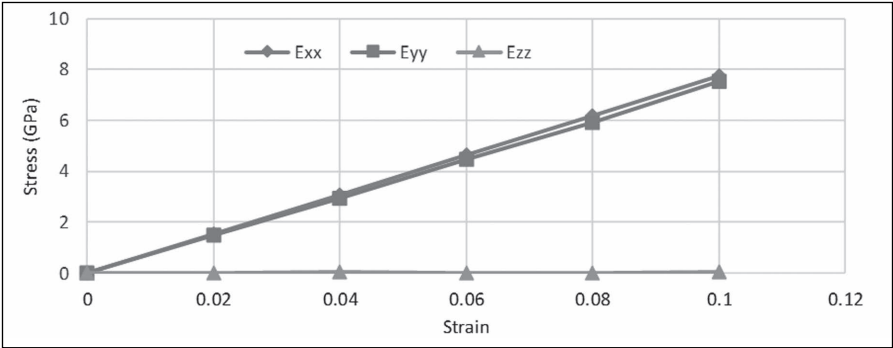


FIGURE 4.31 Stress-strain diagram for double layer (separated) Gr-reinforced TPU.

system remains constant. This is the reason behind to create non-periodic (vacuum) environment to reduce the computational. There is another problem using vacuum environment to control of density during preparation of the system. For further reduce, the computational cost polymer matrix is fixed during extract Gr from polymer matrix. Another important consideration during extraction is that the Gr sheet has been given some constrain condition so that shape of Gr sheet will not be changed so much to affect energy calculation. After every extraction from polymer matrix, energy of the system will increase. For that after each extraction, geometric optimization is performed to minimize the energy.

The interaction energy was estimated from the energy difference ( $\Delta E$ ) between the total PE of the composite and the sum of the potential energies of individual molecules as shown in equation

$$\Delta E = E_{Interaction} = E_{(Graphene+polymer)} - (E_{Graphene} + E_{Polymer}) \quad (4.52)$$

For reduce the computational time, polymer matrix is fixed (i.e.,  $E_{polymer}$  = constant) during extract Gr from polymer matrix.

Separation forces (normal force,  $F_{cohesive}$  and pull out or shear force,  $F_{Adhesive}$ ) calculation is done based on separation energy ( $E_{separation}$ ).

$$E_{separation} = E_{current\ interaction} - E_{initial\ interaction} \quad (4.53)$$

$$\text{Whereas, separation force } (F_{separation}) = \frac{E_{separation}}{Displacement} \quad (4.54)$$

**Normal separation:** Normal displacement of Gr leads us to obtain cohesive mechanism. The cohesive strength (due to normal force,  $F_{cohesive}$ ) is calculated by using following equations,

$$E_{normal\ separation} = \int_0^1 \sigma_{cohesive} \cdot w \cdot L \, dx = \sigma_{cohesive} \cdot w \cdot L = F_{cohesive} \quad (4.55)$$

$$\text{Normal strength} = \sigma_{cohesive} = \frac{F_{cohesive}}{L \cdot W} \quad (4.56)$$

Where, L is length of Gr, W is width of Gr

**Shear separation:** Shear displacement helps us to study the pull-out mechanism. The pull-out force and the average ISS were then determined based on the work done during the pull-out test. In order to minimize the effect from surrounding neighborhood unit cells, the system is non-periodic along the direction of movement. The adhesive strength (due to pull out or shear force,  $F_{Adhesive}$ ) is calculated by using following equations,

$$E_{\text{shear separation}} = \int_0^L \sigma_{\text{adhesive}} \cdot 2 \cdot w \cdot (L - x) dx = \sigma_{\text{adhesive}} \cdot w \cdot L^2 = F_{\text{adhesive}} \cdot L \quad (4.57)$$

$$\text{Shear strength} = \sigma_{\text{Adhesive}} = \frac{F_{\text{Adhesive}}}{w \cdot L} = \frac{E_{\text{Separation}}}{w \cdot L^2} \quad (4.58)$$

Where, W is width of Gr, L is length of Gr.

The factors on which performance of interfacial model depends are

- a) Influence of reinforcement shape (flat or wrinkles),
- b) Influence of matrix character (chain length),
- c) Influence of extraction method,
- d) Influence of agglomeration (increased concentration also enhance possibility of agglomeration in the system), etc.

Interfacial model helps to get full information about the interfacial region between reinforcement and matrix. Interfacial characterization of nanocomposite is very essential for enhancement of nanocomposite properties. Gr-polymer interfacial interactions of modeling are based on (a) C–C covalent bond breaks, (b) Gr pull-out takes place, and (iii) enhancement of interactions due to functionalization, etc.

#### *Model development (unit cell preparation):*

The visualizer tool is used to develop the different Gr-reinforced nanocomposites (interface system) as shown in Figures 4.32 and 4.33. The MD simulation in the Gr-PU interface models is similar to the crystalline models. But the boundary condition is not similar to the periodic system.

The wt% of Gr was taken 3% (wt%) in order to minimize the effect of Gr on vdW interaction between TPU and Gr. Initially, the space between TPU and Gr sheet was maintained approximately 2–3 Å. The cut-off distance was taken for both the model as 14.5 Å. The closes contact method is used to measure this space distance as shown in Figure 4.34.

**Boundary and constraint conditions:** Here, simulations were performed with different constraints, periodicities, and loading conditions. The boundary conditions for cohesive model are taken as  $x$  and  $y$  directions to be periodic and  $z$  direction non-periodic (shrink wrapped). The boundary conditions for the pull out model are taken as  $y$  and  $z$  direction periodic and  $x$  direction non-periodic (shrink wrapped). For normal and shear separations, Gr is free to move in  $z$ -direction and  $x$ -direction, respectively.

Constraint cases have to be imposed in order to separate the two materials from each other; otherwise, movement of the Gr will cause all polymer atoms



to move together with the Gr and there will be no separation. Gr is separated from the polymer keeping all polymer atoms fixed.

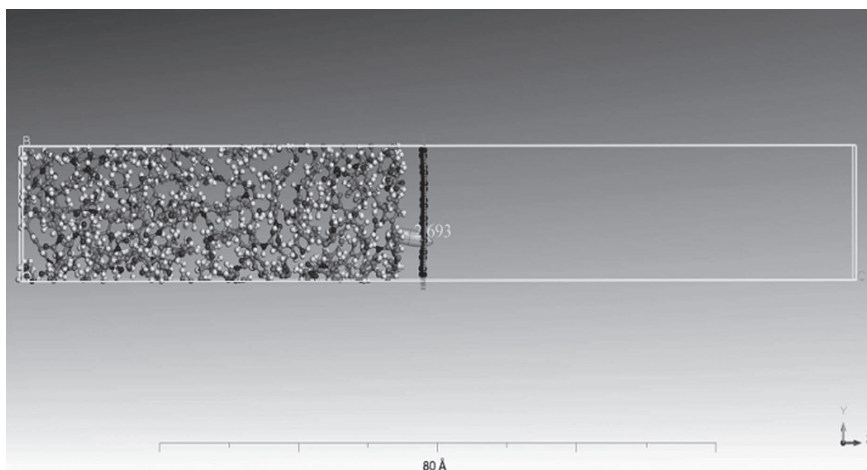


**FIGURE 4.32** Gr/TPU unit cell ( $14.75 \text{ \AA} \times 17.03 \text{ \AA} \times 120 \text{ \AA}$ ) for normal force estimation.

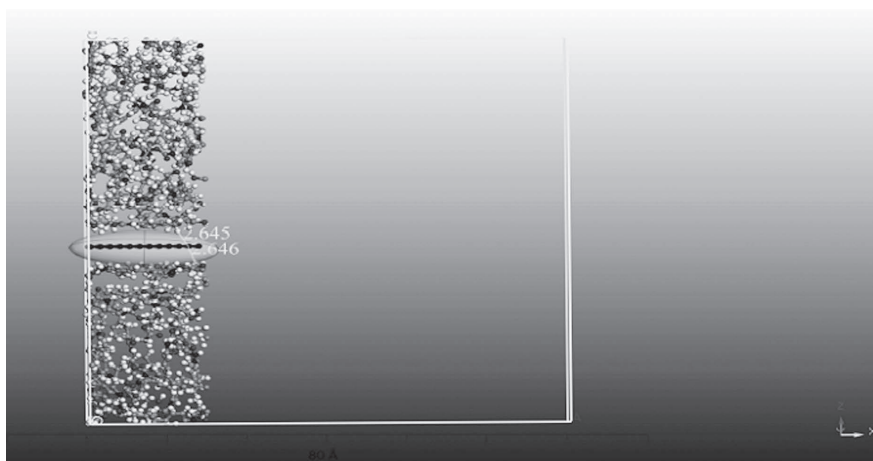


**FIGURE 4.33** Gr/TPU unit cell ( $60 \text{ \AA} \times 17.03 \text{ \AA} \times 60 \text{ \AA}$ ) for shear force estimation.

**Force field:** The COMPASS force field (Sun et al.<sup>46</sup>) was used to model the interactions between atoms. In the COMPASS force field, the total PE  $E_{\text{total}}$  in a molecular system is expressed by:

$$E_{\text{total}} = E_{\text{valence}} + E_{\text{cross-term}} + E_{\text{non-bond}} \quad (4.59)$$

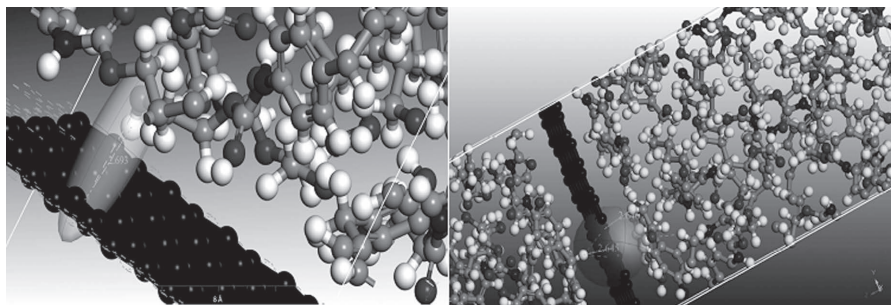


**FIGURE 4.34** Close contact to measure distance between Gr and PU in both models.

**Simulations steps:** Generally, three steps involved in calculation of interfacial mechanical properties.

- i) Prior to transverse or longitudinal movements of Gr plate, energy was using the smart algorithm of MS17. The system was considered as optimized when it satisfied the provided convergence criteria. For reducing the computation time, 5000 iteration steps were performed during the task of geometry optimization. The system was optimized until the change in energy between subsequent steps was less than  $1 \times 10^{-4}$  kcal/mol.
- ii) Each system was equilibrated under NVT for 5000 steps with a step size 1.0 fs. The positions and velocities of the atoms were updated using velocity Verlet time integration scheme under NVT condition. Once the systems are equilibrated, Gr was displaced from the polymer matrix by average translation rate of 0.1 Å/ps for 0.5–3.0 ps in transverse direction (pull-out) and 0.001–0.01 Å/ps for 1.5 ps in longitudinal direction (cohesive). The main purpose of this step is to study energy, density, temperature, and pressure profiles with respect to time and to know about MD equilibration process. After knowing these parameters, it is ensure that the systems are properly equilibrated before deformation.
- iii) The Gr was pulled in the  $x$ -axis direction with increments of 5 Å until complete separation of Gr takes place. Geometry optimization was performed after each separation. During the pull-out process, the Gr was dealt with as a rigid body. Meanwhile, the pull-out process is not dependent on different range of temperature and the pull-out velocity is comparatively fast.

After pull-out, Gr from polymer matrix and total PE is calculated after each pulling process. The results of total PE vs displacement (normal and transverse) calculations are shown in Figures 4.35 and 4.36. The PE at each of these pull-out stages will increase linearly then after it will be constant because after complete pull-out the PE of the composite system does not change since there is no longer any interaction between the Gr and the composite system. The energy required for pull-out is initially higher due to the initial minimized state of the system. After this, energy requirement is constant until the Gr is completely pull-out from the polymer system.

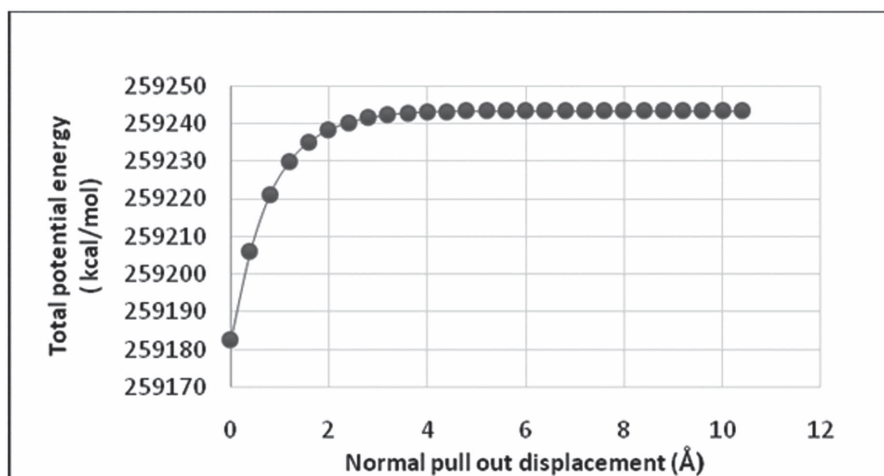


**FIGURE 4.35** Total potential energy–pull-out displacement curve in normal direction.

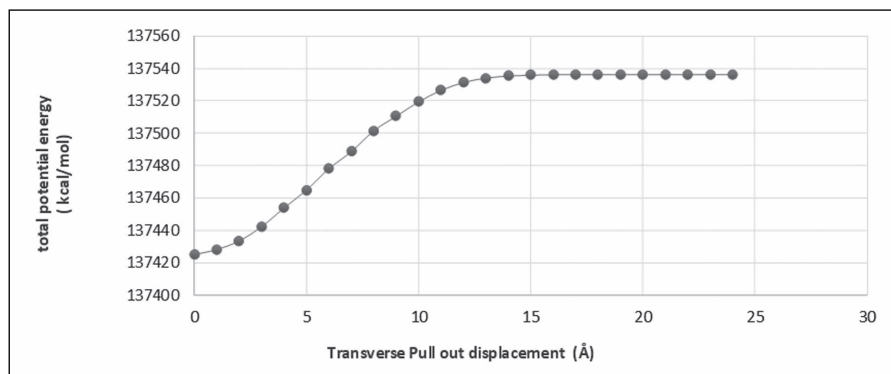


**FIGURE 4.36** Total potential energy–pull-out displacement curve in transverse direction.

The PE at each of these pull-out stages, in turn, was used to calculate the energy increment (i.e., the change in PE relative to the fully embedded configuration). The energy increment is a measure of the work done by the pull-out force. The IE is negative during each stage of the separation showing the existence of attractive interaction between polymer and reinforcement. The energy increment consists of contributions from (i) the variation in the PE of the polymer matrix, (ii) the variation in the PE of the Gr, (iii) the variation in interfacial bonding energy between the Gr and the polymer matrix, and (iv) thermal dissipation.

The results of total interaction energy vs displacement (normal and transverse) calculations are shown in Figures 4.37 and 4.38.

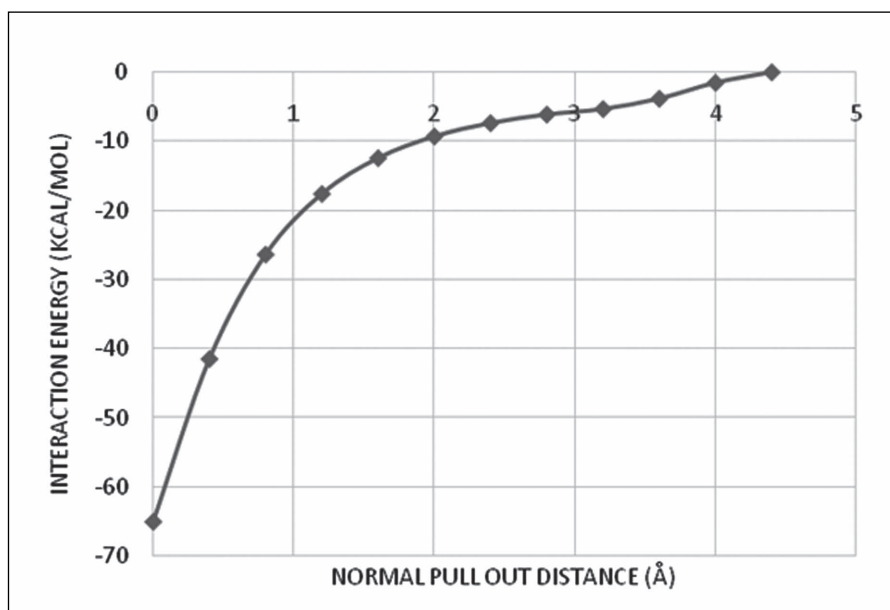


**FIGURE 4.37** Interaction energy–pull-out displacement curve in normal direction.

Normal and shear separation forces were calculated on a slowly displaced Gr sheet from polymer matrix as shown in Figures 4.39 and 4.40. It is seen that maximum pull-out force under shear separation is significantly low compared to normal separation.

For normal separation case, the first pull-out force is increased linearly. It reached a maximum of about 60 kcal/mol/Å after 0.4 Å. Then it reduced gradually and went to zero, as similar previous studies. For shear separation

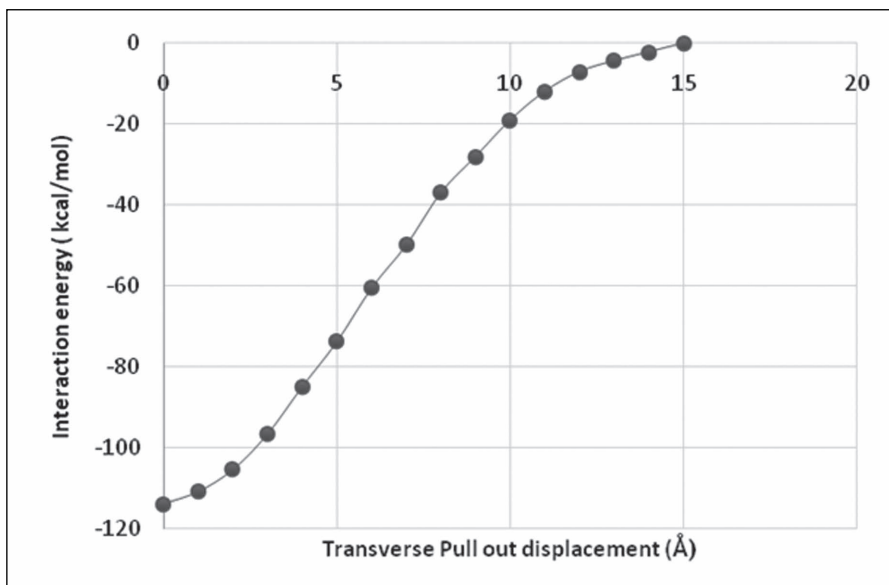


**FIGURE 4.38** Interaction energy–pull-out displacement curve in transverse direction.

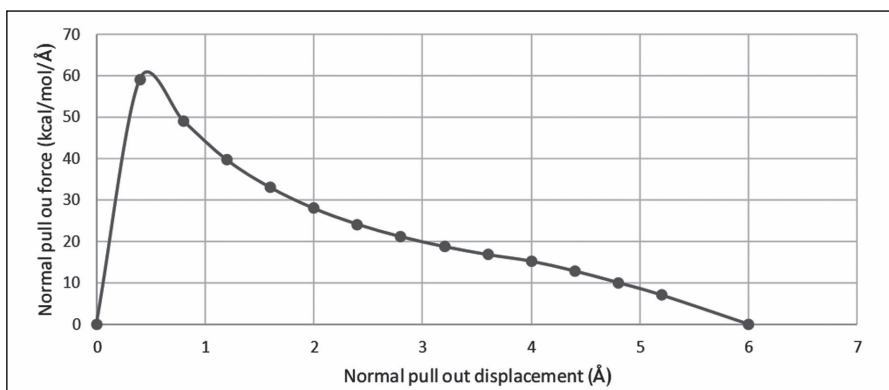


**FIGURE 4.39** Interaction energy–pull-out displacement curve in normal direction.

case, three stages have been seen. Initially, the pull-out force increased linearly, then oscillated around a stable value in the second stage, and finally decreased in the third stage. The variation of energy during the whole pull-out process was equal to the variation of the vdW energy. Simulation results of interfacial system are given in Table 4.6. Here, the IFNS was much higher than the IFSS. As a result, the shear separation failure may occur more easily

than the normal separation. As model was controlled by displacement, certain reaction force was observed in the Gr sheet. Normal displacement of Gr leads us to obtain cohesive law between Gr and TPU whereas shear displacement helps us to study the pull out mechanism. The IFNS (i.e., 1635.29 MPa) between Gr/polymer was larger than that between CNT/polymer. Calculated shear strength of the present model was found 200 MPa. It can be concluded that IFSS between Gr/polymer was better than that of CNT/polymer system. Interfacial properties were mainly dependent on the non-bonded interactions, that is, vdW force. It was observed in Gr-PU system that incorporation of covalent bond enhances interfacial properties significantly. Pull-out force may be increased by minimizing the gap between Gr and polymer or introducing a covalent bond between Gr and polymer. The pull-out force value is increased due to enhanced interfacial surface area under high Gr aspect ratio.



**FIGURE 4.40** Interaction energy–pull-out displacement curve in transverse direction.

**TABLE 4.6** Simulation Result of Interfacial System

Model details	Gr sheet details (Å × Å)	Number of Gr atom	Interfacial maximum force (kcal/mol/Å)	Interfacial maximum stress (MPa)	Maximum displacement (Å)
Cohesive (normal)	(14.76 Å × 96 17.04 Å)	60	1635	200	0.4
Pull-out (shear)		9.6			10

### *Influence of different parameters on interfacial mechanical properties*

These parameters are classified into two categories, namely (i) geometrical parameter effect and (ii) simulation parameter effect. Geometric parameter effect is related to reinforcement, matrix, and reinforcement matrix interface, for example, Gr length, Gr shape, number of Gr layer, number of polymer

chain length, and interface thickness. Simulation parameter effect may be cut-off distance, pull-out velocity, etc.

One of the important simulation parameters may be cut-off distance effect which is vital in interfacial mechanical properties calculation.

*Cut-off distance effect:*

Effect of cut-off distance will affect the accuracy of simulation results. Interaction energy vs cut-off distance in both directions is given in Figures 4.41 and 4.42.

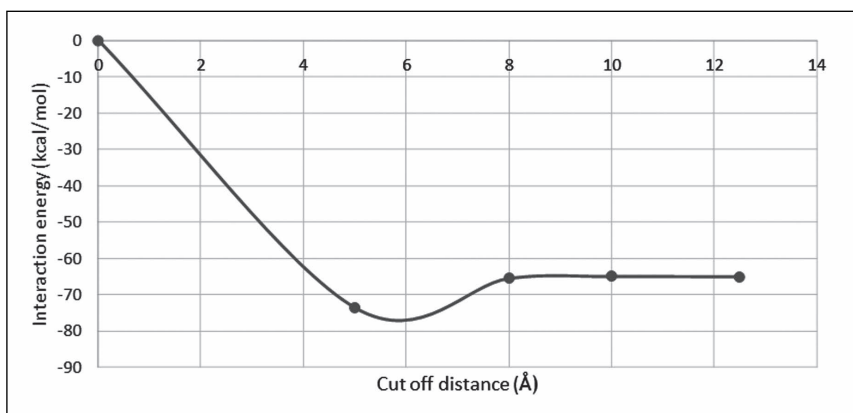


**FIGURE 4.41** Interaction energy vs cut-off distance in normal direction.

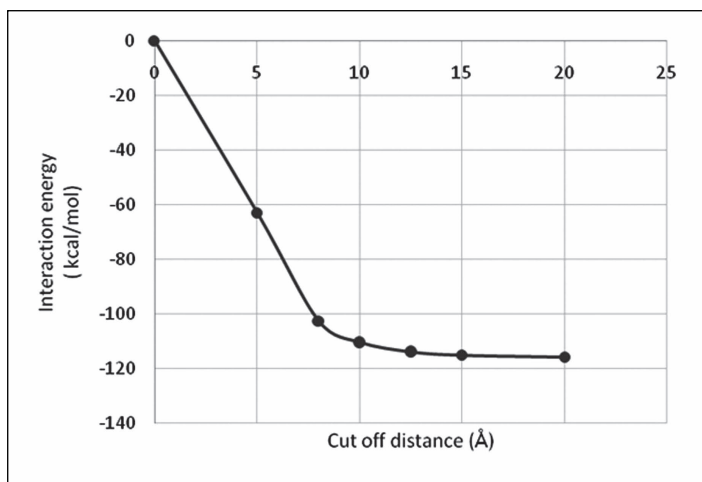


**FIGURE 4.42** Interaction energy vs cut-off distance in transverse direction.

## 4.9 CONCLUDING REMARKS

Classical MD simulation is the most popular method for modeling of carbon-based nanocomposites materials. It adopts interatomic potential or force field to as accurately as possible describe the effect of the electrons on the atomistic interactions and estimate the energy landscape of a large particle system (up to 1 million atoms) to predict different properties of carbon-based nanomaterials for validation with experimental results. The study of the interface model showed that mechanical interactions between Gr and polymer chains are stronger than those among the polymer chains. It is concluded that dispersed Gr provides enhanced in-plane Young's modulus and the out of plane modulus is significantly low compared to in-plane moduli. Gr concentration models show that Young's modulus has decreasing trend with respect to increasing wt% of Gr due to void.

## ACKNOWLEDGMENTS

The authors thank the committee member of TEQIP funded STTP on mechanics of composite using MS 17 in NIT, Durgapur. Also, thanks to Nano HUB for instructions and free uses of MD simulation software online help. Also special thanks to BIOVIA material studio community members who helped and guided me during simulation within the works.

## KEYWORDS

- **molecular dynamics simulation**
- **Gr**
- **thermoplastic polyurethane**
- **Gr reinforced polymer nanocomposite**
- **enhancement of mechanical properties**

## REFERENCES

1. Accelrys Inc. San Francisco. <https://accelrys.com>



2. Alkhateb, H.; Al-Ostaz, A.; Cheng, A.D. Molecular Dynamics Simulations of Graphite-Vinylester Nanocomposites and Their Constituents. *Carbon Lett.* **2010**, *11* (4), 316–324.
3. Atif, R.; Inam, F. Modeling and Simulation of Gr Based Polymer Nanocomposites: Advances in the Last Decade. *Gr* **2016**, *5* (2), 96–142.
4. Awasthi, A. P.; Lagoudas, D. C.; Hammerand, D. C. Modeling of Gr–Polymer Interfacial Mechanical Behavior Using Molecular Dynamics. *Modell. Simulation Mater. Sci. Eng.* **2008**, *17* (1), 015002.
5. Bayer, O.; Rinke, H.; Siefken, W.; Ortner, L.; Schild, H. A Process for the Production of Polyurethanes and Polyureas [Verfahren zur Herstellung von Polyurethanen bzw., Polyharnstoffen. German Patent, 728, 1937.
6. Berendsen, H. J.; Postma, J. V.; van Gunsteren, W. F.; DiNola, A. R. H. J.; Haak, J. R. Molecular Dynamics with Coupling to an External Bath. *J. Chem. Phys.* **1984**, *81* (8), 3684–3690.
7. Bicerano, J. *Prediction of Polymer Properties*; CRC Press, 2002.
8. Brown, D.; Clarke, J. H. Molecular Dynamics Simulation of an Amorphous Polymer Under Tension. *Phenomenol. Macromol.* **1991**, *24* (8), 2075–2082.
9. Chawla, R.; Sharma, S. Molecular Dynamics Simulation of Carbon Nanotube Pull-Out from Polyethylene Matrix. *Compos. Sci. Technol.* **2017**, *144*, 169–177.
10. Chawla, R.; Sharma, S. A Molecular Dynamics Study on Efficient Nanocomposite Formation of Styrene–Butadiene Rubber by Incorporation of Gr. *Gr Technol.* **2018**, 1–9.
11. Chawla, R.; Sharma, S. A Molecular Dynamics Study on Young's Modulus and Tribology of Carbon Nanotube Reinforced Styrene-Butadiene Rubber. *J. Mol. Model.* **2018**, *24* (4), 96.
12. Gao, Y.; Hao, P. Mechanical Properties of Monolayer Gr Under Tensile and Compressive Loading. *Physica E: Low-Dimensional Syst. Nanostruct.* **2009**, *41* (8), 1561–1566.
13. Gupta, S.; Dharamvir, K.; Jindal, V. K. Elastic Moduli of Single-Walled Carbon Nanotubes and Their Ropes. *Phys. Rev. B* **2005**, *72* (16), 165428.
14. Gusev, A. A.; Zehnder, M. M.; Suter, U. W. Fluctuation Formula for Elastic Constants. *Phys. Rev. B* **1996**, *54* (1), 1.
15. Hadden, C. M.; Jensen, B. D.; Bandyopadhyay, A.; Odegard, G. M.; Koo, A.; Liang, R. Molecular Modeling of EPON-862/Graphite Composites: Interfacial Characteristics for Multiple Crosslink Densities. *Compos. Sci. Technol.* **2013**, *76*, 92–99.
16. Hofmann, D.; Fritz, L.; Ulbrich, J.; Schepers, C.; Böhning, M. Detailed-Atomistic Molecular Modeling of Small Molecule Diffusion and Solution Processes in Polymeric Membrane Materials. *Macromol. Theor. Simulations* **2000**, *9* (6), 293–327.
17. Jing, N.; Xue, Q.; Ling, C.; Shan, M.; Zhang, T.; Zhou, X.; Jiao, Z. Effect of Defects on Young's Modulus of Gr Sheets: A Molecular Dynamics Simulation. *RSC Adv.* **2012**, *2* (24), 9124–9129.
18. Kim, S. G. Effect of Polymerization Procedure on Thermal and Mechanical Properties of Polyether Based Thermoplastic Polyurethanes. *Macromol. Res.* **2002**, *10* (6), 365–368.
19. Lee, J. H.; Veyssset, D.; Singer, J. P.; Retsch, M.; Saini, G.; Pezeril, T.; Thomas, E. L. High Strain Rate Deformation of Layered Nanocomposites. *Nat. Commun.* **2012**, *3*, 1164.
20. Lempesis, N.; in't Veld, P. J.; Rutledge, G. C. Atomistic Simulation of a Thermoplastic Polyurethane and Micromechanical Modeling. *Macromolecules* **2017**, *50* (18), 7399–7409.
21. Li, C.; Browning, A. R.; Christensen, S.; Strachan, A. Atomistic Simulations on Multilayer Gr Reinforced Epoxy Composites. *Compos. Part A Appl. Sci. Manuf.* **2012**, *43* (8), 1293–1300.

22. Li, Y.; Wang, S.; Wang, Q. A MD Simulation Study on Enhancement of Mechanical and Tribological Properties of Polymer Composites by Introduction of Gr. *Carbon* **2017**, *111*, 538–545.
23. Li, Y.; Wang, S.; Wang, Q. Enhancement of Tribological Properties of Polymer Composites Reinforced by Functionalized Gr. *Compos. Part B Eng.* **2017**, *120*, 83–91.
24. Li, Y.; Wang, S.; Wang, Q.; Xing, M. Molecular Dynamics Simulations of Tribology Properties of NBR (Nitrile-Butadiene Rubber)/Carbon Nanotube Composites. *Compos. Part B Eng.* **2016**, *97*, 62–67.
25. Lin, F.; Xiang, Y.; Shen, H. S. Temperature Dependent Mechanical Properties of Gr Reinforced Polymer Nanocomposites—A Molecular Dynamics Simulation. *Compos. Part B Eng.* **2017**, *111*, 261–269.
26. Liu, F.; Hu, N.; Ning, H.; Liu, Y.; Li, Y.; Wu, L. Molecular Dynamics Simulation on Interfacial Mechanical Properties of Polymer Nanocomposites with Wrinkled Gr. *Comput. Mater. Sci.* **2015**, *108*, 160–167.
27. Lu, Q.; Huang, R. Nonlinear Mechanics of Single-Atomic-Layer Gr Sheets. *Int. J. Appl. Mech.* **2009**, *1* (03), 443–467.
28. Martienssen, W.; Warlimont, H., Eds. *Springer Handbook of Condensed Matter and Materials Data*; Springer Science & Business Media, 2006.
29. *Materials Studio, User's Manual, Version 8*; Accelrys, Inc.: San Diego, 2008.
30. Nayebi, P.; Zaminpayma, E. A Molecular Dynamic Simulation Study of Mechanical Properties of Gr–Polythiophene Composite with Reax Force Field. *Phys. Lett. A* **2016**, *380* (4), 628–633.
31. Nguyen, V. K.; Li, M. J.; Lee, D. S. *Effects of Hard Segment Length on Solution Viscosities of Ether Based Polyurethanes*; Unpublished Data, 2005.
32. Njoroge, J.; Cagin, T. Molecular Dynamic Simulation of Thermo-mechanical Properties of Amorphous Polyurea/Polyurethane, MRS Fall 2009 Meeting, Boston, MA, 1–4 Dec 2009.
33. Parrinello, M.; Rahman, A. Strain Fluctuations and Elastic Constants. *J. Chem. Phys.* **1982**, *76* (5), 2662–2666.
34. Raaska, T.; Niemela, S.; Sundholm, F. Atom-Based Modeling of Elastic Constants in Amorphous Polystyrene. *Macromolecules* **1994**, *27* (20), 5751–5757.
35. Rafiee, M. A.; Rafiee, J.; Wang, Z.; Song, H.; Yu, Z. Z.; Koratkar, N. Enhanced Mechanical Properties of Nanocomposites at Low Gr Content. *ACS Nano* **2009**, *3* (12), 3884–3890.
36. Rahman, R. The Role of Gr in Enhancing the Stiffness of Polymeric Material: A Molecular Modeling Approach. *J. Appl. Phys.* **2013**, *113* (24), 243503.
37. Rahman, R.; Haque, A. Molecular Dynamic Simulation of Gr Reinforced Nanocomposites for Evaluating Elastic Constants. *Procedia Eng.* **2013**, *56*, 789–794.
38. Roussou, R. E.; Karatasos, K. Gr/Poly (Ethylene Glycol) Nanocomposites as Studied by Molecular Dynamics Simulations. *Mater. Design* **2016**, *97*, 163–174.
39. Schmidt, R.; Thiel, K. O.; von Horsten, F.; Spickermann, C.; Vazhenin, G.; Bäumke, N.; Schreier, H. J. Towards the Mechanism of the Accelerated Corrosion of Decorative Nickel–Chromium Coatings in the Presence of Metals and Their Salts. *Mater. Corrosion* **2014**, *65* (10), 959–967.
40. Seifoori, S.; Hajabdollahi, H. Impact Behavior of Single-Layered Gr Sheets Based on Analytical Model and Molecular Dynamics Simulation. *Appl. Surf. Sci.* **2015**, *351*, 565–572.

41. Sharma, S.; Chandra, R.; Kumar, P.; Kumar, N. Thermo-Mechanical Characterization of Multi-Walled Carbon Nanotube Reinforced Polycarbonate Composites: A Molecular Dynamics Approach. *CR Mecanique* **2015**, *343*, 371–396.
42. Sharma, S.; Chandra, R.; Kumar, P.; Kumar, N. Molecular Dynamics Simulation of Functionalized SWCNT–Polymer Composites. *J. Compos. Mater.* **2016**, 0021998316628973.
43. Sharma, S.; Kumar, P.; Chandra, R. Mechanical and Thermal Properties of Gr–Carbon Nanotube-Reinforced Metal Matrix Composites: A Molecular Dynamics Study. *J. Compos. Mater.* **2017**, *51* (23), 3299–3313.
44. Shiu, S. C.; Tsai, J. L. Characterizing Thermal and Mechanical Properties of Gr/Epoxy Nanocomposites. *Compos. Part B Eng.* **2014**, *56*, 691–697.
45. Singh, V.; Joung, D.; Zhai, L.; Das, S.; Khondaker, S. I.; Seal, S. Gr Based Materials: Past, Present and Future. *Progress Mater. Sci.* **2011**, *56* (8), 1178–1271.
46. Sun, H. COMPASS: An Ab Initio Force-Field Optimized for Condensed-Phase Applications Overview with Details on Alkane and Benzene Compounds. *J. Phys. Chem. B* **1998**, *102* (38), 7338–7364.
47. Talapatra, A.; Datta, D. Properties for Gr Reinforced Polymer Nanocomposite Using Molecular Dynamic Simulation. In *The Proceedings of Fourth International Conference on Nanostructured Materials and Nanocomposites (ICNM 2017) During 10–12th Feb, 2017 at Mahatma Gandhi University, Kottayam, Kerala, India*, Paper no. IL83, 2017; p 127.
48. Talapatra, A.; Datta, D. Characterization of Single Layer Gr Reinforced Polyurethane Nanocomposite Using Multiscale Modelling and Simulation. In *International Conference on Composite Materials and Structures- ICCMS 2017, 27–29th December 2017, IIT Hyderabad*, Paper ID 119, 2017; pp 88–89.
49. Talapatra, A.; Datta, D. Tribological Behaviour of Functionalized Gr Reinforced Thermoplastic Polyurethane Elastomer Nanocomposites Using Molecular Dynamics Simulations. In *International Conference on Advances in Mechanical Engineering and Nanotechnology (ICMEN 2019) on March 8–9, 2019 at Manipal University Jaipur*. Paper ID MSE2222, 2019; p 38.
50. Talapatra, A.; Datta, D. Graphene-Reinforced Thermoplastic Polyurethane Nanocomposites: A Simulation and Experimental Study. *J. Thermoplast. Compos. Mater.* **2019**, *34* (2), 143–161.
51. Talapatra, A.; Datta, D. A Molecular Dynamics-Based Investigation on Tribological Properties of Functionalized Graphene Reinforced Thermoplastic Polyurethanenanocomposites. *Proc. Instit. Mech. Eng. Part J* **2020**, *235* (1), 61–78.
52. Talapatra, A.; Datta, D. Atomistic Investigation of the Interfacial Mechanical Characteristics of Graphene Reinforced Thermoplastic Polyurethane Composite. *Compos. Interfaces* **2020**, *28* (4), 395–427.
53. Talapatra, A.; Datta, D. Estimation of Improvement in Elastic Moduli for Functionalised Defective Graphene-Based Thermoplastic Polyurethane Nanocomposites: A Molecular Dynamics Approach. *Mol. Simul.* **2021**, *47* (7), 602–618.
54. Theodorou, D. N.; Suter, U. W. Atomistic Modeling of Mechanical Properties of Polymeric Glasses. *Macromolecules* **1986**, *19* (1), 139–154.
55. Zhao, H.; Min, K.; Aluru, N. R. Size and Chirality Dependent Elastic Properties of Gr Nanoribbons Under Uniaxial Tension. *Nano Lett.* **2009**, *9* (8), 3012–3015.

56. Zhu, S.; Lempesis, N.; in't Veld, P. J.; Rutledge, G. C. Molecular Simulation of Thermoplastic Polyurethanes Under Large Tensile Deformation. *Macromolecules* **2018**, *51* (5), 1850–1864.
57. Zhou, M. A New Look at the Atomic Level Virial Stress: On Continuum-Molecular System Equivalence. *Proc. R. Soc. London Ser. A* **2003**, *459* (2037), 2347–2392.
58. Zimmerman, J. A.; Webb, E. B.; Hoyt, J. J.; Jones, R. E.; Klein, P. A.; Bammann, D. J. Calculation of Stress in Atomistic Simulation. *Modell. Simulation Mater. Sci. Eng.* **2004**, *12* (4), S319–S332.



## CHAPTER 5

---

# Synthesis and Multifunctional Applications of Polymethyl Methacrylate-Based Nanocomposites: A Review

K. B. BHAVITHA<sup>1,2</sup>, SRINIVASARAOYARAGALLA<sup>3,4</sup>, KALA M. S.<sup>1</sup>,  
NANDAKUMAR KALARIKKAL<sup>2,4</sup>, and SABU THOMAS<sup>2,5</sup>

<sup>1</sup>*Department of Physics, St Teresa's College, Ernakulam, Kerala, India*

<sup>2</sup>*International and Inter University Centre for Nanoscience and Nanotechnology, Mahatma Gandhi University, Kottayam, Kerala, India*

<sup>3</sup>*Guru Nanak Institute of Technical Campus, Hyderabad, Telangana, India*

<sup>4</sup>*Smart Materials Istituto Italiano di Tecnologia, Genova, Italy*

<sup>4</sup>*School of Pure and Applied Physics, Mahatma Gandhi University, Kottayam, Kerala, India*

<sup>5</sup>*School of Chemical Sciences, Mahatma Gandhi University, Kottayam, Kerala, India*

---

### ABSTRACT

A comprehensive review of the synthesis of PMMA nanocomposites and their applications has been presented. The significance of PMMA nanocomposites has been extensively exploited in diverse applications. The coordination effects among the *constituents* of these materials have furnished them as excellent sensing elements and electrical, optical, and optoelectronic applications. PMMA composites are found to be multifunctional materials such as sensors (excellent gas sensor, chemo sensor, strain sensor, plasmonic sensor, etc.), dielectric, optical, and optoelectronics. We hereby gather the

recent studies on PMMA composites for a better understanding of potential applications.

## 5.1 INTRODUCTION

Poly (methyl methacrylate) (PMMA) is a well-established optical polymer that is a transparent thermoplastic. PMMA is a major substitute for glass since it has high impact strength and shear resistance with more strength, less weight, and is transparent. Compared to other polystyrene and polycarbonate optical polymers, its impact strength is better than polystyrene and glass but lower than polycarbonate. Therefore, it is a good substitute for polycarbonate, where high impact strength is not required. PMMA is used for many industrial applications in architecture and construction, automotive and transportation, automotive glazing, electronics and energy, furniture and design, lighting, medical and health, and visual communications.<sup>1</sup>

PMMA itself can be made to nanostructures such as nanotubes,<sup>2</sup> nanospheres,<sup>3</sup> and nanofibers,<sup>4</sup> and so on. The introduction of nanoparticles to PMMA helps to improve the chemical and physical properties and even new properties to the PMMA polymer, extending PMMA to a multifunctional material. The full potential of PMMA is explored by adding secondary components like metal nanoparticles, metal oxide nanoparticles, carbon compounds, chalcogenides, polymers, and so on, and making a new nanocomposite. The nanoparticles are usually stabilized within the polymer matrix by coulomb interactions or van der Waals' interaction. The functionalization of nanoparticles can even lead to the formation of coordination bonds between nanoparticles and the polymer matrix. The nanoparticle incorporation in the polymer matrix can induce structural changes, charge transfer mechanisms, electronic interactions, or the combinations of these mechanisms among the constituents. Anjum Qureshi et al.<sup>5</sup> have synthesized PMMA—Yttrium iron garnet,  $\text{Y}_3\text{Fe}_5\text{O}_{12}$  (YIG); Mohaseen S. Tamboli et al.<sup>6</sup> had prepared PMMA-bismuth ferrite (BFO), which has both magnetic and dielectric properties. Thermal, electrical, and optical properties of the polymer are found to be enhanced concerning the good dispersion and interaction of these nanoparticles with the polymer matrix. Moreover, a small number of nanoparticles are needed for the property enhancement of the polymers, which makes the composites less costly.

This chapter dealt with the synthesis and multifunctional applications of PMMA nanocomposites with the inclusion of various nanoparticles. We concentrate on different synthesis strategies and potential applications

of PMMA nanocomposites in the field of sensing, electrical, optical, and nonlinear optical properties and conclude with future research aspects for PMMA nanocomposites.

## 5.2 SYNTHESIS OF PMMA NANOCOMPOSITES

The synthesis of polymer nanocomposites is of much importance because the synthesis strategies could significantly affect the dimensions and structure of the composites, affecting the properties. The foremost approaches used for the synthesis of nanocomposites are the (i) *in situ* methods<sup>7</sup> and (ii) *ex situ* methods.<sup>7</sup> In the primary scheme, concurrent production of polymerization and nanoparticle production happens. And in the second method, pre-synthesized nanoparticles are incorporated into the monomer, causing nanoparticle inclusion in the polymerized matrix. Researches develop different innovative strategies by using these fundamental methods. The main aim is to precisely tune the dimension, structure, and configuration of the composites. These methods have many advantages and disadvantages, and the methods with different nanoparticle incorporation are given in Table 5.1.

The crucial challenge in the manufacturing process of PMMA nanocomposite is controlling nanoparticle size, distribution, and dispersion in the PMMA matrix. This is a manufacturing challenge since the nanoscale particles have high surface energies and hydrophilicity and are easily aggregated even before adding into the PMMA matrix. Hence, appropriate tailoring and design of nanoparticles and PMMA matrix are needed for the manufacturing of PMMA nanocomposites. Here, we included various manufacturing processes and comparatively discussed them based on the literature.

### *Sol-Gel Route*

This method is a versatile, bottom-up synthesis method, which is low cost, and produce nanoparticles of molecular level domain sizes.<sup>8–10</sup> In this method, a three-dimensional network like inorganic-organic hybrid material is synthesized by hydrolysis and condensation of molecular precursors. Both *in situ* sol-gel, a one-step method, and *ex situ* sol-gel method, in which pre-synthesized nanoparticles are incorporated into the PMMA matrix, are much explored. During the *in situ* sol-gel synthesis, mainly organic chelating agents are used to control the reactivity and sizes of nanoparticles. So, the drawback is that it is difficult to remove the chelating agent from the metallic centers during hydrolysis due to its strong affinity toward metals. This, in



turn, affects the thermomechanical and optical, features of the nanocomposites. Hence, ex situ sol-gel method is the alternative synthesis way to avoid the above problem. The ex situ method has more advantages since it is more controllable at the nanoscale, giving monodisperse nanoscale particles in the polymer matrix.

### *In Situ Formation of Nanoparticles in Polymer Matrices*

This method is a one-step fabrication process and is a current and simplistic technique in which in situ production of nanoparticles from the precursors in the presence of polymer chains is done.<sup>11–13</sup> This method provides good spatial distribution by effectively controlling the particle dimensions, distributing the particles on the polymer matrix, and controlling the agglomerations of the nanoparticles since the polymer matrix does not allow the nanoparticles to meet through diffusion. However, strong interaction between inorganic nanophase and the organic matrix phase is essential for particle size control and polydispersity. Hence, careful tuning and designing are necessary for this process. The main disadvantage is that the unreacted by-products may affect the physical performance of the composites.

### *Ex Situ Synthesis Method*

The ex situ synthesis method is a versatile and large-scale industrial approach for the preparation of polymer nanocomposite for practical applications in which pre-synthesized nanoparticles are integrated into the polymer matrix or monomer, which is consequently polymerized to form composites. The first approach is called the blending route, and the second one is called in situ polymerization. This method controls particle sizes and surface properties since, prior to incorporation into the polymer matrix, the nanoparticles are distinctly synthesized by altering with functionalizing agents and are secluded. The major challenge is the excellent dispersibility and long-term stability of the nanoparticles in the polymer matrix. So, nanoparticles are usually modified using functionalizing agents by chemi or physisorption methods, which stops the aggregation of nanoparticles and changes the surface properties.

### *Blending Route*

The blending method is the most straightforward route. The uniform dispersion of nanoparticles in a polymer or monomer solution is cast into a Petri dish, glass substrate, or plastic substrate by solvent casting, spin coating,

or dip coating methods.<sup>14,15</sup> Then the composite film is peeled off after drying. In this method, the compatibility of nanoparticles and the polymer matrix is a crucial issue. Hence, designing and tuning the structure of nanoparticle and polymer matrix and selecting proper cosolvent is necessary to improve the compatibility and properties of the matrix.

### *In Situ Polymerization*

This method is effective for preparing thick ad bulk polymer nanocomposites.<sup>16–18</sup> The major challenge is to obtain a stable dispersion of nanoparticles since a long polymerization process may cause precipitation of nanoparticles because of its low viscosity compared to the polymer matrix. Hence, the design and tailoring of nanoparticles are crucial to better compatibility with the monomer through interfacial interaction.

#### **5.2.1 NANOCOMPOSITE OF PMMA WITH METAL NANOPARTICLES**

The standard reduction potential of MMA is lesser than that of several noble metal salts. In a one-step redox reaction, MMA is oxidized, and simultaneously the noble metal salts are reduced to zero-valent noble metal nanoparticles, resulting in the formation of a PMMA matrix with metal nanoparticle incorporation. The PMMA composites with Au, Ag, Cu, Pt, etc., can be prepared effectively using this method.

Eda Yilmaz et al.<sup>11</sup> had synthesized PMMA-Au films by spin coating methods on Si or quartz wafers using 1 mM HAuCl<sub>4</sub> and 0.5% (w/v) PMMA in acetone. The reduction of Au<sup>3+</sup> ions to Au<sup>0</sup> nanoparticles was done using 254 nm UV light followed by a UV–Vis–NIR spectrometer. They found an increase in surface conductivity for the films even at low concentrations of incorporated nanoparticles. Hong-Mao Wu et al.<sup>19</sup> have prepared core-shell PMMA–Au composite particles using a facile redox-transmetalation route which gave rise to an electrical resistivity as low as  $3 \times 10^{-2} \Omega \text{ cm}$ .

Mohammed Alsawafta et al.<sup>13</sup> synthesized Gold-poly(methyl methacrylate) nanocomposites by an in situ method by irradiating through UV-, thermal-, and MW-irradiation, respectively, by annealing the samples at temperatures much higher than the PMMA glass transition temperature. The sensitivity of samples synthesized through the three different methods is comparable and is 100 nm/RIU. The results suggest adequate post-synthesis heat treatment, Au-PMMA nanocomposites can be successfully used as plasmonic biosensing platforms.

Lu-Bin Zhong et al.<sup>20</sup> demonstrated the self-assembly of gold nanoparticles on PMMA films by a quick and simple way to fabricate AuNPs/PMMA films, which has a higher potential for in situ ultrasensitive chemical detections on asymmetrical objects. Guo Cai Xu et al.<sup>21</sup> have developed a facile route to synthesize the Ag/PMMA nanocomposites using ultrasonic radiation's bi-in situ emulsion polymerization technique. The synthesis technique is a promising way to prepare a kind of inorganic/polymer nanocomposites with different compositions and sizes.

Hyeyoung Kong et al.<sup>22</sup> synthesized PMMA nanofiber containing silver nanoparticles by radical-mediated dispersion polymerization. The MIC test established that, at the same silver concentration, the antimicrobial efficacy of the silver/PMMA nanofiber had improved with respect to silver nitrate and silver sulfadiazine. Most importantly, the as-synthesized polymer nanofiber had an excellent biocidal potential against Gram-negative bacteria (*E. coli*) as well as Gram-positive bacteria (*S. aureus*). The procedure for the synthesis is as follows. 0.05 wt.% of PVA was dissolved in distilled water (100 mL), and silver precursor, AgNO<sub>3</sub> (0.29  $\mu$ M), was added to the polymeric aqueous solution. After the solution was mixed, 2,2-azobis(isobutyronitrile) (AIBN, 0.29  $\mu$ M) and methyl methacrylate (MMA, 0.02 M) were *sequentially* injected into the aqueous silver solution. MMA monomer was polymerized with vigorous stirring at 60°C for 24 h. After polymerization, the synthesized silver/PMMA nanofiber was precipitated for 24 h and washed by ethanol to remove the residual reagents.

Ki-Young Nam et al.<sup>23</sup> first reported on the synthesis and the antibacterial activity of Pt-PMMA nanocomposite. Platinum nanoparticles (PtN) were successfully loaded and uniformly immobilized into PMMA denture acrylic with proper thermal stability and similar surface morphology as compared to control. Pt NC expressed a significant bacterial anti-adherent effect rather than a bactericidal effect above 50 mg/L PtN loaded compared to pristine PMMA with no or tiny amounts of Pt ion eluted. PMMA denture acrylic loading PtN could be a possible intrinsic antimicrobial denture material with good mechanical characteristics, meeting those specified for denture bases.

Kuan-Ju Lin et al.<sup>24</sup> studied, the electrostatic LbL method, for the pre-treatment of PMMA beads with oppositely charged polyelectrolyte polymers, before the electroless Ni deposition. They have hence modified the surface of colloidal PMMA beads by electrostatic adsorption of cationic poly(allylamine hydrochloride) (PAH) and anionic poly(acrylic acid) (PAA) molecules sequentially. The surface-modified beads were electroless-plated by Ni through the addition of dimethylamine borane in an aqueous

electroless Ni bath so that a continuous Ni film with a reduced crystallite size and a uniform thickness (~100 nm) was formed on the beads, resulting in a pronouncedly reduced electrical resistivity on the packed composite particles.

### **5.2.2 NANOCOMPOSITE OF PMMA WITH METAL OXIDE NANOPARTICLES**

Nanocomposites of PMMA with metal oxide nanoparticles can work as an efficient energy storage device due to the cooperative effects among the components. In addition, magnetorheological fluids are required for pedestals for snubbing and torque transfer, including brakes, clutches, dampers, and semi-active or adaptive vibration control. Zhen Cao et al.<sup>25</sup> have synthesized  $\text{Fe}_3\text{O}_4$ /PMMA nanocomposite particles by one-pot hydrothermal method, and the composite materials were found to exhibit superparamagnetic properties and have higher magnetorheological (MR) effects. Zhang et al.<sup>26</sup> had successfully prepared the PMMA/ $\text{Fe}_3\text{O}_4$  composite fibers using the electrospinning technique and investigated the dielectric and magnetic properties of the composite nanofiber membranes. The prepared PMMA/ $\text{Fe}_3\text{O}_4$  composite fibers were found to have superparamagnetic properties and ultra-low dielectric constant. With increasing  $\text{Fe}_3\text{O}_4$  content, the dielectric permittivity of the PMMA/ $\text{Fe}_3\text{O}_4$  composite fibers decreased. Fang Lan et al.<sup>27</sup> synthesized monodisperse superparamagnetic  $\text{Fe}_3\text{O}_4$ /PMMA composite nanospheres with high saturation magnetization by double mini emulsion polymerization approach. The magnetic polymer composite nanospheres exhibited super paramagnetism with high saturation magnetization up to 39 emu/g. They also studied the use of  $\text{Fe}_3\text{O}_4$ /PMMA composite nanospheres as a nanoplatfrom for multimodal protein separation. R. Rajan Prakash et al.<sup>28</sup> synthesized PMMA- $\text{TiO}_2$  composites using the intercalation method and found that the constant dielectric increases and dielectric loss decrease with an increase in loadings of  $\text{TiO}_2$  filler. Hence, the material is found to be a better substitute for dielectrics and insulation material fabrication. Other research groups<sup>29</sup> synthesized (PMMA)- $\text{TiO}_2$  by in situ sol-gel/polymerization and found ultrafast optical nonlinearity with 780-nm, 250-fs laser pulses, and recovery time of ~1.5 ps. Their findings suggest the potential of nanocomposites for all-optical switching applications. Some researchers<sup>30</sup> prepared PMMA/NiO nanocomposites using in situ bulk polymerization. They investigated TGA and found high thermal stability. The thin films

prepared have potentials for polymeric substrates for flexible polymeric substrates electronic devices.

Xinjian Cheng et al.<sup>31</sup> prepared the SiO<sub>2</sub>/PMMA composite particles with different morphologies such as multicore-shell, raspberry-like, and conventional core-shell, by traditional emulsion polymerization by the aid of acid-base interaction between the silanol groups of unmodified silica particles and the amino groups of 4-vinyl pyridine. The morphologies of composite particles could be controlled by modulating emulsifier content, monomer/silica ratio, silica size, and monomer feed method. El-Bashir et al.<sup>32</sup> prepared PMMA-SiO<sub>2</sub> hybrids as follows. In a fluorescent dye-doped PMMA/MMA solution, SiO<sub>2</sub> nanoparticles were dispersed and stirred for 30 min. with the aid of sonication to obtain a homogeneous mixture. The films were prepared by spin coating method kept in an electrical furnace at 50°C for 3 h. This work has demonstrated the advantages of using a fluorescent dye-doped PMMA/SiO<sub>2</sub> nanohybrid matrix for a luminescent solar concentrator.

Mustafa M. Demir et al.<sup>33</sup> synthesized PMMA-ZnO composites that show visible light transmittance, UV absorption, and moderately high refractive index. Initially, by a precise precipitation through esterification of zinc acetate dihydrate with pentane-1-ol, surface-modified ZnO nanoparticles with 22 nm average diameter were nucleated. In situ, monolayer coverage modified the surface of growing crystalline particles with *tert*-butylphosphonic acid (*t*BuPO<sub>3</sub>H<sub>2</sub>). Second, the surface-modified particles were incorporated into PMMA by in situ bulk polymerization. The composites' refractive index depends linearly on the volume fraction of ZnO and varies from 1.487 to 1.507 ( $\phi = 7.76\%$ ) at 633 nm.

### 5.2.3 NANOCOMPOSITE OF PMMA WITH CNT OR GRAPHENE

Graphene, a well-known honeycomb network with monolayer of carbon atoms, has attracted significant attention due to its exceptional properties such as excellent mechanical, thermal, and electrical properties and its potential use in various fields, such as electronics supercapacitors and sensors. The carbon nanotubes (CNT) are molded by rolling these layers at precise chiral angles. Graphene and CNTs possess an extremely high aspect ratio and exceptional properties, depending on the rolling angle and radius.

Diana Vilela et al.<sup>34</sup> proposed novel single-walled carbon nanotube press-transfer electrodes (SW-PTEs) for microfluidic sensing, in which press-transferring of carbon nanotubes on PMMA substrates was done, efficiently coupled to microfluidic chips, and act as the exclusive transducer

in electrochemical sensing. It was beneficial for the direct coupling of nanomaterials such as carbon nanotubes (CNTs) in microchip end-channel configurations since it avoids the classical casting approach, allowing the direct detection of target analytes on the nanomaterial surface simply and easily. T. Ramanathan et al.<sup>36</sup> fabricated PMMA/functionalized graphene sheets with improved PMMA-graphene interaction. With the addition of 0.05 wt% functionalized graphene sheets in PMMA, an improvement in glass transition temperature, modulus, ultimate strength, and thermal stability is attained. Kar et al.<sup>37</sup> adapted an exceptional method to concentrate multiwall carbon nanotubes wrapped with PMMA to the interface of immiscible PVDF-ABS. They showed enhanced stress transfer, 108% raise in the tensile strength, and 48% improvement in Young's modulus with 3 wt% PMMA wrapped MWNTs compared to the neat blends. The study insights into designing new materials with higher mechanical, electrical conductivity, and EM shielding applications. Shital Patangro Pawr et al.<sup>38</sup> prepared PMMA wrapped MWCNTs to the interface of polycarbonate/styrene-acrylonitrile (PC/SAN) blends with a higher stress transfer across the interface hence improving the mechanical, dynamic mechanical, electrical conductivity, and microwave shielding properties. Shiqiang Song et al.<sup>39</sup> synthesized Pyrene-functionalized PMMA-block-PDMS copolymers and further induced functionalize graphene oxide (GO) with higher tensile strength, Young's modulus, elongation at break, and toughness of PMMA, which is mainly accredited to the consistent dispersion and improved interfacial adhesion between GO@Py-PMMA-b-PDMS and PMMA.

#### **5.2.4 NANOCOMPOSITE OF PMMA WITH CHALCOGENIDES**

The compounds of sulfides, selenides, and tellurides are generally referred to as chalcogenides. Significant performance on optical properties is found by combining PMMA with them. Therefore, the composites have substantial applications in sensors and energy devices.

Santanu Karan et al.<sup>40</sup> employed a microwave (MW) assisted synthesis in preparing cadmium sulfide quantum dots in dimethylformamide in the PMMA solution. Cadmium acetate in DMF was prepared with an appropriate amount of PMMA, thiourea was added to the resulting solution. The solution was then irradiated with microwave radiation for 20–30 s. and it was repeated six times. The solution was then allowed to cool down to room temperature. The PMMA–CdS QDs were centrifuged, washed several times with ethanol and MilliQ water, dried under vacuum, and collected. PMMA–CdS QDs were

characterized by recording the UV–Vis absorption, photoluminescence (PL), and lifetime decay spectra at room temperature.

Qilin Wei et al.<sup>41</sup> introduced CdX (X = S, Se):Ag (Cu) QDs with into a PMMA matrix, with capable applications as a luminescent solar concentrator.

Yuzhen Li et al.<sup>42</sup> formulated ZnS nanoparticles, coated with PMMA, in n-heptane/sodium bis(2-ethylhexyl) sulfosuccinate (AOT)/water microemulsions. The Zn(Ac)<sub>2</sub> and Na<sub>2</sub>S aqueous solutions were set at 0.3 mol/L. Then, aqueous solutions of Zn(Ac)<sub>2</sub> and Na<sub>2</sub>S were prepared and the microemulsions are made by adding the corresponding aqueous solution to the surfactant solution. The microemulsion containing Na<sub>2</sub>S was added slowly into another microemulsion containing Zn(Ac)<sub>2</sub> under stirring. The nano-ZnS UV-Vis absorption peak at about 300 nm, indicates the quantum confinement effect. The PMMA and the water cores play a significant role in controlling particles aggregates. This method can be expected to be used for preparing other kinds of inorganic/polymer nanocomposite.

### 5.2.5 NANOCOMPOSITE OF PMMA WITH POLYMERS

PMMA has been widely incorporated with polymers like polyvinyl alcohol (PVA), polyvinyl acetate (PS), and polymethyl methacrylate (PVDF). The incorporation of these polymers induces mechanical and thermal stability as well as processability.

Cui Mao et al.<sup>43</sup> have designed octadecyl amine-functionalized graphene (GE-ODA) filled immiscible PMMA/PS blends with improved electrical properties. Their results show that the composites' electrical conductivity can be maximum when GE-ODA nanosheets are penetrated in the PS region. Obtained octadecylamine-functionalized graphene used in work by modifying graphene oxide with octadecylamine (ODA) and then reducing it with hydroquinone. PS/PMMA/GE-ODA composites were prepared by solution blending.

Fuminori Arai et al.<sup>44</sup> investigated the crystallization behavior and higher-order structures of Poly (vinylidene fluoride) (PVDF) and isotactic-poly(methyl methacrylate) (i-PMMA) using SAXS, WAXS, and DSC. S. Rajendran et al.<sup>45</sup> synthesized polymer electrolytes based on PMMA/PVdF blend polymer with different salt concentrations were prepared using the solvent casting technique. The ionic conductivity of PMMA/PVDF complexes was found to be the maximum value of  $4.2 \times 10^{-3}$  S/cm.

### 5.2.6 NANOCOMPOSITE OF PMMA WITH MULTI-COMPONENTS

Multi-functional materials are obtained by incorporating PMMA nanocomposites with multicomponents (more than one type of nanomaterial) that have been prepared to receive multiple properties (like electric, optic, and magnetic properties) within the single material or to make significant improvements in the existing properties. The hybrid materials thus made have much wider choice of applications. The commonly fabricated PMMA multicomponent systems are based on PMMA/CNTs.

Qiuyun Ouyang et al.<sup>46</sup> synthesized G/Ag<sub>2</sub>S/PMMA organic glasses and used Z-scan technique to investigate the nonlinear absorption behavior of the G/Ag<sub>2</sub>S/PMMA glasses. They synthesized G/Ag<sub>2</sub>S composites using hydrothermal process. Then G/Ag<sub>2</sub>S composites were dispersed in methyl methacrylate (MMA) to prepare an organic glass by a casting method, and the MMA was polymerized to poly (methyl methacrylate) (PMMA). The results disclosed improved reverse saturable absorption properties for G/Ag<sub>2</sub>S/PMMA with G/Ag<sub>2</sub>S in comparison with G/PMMA and Ag<sub>2</sub>S/PMMA, attributed to the cooperative effects between graphene and Ag<sub>2</sub>S. The effective NLA coefficient  $\beta_{\text{eff}}$  of the G/Ag<sub>2</sub>S/PMMA organic glasses was 103 cm/GW. This material is found to have much application in optical limiting applications.

Gyanaranjan Sahoo et al.<sup>47</sup> fabricated (PMMA/r-GO/Au) nanohybrids by a facile, single-step synthetic method for supercapacitor applications. The protocol includes free radical polymerization of methyl methacrylate (MMA) with the addition of graphene oxide (GO), and following reduction of Au precursor and graphene oxide, hence the formation of Au nanoparticles on (r-GO). The enhancement in electrochemical performance furnished the nanohybrid, a promising candidate for supercapacitor applications.

### 5.2.7 NANOCOMPOSITES OF PMMA WITH NATURAL FIBERS

Farah Fahma et al.<sup>48</sup> prepared poly (methyl methacrylate) (PMMA)-cellulose nanofibers nanocomposite by immersion precipitation method using various nanofiber contents. The as-prepared nanocomposites showed good dispersion of fillers and were transparent. It is also proved by the thermogravimetric and differential scanning calorimetry analyses that the tensile modulus and strength increased with increasing nanofiber content. Also, the nanocomposites' storage modulus increased with increasing nanofiber content from the DMA



measurements. Chuchu Chen et al.<sup>49</sup> prepared PMMA/Chitin nanocomposites by incorporating Ultra-long chitin nanofibers into polymethyl methacrylate (PMMA) resin. They found significant improvement of tensile strength and Young's modulus of the composite with of chitin nanofibers compared to neat PMMA. Light transmittance test showed that the original transparency of PMMA is well conserved. Furthermore, it is shown that the thermal stability of PMMA is improved much by the addition of chitin nanofiber. They propose the composite to various commercial applications, including flexible electronic printing and organic thin-film photovoltaic devices as sustainable green nano-materials.

Alina Sionkowska et al.<sup>50</sup> investigated the properties of composites made of the blends of chitosan and collagen with the addition of poly (methyl methacrylate) and hydroxyapatite. They found the mechanical properties comparable to the spongy part of human bone. They also found that the addition of hydroxyapatite has improved the thermal stability and mechanical properties of the composites. Tao Huang et al.<sup>51</sup> reported the poly (methyl methacrylate)/2,2,6,6-tetramethylpiperidyl-1-oxyl oxidized cellulose nanofiber (PMMA/TOCN) nanocomposites, with good dispersion, excellent mechanical properties, high transparency, and controllable birefringence. The tensile strength and Young's modulus of PMMA were considerably enhanced with the addition of TOCN and the composite is found to have applications in optical devices and in the engineering field. Esra Erbas et al.<sup>14</sup> synthesized poly (methylmethacrylate) (PMMA)-cellulose nanocomposite by solvent casting method. They prepared nanofiber networks with: (i) nanofibrillated cellulose, (ii) cellulose nanocrystals, and (iii) bacterial cellulose from *nata de coca*. They found an increased flexural strength and increased storage modulus. These found that at even low cellulose nanomaterials content enhanced thermal and mechanical properties of PMMA, and the composite can be used for packing, screens, transparent films, and light-weight translucent materials.

### 5.2.8 FUNCTIONALIZATION OF PMMA

Shiqiang Song et al.<sup>39</sup> synthesized pyrene-functionalized poly(methyl methacrylate)-*block*-polydimethylsiloxane (Py-PMMA-*b*-PDMS) copolymers *via* activators regenerated by an electron transfer atom transfer radical polymerization (ARGET ATRP) method and further used to functionalize graphene oxide (GO) through the  $\pi$ - $\pi$  interaction between pyrene and the carbon sheets. The tensile strength, Young's modulus, elongation at break,

**TABLE 5.1** Summary of Synthesis Methods for Different Types of PMMA Composites.

Nanocomposite type	Secondary component	Synthesis method	Applications/References
PMMA/metal	Au	Spin coating, redox-transmetalation, UV-, thermal-, and MW irradiation	Conductive films, plasmonic biosensing, SERS substrate <sup>11,13,19,20</sup>
	Ag	Bi-in situ emulsion polymerization, radical-mediated dispersion polymerization	Enhanced antimicrobial efficacy <sup>21,22</sup>
	Pt	Chemical reduction method followed by ball milling	Antimicrobial denture material <sup>23</sup>
	Ni	Electroless Ni deposition	Reduced electrical resistivity <sup>24</sup>
PMMA/metal oxide	Fe <sub>3</sub> O <sub>4</sub>	One-pot hydrothermal method, Double miniemulsion polymerization	Superparamagnetic properties, multimodal protein separation <sup>25–27</sup>
	TiO <sub>2</sub>	Intercalation method, in situ sol-gel/ polymerization	Dielectric material, optical switching applications <sup>28,29</sup>
	NiO	In situ bulk polymerization	Flexible electronic devices <sup>30</sup>
	SiO <sub>2</sub>	Emulsion polymerization, spin coating method	Luminescent solar concentrator <sup>31,32</sup>
	ZnO	Acid-catalyzed esterification of zinc acetate followed by in situ bulk polymerization	Visible light transmittance, UV absorption, and high refractive index <sup>33</sup>
PMMA/CNT or Graphene	CNT	Press-transferred to PMMA, Bi-in situ emulsion polymerization followed by dip coating	Microfluidic sensing <sup>34,35,37,38</sup>
	Graphene	Functionalized graphene in poly (methyl methacrylate)	High Modulus, ultimate strength and thermal stability <sup>36,39</sup>
PMMA / chalcogenides	CdS	MW-assisted synthesis	Surface trap state photoluminescence <sup>40</sup>
	CdSe	In situ polymerization	Luminescent solar concentrator <sup>41</sup>
	ZnS	Microemulsion method	Controlling particle aggregation <sup>42</sup>
PMMA/polymers	PS	Solution blending	Improved electrical properties <sup>43</sup>

**TABLE 5.1** (Continued)

Nanocomposite type	Secondary component	Synthesis method	Applications/References
	PVDF	Solvent casting	Improved ionic and thermal conductivity <sup>44,45</sup>
PMMA/ multicomponent	G/Ag <sub>2</sub> S	Hydrothermal method followed by solvent casting	Enhanced reverse saturable absorption (RSA) <sup>46</sup>
	r-GO/Au	Free radical polymerization	Symmetric supercapacitor applications <sup>47</sup>
PMMA/Natural fiber	Cellulose	Immersion precipitation, solution casting	Excellent thermal and mechanical properties <sup>48,51,14</sup>
	Chitin	Mechanical and solution casting	Improved thermal and mechanical properties <sup>49</sup>
	Chitosan	Solution casting	Improved thermal and mechanical properties <sup>50</sup>

and toughness of PMMA were increased by 23, 54, 117, and 218%, respectively. The change in decomposition temperature from 349 to 360°C, the haze value from 2.1 to 16.8%, and the refractive index from 1.48 to 1.51 were significant. Hence enlightening the thermomechanical and optical characteristics of PMMA for light-emitting diodes and photovoltaics applications. Functionalization of polymers/nanofillers<sup>52–55</sup> is essential for the varied applications of polymer composites.<sup>56–60</sup>

Poly (methyl methacrylate)-based dielectric materials are attractive for many electronic devices even though the low dielectric constant and hydrophobic nature of PMMA is a drawback. Vijay Kumar Thakur et al.<sup>61</sup> reported synthesis of functionalized PMMA using dopamine (DOPA) to develop polymers with enhanced dielectric properties. They reported the increase of dielectric constant by 70% compared to pristine PMMA films below 100 Hz, which is attributed to the intrinsic properties of DOPA. And a change in the storage modulus and the  $T_g$  was also found. Timothy M. Long et al.<sup>62</sup> reported the formation of trichlorosilane monolayers on SiO<sub>2</sub> with the functionalization of PMMA. Initially, the water-vapor plasma causes hydroxylation. Secondly, plasma-treated PMMA was treated with a trichlorosilane solution to form the functional layer. Suying Wei et al.<sup>63</sup> described the photochemical alteration of PMMA to produce carboxylic acid surface moieties. Additional functionalization of PMMA surfaces can be done due to the chemical patterns formed, and hence various physical properties can be altered.

F. Fixe et al.<sup>64</sup> fabricated PMMA substrates for immobilizing DNA in microarrays by the reaction of PMMA with hexamethylene diamine to form an aminated surface. And it can be useful for making diagnostics devices with functions like sample preparation, treatment, and recognition by means of microfabrication and microelectronic methods. E. Sarantopoulou et al.<sup>65</sup> reported that at 157 nm, laser irradiation on PMMA films makes variations of polymer film thicknesses from sorption of methanol/ethanol analytes by 400%, in comparison to the non-irradiated areas. Depending on the irradiation conditions, surface and volume morphological changes in the nano/microdomain induce the structural changes. Hence, 157 nm laser treatments can make polymer sensor arrays with improved recognition efficacy of liquid/gas molecules.

A. Convetino et al.<sup>66</sup> synthesized TiO<sub>2</sub>/PMMA thin films with different surface ligands (oleic and phosphonic acid). They found that the vapor adsorbing ability, transparency, and refractive index of composites depend on inorganic nanorods (NRs) and the nature of the surface ligands. Alyssa C.

Henry et al.<sup>67</sup> reported the synthesis of amine-terminated PMMA surfaces, demonstrated immobilization of enzymes, and are operative in the constraint digestion of dsDNAs.

### 5.3 APPLICATIONS OF PMMA NANOCOMPOSITES

#### 5.3.1 PMMA NANOCOMPOSITES AS SENSORS

The gas sensors are commonly used for indoor air quality monitoring, carbon monoxide detectors, automobile exhaust monitoring, gas leak detectors, home food spoilage monitors, and smoke detectors. Jose K Abraham et al.<sup>68</sup> fabricated a gas sensor with an altered multiwalled carbon nanotube (*f*-CNT) chemiresistor as the sensing element. They have combined *f*-CNT/polymer composite film patterned on the printed circuit board. The gas sensor works such that the chemiresistor composite film changes the resistance on exposure to different gases. It was found that the *f*-CNT/PMMA composite film demonstrations quick response and change in resistance for varied organic gases. Biju Philip et al.<sup>69</sup> also designed a multiwalled carbon nanotubes (CNTs) and modified multiwalled carbon nanotubes (*f*-CNTs)-PMMA films for gas-sensing applications. Inpil Kang et al.<sup>70</sup> fabricated piezoresistive strain sensor by using CNT/PMMA composites health monitoring applications. They used larger multiwalled carbon nanotubes, improving the sensor's strain transfer, repeatability, and linearity.

Lu-Bin Zhong et al.<sup>20</sup> fabricated a surface-enhanced Raman scattering substrate, which provides excellent optical transparency, good flexibility, and high SERS activity. The AuNPs/PMMA substrate film was fabricated by self-assembly of gold nanoparticles (AuNPs) on PMMA template, which showed the recognition of malachite green isothiocyanate at a concentration of 0.1 nM, and the Raman enhancement factor (EF) was found to be  $(2.4 \pm 0.3) \times 10^7$ .

#### 5.3.2 PMMA NANOCOMPOSITES FOR ELECTRICAL APPLICATIONS

High-*k* polymer nanocomposites are widely used in dielectric applications and energy storage materials because of their flexibility, processing comfort, and low price. For the synthesis of high-*k* polymer nanocomposites, core-shell nanoarchitecture is widely used. Xingyi Huang et al.<sup>71</sup> to propose and prepare high-*k* polymer nanocomposites of core-shell nanoarchitecture.

Liyuan Xie et al.<sup>72</sup> synthesized core-shell BaTiO<sub>3</sub>/(PMMA) nanocomposites by atom transfer radical polymerization of methyl methacrylate from the surface of BaTiO<sub>3</sub> nanoparticles with improved dielectric constant and low loss in a varied range of frequencies. Mi Li et al.<sup>73</sup> prepared PMMA/rPANI@rGO composites were achieving improved dielectric constant and lesser dielectric loss in *comparison* with PMMA/rGO composites. Compared with the PMMA/rGO composites, the PMMA/rPANI@rGO composites have much higher dielectric constants and much lower dielectric loss, which is desirable for practical applications. The considerable increase in dielectric loss in PMMA/rGO composites should be attributed to the percolation network of rGO agglomerates, which causes a dramatic increase in leakage currents with the rise in the rGO content.

Silvia Gross et al.<sup>74</sup> studied the use of PMMA as host matrix for three very different composite materials. The systems concerns (i) the fabrication of composite layers prepared by the UV initiated polymerization of liquid methylmethacrylatemonomer comprising a ZnS:Cu phosphor powder distribution; (ii) the preparation of low- $\kappa$  dielectric films of composition [(PMMA) $x$ (PVC) $y$ ]/(m-SiO<sub>2</sub>) $z$  where  $0 \leq z \leq 38.3$  wt% and  $x = y = (100 - z)/2$  and the investigation of their electrical response, macromolecular interactions and relaxation phenomena; and (iii) methacrylate-functionalized zirconium oxometallate clusters embedded in PMMA and its dielectric characterization.

### 5.3.3 PMMA FOR OPTICAL/OPTOELECTRONIC APPLICATIONS

S. Sugumaran et al.<sup>75</sup> prepared transparent nanocomposite PVA–TiO<sub>2</sub> and PMMA–TiO<sub>2</sub> thin films were by an easy and cost-effective dip-coating method. The high value of dielectric constant ( $\epsilon' = 24.6$  and  $\epsilon' = 26.8$ ) was obtained for the composite films. The conduction in the composite films was found to be due to electrons. The transmittance of the films was above 80% in the visible region, and the optical band gap calculated using Tauc's plot was about 3.77 eV and 3.78 eV, respectively for PVA–TiO<sub>2</sub> and PMMA–TiO<sub>2</sub> films. The refractive index ( $n$ ) values were calculated as between 1.6 and 2.3. The observed amorphous structure, good optical properties, and dielectric behavior of the prepared nanocomposite thin films indicated that these films could be used in opto-electronic devices and thin film transistors.

H. Althues et al.<sup>76</sup> have presented an efficient method for the generation of ZnS:Mn/PMMA luminescent inorganic-organic hybrid materials. Transparent luminescent nanocomposites were obtained using the bulk polymerization of transparent dispersions containing manganese-doped ZnS

nanoparticles in a blend of MMA and acrylic acid. In the nanocomposites, highly transparent acrylic glasses with a transmittance of 87% due to the small particle size and high degree of dispersion.

Jingang Hu et al.<sup>77</sup> prepared multifunctional optical diffusers based on hybrid polysiloxane@CeO<sub>2</sub>@PMMA microspheres by UV curing process. The novel diffusers had enhanced UV shielding effect, heat resistance, mechanical, fluorescence, anti-aging properties, and showed a strong NIR absorption, which had a potential application in absorbing materials. Feng Jin et al.<sup>78</sup> fabricated a PMMA-SH/CdSe–Au nanocomposite thin films by a layer-by-layer assembly method which showed excellent transparency, thermal stability, and optical limiting response to a 532 nm pulsed laser. The optical limiting threshold value was found to be 13 J/cm<sup>2</sup> and was found to be a good candidate for laser optical limiting applications.

Yu Zhang et al.<sup>79</sup> have successfully employed a two-step polymerization process to synthesize highly luminescent and transparent bulk PMMA/ZnO nanocomposites. The resulted PMMA/ZnO nanocomposites showed excellent homogeneity, transparency, luminescence, and UV-shielding ability, which is primarily attributed to the existing defects states in the quantum-sized ZnO particles.

Ranadip Bera et al.<sup>80</sup> synthesized single-wall carbon nanohorn (SWCNH)/graphene nanoplates (GNP)/poly(methyl methacrylate) (PMMA) nanocomposites with high electrical conductivity ( $4.54 \times 10^{-2}$  S/cm) and high EMI SE value  $\sim (-23.6$  dB) even at a lower loading of fillers.

Kenichi Hayashida et al.<sup>81</sup> prepared PMMA–ZnO composites using surface-initiated polymerization technique and found that the dielectric constant  $\epsilon_r'$  was highly improved by irradiation of UV light which was attributed due to the Maxwell–Wagner polarization of the free electrons. The composite showed strong absorption of UV light and low light scattering and was found to be a capable material for high sensitivity and less-loss UV light sensors.

Anshu Singhal et al.<sup>82</sup> prepared self-supporting poly(methyl methacrylate) (PMMA)/In<sub>2</sub>O<sub>3</sub> with varying In<sub>2</sub>O<sub>3</sub> nanocomposite films by solution-casting and spin-coating techniques. The results showed that with the small loading of filler NPs, the thermal stability, UV-absorbing capacity and transparency in the visible region was extremely enhanced.

Haider Mohammed Shanshool et al.<sup>83</sup> prepared the polymethyl methacrylate (PMMA)/ZnO nanocomposites as foils by using the casting method. Nanocomposites have been prepared by increasing concentrations of ZnO nanoparticles as fillers within the PMMA matrix. The real, imaginary parts and the absolute

value of the third-order nonlinear optical susceptibility  $\chi(3)$  have been calculated in the order of  $10^{-7}$  e.s.u. Hence, the nanocomposites indicate a promising candidate to be used as an optical limiter.

### 5.3.4 OTHER APPLICATIONS

PMMA and PMMA composites are also used in other applications such as biomedical, packaging, electronics, mechanical, etc. Dan Kai et al.<sup>84</sup> prepared a series of poly(methyl methacrylate) (PMMA) grafted lignin copolymers by atom transfer radical polymerization. This lignin–PMMA copolymers were further blended with poly( $\epsilon$ -caprolactone) (PCL) and made nanofibrous composites by electrospinning. They carried out cell culture studies of PCL/lignin–PMMA nanofibers and found that they are biocompatible and promoted the proliferation, attachment, and interactions of human dermal fibroblasts. This study suggests that the electrospun nanofibers are potentially useful as biomaterial substrates for biomedical applications. Yue Sa et al.<sup>85</sup> prepared injectable *p*-PMMA/CS–GP/nano-HA/GM cement in which PMMA/chitosan–glycerophosphate (CS–GP) hydrogel, which is the pore-forming mediator which helps bone tissue ingrowth and hydroxyapatite (nano-HA)/antibiotic gentamicin (GM) which is the transporter. The hybrid cement enhances the properties, including antibacterial activities of PMMA which is recommended the material for bone reconstruction applications.

Elke Van De Walle et al.<sup>86</sup> fabricated cell-interactivity coating for methacrylate-based materials. They described the fabrication of (PMMAPEG)/(PDA)/gelatin material with cell interactivities, regardless of the physical and chemical properties of the substrate, and hence can be a promising material for medical device and organic electronic device packing. Y Kim et al.<sup>87</sup> reported the interfacial fracture toughness of SiNx–PMMA multilayer material. Four-point bending assessments showed that the adhesion improved from 4.8 to 10 J/m<sup>2</sup>, and the adhesion strength amplified to 28 J/m<sup>2</sup>.

In microelectronics technology, materials with high-thermal-conductivity and less-dielectric-loss composites are crucial. Abhilash Pullanchiyodan et al.<sup>88</sup> reported the development of (AgNP)/boron nitride nanosheets (BNNs)/(PMMA) composites with high thermal conductivity, low dielectric constant, and less-loss nanocomposite. The thermal conductivity (TC) improvement of around 363% was found for nanocomposite of 0.35 V/f of hybrid filler (1.48 W/m K). A low dielectric constant ( $<5$ ), low loss ( $10^{-2}$ ), and low alternating current conductivity ( $10^{-7}$  S/cm) was found using dielectric measurements.



Viet Hung Pham et al.<sup>89</sup> reported a facile method for preparing conductive PMMA-RGO composites with high electrical conductivity of 64 S/m. Moreover, even at lower filler loadings, the storage modulus improved by 30%, and glass transition temperature changed by 15°C. This composite could be a good opponent to other polymer graphene composites for varied applications.<sup>90–94</sup>

Laida Cano et al.<sup>95</sup> prepared a diglycidyl ether of bisphenol A (DGEBA) epoxy monomer-polystyrene-*block*-polymethyl methacrylate (PS-*b*-PMMA) composites and found the mechanical property improvements such as fracture toughness. Also, the AFM studies showed exhibited an enhancement of the elastic modulus of the PMMA/(DGEBA-MCDEA) matrix up to 25 wt% PS-*b*-PMMA content. Changanti Srinivasa Reddy et al.<sup>96</sup> reported the fabrication of Tungsten disulfide inorganic nanotubes (WS<sub>2</sub> INTs) embedded into a PMMA nanofiber matrix by electrospinning technique. The elastic modulus improved 10 times and 22 for 1 wt% and 2 wt%, loading of WS<sub>2</sub> INTs, respectively. Also, the increment in tensile strength by 35%, the toughness by 30% and the dielectric constant by 61% higher were noted. Hence, the composites were found to have applications in high-energy absorption materials.

## 5.4 CONCLUSION AND REMARKS

PMMA nanocomposites have shown much promise as an electrical, optical, optoelectronics, and sensing element, as many applications have shown. Nanocomposites of PMMA showed improved properties with respect to pristine PMMA. PMMA nanocomposites offer safer detection of chemicals by inducing higher selectivity and sensitivity. These PMMA-based composites and hybrids have proven to be exciting materials for developing electroluminescent devices and dielectric films for microelectronic applications. The reasons for the choice of PMMA as host matrix are due to some exciting features of this polymer that can be listed as follows:

1. PMMA can be readily available starting from a liquid monomer. Since the use of a liquid precursor allows a molecular mixing with the inorganic nanoparticles already in the starting solution, thus ensuring a uniform distribution of the nanoparticles in the organic backbone;
2. The polymer can be easily cast into a film. Thus, the shape of the final material can be tuned according to the device requirements;
3. The low value of the dielectric constant of pure PMMA, is a good starting point for further tuning this critical property; (4) It showed

excellent thermal stability, optical lucidity, and weather and chemical resistance.<sup>65</sup> Finally, to identify the fundamental mechanism involved in PMMA and its nanocomposites, such as analyte sensing and electric and optoelectronic properties, novel approaches are vital, which will empower us to fabricate and commercialize highly selective materials for specific agents.

## KEYWORDS

- **polymethyl methacrylate**
- **nanocomposites**
- **electrical properties**
- **optical**

## REFERENCES

1. Pawar, E. A Review Article on Acrylic PMMA. *IOSR J. Mech. Civil Eng.* **2016**, *13*, 1–4. DOI: 10.9790/1684-1302010104.
2. Lee, S.; Müller, A. M.; Al-Kaysi, R.; Bardeen, C. J. Using Perylene-Doped Polymer Nanotubes as Fluorescence Sensors. *Nano Lett.* **2006**, *6*, 1420–1424. DOI: 10.1021/nl060446z.
3. Chen, W.; Liu, X.; Liu, Y.; Bang, Y.; Il Kim, H. Synthesis of PMMA and PMMA/PS Nanoparticles by Microemulsion Polymerization with a New Vapor Monomer Feeding System. *Colloids Surf. A* **2010**, *364*, 145–150. DOI: 10.1016/j.colsurfa.2010.05.010.
4. Piperno, S.; Lozzi, L.; Rastelli, R.; Passacantando, M.; Santucci, S. PMMA Nanofibers Production by Electrospinning. *Appl. Surf. Sci.* **2006**, *252*, 5583–5586. DOI: 10.1016/j.apsusc.2005.12.142.
5. Qureshi, A.; Mergen, A.; Aktaş, B. Dielectric and Magnetic Properties of YIG/PMMA Nanocomposites. *J. Phys.: Conf. Ser.* **2009**, *153*, 012061. DOI: 10.1088/1742-6596/153/1/012061.
6. Tamboli, M. S.; Palei, P. K.; Patil, S. S.; Kulkarni, M. V.; Maldar, N. N.; Kale, B. B. Polymethyl Methacrylate (PMMA)-Bismuth Ferrite (BFO) Nanocomposite: Low Loss and High Dielectric Constant Materials with Perceptible Magnetic Properties. *Dalton Trans.* **2014**, *43*, 13232–13241. DOI: 10.1039/c4dt00947a.
7. Lü, C.; Yang, B. High Refractive Index Organic–Inorganic Nanocomposites: Design, Synthesis and Application. *J. Mater. Chem.* **2009**, *19*, 2884. DOI: 10.1039/b816254a.
8. Morselli, D.; Bondioli, F.; Fiorini, M.; Messori, M.; Poly(Methyl Methacrylate)-TiO<sub>2</sub> Nanocomposites Obtained by Non-Hydrolytic Sol-Gel Synthesis: The Innovative Tert-Butyl Alcohol Route. *J. Mater. Sci.* **2012**. DOI: 10.1007/s10853-012-6651-4.

9. Kuan, H. C.; Chiu, S. L.; Chen, C. H.; Kuan, C. F.; Chiang, C. L. Synthesis, Characterization, and Thermal Stability of PMMA/SiO<sub>2</sub>/TiO<sub>2</sub> Tertiary Nanocomposites via Non-Hydrolytic Sol-Gel Method. *J. Appl. Polym. Sci.* **2009**. DOI: 10.1002/app.30201.
10. Yeh, J. M.; Huang, K. Y.; Dai, C. F.; Chand, B. G.; Weng, C. J. Organic-Acid-Catalyzed Sol-Gel Route for Preparing Poly(Methyl Methacrylate)-Silica Hybrid Materials. *J. Appl. Polym. Sci.* **2008**. DOI: 10.1002/app.28778.
11. Yilmaz, E.; Suzer, S. Au Nanoparticles in PMMA Matrix: In Situ Synthesis and the Effect of Au Nanoparticles on PMMA Conductivity. *Appl. Surf. Sci.* **2010**, 256, 6630–6633. DOI: 10.1016/j.apsusc.2010.04.060.
12. Kassaei, M. Z.; Mohammadkhani, M.; Akhavan, A.; Mohammadi, R. In Situ Formation of Silver Nanoparticles in PMMA via Reduction of Silver Ions by Butylated Hydroxytoluene. *Struct. Chem.* **2011**, 22, 11–15. DOI: 10.1007/s11224-010-9671-1.
13. Alsawafta, M.; Badilescu, S.; Paneri, A.; Truong, V.-V.; Packirisamy, M. Gold-Poly(Methyl Methacrylate) Nanocomposite Films for Plasmonic Biosensing Applications. *Polymers* **2011**, 3, 1833–1848. DOI: 10.3390/polym3041833.
14. Erbas Kiziltas, E.; Kiziltas, A.; Bollin, S. C.; Gardner, D. J. Preparation and Characterization of Transparent PMMA–Cellulose-Based Nanocomposites. *Carbohydr. Polym.* **2015**, 127, 381–389. DOI: 10.1016/j.carbpol.2015.03.029.
15. Chau, J. L. H.; Hsieh, C. C.; Lin, Y. M.; Li, A. K. Preparation of Transparent Silica-PMMA Nanocomposite Hard Coatings. *Progress Org. Coat.* **2008**. DOI: 10.1016/j.porgcoat.2008.02.005.
16. Meneghetti, P.; Qutubuddin, S. Synthesis of Poly(Methyl Methacrylate) Nanocomposites via Emulsion Polymerization Using a Zwitterionic Surfactant. *Langmuir* **2007**. DOI: 10.1021/la0357099.
17. Prado, B. R.; Bartoli, J. R. Synthesis and Characterization of PMMA and Organic Modified Montmorillonites Nanocomposites via In Situ Polymerization Assisted by Sonication. *Appl. Clay Sci.* **2018**, 160, 132–143. DOI: 10.1016/j.clay.2018.02.035.
18. Sain, S.; Ray, D.; Mukhopadhyay, A.; Sengupta, S.; Kar, T.; Ennis, C. J.; Rahman, P. K. S. M. Synthesis and Characterization of PMMA-Cellulose Nanocomposites by In Situ Polymerization Technique. *J. Appl. Polym. Sci.* **2012**. DOI: 10.1002/app.36723.
19. Wu, H.; Lin, K.; Yu, Y.; Ho, C.; Wei, M.; Lu, F.; Tseng, W. J. Effect of pH on Film Structure and Electrical Property of PMMA–Au Composite Particles Prepared by Redox Transmetalation. *Appl. Surf. Sci.* **2014**, 289, 524–528. DOI: 10.1016/j.apsusc.2013.11.028.
20. Zhong, L.; Yin, J.; Zheng, Y.; Liu, Q.; Cheng, X.; Luo, F. Self-Assembly of Au Nanoparticles on PMMA Template as Flexible, Transparent, and Highly Active SERS Substrates. *Analy. Chem.* **2014**, 86, 6262–6267.
21. Guo, Y. L. W.; Xu, C.; Xiong, J. Y.; Ji, X. L. Synthesis of Nanosilver/PMMA Composites Via Ultrasonically Bi-In Situ Emulsion Polymerization. *J. Thermoplast. Compos. Mater.* **2007**, 20, 523–533. DOI: 10.1177/0892705707083633.
22. Kong, H.; Jang, J. Antibacterial Properties of Novel Poly(Methyl Methacrylate) Nanofiber Containing Silver Nanoparticles. *Langmuir* **2008**, 24, 2051–2056. DOI: 10.1021/la703085e.
23. Nam, K. Characterization and Bacterial Anti-Adherent Effect on Modified PMMA Denture Acrylic Resin Containing Platinum Nanoparticles **2014**, 207–214.
24. Lin, K.-J.; Wu, H.-M.; Yu, Y.-H.; Ho, C.-Y.; Wei, M.-H.; Lu, F.; Tseng, W. J. Preparation of PMMA-Ni Core-Shell Composite Particles by Electroless Plating on Polyelectrolyte-Modified PMMA Beads. *Appl. Surf. Sci.* **2013**, 282, 741–745. DOI: 10.1016/j.apsusc.2013.04.175.

25. Cao, Z.; Jiang, W.; Ye, X.; Gong, X. Preparation of Superparamagnetic Fe<sub>3</sub>O<sub>4</sub>/PMMA Nano Composites and Their Magnetorheological Characteristics. *J. Magn. Magn. Mater.* **2008**, *320*, 1499–1502. DOI: 10.1016/j.jmmm.2007.12.007.
26. Zhang, C. C.; Li, X.; Yang, Y.; Wang, C. Polymethylmethacrylate/Fe<sub>3</sub>O<sub>4</sub> Composite Nanofiber Membranes with Ultra-Low Dielectric Permittivity. *Appl. Phys. A* **2009**, *97*, 281–285. DOI: 10.1007/s00339-009-5378-9.
27. Lan, F.; Liu, K.-X.; Jiang, W.; Zeng, X.-B.; Wu, Y.; Gu, Z.-W. Facile Synthesis of Monodisperse Superparamagnetic Fe<sub>3</sub>O<sub>4</sub>/PMMA Composite Nanospheres with High Magnetization. *Nanotechnology* **2011**, *22*, 225604. DOI: 10.1088/0957-4484/22/22/225604.
28. Rajan Prakash, R.; Pandiarajan, S.; Venkatesh, P.; Kamaraj, N. Performance Analysis of PMMA—TiO<sub>2</sub> Nanocomposite Dielectrics. In *2011 International Conference on Emerging Trends in Electrical and Computer Technology*; IEEE, 2011; pp 46–49. DOI: 10.1109/ICETECT.2011.5760089
29. Yuwono, A. H.; Xue, J.; Wang, J.; Elim, H. I.; Ji, W.; Li, Y.; White, T. J. Transparent Nanohybrids of Nanocrystalline TiO<sub>2</sub> in PMMA with Unique Nonlinear Optical Behavior. *J. Mater. Chem.* **2003**, *13*, 1475. DOI: 10.1039/b211976e.
30. García-Cerda, L. A.; Romo-Mendoza, L. E.; Quevedo-López, M. A. Synthesis and Characterization of NiO Nanoparticles and Their PMMA Nanocomposites Obtained by In Situ Bulk Polymerization. *J. Mater. Sci.* **2009**, *44*, 4553–4556. DOI: 10.1007/s10853-009-3690-6.
31. Cheng, X.; Chen, M.; Zhou, S.; Wu, L. Preparation of SiO<sub>2</sub>/PMMA Composite Particles via Conventional Emulsion Polymerization. *J. Polym. Sci. Part A* **2006**, *44*, 3807–3816.
32. El-Bashir, S. M. Photophysical Properties of Fluorescent PMMA/SiO<sub>2</sub> Nanohybrids for Solar Energy Applications. *J. Luminescence* **2012**, *132*, 1786–1791. DOI: 10.1016/j.jlumin.2012.02.010.
33. Demir, M. M.; Koynov, K.; Akbey, Ü.; Bubeck, C.; Park, I.; Lieberwirth, I.; Wegner, G. Optical Properties of Composites of PMMA and Surface-Modified Zincite Nanoparticles. *Macromolecules* **2007**, *40*, 1089–1100. DOI: 10.1021/ma062184t.
34. Vilela, D.; Garoz, J.; Colina, Á.; Gonz, M. C.ález, Escarpa, A. Carbon Nanotubes Press-Transferred on PMMA Substrates as Exclusive Transducers for Electrochemical Microfluidic Sensing. *Analyt. Chem.* **2012**, *84*, 10838–10844. DOI: 10.1021/ac303049x.
35. Harb, S. V.; Pulcinelli, S. H.; Santilli, C. V.; Knowles, K. M.; Hammer, P. A Comparative Study on Graphene Oxide and Carbon Nanotube Reinforcement of PMMA-Siloxane-Silica Anticorrosive Coatings. *ACS Appl. Mater. Interfaces* **2016**, *8*, 16339–16350. DOI: 10.1021/acsami.6b04780.
36. Ramanathan, T.; Abdala, A. A.; Stankovich, S.; Dikin, D. A.; M. Herrera-Alonso, Piner, R. D.; Adamson, D. H.; Schniepp, H. C.; Chen, X.; Ruoff, R. S.; Nguyen, S. T.; Aksay, I. A.; R. K. Prud'Homme, Brinson, L. C. Functionalized Graphene Sheets for Polymer Nanocomposites. *Nat. Nanotechnol.* **2008**, *3*, 327–331. DOI: 10.1038/nnano.2008.96.
37. Kar, G. P.; Biswas, S.; Bose, S. Simultaneous Enhancement in Mechanical Strength, Electrical Conductivity, and Electromagnetic Shielding Properties in PVDF–ABS Blends Containing PMMA Wrapped Multiwall Carbon Nanotubes. *Phys. Chem. Chem. Phys.* **2015**, *17*, 14856–14865. DOI: 10.1039/C5CP01452B.
38. Pawar, S. P.; Bhingardive, V.; Jadhav, A.; Bose, S. An Efficient Strategy to Develop Microwave Shielding Materials with Enhanced Attenuation Constant. *RSC Adv.* **2015**, *5*, 89461–89471. DOI: 10.1039/C5RA17624G.

39. Song, S.; Wan, C.; Zhang, Y. Non-Covalent Functionalization of Graphene Oxide by Pyrene-Block Copolymers for Enhancing Physical Properties of Poly(Methyl Methacrylate). *RSC Adv.* **2015**, *5*, 79947–79955. DOI: 10.1039/C5RA14967C.
40. Karan, S.; Majumder, M.; Mallik, B. Controlled Surface Trap State Photoluminescence from CdS QDs Impregnated in Poly(Methyl Methacrylate). *Photochem. Photobiol. Sci.* **2012**, *11*, 1220. DOI: 10.1039/c2pp25023c.
41. Wei, Q.; Zhao, Y.; Di, Q.; Liu, J.; Xu, M.; Liu, J.; Zhang, J. Good Dispersion of Large-Stokes-Shift Heterovalent-Doped CdX Quantum Dots into Bulk PMMA Matrix and Their Optical Properties Characterization. *J. Phys. Chem. C* **2017**, *121*, 6152–6159. DOI: 10.1021/acs.jpcc.7b00207.
42. Li, Y.; Zhang, S.; Gao, L.; Chen, W.; Gao, L.; Zhang, W.; Cui, J.; Yan, S. The Preparation and Characterization of ZnS/PMMA Nanocomposites, Synthesis and Reactivity in Inorganic. *Metal-Org. Nano-Metal Chem.* **2014**, *44*, 942–945. DOI: 10.1080/15533174.2013.797444.
43. Mao, C.; Zhu, Y.; Jiang, W. Design of Electrical Conductive Composites: Tuning the Morphology to Improve the Electrical Properties of Graphene Filled Immiscible Polymer Blends. *ACS Appl. Mater. Interf.* **2012**, *4*, 5281–5286. DOI: 10.1021/am301230q.
44. Arai, F.; Shinohara, K.; Nagasawa, N.; Takeshita, H.; Takenaka, K.; Miya, M.; Shiomi, T. Crystallization Behavior and Higher-Order Structure in Miscible Crystalline/Crystalline Polymer Blends. *Polym. J.* **2013**, *45*, 921–928. DOI: 10.1038/pj.2013.5.
45. Rajendran, S.; Mahendran, O.; Mahalingam, T. Thermal and Ionic Conductivity Studies of Plasticized PMMA/PVdF Blend Polymer Electrolytes. *Eur. Polym. J.* **2002**, *38*, 49–55. DOI: 10.1016/S0014-3057(01)00140-9.
46. Ouyang, Q.; Di, X.; Lei, Z.; Qi, L.; Li, C.; Chen, Y. Enhanced Reverse Saturable Absorption in Graphene/Ag<sub>2</sub>S Organic Glasses. *Phys. Chem. Chem. Phys.* **2013**, *15*, 11048. DOI: 10.1039/c3cp51154e.
47. Sahoo, G.; Sarkar, N.; Sahu, D.; Swain, S. K. Nano Gold Decorated Reduced Graphene Oxide Wrapped Polymethylmethacrylate for Supercapacitor Applications. *RSC Adv.* **2017**, *7*, 2137–2150. DOI: 10.1039/C6RA26930C.
48. Fahma, F.; Hori, N.; Iwata, T.; Takemura, A. The Morphology and Properties of Poly (Methyl Methacrylate)-Cellulose Nanocomposites Prepared by Immersion Precipitation Method. *J. Appl. Polym. Sci.* **2013**, *128*, 1563–1568.
49. Chen, C.; Li, D.; Hu, Q.; Wang, R.; Properties of Polymethyl Methacrylate-Based Nanocomposites: Reinforced with Ultra-Long Chitin Nanofiber Extracted from Crab Shells. *Mater. Des. (1980–2015)*. **2014**, *56*, 1049–1056. DOI: 10.1016/j.matdes.2013.11.057.
50. Sionkowska, A.; Kaczmarek, B.; Trokowska, P.; Antoniac, I. V.; Properties and Characterization of Chitosan/Collagen/PMMA Composites Containing Hydroxyapatite. *Key Eng. Mater.* **2016**, *672*, 247–256. DOI: 10.4028/www.scientific.net/KEM.672.247.
51. Huang, T.; Kuboyama, K.; Fukuzumi, H.; Ougizawa, T. PMMA/TEMPO-Oxidized Cellulose Nanofiber Nanocomposite with Improved Mechanical Properties, High Transparency and Tunable Birefringence. *Cellulose.* **2018**, *25*, 2393–2403.
52. Yaragalla, S. Preparation of Epoxy Graphene and Its Structural and Optical Properties. *Adv. Mater. Lett.* **2015**, *6*, 848–852. DOI: 10.5185/amlett.2015.5914.
53. Yaragalla, S.; Mishra, R.; Thomas, S.; Kalarikkal, N.; Maria, H. J. *Carbon-Based Nanofillers and Their Rubber Nanocomposites*; Elsevier, 2019. DOI: 10.1016/C2016-0-03648-3.

54. Yaragalla, S.; Anilkumar, G.; Kalarikkal, N.; Thomas, S. Structural and Optical Properties of Functionalized Multi-Walled Carbon Nanotubes. *Mater. Sci. Semicond. Process.* **2016**, *41*, 491–496. DOI: 10.1016/j.mssp.2015.10.022.
55. Yaragalla, S.; Rajendran, R.; Jose, J.; AlMaadeed, M. A.; Kalarikkal, N.; Thomas, S. Preparation and Characterization of Green Graphene Using Grape Seed Extract for Bioapplications. *Mater. Sci. Eng. C* **2016**, *65*, 345–353. DOI: 10.1016/j.msec.2016.04.050.
56. Yaragalla, S.; Zahid, M.; Panda, J. K.; Tsagarakis, N.; Cingolani, R.; Athanassiou, A. Comprehensive Enhancement in Thermomechanical Performance of Melt-Extruded PEEK Filaments by Graphene Incorporation. *Polymers (Basel)*. **2021**, *13*, 1425. DOI: 10.3390/polym13091425.
57. Ponnammma, D.; C. Jose Chirayil, Sadasivuni, K. K.; Somasekharan, L.; Yaragalla, S.; Abraham, J.; Thomas, S. Special Purpose Elastomers: Synthesis, Structure-Property Relationship, Compounding, Processing and Applications. In: 2013; pp 47–82. DOI: 10.1007/978-3-642-20925-3\_3.
58. Yaragalla, S.; Thomas, S.; Maria, H. J.; Mishra, R. K.; Kalarikkal, N. *Carbon-Based Nanofillers and Their Rubber Nanocomposites*; Elsevier, 2019. DOI: 10.1016/C2018-0-02522-0.
59. Yaragalla, S.; Bhavitha, K. B.; Kalarikkal, N.; Thomas, S. Novel Graphene-Based Polymer Nanocomposites. In: *Handbook of Polymer Ceramic Nanotechnology*; Springer International Publishing: Cham, 2020; pp 1–21. DOI: 10.1007/978-3-030-10614-0\_29-1.
60. Bhavitha, K. B.; Yaragalla, S.; C. H. China Satyanarayana, Kalarikkal, N. Thomas, S. *Natural Rubber/Graphene Nanocomposites and Their Applications*; Springer, 2021; pp 203–220. DOI: 10.1007/978-981-15-9180-8\_11.
61. Thakur, V. K.; Vennerberg, D.; Madbouly, S. A.; Kessler, M. R. Bio-Inspired Green Surface Functionalization of PMMA for Multifunctional Capacitors. *RSC Adv.* **2014**. DOI: 10.1039/c3ra46592f.
62. Long, T. M.; Prakash, S.; Shannon, M. A.; Moore, J. S. Water-Vapor Plasma-Based Surface Activation for Trichlorosilane Modification of PMMA. *Langmuir* **2006**. DOI: 10.1021/la052977t.
63. Wei, S.; Vaidya, B.; Patel, A. B.; Soper, S. A.; McCarley, R. L. Photochemically Patterned Poly(Methyl Methacrylate) Surfaces Used in the Fabrication of Microanalytical Devices. *J. Phys. Chem. B*. **2005**. DOI: 10.1021/jp051550s
64. Fixe, F. Functionalization of Poly(Methyl Methacrylate) (PMMA) as a Substrate for DNA Microarrays. *Nucleic Acids Res.* **2004**. DOI: 10.1093/nar/gng157.
65. Sarantopoulou, E.; Kollia, Z.; Cefalas, A. C.; Manoli, K.; Sanopoulou, M.; Goustouridis, D.; Chatzandroulis, S.; Raptis, I. Surface Nano/Micro Functionalization of PMMA Thin Films by 157 nm Irradiation for Sensing Applications. *Appl. Surf. Sci.* **2008**, *254*, 1710–1719.
66. Convertino, A.; Leo, G.; Tamborra, M.; Sciancalepore, C.; Striccoli, M.; Curri, M. L.; Agostiano, A. TiO<sub>2</sub> Colloidal Nanocrystals Functionalization of PMMA: A Tailoring of Optical Properties and Chemical Adsorption. *Sens. Actuat. B: Chem.* **2007**. DOI: 10.1016/j.snb.2006.11.043.
67. Henry, A. C.; Tutt, T. J.; Galloway, M.; Davidson, Y. Y.; McWhorter, C. S.; Soper, S. A.; McCarley, R. L. Surface Modification of Poly(Methyl Methacrylate) Used in the Fabrication of Microanalytical Devices. *Analyt. Chem.* **2000**. DOI: 10.1021/ac000685l.
68. Abraham, J. K.; Philip, B.; Witchurch, A.; Varadan, V. K.; Reddy, C. C. A Compact Wireless Gas Sensor Using a Carbon Nanotube/PMMA Thin Film Chemiresistor. *Smart Mater. Struct.* **2004**, *13*, 1045–1049. DOI: 10.1088/0964-1726/13/5/010.

69. Philip, B.; Abraham, J. K.; Chandrasekhar, A. Carbon Nanotube / PMMA Composite Thin Films for Gas-Sensing Applications. *Smart Mater. Struct.* **2003**, *9*35, 1–6. DOI: stacks.iop.org/SMS/12/935.
70. Kang, I.; Schulz, M. J.; Kim, J. H.; Shanov, V.; Shi, D. A Carbon Nanotube Strain Sensor for Structural Health Monitoring. *Smart Mater. Struct.* **2006**, *15*, 737–748. DOI: 10.1088/0964-1726/15/3/009.
71. Huang, X.; Jiang, P.; Core-Shell Structured High- $\kappa$  Polymer Nanocomposites for Energy Storage and Dielectric Applications. *Adv. Mater.* **2015**, *27*, 546–554. DOI: 10.1002/adma.201401310.
72. Xie, L.; Huang, X.; Wu, C.; Jiang, P.; Core-Shell Structured Poly(Methyl Methacrylate)/BaTiO<sub>3</sub> Nanocomposites Prepared by In Situ Atom Transfer Radical Polymerization: A Route to High Dielectric Constant Materials with the Inherent Low Loss of the Base Polymer. *J. Mater. Chem.* **2011**, *21*, 5897. DOI: 10.1039/c0jm04574h.
73. Li, M.; Huang, X.; Wu, C.; Xu, H.; Jiang, P.; Tanaka, T. Fabrication of Two-Dimensional Hybrid Sheets by Decorating Insulating PANI on Reduced Graphene Oxide for Polymer Nanocomposites with Low Dielectric Loss and High Dielectric Constant. *J. Mater. Chem.* **2012**, *22*, 23477. DOI: 10.1039/c2jm34683d.
74. Gross, S.; Camozzo, D.; V. Di Noto, Armelao, L.; Tondello, E. PMMA: A Key Macromolecular Component for Dielectric Low- $\kappa$  Hybrid Inorganic–Organic Polymer Films. *Eur. Polym. J.* **2007**, *43*, 673–696. DOI: 10.1016/j.eurpolymj.2006.12.012.
75. Sugumaran, S.; Bellan, C. S. Transparent Nano Composite PVA-TiO<sub>2</sub> and PMMA-TiO<sub>2</sub> Thin Films: Optical and Dielectric Properties. *Optik.* **2014**, *125*, 5128–5133. DOI: 10.1016/j.ijleo.2014.04.077.
76. Althues, H.; Palkovits, R.; Rumpelcker, A.; Simon, P.; Sigle, W.; Bredol, M.; Kynast, U.; Kaskel, S. Synthesis and Characterization of Transparent Luminescent ZnS:Mn/PMMA Nanocomposites. *Chem. Mater.* **2006**, *18*, 1068–1072. DOI: 10.1021/cm0477422.
77. Hu, J.; Zhou, Y.; Sheng, X. Optical Diffusers with Enhanced Properties Based on Novel Polysiloxane@CeO<sub>2</sub>@PMMA Fillers. *J. Mater. Chem. C.* **2015**, *3*, 2223–2230. DOI: 10.1039/C4TC02287D.
78. Jin, F.; M.-L. Zheng, Z.-H. Liu, Y.-M. Fan, Xu, K.; Z.-S. Zhao, X.-M. Duan, Layer-by-Layer Assembled PMMA-SH/CdSe-Au Nanocomposite Thin Films and the Optical Limiting Property. *RSC Adv.* **2016**, *6*, 25401–25408. DOI: 10.1039/C6RA02893D.
79. Zhang, Y.; Wang, X.; Liu, Y.; Song, S.; Liu, D. Highly Transparent Bulk PMMA/ZnO Nanocomposites with Bright Visible Luminescence and Efficient UV-Shielding Capability. *J. Mater. Chem.* **2012**, *22*, 11971. DOI: 10.1039/c2jm30672g.
80. Bera, R.; Karan, S. K.; Das, A. K.; Paria, S.; Khatua, B. B.; Single Wall Carbon Nanohorn (SWCNH)/Graphene Nanoplate/Poly(Methyl Methacrylate) Nanocomposites: A Promising Material for Electromagnetic Interference Shielding Applications. *RSC Adv.* **2015**, *5*, 70482–70493. DOI: 10.1039/C5RA07718D.
81. Hayashida, K.; Takatani, Y.; Poly(Methyl Methacrylate)-Grafted ZnO Nanocomposites with Variable Dielectric Constants by UV Light Irradiation. *J. Mater. Chem. C.* **2016**, *4*, 3640–3645. DOI: 10.1039/C6TC00882H.
82. Singhal, A.; Dubey, K. A.; Bhardwaj, Y. K.; Jain, D.; Choudhury, S.; Tyagi, A. K.; UV-Shielding Transparent PMMA/In<sub>2</sub>O<sub>3</sub> Nanocomposite Films Based on In<sub>2</sub>O<sub>3</sub> Nanoparticles. *RSC Adv.* **2013**, *3*, 20913–20921. DOI: 10.1039/C3RA42244E.
83. Shanshoal, H. M.; Yahaya, M.; Yunus, W. M. M.; Abdullah, I. Y.; Third Order Nonlinearity of PMMA/ZnO Nanocomposites as Foils. *Opt. Quant. Electron.* **2016**, *48*, 1–14. DOI: 10.1007/s11082-015-0267-2.



84. Kai, D.; Jiang, S.; Low, Z. W.; Loh, X. J. Engineering Highly Stretchable Lignin-Based Electrospun Nanofibers for Potential Biomedical Applications. *J. Mater. Chem B* **2015**. DOI: 10.1039/c5tb00765h.
85. Sa, Y.; Wang, M.; Deng, H.; Wang, Y.; Jiang, T. Beneficial Effects of Biomimetic Nano-Sized Hydroxyapatite/Antibiotic Gentamicin Enriched Chitosan–Glycerophosphate Hydrogel on the Performance of Injectable Polymethylmethacrylate. *RSC Adv.* **2015**, 5, 91082–91092.
86. E. Van De Walle, I. Van Nieuwenhove, Vanderleyden, E.; Declercq, H.; Gellynck, K.; Schaubroeck, D.; Ottevaere, H.; Thienpont, H.; W. H. De Vos, Cornelissen, M.; S. Van Vlierbergh, Dubrue, P. Polydopamine-Gelatin as Universal Cell-Interactive Coating for Methacrylate-Based Medical Device Packaging Materials: When Surface Chemistry Overrules Substrate Bulk Properties. *Biomacromolecules* **2016**. DOI: 10.1021/acs.biomac.5b01094.
87. Kim, Y.; Bulusu, A.; Giordano, A. J.; Marder, S. R.; Dauskardt, R.; Graham, S. Experimental Study of Interfacial Fracture Toughness in a SiN x/PMMA Barrier Film. *ACS Appl. Mater. Interfaces* **2012**, 4, 6711–6719.
88. Pullanchiyodan, A.; K. S. Nair, Surendran, K. P.; Silver-Decorated Boron Nitride Nanosheets as an Effective Hybrid Filler in PMMA for High-Thermal-Conductivity Electronic Substrates. *ACS Omega* **2017**. DOI: 10.1021/acsomega.7b01436.
89. Pham, V. H.; Dang, T. T.; Hur, S. H.; Kim, E. J.; Chung, J. S. Highly Conductive Poly (Methyl Methacrylate)(PMMA)-Reduced Graphene Oxide Composite Prepared by Self-Assembly of PMMA Latex and Graphene Oxide Through Electrostatic Interaction. *ACS Appl. Mater. Interfaces* **2012**, 4, 2630–2636.
90. Yaragalla, S.; M. A. P.; Kalarikkal, N.; Thomas, S. Chemistry Associated with Natural Rubber–Graphene Nanocomposites and Its Effect on Physical and Structural Properties. *Ind. Crops Prod.* **2015**, 74, 792–802. DOI: 10.1016/j.indcrop.2015.05.079.
91. Yaragalla, S.; Dussoni, S.; Zahid, M.; Maggiali, M.; Metta, G.; Athanasiou, A.; Bayer, I. S. Stretchable Graphene and Carbon Nanofiber Capacitive Touch Sensors for Robotic Skin Applications. *J. Ind. Eng. Chem.* **2021**, 101, 348–358. DOI: 10.1016/j.jiec.2021.05.048.
92. Srinivasarao, Y.; Ri, Y. S. Hanum, Chan, C. H.; Nandakumar, K.; Sabu, T. Electrical Properties of Graphene Filled Natural Rubber Composites. *Adv. Mater. Res.* **2013**, 812, 263–266. DOI: 10.4028/www.scientific.net/AMR.812.263.
93. Yaragalla, S.; Sindam, B.; Abraham, J.; Raju, K. C. J.; Kalarikkal, N.; Thomas, S. Fabrication of Graphite-Graphene-Ionic Liquid Modified Carbon Nanotubes Filled Natural Rubber Thin Films for Microwave and Energy Storage Applications. *J. Polym. Res.* **2015**, 22, 137. DOI: 10.1007/s10965-015-0776-5.
94. Yaragalla, S.; Chandran, C. S.; Kalarikkal, N.; Subban, R. H. Y.; Chan, C. H.; Thomas, S. Effect of Reinforcement on the Barrier and Dielectric Properties of Epoxidized Natural Rubber-Graphene Nanocomposites. *Polym. Eng. Sci.* **2015**, 55, 2439–2447. DOI: 10.1002/pen.24131.
95. Cano, L.; Gutierrez, J.; Tercjak, A. Enhancement of the Mechanical Properties at the Macro and Nanoscale of Thermosetting Systems Modified with a Polystyrene-Block-Polymethyl Methacrylate Block Copolymer. *RSC Adv.* **2015**. DOI: 10.1039/c5ra21857h.
96. Reddy, C. S.; Zak, A.; Zussman, E. WS2 Nanotubes Embedded in PMMA nanofibers as Energy Absorptive Material. *J. Mater. Chem.* **2011**. DOI: 10.1039/c1jm12700d.





## CHAPTER 6

---

# MnO<sub>2</sub>-Based Nanostructure Synthesis, Properties, and Applications

SANAL SEBASTIAN PAYYAPPILLY<sup>1</sup>, VYSHNAVI SANTOSH<sup>2</sup>,  
SNEHA SABU MATHEW<sup>3,4</sup>, and ASHINA MUHAMMED<sup>1</sup>

*<sup>1</sup>International and Inter University Centre for Nanoscience and Nanotechnology, Mahatma Gandhi University, Kottayam, Kerala, India*

*<sup>2</sup>Department of Chemistry, Baselius College, Kottayam, Kerala, India*

*<sup>3</sup>School of energy materials, Mahatma Gandhi University, Kottayam, Kerala, India*

*<sup>4</sup>School of chemical sciences, Mahatma Gandhi University, Kottayam, Kerala, India*

---

### ABSTRACT

Manganese dioxide (MnO<sub>2</sub>) nanostructures have garnered considerable attention due to their exceptional electrochemical properties. This chapter provides an in-depth exploration of MnO<sub>2</sub>-based nanostructures, encompassing synthesis methods, properties, and versatile applications. The synthesis techniques covered include template-assisted, sol-gel, hydrothermal, chemical co-precipitation, electrospinning, and electrochemical deposition. These methodologies enable the creation of tailored MnO<sub>2</sub> nanostructures with distinct crystalline structures, morphologies, and porosities to meet specific application requirements. The chapter elaborates on their diverse applications across various domains, including supercapacitors, batteries, water treatment, and electrochemical biosensing, highlighting their extensive utility. MnO<sub>2</sub>-based nanostructures are poised to make significant contributions to supercapacitors,

batteries, water purification, and biosensing applications, ultimately benefiting diverse industries and advancing technology.

## 6.1 INTRODUCTION

In the present scenario, transition metal oxide-based nanostructures are attracting the interest of researchers because of their superior electrochemical properties.<sup>1</sup> One-dimensional transition metal oxide nanostructures are promising for application in microelectronic and optoelectronic devices. Transition metal oxides, such as ruthenium dioxide ( $\text{RuO}_2$ ), vanadium oxide ( $\text{V}_2\text{O}_5$ ), manganese dioxide ( $\text{MnO}_2$ ), cobalt oxide ( $\text{Co}_3\text{O}_4$ ), and nickel oxide ( $\text{NiO}$ ), are widely studied for electrochemical applications.<sup>2,3</sup> Electrochemical properties of  $\text{RuO}_2$  are best when considered among other transition metal oxides and hence are used as an electrode material for supercapacitors. But this metal oxide is quite rare in the earth's crust and its toxicity level is considerably high, which limits its applications.

Manganese oxides ( $\text{MnO}_x$ ) are of great importance because of their attractive properties which include variability in oxidation states, diversity in morphology, redox ability and their natural abundance. Manganese oxides exist in different forms:  $\alpha$ - $\text{MnO}_2$ ,  $\beta$ - $\text{MnO}_2$ ,  $\gamma$ - $\text{MnO}_2$ ,  $\alpha$ - $\text{Mn}_3\text{O}_4$ ,  $\gamma$ - $\text{Mn}_2\text{O}_3$ ,  $\alpha$ - $\text{Mn}_2\text{O}_3$ , and  $\text{Mn}_5\text{O}_8$ . Recently,  $\text{MnO}_2$ -based materials have attracted wide attention due to their high theoretical specific capacitance, natural abundance, and low cost. Manganese dioxide exists naturally in the earth's crust, mainly in the form of pyrolusite ( $\beta$ - $\text{MnO}_2$ ), an ore of manganese. It is non-poisonous and is in the form of black powder. The molecular weight of it is about  $86.93 \text{ g mol}^{-1}$ , density is  $5.026 \times 10^3 \text{ kg m}^{-3}$ , bulk density is about  $1.7\text{--}2.5 \text{ g cm}^{-3}$ , and surface area is  $30\text{--}60 \text{ m}^2 \text{ g}^{-1}$ . The fascinating physical and chemical properties of  $\text{MnO}_2$  make it an important functional metal oxide for a variety of applications, such as catalyst, ion exchange, and biosensors.<sup>4-6</sup> It possesses good electrolytic properties and can be used as the cathode material in most of the latest alkaline batteries, lithium manganese primary batteries, and electrochemical supercapacitors. The wide use of electrolytic manganese dioxide is due to its natural abundance, low cost of production, high redox potential, good execution over a wide range of temperature, and its storage capability.

Manganese dioxides are commercially available in four different forms: (1) natural manganese dioxide, produced directly from natural deposits; (2) chemical manganese dioxide, produced by roasting and treatment with acid; (3) electrolytic manganese dioxide, produced by oxidation of divalent manganese in acidic medium, and (4) synthetic hydrate forms.

The basic structural units of MnO<sub>2</sub> crystal structures are MnO<sub>6</sub> octahedrons. MnO<sub>2</sub> can exist in different crystal forms, such as  $\alpha$ ,  $\beta$ ,  $\gamma$ ,  $\epsilon$ , and  $\delta$ .<sup>7</sup> The difference in crystal structure forms arises due to the difference in the arrangement of Mn<sup>4+</sup> ions at various octahedral sites. According to the linkage of these structural units, MnO<sub>2</sub> have different forms such as  $\alpha$ ,  $\beta$ ,  $\gamma$ ,  $\delta$ ,  $\epsilon$ , and  $\lambda$  forms. Broadly, they can be again divided into three classes:

- 1) Chain-like tunnel structures which include  $\alpha$ -,  $\beta$ - and  $\gamma$ - MnO<sub>2</sub> forms
- 2) Sheet-like layered structures which include  $\delta$ -MnO<sub>2</sub> forms
- 3) 3D structures, such as  $\lambda$  and  $\epsilon$  forms

During crystallization, in most cases, a chain of MnO<sub>6</sub> octahedrons is formed with the formation of tunnel structures. Different crystal structures formed can be identified by the size of the tunnel in the case of a tunnel-type structure.  $2 \times 2$  tunnels and  $1 \times 1$  tunnel structures indicate the formation of  $\alpha$ ,  $\beta$  crystal forms, respectively.  $\lambda$ -MnO<sub>2</sub> has a 3D spinel-type tunnel structure. Figure 6.1 shows the structures of  $\alpha$ -,  $\beta$ -,  $\gamma$ -,  $\delta$ -, and  $\lambda$ -MnO<sub>2</sub>. Birnessite form or  $\delta$ -MnO<sub>2</sub> is the only 2D form of MnO<sub>2</sub>. Interlayer distance between  $\delta$ -MnO<sub>2</sub> layers is around 0.55–1.0 nm.

## 6.2 SYNTHESIS OF MnO<sub>2</sub> NANOSTRUCTURES

### 6.2.1 TEMPLATE-ASSISTED METHOD

Template-assisted method is one of the widely used methods for producing metal oxide nanoparticles with desired size and shape. Templates are scaffolds used during synthesis to get the desired shape and morphology. Templates are classified as hard and soft templates depending upon the nature of the material used as the template. SiO<sub>2</sub> spheres, diatomite, polycarbonate membranes, and porous aluminum oxide, etc., are used as hard templates for the synthesis of MnO<sub>2</sub> structures. Sodium dodecyl sulfate, tetraoctyl ammonium bromide (TOAB), pluronic P123 (PEO- PPO-PEO triblock copolymer), and polyvinylpyrrolidone (PVP) are some of the soft templates studied for the MnO<sub>2</sub> nanostructures.<sup>9</sup>

Diatomite is a promising template for producing porous MnO<sub>2</sub> nanostructures due to its high porosity and chemical stability. 3D hollow structured MnO<sub>2</sub> with a high surface area were prepared by hydrothermal method using diatomite as a template. MnO<sub>2</sub> nanostructures were grown into the diatomite template hydrothermally using KmnO<sub>4</sub> as the reagent. Thereafter, diatomite is removed to obtain MnO<sub>2</sub> hollow structures.<sup>10</sup> Anodic aluminum oxide

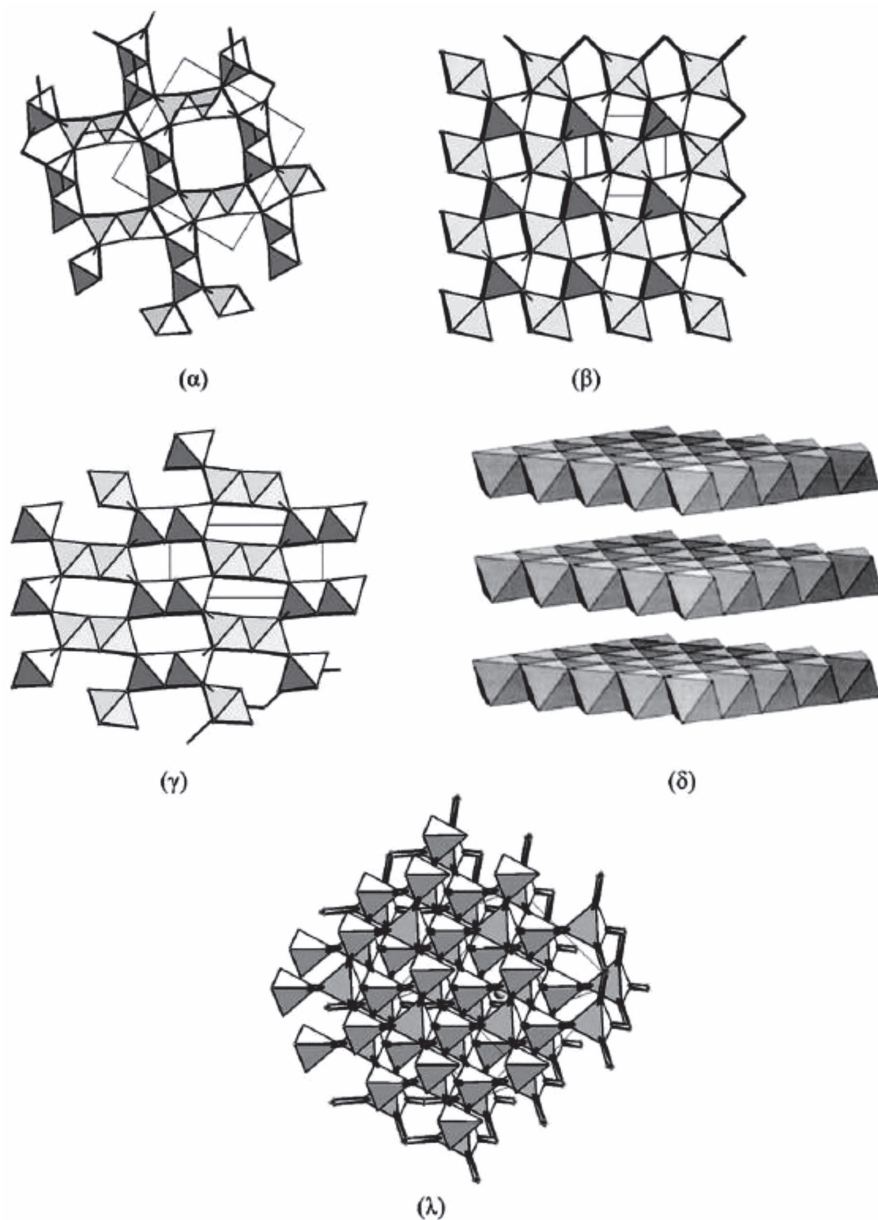


**FIGURE 6.1** Crystal structures of  $\alpha$ -,  $\beta$ -,  $\gamma$ -,  $\delta$ -, and  $\lambda$ - $\text{MnO}_2$ .

Source: Reprinted with permission from Ref. [8]. Copyright 2008, © 2008 American Chemical Society.

templates were also used to produce anisotropic porous structures. It has a highly porous structure with long pores length ranging from 1 to 50 mm and diameter ranging from 10 to 200 nm. A major drawback of anodic aluminum oxide templates is their high cost. Huang et al. used polycarbonate-based membrane as a template in the hydrothermal process and synthesized porous MnO<sub>2</sub> nanotubes.<sup>11</sup> The thickness and diameter of the nanotubes can be controlled by using polycarbonate membranes with appropriate pore sizes. Hard templates-based synthesis are very useful for the synthesis of MnO<sub>2</sub> nanostructures with the required nanoarchitecture. However, the high cost and requirement to remove templates using complicated processes are some of the drawbacks of this process.

Soft templates self-assemble into different nanoarchitectures and adsorb and guide the formed MnO<sub>2</sub> nuclei to the formation of MnO<sub>2</sub> nanostructures. Block copolymer surfactants are widely studied as a soft template for synthesis. Nayak et al. prepared mesoporous MnO<sub>2</sub> using pluronic P123 and KMnO<sub>4</sub>. KMnO<sub>4</sub> was added to the P123 aqueous solution and stirred for hours for the formation of the nanoparticles. Interestingly, the morphology of nanoparticles changed to nanorods during the annealing process.<sup>12</sup> Hu et al. synthesized ultralong MnO<sub>2</sub> nanowires using polyvinylpyrrolidone (PVP) as a template in hydrothermal synthesis. PVP adsorbs the formed MnO<sub>2</sub> nuclei and guides the formation of nanowires.<sup>13</sup> Single-layered MnO<sub>2</sub> nanosheets were prepared using sodium dodecyl sulfate as the soft template. In this reaction, SDS acts as a reducer for KMnO<sub>4</sub> and also assists the formation of single layer-nanosheets.<sup>14</sup> The disadvantage of the soft template-based method is the lengthy time-consuming removal procedure of the template. There is also a chance that the remaining surfactant decreases the charge storage capacity of the prepared MnO<sub>2</sub> nanostructures by enveloping it.

### **6.2.2 SOL-GEL METHOD**

This method is commonly used for the fabrication of metal oxides, especially for metals like silicon and titanium. It is a wet chemical method, where precursor solution (usually metal alkoxides) readily reacts with water (or alcohol) to form a sol that is heterogeneous. The prepared sol undergoes condensation and transforms into a homogeneous gel. Condensation continues till a rigid and porous inorganic network completely covered with a liquid phase is obtained. And this transformation is called the Sol-Gel transition. Oxide materials are finally obtained by sintering at a specific temperature.

Anderson and coworkers prepared thin-film electrodes by dipping and dropping method. Manganese perchlorate  $\text{Mn}(\text{ClO}_4)_2$  was oxidized to  $\text{MnO}_2$  using  $\text{KMnO}_4$  at a pH of 10.5.<sup>15</sup> Temperature, pH, reaction time, solution concentration along with the chelating agent play a key role in the crystalline formation of  $\text{MnO}_2$ .

The sol-gel method has many advantages in synthesizing functional nanomaterials. This method is controllable at a molecular level and geometry can be predicted under the mesoscopic level. Products obtained by this process are of high purity and chemical homogeneity. Even multi-component oxide films are easy to fabricate economically by this method. But this process is time-consuming and is prone to agglomeration of nanomaterials during the heating stage.<sup>16</sup>

### 6.2.3 HYDROTHERMAL SYNTHESIS

Hydrothermal synthesis is a common technique used for the synthesis of crystal substances. It requires a special apparatus called autoclave which supplies high temperature and vapor pressure throughout the process. A remarkable advantage of this method is that water is used as the reaction medium. High temperature and pressure used in this method allow the dissolution and recrystallization of insoluble and partially soluble materials. Another advantage is that crystallization is carried out in a single step. Crystals with good orientation and predictable stoichiometry can be obtained through the hydrothermal synthesis method. Normally, one-dimensional nanostructures are prepared with the help of templates and catalysts. But the low temperature hydrothermal method requires no template or catalyst for the nanostructure synthesis and thus impurity in the final product also can be reduced. This also contributes much to the wide acceptance of this route of synthesis. Nanostructures produced by the hydrothermal route have a lot of advantages as described above but also have some drawbacks such as a longer time duration. One drawback with this method is that as the autoclave is sealed and therefore reaction growth cannot be traced in between and any adjustments can be done only after the completion of the reaction.<sup>16</sup>

Li et al. synthesized  $\alpha$ -,  $\beta$ -,  $\gamma$ -, and  $\delta$ - $\text{MnO}_2$  using the hydrothermal method by varying reactant concentration. In all the cases,  $\text{MnO}_2$  initially forms the  $\delta$ - $\text{MnO}_2$  layer structure before transforming into other crystal forms. Formed  $\delta$ - $\text{MnO}_2$  is in a metastable state. If there are sufficient cations, it will retain its layered structure otherwise it will collapse to form a  $2 \times 2$  tunnel structure of  $\alpha$   $\text{MnO}_2$  or a  $1 \times 2$  tunnel structure of  $\gamma$ - $\text{MnO}_2$ .  $\beta$   $\text{MnO}_2$  structure is

formed by the collapse of  $2 \times 2$  and  $1 \times 2$  structures into  $1 \times 1$  structures. They proposed a rolling mechanism of  $\delta$ -MnO<sub>2</sub> layer structure to account for this phenomenon. Curling lamellar structures and tunnel structures grow and form nanowire structures. During the hydrothermal process, the Ostwald ripening process causes shorter nanowires to dissolve and larger ones to grow in size.<sup>17</sup> Figure 6.2 shows the TEM images of the formed nanostructures.

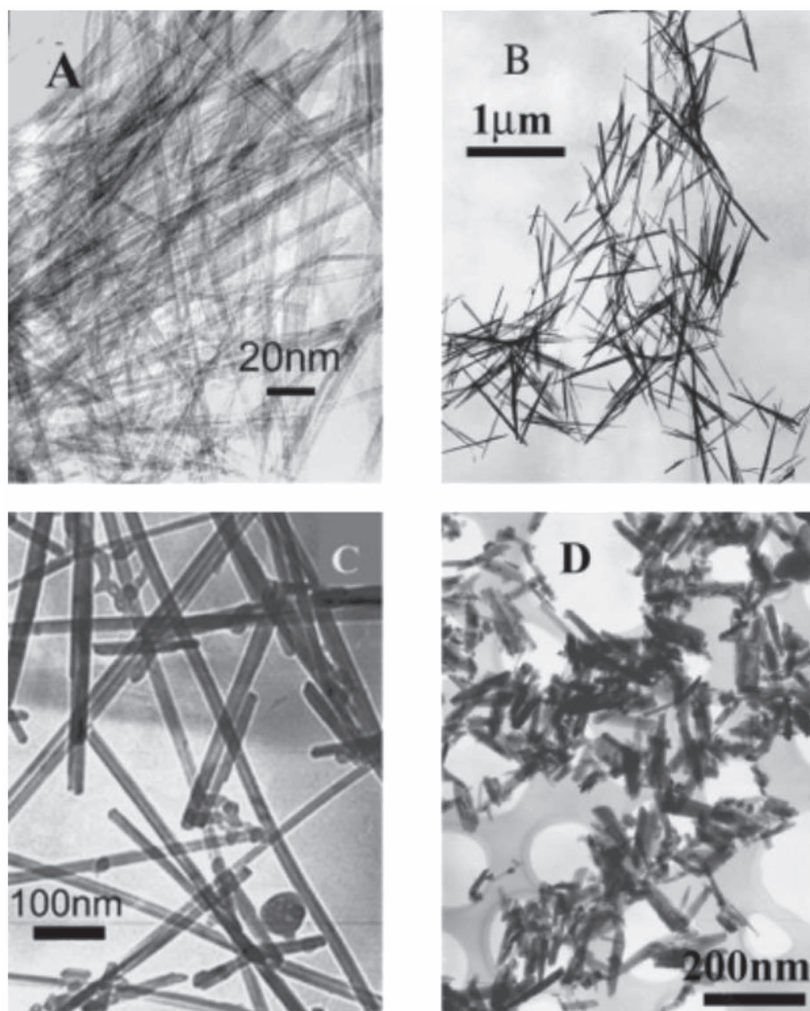


**FIGURE 6.2** TEM images of A)  $\alpha$ -MnO<sub>2</sub> ribbonlike nanowires B)  $\beta$ -MnO<sub>2</sub> nanorods; C)  $\beta$ -MnO<sub>2</sub> nanorods; D)  $\gamma$ -MnO<sub>2</sub> nanorods.

Source: Reprinted with permission from Ref. [17]. © 2012 Elsevier.



Wang et al. synthesized  $\alpha$ - and  $\beta$ - $\text{MnO}_2$  nanostructures without using any templates by hydrothermal method.<sup>18</sup> A homogeneous solution of manganese sulfate hydrate and ammonium persulfate were prepared in distilled water and then kept into a Teflon-lined airtight autoclave and held at 120°C for 12 h. Black solid  $\text{MnO}_2$  was obtained at the end of the reaction. It was then filtered, washed, and dried. Prepared nanoparticles were found to be of  $\beta$ - $\text{MnO}_2$  nanorods.  $\alpha$ - $\text{MnO}_2$  nanoparticles were also prepared following the same procedure, except adding ammonium persulfate. TEM studies showed the morphological difference of  $\alpha$ - and  $\beta$ -nanostructures.  $\alpha$ -  $\text{MnO}_2$  samples exhibited nanowire-like structures with diameters 5–20 nm and lengths ranging between 5 and 10  $\mu\text{m}$ . Whereas,  $\beta$ - $\text{MnO}_2$  samples exhibited nanorod-like structure morphology with diameters 40–100 nm and lengths ranging between 2.5 and 4.0  $\mu\text{m}$ . It was also noticed that double chains of  $\text{MnO}_6$  octahedra form the basis for  $\alpha$ - $\text{MnO}_2$  and resulted in  $2 \times 2$  tunnels, whereas single chains of octahedra form the basis for  $\beta$ - $\text{MnO}_2$ . By the same hydrothermal method, Deng et al. produced rod-like  $\alpha$ - $\text{MnO}_2$  which were about 50–70 nm in diameter with considerable dispersion and uniform structure using  $\text{KMnO}_4$  and  $\text{Mn}(\text{CH}_3\text{COO})_2$  as reagents.<sup>19</sup>

#### 6.2.4 CHEMICAL CO-PRECIPITATION METHOD

Co-precipitation, also known as carrying down, is one of the most usual techniques for nanoparticle synthesis. Manganese oxide nanoparticles are obtained in the aqueous solution of metal salts like  $\text{KMnO}_4$ , by the addition of metal cation reductants like  $\text{MnSO}_4$ ,  $\text{MnCl}_2$ , and  $\text{Mn}(\text{OAc})_2$ , etc. under appropriate conditions. In this method,  $\text{Mn}(\text{II})$  and  $\text{Mn}(\text{VII})$  salts are mixed in a fixed ratio in an aqueous solution for the synthesis of manganese oxide nanostructures.

Nam et al. succeeded in fabricating  $\text{MnO}_2$  nanowires through this method using  $\text{KMnO}_4$  and  $\text{MnCl}_2$  as reagents.<sup>20</sup> Kumar and coworkers used manganese sulfate and manganese oxalate to obtain  $\text{MnO}_2$  nanostructures of simple cubic structures.<sup>21</sup> The wide acceptance of this method is due to the fact that preparation is very simple and rapid, composition and particle size can be easily controlled, low synthesis temperature, and overall homogeneity. At the same time, a major challenge regarding this method is that it is prone to form hard aggregates. However, this problem can be resolved by controlling pH of the solution and the concentration of the reactants.<sup>20,21</sup>

### 6.2.5 ELECTROSPINNING

Electrospinning is a convenient method for fabricating micro and nano-fibers. This method uses a high voltage to fabricate fibers of nano and micro diameter range. Zhang et al. prepared free-standing composite fiber electrodes using the electrospinning technique. Polyacrylonitrile solution containing Mn(CH<sub>3</sub>COO)<sub>2</sub>·H<sub>2</sub>O was electrospun into a fiber mat. Prepared fiber mats were carbonized at high temperatures to produce a freestanding MnO<sub>2</sub>-carbon fiber composite electrode with excellent properties.<sup>22</sup>

### 6.2.6 LOW-TEMPERATURE SOLID-PHASE SYNTHESIS

Solid-phase synthesis is a relatively new technique in nanoparticle synthesis, which involves the direct mixing of solid materials followed by grinding. Basically, this method is a four-step process that includes (1) diffusion, (2) reaction, (3) nucleation, and (4) growth. Initially, diffusion takes place and reactant molecules come into contact with each other which leads to the reaction. Crystal nuclei appear only after the accumulation of product molecules to a minimum size. These nuclei then grow until a single crystalline product is obtained. Diffusion and nucleation were considered as the crucial rate-determining steps in the whole process. At low temperatures, this process is slow and it may be the rate-determining step. Yuan et al. synthesized MnO<sub>2</sub> nanostructures using this method.<sup>23</sup> Initially, MnSO<sub>4</sub> and MnCl<sub>2</sub> underwent solid-state reaction with (NH<sub>4</sub>)<sub>2</sub>C<sub>2</sub>O<sub>4</sub> to form MnC<sub>2</sub>O<sub>4</sub>. Calcination of the formed MnC<sub>2</sub>O<sub>4</sub> produced MnO<sub>2</sub> nanostructures. Noticeable advantages of low-temperature solid-phase synthesis include high product yield, good selectivity, no requirement solvents, and fewer environmental threats. But the sensitivity of MnO<sub>2</sub> to temperature and grinding should be kept in mind while fabrication using this method.

### 6.2.7 MICROWAVE-ASSISTED SYNTHESIS

Recently, microwave-assisted syntheses have received wide attention as it can greatly shorten the reaction time and energy consumption. Microwaves can heat the medium uniformly and thereby induce homogenize crystallization. It consumes less energy compared to other methods and also shortens the crystallization time. Zhang et al. synthesized urchin-like γ-MnO<sub>2</sub>

nanostructures using microwave-assisted synthesis. In this reaction, potassium persulfate and manganese sulfate were kept in a microwave at 98°C for 30 min. Figure 6.3 shows FESEM images of prepared  $\text{MnO}_2$  nanostructures.<sup>24</sup>

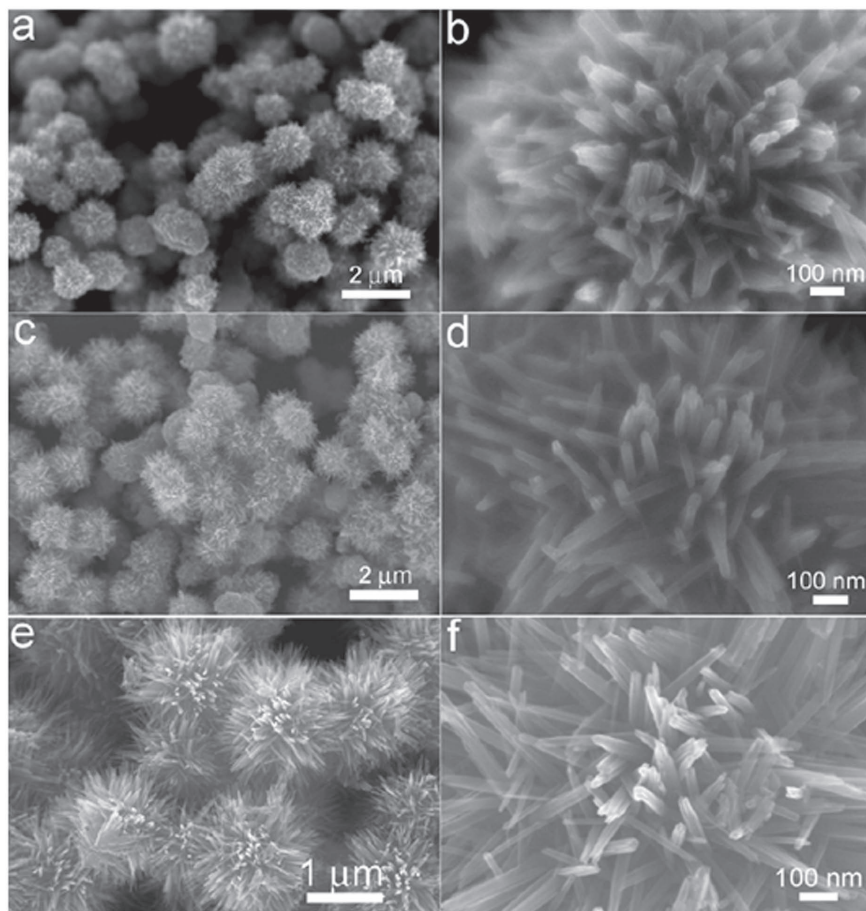


**FIGURE 6.3** FESEM images of  $\text{MnO}_2$  nanostructures with different time duration: (a) 5 min; (b) 5 min; (c) 10 min; (d) 10 min; (e) 30 min; and (f) 30 min.

*Source:* Reprinted with permission from Ref. [24]. © 2012 Elsevier.

### 6.2.8 ELECTROCHEMICAL DEPOSITION

The electrochemical deposition process involves the reduction of dissolved metal ions using electric current which results in the formation of a coherent

metal coating on an electrode. By controlling the deposition rate, ions will be deposited on the electrode plates with grain sizes of about 1–100 nm range. Huang et al. prepared MnO<sub>2</sub> using different types of electrodeposition such as galvanostatic electrodeposition, constant-voltage electrodeposition, and cyclic voltammetry electrodeposition. Metal oxide prepared by galvanostatic electrode deposition showed greater capacitance. This process requires relatively simple conditions.<sup>25</sup> MnO<sub>2</sub> nanostructures with high-temperature resistance, greater density, and smaller porosity can be obtained by this process. The major demerit regarding this method is the large particle size and uneven thickness of the film. Correction to this problem can be done by monitoring the deposition rate which can be controlled by adjusting current density and solution concentration.

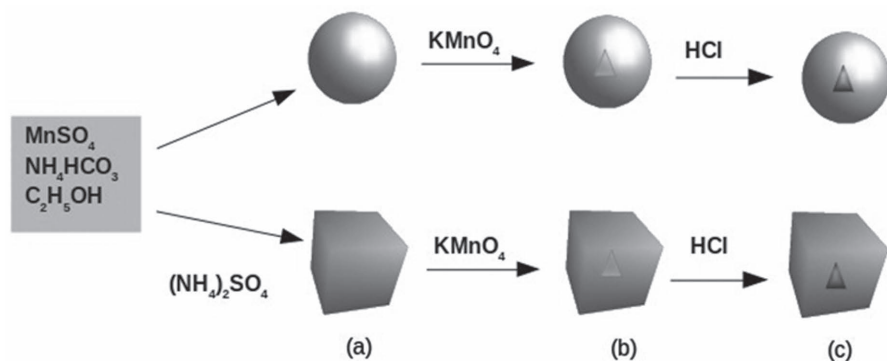


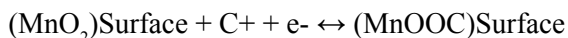
**FIGURE 6.4** Schematic illustration of MnO<sub>2</sub> hierarchical hollow nanostructures fabrication. (a) intermediate MnO<sub>2</sub> crystals; (b) MnCO<sub>3</sub>-MnCO<sub>2</sub> core-shell structures; (c) MnO<sub>2</sub> hierarchical hollow nanostructures.

Hierarchical hollow nanostructures consisting of metal oxide nanoparticles have attracted significant interest due to potential applications in biomedicine, acoustic insulation, catalysis, and photonic crystals. Fei et al. synthesized MnO<sub>2</sub> hierarchical hollow nanostructures using a three-step process.<sup>26</sup> Figure 6.4 shows the schematic diagram of the synthesis of the MnO<sub>2</sub> hollow nanostructures. In the first step, intermediate MnCO<sub>3</sub> spherical crystals were prepared by the reaction of MnSO<sub>4</sub>, NH<sub>4</sub>HCO<sub>3</sub>, and C<sub>2</sub>H<sub>5</sub>OH. Nanostructures with cubic morphology were formed when the reaction was carried out in the presence (NH<sub>4</sub>)<sub>2</sub>SO<sub>4</sub>. In the second step, formed MnCO<sub>3</sub> crystals were converted to MnO<sub>2</sub> nanostructures by the addition of KMnO<sub>4</sub>. In the third step, HCl was used to remove unreacted MnCO<sub>3</sub> at the core to get MnO<sub>2</sub> hollow nanostructures.

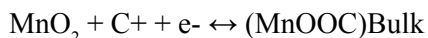
### 6.3 PROPERTIES AND APPLICATIONS OF $\text{MnO}_2$

Due to its structural diversity, manganese dioxide finds vast applications in the field of electrochemistry.  $\alpha$ -, and  $\delta$ -form of  $\text{MnO}_2$  are the most electrochemically active crystallographic forms of  $\text{MnO}_2$ . The greater interlayer spacing (7.0 Å) and bigger tunnel size (4.6 Å) of layered  $\delta$ - $\text{MnO}_2$  and  $\alpha$ - $\text{MnO}_2$  are attributed to their high SC values.<sup>27</sup>  $\gamma$ - $\text{MnO}_2$  is also known as Nsutite and is commonly used for battery applications. It can be synthesized by both chemical and electrochemical methods. Electrochemically synthesized  $\gamma$ - $\text{MnO}_2$  shows better performance compared to chemically synthesized counterparts. The electrochemical activity of the  $\beta$ - $\text{MnO}_2$  form is the least when compared to other crystal forms.<sup>28</sup>

The main demerits of  $\text{MnO}_2$ -based materials are their low electrical conductivity and partial dissolution. Many researches have been conducted in order to increase the efficiency of  $\text{MnO}_2$ -based supercapacitors by using conductive polymers such as polyaniline, polypyrrole, etc. Studies have also been conducted by using carbon nanotubes, carbon fibers, and graphene to improve the performance of  $\text{MnO}_2$ -based electrodes. Commonly used electrode materials can function well only in the presence of acidic or alkaline electrolytes but  $\text{MnO}_2$ -based electrodes can also function in neutral aqueous electrolytic mediums, such as  $\text{Na}_2\text{SO}_4$ ,  $\text{K}_2\text{SO}_4$ ,  $\text{KCl}$ , etc.<sup>16</sup> Basically, there are two charge storage mechanisms in  $\text{MnO}_2$ : (i) surface charge storage (ii) bulk charge storage. In the surface charge storage mechanism, adsorption or desorption on the  $\text{MnO}_2$  surface takes place by the electrolytic cations ( $\text{C}^+$ ). This reaction is known as a Faradaic reaction. The reaction can be represented as:



In the second type, bulk Faradaic reaction occurs where the electrolytic cations enter and react with the bulk of  $\text{MnO}_2$ . The reaction can be represented as:



Crystalline  $\text{MnO}_2$  is mostly functioned by the second mechanism.  $\text{MnO}_2$ -based electrodes get charged and discharged at a constant rate over an applied voltage, and they have good specific capacitance and rate capability. These properties attract the use of  $\text{MnO}_2$ -based electrodes in the field of electrochemistry.<sup>7</sup>

### **6.3.1 APPLICATION OF MnO<sub>2</sub> IN SUPERCAPACITORS**

Energy which is one of the major sources of economic development needs to be stored and converted in a sustainable manner, for that, various effective technologies have been raised. Batteries, fuel cells, and electrochemical supercapacitors are some of those effective technologies. Electrochemical supercapacitors or ultra-capacitors are one of the most interesting concepts because of their high power density and long cycle life. They bridge the functional gap between traditional dielectric capacitors and batteries. Dielectric capacitors have high power output on the other side batteries have high energy storage capacity.<sup>29</sup> There are two types of charge storage mechanisms involved in supercapacitors as is explained below. If the electrode materials used are inert, possess high surface area, and are conducting, then storage and release of energy are operated by a charge separation mechanism between electrode and electrolyte. This charge storage mechanism is known as electrochemical double-layer capacitance. If the electrode materials used are redox-active, then storage and release of energy are operated by redox reactions. This charge storage mechanism is also known as pseudocapacitance.

Generally, carbon-based nanostructures such as CNTs, active carbon, and graphene store and release energy using double-layer capacitance. Transition metal oxides such as MnO<sub>2</sub> store and release energy by the pseudocapacitance mechanism.<sup>28</sup> MnO<sub>2</sub>-based electrodes have high potential and theoretical capacitance value and are used in aqueous supercapacitors, and are considered to be much safer and of low cost. It is expected that such types of supercapacitors can replace electrochemical double-layer capacitors and RuO<sub>2</sub>-based acid supercapacitors.<sup>7</sup> MnO<sub>2</sub> is considered to be one of the most suitable materials for supercapacitor applications because of its attractive properties, such as high theoretical specific capacitance, low cost, low toxicity, and easy availability. However, electronic and ionic conductivities of MnO<sub>2</sub> are not good as expected, and hence it shows low power density and poor cycling performance. By the “conducting wrapping” method, the performance of supercapacitors with MnO<sub>2</sub>-based nanostructures electrodes can be enhanced. Carbon nanotubes and conducting polymers are used for the conducting wrapping of graphene/MnO<sub>2</sub> nanostructures which can increase the specific capacitance by approximately 20% and 45%, respectively. Figure 6.5 shows the schematic representation of conducting wrapping of graphene/MnO<sub>2</sub> by CNTs (GMC), and by conducting polymer (GMP). These modified

electrodes also showed excellent cycling performance with the maintenance and retention of capacitance (95%) for over 3000 cycles.

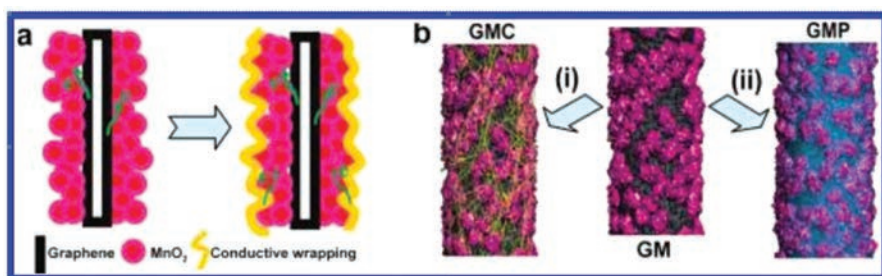


**FIGURE 6.5** (a) Schematic diagram of conductive wrapping of the graphene/MnO<sub>2</sub> to introduce more electron transport path. (b) GMC and GMP systems fabricated by wrapping graphene/MnO<sub>2</sub> nanostructures with CNTs or conducting polymers (rose-MnO<sub>2</sub>; black-graphene; blue-conducting polymer; yellow-CNTs).

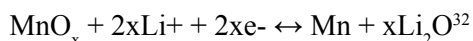
Source: Reprinted with permission from Ref. [30]. © 2011 American Chemical Society.

The electrochemical properties of graphene oxide-MnO<sub>2</sub> nanocomposites are of much interest because of the chemical interaction between GO and MnO<sub>2</sub>. MnO<sub>2</sub> nanoparticles get deposited on the graphene oxide sheets and can be used for advanced technical applications.<sup>31</sup>

### 6.3.2 APPLICATIONS OF MnO<sub>2</sub> IN BATTERIES

Manganese-based oxides are superior to iron, cobalt, and nickel-based oxides, because of their high specific capacitance, lower cost, low level of toxicity, and requirement of low operating voltage. Standard cells, that is, Leclanche cells, use natural manganese dioxide (NMD) in the cathode. Chemical manganese dioxide (CMD) is used in alkaline and lithium batteries. The content of manganese is high in electrolytic manganese dioxide (EMD) compared to NMD and CMD, so it is mainly used in modern commercial alkaline batteries.<sup>28</sup> Manganese-based oxides are also used as anode materials in lithium-ion batteries. Rechargeable lithium-ion batteries are used in electronic devices, electric vehicles, and hybrid electric vehicles.

In Li/MnO<sub>x</sub> half-cell, electrochemical process can be represented as:



One-dimensional  $\alpha$ -MnO<sub>2</sub> and  $\gamma$ -MnO<sub>2</sub> nanostructures synthesized via hydrothermal route show highly effective discharge performance and



are used as cathode material in both primary alkaline Zn–MnO<sub>2</sub> cells and rechargeable Li–MnO<sub>2</sub> cells.<sup>4</sup>  $\alpha$ -MnO<sub>2</sub> hollow urchins prepared using the reduction method are also found to be promising for battery applications. In this method, the temperature is maintained at about 60°C without the use of any templates or surfactants for producing the hollow urchin structured MnO<sub>2</sub> nanoparticles. MnO<sub>2</sub> nanostructures with high surface area and mesoporous structure show enhanced electrochemical properties and hence improved battery performance.<sup>33</sup>

### **6.3.3 MnO<sub>2</sub> NANOSTRUCTURES FOR WATER TREATMENT**

Organic waste present in water bodies can be removed effectively by transition metal oxides. Metal oxides, especially manganese oxides, show catalytic properties and are used as a major component in water treatment systems. It can also act as an efficient adsorbent because of its structural flexibility.<sup>26</sup> Chen et al. prepared birnessite MnO<sub>2</sub> materials using a soft chemistry route, which showed excellent low-temperature oxidative decomposition of formaldehyde. The same group also developed porous MnO<sub>2</sub> with a high adsorption capacity of organic pollutants and wastewater treatment capacity. Wastewater treatment studies using the prepared MnO<sub>2</sub> studies showed better performance compared to the presently used Red mud and MCM-22.<sup>34</sup> MnO<sub>2</sub>-based hierarchical hollow nanostructures can be used as an efficient adsorbent to remove organic pollutants. MnO<sub>2</sub>-based hierarchical hollow nanostructures could remove up to 90% of Congo red at room temperature.<sup>26</sup>

MnO<sub>2</sub> is also can be used to remove heavy metals from wastewater. Industrial wastewater sometimes contains a high level of Nickel, a toxic heavy metal ion. Nickel ions are produced by industrial processes such as smelting, dyeing operation, galvanization, and battery manufacturing. A high level of nickel can cause a variety of diseases, such as renal edema, gastrointestinal disorder, and lung cancer. Ren et al. synthesized a composite of graphene nanosheet and MnO<sub>2</sub> using the microwave-assisted method.<sup>35</sup> Prepared composites were studied in detail to determine their removal ability of Ni (II) ions. The adsorption capacity of the prepared nanocomposite was 46.6 mg g<sup>-1</sup>. MnO<sub>2</sub> nanosheets showed 1.5 and 15 times adsorption capacity compared to graphene sheet and MnO<sub>2</sub>, respectively. Prepared composite materials also showed better dispersion and fewer conglomerations. Prepared MnO<sub>2</sub>-graphene nanocomposite retained its adsorption property even after five cycles and thereby is reusable.



### 6.3.4 APPLICATION OF $\text{MnO}_2$ -BASED NANOFIBERS FOR ELECTROCHEMICAL BIOSENSING

A sensor, which can give precise measurement using biomolecular recognition element (receptor) and integrated biochip is known as an electrochemical biosensor. The physiological changes that take place in biomolecules are detected, recorded, and transmitted using biosensors. Nanostructured materials play an important role in the field of biosensing and biomedical applications. Recently, the synthesis of nanofibers of polymers, metals, and metal oxides by electrospinning technique has attracted much attention. The electrospinning technique can be used to generate biocompatible and biodegradable nanofibers with optimum properties. The level of glucose, cholesterol, triglyceride, and low-density lipoprotein affinity in the blood can be determined by biosensors with high sensitivity. Electrospun nanofibers are highly porous and their surface-to-volume ratio is comparatively very high. These properties make them highly sensitive and quite suitable to be used as a biosensor. Figure 6.6 shows the schematic diagram of a biosensor.

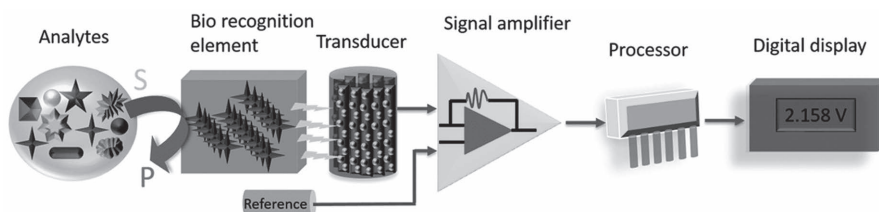


**FIGURE 6.6** Schematic diagram of a biosensor.

Source: Reprinted with permission from Ref. [36]. © 2016 Royal Society of Chemistry.

Electrospun nanofibers containing  $\text{MnO}_2$  can be used for cancer treatment.<sup>37</sup> Metal oxide nanoparticles synthesized by the electrospinning technique are highly sensitive due to their charge separation, high enzyme loading capacity, and also its ability to form covalent bonds with biomolecules. These unique properties make it very useful for the application as biosensors.<sup>38</sup> Xu et al. prepared a sensitive enzyme-based field effect transistor (FET) biosensor for lactate using  $\text{MnO}_2$  nanostructures at the gate surface.  $\text{MnO}_2$  nanostructures were used as oxidants with  $\text{H}_2\text{O}_2$ . In presence of lactase oxidase, lactate is converted to pyruvate by oxidation reaction. Hydrogen peroxide is produced as a byproduct in this process as a result of the reduction of oxygen.  $\text{MnO}_2$  nanoparticles react with the formed hydrogen peroxide and form  $\text{Mn}^{2+}$  and

O<sub>2</sub> consuming two hydrogen ions. Change in pH due to the consumption of hydrogen ions was monitored and correlated with the lactate concentration. The prepared biosensor showed good sensitivity even at low lactate concentrations.<sup>39</sup>

Xu et al. used MnO<sub>2</sub> nanoparticles in glucose biosensors to eliminate the interference from ascorbic acid. In this work, MnO<sub>2</sub> was co-deposited with chitosan by an electrochemical method to form a membrane on the surface of the glucose oxidase modified electrode.<sup>40</sup> The hydrogen peroxide formed as a resultant of the reaction between glucose oxidase and glucose is detected by this detector. However, ascorbic acid, which is also electroactive in the determination potential range of hydrogen peroxide acts as interference in glucose measurement. The anti-interference property of the prepared MnO<sub>2</sub>-based electrode is due to the pre-oxidation of ascorbic acid by MnO<sub>2</sub>. The prepared biosensor showed promising results as an interference-free glucose sensor.

### **6.3.5 MnO<sub>2</sub> NANOSTRUCTURES FOR HETEROGENEOUS CATALYSIS**

A heterogeneous catalyst needs to have a wide surface area, large pore volumes, excellent catalytic activity, and temperature stability to function well. During the reaction, reactants diffuse and get adsorbed on the surface of the catalyst for the reaction to happen. Nanostructured metal oxides are one such compound and have attained great attention in this field. In an efficient catalyst process, the catalyst must be easily separated and recovered from the reaction mixture. In metal oxide- assisted catalysis, the catalyst needs to be in a phase that is different from that of reactants and products, so that it can be easily separated after the reaction. In the case of porous metal oxide catalysts, both interior and exterior interaction takes place between the reactants and catalyst which clearly differentiates them from other non-porous catalysts.

By modifying the porosity in a solid catalyst, the surface area can be increased. Depending upon the pore size, porous metal oxide materials can be classified:

Microporous: pore diameter < 2 nm

Mesoporous: 2nm < pore diameter < 50 nm

Macroporous: pore diameter > 50 nm

MnO<sub>2</sub> can be used as a catalyst and as an electrode in energy storage devices. Ye et al. synthesized  $\alpha$ -MnO<sub>2</sub> supported silver catalyst. The prepared catalyst could efficiently carry out the oxidation of CO and benzene at low

temperatures.<sup>41</sup> They also prepared  $\beta$ - $\text{MnO}_2$  supported Au catalyst with mesoporous structure and three-dimensional orientation. The prepared catalyst could efficiently oxidize CO, toluene, and benzene at low temperatures.<sup>42</sup> Wang et al. prepared  $\alpha$ - $\text{MnO}_2$  nanoparticles of distinct morphology—rod, tubular, wire, etc. These nanoparticles were fabricated using a hydrothermal method and carbon tetrachloride solution method. Prepared nanostructures were studied for the removal of toluene. Rod-like  $\alpha$ - $\text{MnO}_2$  was found to have greater efficiency to remove toluene. This can be due to the higher concentration of oxygen present in  $\alpha$ - $\text{MnO}_2$ .<sup>43</sup>

## 6.4 CONCLUSIONS

$\text{MnO}_2$  is one of the most promising metal oxides due to their abundance, low cost, pseudocapacitance, and low toxicity. However, they have some disadvantages such as low conductivity and partial dissolution. Hybridization of  $\text{MnO}_2$  with carbon nanotubes, graphene, and conducting polymers yields excellent results. Nanostructures with required crystalline structures, morphology, and porosity can be synthesized using various synthesis methods.  $\text{MnO}_2$ -based nanostructures especially their hybrid forms have a promising future in applications such as supercapacitors, batteries, water purification, and biosensors.

## ACKNOWLEDGMENT

Dr. Sanal Sebastian Payyappilly is grateful for the national postdoctoral fellowship from Science Engineering Research Board (SERB) (No. PDF/2016/004115/ES).

## KEYWORDS

- $\text{MnO}_2$
- nanostructures
- synthesis
- nanoparticles
- electrospinning

## REFERENCES

1. Yuan, S. et al., Recent Progress on Transition Metal Oxides as Advanced Materials for Energy Conversion and Storage. *Energy Storage Mater.* **2021**.
2. Wang, Y.; Arandiyani, H.; Scott, J.; Bagheri, A.; Dai, H.; Amal, R. Recent Advances in Ordered Meso/Macroporous Metal Oxides for Heterogeneous Catalysis: A Review. *J. Mater. Chem. A* **2017**, *5* (19), 8825–8846.
3. Fang, S.; Bresser, D.; Passerini, S. Transition Metal Oxide Anodes for Electrochemical Energy Storage in Lithium- and Sodium-Ion Batteries. *Adv. Energy Mater.* **2020**, *10* (1), 1902485.
4. Cheng, F. et al. Facile Controlled Synthesis of MnO<sub>2</sub> Nanostructures of Novel Shapes and Their Application in Batteries. *Inorg. Chem.* **2006**, *45* (5), 2038–2044.
5. Yang, R. et al. Oxygen Defect Engineering of  $\beta$ -MnO<sub>2</sub> Catalysts via Phase Transformation for Selective Catalytic Reduction of NO. *Small* **2021**, 2102408.
6. Iftikhar, T. et al. Tuning Electrocatalytic Aptitude by Incorporating  $\alpha$ -MnO<sub>2</sub> Nanorods in Cu-MOF/rGO/CuO Hybrids: Electrochemical Sensing of Resorcinol for Practical Applications. *ACS Appl. Mater. Interfaces* **2021**, *13* (27), 31462–31473.
7. Zhang, Y.; Xue, D. Recent Advances in MnO<sub>2</sub>: Chemical Synthesis and Supercapacitance. *Mater. Focus* **2013**, *2* (3), 161–173.
8. Devaraj, S.; Munichandraiah, N. Effect of Crystallographic Structure of MnO<sub>2</sub> on Its Electrochemical Capacitance Properties. *J. Phys. Chem. C* **2008**, *112* (11), 4406–4417.
9. Huang, M.; Li, F.; Dong, F.; Zhang, Y. X.; Zhang, L. L. MnO<sub>2</sub>-Based Nanostructures for High-Performance Supercapacitors. *J. Mater. Chem. A* **2015**, *3* (43), 21380–21423.
10. Li, F. et al. MnO<sub>2</sub> Nanostructures with Three-Dimensional (3D) Morphology Replicated from Diatoms for High-Performance Supercapacitors. *J. Mater. Chem. A* **2015**, *3* (15), 7855–7861.
11. Huang, M. et al. Self-Assembly of Mesoporous Nanotubes Assembled from Interwoven Ultrathin Birnessite-Type MnO<sub>2</sub> Nanosheets for Asymmetric Supercapacitors. *Sci. Rep.* **2014**, *4*, 3878.
12. Nayak, P. K.; Munichandraiah, N. Mesoporous MnO<sub>2</sub> Synthesized by Using a Tri-Block Copolymer for Electrochemical Supercapacitor Studies. *Microporous Mesoporous Mater.* **2011**, *143* (1), 206–214.
13. Li, W. et al. MnO<sub>2</sub> Ultralong Nanowires with Better Electrical Conductivity and Enhanced Supercapacitor Performances. *J. Mater. Chem.* **2012**, *22* (30), 14864–14867.
14. Liu, Z.; Xu, K.; Sun, H.; Yin, S. One-Step Synthesis of Single Layer MnO<sub>2</sub> Nanosheets with Multi- Role Sodium Dodecyl Sulfate for High-Performance Pseudocapacitors. *Small* **2015**, *11* (18), 2182–2191.
15. Pang, S.-C.; Anderson, M. A. Novel Electrode Materials for Thin-Film Ultracapacitors: Comparison of Electrochemical Properties of Sol-Gel-Derived and Electrodeposited Manganese Dioxide. *J. Mater. Res.* **2000**, *15* (10), 2096–2106.
16. Liu, T. T.; Shao, G. J.; Ji, M. T.; Ma, Z. P. Research Progress in Nano-Structured MnO<sub>2</sub> as Electrode Materials for Supercapacitors, *Asian J. Chem.* **2013**, *25* (13), 7065–7070.
17. Wang, X.; Li, Y. Synthesis and Formation Mechanism of Manganese Dioxide Nanowires/Nanorods. *Chemistry* **2003**, *9* (1), 300–306.
18. Wang, X.; Li, Y. Selected-Control Hydrothermal Synthesis of  $\alpha$ - and  $\beta$ -MnO<sub>2</sub> Single Crystal Nanowires. *J. Am. Chem. Soc.* **2002**, *124* (12), 2880–2881.

19. Deng, M.-G.; Feng, Y.-H.; Fang, Q.; Chen, Y.-F. Hydrothermal Synthesis and Characterization of  $\text{MnO}_2$  Nanorods for Supercapacitor. *Gongneng Cailiao yu Qijian Xuebao/J. Funct. Mater. Devices* **2009**, *15* (5), 503–506.
20. Nam, H. S.; Kwon, J. S.; Kim, K. M.; Ko, J. M.; Kim, J. D. Supercapacitive Properties of a Nanowire-Structured  $\text{MnO}_2$  Electrode in the Gel Electrolyte Containing Silica. *Electrochim. Acta* **2010**, *55* (25), 7443–7446.
21. Kumar, H.; Sangwan, P. Synthesis and Characterization of  $\text{MnO}_2$  Nanoparticles Using Co-precipitation Technique. *Int. J. Chem. Chem. Eng.* **2013**, *3* (3), 2248–9924.
22. Huang, T. et al., Flexible High Performance Wet-Spun Graphene Fiber Supercapacitors. *RSC Adv.* **2013**, *3* (46), 23957–23962.
23. Yuan, A.; Wang, X.; Wang, Y.; Hu, J. Comparison of Nano- $\text{MnO}_2$  Derived from Different Manganese Sources and Influence of Active Material Weight Ratio on Performance of Nano- $\text{MnO}_2$ /Activated Carbon Supercapacitor. *Energy Convers. Manag.* **2010**, *51*, (12), 2588–2594.
24. Zhang, X.; Sun, X.; Zhang, H.; Zhang, D.; Ma, Y. Microwave-Assisted Reflux Rapid Synthesis of  $\text{MnO}_2$  Nanostructures and Their Application in Supercapacitors. *Electrochim. Acta* **2013**, *87* 637–644.
25. Huang, Q.; Wang, X.; Wang, X.; Li, J.; Huang, W. Studies of Electrochemical Preparation and Performance of  $\text{MnO}_2$  for the Application of Supercapacitor. *Chinese J. Power Sources* **2005**, *29* (7), 470.
26. Fei, J. B. et al. Controlled Preparation of  $\text{MnO}_2$  Hierarchical Hollow Nanostructures and Their Application in Water Treatment. *Adv. Mater.* **2008**, *20* (3), 452–456.
27. Innovations, F. *No Title*.
28. Biswal, A.; Tripathy, C.; Sanjay, K. RSC Advances Perspective on Worldwide Production, Reserves and Its Role in Electrochemistry. *RSC Adv.* **2015**, *5*, 58255–58283.
29. Wang, G.; Zhang, L.; Zhang, J. A Review of Electrode Materials for Electrochemical Supercapacitors. *Chem. Soc. Rev.* **2012**, *41* (2), 797–828.
30. Yu, G. et al. Enhancing the Supercapacitor Performance of Graphene/ $\text{MnO}_2$  Nanostructured Electrodes by Conductive Wrapping. *Nano Lett.* **2011**, *11* (10), 4438–4442.
31. Rani, J.; Thangavel, R.; Kim, M.; Lee, Y. S.; Jang, J.-H. Ultra-High Energy Density Hybrid Supercapacitors Using  $\text{MnO}_2$ /Reduced Graphene Oxide Hybrid Nanoscrolls. *Nanomaterials* **2020**, *10* (10), 2049.
32. Online, V. A.; Qin, X.; Chen, G. *RSC Adv.* **2014**.
33. Li, B.; Rong, G.; Xie, Y.; Huang, L.; Feng, C. Low-Temperature Synthesis of  $\alpha$ - $\text{MnO}_2$  Hollow Urchins and Their Application in Rechargeable  $\text{Li}^+$  Batteries. *Inorg. Chem.* **2006**, *45* (16), 6404–6410.
34. Chen, H.; He, J. Facile Synthesis of Monodisperse Manganese Oxide Nanostructures and Their Application in Water Treatment. *J. Phys. Chem. C* **2008**, *112* (45), 17540–17545.
35. Ren, Y. et al. Graphene/ $\delta$ - $\text{MnO}_2$  Composite as Adsorbent for the Removal of Nickel Ions from Wastewater. *Chem. Eng. J.* **2011**, *175*, 1–7.
36. Mondal, K.; Sharma, A. Recent Advances in Electrospun Metal-Oxide Nanofiber Based Interfaces for Electrochemical Biosensing, *RSC Adv.* **2016**, *6* (97), 94595–94616.
37. Luo, H.; Jie, T.; Zheng, L.; Huang, C.; Chen, G.; Cui, W. Electrospun Nanofibers for Cancer Therapy. *Bio-Nanomed. Cancer Ther.* **2021**, 163–190.
38. Wei, J. et al. Binary  $\text{MnO}_2/\text{Co}_3\text{O}_4$ @ Well-Aligned Electrospun Carbon Nanofibers for Sensitive, Nonenzymatic Glucose Sensing. *ECS Meeting Abstracts* **2020**, *27*, 1883.

39. Xu, J. J.; Zhao, W.; Luo, X. L.; Chen, H. Y. A Sensitive Biosensor for Lactate Based on Layer-by-Layer Assembling MnO<sub>2</sub> Nanoparticles and Lactate Oxidase on Ion-Sensitive Field- Effect Transistors. *Chem. Commun.* **2005**, 6, 792–794.
40. Xu, J. J.; Luo, X. L.; Du, Y.; Chen, H. Y. Application of MnO<sub>2</sub> Nanoparticles as an Eliminator of Ascorbate Interference to Amperometric Glucose Biosensors. *Electrochem. Commun.* **2004**, 6 (11), 1169–1173.
41. Ye, Q. et al. Nanosized Ag/ $\alpha$ -MnO<sub>2</sub> Catalysts Highly Active for the Low-Temperature Oxidation of Carbon Monoxide and Benzene. *Catal. Today* **2011**, 175, (1), 603–609.
42. Ye, Q. et al. Nanosized Au Supported on Three-Dimensionally Ordered Mesoporous  $\beta$ - MnO<sub>2</sub>: Highly Active Catalysts for the Low-Temperature Oxidation of Carbon Monoxide, Benzene, and Toluene. *Microporous Mesoporous Mater.* **2013**, 172, 20–29.
43. Wang, F.; Dai, H.; Deng, J.; Bai, G.; Ji, K.; Liu, Y. Manganese Oxides with Rod-, Wire-, Tube-, and Flower-Like Morphologies: Highly Effective Catalysts for the Removal of Toluene. *Environ. Sci. Technol.* **2012**, 46 (7), 4034–4041.



# Dye Removal Using Nanocomposites

SANTRA SANTHOSH<sup>1</sup> and DHANYA K. R.<sup>2</sup>

<sup>1</sup>*Indian Institute of Science Education and Research, Thiruvananthapuram, India*

<sup>2</sup>*IIUCNN, Mahatma Gandhi University, Kottayam, Kerala, India*

---

## ABSTRACT

Textile dyeing industry is one of the largest causes of water pollution. It releases many hazardous dyes and metals into the water bodies, making them unusable and poisonous. A vast range of nanomaterials are synthesized widely with unique properties. Nanocomposites with enhanced catalytic or adsorbing behavior are used for removing pollutants, especially dyes from water bodies. This chapter discusses different types of dyes and nanocomposites and dye removal using nanocomposites.

## 7.1 INTRODUCTION

Nanotechnology is the promising technology of the future in every field. Nanocomposites are the most interesting part of technology nowadays. Unlike the conventional composite materials, nanocomposites possess unique designs and combinations of properties.

Nanocomposites are polyphase solid materials. One or more dimensions of one of the phases in a nanocomposite come in the size range of 1–100 nm. Most of the physical and chemical properties such as mechanical, electrical, thermal, optical, electrochemical, catalytic properties of them are different from its component materials. The critical size of the nanocomposites gives



its particular properties.<sup>1</sup> For catalytic activity, the required size is  $<5$  nm. Similarly,  $<50$  nm,  $<100$  nm for refractive index changes and for achieving superparamagnetism and other electromagnetic phenomena are the required critical sizes, respectively. As the dimensions will be in nanometer scale, interactions at phase interfaces become largely improved which is important to upgrade the properties of materials. In mechanical terms, due to the exceptionally high surface-to-volume ratio of the reinforcing phase nanocomposites differ from traditional composite materials. Relatively, a small amount of nanoscale reinforcement can have a recognizable effect on the macroscale properties of the composite. Structures of abalone shells and bones are examples of natural nanocomposites.

Matrix materials nanocomposites are classified into three according to their: ceramic–matrix nanocomposites (CMNC), metal–matrix nanocomposites (MMNC), and polymer matrix nanocomposites (PMNC).

## **7.2 STRUCTURE AND PROPERTIES OF NANOCOMPOSITES**

The structure of nanocomposites contains matrix material containing nanoparticles in the shape of fibers, nanotubes, spheres, etc.<sup>2</sup> The different techniques used for the characterizations of PMNCs include thermal analysis techniques, such as TGA, DTA, DSC, TMA, and DMA and microscopic techniques, such as atomic force microscopy (AFM), scanning tunneling microscopy (STM), nuclear magnetic resonance (NMR), Fourier transformed infrared spectroscopy (FTIR), X-ray photoelectron spectroscopy (XPS), differential scanning calorimetry (DSC), scanning electron microscopy (SEM), transmission electron microscopy (TEM), Raman and X-ray diffraction techniques. The presence of a polymer matrix enhances the thermal stability of the polymer significantly. Thermal analytical techniques have been used for this purpose frequently.<sup>3</sup>

Scanning electron microscopy (SEM) provides images of the sample's properties, such as homogeneity, porosity, roughness, compatibility, and lattice mismatch. Scanning probe microscopy (SPM) and scanning tunneling microscopy (STM) are used to characterize PMNCs.<sup>4</sup> The AFM is used to scan across the sample to evaluate the roughness of morphology.<sup>5</sup> In some cases, transmission electron microscopy (TEM) helps in qualitative understanding of the internal structure and spatial distribution of the various phases through direct visualization of PMNCs. Wide angle X-ray diffraction (WAXD) and small angle X-ray scattering (SAXS) provide details about the crystallinity and lattice structure of nanocomposite.

The PMNC prepared from inorganic materials using *in situ* polymerization and composite formation are suitable as catalysts, sensors, reducing agents, and microbe-killing agents.<sup>6</sup> Scientists have synthesized zinc oxide polyaniline nanocomposite which has improved interface. Due to its synergistic effects, it exhibited a thousand times better electrical conductivity.<sup>7</sup>

The addition of nanoparticles in the polymer matrix improves the polymer properties and produce PNCs with desired properties. Catalytic, adsorption, and mechanical properties of PNCs are generally used for the purification of water. These properties of PNCs are briefly discussed below.

### 7.2.1 CATALYST

Some metals, metal oxides, and sulfides are used as catalysts for the purification of water both in the presence and absence of light.<sup>8</sup> Reports say that a wide variety of compounds are catalytically degraded.<sup>9</sup> Metal compounds, such as  $\text{TiO}_2$ ,  $\text{ZnO}$ ,  $\text{Fe}_2\text{O}_3$ ,  $\text{CdS}$ ,  $\text{GaP}$ , and  $\text{ZnS}$  are used for catalytic degradation due to their interaction with the ionic surface and its modified surface tension.<sup>10</sup> Titanium dioxide ( $\text{TiO}_2$ ) and zinc oxide ( $\text{ZnO}$ ) are low cost and have high photocatalytic activity and stability and have great importance.<sup>11,12</sup> For example,  $\text{ZnO/PMMA}$  nanocomposite is used for the photocatalytic degradation of phenol and methylene blue (see Figure 7.1a).<sup>13</sup>

Electrons are released by these metal oxides on irradiation with UV light. This will react with the  $\text{H}_2\text{O}$  and  $\text{O}_2$  molecules which are adhered to its surface. It results in the production of highly reactive oxygen species (ROS) like peroxides, superoxide, singlet oxygen, and hydroxyl radicals which are capable of degrading organic water pollutants efficiently.<sup>14</sup> ROS also has an antibacterial effect and it could inactivate the microbes present in the polluted water.<sup>15</sup> But the presence of these metals in water is harmful to the ecosystem and human life. Therefore, we use nanocomposites in which these metals are inserted. This could help in the sustained release of ions or electrons. Examples are Titana/PMMA nanocomposite, silver-embedded aluminum oxyhydroxide–chitosan nanocomposite, etc.<sup>16,17</sup>

### 7.2.2 ADSORPTION BEHAVIOR

Due to the high surface area of nanoparticles, nanocomposites are known for their high adsorption behavior. Since it is optimized, it can be used for applications, such as water purification, drug delivery, chemical sensor.

Toxic dyes, metal ions, and microbes are easily removed using this from wastewater.

Adsorption is dependent on the ionic or surface interaction. It needs a selective interaction site. This can be synchronized by having hydrophobic and hydrophilic behaviors in the matrix. Most of the nanocomposites possess this quality which makes them a perfect adsorbent. The interpenetrating nature and magnetic nature of the nanocomposites also increase the adsorption capacity.

Nanocomposites that consist of carbon nanotubes (CNT) have high porosity, the affinity of solvents, better selectivity, and reactivity of molecules and ions.<sup>18</sup> Nanocomposites that have optimized porosity are good in mass transfer, lighter weight, and liquid retention. Chitosan and its nanoderivatives are reported as good adsorbents for the removal of water contaminants. But like everything in the world, it too has a disadvantage as it has low mechanical strength (see Figure 7.1b).<sup>19</sup>

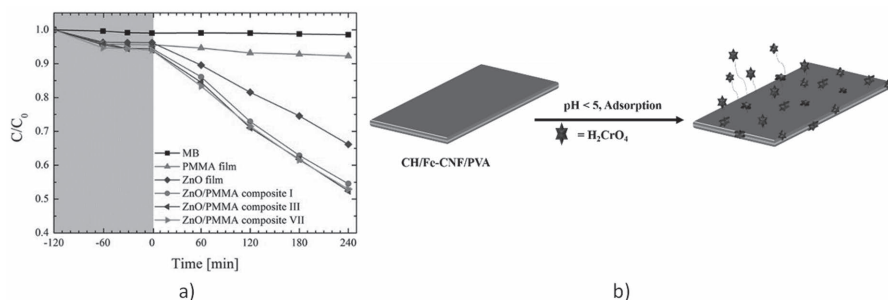


**FIGURE 7.1** (a) Photocatalytic degradation methylene blue over ZnO/PMMA composites as a function of the irradiation time for four aqueous solutions respectively with: MB (squares), MB with a PMMA film (up triangles), MB with a ZnO film (diamonds), and MB with a ZnO/PMMA composite (circles) (with permission from Impellizzeri, G<sup>13</sup>). (b) Schematic illustration for chromium adsorption on Chitosan/Fe-Carbon nanofibers and polyvinyl alcohol nanocomposite.

Source: Reprinted/Adapted from Refs. [13, 18, 19]

### 7.3 APPLICATIONS OF NANOCOMPOSITES

Nanocomposites are well known for their wider applications. Biosensors with high sensitivity, selectivity, and high biocompatibility are required in medical industries for the detection of biomolecules with high precision. Graphene-based nanocomposites are widely used as biosensors of glucose, cholesterol, oligonucleotides,  $H_2O_2$ , dopamine, NADH, ascorbic acid, uric

acid, pathogens, and various cancer biomarker detection.<sup>20–31</sup> Oxygenated graphene makes the graphene nanocomposites strongly hydrophilic and thereby more chemically functionalized.<sup>32</sup> Incorporation of them with other organic and inorganic nanoparticles provides them unique properties required for biointeractions, which makes them the best candidate for biomolecule detection.

Nanocomposites find their applications in drug delivery, cancer therapeutics, gene therapy, and tissue engineering.<sup>33–36</sup> Mainly, chitosan-based nanocomposites are used due to their biocompatibility. Chitosan can be dissolved in mildly acidic pH, which is similar to the pH of cancer cells. Because of this, chitosan-based nanocomposites have found their applications in cancer theranostics.<sup>37</sup>

High barrier film gives enhanced thermal and mechanical characteristics for materials. Graphene nanoplates have shown improved heat resistance and barrier properties.<sup>38</sup> For food packaging applications, materials that provide good shelf life, flavor, color, and texture to food are required. Biopolymer/clay nanocomposites are widely used for this due to their higher tensile strength, augmented thermal stability, and better gas barrier properties.<sup>39–44</sup> Silver and oxides of copper, titanium, and zinc are used with the nanocomposites because of their antimicrobial properties.<sup>45</sup>

Batteries, capacitors, supercapacitors, and other energy storage devices can be made from nanocomposites of conducting polymers, metal oxides, graphene, and other electroactive materials. The morphology and interfacial characteristics of them give increased electrical properties and mechanical durability.<sup>46–51</sup>

Re-enforced nanocomposites are used in oil and gas pipelines because of their anisotropic characteristics, structurally integrated sensors, corrosion resistance, and damage tolerance.<sup>52–54</sup> Nanoparticles used as a blend against plastics have high strength and can be used as automobile parts which are more prone to wear and tear. These polymer nanocomposites are used over the following aspects like weight reduction, recyclability, and improved performance.<sup>55, 56</sup>

Water resources are getting polluted with industrial pollutants, such as hazardous metals, dyes, and microbes. Nanocomposites are used for their removal according to its special properties.<sup>57</sup> Dispersion of nanosilicate layer results in the improvement in mechanical, barrier properties, ablation performance, thermal stability, controlled release of drugs, electrical conductivity, fire retardancy, and photoactivity. So, they are used for aerospace food packaging, and tissue engineering. There are many other applications for

nanocomposites, and researchers are currently working on these to develop the world through the field of nanotechnology.

## 7.4 DYES

Before discussing about dye removal, we must know the structure and properties of the dyes to find out the appropriate method for dye removal.

According to Otto Witt's theory, a dye compound has two components – a chromophore and an auxochrome. Chromophore is an unsaturated functional group that causes the dye to be colored, while an auxochrome is a functional group which can alter the color of the chromophore. A dyeing process is the interaction between the fabric/fiber and the dye. According to the target fabric material, the dye also changes. Different kinds of dyes used in the textile industries are the following according to their solubility and chemical properties (see Table 7.1).

### 7.4.1 REACTIVE DYES

Reactive dyes have a reactive group that creates a covalent bonding with the substrate. It is mostly used with cellulosic fibers, such as cotton, flax, and also wool and polyamides. These dyes are soluble in water but have very good wash fastness because of their strong bonding with fiber.



**FIGURE 7.2** General structure of a reactive dye.

*Source:* Reprinted/Adapted from Ref. [58]

### 7.4.2 DIRECT DYES

Direct dyes are water soluble and can be applied directly on cotton, paper, wool, silk, leather, and nylon. They are dull in color and do not wash fast. A slightly alkaline bath is required for dyeing. Direct dye compounds mainly consist of poly azo groups.

### **7.4.3 DISPERSE DYES**

Disperse dyes are used in paste or powder form. Since they are water-insoluble, a dispersing agent is used here. They were specially made for dyeing cellulose acetate. Now it is used in dyeing nylon, acrylic fibers, and polyesters. A high dyeing temperature and pressurized bath are required for this dyeing process. Disperse dye compounds generally contain azo, anthraquinone, nitro, and styryl groups.

### **7.4.4 ACID DYES**

Acid dyes are best for dyeing protein fabrics. Silk, wool, nylon, and some acrylic fibers are dyed using acid dye baths. They are water-soluble anionic dyes. The anionic group of acid dye forms a salt with the cationic group of the fiber. Most synthetic colors are of this type. It is sometimes used as food and cosmetic color also. Acid dye compounds have azo, azine, anthraquinone, nitro, and nitroso groups.

### **7.4.5 BASIC DYES**

Basic dyes are water-soluble cationic dyes. It bonds with the fiber through salt formation similar to acid dyes. It is used in weakly acidic dye baths so that it increases the adsorption of the dye to the fiber. Basic dyes are used to dye pure silk, wool, paper, modified nylon, and modified acrylic fibers. Basic dye compounds have cyanines, thiazine, and oxazine.

### **7.4.6 VAT DYES**

VAT dyes are water-insoluble. They are chemically more complex and contain anthraquinones or indigoids. It requires a reducing agent to get adsorbed to the fabric. Indigo, a VAT dye is used for dyeing denim.

### **7.4.7 AZO DYES**

Azoic dyes contain insoluble azo groups and therefore have enhanced water fastness. They are synthesized by reacting a coupling compound and diazo compound.

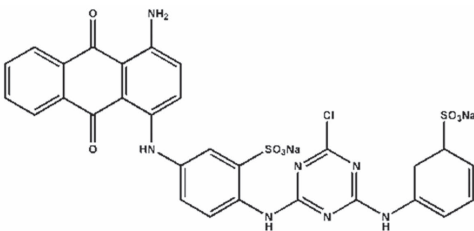
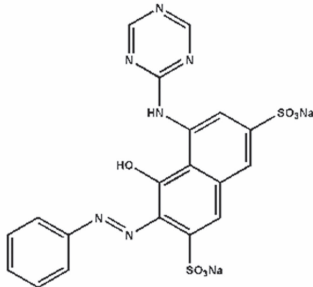
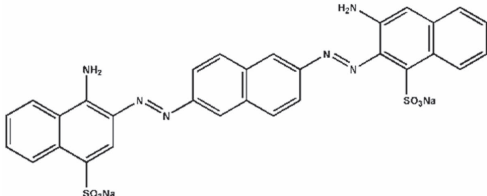
### 7.4.8 SULFUR DYES

Sulfur dye compounds have sulfur or sodium sulfide groups. It is the most inexpensive and easiest method of dyeing cotton.

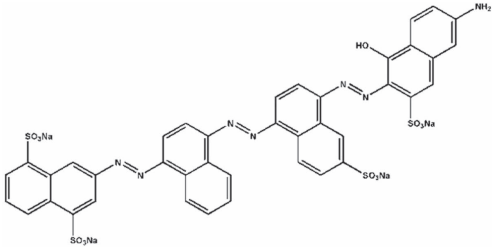
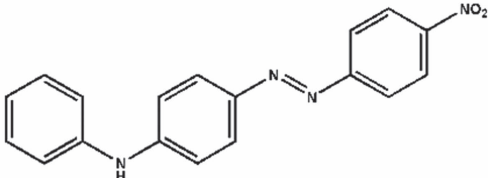
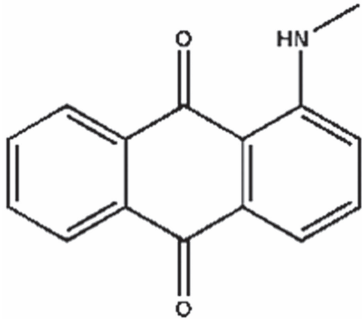
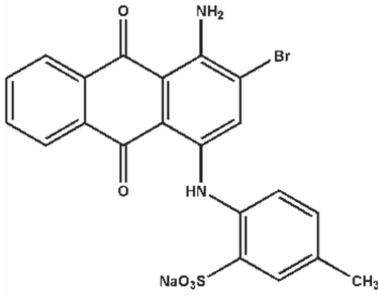
### 7.4.9 MORDANT DYES

Mordant dyes are called so because they require a mordant which increases their fastness against water, light, and perspiration. Most natural dyes are of this type. Many mordants can be poisonous.

**TABLE 7.1** Different Types of Dyes With Examples.

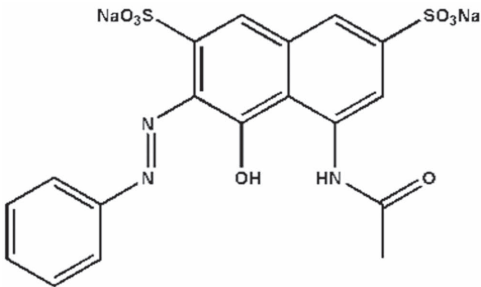
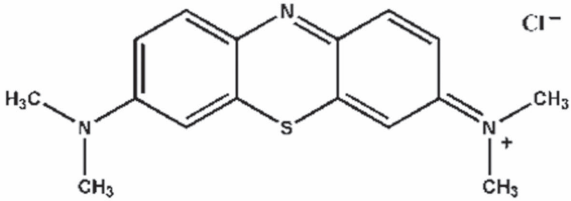
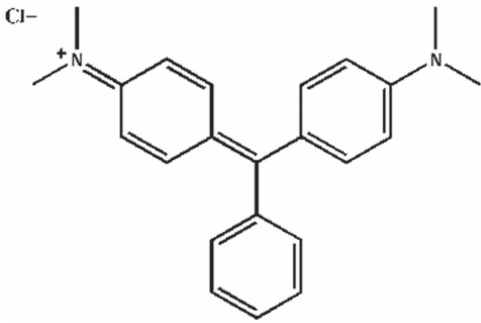
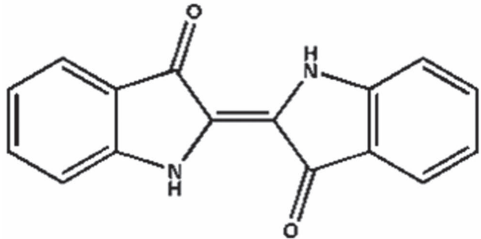
Type of dye	Examples
Reactive	<p>Levafix Brilliant Red</p>  <p>Procion Red MX 5B</p> 
Direct	<p>Congo Red</p> 

**TABLE 7.1** (Continued)

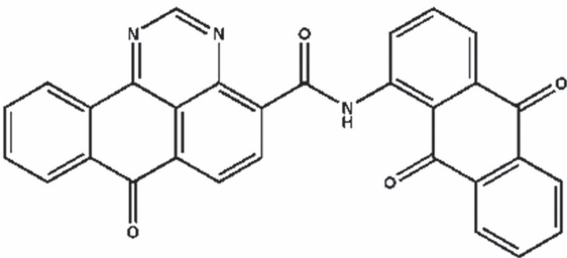
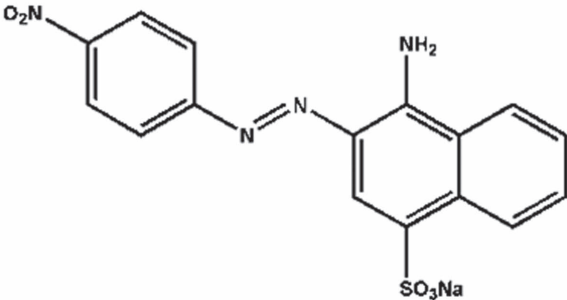
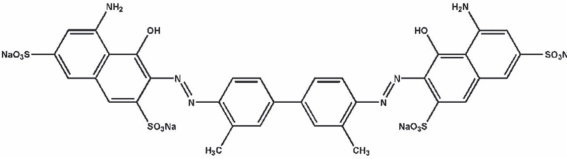
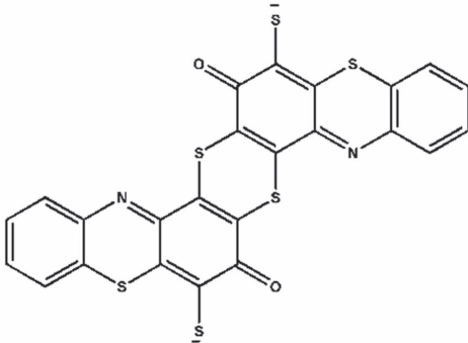
Type of dye	Examples
Direct	Direct Blue 71
	
Disperse	Disperse Orange 1B
	
	Disperse Red 9
	
Acid	Acid Blue 78
	



**TABLE 7.1** (Continued)

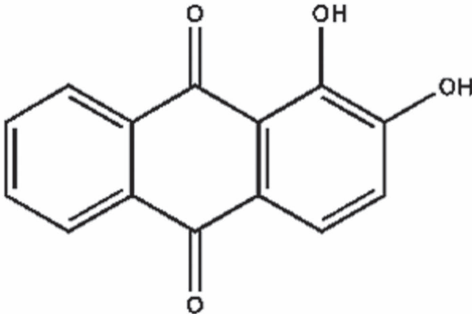
Type of dye	Examples
	<p>Acid Red 1</p> 
Basic	<p>Methylene Blue</p> 
	<p>Malachite Green</p> 
Vat	<p>Indigo</p> 

**TABLE 7.1** (Continued)

Type of dye	Examples
	Pigment Yellow 108
	
Azo	Acid Red Dye 74
	
	Trypan Blue
	
Sulfur	Sulfur Black
	

**TABLE 7.1** (Continued)

Type of dye	Examples
Mordant	Alizarin



## 7.5 DYE REMOVAL USING NANOCOMPOSITE

Dyes are discharged into water resources in a good amount on daily basis from textile, printing, and cosmetics industries. Less than a milligram of dye can be visible and affects the transparency of water. It is easily soluble in water and reduces the gas solubility of water bodies. It adsorbs and reflects the sunlight and interferes with the growth of aquatic species by hindering photosynthesis. Thus, dyes affect the aquatic life adversely. Generally, the structure of dyes is complex, the and presence of heavy metals makes the wastewater effluent more toxic and it even becomes carcinogenic. On long-term exposure, tumors and cancers can affect on skin, liver, and kidney. Various physical and chemical techniques have been studied for the treatment of wastewater containing dyes. Of all the processes, the adsorption technique is the most reliable as it generates very less sludge and it is cheap. Adsorption is widely used for dye removal as it is the easiest and cheapest method of all. Water treatment needs the removal of both organic and inorganic micropollutants, such as dye and others. Clay-polymer nanocomposites (CPN) adsorb and flocculate these effectively.<sup>59</sup>

### 7.5.1 CERAMIC-MATRIX NANOCOMPOSITES

Ceramics have high thermal and chemical stability and wear resistance. But they are poor in toughness. In order to overcome this, CMNC are used, which have enhanced mechanical properties than ceramics. The main part

of the volume of these nanocomposites consists of ceramic. Generally, the second component of CMNC is metal. In ideal conditions, both metal and ceramic are finely dispersed in each other to show their particular nanoscopic properties. CMNC have improved properties of optical, electrical, magnetic corrosion resistance, and others.<sup>60</sup>

Removal of basic blue 3 (BB3) from water showed the sonocatalytic performance of  $\text{TiO}_2/\text{Montmorillonite K}_{10}$  ( $\text{TiO}_2/\text{MMT}$ ). The results revealed that  $\text{TiO}_2/\text{MMT}$  shows higher sonocatalytic activity than that of pure  $\text{TiO}_2$  and MMT. Increasing  $\text{TiO}_2/\text{MMT}$  nanocomposites dosage and power of the ultrasonic generator and decreasing the initial concentration of BB3 increases the decolorization efficiency. Inorganic anions also have effects on decolorization of BB3 in the following order:  $\text{Cl}^- > \text{CO}_3^{2-} > \text{SO}_4^{2-}$ .<sup>61</sup>

Similarly, studies have shown that Stishovite- $\text{TiO}_2$  nanocomposite and Stishovite clay are good adsorbents of malachite green. Both followed a pseudo-second-order kinetic model. Langmuir and Freundlich adsorption models and Elkovich chemisorptive kinetic model give the data of kinetics of this process. Since its desorption level is very low, we can conclude that this process undergoes chemisorption. The adsorption rate depends on the pH initial dye concentration, dosage of adsorbent, and temperature. This study shows that Stishovite- $\text{TiO}_2$  nanocomposite removes MG more efficiently than Stishovite clay.<sup>62</sup>

Nickel-modified  $\text{SiOC(H)}$  ceramic nanocomposites show ferromagnetic behavior and are predominantly mesoporous. Therefore, it shows higher adsorptive properties toward a template dye acid fuschin.<sup>63</sup>

### 7.5.2 METAL-MATRIX NANOCOMPOSITES

Metal matrix nanocomposites (MMNC) are metal matrix which contains nanosized reinforcement material. These can be classified as continuous and non-continuous reinforced materials. These nanocomposites possess the combined properties of metal and ceramic, such as ductility, toughness, and therefore are used in the production of materials having high strength in shear/compression processes and high service temperature capabilities.

Low-cost adsorbent like activated carbon- $\text{MnO}_2$  nanocomposite ( $\text{AC-MnO}_2\text{-NC}$ ) has shown the efficient removal of malachite green, a basic dye. Desorption with acetic acid after the regeneration of adsorbent and its other thermodynamic parameters showed that it is a thermodynamically favorable physisorption. By using appropriate dosages of adsorbent and pH of wastewater we can completely remove the dye. Most importantly,

the raw material is available in large quantities and therefore it is more economical.<sup>64</sup>

We can see that nickel nanocomposites are widely used for dye removal. UV–vis spectroscopy showed that the supported nickel nanoparticles/carbon porous materials (Ni/CPM) exhibit an excellent activity of catalytic reduction of organic dyes like Rhodamine B (RB) and methylene blue (MB). In addition, electrochemical measurements by cyclic voltammetry (CV) and differential pulse voltammetry (DPV) demonstrated this nanocomposite has high sensitivity and a low detection limit toward the detection of Hg(II) ion (see Figure 7.3). It is user-friendly and highly effective for catalytic reduction of organic dyes and detection of heavy metals in trace levels.<sup>65</sup>

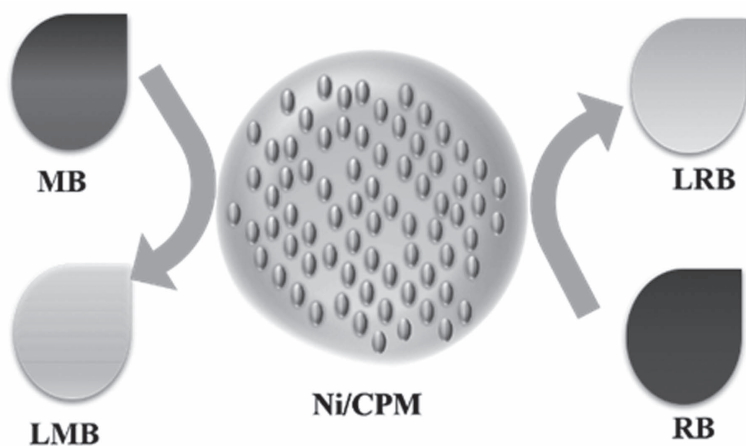


**FIGURE 7.3** Schematic diagram of dye removal by Ni/CPM.

In another case, it was shown that Rhodamine B (RB) can be removed from the aqueous solution using magnetic  $\text{ZnFe}_2\text{O}_4$  nanocomposite (ZnFe-NC). The adsorption capacity increased with an increase in the initial concentration of dye. The experiment was well-fitted with Langmuir isotherm model and low pH is preferred for this.<sup>66</sup>

Nickel nanocomposites were made to decolorize C I Reactive Blue 21 and polyvinyl pyrrolidone (PVP) was used as a stabilizer. FTIR was done to study the attachment of degraded dye onto the nanoparticles. RB21 dye has a complex structure with less percent exhaustion and that is why it was taken for this experiment. Degradation of dye varied with pH dye and nanoparticle concentration, addition of alkali and salts, and contact time. The percentage of decolorization can be found from the calibration curve.<sup>67</sup>

Another widely used agent for dye removal is magnetite nanocomposites due to their magnetic properties. Halloysite–magnetite ( $\text{HNT-Fe}_3\text{O}_4$ ) nanocomposite is used for the adsorption of methyl violet (MV) 2B which has broad applications in textiles, paints, and printing industries. MV has been used as a disinfectant, but it is also found out that it is poisonous to most animals.  $\text{HNT-Fe}_3\text{O}_4$  is reusable too. Since it is magnetic, it causes less contamination. Experimental conditions, such as rate of stirring, dosage of adsorbent, contact time, initial pH, and dye concentration alter the adsorption rate. The kinetics of this adsorption follows pseudo-second-order model and it is a spontaneous and exothermal process.<sup>68</sup>

Malachite green (MG) was removed by batch method using herein, trisodium citrate-based magnetite nanocomposites ( $\text{Fe}_3\text{O}_4\text{-TSC}$ ). The thermodynamic analysis showed that this process is impulsive and exothermic. The adsorption percentage decreased with increasing the temperature. MG can be recovered by using 0.1 HCl and  $\text{Fe}_3\text{O}_4\text{-TSC}$  can be separated from mixed solutions by applying an external magnetic field (see Figure 7.4). MG adsorption onto  $\text{Fe}_3\text{O}_4\text{-TSC}$  followed pseudo-second-order kinetic model and fitted well for Langmuir model.<sup>69</sup>

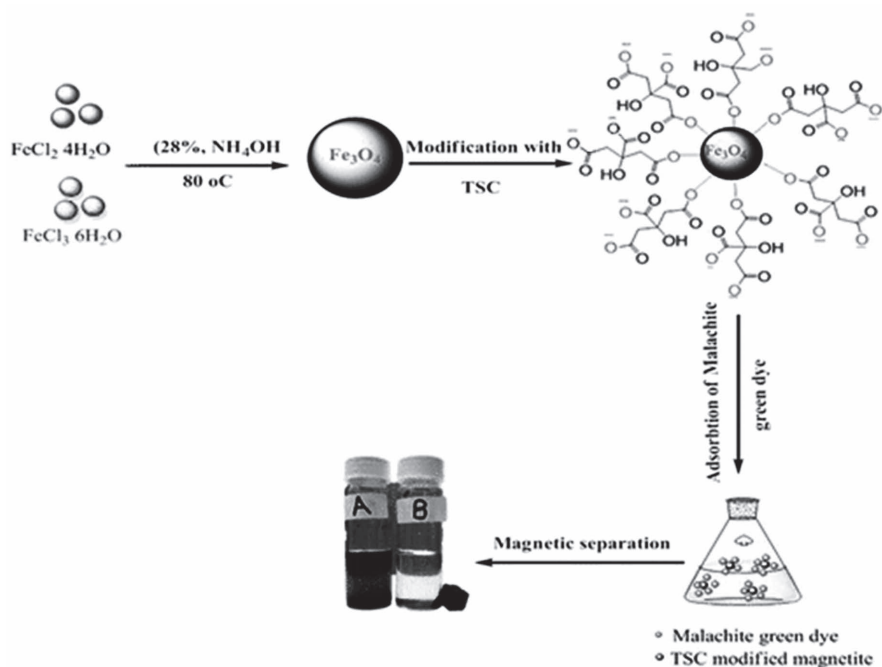


**FIGURE 7.4** Removal of Malachite Green using  $\text{Fe}_3\text{O}_4\text{-TSC}$ .

Source: Reprinted with permission from Ref. [69]

Graphene has good thermal, optical, electronic, mechanical, and chemical tolerance capabilities and high surface-to-volume ratio<sup>70</sup>. Therefore, it is used for making nanocomposites with polymers, metals, and metal–organic nanoparticles, etc. Generally, inorganic metal oxide-based nanocomposites are used for applying photovoltaics, photodegradation, wastewater treatment, photochromism, etc. because of its physiochemical properties.

Combined properties of graphene oxide, magnetite, and chitosan are expressed in chitosan/Fe<sub>3</sub>O<sub>4</sub>/graphene oxide (CS/Fe<sub>3</sub>O<sub>4</sub>/GO) nanocomposites. Therefore, it is used for the efficient removal of methylene blue. CS/Fe<sub>3</sub>O<sub>4</sub>/GO nanocomposites are cheap and efficient adsorbents of cationic dyes. Also, it is a recoverable and recyclable adsorbent.<sup>71</sup>

Magnetite/reduced graphene oxide (MRGO) nanocomposites are prepared by a simple solvothermal strategy. Nontoxic materials are used to prepare this and are used to remove dye pollutants. From studies, it is found that it shows higher removal efficiency of over 94% for malachite green and over 91% for rhodamine due to the combined properties of graphene and magnetic nanoparticles. But the performance of MRGO depends on the loading of magnetite and the pH value. Loading more amount of Fe<sub>3</sub>O<sub>4</sub> will complement the magnetic properties but at the same time, it will reduce the availability of exposed surface area. This could result in a lower adsorption capacity of MRGO. Its magnetic characterization is done using a superconducting quantum interference device (SQUID). High pH will increase the negative charge over the surface of MRGO which increases the electrostatic interaction and thereby adsorption of positively charged dyes like malachite green. For lower pH, negatively charged dyes like rhodamine get easily adsorbed. It is widely used for the removal of dye from the industrial wastewater and lake water.<sup>72</sup>

Graphene oxide has shown efficiency in removing both heavy metal ions and ionic dyes in wastewater, but it has segregation inconvenience. Magnetic graphene oxide was composed of oxides of graphene and iron. MGO is used for the simultaneous removal of ionic dyes like methylene blue (MB) and orange G (OG) and Cd(II) ion. However, the sorption capacities differed for both dyes with respect to the pH of the system. Synergistic adsorption and suppression adsorption were observed for OG in Cd(II)-OG binary system and Cd(II) in Cd(II)-MB binary system. As the concentration of MB was increased sorption of Cd(II) decreased. But variation in concentration of Cd(II) did not affect MB in Cd(II)-MB system. Increasing the concentration of Cd(II) increased the sorption capacity of OG and Cd(II) was independent of OG in Cd(II)-OG system.<sup>73</sup> Similarly, a case of Cr (VI) removal from aqueous solutions was done using magnetite modified chitosan cinnamaldehyde.<sup>74</sup>

The photocatalytic degradation of methylene blue by graphene oxide/zinc oxide nanocomposites was analyzed and compared with that of zinc oxide, graphene oxide, and carbon nanotube/zinc oxide. Optimum conditions of photocatalytic dosages,  $\text{H}_2\text{O}_2$  concentration, and initial pH were taken into account in this process. It revealed that the removal of MB over GO/ZnO was more efficient than that over GO and CNT/ZnO. A second-order model was developed for this photocatalytic process.<sup>75</sup> Similarly, CH-GEL/ZSPNC was used to remove Rhodamine B through photocatalysis (see Figure 7.5).<sup>76</sup>

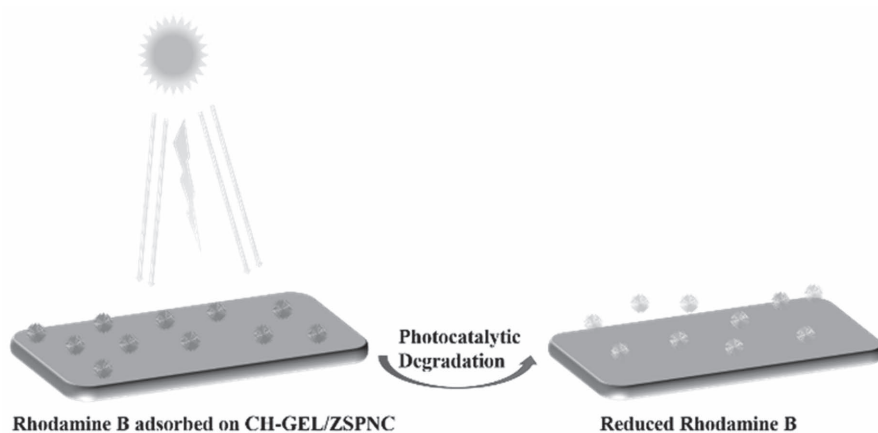


**FIGURE 7.5** Photocatalytic degradation of Rhodamine B by CH-GEL/ZSPNC.

In a study, graphene-based nanocomposites ( $\text{G}/\text{Fe}_3\text{O}_4$ ) were prepared for the removal of an organic dye fuchsine. SEM and XRD were used to study the morphology and inner structure of the composite. Adsorption capacity of adsorbent, adsorption kinetics, the effect of dye and adsorbent concentration, and pH were studied in this experiment. Adsorption isotherms were studied using Langmuir and Freundlich models and the kinetic data fitted the pseudo-second-order kinetics.<sup>77</sup>

(PANI)-coated graphene oxide doped with  $\text{SrTiO}_3$  nanocubes were synthesized through in situ oxidative polymerization. It is made with the aim of removing carcinogenic dyes, such as methylene blue (MB) and methyl orange (MO), which are cationic dye and anionic dye, respectively. The cationic and anionic nature is imparted to the nanocomposite by the nitrogen-containing functional groups in polyaniline and oxygenated functional groups in graphene oxide.  $\text{SrTiO}_3$  acts as a spacer and increases the surface area of the nanocomposite. Field emission scanning electron



microscopy (FESEM), thermo gravimetric analysis (TGA), TEM, XRD, and FTIR were used to characterize the nanocomposite. FESEM analysis revealed that on incorporating PANI and  $\text{SrTiO}_3$  to GO the aggregated sheet form of it changed to a segregated one.

Electrostatic attraction is one of the major factors that act in the removal of MO and MB dyes as they are anionic and cationic, respectively. The negative polarization on GO due to the oxygenated functional groups on it along with  $\text{sp}_2$  hybridized framework helps to form a strong electrostatic interaction with MB for its removal. The presence of the positively charged polymeric backbone on PANI helps it in the removal of MO. The lone pair electrons on the nitrogen of MB and MO form intermolecular H-bonding with the hydroxyl and carboxyl groups on the surface of GOPSr-2, which aids in the efficient removal of the dye. The given nanocomposites have aromatic backbone and it will have a  $\pi$ - $\pi$  interaction with MB and MO which are also planar molecules. So, all these interactions help in the efficient removal of dyes in a short period of time. The removal efficiency of MB was pH independent whereas that of MO was pH-dependent.<sup>78</sup>

Magnetic multiwall carbon nanotube (MMWCNT) was composed of multiwall CNT and iron oxide nanoparticles. It was used for the adsorption of cationic dyes, such as neutral red, methylene blue, and brilliant cresyl blue. It showed the advantage of separation convenience.<sup>79</sup>

Magnetic nanocomposites were made using saponite clay and magnetite. Characterization studies revealed that they have more microporosity and mesoporosity when compared with saponite clay and this is due to the stabilization of  $\text{Fe}_3\text{O}_4$  layer on the surface of saponite clay. This property helps in the removal of dye from the aqueous solution. These waste composite magnetic sorbents can be removed from water by magnetic separation.<sup>80</sup>

Magnetic  $\text{Fe}_3\text{O}_4$ -activated carbon nanocomposites have relatively large pore size, high surface area, and high saturation magnetization. This system has high adsorption capacity and better magnetic separation performance. It is used for the adsorption of methylene blue from aqueous solution.<sup>81</sup>

The chemical co-precipitation method was used to prepare magnetic  $\text{Fe}_3\text{O}_4$ /bentonite nanocomposites. Magnetic  $\text{Fe}_3\text{O}_4$  nanoparticles were implanted onto the surface of bentonite. This produced a porous surface of high surface area, which is suitable for the adsorption of basic dyes. Batch adsorption experiments were conducted for the study of using  $\text{Fe}_3\text{O}_4$ /bentonite nanocomposite removal of methylene blue (MB) from aqueous solutions. pH of the initial dye solution, contact time on the adsorption capacity, and mass of the adsorbent were checked in this experiment. By increasing the initial pH

of the solution and contact time the adsorption capacity also increased and decreased by increasing the mass of the adsorbent. The kinetic data showed that this adsorption technique is in good agreement with the intra-particle diffusion model and it followed pseudo-second-order kinetic model.<sup>82</sup>

Zinc oxide was added to magnetic nanoparticles by a chemical method to adsorb reactive black 5 (RB5) from aqueous solutions. Characterization studies of the nanocomposite using FTIR, EDX, SEM, and XRD revealed the functional group's structure and porous surface. Removal efficiency by ZnO-Fe<sub>3</sub>O<sub>4</sub> varied with pH concentration of adsorbent dye and H<sub>2</sub>O<sub>2</sub> and ionic strength (salts of sodium). The removal efficiency of ZnO-Fe<sub>3</sub>O<sub>4</sub> was higher than the individual components and it increased with increasing the initial concentration of H<sub>2</sub>O<sub>2</sub> from 2 to 5 mM but decreased after 5 mM. Also increasing the contact time and adsorbent dosage increased the adsorbing activity whereas increasing the dye concentration decreased the activity. Adsorption capacity increased in the presence of sodium chloride, whereas it decreased greatly in the presence of carbonate, bicarbonate, and sulfate ion. This adsorption technique followed pseudo-second-order and was well-fitted for Langmuir equation.<sup>83</sup>

A study on the removal of MB using magnetic nanoparticles (MNPs) and gum arabic (GA)-coated MNPs was conducted. It showed that GA-MNPs are highly efficient in the removal of MB from wastewater. The adsorption increased with temperature indicating that it is an endothermic process and it fitted Langmuir model.<sup>84</sup>

### 7.5.3 POLYMER-MATRIX NANOCOMPOSITES

Polymer-matrix nanocomposites are nanocomposites in which nanofillers are implanted into the matrix to produce a composite with equal or better mechanical, physical, and chemical properties. These are also described as nano-filled polymer composites. At least one dimension of this multiphased-composite will be in nano range. Since PMNCs have a lot of properties, such as dimensional variability, film-forming ability, and activated functionalities, PMNC has become one of the most important areas of research and development now.<sup>85,86</sup>

Graft copolymerization of vinyl acetate onto starch in the presence of magnetic nanoparticles produced starch-g-poly (vinyl sulfate) (MNP@St-g-PVS), a magnetic nanocomposite. This was used for the removal of typical cationic dyes like methylene blue (MB) and malachite green (MG) from its aqueous solutions (see Figure 7.6). This adsorbent has a robust structure and

is also recoverable without the loss of its adsorption ability. The efficiency of dye removal by an adsorbent depends upon factors, such as pH, time of adsorption, agitation speed, initial concentration of adsorbent and dye, and temperature. Modified polysaccharides are being used for the removal of toxic dyes from wastewater effluents even though they have limited hydrodynamic volume, poor thermal stability, and lower surface area. Due to the synergistic effect between inorganic nanofiller and organic polymer matrix, these biodegradable nanocomposites show improved mechanical and thermal properties along with large surface area and hydrodynamic volume.<sup>87</sup>



**FIGURE 7.6** Mechanism of dye removal using MNP@St-g-PVS.

During the polymerization of acrylamide using ammonium persulfate and N,N'-methylenebis(acrylamide) nanoparticles were added to synthesize a photocatalyst polyacrylamide/ $\text{Ni}_{0.002}\text{Zn}_{0.98}\text{O}$  (PAM/ZNP). This material possesses good photoactivity along with high adsorption capacity. This was used for the removal of malachite green (MG) and rhodamine B (RB) from water effluents. Simultaneous adsorption and photocatalysis by PAM/ZNP under natural sunlight irradiation makes it a good dye-removing agent.<sup>88</sup>

Polyaniline belongs to the polymer family and it also has efficient thermal and environmental stability but it has some drawbacks, such as poor mechanical properties, less surface area, and poor solubility.<sup>89</sup> In order to overcome these drawbacks, PANI is implanted into different types of organic and inorganic materials. PANI-based nanocomposites are used as adsorbents for dye removal from wastewater effluents.

Polyaniline-coated sawdust, a polyaniline nanocomposite was exploited for the removal of Acid Violet 49, an acid dye from aqueous solutions. Removal of AV49 dye is pH-dependent. In acidic condition, the proton gradient increases and it makes the surface of the adsorbent positively charged. It will increase the interaction between the positive surface and anionic dye. As the initial concentration of dye increases, the number of molecules of dye near the adsorbent also increases. Therefore, the amount of dye adsorption also increases. Since adsorption increases here as the temperature is increased, it

is an endothermic process. The experimental data showed that this process followed pseudo-second-order model. It was concluded from the energy of activation that this adsorption involves a physisorption mechanism. By utilizing an alkaline solution of a pH of 8–9, desorption of acidic dye from the nanocomposites becomes easier. From this study, it was suggested that polyaniline nanocomposites can be used as a potential adsorbent of acidic dyes from aqueous solutions.<sup>90</sup>

Cations such as  $\text{Na}^+$ ,  $\text{K}^+$ ,  $\text{Mg}^{2+}$ , and  $\text{Ca}^{2+}$  located on the natural zeolite of clinoptilolite were exchanged with anilinium cations which resulted in the formation of polyaniline/clinoptilolite (PANI/CPL) nanocomposite. This was used for the adsorption of methyl orange. Modified clinoptilolite has the properties of high adsorption capacity, low contact time, and low cost which makes it an efficient adsorbent of MO from aqueous solutions. PANI is in the doped state in PANI/CPL and positively charged  $\text{NH}^+$  is in the center of PANI which enables its interaction with methyl orange, an anionic dye. Also, the positive charge on methyl orange interacts with free nitrogen groups of PANI and increases its removal efficiency.<sup>91</sup>

PANI- $\text{Fe}_2\text{O}_3$  nanocomposite is synthesized successfully in situ by self-polymerization of aniline monomer. EDS technique, SEM, and XRD provide the elemental composition and morphological features of it. It is used for the removal of carcinogenic acid violet 19 dye. The adsorption rate increased by increasing the amount of adsorbent and decreased with increasing the concentration of dye. As with most of the other dye removal techniques, this technique also follows pseudo-second-order kinetics. Also, the Elvoich model has a good correlation with  $R^2$  values and this indicates that the process involved in this technique is chemisorption.<sup>92</sup>

The nanocomposite of hydrolyzed polyacrylamide grafted xanthan gum and incorporated nanosilica was synthesized by the saponification of grafted polyacrylamide and the in situ formation of  $\text{SiO}_2$  by a sol–gel reaction. This was developed for the efficient adsorption of MB and MV from the aqueous solution. Adsorbing process was in accordance with the pseudo-second-order kinetic model and Langmuir isotherm. This process was entropy driven and strongly depended on the point of zero charge (pzc) of the adsorbent. The high adsorption capacity is due to the H-bonding, dipole–dipole, and electrostatic interactions formed between the adsorbent and dye. This also has excellent regeneration capacity.<sup>93</sup>

Nowadays, natural polymers are used for dye removal, as they are biodegradable and nontoxic.<sup>94</sup> Chitosan is a biopolymer synthesized by deacetylation of chitin. Chitosan-based nanocomposites have high surface-to-volume

ratios and therefore they depict extraordinary reinforcement qualities, high electrical stiffness and strength. Compared with the conventional polymeric composites, they also exhibit enhanced barrier resistance, wear resistance, decreased permeability, and flame retardancy. As a result, chitosan nanocomposites have versatile applications. They are now used in medical, food, fiber, textile and automotive industries.<sup>95,96</sup>

Chitosan zinc oxide nanocomposite was used as an adsorbent of Reactive Black HN and Reactive Magenta HB from dyeing industry effluent in this study. Batch adsorption experiments of color removal were done using this nanocomposite. From the results, it was concluded that color adsorption increases and the turbidity decreases with the increase of the dosage of composite and more time of contact of solution. It was found that under optimum conditions about 99% of the dye could be removed.<sup>97</sup>

Chitosan/montmorillonite (CTS/MMT) nanocomposites were used to adsorb Congo Red (CR) dye. The experiments showed that CTS/MMT nanocomposites have higher adsorption capacity and flocculation ability than that of CTS and MMT individually. This process is dependent on the molar ratios of CTS and MMT. The adsorption kinetics of CTS/MMT followed pseudo-second-order and fitted the Langmuir monolayer model.<sup>98</sup>

Chitosan-g-poly (acrylic acid)/montmorillonite (CTS-g-PAA/MMT) nanocomposites were used to conduct batch adsorption experiments on the removal of methylene blue. The study showed that the weight ratio of AA to CTS and introducing a small amount of MMT improves the adsorbing capacity of CTS-g-PPA. This adsorption follows pseudo-second-order kinetics and is well-fitted with the Langmuir equation. The desorption studies showed that these nanocomposites have the ability for regeneration and can be reused after MB dye adsorption.<sup>99</sup>

#### **7.5.4 HYDROGEL/CLAY NANOCOMPOSITES AND OTHERS**

Hydrogel/clay nanocomposites are emphasized for their improved features like mechanical, rheological, thermal, and optical properties, as well as swelling and adsorption capacity. Consequently, a wide range of possible applications of them are explored.

Safranin-Tand Brilliant Cresyl Blue dyes were used to study the swelling and diffusion parameters of Acrylamide (AAm)-2-acrylamide-2-methylpropanesulfonic acid sodium salt (AMPSNa) hydrogel and AAm-AMPSNa/clay hydrogel nanocomposite. It was shown that AAm-AMPSNa/clay hydrogel

nanocomposite has enhanced swelling capacity when compared with AAm-AMPSNa hydrogel. The incorporation of clay into hydrogel increased the rate of adsorption.<sup>100</sup>

An efficient MB adsorbent was synthesized using starch/cellulose nanowhiskers hydrogel composite. On increasing the initial MB concentration, adsorption capacity increased. The negatively charged  $\text{COO}^-$  groups are generated when  $\text{pH} \geq 5$  interact with the positively charged MB, thereby helping in the efficient removal of MB. This biodegradable nanocomposite follows pseudo-second-order kinetics and it is based on chemisorption phenomenon. Desorption studies revealed that the adsorbent can be reused.<sup>101</sup>

Most of the good dye removal agents are photocatalysts. They release ROS on irradiation with UV. Now, some nanocomposites are discovered which can release ROS both in the presence and absence of light. Zinc oxide polypyrrole nanocomposite ( $\text{ZnO}_2/\text{ppy}$ ) degrades dyes in the dark through an advanced oxidation process which does not need additional reagents. It will remain stable even in the presence of UV light.<sup>102</sup>

## 7.6 SUMMARY

Dye removal is essential for the effective balancing of the ecosystem. The usage of nanocomposites depends upon varying factors, such as initial concentration of dye, adsorbent dosage, pH, temperature, contact time of solvent, and intraparticle diffusion. The advantages and disadvantages of nanocomposites depend upon the applications where it is used. Mechanical properties of the individual compounds are enhanced when they are modified into nanocomposite, but their viscosity will increase which limits their processing ability. Production of nanocomposites by spray pyrolysis helps in the effective preparation of homogenous, ultrafine, and spherical powders. But the large-scale production of uniform particles is not economical. Also, many parameters have to be characterized for a newly prepared nanoparticle which is money-consuming and relatively a complex program.<sup>103</sup> Some available data show that nanoclay modification of some polymers could reduce their impact performance. It could affect their further applications. Nanocomposites are used as gas barriers but they have dispersion difficulties. Even though it has some limitations, it excels in its wider applications. So, the novel properties of nanocomposites are giving a promising future for the technological world.

## KEYWORDS

- dye removal
- nanocomposites
- adsorptive removal
- photocatalytic degradation

## REFERENCES

1. Kamigaito, O. What Can Be Improved by Nanometer Composites. *J. Jpn Soc. Powder Powder Metall.* **1991**, 38, 315–321.
2. Biswas, M.; Ray, S. S. Recent Progress in Synthesis and Evaluation of Polymer-Montmorillonite Nanocomposites. In *New Polymerization Techniques and Synthetic Methodologies*; Springer: Berlin, Heidelberg, 2001; pp 167–221.
3. Meneghetti, P.; Qutubuddin, S. Synthesis, Thermal Properties and Applications of Polymer-Clay Nanocomposites. *Thermochim. Acta* **2006**, 442 (1–2), 74–77.
4. Cobut, A.; Sehaqui, H.; Berglund, L. A. Cellulose Nanocomposites by Melt Compounding of TEMPO-Treated Wood Fibers in Thermoplastic Starch Matrix. *BioResources* **2014**, 9 (2).
5. Magonov, S. N.; Reneker, D. H. Characterization of Polymer Surfaces with Atomic Force Microscopy. *Annu. Rev. Mater. Sci.* **1997**, 27 (1), 175–222.
6. Pandey, N.; Shukla, S. K.; Singh, N. B. Water Purification by Polymer Nanocomposites: An Overview. *Nanocomposites* **2017**, 3 (2), 47–66.
7. Li, L.; Duan, H.; Wang, X.; Luo, C. Fabrication of Novel Magnetic Nanocomposite with a Number of Adsorption Sites for the Removal of Dye. (1879–0003 (Electronic)).
8. Petronella, F.; Truppi, A.; Ingrosso, C.; Placido, T.; Striccoli, M.; Curri, M. L.; Agostiano, A.; Comparelli, R. Nanocomposite Materials for Photocatalytic Degradation of Pollutants. *Catal. Today* **2017**, 281, 85–100.
9. Peng, C.; Yao, B. H.; Li, J. X.; Niu, J. F. Preparation and Characterization of Conjugated Microspheres FeTCPP-SSA-TiO<sub>2</sub>. *Mater. Sci. Forum* **2016**, 852, 244–251.
10. Singh, S.; Barick, K. C.; Bahadur, D. Functional Oxide Nanomaterials and Nanocomposites for the Removal of Heavy Metals and Dyes. *Nanomater. Nanotechnol.* **2013**, 3, 20.
11. Sunandan, B.; Samir, K. P.; Joydeep, D. Nanostructured Zinc Oxide for Water Treatment. *Nanosci. Nanotechnol.-Asia* **2012**, 2 (2), 90–102.
12. Lazar, M. A.; Varghese, S.; Nair, S. S. Photocatalytic Water Treatment by Titanium Dioxide: Recent Updates. *Catalysts* **2012**, 2 (4), 572–601.
13. Di Mauro, A.; Cantarella, M.; Nicotra, G.; Pellegrino, G.; Gulino, A.; Brundo, M. V.; Privitera, V.; Impellizzeri, G. Novel Synthesis of ZnO/PMMA Nanocomposites for Photocatalytic Applications. *Sci. Rep.* **2017**, 7, 40895.
14. Brillas, E.; Martínez-Huitle, C. A. Decontamination of Wastewaters Containing Synthetic Organic Dyes by Electrochemical Methods: An Updated Review. *Appl. Catal. B Environ.* **2015**, 166–167, 603–643.

15. Han, C.; Lalley, J.; Namboodiri, D.; Cromer, K.; Nadagouda, M. N. Titanium Dioxide-Based Antibacterial Surfaces for Water Treatment. *Curr. Opin. Chem. Eng.* **2016**, *11*, 46–51.
16. Sankar, M. U.; Aigal, S.; Maliyekkal, S. M.; Chaudhary, A.; Anshup; Kumar, A. A.; Chaudhari, K.; Pradeep, T. Biopolymer-Reinforced Synthetic Granular Nanocomposites for Affordable Point-of-Use Water Purification. *Proc. Natl. Acad. Sci. USA* **2013**, *110* (21), 8459–8464.
17. Damodar, R. A.; You, S. J.; Chou, H. H. Study the Self Cleaning, Antibacterial and Photocatalytic Properties of TiO<sub>2</sub> Entrapped PVDF Membranes. *J. Hazard Mater.* **2009**, *172* (2–3), 1321–8.
18. Mittal, G.; Dhand, V.; Rhee, K. Y.; Park, S.-J.; Lee, W. R. A Review on Carbon Nanotubes and Graphene as Fillers in Reinforced Polymer Nanocomposites. *J. Ind. Eng. Chem.* **2015**, *21*, 11–25.
19. Khare, P.; Yadav, A.; Ramkumar, J.; Verma, N. Microchannel-Embedded Metal–Carbon–Polymer Nanocomposite as a Novel Support for Chitosan for Efficient Removal of Hexavalent Chromium from Water Under Dynamic Conditions. *Chem. Eng. J.* **2016**, *293*, 44–54.
20. Bai, Y.; Xu, T.; Zhang, X. Graphene-Based Biosensors for Detection of Biomarkers. *Micromachines* **2020**, *11* (1).
21. Cao, S.; Zhang, L.; Chai, Y.; Yuan, R.; Yuan, R. An Integrated Sensing System for Detection of Cholesterol Based on TiO<sub>2</sub>-Graphene-Pt-Pd Hybrid Nanocomposites (1873–4235 (Electronic)).
22. Chen, X.; Jia, X.; Han, J.; Ma, J.; Ma, Z. Electrochemical Immunosensor for Simultaneous Detection of Multiplex Cancer Biomarkers Based on Graphene Nanocomposites (1873–4235 (Electronic)).
23. Jia, X.; Liu, Z.; Liu, N.; Ma, Z. A Label-Free Immunosensor Based on Graphene Nanocomposites for Simultaneous Multiplexed Electrochemical Determination of Tumor Markers (1873–4235 (Electronic)).
24. Manivel, P.; Dhakshnamoorthy, M.; Balamurugan, A.; Ponpandian, N.; Mangalaraj, D.; Viswanathan, C. Conducting Polyaniline-Graphene Oxide Fibrous Nanocomposites: Preparation, Characterization and Simultaneous Electrochemical Detection of Ascorbic Acid, Dopamine and Uric Acid. *RSC Adv.* **2013**, *3* (34), 14428–14437.
25. Qi, M.; Zhang, Y.; Cao, C.; Lu, Y.; Liu, G. Increased Sensitivity of Extracellular Glucose Monitoring Based on AuNP Decorated GO Nanocomposites. *RSC Adv.* **2016**, *6* (45), 39180–39187.
26. Sangamithirai, D.; Narayanan, V.; Muthuraaman, B.; Stephen, A. Investigations on the Performance of Poly(O-Anisidine)/Graphene Nanocomposites for the Electrochemical Detection of NADH (1873–0191 (Electronic)).
27. Shan, C.; Yang, H.; Han, D.; Zhang, Q.; Ivaska, A.; Niu, L. Graphene/AuNPs/Chitosan Nanocomposites Film for Glucose Biosensing (1873–4235 (Electronic)).
28. Shukla, S.; Haldorai, Y.; Bajpai, V. K.; Rengaraj, A.; Hwang, S. K.; Song, X.; Kim, M.; Huh, Y. S.; Han, Y. K. Electrochemical Coupled Immunosensing Platform Based on Graphene Oxide/Gold Nanocomposite for Sensitive Detection of Cronobacter Sakazakii in Powdered Infant Formula (1873–4235 (Electronic)).
29. Sun, C. L.; Lee, Hh.; Yang, J.-M.; Wu, C.-C. The Simultaneous Electrochemical Detection of Ascorbic Acid, Dopamine, and Uric Acid Using Graphene/Size-Selected Pt Nanocomposites (1873–4235 (Electronic)).



30. Zhang, H.; Ba, S.; Yang, Z.; Wang, T.; Lee, J. Y.; Li, T.; Shao, F. Graphene Quantum Dot-Based Nanocomposites for Diagnosing Cancer Biomarker APE1 in Living Cells. *ACS Appl. Mater. Interfaces* **2020**, *12* (12), 13634–13643.
31. Zhang, Y.; Bai X.; Wang, X.; Shiu, K.-K.; Zhu, Y.; Jiang, H. Highly Sensitive Graphene-Pt Nanocomposites Amperometric Biosensor and Its Application in Living Cell H<sub>2</sub>O<sub>2</sub> Detection (1520–6882 (Electronic)).
32. Krishnan, S. K.; Singh, E.; Singh, P.; Meyyappan, M.; Nalwa, H. S. A Review on Graphene-Based Nanocomposites for Electrochemical and Fluorescent Biosensors. *RSC Adv.* **2019**, *9* (16), 8778–8881.
33. Li, C.; Chen, G.; Zhang, Y.; Wu, F.; Wang, Q. Advanced Fluorescence Imaging Technology in the Near-Infrared-II Window for Biomedical Applications. *J. Am. Chem. Soc.* **2020**, *142* (35), 14789–14804.
34. Pathania, D.; Kumari, S. Nanocomposites Based on Biopolymer for Biomedical and Antibacterial Applications. In *Adapting 2D Nanomaterials for Advanced Applications*, Vol. 1353; American Chemical Society, 2020; pp 375–391.
35. Shen, H.; Tan, J.; Saltzman, W. M. Surface-Mediated Gene Transfer from Nanocomposites of Controlled Texture. *Nat. Mater.* **2004**, *3* (8), 569–574.
36. Wang, R.; Gu, X.; Li, Q.; Gao, J.; Shi, B.; Xu, G.; Zhu, T.; Tian, H.; Zhao, C. Aggregation Enhanced Responsiveness of Rationally Designed Probes to Hydrogen Sulfide for Targeted Cancer Imaging. *J. Am. Chem. Soc.* **2020**, *142* (35), 15084–15090.
37. Ashrafizadeh, M.; Ahmadi, Z.; Mohamadi, N.; Zarrabi, A.; Abasi, S.; Dehghannoudeh, G.; Tamaddondoust, R. N.; Khanbabaei, H.; Mohammadinejad, R.; Thakur, V. K. Chitosan-Based Advanced Materials for Docetaxel and Paclitaxel Delivery: Recent Advances and Future Directions in Cancer Theranostics (1879–0003 (Electronic)).
38. Ramanathan, T.; Abdala Aa.; Stankovich, S.; Dikin, D. A.; Herrera-Alonso, M.; Piner, R. D.; Adamson, D. H.; Schniepp, H. C.; Chen, X.; Ruoff, R. S.; Nguyen, S. T.; Aksay, I. A.; Prud'Homme, R. K.; Brinson, L. C. Functionalized Graphene Sheets for Polymer Nanocomposites (1748–3395 (Electronic)).
39. Ates, B.; Koytepe, S.; Ulu, A.; Gurses, C.; Thakur, V. K. Chemistry, Structures, and Advanced Applications of Nanocomposites from Biorenewable Resources. *Chem. Rev.* **2020**, *120* (17), 9304–9362.
40. Avella, M.; De Vlieger, J. J.; Errico, M. E.; Fischer, S.; Vacca, P.; Volpe, M. G. Biodegradable Starch/Clay Nanocomposite Films for Food Packaging Applications. *Food Chem.* **2005**, *93* (3), 467–474.
41. Azeredo, H. M. C. d. Nanocomposites for Food Packaging Applications. *Food Res. Int.* **2009**, *42* (9), 1240–1253.
42. Ray, S.; Quek, S. Y.; Easteal, A.; Chen, X. D. The Potential Use of Polymer-Clay Nanocomposites in Food Packaging. *Int. J. Food Eng.* **2006**, *2* (4).
43. Sarfraz, J.; Gulin-Sarfraz, T.; Nilsen-Nygaard, J.; Pettersen, M. K. Nanocomposites for Food Packaging Applications: An Overview. LID—10.3390/nano11010010 [doi] LID—10 (2079–4991 (Print)).
44. Sorrentino, A.; Gorrasi, G.; Vittoria, V. Potential Perspectives of Bio-Nanocomposites for Food Packaging Applications. *Trends Food Sci. Technol.* **2007**, *18*, 84–95.
45. Duncan, T. V. Applications of Nanotechnology in Food Packaging and Food Safety: Barrier Materials, Antimicrobials and Sensors (1095–7103 (Electronic)).
46. Siwal, S. S.; Zhang, Q.; Devi, N.; Thakur, V. K. Carbon-Based Polymer Nanocomposite for High-Performance Energy Storage Applications. *Polymers* **2020**, *12* (3).

47. Yang, D. Application of Nanocomposites for Supercapacitors: Characteristics and Properties. 2012.
48. Yang, S.; Sun, L.; An, X.; Qian, X. Construction of Flexible Electrodes Based on Ternary Polypyrrole@Cobalt Oxyhydroxide/Cellulose Fiber Composite for Supercapacitor (1879–1344 (Electronic)).
49. Yi, T.-F.; Pan, J.-J.; Wei, T.-T.; Li, Y.; Cao, G. NiCo<sub>2</sub>S<sub>4</sub>-Based Nanocomposites for Energy Storage in Supercapacitors and Batteries. *Nano Today* **2020**, *33*, 100894.
50. Yi, T.-F.; Sari, H. M. K.; Li, X.; Wang, F.; Zhu, Y.-R.; Hu, J.; Zhang, J.; Li, X. A Review of Niobium Oxides Based Nanocomposites for Lithium-Ion Batteries, Sodium-Ion Batteries and Supercapacitors. *Nano Energy* **2021**, *85*, 105955.
51. Yu, L.; Liu, J.; He, S.; Huang, C.; Gong, Z.; Gan, L.; Long, M. N-doped rGO/C@Si Composites Using Sustainable Chitosan as the Carbon Source for Lithium-Ion Batteries. *Appl. Surf. Sci.* **2020**, *501*, 144136.
52. Saliba, P. A.; Mansur, A. A. P.; Mansur, H. S. Advanced Nanocomposite Coatings of Fusion Bonded Epoxy Reinforced with Amino-Functionalized Nanoparticles for Applications in Underwater Oil Pipelines. *J. Nanomater.* **2016**, *2016*, 7281726.
53. Savino, V.; Fallatah, G.; Mehdi, M. Applications of Nanocomposite Materials in the Oil and Gas Industry. *Adv. Mater. Res.* **2009**, *83–86*, 771–776.
54. Wang, X.; Tang, F.; Qi, X.; Lin, Z.; Battocchi, D.; Chen, X. Enhanced Protective Coatings Based on Nanoparticle fullerene C60 for Oil & Gas Pipeline Corrosion Mitigation. *Nanomaterials* **2019**, *9* (10).
55. Chandra, A. K.; Kumar, N. R. Polymer Nanocomposites for Automobile Engineering Applications. In *Properties and Applications of Polymer Nanocomposites: Clay and Carbon Based Polymer Nanocomposites*; Tripathy, D. K., Sahoo, B. P., Eds.; Springer: Berlin, Heidelberg, 2017; pp 139–172.
56. Veličković Gajević, S.; Stojanovic, B.; Ivanovic, L.; Miladinović, S.; Milojević, S. *Application of Nanocomposites in the Automotive Industry*; 2018.
57. Amin, M. T.; Alazba, A. A.; Manzoor, U. A Review of Removal of Pollutants from Water/Wastewater Using Different Types of Nanomaterials. *Adv. Mater. Sci. Eng.* **2014**, *2014*, 825910.
58. Pal, P. Chapter 6: Industry-Specific Water Treatment: Case Studies. In *Industrial Water Treatment Process Technology*; Pal, P. Ed.; Butterworth-Heinemann, 2017; pp 243–511.
59. Unuabonah, E. I.; Taubert, A. Clay–Polymer Nanocomposites (CPNs): Adsorbents of the Future for Water Treatment. *Appl. Clay Sci.* **2014**, *99*, 83–92.
60. Zhang, S.; Sun, D.; Fu, Y. Q.; Du, H. Recent Advances of Superhard Nanocomposite Coatings. *Surf. Coat. Technol.* **2003**, *167*, 113–119.
61. Khataee, A.; Sheydaei, M.; Hassani, A.; Taseidifar, M.; Karaca, S. Sonocatalytic Removal of an Organic Dye Using TiO<sub>2</sub>/Montmorillonite Nanocomposite. *Ultrason. Sonochem.* **2015**, *22*, 404–11.
62. V. VENKATESWARAN, V. T. P. a. P. B. Removal of Malachite Green by Stishovite-TiO<sub>2</sub> Nanocomposite and Stishovite Clay—A Comparative Study. *Chem. Sci. Trans.* **2013**, *2* (3), 771–780
63. Yu, Z.; Li, S.; Zhang, P.; Feng, Y.; Liu, X. Polymer-Derived Mesoporous Ni/SiOC(H) Ceramic Nanocomposites for Efficient Removal of Acid Fuchsin. *Ceram. Int.* **2017**, *43* (5), 4520–4526.
64. Santhi et al. Removal of Malachite Green Dyes By Adsorption onto Activated Carbon—MnO<sub>2</sub>—Nanocomposite—Kinetic Study and Equilibrium Isotherm Analyses. *IOSR J. Appl. Chem.* **2015**, *8* (4), 33–41.

65. Veerakumar, P.; Chen, S. M.; Madhu, R.; Veeramani, V.; Hung, C. T.; Liu, S. B. Nickel Nanoparticle-Decorated Porous Carbons for Highly Active Catalytic Reduction of Organic Dyes and Sensitive Detection of Hg(II) Ions. *ACS Appl. Mater. Interfaces* **2015**, 7 (44), 24810–21.
66. Konicki, W.; Siber, D.; Narkiewicz, U. Removal of Rhodamine B from Aqueous Solution by ZnFe<sub>2</sub>O<sub>4</sub> Nanocomposite with Magnetic Separation Performance. *Polish J. Chem. Technol.* **2017**, 19.
67. Kale, R. D.; Kane, P. B. Colour Removal Using Nanoparticles. *Text. Cloth. Sustain.* **2016**, 2 (1), 4.
68. Bonetto, L. R.; Ferrarini, F.; de Marco, C.; Crespo, J. S.; Guégan, R.; Giovanela, M. Removal of Methyl Violet 2B Dye from Aqueous Solution Using a Magnetic Composite as an Adsorbent. *J. Water Process Eng.* **2015**, 6 (Complete), 11–20.
69. Alqadami, A. A.; Naushad, M.; Abdalla, M. A.; Khan, M. R.; Alothman, Z. A. Adsorptive Removal of Toxic Dye Using Fe<sub>3</sub>O<sub>4</sub>-TSC Nanocomposite: Equilibrium, Kinetic, and Thermodynamic Studies. *J. Chem. Eng. Data* **2016**, 61 (11), 3806–3813.
70. Zhu, Y.; Murali, S.; Cai, W.; Li, X.; Suk, J. W.; Potts, J. R.; Ruoff, R. S. Graphene and Graphene Oxide: Synthesis, Properties, and Applications. *Adv. Mater.* **2010**, 22 (35), 3906–24.
71. Tran, H. V.; Bui, L. T.; Dinh, T. T.; Le, D. H.; Huynh, C. D.; Trinh, A. X. Graphene Oxide/Fe<sub>3</sub>O<sub>4</sub>/Chitosan Nanocomposite: A Recoverable and RECYCLABLE ADSORBENT for Organic Dyes Removal: Application to Methylene Blue. *Mater. Res. Express* **2017**, 4 (3), 035701.
72. Sun, H.; Cao, L.; Lu, L. Magnetite/Reduced Graphene Oxide Nanocomposites: One Step Solvothermal Synthesis and Use as a Novel Platform for Removal of Dye Pollutants. *Nano Res.* **2011**, 4 (6), 550–562.
73. Deng, J.-H.; Zhang, X.-R.; Zeng, G.-M.; Gong, J.-L.; Niu, Q.-Y.; Liang, J. Simultaneous Removal of Cd(II) and Ionic Dyes from Aqueous Solution Using Magnetic Graphene Oxide Nanocomposite as an Adsorbent. *Chem. Eng. J.* **2013**, 226, 189–200.
74. E. Khalil, T.; Elhusseiny, A.; El-Dissouky, A.; Ibrahim, N. Functionalized Chitosan Nanocomposites for Removal of Toxic Cr (VI) from Aqueous Solution. *React. Funct. Polym.* **2019**, 146, 104407.
75. Hosseini, S. A.; Babaei, S. Graphene Oxide/Zinc Oxide (GO/ZnO) Nanocomposite as a Superior Photocatalyst for Degradation of Methylene Blue (MB)-Process Modeling by Response Surface Methodology (RSM). *J. Braz. Chem. Soc.* **2016**.
76. Kaur, K.; Jindal, R. Synergistic Effect of Organic-Inorganic Hybrid Nanocomposite Ion Exchanger on Photocatalytic Degradation of Rhodamine-B Dye and Heavy Metal Ion Removal from Industrial Effluents. *J. Environ. Chem. Eng.* **2018**, 6 (6), 7091–7101.
77. Wang, C.; Feng, C.; Gao, Y.; Ma, X.; Wu, Q.; Wang, Z. Preparation of a Graphene-Based Magnetic Nanocomposite for the Removal of an Organic Dye from Aqueous Solution. *Chem. Eng. J.* **2011**, 173 (1), 92–97.
78. Shahabuddin, S.; Sarih, N. M.; Afzal Kamboh, M.; Rashidi Nodeh, H.; Mohamad, S. Synthesis of Polyaniline-Coated Graphene Oxide@SrTiO<sub>3</sub> Nanocube Nanocomposites for Enhanced Removal of Carcinogenic Dyes from Aqueous Solution. *Polym.* **2016**, 8 (9).
79. Gong, J. L.; Wang, B.; Zeng, G. M.; Yang, C. P.; Niu, C. G.; Niu, Q. Y.; Zhou, W. J.; Liang, Y. Removal of Cationic Dyes from Aqueous Solution Using Magnetic Multi-Wall Carbon Nanotube Nanocomposite as Adsorbent. *J. Hazard. Mater.* **2009**, 164 (2–3), 1517–22.

80. Makarchuk, O. V.; Dontsova, T. A.; Astrelin, I. M. Magnetic Nanocomposites as Efficient Sorption Materials for Removing Dyes from Aqueous Solutions. *Nanoscale Res. Lett.* **2016**, *11* (1), 161.
81. Yang, N.; Zhu, S.; Zhang, D.; Xu, S. Synthesis and Properties of Magnetic Fe<sub>3</sub>O<sub>4</sub>-Activated Carbon Nanocomposite Particles for Dye Removal. *Mater. Lett.* **2008**, *62* (4), 645–647.
82. Hashem, F. Adsorption of Methylene Blue from Aqueous Solutions using Fe<sub>3</sub>O<sub>4</sub>/Bentonite Nanocomposite. *Hydrol. Curr. Res.* **2012**, *3*, 1–6.
83. Farrokhi, M.; Hosseini, S.-C.; Yang, J.-K.; Shirzad-Siboni, M. Application of ZnO–Fe<sub>3</sub>O<sub>4</sub> Nanocomposite on the Removal of Azo Dye from Aqueous Solutions: Kinetics and Equilibrium Studies. *Water, Air, Soil Pollut.* **2014**, *225* (9).
84. Alzahrani, E. Gum Arabic-Coated Magnetic Nanoparticles For Methylene Blue Removal. *Int. J. Innov. Res. Sci. Eng. Technol.* **2014**, *03* (08), 15118–15129.
85. Riedel, R.; Seher, M.; Mayer, J.; Szabó, D. V. Polymer-Derived Si-Based Bulk Ceramics, Part I: Preparation, Processing and Properties. *J. Eur. Ceram. Soc.* **1995**, *15* (8), 703–715.
86. Viart, N.; Richard-Plouet, M.; Muller, D.; Pourroy, G. Synthesis and characterization of Co/ZnO Nanocomposites: Towards New Perspectives Offered by Metal/Piezoelectric Composite Materials. *Thin Solid Films* **2003**, *437* (1), 1–9.
87. Pourjavadi, A.; Abedin-Moghanaki, A.; Tavakoli, A. Efficient Removal of Cationic Dyes Using a New Magnetic Nanocomposite Based on Starch-g-Poly(Vinylalcohol) and Functionalized with Sulfate Groups. *RSC Adv.* **2016**, *6* (44), 38042–38051.
88. Kumar, A.; Sharma, G.; Naushad, M.; Singh, P.; Kalia, S. Polyacrylamide/Ni<sub>0.02</sub>Zn<sub>0.98</sub>O Nanocomposite with High Solar Light Photocatalytic Activity and Efficient Adsorption Capacity for Toxic Dye Removal. *Ind. Eng. Chem. Res.* **2014**, *53* (40), 15549–15560.
89. Pouretedal, H. R.; Norozi, A.; Keshavarz, M. H.; Semnani, A. Nanoparticles of Zinc Sulfide Doped with Manganese, Nickel and Copper as Nanophotocatalyst in the Degradation of Organic Dyes. *J. Hazard Mater.* **2009**, *162* (2–3), 674–81.
90. Baseri, R.; Palanisamy, P. N.; Sivakumar, P. Application of Polyaniline Nano Composite for the Adsorption of Acid Dye from Aqueous Solutions. *J. Chem.* **2012**, *9*.
91. Zaremotlagh, S.; Hezarkhani, A. Removal of Textile Dyes from Aqueous Solution by Conducting Polymer Modified Clinoptilolite. *Environ. Earth Sci.* **2013**, *71* (7), 2999–3006.
92. Patil, M.; Shrivastava, V. Adsorption Removal of Carcinogenic Acid Violet19 Dye from Aqueous Solution by Polyaniline-Fe<sub>2</sub>O<sub>3</sub> Magnetic Nano-Composite. *J. Mater. Environ. Sci.* **2015**, *6*, 11–21.
93. Ghorai, S.; Sarkar, A.; Raoufi, M.; Panda, A. B.; Schönherr, H.; Pal, S. Enhanced Removal of Methylene Blue and Methyl Violet Dyes from Aqueous Solution Using a Nanocomposite of Hydrolyzed Polyacrylamide Grafted Xanthan Gum and Incorporated Nanosilica. *ACS Appl. Mater. Interfaces* **2014**, *6* (7), 4766–4777.
94. Chang, M. Y.; Juang, R. S. Adsorption of Tannic Acid, Humic Acid, and Dyes from Water Using the Composite of Chitosan and Activated Clay. *J. Colloid Interface Sci.* **2004**, *278* (1), 18–25.
95. Yadav, T.; Saxena, P.; Srivastava, A. K.; Yadav, R.; Prasad, R.; Pruthi, V. Potential Applications of Chitosan Nanocomposites: Recent Trends and Challenges, 2019.
96. Vieira, R. S.; Beppu, M. M. Interaction of Natural and Crosslinked Chitosan Membranes with Hg(II) Ions. *Colloids Surfaces A* **2006**, *279* (1–3), 196–207.
97. Sabrin A, A. A. Textile Dye Removal from Wastewater Effluents Using Chitosan-ZnO Nanocomposite. *J. Text. Sci. Eng.* **2015**, *05* (03).

98. Wang, L.; Wang, A. Adsorption Characteristics of Congo Red onto the Chitosan/Montmorillonite Nanocomposite. *J. Hazard. Mater.* **2007**, *147* (3), 979–985.
99. Wang, L.; Zhang, J.; Wang, A. Removal of Methylene Blue from Aqueous Solution Using Chitosan-g-Poly(Acrylic Acid)/Montmorillonite Superadsorbent Nanocomposite. *Colloids Surfaces A* **2008**, *322* (1), 47–53.
100. Kaşgöz, H.; Durmus, A. Dye Removal by a Novel Hydrogel-Clay Nanocomposite with Enhanced Swelling Properties. *Polym. Adv. Technol.* **2008**, *19* (7), 838–845.
101. Gomes, R. F.; de Azevedo, A. C.; Pereira, A. G.; Muniz, E. C.; Fajardo, A. R.; Rodrigues, F. H. Fast Dye Removal from Water by Starch-Based Nanocomposites. *J. Colloid Interface Sci.* **2015**, *454*, 200–209.
102. Prasanna, V. L.; Rajagopalan, V. A New Synergetic Nanocomposite for Dye Degradation in Dark and Light. *Scientific Reports* [Online], 2016, p. 38606. PubMed. <http://europepmc.org/abstract/MED/27929084>; <https://doi.org/10.1038/srep38606>; <https://europepmc.org/articles/PMC5144144>; <https://europepmc.org/articles/PMC5144144?pdf=render> (accessed 2016/12//).
103. Pandya, S. Nanocomposites and It's Application—Review. *Int. J. Pharma. Sci. Res.* **2013**, *4* (1), 19–28.

## CHAPTER 8

---

# Bionanomaterials: Significance, Classification, and Application

NEETHA JOHN, ABHIJITH KRISHNA, and JEFFY JOJI

*CIPET-Central Institute of Petrochemical Engineering and Technology,  
Udyogamandal P.O., Kochi, Kerala, India*

---

### ABSTRACT

Today, everything is about miniaturization. There was a time when thousands of pages were printed out, clipped together and made into files for future references. But today, a huge amount of data can be so small that we may not be able to see with our naked eyes. Yes! This is the age of nanomaterials. When these materials are composed partially or completely of biological molecules or in other cases used for biological applications, they become bionanomaterials. Bionanomaterials always have been a kickstart for different breakthroughs in a wide variety of areas. They are now being highly commercialized that we are just a step behind to a life where we use nanomaterials everyday even for our food. In this review, we go through the basic idea of bionanomaterials. We start with different classification of bionanomaterials followed by the major application areas. Toward the end, we point out a few remarkable aspects which give the reader an idea of the significance of the word “Bio-nano” in today’s world. Finally, the review ends on a good note on the possibilities of growth and advancements in this field.

### 8.1 INTRODUCTION

The present trend to reduce the dimensions of materials originated from our need to access new materialistic and performance properties that only

---

Functional Nanocomposites and Their Applications. Dhanya K. R., Sanal P. S., Sabu Thomas, & Nandakumar Kalarikkal (Eds.)

© 2025 Apple Academic Press, Inc. Co-published with CRC Press (Taylor & Francis)

unlock when we look at molecules in the nano range.<sup>1</sup> When compared with other tiny or macroscopic structures, nanoscale materials can have unique mechanical, electrical, and optical characteristics.<sup>2</sup> The increase in surface area when the size of the molecule decreases also plays an important role in improving properties like surface morphology and composition, which are two of the most important properties of NP's because they decrease the coordination number and control the reactivity of the NP's up to a certain extent, that is, it increases the surface reactivity compared with their bulk counterparts. Another reason for the high surface reactivity is due to the deviation of NP's from Gibbs-Thomson relation which describes that the chemical energy of an atom in nanophase exceeds its potential compared with the same atom present in the bulk state.<sup>3</sup> Nanotechnology deals with molecules and interactions in the range of 1–100 nm and gives us an idea about the arrangement or organization of almost all natural and manmade nanomaterials in the nano range to form large molecules.<sup>4</sup>

Nanomaterials are used in a wide range of sectors, from medical and cosmetics to environmental preservation and air purification, mainly because of their capacity to produce materials in a precise way to perform a specified function.<sup>5</sup> Nanoparticles or nanomaterials can be mainly classified into two types: organic and inorganic. Carbon nanoparticles like fullerenes are examples of organic nanoparticles, whereas inorganic nanoparticles consist of noble metal and magnetic nanoparticles.<sup>6</sup> Nanomaterials can exist naturally, be formed as by-products of combustion processes, or be engineered specifically to fulfill a certain job. The physical and chemical characteristics of these materials may differ from those of their bulk-form equivalents. Of the many signs of progress in the field of nanomaterials, the advancements in the area of functional nanomaterials, especially bionanomaterials are of huge impact in the current era of science and technology.<sup>6</sup> According to John F Honek Bionanomaterials can be defined as molecular materials made up largely or entirely of biological molecules, such as antibodies, proteins/enzymes, DNA, RNA, lipids, oligosaccharides, viruses, cells, and leading to molecular structures with a nanoscale dimension.<sup>7</sup>

A nanometer is equal to one billionth of a meter ( $10^{-9}\text{m}$ ). To put things into perspective, a single sheet of paper is around 100,000 nm thick and a single human strand of DNA is 2.5 nm in diameters.<sup>2,8</sup> Table 8.1 presents some of the examples of commonly used nanoparticles.<sup>9</sup> Physical, mechanical, and chemical approaches are normally used to synthesize nanoparticles.<sup>10,11</sup> These procedures are extremely expensive and some require the use of dangerous substances. Traditionally, nanoparticles are mainly prepared by

two methods: Bottoms up approach (BUA)<sup>12,13</sup> and Top-down approach (TDA).<sup>14,15</sup> In BUA, a chemical reaction takes place where the reactants are mixed and a resultant solid phase/crystal is formed with a diameter of 1–2 nm or smaller. This step is called nucleation. These tiny crystals develop into bigger crystals through a thermodynamically favorable process. Electrostatic repulsion or steric stabilization, or both, can explain the colloidal stability. In the case of TDA, the bulk material is broken down into nanometric structures or particles. Nanometer-sized particles have been synthesized using top-down synthesis techniques, which are in a sense an extension of the techniques already in use for the preparation of micron-sized particles. But both of these methods have some major disadvantages, material interactions that may lead to toxicological consequences might emerge from changes in the physicochemical and structural characteristics of nanoscale materials as a result of their size reduction. As a result, the need for another biosynthesis method for the preparation of NP rose out of necessity to take care of these negative factors.<sup>16</sup> Biosynthesis/biogenesis is a kind of BUA in which the primary reaction is reduction/oxidation. As part of current and realistic biosynthetic methods, biological sources, such as algae, bacteria, fungus, viruses, and plant components can catalyze particular processes.<sup>17,18</sup>

**TABLE 8.1** Various Types of Organic and Inorganic Nanoparticles.

	Types	Examples	Size range (nm)
Inorganic compounds	Metallic	Gold and silver particles	<50
	Magnetic	Superparamagnetic iron oxide particles	5–100
	Nanoshells	Dielectric silica core in a thin gold metal shell	10–300
	Ceramics	Inorganic porous biocompatible materials	<100
Organic compounds	Carbon tubes	Cylindrical graphite sheets	1.5–5000
	Quantum dots	Semiconductor crystals with a cadmium core and metal shell	<10
	Dendrimers	Highly branched macromolecules	5–20
	Liposomes	Phospholipids	5–100
	Polymers	Colloidal particles	10–1000

A new frontier in the fields of life science and material science is emerging with bionanomaterial research during the past several years, with DNA, RNA, and peptides playing an important role in bionanomaterial design for the



basic advancement of biotechnology and nanomaterials.<sup>19</sup> Bionanomaterial research is a deeply interdisciplinary field in which chemistry, immunology, materials science, physics, biochemistry, engineering, and mathematics plays some very major roles.<sup>7</sup> Nanocomposite materials, nanoscale biomimetic materials, nano-biochip materials, nanomotors, nanodrug delivery systems, nanobiosensors, and interface biomaterials offer great potential for industrial, defense, and clinical medical applications.<sup>20</sup> Bionanomaterials rely heavily on biomolecular components. Examples include polysaccharides, such as cellulose, chitosan, and chitin which are plentiful in nature and can be utilized for drug administration, cell-encapsulating biomaterials, scaffolding tissue engineering, and regenerative medicine. They are also biodegradable, biocompatible, and very cheap. Different carbon-based NP's are also being used as novel biomaterials for many different applications, such as drug delivery, scaffold, transcellular transportation etc.<sup>21</sup> Plant proteins like zein, soy, and wheat proteins, clay, keratin, etc. are some of the other biomaterials used for the preparation of bionanomaterials.

## **8.2 CLASSIFICATION OF BIONANOMATERIALS**

### **8.2.1 METAL/METAL OXIDE NANOPARTICLE**

#### **8.2.1.1 GOLD NANOPARTICLES**

Gold was the second metal discovered along with silver early in 2500 BC. "Gold is where you find it" as the saying goes, numerous properties of gold has made it suitable for multiple application. As early as its discovery, it was a cure for conditions from mental diseases to contagious diseases like leprosy. Gold nanoparticles are usually synthesized as nanosphere,<sup>22</sup> nanostars,<sup>23</sup> nanorods, nanoshells, bipyramids,<sup>24</sup> nanocubes<sup>25</sup> or even nanonecklaces.<sup>26</sup> All these reported works prove its ability to change the shape during synthesis which in turn helps in tuning the optical properties.<sup>27</sup> Today, the applications of gold nanoparticle include but not confined to drug delivery, sensing, cancer therapy, diagnostics, electronic chipping, etc. properties, such as less toxicity, biocompatibility, and its small dimension makes it an excellent choice for biomedical application.<sup>28</sup> For instance, in 2018, yang et al. reported their work on functionalized gold nanoparticles with an anticancer drug and peptide sequence, and the nanoparticle drug complex was found to decrease the survival rate of the human breast cancer cells.<sup>29</sup>

### 8.2.1.2 SILVER NANOPARTICLES

Just like Gold nanoparticles, colloidal silver also has a similar story since its successful synthesis in M.C. Lea in 1889.<sup>30</sup> Silver nanoparticles are known for its excellent optical properties, such as surface plasmon resonance, electrical properties, such as high conductivity,<sup>31</sup> excellent mechanical strength<sup>32</sup> and also its way of synthesizing to extract from plants.<sup>33</sup> Krithiga et al. reported the green synthesis of silver nanoparticles and its morphological studies were done. Silver particles are always recognized for their antimicrobial and anti-inflammatory properties. *Clitoria ternatea* and *Solanum nigrum* leaves were extracted and precipitated with silver nitrate ( $\text{AgNO}_3$ ) to prepare silver nanoparticles. The results showed excellent antibacterial effects against common nosocomial pathogens.<sup>34</sup> Similarly, silver nanoparticles were extracted from various plants like *Melia azadirachta* for wound healing; it has antidiabetic and antioxidant properties.<sup>35</sup> Apart from the biomedical field, other areas of application include cosmetic production, textile industry, optical devices, etc.

### 8.2.1.3 TITANIUM DIOXIDE

Not only metals but metal oxides are also included in the category of bionanomaterials. Metal oxides like titanium dioxide are exploited because of their photolytic properties and their industrial application thus increasing its use in sunscreen, cosmetic products, etc., other metal oxide nanoparticles include iron oxide, cerium dioxide, chromium dioxide, molybdenum trioxide, bismuthtrioxide, and binary oxides (e.g., indium-tin oxide)<sup>36</sup>

$\text{TiO}_2$  is long known for its nontoxic nature, low cost, and chemical stability. In addition to the long list of biomedical applications,  $\text{TiO}_2$  is also used in toothpaste, whiteners, food supplements, food colors, etc. they are also reported to be useful or reduction of water pollutants.<sup>37</sup> Usually,  $\text{TiO}_2$  nanoparticles are synthesized by chemical vapor deposition, microemulsion, sol-gel method<sup>38</sup> but due to the increasing toxicity of the material used for the synthesis the method of synthesis is being switched over to green synthesis where it's extracted from plants.<sup>39</sup>

## 8.2.2 POLYMERIC BIONANOPARTICLES AND NANOCOMPOSITES

Researchers undertaken on polymeric bionanomaterials are numerous due to their easy processibility, biocompatibility, less toxicity, and less cost.

Depending on the nature, it can be natural and hydrophilic, such as polysaccharides (starch, alginate, chitosan, etc.) or protein (collagen, silk, albumin, lipoprotein, etc.). they can also be synthetic and hydrophobic materials, such as polylactic acid, polyglycolic acid, poly( $\epsilon$ -caprolactone), etc. the polymers like polylactic acid have high advantage due to its chiral nature where their stereo complexity can be adjusted to increase the metallic and thermal properties.<sup>40</sup> Calciumphosphate fillers like hydroxyapatite are incorporated to increase its apatite activity for bone regeneration activities. They are also widely used in drug delivery, scaffold, wound healing, etc.<sup>41,42</sup>

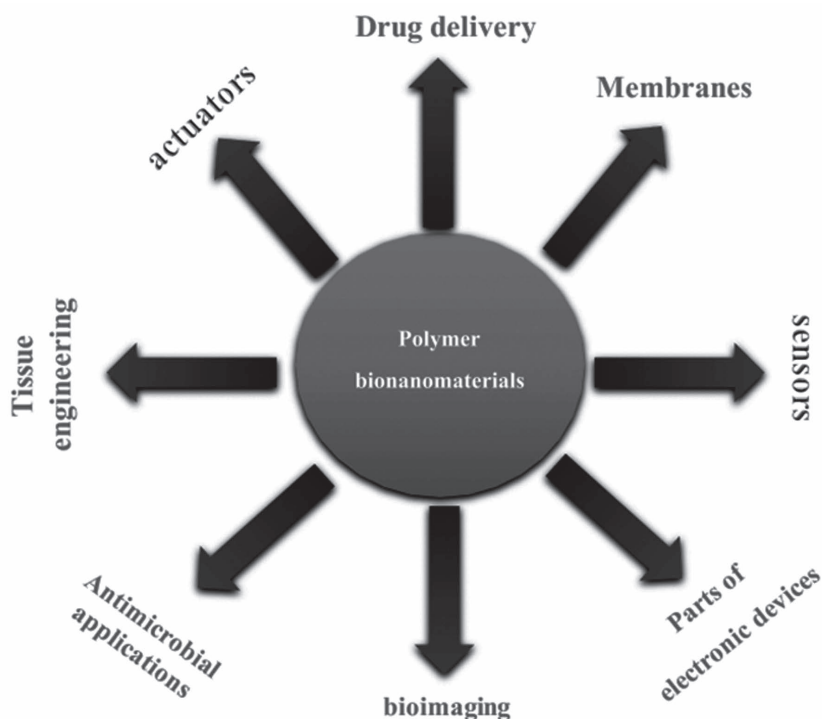


**FIGURE 8.1** Major areas of application of polymeric bionanomaterials.

One another significant example is a chitosan nanoparticle extracted from chitin, the major constituent of the exoskeleton in arthropods. They have charged surface and mucoadhesive properties due to the interactions of mucin and the polymer.<sup>43</sup> As a result, chitosan nanoparticles have increased drug loading capacity and controlled drug release. Similarly, biopolymers and nanofiller-incorporated biomaterials are prominent research areas among scientists.

### **8.2.3 BIOGENIC NANOPARTICLES**

#### **8.2.3.1 DNA**

By the year 2023, it will be 70 years since the discovery of double-helical structure of DNA. From being the complex molecule that contains all of the information necessary to build and maintain an organism, the concept of DNA has evolved in the decade. Now, DNA is widely used as a nanoparticle in the field of bioelectronics, drug delivery, biochemical industry, and many others. It is surprising to know that today DNA can easily be used as a conductive nanowire for synthesizing biosensor<sup>44</sup> or origami nanomachines for biology-related fields.<sup>45</sup> The evolution of DNA as a nanomaterial significantly relied on improvised methodology to control DNA hybridization, for example, by using moieties like photo-switchable molecular glue and the easy synthesis and assembly of DNA oligonucleotides.<sup>46,47</sup> Quoting the before mentioned, DNA origami is one of the milestone advantages that happened in this field where DNA is used as the building block for fabricating nanomaterials. Long DNA strands are folded into 3D scaffolds of staple strands containing up to 100–400 nucleotides just like a craft paper is folded into an arbitrary form.<sup>47</sup> In 2016, Matthies et al. developed DNA trusses, where rather than building up flat trusses, they folded tetrahedral, octahedral, and dodecahedral trusses which in turn helped in saving the volume of the material.<sup>48</sup> This proves how fast DNA nanotechnology is evolving. Other developments include but are not confined to the usage of DNA as molecular tags in combinatorial chemistry, DNA machines containing<sup>49</sup> nanofuels, DNA computing<sup>50</sup> and Molecular recognition element.

#### **8.2.3.2 VIRAL NANOPARTICLES**

It has been almost 30 years since the virus has been introduced as nanoparticles. The versatile nature, biocompatibility, biodegradability, and the ability to synthesize using both genetic and chemical protocols are some of its factors resulting in wide application. The application of viruses as nanomaterials have confined to the biomedical sector due to these characteristics. They are used in drug delivery, immunotherapy, therapeutic interventions, etc. The use of viruses as vaccines goes way before three centuries. Even though many vaccines like for HIV are still ambiguous and elusive, there is a huge list of dreadful infectious diseases eradicated from the universe. The scenario of COVID-19 pandemic is a significant example. Despite being struck worldwide

in a devastating scale, there has been much hope because of the development of vaccines, and millions of lives were also saved. Different strains of viral nanoparticles are available, all of which can be tailor-made and used depending on the application. For example, capsid assembly of icosahedral plan virus is exploited to fabricate 3D nanostructures for applications, such as self-assembly, biomineralization, and microencapsulation.<sup>51,52</sup> Among the disadvantages, toxicity, problems associated with pharmacokinetics, and risk factors of pathogenicity have always been of wide concern when dealing with viral particles. An increasing number of studies is being reported recently in either synthesizing benign viral particles or in decreasing the toxicity of the nanoparticles.<sup>53</sup> Whatsoever, in coming years, viral nanoparticles are expected to restructure many areas not only limited to biomedical field but even agricultural and even industrial sectors.

#### 8.2.3.3 AMYLOID FIBRILS

Amyloid fibrils are insoluble fibrous proteinaceous substances. They can be self-assembled from different polypeptides and contains cross  $\beta$ -sheet structure. They have comparable mechanical strength. These proteins are widely associated with many incurable diseases like Alzheimer's and Parkinson disease.<sup>54</sup> Although amyloid has always been on the bad and detested side being the source to mainly diseases, the increasing researches are a proof that these substances play vital functions in human body. These are called functional amyloids and these play a non-speaking part in curing diseases rather than creating them. Some of the basic functional amyloids include Microcin E492 which is found in bacteria and helps in pore formation of membranes,<sup>55,56</sup> Yeast pyruvate kinase Cdc19 found in *Saccharomyces cerevisiae* act as a catalyst for the transfer of a phosphate group from phosphoenolpyruvate to adenosine diphosphate in the final stage of glycolysis, Pmel17 in mammals which catalyzes the process of melanogenesis.

#### 8.2.4 CARBON-BASED NANOPARTICLES

These classes of nanomaterials have gained high attention due to their excellent mechanical, thermal, and electrical properties. Carbon nanotubes, graphene compounds, and graphene quantum dots are widely used in drug delivery, cancer therapy, diagnosis, and many other biomedical applications. They have also exhibited their catalytic applications which include

photocatalysis, acid–base catalysis, and electrocatalysis<sup>57</sup> Existence of different allotropic forms of carbon is one of the main factors for these wide varieties of carbon nanoparticles.

CNTs manifest high tensile strength, chemical stability, and ultra-lightweight making them a good choice for researchers. CNTs are the best option for sorption gas sensors in which adsorbed gas molecules give or take an electron from CNT. This in turn changes the electrical properties of CNT and can be sensed.<sup>58</sup> Similarly, graphene compounds like graphene oxide are an excellent choice for membrane preparation either as the base material or as the filler.<sup>59</sup> Due to selective torturous pathways created by GO, they are widely used for mixed-matrix gas separation membranes.

Some other common classifications include ceramic-based nanomaterials and semiconductor-based nanomaterial, a significant number of reviews and research papers have been reported in the last couple of decades about them.

### **8.3 APPLICATIONS OF BIONANOMATERIALS**

Nanotechnology has provided important advances in the area of novel interfaces, compounds, and morphologies, all of which have uses throughout the healthcare sector. Many of the existing medical processes such as tissue engineering, biosensors, smart sensors, and sustained release systems are just a few of the examples which can greatly benefit from incorporating nanotechnology into the mix.<sup>60</sup> Despite the fact that bionanomaterials have been used in a variety of biomedical sectors, the precise surface interaction between cells/tissues and nanomaterials is still unknown, and the risk and cytotoxicity associated with them are still to be properly studied.<sup>61</sup> The reason why they are advantageous compared with traditional substances include their large specific surface area which is favorable for a more efficient biochemical reaction and because of the many mechanisms dependent on their chemistry, mechanical characteristics are greatly improved.<sup>62</sup> Also, since the reactions are occurring in a molecular and/or atomic level, their level of purity and homogeneousness is also high.

#### **8.3.1 TISSUE ENGINEERING**

Tissue engineering is a relatively new branch of regenerative medicine that attempts to create a suitable biological replacement capable of repairing, preserving, or enhancing the real function of a damaged tissue. Even

though the ability of tissue engineering to repair damaged tissues and organs has already been proven, the majority of conditions of significance are still unexplored.<sup>63,64</sup> Nanostructured synthetic/natural matrices appear to be the next-generation scaffolds, presenting new opportunities for tissue regeneration while also posing new difficulties.<sup>65</sup> Cells, scaffolds, and growth factors, together known as the “tissue engineering trinity,” are the fundamental ingredients that form the foundation of the field.<sup>66</sup>

**TABLE 8.2** Application of Nanotechnology in Different Fields.

Field	Application
Medicine	<ul style="list-style-type: none"> <li>• Diagnosis</li> <li>• Medication records</li> <li>• Tissue engineering</li> </ul>
Chemistry and environment	<ul style="list-style-type: none"> <li>• Catalysis</li> <li>• Filtration</li> </ul>
Energy	<ul style="list-style-type: none"> <li>• Reduction of energy consumption</li> <li>• Increase in energy efficiency production</li> <li>• Use of more environmentally friendly energy systems</li> <li>• Battery recycling</li> </ul>
Information and communication	<ul style="list-style-type: none"> <li>• New semiconductor devices</li> <li>• New optoelectronic devices</li> <li>• Screens</li> <li>• Quantum computers</li> </ul>
Heavy industry	<ul style="list-style-type: none"> <li>• Aerospace</li> <li>• Refineries</li> <li>• Automobile industry</li> <li>• Consumer goods</li> <li>• Food</li> </ul>

Recently, development in nanotechnology has made the design of a nanoscale material capable of mimicking the properties of an extracellular matrix (ECM) which surrounds cells in tissues, provides support, and directs their activity possible. As a result, nanostructured materials may be used to create bioconstructs with unique mechanical, electrical, and biochemical characteristics that replicate tissue-specific environments.<sup>67</sup> Also, the cells’ interaction with the biomimetic nanomaterial can promote stem cell differentiation without any external factor. Zeng et al.<sup>68</sup> produced a variety of

magnetic nanoparticles-hydroxyapatite (MNP-HA) magnetic scaffolds with varying MNP concentrations (from 0.2 to 2%) by immersing HA scaffolds in MNP colloid. The magnetic scaffold was found to react to an external magnetic field and have high effectiveness on cell growth and division by amplifying the positive impact of a magnetic field on cells. Biopolymers can also be used as scaffolds for TE application, for example, natural polymers, such as collagen, chitosan, silk, alginate, fibrin, gelatine, or synthetic polymers, such as PLA, PGA, PCL, PLGA, poly(L-lactic acid), polyacrylamide, PU, PET, PMMA, polyethylene oxide, and PVA are used. Nano-scaffold systems, such as nanofibers, nanogels, or nanocomposites can be prepared from these polymers through different synthesis method of which electrospinning is the most extensively used one.<sup>69</sup> But they generally provide a smooth surface to the scaffold and can adversely impact the adhesion, growth and proliferation of the cell, as a result, other reinforcement specific to the biological sites needs to be provided. Table 8.2 presents a detailed description about different nanostructured scaffolds used for tissue engineering

**TABLE 8.3** Different Nanostructured Scaffolds and Synthesis Method Used for Tissue Engineering.

Nanostructure scaffold system	Polymer used	Synthesis method
Electrospun nanofibers <sup>70</sup>	Poly (lactide-co-caprolactone)	Electrospinning
Nanofibrous hollow microspheres <sup>71</sup>	PLLA polymer from PAMAM dendrimers	TIPS
Sol-gel fibermats <sup>72</sup>	PCL	Sol-gel process and electrospinning
Nanodiamond structured scaffolds <sup>73</sup>	Poly(LLA-co-CL)	Solvent casting Particulate leaching method
Magnetic nanoparticle structured biomimetic scaffolds <sup>68</sup>	HA scaffold	Microwave-assisted heating and sintering
3D printed nanobiocomposite scaffolds <sup>74</sup>	PCL	3D printing via robotic system

### 8.3.2 DRUG DELIVERY

The amount of literature published on the use of different NPs for drug delivery applications is very high in the recent years like mesoporous silica NPs used as a delivery agent, but they have disadvantages, such as low biodegradability, high porosity, immune rejection, etc. Conventional therapies have negative side effects and target normal/healthy cells as well as sick cells.<sup>75</sup> While



NP-based drug delivery is used to treat a variety of diseases, this form of therapy helps to reduce the drug's harmful effects, does not harm healthy cells, and only targets damaged cells. The use of biocompatible nanoscale inorganic materials for bioencapsulation and drug delivery with a sustained release strategy is one of the latest research areas which is capable of solving this crisis. Nanodimensional drug delivery systems are of great clinical importance because they have the potential to change the therapeutic efficacy of drug molecules, allowing them to concentrate more in the target tissues.<sup>76</sup>

Active and Passive targeting are the two modes that are currently being employed for the drug delivery of NPs. In passive targeting the nanoparticles infiltrate through tissue and increase in concentration at the target location due to enhanced permeability and retention but in the case of Active targeting which uses a receptor-mediated endocytosis for build-up and intake. Sometimes, ligands can also be used to bind NP's at the receptor site. Both active and passive NP targeting system, enhances the intracellular levels of medicines in tumor/target cells while posing no risk to normal cells. In the field of drug and gene delivery, nanoparticles, such as silica, gelatine, PEG, biodegradable chitosan,<sup>77</sup> liposomes, dextran, and non-biodegradable polymers, such as polystyrene, polycyanoacrylate, PMMA, polyacrylamide, polyphosphazene derivatives, etc. are being investigated. Magnetic NPs can be used for targeted drug delivery in which a cytotoxic medication is linked to an NP carrier, which enters the bloodstream and is targeted by magnetic fields to reach a specific location within the body. After arriving at the target location, the drug is released either by enzymatic activity or by changing physiological factors, such as osmolality, pH, temperature, etc.<sup>78</sup> For example, Liang et al.<sup>79</sup> developed a (FA)-functionalized lipoproteins (LDL)/sodium carboxymethyl cellulose (CMC) nanoparticles (NP) having low density for pH-assisted drug release and KB cells and A549 cells were used to assess the active targeting efficiency. With the active targeting capacity provided by FA moieties, the drug-loaded FA-CMC/LDL NP was predicted to accomplish site-specific and intracellular triggered release of therapeutic drugs. In the work done by Hardiansyah et al.,<sup>80</sup> the hydrophobic drug curcumin was incorporated into PEGylated magnetic liposomes as a drug carrier platform for regulated drug release. Drug release was accelerated by inductive magnetic heating (hyperthermia). The study showed that at 37°C, the drug carriers did not release any substantial amounts of curcumin, whereas at 45°C, they released a large amount of curcumin very quickly and under the influence of high-frequency magnetic fields (HFMFs), it was further increased (three times more).

### **8.3.3 BIOSENSING**

Nanotechnology, nanostructured capabilities, and miniaturized electronics, along with innovative biochemical detection approaches, result in highly precise and quick screenings for the recognition of specified biomolecules in a number of diverse areas.<sup>81</sup> Distinct types of biosensors are employed, each with its own set of benefits and drawbacks, along with a distinct actuator/sensor to construct biosensing devices for the detection of various sorts of desired biomolecules.<sup>82</sup> Different nanomolecules including DNA, RNA, peptides, etc. can be used to fabricate biomaterials such as nanobiomimetic materials, nanocomposite materials, nanodrug delivery systems, interface biomaterials, nano-biosensors. Biosensors are a new multidisciplinary field of study.<sup>83</sup>

Peptide nucleic acid (PNA) is a new type of probe that is replacing DNA for various therapeutic and pharmaceutical applications, including the development of sensors, arrays, chips. PNAs are a viable linker for the construction of DNA-based nanomaterials<sup>84</sup> because of their remarkable capacity to strand invade and hybridize to sequences inside duplex DNA.<sup>85</sup> PNA has been utilized for nanostructure construction before, with applications, such as DNA tagging and strand invasion into DNA hairpins and tetra loop patterns.<sup>86</sup> The design of synchronized nanobiosensors combines advantageous properties and characteristics of the individual components: polypeptide mechanism for precision of binding, peptide or oligonucleotide chemistry for matching the numerous electron-transducing components, and nanoelectrodes for enhancement.<sup>87</sup> The findings from these approaches highlight the potential benefits of utilizing nanoscale biosensors, which will dramatically alter biomedical diagnostics and therapies. The development and implementation of nano-devices in biology and medicine will have huge societal and health ramifications.

### **8.3.4 MOLECULAR IMAGING**

The branch of medical imaging known as molecular imaging focuses on visualizing molecules of medical relevance within living patients. This is in contradiction to histology, which is a common approach for extracting biological information from preserved tissue samples. This area provides a noninvasive approach to identifying molecular and cellular processes within a living organism, which can be carried out in physiological circumstances

that are similar to those encountered in clinical settings.<sup>88</sup> Molecular imaging usually necessitates the use of a substance to generate signals that can be detected by imaging equipment. Contrast agents, molecular probes, tracers, and reporters are all terms used to describe these substances. Molecular probes are divided into two types: passive and responsive (or “smart”) probes.<sup>89</sup> The responsive probe reports on the biological activities of the target tissues, cells and molecules, as opposed to passive tracers that allow for in vivo imaging.

For imaging techniques, cells could be transduced with a reporter gene. An injection of a reporter probe can identify a chemical produced by transduced cells. As only viable cells can be detected, this provides a means to distinguish between viable and nonviable cells. HSV-1 thymidine kinase (HSV-Tk) is the most widely used nuclear imaging reporter gene.<sup>90</sup> As well as being biocompatible, liposomes have the ability to be surface functionalized and protect radionuclides from a potentially unstable environment. Various techniques have been used to produce radio labeled liposomes, however, the two methods having the highest labeling efficiency and in vivo stability are: (1) radiolabeled amphiphilic chelators are introduced into the bilayers of premade liposomes, which encase chelators with greater affinity for the radionuclides, therefore trapping them inside the liposomes<sup>91</sup> and (2) after loading radionuclides with lipophilic molecules, liposomes enclose chelators with a greater affinity for radionuclides, trapping them within.<sup>92</sup> Aziz et al.<sup>93</sup> studied the efficacy of gold and silver NPs and found that porous AuNPs were more effective than solid AuNPs for direct CT scanning (45 HU contrast) (26 HU). Naha et al.<sup>94</sup> developed GSAN, which are gold–silver alloy nanoparticles with strong DEM (dual-energy mammography) contrast characteristics and enhanced biocompatibility. It was shown that GSANs provided significant DEM and CT contrast and accumulated in tumors before being excreted via urine and feces in mice breast tumor imaging studies.

### **8.3.5 IMMUNOTHERAPY**

They are considered an excellent technique for developing novel vaccines since they dramatically boost the antibody reaction to soluble antigens. Also, the oral administration of vaccinations can be improved by using nanoparticles, as compared with traditional formulations.<sup>95</sup> Marques Neto et al.,<sup>96</sup> in order to assess the development of their usage in vaccinology and their potential uses as adjuvants, they examined the use of Metallic NPs in formulations against infectious illnesses. The immunostimulatory capability

of Metallic NPs is well-established, and they have the ability to elicit a variety of responses at various stages of vaccine production. All of these capacities were connected to the physical properties of nanoparticles (NPs), including size, charge, and hydrophobicity. It was found that T-helper 1 and T-helper 17 were shown to promote the development of cellular immunological response, suggesting that Metallic NPs might be used as adjuvants for subunit vaccines.

Immunotherapy, a novel idea in cancer treatment, has demonstrated exceptional outcomes in patients treated with solid tumors, according to the FDA.<sup>97</sup> There has been a rapid advancement in cancer immunotherapy to create nanosystems for targeted therapies and chemotherapies. Functionalized nanomaterials, in specific, bring numerous benefits for cancer immunotherapy delivery, including active targeting to lymphocytes, co-delivery of chemotherapeutic drugs, reduced negative outcomes, obstructed immune checkpoint cells, and activation of immune responses through the use of triggers or immunostimulatory materials.<sup>98,99</sup>

#### **8.4 SIGNIFICANCE OF BIONANOMATERIALS**

Almost 60 years have passed since the introduction of bionanomaterials and nanotechnology, it is not wrong to say the discovery of this whole different class of materials has revolutionized the technology as well as industry. The main benefit of bionanomaterials lies in the fact that we are able to develop tailored products even at an extremely small scale to achieve specific properties. They can be made more conductive or insulative, lightweight or heavy weight, more or less durable, and many more. Moreover, they can be easily extracted from plants and animals. Even everyday commercial small-scale products in the market nowadays depend on nanoscience. Their extraordinary features, properties, synthesis methods, and application range make them the main focus of the entire world. The versatility of green nanocomposites makes it an entirely different class prone to a plethora of advances. Unlike other nanomaterials, these groups can be easily synthesized using plant and animal resources.

Nano additives are nowadays used as colorant, flavoring substance, or supplements. They highly help in absorption because of their larger surface area. Many countries use nano supplements and nanosalts as daily ingredients. Nanosalt not only has high nutrient value but it is said that a little amount can provide more flavor than common salt.<sup>100</sup> Similar benefits are seen in the case of meat. Encapsulated nano additives and fillers are added

to increase the shelf life and quality.<sup>101</sup> This tells that it has reached to a point that we are surviving on a nanoscale basis for our basic necessities. Not only confined to food processing, bionanomaterials also have had their significant advances in packaging application as well as agricultural application. Nanoformulations for insecticides and pesticides in the form of nanocapsules, nanospheres, micelles, nanogels, and nanofibers where a nanocarrier mechanism that allows the regulated release of the substance in insect, ensuring that the proper concentration of this active ingredient is maintained till the insect's larvae stage. Bionanomaterials have also reached a milestone in the area of active and intelligent packaging. Materials like nanosilver shows high performance in the packaging industry due to its exceptional antimicrobial and barrier properties. There are many reported researches where nanosilver is made composites with agar, gelatine, LDPE, PLA, CMC, and the list goes on.<sup>102–104</sup>

Just like bionanomaterials have changed the perspective in bio-related areas, the significance of nanomaterials in the field of energy is noteworthy. There is a whole different future of energy enabled by nanomaterials. As we discussed above, since these materials can be attuned and modified into different conductivity and ionic transport, they can endure a high number of currents making them promising in the field of energy storage, generation, and conservation.<sup>105</sup> Nanobiomaterials have been a source of study for many years and today they are part of almost every study taking place in the field of science and technology. Just like the few significant applications mentioned above, there's a wide variety of realms, where "bionano" is a part.

## **8.5 CONCLUSION**

Researchers are searching for innovative materials that are most compatible with the human body, while a new concept of sustainable development has developed rapidly. In the future, new biomedical devices might be designed with the help of cellular and tissue-interfacing nanostructured materials derived from biological sources. Also, bio-based materials may be easily adjusted in terms of chemical, physical, and mechanical characteristics to fit a range of target tissues. There are now easy-to-prepare nanoparticles that are less harmful and have a wide variety of uses based on their size or form thanks to biogenic nanoparticle production. In this chapter, we have discussed the evolving field of bionanomaterials, their classifications, and some major biomedical applications.

Even though bio-based nanomaterials are still in their infancy, efforts are being made to improve procedures for clinical applications. There is still more to be done to fulfill the capabilities of bionanomaterials in medicine and surgery. To ensure dependable, cost-effective, and scalable manufacturing of bioderived polymers with the appropriate chemical, biological physical, and mechanical characteristics requires efficient process development as well.

## KEYWORDS

- **bionanomaterials**
- **nanoparticles**
- **biomedical**
- **tissue engineering**
- **biogenic**

## REFERENCES

1. Bayda, S.; Adeel, M.; Tuccinardi, T.; Cordani, M. Rizzolio, F. The History of Nanoscience and Nanotechnology: From Chemical-Physical Applications to Nanomedicine. *Molecules* **2020**, *25*(1). DOI: 10.3390/molecules25010112.
2. Poole, C. P.; Frank Owens, J. J. Introduction to Nanotechnology. 2003. www.copyright.com
3. Wu, N.; Lu, X.; An, R.; Ji, X. Thermodynamic analysis and modification of Gibbs–Thomson equation for melting point depression of metal nanoparticles. *Chin J. Chem. Eng.* **2021**, *31*, 198–205. DOI: 10.1016/J.CJCHE.2020.11.035.
4. Thangadurai, D.; Sangeetha, J.; Prasad, R. Functional Bionano-Materials From Biomolecules to Nanoparticles. <http://www.springer.com/series/15921>
5. Has Irc, V. I et al. Nanobiomaterials: A Review of the Existing Science and Technology, and New Approaches. 2006.
6. Sahayaraj, K. Bionanomaterials: Synthesis and Applications, 2012.
7. Honek, J. F. Bionanotechnology and Bionanomaterials: John Honek Explains the Good Things That Can Come in Very Small Packages. *BMC Biochem.* **2013**, *14*(1). DOI: 10.1186/1471-2091-14-29
8. Bhushan, B. Springer of Nanotechnology.
9. Palmer, R. E.; de La Fuente, J. M.; Grazu, V. Atomic and Molecular Manipulation edited by www.elsevierdirect.com
10. Jamkhande, P. G.; Ghule, N. W.; Bamer, A. H.; Kalaskar, M. G. Metal Nanoparticles Synthesis: An Overview on Methods of Preparation, Advantages and Disadvantages,

- and Applications. *J. Drug Deliv. Sci. Technol.* **2019**, *53*, 101174. DOI: 10.1016/J.JDDST.2019.101174.
11. Thakkar, K. N.; Mhatre, S. S.; Parikh, R. Y. Biological Synthesis of Metallic Nanoparticles. *Nanomed.: Nanotechnol. Biol. Med* **2010**, *6*(2), 257–262. DOI: 10.1016/J.NANO.2009.07.002.
  12. de Oliveira, P. F. M.; Torresi, R. M.; Emmerling, F.; Camargo, P. H. C. Challenges and Opportunities in the Bottom-Up Mechanochemical Synthesis of Noble Metal Nanoparticles. *J. Mater. Chem. A* **2020**, *8*(32), 16114–16141. DOI: 10.1039/d0ta05183g.
  13. Bayda, S. et al. Bottom-Up Synthesis of Carbon Nanoparticles with Higher Doxorubicin Efficacy. *J. Control. Release* **2017**, *248*, 144–152. DOI: 10.1016/j.jconrel.2017.01.022.
  14. Mignot, A. et al. A Top-Down Synthesis Route to Ultrasmall Multifunctional Gd-Based Silica Nanoparticles for Theranostic Applications. *Chem.—A Eur. J.* **2013**, *19*(19), 6122–6136. DOI: 10.1002/chem.201203003.
  15. Amendola, V. et al. Top-Down Synthesis of Multifunctional Iron Oxide Nanoparticles for Macrophage Labelling and Manipulation. *J. Mater. Chem.* **2011**, *21*(11), 3803–3813. DOI: 10.1039/c0jm03863f.
  16. Mohanpuria, P.; Rana, N. K.; Yadav, S. K. Biosynthesis of Nanoparticles: Technological Concepts and Future Applications. *J. Nanopart. Res.* **2008**, *10*(3), 507–517. DOI: 10.1007/s11051-007-9275-x.
  17. Vithiya, K.; Sen, S. Biosynthesis of Nanoparticles. **2011**, *2*(11), 2781–2785. www.ijpsr.com
  18. Li, X.; Xu, H.; Chen, Z. S.; Chen, G. Biosynthesis of Nanoparticles by Microorganisms and Their Applications. *J. Nanomater.* **2011**, *2011*. DOI: 10.1155/2011/270974.
  19. R. Mishra, K.; S. Ha, K.; Verma, K.; Tiwari, S. K. Recent Progress in Selected Bio-Nanomaterials and Their Engineering Applications: An Overview. *J. Sci.: Adv. Mater. Devices* **2018**, *3*(3), 263–288. DOI: 10.1016/j.jsamd.2018.05.003.
  20. Antón, P. S.; Silbergliitt, R. S.; Schneider, J. *The Global Technology Revolution: Bio/Nano/Materials Trends and Their Synergies with Information Technology by 2015*; RAND, 2001.
  21. Wang, X.; Ramalingam, M.; Kong, X.; Zhao, L. *Nanobiomaterials: Classification, Fabrication and Biomedical Applications*.
  22. Schwartzberg, A. M.; Olson, T. Y.; Talley, C. E.; Zhang, J. Z. Synthesis, Characterization, and Tunable Optical Properties of Hollow Gold Nanospheres. *J. Phys. Chem. B* **2006**, *110*(40), 19935–19944. DOI: 10.1021/jp062136a.
  23. Nehl, C. L.; Liao, H.; Hafner, J. H. Optical Properties of Star-Shaped Gold Nanoparticles. *Nano Lett.* **2006**, *6*(4), 683–688, **2006**, DOI: 10.1021/nl052409y.
  24. Pylaev, T. E.; Khanadeev, V. A.; Khlebtsov, B. N.; Dykman, L. A.; Bogatyrev, V. A.; Khlebtsov, N. G. Effects of Shape and Charge of Colloidal Gold Nanoparticles in Colorimetric Determination of DNA Sequences. *Colloid J.* **2011**, *73*(3), 368–377. DOI: 10.1134/S1061933X11020104.
  25. Grzelczak, M.; Pérez-Juste, J.; Mulvaney, P.; Liz-Marzán, L. M. Shape Control in Gold Nanoparticle Synthesis. *Chem. Soc. Rev.* **2008**, *37*(9), 1783–1791. DOI: 10.1039/b711490g.
  26. Ramakrishna, G.; Dai, Q.; Zou, J.; Huo, Q.; Goodson, T. Interparticle Electromagnetic Coupling in Assembled Gold-Necklace Nanoparticles. *J. Am. Chem. Soc.* **2007**, *129*(7), 1848–1849. DOI: 10.1021/ja067123p.
  27. Huang, X.; El-Sayed, M. A. Gold Nanoparticles: Optical Properties and Implementations in Cancer Diagnosis and Photothermal Therapy. *J. Adv. Res.* **2010**, *1*(1), 13–28. DOI: 10.1016/j.jare.2010.02.002.

28. Dykman, L.; Khlebtsov, N. Gold Nanoparticles in Biomedical Applications: Recent Advances and Perspectives. *Chem. Soc. Rev.* **2012**, *41*(6), 2256–2282. DOI: 10.1039/c1cs15166e.
29. Yang, C.; Bromma, K.; Di Ciano-Oliveira, C.; Zafarana, G.; van Prooijen, M.; Chithrani, D. B. Gold Nanoparticle Mediated Combined Cancer Therapy. *Cancer Nanotechnol.* **2018**, *9*(1). DOI: 10.1186/s12645-018-0039-3.
30. Nowack, B.; Krug, H. F.; Height, M. 120 Years of Nanosilver History: Implications for Policy Makers. *Environ. Sci. Technol.* **2011**, *45*(4), 1177–1183. DOI: 10.1021/es103316q.
31. Diantoro, M. et al. Modification of Electrical Properties of Silver Nanoparticle. In *Silver Nanoparticles—Fabrication, Characterization and Applications*; InTech, 2018. DOI: 10.5772/intechopen.75682.
32. Guo, D.; Xie, G.; Luo, J. Mechanical Properties of Nanoparticles: Basics and Applications. *J. Phys. D: Appl. Phys.* **2014**, *47*(1). DOI: 10.1088/0022-3727/47/1/013001.
33. Ponarulselvam, S.; Panneerselvam, C.; Murugan, K.; Aarthi, N.; Kalimuthu, K.; Thangamani, S. Synthesis of Silver Nanoparticles Using Leaves of *Catharanthus roseus* Linn. G. Don and Their Antiplasmodial Activities. *Asian Pac. J. Trop. Biomed.* **2012**, *2*(7), 574–580. DOI: 10.1016/S2221-1691(12)60100-2.
34. Krithiga, N.; Rajalakshmi, A.; Jayachitra, A. Green Synthesis of Silver Nanoparticles Using Leaf Extracts of *Clitoria ternatea* and *Solanum nigrum* and Study of Its Antibacterial Effect Against Common Nosocomial Pathogens. *J. Nanosci.* **2015**, *2015*, 1–8. DOI: 10.1155/2015/928204.
35. Chinnasamy, G.; Chandrasekharan, S.; Bhatnagar, S. Biosynthesis of Silver Nanoparticles from *Melia azedarach*: Enhancement of Antibacterial, Wound Healing, Antidiabetic and Antioxidant Activities. *Int. J. Nanomed.* **2019**, *14*, 9823–9836. DOI: 10.2147/IJN.S231340.
36. Farré, M.; Barceló, D. *Introduction to the Analysis and Risk of Nanomaterials in Environmental and Food Samples* **2012**, *59*. DOI: 10.1016/B978-0-444-56328-6.00001-3.
37. Lusvardi, G.; Barani, C.; Giubertoni, F.; Paganelli, G. Synthesis and Characterization of TiO<sub>2</sub> Nanoparticles for the Reduction of Water Pollutants. *Materials* **2017**, *10*(10), 1–11. DOI: 10.3390/ma10101208.
38. MuhdJulkapli, N.; Bagheri, S.; Bee Abd Hamid, S. Recent Advances in Heterogeneous Photocatalytic Decolorization of Synthetic Dyes. *Sci. World J.* **2014**, *2014*. DOI: 10.1155/2014/692307.
39. Ponarulselvam, S.; Panneerselvam, C.; Murugan, K.; Aarthi, N.; Kalimuthu, K.; Thangamani, S. Synthesis of Silver Nanoparticles Using Leaves of *Catharanthus roseus* Linn. G. Don and Their Antiplasmodial Activities. *Asian Pac. J. Trop. Biomed.* **2012**, *2*(7), 574–580. DOI: 10.1016/S2221-1691(12)60100-2.
40. Fomby, P. et al. Stem Cells and Cell Therapies in Lung Biology and Diseases: Conference Report. *Ann. Am. Thoracic Soc.* **2010**, *12*(3), 181–204. DOI: 10.1002/term.
41. Tsuji, H. Poly(Lactic Acid) Stereocomplexes: A Decade of Progress. *Adv. Drug Deliv. Rev.* **2016**, *107*, 97–135. DOI: 10.1016/j.addr.2016.04.017.
42. Mao, D.; Li, Q.; Bai, N.; Dong, H.; Li, D. Porous Stable Poly(Lactic Acid)/Ethyl Cellulose/Hydroxyapatite Composite Scaffolds Prepared by a Combined Method for Bone Regeneration. *Carbohydr. Polym.* **2018**, *180* (July 2017), 104–111, **2018**, DOI: 10.1016/j.carbpol.2017.10.031.
43. Sogias, I. A.; Williams, A. C.; Khutoryanskiy, V. V. Why Is Chitosan Mucoadhesive? *Biomacromolecules* **2008**, *9*(7), 1837–1842. DOI: 10.1021/bm800276d.



44. Srivastava, R. Introductory Chapter: DNA as Nanowires. In *Bio-Inspired Technology [Working Title]*, 2019; pp1–8. DOI: 10.5772/intechopen.85172.
45. Endo, M.; Sugiyama, H. DNA Origami Nanomachines. *Molecules* **2018**, *23*, (7). DOI: 10.3390/molecules23071766.
46. Dohno, C.; Nakatani, K. Control of DNA Hybridization by Photoswitchable Molecular Glue. *Chem. Soc. Rev.* **2011**, *40*(12), 5718–5729. DOI: 10.1039/c1cs15062f.
47. Hughes, R. A.; A. Ellington, D. Synthetic DNA Synthesis and Assembly: Putting the Synthetic in Synthetic Biology. *Cold Spring Harbor Perspect. Biol.* **2017**, *9*(1). DOI: 10.1101/cshperspect.a023812.
48. Matthies, M.; Agarwal, N. P.; Schmidt, T. L. Design and Synthesis of Triangulated DNA Origami Trusses. *Nano Lett.* **2016**, *16*(3), 2108–2113. DOI: 10.1021/acs.nanolett.6b00381.
49. Beyer, C. et al. A DNA-Fuelled Molecular Ma. *J. Am. Chem. Soc.* **2006**, *128*, 3, 10092–10102.
50. Huang, Y.; He, L. DNA Computing Research Progress and Application. *ICCSE 2011—6th International Conference on Computer Science and Education, Final Program and Proceedings*, no. ICCSE, 2011; pp 232–235. DOI: 10.1109/ICCSE.2011.6028624.
51. Zlotnick, A.; Aldrich, R.; Johnson, J. M.; Ceres, P.; Young, M. J. Mechanism of Capsid Assembly for an Icosahedral Plant Virus. *Virology* **2000**, *277*(2), 450–456. DOI: 10.1006/viro.2000.0619.
52. Narayanan, K. B.; Han, S. S. Icosahedral Plant Viral Nanoparticles—Bioinspired Synthesis of Nanomaterials/Nanostructures. *Adv. Coll. Interface Sci.* **2017**, *248*, 1–19. DOI: 10.1016/j.cis.2017.08.005.
53. Esfandiari, N.; Arzanani, M. K.; Koohi-Habibi, M. The Study of Toxicity and Pathogenicity Risk of Potato Virus X/Herceptin Nanoparticles as Agents for Cancer Therapy. *Cancer Nanotechnol.* **2018**, *9*(1), 1–13. DOI: 10.1186/s12645-018-0036-6.
54. Ow, S. Y.; Dunstan, D. E. A Brief Overview of Amyloids and Alzheimer’s Disease. *Protein Sci.* **2014**, *23*(10), 1315–1331. DOI: 10.1002/pro.2524.
55. Otzen, D.; Riek, R. Functional Amyloids. *Cold Spring Harbor Perspect. Biol.* **2019**, *11*(12). DOI: 10.1101/cshperspect.a033860.
56. Berson, J. F.; Harper, D. C.; Tenza, D.; Raposo, G.; Marks, M. S. Pmel17 Initiates Premelanosome Morphogenesis within Multivesicular Bodies, 2001.
57. Testa, C.; Zammataro, A.; Pappalardo, A.; Trusso Sfrazzetto, G. Catalysis with Carbon Nanoparticles. *RSC Adv.* **2019**, *9*(47), 27659–27664. DOI: 10.1039/c9ra05689k.
58. De Zhang, W.; Zhang, W. H. Carbon Nanotubes as Active Components for Gas Sensors. *J. Sens.* **2009**, *2009*. DOI: 10.1155/2009/160698.
59. Janakiram, S.; Martín Espejo, J. L.; Yu, X.; Ansaloni, L.; Deng, L. Facilitated Transport Membranes Containing Graphene Oxide-Based Nanoplatelets for CO<sub>2</sub> Separation: Effect of 2D Filler Properties. *J. Membr. Sci.* **2020**, *616*(August), 118626. DOI: 10.1016/j.memsci.2020.118626.
60. Sitharaman, B. *Nanobiomaterials Handbook*, 2011.
61. Jeevanandam, J.; Barhoum, A.; Chan, Y. S.; Dufresne, A.; Danquah, M. K. Review on Nanoparticles and Nanostructured Materials: History, Sources, Toxicity and Regulations. *Beilstein J. Nanotechnol.* **2018**, *9*(1), 1050–1074. DOI: 10.3762/bjnano.9.98.
62. Singh, T. G.; Dhiman, S.; Jindal, M.; Sandhu, I. S.; Chitkara, M. Nanobiomaterials: Applications in Biomedicine and Biotechnology. In *Fabrication and Self-Assembly of Nanobiomaterials: Applications of Nanobiomaterials*; Elsevier Inc., 2016; pp 401–429. DOI: 10.1016/B978-0-323-41533-0.00013-1.

63. Grumezescu, A. M. *Nanobiomaterials in Hard Tissue Engineering: Applications of Nanobiomaterials*; William Andrew is an imprint of Elsevier, 2016.
64. Grumezescu, A. M. *Nanobiomaterials in Soft Tissue Engineering: Applications of Nanobiomaterials*.
65. Scott, T. G. et al. Advances in Bionanomaterials for Bone Tissue Engineering. *J. Nanosci. Nanotechnol.* **2013**, 13, no. 1. 1–22. DOI: 10.1166/jnn.2013.6733.
66. Cui, L.; Liang, J.; Liu, H.; Zhang, K.; Li, J. Nanomaterials for Angiogenesis in Skin Tissue Engineering. *Tissue Eng. Part B: Rev.* **2020**, 26(3), 203–216. DOI: 10.1089/ten.teb.2019.0337.
67. Cui, L.; Liang, J.; Liu, H.; Zhang, K.; Li, J. Nanomaterials for Angiogenesis in Skin Tissue Engineering. *Tissue Eng. Part B: Rev.* **2020**, 26(3), 203–216. DOI: 10.1089/ten.teb.2019.0337.
68. Zeng, X. B. et al. Magnetic Responsive Hydroxyapatite Composite Scaffolds Construction for Bone Defect Reparation. *Int. J. Nanomed.* **2012**, 7, 3365–3378. DOI: 10.2147/IJN.S32264.
69. Mostafavi, E.; Medina-Cruz, D.; Kalantari, K.; Taymoori, A.; Soltantabar, P.; Webster, T. J. Electroconductive Nanobiomaterials for Tissue Engineering and Regenerative Medicine. *Bioelectricity* **2020**, 2(2), 120–149. DOI: 10.1089/bioe.2020.0021.
70. Holzwarth, J. M.; Ma, P. X. Biomimetic Nanofibrous Scaffolds for Bone Tissue Engineering. *Biomaterials* **2011**, 32, no. 36. 9622–9629. DOI: 10.1016/j.biomaterials.2011.09.009.
71. Liu, X.; Jin, X.; Ma, P. X. Nanofibrous Hollow Microspheres Self-Assembled from Star-Shaped Polymers as Injectable Cell Carriers for Knee Repair. *Nat. Mater.* **2011**, 10, 5, 398–406. DOI: 10.1038/nmat2999.
72. Lee, E. J. et al. Nanostructured Poly( $\epsilon$ -Caprolactone)-Silica Xerogel Fibrous Membrane for Guided Bone Regeneration. *Acta Biomater.* **2010**, 6(9), 3557–3565. DOI: 10.1016/j.actbio.2010.03.022.
73. Xing, Z. et al. Biological Effects of Functionalizing Copolymer Scaffolds with Nanodiamond Particles. *Tissue Eng.—Part A* **2013**, 19(15–16), 1783–1791. DOI: 10.1089/ten.tea.2012.0336.
74. Ye, L.; Zeng, X.; Li, H.; Ai, Y. Fabrication and Biocompatibility of Nano Non-Stoichiometric Apatite and Poly( $\epsilon$ -Caprolactone) Composite Scaffold by Using Prototyping Controlled Process. *J. Mater. Sci.* **2010**, 21(2), 753–760. DOI: 10.1007/s10856-009-3872-4.
75. Nanomaterials in Drug Delivery, Imaging, and Tissue Engineering.
76. Fernandez-Fernandez, A.; Manchanda, R.; McGoron, A. J. Theranostic Applications of Nanomaterials in Cancer: Drug Delivery, Image-Guided Therapy, and Multifunctional Platforms. *Appl. Biochem. Biotechnol.* **2011**, 165(7–8), 1628–1651. DOI: 10.1007/s12010-011-9383-z.
77. Yang, Y.; Wang, S.; Wang, Y.; Wang, X.; Wang, Q.; Chen, M. Advances in Self-Assembled Chitosan Nanomaterials for Drug Delivery. *Biotechnol. Adv.* **2014**, 32(7), 1301–1316. DOI: 10.1016/J.BIOTECHADV.2014.07.007.
78. Jacob, J.; Haponiuk, J. T.; Thomas, S.; Gopi, S. Biopolymer Based Nanomaterials in Drug Delivery Systems: A Review. *Mater. Today Chem.* **2018**, 9, 43–55. DOI: 10.1016/J.MTCHEM.2018.05.002.
79. Liang, H.; He, L.; Zhou, B.; Li, B.; Li, J. Folate-Functionalized Assembly of Low Density Lipoprotein/Sodium Carboxymethyl Cellulose Nanoparticles for Targeted Delivery. *Colloids Surfaces B* **2017**, 156, 19–28. DOI: 10.1016/j.colsurfb.2017.05.004.

80. Hardiansyah, A.; Yang, M. C.; Liu, T. Y.; Kuo, C. Y.; Huang, L. Y.; Chan, T. Y. Hydrophobic Drug-Loaded PEGylated Magnetic Liposomes for Drug-Controlled Release. *Nanoscale Res. Lett.* **2017**, *12*. DOI: 10.1186/s11671-017-2119-4.
81. Jianrong, C.; Yuqing, M.; Nongyue, H.; Xiaohua, W.; Sijiao, L. Nanotechnology and Biosensors. *Biotechnol. Adv.* **2004**, *22*(7), 505–518. DOI: 10.1016/j.biotechadv.2004.03.004.
82. *Frontiers of Nano-Optoelectronic Systems*; Springer: Netherlands, 2000. DOI: 10.1007/978-94-010-0890-7.
83. Singh, R. P.; Choi, J. W. Bio-Nanomaterials for Versatile Bio-Molecules Detection Technology. *Adv. Mater. Lett.* **2010**, *1*(1), 83–84. DOI: 10.5185/amlett.2010.4109.
84. Park, S. J.; Taton, T. A.; Mirkin, C. A. Array-Based Electrical Detection of DNA with Nanoparticle Probes. *Science* **2002**, *295*(5559), 1503–1506. DOI: 10.1126/science.1067003.
85. Tombelli, S.; Minunni, M.; Mascini, M. Analytical Applications of Aptamers. *Biosens. Bioelectron.* **2005**, *20*(12), 2424–2434. DOI: 10.1016/j.bios.2004.11.006.
86. Singh, R. P.; Choi, J. W. Bio-Nanomaterials for Versatile Bio-Molecules Detection Technology. *Adv. Mater. Lett.* **2010**, *1*(1), 83–84. DOI: 10.5185/amlett.2010.4109.
87. turberfield2000.
88. Krestin, G. P.; Bernsen, M. R. Molecular Imaging in Radiology: The Latest Fad or the New Frontier? *Eur. Radiol.* **2006**, *16*(11), 2383–2385. DOI: 10.1007/s00330-006-0454-4.
89. Sherry, A. D.; Woods, M. Chemical Exchange Saturation Transfer Contrast Agents for Magnetic Resonance Imaging. *Annu. Rev. Biomed. Eng.* **2008**, *10*, 391–411. DOI: 10.1146/annurev.bioeng.9.060906.151929.
90. Cao, F. et al. In Vivo Visualization of Embryonic Stem Cell Survival, Proliferation, and Migration After Cardiac Delivery. *Circulation* **2006**, *113*(7), 1005–1014. DOI: 10.1161/CIRCULATIONAHA.105.588954.
91. Man, F.; Gawne, P. J.; de Rosales, R. T.M. Nuclear Imaging of Liposomal Drug Delivery Systems: A Critical Review of Radiolabelling Methods and Applications in Nanomedicine. *Adv. Drug Deliv. Rev.* **2019**, *143*, 134–160. DOI: 10.1016/j.addr.2019.05.012.
92. A Novel Liposome Radiolabeling Method Using <sup>99m</sup>Tc.
93. Aziz, F. et al. Novel Route Synthesis of Porous and Solid Gold Nanoparticles for Investigating Their Comparative Performance as Contrast Agent in Computed Tomography Scan and Effect on Liver and Kidney Function. *Int. J. Nanomed.* **2017**, *12*, 1555–1563. DOI: 10.2147/IJN.S127996.
94. Naha, P. C. et al. Gold Silver Alloy Nanoparticles (GSAN): An Imaging Probe for Breast Cancer Screening with Dual-Energy Mammography or Computed Tomography. *Nanoscale* **2016**, *8*(28), 13740–13754. DOI: 10.1039/c6nr02618d.
95. Salatin, S.; Barar, J.; Barzegar-Jalali, M.; Adibkia, K.; Milani, M. A.; Jelvehgari, M. Hydrogel Nanoparticles and Nanocomposites for Nasal Drug/Vaccine Delivery. *Arch. Pharm. Res.* **2016**, *39*(9), 1181–1192. DOI: 10.1007/s12272-016-0782-0.
96. Marques Neto, L. M.; Kipnis, A.; Junqueira-Kipnis, A. P. Role of Metallic Nanoparticles in Vaccinology: Implications for Infectious Disease Vaccine Development. *Front. Immunol.* **2017**, *8*(MAR). DOI: 10.3389/fimmu.2017.00239.
97. Saleh, T.; Shojaosadati, S. A. Multifunctional Nanoparticles for Cancer Immunotherapy. *Human Vaccines Immunotherap.* **2016**, *12*(7), 1863–1875. DOI: 10.1080/21645515.2016.1147635.

98. Fontana, F.; Liu, D.; Hirvonen, J.; Santos, H. A. Delivery of Therapeutics with Nanoparticles: What's New in Cancer Immunotherapy? *Wiley Interdiscip. Rev.: Nanomed. Nanobiotechnol.* **2017**, 9(1). DOI: 10.1002/wnan.1421.
99. Yue, H. et al. Exploration of Graphene Oxide as an Intelligent Platform for Cancer Vaccines. *Nanoscale* **2015**, 7(47), 19949–19957. DOI: 10.1039/c5nr04986e.
100. Shabnam; Perwez, M.; Mazumder, J. A.; Sardar, M. *Phytonanotechnology: A New Horizon for the Food Industry*; Elsevier Inc., 2020. DOI: 10.1016/b978-0-12-822348-2.00012-7.
101. Singh, P. K.; Jairath, G.; Ahlawat, S. S. Nanotechnology: A Future Tool to Improve Quality and Safety in Meat Industry. *J. Food Sci. Technol.* **2016**, 53(4), 1739–1749. DOI: 10.1007/s13197-015-2090-y.
102. Fortunati, E. et al. Nano-Biocomposite Films with Modified Cellulose Nanocrystals and Synthesized Silver Nanoparticles. *Carbohydr. Polym.* **2014**, 101(1), 1122–1133. DOI: 10.1016/j.carbpol.2013.10.055.
103. Kanmani, P.; Rhim, J. W. Physicochemical Properties of Gelatin/Silver Nanoparticle Antimicrobial Composite Films. *Food Chem.* **2014**, 148, 162–169. DOI: 10.1016/j.foodchem.2013.10.047.
104. Othman, S. H. Bio-Nanocomposite Materials for Food Packaging Applications: Types of Biopolymer and Nano-Sized Filler. *Agric. Agric. Sci. Procedia* **2014**, 2, 296–303. DOI: 10.1016/j.aaspro.2014.11.042.
105. Pomerantseva, E.; Bonaccorso, F.; Feng, X.; Cui, Y.; Gogotsi, Y. Energy Storage: The Future Enabled by Nanomaterials. *Science* **2019**, 366(6468). DOI: 10.1126/science.aan8285.



## CHAPTER 9

---

# Luminescent Properties of Pure and Lanthanide Doped Rare Earth Sesquioxide Nanoparticles

MORRIS MARIELI ANTOINETTE<sup>1</sup> and SUJIN P. JOSE<sup>2</sup>

<sup>1</sup>*Department of Physics, St. Joseph's College, Alappuzha, Kerala, India*

<sup>2</sup>*School of Physics, Madurai Kamaraj University, Madurai, Tamil Nadu, India*

---

### ABSTRACT

Some rare earth oxide nanophosphors have been investigated at length during the last decade due to their potential use in various high-performance novel displays and applications. In this chapter, we review the luminescent properties of pure and lanthanide ( $\text{Ln}^{3+}$ ) doped rare earth sesquioxide nanophosphors synthesized using various methods. Solid state, combustion, sol-gel, microwave, and hydrothermal/solvothermal are the common methods of synthesis. The structure of the synthesized materials is obtained from the X-ray diffraction (XRD) results and the morphology from the images of scanning electron microscopy (SEM) and transmission electron microscopy (TEM). The structure and the morphology of the materials depend upon the precursors, method of synthesis, and the temperature at which these are synthesized. The emission intensity observed from the PL spectra reveals their potentials for various optical applications. The most commonly prepared sesquioxides are found to be  $\text{Nd}_2\text{O}_3$ ,  $\text{Gd}_2\text{O}_3$ , and  $\text{Dy}_2\text{O}_3$ .

## 9.1 INTRODUCTION

Nanoscience, the study on materials at atomic and molecular scales, is a promising area of research where the properties of materials can vary tangibly in comparison with its bulk. Studying materials at nanometer scale has resulted in the exploration of many amazing novel materials that possess distinguished properties in comparison with its bulk state. While the bulk materials possess constant physical properties, the materials at the nanoscale have size-dependent properties. Hence, in general, the properties of materials change significantly as their size approaches the nanoscale which is very much different from that of their bulk counterparts. Nanotechnology deals with the technological applications of nanoscience, which includes the synthesis, design, characterization and applications of structures, devices and systems at nanometer scale.

The development of nanotechnology in the past two decades has helped, to a great extent, to control materials at the nanometer scale and has opened up exciting opportunities in designing materials with desirable electronic, ionic, photonic, and mechanical properties. In recent years, studies related to the synthesis of nanomaterials and nanoparticles with unique and desired properties have attracted a great deal of attention due to their features like small size, multifunctionality, surface tailorability, and biocompatibility. Moreover, these features have also led to nanomaterials being used in an increasing number of applications in various branches of science, industry, and in daily life. Nanotechnology has brought about several innovative products in the field of engineering because of its unique and rewarding chemical, physical, and mechanical properties. It has also helped to considerably improve, even revolutionize, many sectors like information technology, homeland security, medicine, transportation, energy, food safety, environmental science, and so on and so forth.

Today, nanotechnology is used for many important and interesting applications in the various fields of science and technology. It is used in the manufacture of both strong and light weight nanomaterials that are suitable for different applications namely, to build electronic parts, fuel cells, solar cells, batteries, chemical sensors, fabrics, memory devices, spacecraft, and in cosmetics like sunscreens too. Also, nanostructured catalysts help make chemical manufacturing processes more efficient as they save energy and reduce waste. Moreover, nano particles are used to remove the contaminations in the groundwater at a lower cost. Nanomaterials are used in healthcare as well. For example, they are used in the detection and treatment of cancer.

Some nanoceramics are used in specific dental implants or to fill holes in diseased bones, as their mechanical and chemical properties can be altered to attract bone cells from the surrounding tissue to make new bone. Thus, as the possible benefits of nanoparticles are almost endless, they are of immense scientific interest.

## 9.2 LANTHANIDES

The lanthanide (Ln) elements consist of a distinctive series of metals in the periodic table. These are unique in terms of valence orbitals, size, electrophilicity, optical, electronic and magnetic properties. Hence, certain elements of the series are at present the most excellent metals for potential industrial and technological applications. For reactions in which a large trivalent ion is required these may be the most excellent ones.

Rare earth (RE) ions play a vital role in modern industries and optical technologies as the vital constituents in producing numerous essential novel materials. The lanthanides are Lanthanum (La), Cerium (Ce), Praseodymium (Pr), Neodymium (Nd), Promethium (Pm), Samarium (Sm), Europium (Eu), Gadolinium (Gd), Terbium (Tb), Dysprosium (Dy), Holmium (Ho), Erbium (Er), Thulium (Tm), Ytterbium (Yb), and Lutetium (Lu). All these show generally oxidation state which is the stable oxidation state in the whole series. On the other hand, some of the RE ions such as samarium, europium, and ytterbium can exist in a divalent oxidation state as well. Furthermore, Cerium and terbium can be present in a tetravalent oxidation state.

Lanthanides are a group of elements in the periodic table that come after lanthanum with atomic number ranging from 58 to 71. Their normal configurations are given in Table 9.1. The sharp emission lines and long excited state lifetime values from lanthanide ions may be due to the shielding of 4f electron by 5d and 6s electrons. The 4f<sup>N</sup> electrons which are partially filled are efficiently shielded by the filled 5s and 5p electron shells, crystal-field (CF) environment, and /or the ligand. Hence, even in solid materials, they have only little influence on the electronic cloud of these trivalent ions. Hence, it can be considered as a perturbation known as the crystal field interaction, which is mainly responsible for the fine spectral structure of Ln<sup>3+</sup> ions.<sup>1,2</sup> As the lanthanides are comparatively abundant in nature, on the worldwide market, their price is low and used in different potential applications.



**TABLE 9.1** Configurations of Lanthanide Ions and Their Radii.

At. No.	Lanthanide	$\text{Ln}^{3+}$ (ground state)	Radii of $\text{Ln}^{3+}$ (Å)
58	Cerium (Ce)	$4f^15s^25p^6 (^4F_{5/2})$	1.034
59	Praseodymium (Pr)	$4f^25s^25p^6 (^3H_4)$	1.013
60	Neodymium (Nd)	$4f^35s^25p^6 (^4I_{9/2})$	0.995
61	Promethium (Pm)	$4f^45s^25p^6 (^5I_4)$	0.980
62	Samarium (Sm)	$4f^55s^25p^6 (^6H_{5/2})$	0.964
63	Europium (Eu)	$4f^65s^25p^6 (^7F_0)$	0.950
64	Gadolinium (Gd)	$4f^75s^25p^6 (^8S_{7/2})$	0.938
65	Terbium (Tb)	$4f^85s^25p^6 (^7F_6)$	0.923
66	Dysprosium (Dy)	$4f^95s^25p^6 (^6H_{15/2})$	0.908
67	Holmium (Ho)	$4f^{10}5s^25p^6 (^5I_8)$	0.894
68	Erbium (Er)	$4f^{11}5s^25p^6 (^4I_{15/2})$	0.881
69	Thulium (Tm)	$4f^{12}5s^25p^6 (^3H_6)$	0.869
70	Ytterbium (Yb)	$4f^{13}5s^25p^6 (^2F_{7/2})$	0.858
71	Lutetium (Lu)	$4f^{14}5s^25p^6 (^1S_0)$	0.848

The unique properties of the lanthanides are:

- Largest nonradioactive metals in the periodic table, and so used in reactions where a large trivalent ion is required
- Quite electropositive and by itself have a high affinity for oxygen and the halides, and hence is utilized as catalytic converters in fuel cells and automobiles.
- Sharp 4f–4f emission and absorption spectra which result in explicit and efficient optical processes in optical devices like lasers (e.g., Nd:YAG), color television, energy-saving phosphors etc.
- High magnetic moments suitable for applications ranging from magnetic resonance imaging (MRI) to low weight high power magnets which are used in airplanes, cars, and appliances.

Lanthanide ions ( $\text{Ln}^{3+}$ ) are important constituents in many optical materials. They have an extensive variety of applications, including phosphors for fluorescent lighting, amplifiers for fiber-optic communication, materials for display monitors, X-ray imaging, scintillators, lasers, etc. Lanthanide based luminescent materials are prepared either by complexing  $\text{Ln}^{3+}$  ions with suitable organic ligands or by doping  $\text{Ln}^{3+}$  ion an appropriate inorganic lattices having different dimensions. The reduced optical scattering of

nanometer-sized particles makes it helpful as active materials in polymer or glass-based lasers and amplifiers. Such nanoparticles can be stabilized with suitable ligands during the synthesis and can be incorporated in different types of matrices.

Composites consisting of luminescent nanoparticles dispersed in a polymer matrix have certain advantages as the polymer lattice. This offers desirable mechanical properties while the inorganic luminescent material gives high luminescence efficiency and long-term chemical stability. Of late, inorganic nanophosphors doped with rare earth metal ions have attracted immense attention due to their fascinating luminescence and potential applications, commonly referring as X-ray imaging, radiation dosimetry, lamp industry, and color display.<sup>3-5</sup>

Each lanthanide ion gives a characteristic absorption and emission spectra which result in emission in the regions of near-ultraviolet (n-UV), visible (Vis), near infrared (NIR), and infrared (IR) of the electromagnetic spectrum. The unfilled 4f electronic structure of the lanthanide ions results in the exhibition of magnetic, luminescent, catalytic, and electronic properties which are highly beneficial in developing novel materials which find applications like as magnetic materials, phosphors, biomedicine, catalysts, and memory devices. The luminescence of rare earth ions has captured great attention in technological and industrial applications. Hence, stupendous research is on progress in the field of luminescent materials for displays and solid-state lightings. Dieke et al. explain the universal scheme of the essential lanthanide absorption and emission bands.<sup>6</sup>

### 9.3 LUMINESCENCE

Luminescent materials, also called phosphors, are mostly inorganic materials emitting light in the visible region when exposed to radiations such as ultraviolet light or an electron beam. Absorbing a photon, the electrons are excited to a higher energy level, and later return to the ground state by emitting radiations in the regions between UV and IR. The schematic diagram of the emission process is shown in Figure 9.1.

Luminescence can be classified into various types according to their method of excitation. Emission resulting from the absorption of electromagnetic waves, electric field, an electron beam, X-rays, and chemical reaction is referred to as photoluminescence, electroluminescence, cathodoluminescence, X-ray luminescence, and chemiluminescence, respectively.

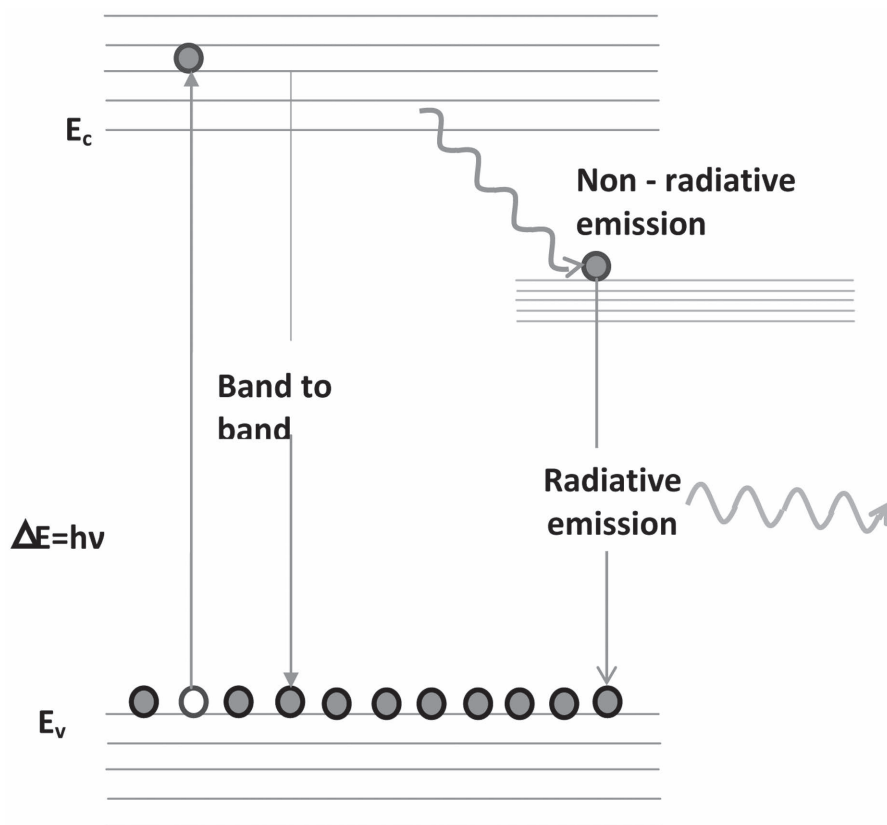


**FIGURE 9.1** Schematic diagram of the emission process.

Phosphors in nano-sized form show markedly different structural, optical, and electrical properties as compared to those in the bulk form. When an impurity is doped in a quantum-confined structure, the phosphor host materials exhibit significant size-dependent luminescent properties. The emissions of the luminescent materials are tailored in nanocrystalline form. Moreover, the absorption edge shifts to high energy owing to quantum confinement, and hence these materials have a degree of tailorability. Evidently, all these properties of doped nanocrystalline phosphors make them exceptionally useful for optoelectronic devices.

Numerous phosphors possessing unique characteristic color emission have been synthesized. Phosphor material having narrow size distribution and spherical morphology shows good luminescence characteristics. In the past decade, a vast research has been carried out in the field of lanthanide-based

luminescent materials. The luminescence of lanthanide ions has applications ranging from displays to bio imaging and sensing. Hence, incorporation of appropriate lanthanide ions into a strong and compatible matrix has an immense effect on the luminescence which makes it suitable for an intended application. Recently, rare earths (RE) sesquioxides have found a variety of applications in solid-state lasers, display devices, X-ray radiography, luminescent materials due to their high thermal and chemical stability, and maximum power output.

## 9.4 RARE-EARTH OXIDES

Rare-earth oxide nanomaterials have been extensively studied due to their varied interesting optical, magnetic and electrical properties, and applications. The rare-earth-based materials synthesized from rare-earth oxides are used for various applications such as catalysis, sensors, phosphors, and biomedicine.<sup>7–12</sup> Most of the rare-earth oxides exist in three phases: cubic, monoclinic, and hexagonal depending on the conditions of synthesis (Figure 9.2).

The rare-earth ions in the rare-earth oxides usually have +3 oxidation state as this state is highly stable when compared to the other states. Hence, all rare-earth ions have sesquioxides (three atoms of oxygen with two atoms/radicals of another element). The physical and chemical properties of rare-earth oxides are more or less similar due to their electronic arrangement. The optical properties arise due to their incompletely filled  $4f$  shells which are shielded by the outer  $5s$  and  $5p$  shells. Interestingly, doping with rare-earth (RE) ions results in an enhanced emission from the UV to the NIR regions and so RE-doped nanomaterials show advanced optical and chemical properties. Therefore, doping with rare-earth ions produces a novel material with improved optical properties. The rare-earth oxides slightly differ from the other oxides in their magnetic properties due to the filling of the  $4f$  orbitals with the unpaired electrons according to Hund's rule. The electrical conductivity of the rare-earth oxides is low, and the conductivity decreases with the increase in atomic number of the rare-earth ion.<sup>13</sup>

### 9.4.1 SYNTHESIS OF RARE-EARTH OXIDES

The primary requisite of any novel study on a nano oxide is the method of synthesis of the material. In general, nanomaterials can be synthesized

into two broad categories: the top-down method and the bottom-up method. The schematic representation of top-down and bottom-up nanomaterials synthesis is shown in Figure 9.3.

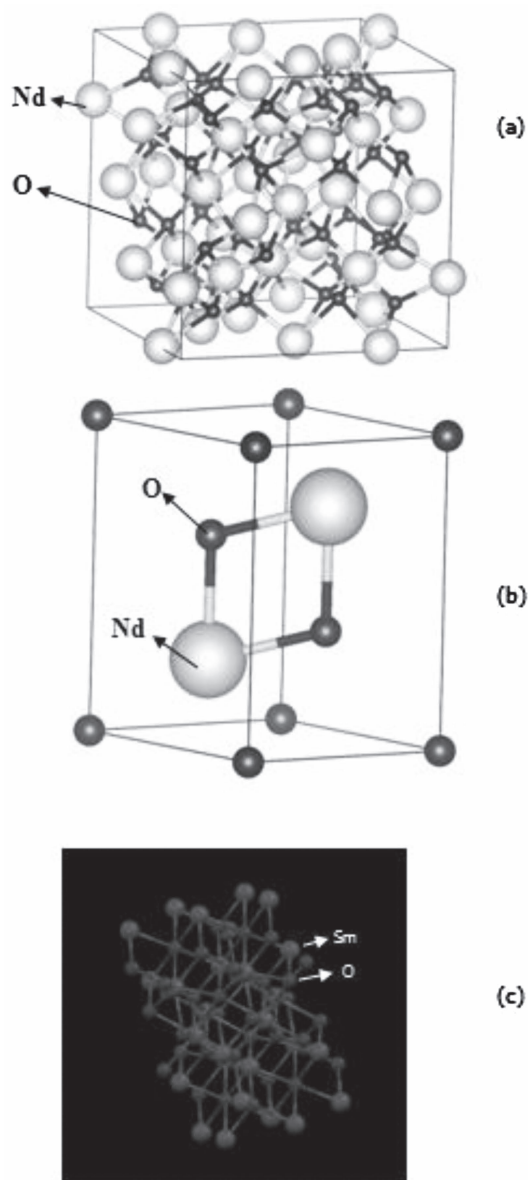


**FIGURE 9.2** Crystal structure of rare earth oxides (a) cubic, (b) hexagonal, (c) monoclinic.

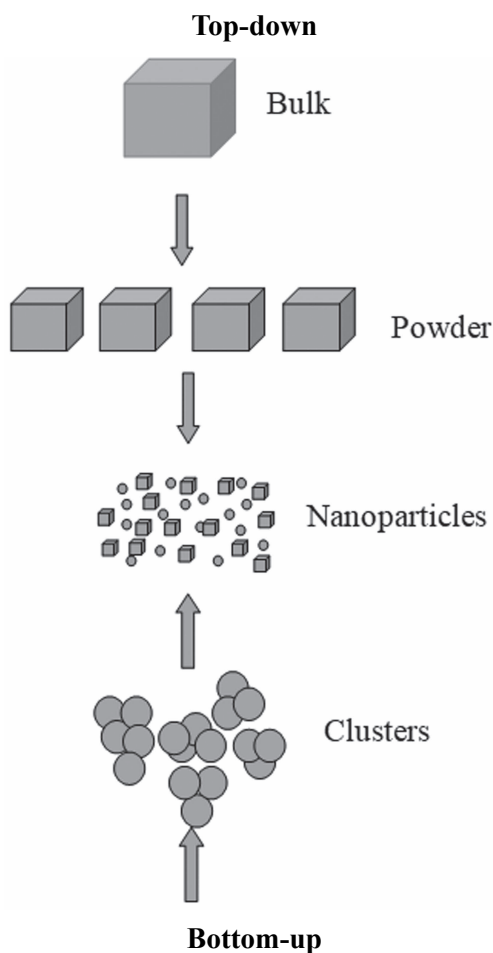


**FIGURE 9.3** Schematic representation of top-down and bottom-up nanomaterials synthesis.

**a) Top-down Method**

Top-down method is one of the initial methods used by experimentalists to synthesize nanomaterials from its bulk counterparts. In this method, bulk material is reduced to nanosize either by successive cutting or by milling. Of the various top-down methods like ball milling, etching, mechanical grinding, photolithography, and so on, photolithography is the most popular.

**b) Bottom-up Method**

Bottom-up method, the most extensively and usually used method for the synthesis of nanomaterials is the reverse of the top-down method.

In this method, materials are synthesized in the nanoscale regime from the bottom, atom by atom, molecule by molecule, or cluster by cluster. Self-assembly of nanoparticles occurs naturally in this process.<sup>14</sup> This method is particularly used to synthesize materials with relatively less defects and to maintain homogeneous chemical composition in the grown products. The various kinds of bottom-up methods are chemical precipitation method, sol–gel method, hydrothermal method, solvothermal method, microwave synthesis, and so on and so forth.

Rare earth oxides are mainly prepared using the bottom up method. The initial requisite of any novel study of nano oxides is to have a suitable method of synthesis. The methodical study of the synthesis of these nanoparticles is vital. Controlling the size and chemical homogeneity of these nanoparticles is a tremendous task. Nevertheless, the usage of surfactants and sonochemical methods emerge as both novel and feasible alternatives to optimize the resulting solid morphological characteristics.

It is challenging to synthesize pure and efficient chemical products that are of nanometer dimensions (generally in the range of 1–100 nm).<sup>15</sup> Hence, the challenge of the ongoing research community is to devise perfect methodologies which produce pure cost-effective nanoparticles of desired particle size, particle size distribution, and uniformity in terms both structure and composition. The rare earth oxides have been synthesized by a wide variety of methods including microwave-assisted, solvothermal, sol gel, hydrothermal, solution combustion, co-precipitation, etc.<sup>16–21</sup>

#### **9.4.2 NEODYMIUM (III) OXIDE**

Neodymium sesquioxide ( $\text{Nd}_2\text{O}_3$ ), a rare earth oxide consisting of neodymium and oxygen, is soluble in acid and insoluble in water. It has a very high melting point of  $2233^\circ$  and density of  $7.24 \text{ g cm}^{-3}$ . It forms blue hexagonal crystals.

The key applications of neodymium oxide nanoparticles are as follows:

- Used as dopant for high-efficiency solid-state lasers
- Used as sintering additives, and additives for Mg or Al alloys and polymers
- Used as coloring agent of glass and ceramics
- Used in catalytic applications
- Used as the raw materials of the neodymium metal and neodymium alloy
- Used in electric capacitors

Unlike the traditional neodymium oxides, the study of  $\text{Nd}_2\text{O}_3$  nanoparticles is of immense interest because of their potential applications resulting from their interfacial surface effect, quantum size effect, and tunneling effect. Therefore, research studies on  $\text{Nd}_2\text{O}_3$  nanoparticles are in progress. In particular,  $\text{Nd}_2\text{O}_3$  nanoparticles find potential applications in photonics,<sup>22–24</sup> luminescent and thermoluminescent materials,<sup>25,26</sup> protective coatings,<sup>27,28</sup> and thin films<sup>29</sup> due to their nanoscale dimension and large surface area.

$\text{Nd}_2\text{O}_3$  has attracted many researchers and deserves special attention due to its promising wide range of applications. The  $\text{Nd}^{3+}$  ion is recognized among the rare-earth ions, as one of the most efficient ions for solid-state lasers. Neodymium ions are also used in upconversion fluorescence and lasers.<sup>30,31</sup> It is used in ceramic capacitors, color television (TV) tubes, coloring glass, catalyst for automotive industry, ultraviolet absorbent, etc.<sup>32</sup>

Jian-Hua et al.<sup>32</sup> reported the synthesis of  $\text{Nd}_2\text{O}_3$  nanoparticles by using the microemulsion method in the sodium bis (2-ethylhexyl) sulfosuccinate (AOT) AOT/ toluene and propanol. Two emission bands at 344 nm corresponding to  $^4D_{3/2} \rightarrow ^4I_{9/2}$  and at 361 nm corresponding to  $^2P_{3/2} \rightarrow ^4I_{11/2}$  or  $^4D_{3/2} \rightarrow ^4I_{13/2}$  transition were observed. The intensity of the emission increased with the decrease of the particle size of  $\text{Nd}_2\text{O}_3$ .

Dhamale et al.<sup>33</sup> synthesized nanocrystalline  $\text{Nd}_2\text{O}_3$  with hexagonal structure through radiofrequency (RF) thermal plasma route. The TEM image of the synthesized  $\text{Nd}_2\text{O}_3$  nanoparticles exhibited the faceted morphology of the particles with good uniformity in size and shape, having average size around 20 nm. The thermoluminescence results showed that on comparing with its bulk there was an enhancement of the luminescent properties of the synthesized nanoparticles.

Goel et al.<sup>34</sup> investigated the mechanism of enhancing and quenching photoluminescence in  $\text{Nd}_2\text{O}_3$  nanoparticles—ferroelectric liquid crystal nanocomposites using UV-Vis and photoluminescence (PL) spectroscopy techniques. They had observed that emissions varied in accordance with the exciting wavelengths. They have recorded PL emission of pure  $\text{Nd}_2\text{O}_3$  nanoparticles at 205 nm, 248 nm, and 292 nm excitation wavelengths. The maximum emission intensity was observed for 248 nm excitation. The emission peaks obtained were in the range of ~345–397 nm, ~425–475 nm, ~545–560, and ~613 nm wavelength regions.

Neodymium oxide nanoparticles of various morphologies were synthesized by Kepinski et al.<sup>35</sup> using the hydrothermal method. It was observed that the structure and the morphology depended upon the temperature at which the reaction was carried out. At temperatures 200°C up to 400°C, fiber-like structures were observed. At 600°C flake-like structures occurred



which later changed into irregular morphology of an array of interconnected units at 800°C. There was a slow transformation from cubic to trigonal  $\text{Nd}_2\text{O}_3$  when the temperature approached 800°C.

Spherical and rod-like structures of  $\text{Nd}_2\text{O}_3$  nanocrystals were synthesized by Umesh et al.<sup>36</sup> using hydrothermal and combustion methods respectively. Spherical particles of size ranging from 20 to 100 nm were formed using the combustion method and nanorods of size ranging from 25 to 90 nm were formed in the hydrothermal method. The PL spectrum resulted in a series of emission bands in the UV, blue, green, and red regions as shown in Figure 9.4 which can find applications in display technology and can be promising candidates for white light emitting diodes (LEDs).

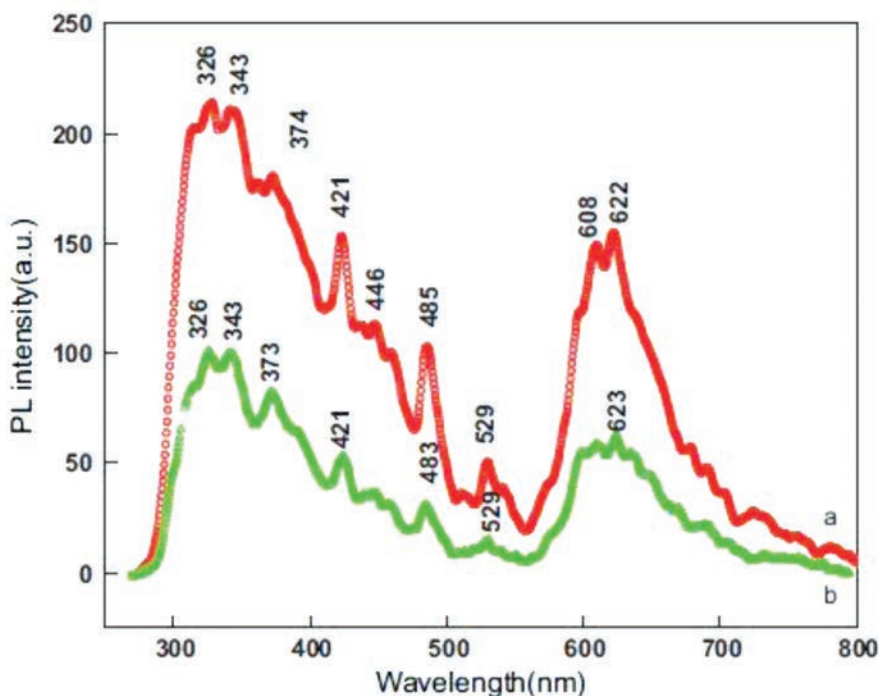


**FIGURE 9.4** PL spectra of  $\text{Nd}_2\text{O}_3$  calcinated at 900°C for 3h (a) combustion synthesis and (b) hydrothermal synthesis.

Antoinette et al.<sup>37</sup> synthesized pure and  $\text{Sm}^{3+}$  doped  $\text{Nd}_2\text{O}_3$  nanophosphors at 750°C using the modified Pechini method. The HRTEM results showed that the synthesized particles were around 25–35 nm and highly crystalline in nature. The optimal doping molar concentration was found to be 6% of

samarium which gave the maximum intensity peak at 397 nm which proved that these materials can have potential applications pertaining to solid-state lightings especially near-ultraviolet light-emitting diodes (NUV-LEDs).

### 9.4.3 GADOLINIUM (III) OXIDE

Gadolinium oxide ( $\text{Gd}_2\text{O}_3$ ) is chemically and thermally stable. Its melting point,  $2420^\circ\text{C}$  and density,  $7.41\text{ g cm}^{-3}$  make it a good host for both upconversion and down conversion process. Having a low phonon energy of around  $600\text{ cm}^{-1}$  and maximum number of unpaired electrons, makes it an efficient phosphor material. The luminescence efficiency is enhanced by doping it with other rare-earth ions.

Di et al.<sup>38</sup> reported the fabrication of the mesoporous gadolinium oxides using the solid-state thermal decomposition process. The mesoporous  $\text{Gd}_2\text{O}_3$  when doped with  $\text{Eu}^{3+}$  ions showed strong luminescence with a high quantum yield of 0.78. Strong luminescence and mesoporous nature of  $\text{Gd}_2\text{O}_3:\text{Eu}^{3+}$  indicated that these may be highly useful for biological uses as fluorescence labels and drug delivery vehicles.

$\text{Gd}_2\text{O}_3:\text{Eu}^{3+}$  nanopowders with cubic structure were prepared by the microwave-assisted hydrothermal method by de Moura et al.<sup>39</sup> FESEM images showed that the prepared  $\text{Gd}_2\text{O}_3:\text{Eu}^{3+}$  powders consisted of aggregated nanorods-like morphology with size ranging from 8 to 20 nm. Intense emission peak was observed at 612 nm when  $\text{Gd}_2\text{O}_3:\text{Eu}^{3+}$  nanopowders were excited at wavelength of 263 nm.

Zhou et al.<sup>40</sup> synthesized  $\text{Er}^{3+}$ ,  $\text{Yb}^{3+}$ , and  $\text{Tm}^{3+}$  ion-doped  $\text{Gd}_2\text{O}_3$  nanoparticles using the hydrothermal method in the presence of urea and glycerol. The doping resulted in strong upconversion (UC) fluorescence when it was excited at 980 nm. The *in vitro*/ *in vivo* optical imaging showed that these nanoparticles could be suitable for biomedical applications like bio-imaging.

Using the hydrothermal method, 1-D rod like  $\text{Eu}:\text{Gd}_2\text{O}_3$  red phosphor suitable for applications in the field of luminescent devices was successfully synthesized by Chang et al.<sup>41</sup> Upon UV illumination, strong emission was observed at 610 nm which confirmed that these can have potential applications in the field of luminescent devices.

Luminescence properties of monodisperse  $\text{Gd}_2\text{O}_3:\text{Eu}^{3+}$  were studied by Wang et al.<sup>42</sup> using the solvothermal method. Iron was used as a catalyst and Cetyltrimethyl Ammonium Bromide (CTAB) and Polyvinylpyrrolidone (PVP) were used as surfactants. Nanospheres of less than 100 nm were formed. Upon 253-nm excitation, intense emission was found at 612 nm.

By means of combustion synthesis, Jayasimhadri et al.<sup>43</sup> synthesized  $\text{Gd}_2\text{O}_3$  nanophosphors with and without doping of  $\text{Dy}^{3+}$  ions. Under UV excitation the  $\text{Gd}_2\text{O}_3$  nanophosphors exhibited green color and when it was doped with  $\text{Dy}^{3+}$  ions, it exhibited white color which proved that these nanophosphors could be used in flat panel displays.

Dhananjaya et al.<sup>44</sup> studied the effect of glycine, urea, citric acid, and ODH as fuel in the synthesis of  $\text{Gd}_2\text{O}_3$  nanoparticles. ODH fuel gave the most effective results in the case of photoluminescence studies as shown in Figure 9.5 while urea gave the best results in thermoluminescence studies. The photoluminescence studies revealed that these can be highly promising candidates for optical materials and light-emitting diodes. The thermoluminescence studies showed that it can be useful for radiation dosimetry.

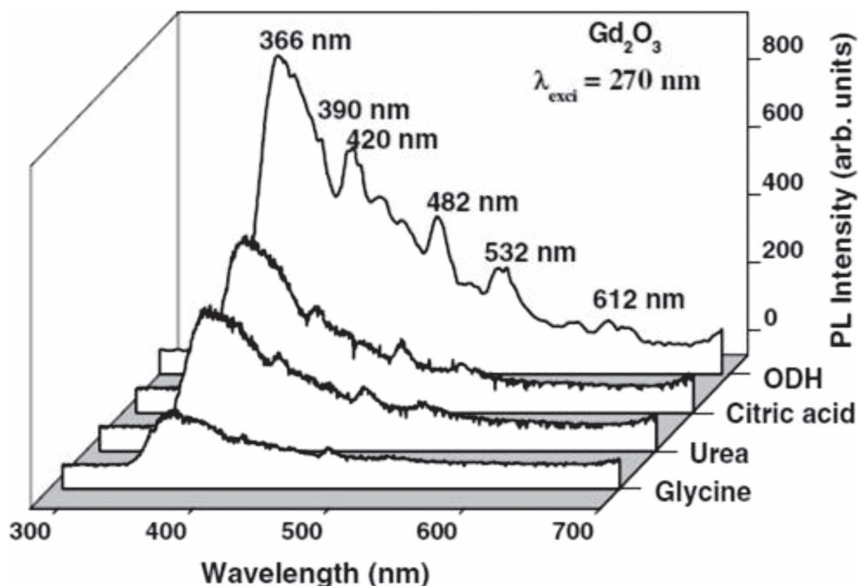


**FIGURE 9.5** PL emission spectra of  $\text{Gd}_2\text{O}_3$  nanoparticles synthesized using different fuels excited at a wavelength of 270 nm.

Dhananjaya et al.<sup>45</sup> compared the rod-like and spherical nanocrystalline  $\text{Gd}_2\text{O}_3:\text{Eu}^{3+}$  red phosphors obtained on synthesis using the hydrothermal and solution combustion methods. Cubic phase of  $\text{Gd}_2\text{O}_3:\text{Eu}^{3+}$  was observed after the calcination at  $800^\circ\text{C}$  for 3 hours using the combustion method and at  $600^\circ\text{C}$  for 3 hours using the hydrothermal method, respectively. Nanorods of around 15 nm and length in the range of about 50 to 150 nm were observed

from the TEM micrographs of hydrothermally prepared  $\text{Gd}_2\text{O}_3:\text{Eu}^{3+}$ , whereas particles of irregular shape were obtained from the combustion product with different sizes in the range 50–250 nm. In cubic  $\text{Gd}_2\text{O}_3:\text{Eu}^{3+}$ , intense red emission was observed at 612 nm when excited under 254 nm wavelength which shows that these can be promising candidates for high-performance display materials.

Tamrakar et al.<sup>46</sup> synthesized  $\text{Er}^{3+}$ -doped  $\text{Gd}_2\text{O}_3$  nanophosphors using the combustion synthesis method. It was found that the average crystallite size was around 28 nm for  $\text{Gd}_2\text{O}_3$  containing 1 mol%  $\text{Er}^{3+}$  concentration and around 38 nm for  $\text{Gd}_2\text{O}_3$  containing 2 mol%  $\text{Er}^{3+}$  concentration. The nanocrystals showed strong green visible photoluminescence under 275-nm excitation. There was an enhancement in the luminescence intensity with the increase of  $\text{Er}^{3+}$  ion concentration as well as with the increase of annealing temperature. From the emission spectra of the nanophosphor, it was observed that the  $\text{Gd}_2\text{O}_3:\text{Er}^{3+}$  phosphors showed downconversion process under 275-nm excitation.

Seo et al.<sup>47</sup> reported the controlled-shape synthesis of colloidal nanocrystalline  $\text{Gd}_2\text{O}_3:\text{Eu}^{3+}$  or  $\text{Tb}^{3+}$  using nonhydrolytic high-temperature solution growth methods. Different shapes like spheres, plates, and curved rods of  $\text{Gd}_2\text{O}_3$  nanocrystals were synthesized. It was found that the synthesis parameters, like type of metal precursor and surfactant, and their concentration ratio influenced the shape

of the nanocrystals. The emission intensity of the PL spectra of the rare earth doped  $\text{Gd}_2\text{O}_3$  was found to increase from nanoplates to nanospheres, as shown in Figure 9.6. This showed that the photoluminescence properties depended upon the doping efficiency, crystal structure, and ratio of surface to volume.

Tamrakar et al.<sup>48</sup> synthesized  $\text{Eu}^{3+}$ -doped  $\text{Gd}_2\text{O}_3$  with cubic structure using the solid-state reaction method. The crystallite size was found to be around 76 nm. The emission intensity for different doping concentrations showed that there was an increase for lower concentrations and then a decrease after a particular increase in the doping concentration. The increase in the emission intensity was due to the cross relaxation process taking place between two nearby  $\text{Eu}^{3+} \rightarrow \text{Eu}^{3+}$  ions. The emission intensity began to decrease after a particular concentration of  $\text{Eu}^{3+}$  ion with further increase in  $\text{Eu}^{3+}$  concentration due to  $\text{Eu}^{3+} \rightarrow \text{O}^{2-}$  energy transfer. It was also seen from the CIE diagram and the X and Y coordinates of CIE that tuning of the emitted color is possible if the same  $\text{Gd}_2\text{O}_3:\text{Eu}^{3+}$  phosphor is excited at various wavelengths.

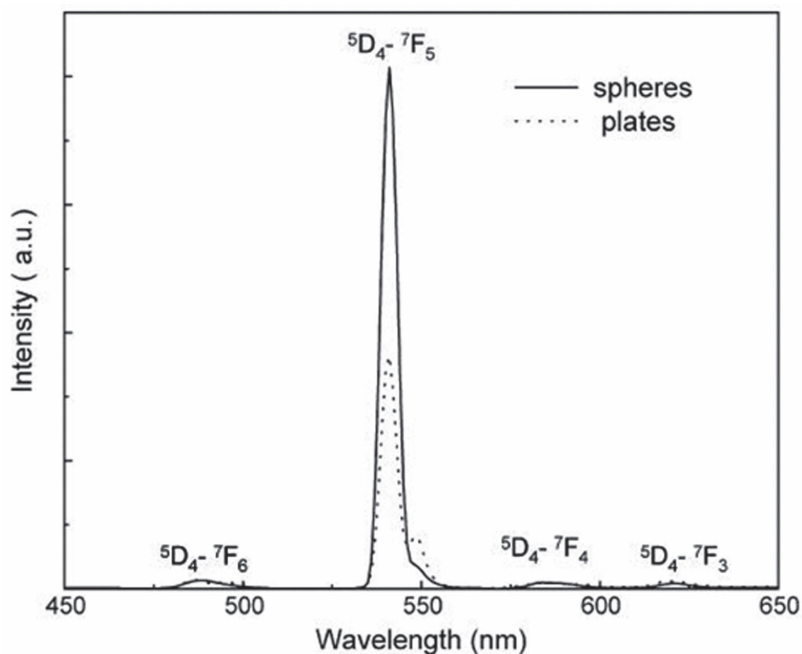


**FIGURE 9.6** PL emission spectra of  $\text{Gd}_2\text{O}_3:\text{Tb}^{3+}$  (10 mol%) nanocrystals

#### 9.4.4 DYSPROSIUM (III) OXIDE

Dysprosium oxide ( $\text{Dy}_2\text{O}_3$ ) is a basic metal oxide which is highly insoluble and thermally stable. It has a very high melting point of  $2420^\circ$  and density of  $7.41 \text{ g cm}^{-3}$ . The specific properties of dysprosium make it one of the important rare earth elements that can be used for various industrial applications. Dysprosium oxide crystallizes as a cubic structure at temperatures below  $1870^\circ\text{C}$ . It finds applications in optical and laser devices.

Chandrasekhar et al.<sup>49</sup> reported the synthesis of  $\text{Dy}_2\text{O}_3$  nanophosphor using the combustion method using sugar and oxalyl dihydrazine (ODH) as fuels. Thermoluminescence (TL) of  $\text{Dy}_2\text{O}_3$  was studied for both the samples by irradiating with gamma and UV rays. It was observed that TL intensity was more in gamma-irradiated  $\text{Dy}_2\text{O}_3$  nanophosphor and can be useful in radiation dosimetry for higher temperatures. Also, it was observed that the luminescence intensity in combustion synthesis can be tuned by varying the fuels as the PL intensity was high when ODH was used as the fuel when compared with sugar as shown in Figure 9.7. The inset of Figure 9.7 shows the PLE spectrum of  $\text{Dy}_2\text{O}_3$  nanophosphor

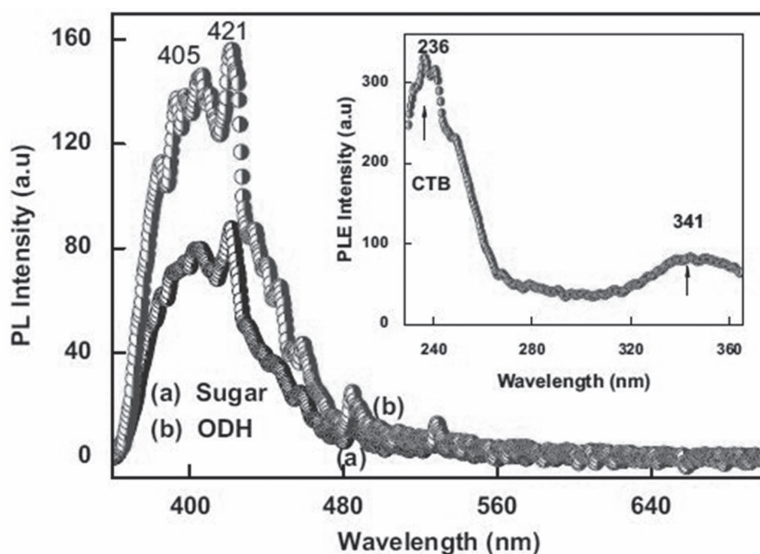


**FIGURE 9.7** PL emission spectra of  $\text{Dy}_2\text{O}_3$  nanophosphor synthesized using (a) sugar and (b) ODH fuel.

Sreethawong et al.<sup>50</sup> prepared mesoporous  $\text{Dy}_2\text{O}_3$  nanocrystal using the sol-gel method. They used laurylamine hydrochloride as the surfactant for the synthesis. The results of their studies revealed that mesoporous  $\text{Dy}_2\text{O}_3$  nanocrystal can be used in magneto-optical recording materials, catalytic applications, luminescence, optical and laser-based devices, glass additive, and rare-earth permanent magnet materials.

Han et al.<sup>51</sup> studied the photoluminescence properties of  $\text{Dy}_2\text{O}_3$  microspheres and tripod-like structures using the hydrothermal method. They observed that the PL intensity of  $\text{Dy}_2\text{O}_3$  tripod-like structures when compared to the microspheres was high which in turn may find novel applications in optical materials.

Chandar et al.<sup>52</sup> synthesized pure and gadolinium-doped  $\text{Dy}_2\text{O}_3$  nanoparticles using a wet chemical synthesis route. Structural, morphological, thermal, and optical studies were done. It was observed that the particle size, lattice parameters, and band gap energies depended on the dopant gadolinium. The XRD results confirmed the formation of pure and  $\text{Ce:Dy}_2\text{O}_3$  nanoparticles with the cubic structure. TEM micrograph showed the particle size of  $\text{Gd:Dy}_2\text{O}_3$  nanoparticles was around 10 nm. Enhanced optical absorption in the UV region was observed for Gd doped  $\text{Dy}_2\text{O}_3$ . The direct bandgap was found to be 4.03 and 4.26 eV for pure and Gd-doped  $\text{Dy}_2\text{O}_3$  respectively.

Strong emission in the visible region was observed which revealed that the prepared samples might find potential applications as photoluminescent and UV blocking materials.

Chandrasekhar et al.<sup>53</sup> reported the synthesis of  $\text{Dy}_2\text{O}_3$  nanopowders by co-precipitation and green combustion synthesis using *E. tirucalli* plant latex as the fuel. Rods and particles were observed from the SEM micrographs of the synthesized  $\text{Dy}_2\text{O}_3$  nanopowders using the co-precipitation and green combustion routes respectively. The TEM image showed that rods with different lengths and diameters of around 50–90 nm were formed using co-precipitation route and irregular shaped particles of average size around 40 nm were formed using green combustion routes. The emissions were observed at 481, 577, 666, and 756 nm for both the samples which matched well with the transitions of  $\text{Dy}^{3+}$  ions. Intense emission peak at 577 nm was observed in the case of co-precipitation route. The white emission was confirmed by the CIE diagram which revealed that the product can be highly effective in the fabrication of WLEDs.

Chandar et al.<sup>53</sup> prepared pure and cerium-doped  $\text{Dy}_2\text{O}_3$  nanoparticles using the wet chemical synthesis route. The XRD results revealed the formation of cubic bixbyite structure of pure and Ce:  $\text{Dy}_2\text{O}_3$  nanoparticles. The TEM micrographs confirmed that the particles were formed in nano regime and found to be around 10 nm. The band gap was found to decrease when cerium was doped from 4.26 to 4.01 eV. The PL spectrum given in Figure 9.8 showed emissions at 482 nm (blue), 575 nm (yellow), and 670 nm (red) and the difference in the emission intensity may be attributed to surface-specific defects. The strong white light emission shows that these materials can be used for optoelectronic or photoluminescent applications.

#### 9.4.5 SAMARIUM (III) OXIDE

Samarium oxide ( $\text{Sm}_2\text{O}_3$ ), an important rare earth oxide, has been widely studied as it possesses variable valence properties. Samarium oxide nanoparticles are both chemically and thermally stable, and are suitable for applications related to ceramics, glass, optics, catalysis, etc.<sup>54,55</sup>

Antoinette et al.<sup>56</sup> reported the synthesis of pure and  $\text{Ce}^{3+}$ -doped  $\text{Sm}_2\text{O}_3$  nanoparticles using the solvothermal method at 900°C. The HRTEM results of the synthesized nanoparticles showed that they were almost spherical in shape and in the size range of 14–26 nm. On 400-nm excitation, they showed a sharp emission band at 604 nm. The optimal doping molar concentration of cerium dopant in  $\text{Sm}_2\text{O}_3$ , which is responsible for the strong emission peak,

was found to be 4%. The CIE color co-ordinate values located in orange-red region revealed that these materials were promising candidates in applications for ultraviolet light-emitting diodes (UV-LEDs) and can be effectively used in near-UV LED chips for potential usage as WLEDs.

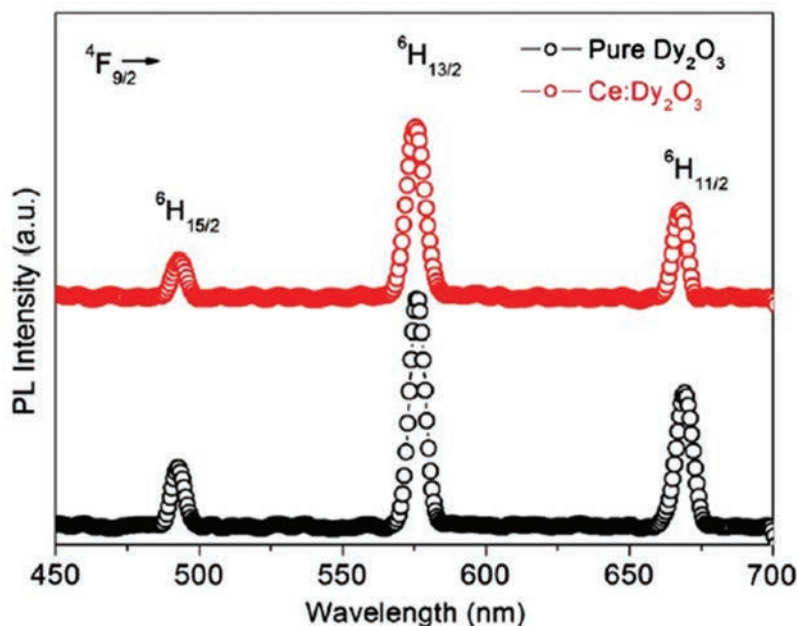


**FIGURE 9.8** PL spectra of the pure and Ce:  $\text{Dy}_2\text{O}_3$  particles calcined at  $600^\circ\text{C}$  in air.

Ghosh et al.<sup>57</sup> prepared  $\text{Sm}_2\text{O}_3$  particles with various morphologies nanoparticles like nanorods and nanoplates by solution-based techniques. Cetyl trimethyl ammonium bromide (CTAB) was used as surfactant, and their liquid mixtures were processed using the hydrothermal method. SEM micrographs showed that the particles were in nano range. The PL emission peaks were observed at 610 and 656 nm under excitation 370 nm, but when the excitation wavelength was tuned to 400 nm emission bands at 545, 610, and 656 nm were observed which showed that there was a chromatic change in the PL emission when the exciting wavelength was tuned.

Pure and  $\text{Gd}^{3+}$ -doped  $\text{Sm}_2\text{O}_3$  nanoparticles were synthesized using the combustion method by Antoinette et al.<sup>58</sup> The average crystallite size of the synthesized pure and  $\text{Gd}^{3+}$ -doped  $\text{Sm}_2\text{O}_3$  samples was found to be 4–9 nm. The optical band gap of the pure and  $\text{Gd}^{3+}$ -doped  $\text{Sm}_2\text{O}_3$  nanoparticles calculated from the UV-Vis-NIR absorption studies was found to be the least



at  $x=0.06$  which might be due to the concentration quenching. The optimal molar concentration of the  $Gd^{3+}$  dopant was found to be 6% which gave the highest emission intensity when excited at 404 nm. The CIE chromaticity diagram showed that the color of emission was orange-red which proved that these materials can have potential applications in solid-state lightings especially in white light-emitting diodes (W-LEDs).

#### 9.4.6 OTHER RARE EARTH OXIDES

Li et al.<sup>59</sup> synthesized  $Lu_2O_3:Yb^{3+},Tm^{3+}$  nanocrystals with cubic structure using the reverse-like co-precipitation method in which ammonium hydrogen carbonate was taken as the precipitant. They investigated on the effects of calcination temperature and the molar fractions of the dopants  $Tm^{3+}$ ,  $Yb^{3+}$  on the structural and upconversion luminescent properties of the prepared  $Lu_2O_3$  nanocrystals. The optimal molar concentrations of the dopants  $Tm^{3+}$  and  $Yb^{3+}$  were found to be 0.2% and 2%, respectively. Upon 980-nm laser excitation, strong blue (490 nm) and the weak red (653 nm) emissions were observed. The upconversion intensities gradually increased with the increase of temperature and may be due to the effect of the reducing number of OH-groups and the increase in the nanocrystal size. These nanocrystals were found to be useful in the development of upconversion ceramic laser.

$Lu_2O_3$  nanocrystals doped with Yb were synthesized by Galceran et al.<sup>60</sup> via the modified Pechini method using ethylenediaminetetra-acetic acid (EDTA), acting as a chelating agent and ethylene glycol (EG) as the polymerizing agent. The maximum emission at room temperature was at 1032 nm. Nanocrystals of size in the range 50–100 nm were formed. The observed optical absorption at 976 nm proved that these can be efficiently pumped by both Ti:Shapphire laser and diode around 940 nm, where absorbance was present.

Xiao et al.<sup>61</sup> reported the synthesis of nanostructured rare earth oxides  $Sm_2O_3$ ,  $Gd_2O_3$ ,  $Dy_2O_3$ , and  $Gd_2O_3:Eu^{3+}$  by using rare earth acetylacetonates as the starting materials. The synthesized  $Sm_2O_3$  consisted of stacks of ultrathin nanodisks and  $Gd_2O_3$  and  $Dy_2O_3$  were in the form of hierarchical nanosheet microspheres. Under ultraviolet excitation (260 nm),  $Gd_2O_3:Eu^{3+}$  nanophosphors showed strong red emission at 612 nm confirming that these will find potential applications in fluorescent lamps and field emission displays.

Mendez et al.<sup>62</sup> reported the synthesis of  $Eu^{3+}$ -doped  $La_2O_3$  nanocrystals using the modified Pechini method. TEM images show that agglomerated nanoparticles were formed in the range of 50 to 200 nm. Luminescent

properties investigated using photoluminescence and cathodoluminescence show similar results. The maximum emission intensity is observed at 626 nm, thus revealing that these can be used as red-emitting nanophosphors.

## 9.5 CONCLUSIONS

From the above-mentioned studies, we can conclude that pure and lanthanide-doped rare earth sesquioxides can be prepared by various methods which result in their unique structural, morphological properties which will in turn influence their luminescent behavior. The particle size also influences the luminescent properties. The emission intensities can be tuned by varying the fuels and the excitation wavelengths. On doping the lanthanide ions in rare earth sesquioxides, their photoluminescent properties can be enhanced. This makes these ions highly useful in the potential applications in the modern-day industrial and optical technologies. There are only a few reported literatures on the synthesis and applications of lanthanide-doped rare earth sesquioxides and there is a lot more to be explored.

## ACKNOWLEDGMENTS

One of the authors, Morris Marieli Antoinette, is grateful to the Management, St. Joseph's College for Women, Alappuzha for their continued encouragement and support.

## KEYWORDS

- rare earth sesquioxides
- photoluminescence

## REFERENCES

1. Wybourne, B. G. *Spectroscopic Properties of Rare Earths*; Wiley-Interscience: New York, 1965.
2. Liu, G., Jacquier, B. *Spectroscopic Properties of Rare Earths in Optical Materials*, Vol. 83, Springer Series in Materials Science; Springer: Berlin, 2005.

3. Van den Eeckhout, K.; Smet, P. F.; Poelman, D. Persistent Luminescence in  $\text{Eu}^{2+}$ -Doped Compounds: A Review. *Materials* **2010**, *3*, 2536–2566.
4. Saines, P. J.; Elcombe, M. M.; Kennedy, B. J.; Lanthanide Distribution in Some Doped Alkaline Earth Aluminates and Gallates. *J. Solid State Chem.* **2006**, *179*, 613–622.
5. Kim, D. Recent Developments in Lanthanide-Doped Alkaline Earth Aluminate Phosphors with Enhanced and Long-Persistent Luminescence. *Nanomaterials* **2021**, *11*, 723.
6. Dieke, G. H.; Crosswhite, H. M. The Spectra of the Doubly and Triply Ionized Rare Earths. *Appl. Optics*. **1963**, *2*, 675–686.
7. Hodgson, G. K.; Impellizzeri, S.; Scaiano, J. C. Single Molecule Study of Samarium Oxide Nanoparticles as a Purely Heterogeneous Catalyst for One- Pot Aldehyde Chemistry. *Catal. Sci. Technol.* **2016**. DOI: 10.1039/C6CY00894A.
8. Gao, J., Zhao, Y., W. Yang, Tian, J., F. Guan, Ma, Y., Hou, J., Kang, J., Wang, Y., Preparation of Samarium Oxide Nanoparticles and Its Catalytic Activity on the Esterification. *Mater. Chem. Phys.* **2001**, *77*, 65–69.
9. Michel, C. R.; Martinez-Preciado, A. H.; Parra, R.; Aldao, C. M.; Ponce, M. A. Novel  $\text{CO}_2$  and  $\text{CO}$  Gas Sensor Based on Nanostructured  $\text{Sm}_2\text{O}_3$  Hollow Microspheres. *Sens. Actuator B* **2014**, *202*, 1220–1228.
10. Dhananjaya, N.; Nagabhushana, H.; Sharma, S. C.; Rudraswamy, B.; Shivakumara, C.; Nagabhushana, B. M. Hydrothermal Synthesis of  $\text{Gd}_2\text{O}_3:\text{Eu}^{3+}$  Nanophosphors: Effect of Surfactant on Structural and Luminescence Properties. *J. Alloys Compd.* **2014**, *587*, 755–762.
11. Zhou, L.; Gu, Z.; Liu, X.; Yin, W.; Tian, G.; Yan, L.; Jin, S.; Ren, W.; Xing, G.; Li, W.; Chang, X.; Hu, Z.; Zhao, Y. Size-Tunable Synthesis of Lanthanide-Doped  $\text{Gd}_2\text{O}_3$  Nanoparticles and Their Applications for Optical and Magnetic Resonance Imaging. *J. Mater. Chem.*, **2012**, *22*, 966.
12. Di, W.; Ren, X.; Zhang, L.; Liu, C.; Lu, S. A Facile Template-Free Route to Fabricate Highly Luminescent Mesoporous Gadolinium Oxides. *Cryst. Eng. Commun.*, **2011**, *13*, 4831–4833.
13. Rao, G. V. S.; Ramdas, S.; Mehrotra, P. N.; Rao, C. N. R. Electrical Transport in Rare-Earth Oxides. *J. Solid State Chem.* **1970**, *2*, 377–384.
14. Chattopadhyay, K. K.; Banerjee, A. N. *Introduction to Nanoscience and Nanotechnology*; PHI Learning Private Limited: New Delhi, 2012.
15. Prasad Paras, N. *Nanophotonics*; John Wiley & Sons, Inc., Publication, 2004.
16. Zawadzki, M. Microwave-Assisted Synthesis and Characterization of Ultrafine Neodymium Oxide Particles. *J. Alloys Compd.* **2008**, *451*, 297–300.
17. Yang, J.; Quan, Z.; Kong, D.; Liu, X.; Lin, J.  $\text{Y}_2\text{O}_3:\text{Eu}^{3+}$  Microspheres: Solvothermal Synthesis and Luminescence Properties. *Cryst. Growth Des.* **2007**, *7*, 730–735.
18. Liu, L.; Jiang, H.; Chen, Y.; Zhang, X.; Zhang, Z.; Wang, Y. Power Dependence of Upconversion Luminescence of  $\text{Er}^{3+}$  Doped Yttria Nanocrystals and Their Bulk Counterpart. *J. Lumin.* **2013**, *143*, 423–431.
19. Liu, G.; Hong, G.; Wang, J.; Dong, X. Hydrothermal Synthesis of Spherical and Hollow  $\text{Gd}_2\text{O}_3:\text{Eu}^{3+}$  Phosphors. *J. Alloys Compd.* **2007**, *432*, 200.
20. Fu, Y. P.; Wen, S. B.; Hsu, C. S. Preparation and Characterization of  $\text{Y}_3\text{Al}_5\text{O}_{12}:\text{Ce}$  and  $\text{Y}_2\text{O}_3:\text{Eu}$  Phosphors Powders by Combustion Process. *J. Alloys Compd.* **2008**, *458*, 318–322.
21. Chandrasekhar, M.; Nagabhushana H.; Sudheerkumar K. H.; Dhananjaya N.; Sharma S. C.; Kavyashree D.; Shivakumara C.; Nagabhushana B. M. Comparison of Structural and

- Luminescence Properties of  $\text{Dy}_2\text{O}_3$  Nanopowders Synthesized by Co-Precipitation and Green Combustion Routes. *Mater. Res. Bull.* **2014**, *55*, 237–245.
22. Zhang, Q. Y.; Huang, X. Y. Recent Progress in Quantum Cutting Phosphors. *Prog. Mater. Sci.* **2010**, *55*, 353–427.
23. Peng, Y.; Chen, X.; Gao, Z. Determination of Trace Amounts of Mercury Using Hierarchically Nanostructured Europium Oxide. *Talanta* **2010**, *82*, 1924–1928.
24. Sreethawong, T.; Chavadej, S.; Ngamsinlapasathian, S.; Yoshikawa, S. Sol–Gel Synthesis of Mesoporous Assembly of  $\text{Nd}_2\text{O}_3$  Nanocrystals with the Aid of Structure-Directing Surfactant. *Solid State Sci.* **2008**, *10*, 20–25.
25. Bazzi, R.; Flores-Gonzalez, M. A.; Louis, C.; Lebbou, K.; Dujardin, C.; Brenier, A.; Zhang, W.; Tillement, O.; Bernstein, E.; Perriat, P. Synthesis and Luminescent Properties of Sub-5-nm Lanthanide Oxides Nanoparticles. *J. Lumin.* **2003**, *102*, 445–450.
26. Soliman, C. Neodymium Oxide: A New Thermoluminescent Material for Gamma Dosimetry. *Nucl. Instrum. Methods Phys. Res. B* **2006**, *251*, 441–444.
27. Zawadzki, M.; Kepinski, L. Synthesis and Characterization of Neodymium Oxide Nanoparticles. *J. Alloys Compd.* **2004**, *380*, 255–259.
28. Zhaorigetu, B.; Ga, R.; Li, M. Preparation of  $\text{Nd}_2\text{O}_3$  Nanoparticles by Tartrate Route. *J. Alloys Compd.* **2007**, *427*, 235–237.
29. Kosola, A.; Paivasaari J.; Putkonen M.; Niinisto L. Neodymium Oxide and Neodymium Aluminate Thin Films by Atomic Layer Deposition. *Thin Solid Films* **2005**, *79*, 152–159.
30. Que, W.; Kam, C. H.; Zhou, Y.; Lam, Y. L.; Chan, Y. C. Yellow-to- Violet Upconversion in Neodymium Oxide Nanocrystals/Titania/Ormosil Composite Sol–Gel Films Derived at Low Temperature. *J. Appl. Phys.* **2001**, *90*, 4865–4867.
31. Lupei, V.; Lupei, A.; Ikesue, A. Transparent Nd and (Nd, Yb)—Doped  $\text{Sc}_2\text{O}_3$  Ceramics as Potential New Laser Materials. *Appl. Phys. Lett.* **2005**, *86*, 111118.
32. Jian-Hua, R.; Tong-Gang, Z.; Jian-Hua, L.; Juan, K.; Jia-Xin, H.; Lin, G. Synthesis and Photoluminescence Properties of  $\text{Nd}_2\text{O}_3$  Nanoparticles Modified by Sodium bis(2-Ethylhexyl) Sulfosuccinate. *Chin. Phys. B.* **2008**, *17*, 4669–4672.
33. Dhamale, G. D.; Mathe, V. L.; Bhoraskar, S. V.; Sahasrabudhe, S. N.; Dhole, S. D.; Ghorui, S. Synthesis and Characterization of  $\text{Nd}_2\text{O}_3$  Nanoparticles in a Radiofrequency Thermal Plasma Reactor. *Nanotechnology* **2016**, *27*, 085603.
34. Goel, P.; Arora, M. Mechanism of Photoluminescence Enhancement and Quenching in  $\text{Nd}_2\text{O}_3$  Nanoparticles–Ferroelectric Liquid Crystal Nanocomposites. *RSC Adv.* **2015**, *5*, 14974.
35. Kepinski, L.; Zawadzki, M.; Mista, W. Hydrothermal Synthesis of Precursors of Neodymium Oxide Nanoparticles. *Solid State Sci.* **2004**, *6*, 1327–1336.
36. Umesh, B.; Eraiah, B.; Nagabhushana, H.; Nagabhushana, B.M; Nagaraja, G.; Shivakumara, C.; Chakradhar, R. P. S. Synthesis and Characterization of Spherical and Rod Like Nanocrystalline  $\text{Nd}_2\text{O}_3$  Phosphors. *J. Alloys Compd.* **2011**, *509*, 1146–1151.
37. Antoinette, M. M.; Israel, S.; Sathya, G.; Amali, A. J.; Berchmans, J. L.; Sujatha, K.; Anzline C.; Devi, R. N. Experimental Charge Density Distribution and Its Correlation to Structural and Optical Properties of  $\text{Sm}_3+$  Doped  $\text{Nd}_2\text{O}_3$  Nanophosphors. *J. Rare Earths* **2017**, *35*, 1102–1114.
38. Di, W.; Ren, X.; Zhang, L.; Liu, C.; Lu, S. A Facile Template-Free Route to Fabricate Highly Luminescent Mesoporous Gadolinium Oxides. *CrystEnggComm* **2011**, *13*, 4831–4833.
39. de Moura, A. P.; Oliveira, L. H.; Nogueira, I. C.; Pereira, P. F. S.; Li, M. S.; Longo, E.; Varela, J. A.; Rosa, I. L. V. Synthesis, Structural and Photophysical Properties of

- Gd<sub>2</sub>O<sub>3</sub>:Eu<sup>3+</sup> Nanostructures Prepared by a Microwave Sintering Process. *Adv. Chem. Eng. Sci.* **2014**, *4*, 374–388.
40. Zhou, L.; Gu, Z.; Liu, X.; Yin, W.; Tian, G.; Yan, L.; Jin, S.; Ren, W.; Xing, G.; Li, W.; Chang, X.; Hu, Z.; Zhao, Y. Size-Tunable Synthesis of Lanthanide-Doped Gd<sub>2</sub>O<sub>3</sub> Nanoparticles and Their Applications for Optical and Magnetic Resonance Imaging. *J. Mater. Chem.* **2012**, *22*, 966–974.
  41. Chang, C.; Kimura, F.; Kimura, T.; Wada, H. Preparation and Characterization of Rod-Like Eu: Gd<sub>2</sub>O<sub>3</sub> Phosphor Through a Hydrothermal Routine. *Mater. Lett.* **2005**, *59*, 1037–1041.
  42. Wang, Y.; Bai, X.; Liu, T.; Dong, B.; Xu, L.; Liu, Q.; Song, H. Solvothermal Synthesis and Luminescence Properties of Monodisperse Gd<sub>2</sub>O<sub>3</sub>: Eu<sup>3+</sup> and Gd<sub>2</sub>O<sub>3</sub>:Eu<sup>3+</sup>@SiO<sub>2</sub> Nanospheres. *J. Solid State Chem.* **2010**, *183*, 2779–2785.
  43. Jayasimhadri, M.; Ratnam, B. V.; Jang, K.; Lee, H. S.; Yi, S.-S.; Jeong, J.-H. Conversion of Green Emission into White Light in Gd<sub>2</sub>O<sub>3</sub> Nanophosphors. *Thin Solid Films* **2010**, *518*, 6210–6213.
  44. Dhananjaya, N.; Nagabhushana, H.; Nagabhushana, B. M.; Rudraswamy, B.; Sharma, S. C.; Sunitha, D. V.; Shivakumara, C.; Chakradhar, R. P. S. Effect of Different Fuels on Structural, Thermo and Photoluminescent Properties of Gd<sub>2</sub>O<sub>3</sub> Nanoparticles. *Spectrochim. Acta, Part A* **2012**, *96*, 532–540.
  45. Dhananjaya, N.; Nagabhushana, H.; Nagabhushana, B. M.; Rudraswamy, B.; Shivakumara, C.; Chakradhar, R. P. S. Spherical and Rod-Like Gd<sub>2</sub>O<sub>3</sub>:Eu<sup>3+</sup> Nanophosphors—Structural and Luminescent Properties. *Bull. Mater. Sci.* **2012**, *35*, 519–527.
  46. Tamrakar, R. K.; Bisen, D. P.; K. Upadhyay; Sahu, I. P.; Sahu, M. The Down Conversion Properties of a Gd<sub>2</sub>O<sub>3</sub>:Er<sup>3+</sup> Phosphor Prepared via a Combustion Synthesis Method. *RSC Adv.* **2016**, *6*, 92360–92370.
  47. Seo, S.; Yang, H.; Holloway, P. H. Controlled Shape Growth of Eu- or Tb- Doped Luminescent Gd<sub>2</sub>O<sub>3</sub> Colloidal Nanocrystals. *J. Colloid Interface. Sci.* **2009**, *331*, 236–242.
  48. Tamrakar, R. K.; Upadhyay, K.; Sahu, I. P.; Bisen, D. P. Tuning of Photoluminescence Emission Properties of Eu<sup>3+</sup>doped Gd<sub>2</sub>O<sub>3</sub> by Different Excitations. *Optik.* **2017**, *135*, 281–289.
  49. Chandrasekhar, M.; Sunitha, D. V.; Dhananjaya, N.; Nagabhushana, H.; Sharma, S. C.; Nagabhushana, B. M.; Shivakumara, C.; Chakradhar, R. P. S.; Thermoluminescence Response in Gamma and UV Irradiated Dy<sub>2</sub>O<sub>3</sub> Nanophosphor. *J. Lumin.* **2012**, *132*, 1798–1806.
  50. Sreethawong, T.; Chavadej, S.; Ngamsinlapasathian, S.; Yoshikawa, S. A Simple Route Utilizing Surfactant-Assisted Templating Sol–Gel Process for Synthesis of Mesoporous Dy<sub>2</sub>O<sub>3</sub> Nanocrystal. *J. Colloid Interface. Sci.* **2006**, *300*, 219–224.
  51. Han, K.; Zhang, Y.; Cheng, T.; Fang, Z.; Gao, M.; Xu, Z.; Yin, X. Self-Assembled Synthesis and Photoluminescence Properties of Uniform Dy<sub>2</sub>O<sub>3</sub> Microspheres and Tripod-Like Structures. *Mater. Chem. Phys.* **2009**, *114*, 430–433.
  52. Chandar, N. K.; Jayavel, R. Room Temperature Synthesis and Properties of Pure and Gadolinium Doped Dy<sub>2</sub>O<sub>3</sub> Nanoparticles. *Adv. Mat. Res.* **2012**, *584*, 285–289.
  53. Chandar, N. K.; Jayavel, R. Wet Chemical Synthesis and Characterization Of Pure And Cerium Doped Dy<sub>2</sub>O<sub>3</sub> Nanoparticles. *J. Phys. Chem. Solids.* **2012**, *73*, 1164–1169.
  54. Hodgson, G. K.; Impellizzeri, S.; L Hallett-Tapley, G.; Scaiano, J. C. Photochemical Synthesis and Characterization of Novel Samarium Oxide Nanoparticles: Toward a Heterogeneous Bronsted Acid Catalyst. *RSC Adv.* **2015**, *5*, 3728.

55. El-Zaiat, S. Y.; El-Den, M. B.; El-Kameesy, S. U.; El-Gammam, Y. A. Spectral Dispersion Of Linear Optical Properties For  $\text{Sm}_2\text{O}_3$  Doped  $\text{B}_2\text{O}_3$ – $\text{PbO}$ – $\text{Al}_2\text{O}_3$  Glasses. *Opt. Laser Technol.* **2012**, *44*, 1270.
56. Antoinette, M. M.; Israel, S.; Amali, A. J.; Berchmans, J. L.; Kumar, B. S.; Manoj G. J.; Usmaniya, U. M. A Novel Synthesis of Orange-Red Emitting  $(\text{Sm}_{1-x}\text{Ce}_x)_2\text{O}_3$  Nanophosphors for UV LEDs. *Nano Struct. Nano Objects* **2018**, *13*, 51–58.
57. P. Ghosh, S. Kundu, A. Kar, Ramanujachary, K. V., S. Lofland, A. Patra, Synthesis and Characterization of Different Shaped  $\text{Sm}_2\text{O}_3$  Nanocrystals. *J. Phys. D: Appl. Phys.* **2010**, *43*, 405401.
58. Antoinette, M. M.; Israel, S.; Berchmans, J. L.; Manoj, G. J. Enhanced Photoluminescence and Charge Density Studies of Novel  $(\text{Sm}_{1-x}\text{Gd}_x)_2\text{O}_3$  Nanophosphors for LED Applications. *J. Mater. Sci.: Mater. Electron.* **2018**. doi:10.1007/s10854–018- 00661.
59. Li, L.; Xue-qin, C.; You, Z.; Chang-xin, G. Synthesis and Upconversion Luminescence of  $\text{Lu}_2\text{O}_3\text{:Yb}_3^+, \text{Tm}_3^+$  Nanocrystals. *Trans. Nonferrous Met. Soc. China* **2012**, *22*, 373–379.
60. Galceran, M.; Pujol, M. C.; Aguilo, M.; Diaz, F. Synthesis and Characterization of Nanocrystalline  $\text{Yb:Lu}_2\text{O}_3$  by Modified Pechini Method. *Mat. Sci. Eng. B.* 2008, *146*, 7–15.
61. Xiao, H.; Li, P.; Jia, F.; Zhang, L. General Nonaqueous Sol–Gel Synthesis of Nanostructured  $\text{Sm}_2\text{O}_3$ ,  $\text{Gd}_2\text{O}_3$ ,  $\text{Dy}_2\text{O}_3$ , and  $\text{Gd}_2\text{O}_3\text{:Eu}^{3+}$  Phosphor. *J. Phys. Chem. C* **2009**, *113*, 21034–21041.
62. Mendez, M.; Carvajal, J. J.; Cesteros, Y.; Aguilo, M.; Díaz, F.; Giguere, A.; Drouin, D.; Martinez-Ferrero, E.; Salagre, P.; Formentin, P.; Pallares, J.; Marsal, L. F. Sol–Gel Pechini Synthesis and Optical Spectroscopy of Nanocrystalline  $\text{La}_2\text{O}_3$  Doped with  $\text{Eu}^{3+}$ . *Opt. Mater.* **2010**, *32*, 1686–1692.



## CHAPTER 10

---

# Composites and their Applications in Light-Source-Enhanced Destruction of Organic Wastes

I. PRABHA

*Department of Chemistry, Bharathiar University, Coimbatore, Tamil Nadu, India*

---

### ABSTRACT

The synthesis, characterization, and applications of metal oxide nanocomposites, metal nanoparticles, and substrate-supported nanomaterials have been undergone the studies for various properties and applications. Wide band-gap mixed semiconductor materials extensively attracted a great deal of consideration from experimental and theoretical view points, due to their potential advantages in natural light energy renovation, light-mediated catalysis from their size-dependent optical properties. Compared to bulk semiconductors, nanocomposites are focused in the research in functional-based materials due to the evidence of novel electrical, catalytic, and optical nonlinear, photoelectric switch and piezoelectric properties. One of the material terminologies like surface influences the luminescence behaviors of mixed semiconductor nanomaterials. This chapter deals about the brief introduction about the nanocomposite materials with some suitable examples, efficient properties, and applications. Next, it elaborates the categorization, advantages, and economical applications of nanocomposites. One of the nanophotocomposites ZnO-TiO<sub>2</sub> has been selected and the reactive red 198 dye as a model compound for the photocatalytic degradation reaction in UV light source. In these experimental studies photodegradability of the nanocatalyst, effect of incident wavelength, effect of concentration of the dye,

---

Functional Nanocomposites and Their Applications. Dhanya K. R., Sanal P. S., Sabu Thomas, & Nandakumar Kalarikkal (Eds.)

© 2025 Apple Academic Press, Inc. Co-published with CRC Press (Taylor & Francis)



and the total organic carbon analysis were done. The experimental results showed that ZnO-TiO<sub>2</sub> nanocomposite particles displayed significant UV absorption and effective transparency. The photolight-supported efficiency of ZnO-TiO<sub>2</sub> material is appropriate for the reduction of organic contaminants in the wastewater.

## **10.1 INTRODUCTION**

Nanotechnology is an empowering scientific field that has evidenced in humanizing numerous life aspects ranging from Medication to Industrial materials. It has been a relentless endeavor of mankind to improve existing technologies and materials to attain maximum potentialities. Many exotic structural materials have been developed and one of the most promising materials is advanced composites. This branch of materials includes a wide variety of combinations of reinforcements and matrices and the usual reinforcements have the smallest dimension in micrometer. With the advent of nanotechnologies, the interest of scientists and engineers has enormously increased in the development of nanocomposites which have one phase, usually called reinforcing phase on nanometric scale. Like regular advanced composites, composites exhibited a variety of material options in reinforcement and matrices. Among these properties, physical, mechanical, chemical, thermal, and optical properties are much specific and unique which tends the benefits of industrial side and in effective engineering fields for upcoming challenges and demands. The behavior of the nanomaterials is majorly based on their matrix and reinforcement. Heterogeneous chemical species as reinforcement and matrices to obtain nanocomposites with different properties are known to be multi-functional. Nanocomposites are the new generation of novel materials formed by mixing of one or more dissimilar materials to control as well as develop new and improved structural materials with advanced properties.

It incorporates a wide range of materials from dimensional lamellar defining many variations of nano-mixed and layered materials. The properties of nanocomposites depend on the usage of individual components, morphology, and the interface characteristics. Active materials and smart structures provide a wealth of novel opportunities to human ingenuity and engineering technology. It has the attributes of adaptability, flexibility, and intelligence. The active materials with nanostructures are enabling factors that make smart composite structures with unique properties and applications.

Some of the specific composites are discussed along with their properties and its applications. Zn-Al-based nanocomposites have been continued to find relevance in several technological applications<sup>1</sup> due to the sustainable combination of physical, mechanical, and technological properties such as high strength, excellency in physico-chemical properties. It has been formed between the MWCNTs and the Cu-Cr matrix which enhance the strength of the composites.

Carbon nanotubes (CNTs) could be the ideal reinforcement for composite materials due to their excellent properties such as high tensile strength ( $\sim 110$  GPa), high Young's modulus ( $\sim 1$  TPa), superior thermal conductivity ( $\sim 3000 \text{ W m}^{-1} \text{ K}^{-1}$ ), and good electrical conductivity ( $\sim 2 \times 10^7 \text{ s m}^{-1}$ ). Recently, extensive attention has been paid to multi-walled carbon nanotubes (MWCNT) reinforced by metal matrix composites (MMCs). The challenge of uniformly dispersing MWCNTs need to be addressed in order to fully exploit the excellent properties of MWCNTs incorporated in MMCs. In current eras, there are more advanced synthesized techniques that are offered, for example, high-energy ball milling, flake powder metallurgy, polymer pyrolysis, chemical vapor deposition, friction stir-processing, and in-situ growth have been employed to disperse the MWCNTs into the Al matrix. The ultimate tensile strength (UTS) of pure Al, which has improved only by 21%, by incorporating of 2.6% of MWCNTs, which are effectively and remarkably increasing the intrinsic behavior of MWCNTs has not fully exploited.<sup>2</sup>

### **10.1.1 CLASSIFICATION OF COMPOSITES IN NANOTECHNOLOGY**

Investigating the various fields of composites in the nanoworld, different nanotechnologies have been developed. Generally, technologies are classified into three groups such as composites of wet nanotechnology, dry nanotechnology, and computational nanotechnology. Wet nanotechnology deals with biological processes and management systems primarily existing water in environments. The nanocomposites have been investigated in wet nanotechnology mainly consisting of membranes, enzymes, DNA, additional cellular components, and function. Dry technology is emerged from physical chemistry and surface sciences. This is concentrate on the synthesis and characterization of nanostructured composites in dry environment such as carbon nanocomposites and silicon nanocomposites. In the computational nanotechnology, the analytical and predictive power of computation is used to model and stimulate complicated nanocomposite materials and its structures.

### **10.1.2 ADVANTAGES OF NANOCOMPOSITE MATERIALS**

- Displays a lower specific gravity
- Indicates the advanced stiffness of nanomaterials
- Maintains the authentic weight at applied temperature
- Shows improved and constant toughness throughout the process reproducibility and fabrication method is the easier
- Keeps the better fatigue and creep strength as the constant
- Brings the controlled electrical conductivity
- Confirms the resistance to corrosion and oxidation
- Exhibits extremely high thermal conductivity
- Specifies extremely high stiffness
- Sustains low density of carbon fiber-reinforced polymers

### **10.1.3 APPLICATIONS OF NANOCOMPOSITE MATERIALS**

It shows the excellent contribution in Automobile Industries such as Steel and Aluminum body.

It finds applications in Marine engineering. Examples: Shafts, hulls, and spars (racing boats)

It gives the tremendous applications to the field of Aeronautical.

It provides the outstanding services in electronic and communication technologies such as PCB, etc.

It displays merits in safety equipment like ballistic protection and air bags of cars etc.

### **10.1.4 METAL, POLYMER, AND GREEN SUPPORTED NANOCOMPOSITES**

The novel metal nanocomposites show a variety of unconventional uses in multidisciplinary areas like, for example, alteration of natural resource into thermal remedy which is recently implemented efficiently for the application of tumor therapy and in anticancer drug doxorubicin.

Due to the variation in the heat energy the magnetic nanocomposites have been used in the measurement of heat energy which is conducted using a high radio frequency.

Nowadays, there is an increasing interest about the synthesis of cellulose mediated polymeric composites and micro or nanohydroxyapatite particles,

mainly used for osteo integration. The prime reason for this is the widespread nature of cellulose due to (the material with the highest abundance  $5 \times 10^{11}$  tons generated annually in the biosphere), good mechanical strength, thermal stability, and easy availability.

Applications of polymer-supported nanocomposites are observed in aerospace such as wings, fuselages, landing gears, rudders/elevators, rotor, blades, and satellite structures etc. It enhances frames, bumpers, leaf springs, drive shafts, seat housing, tires, and other ground transportation vehicles (bullet train). It gives the evidences in marine engineering (e.g., Catamaran) such as the boat hulls, decks, masts, propeller shafts, and wind surfer. It shows the applications in various parts of the chemical plants such as the process pipes, tanks, pressure vessels, and oil field structures.

### 10.1.5 GREEN NANOCOMPOSITES

Figure 10.1 shows the synthesis of green composites. The advancement of green composite materials can be (economically) competitive replacements for Glass Fibre Reinforced Polymer (GFRP) composites which is an important area of research. Green' composite is to be classified and is an alternative to the sustainable composites; the manufacture, use, and disposal phases need to be considered.

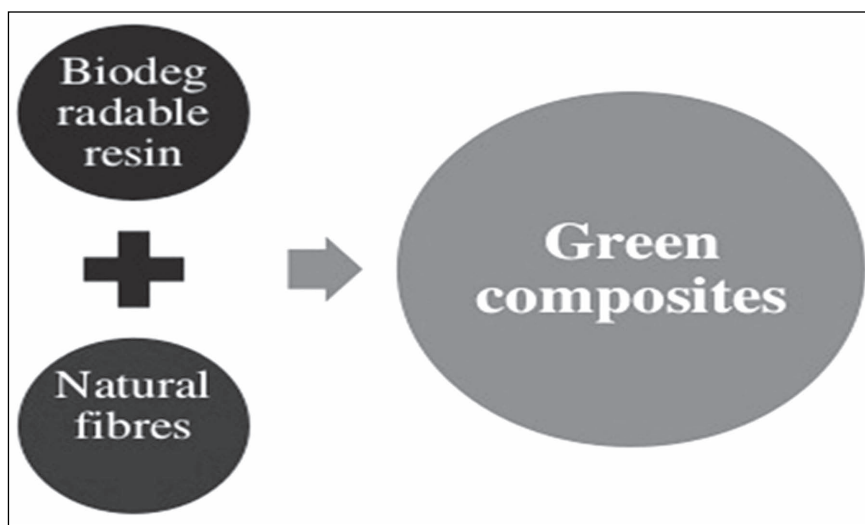


**FIGURE 10.1** Fabrication of green composites.

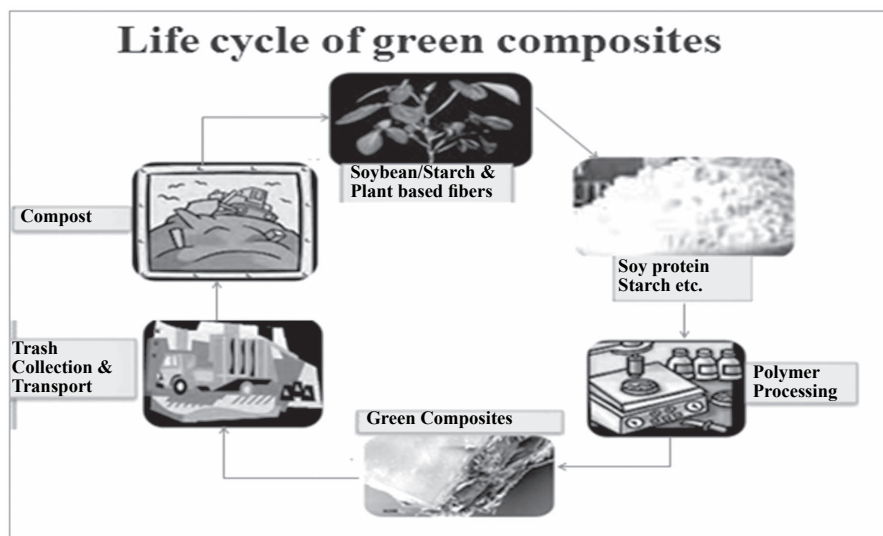


**FIGURE 10.2** Green composites pathway.

The fabrication of composite material attained by the accumulation of ordinary or artificial fibers to polymer matrices allows improving the mechanical and thermal properties. Natural fibers such as hemp, flax, kenaf, jute, abaca, sisal, and agave serve as reinforcements, offering numerous advantages when compared to artificial fibers including low density, renewability, biodegradability, low-cost, non-hazardous nature and favorable physico-chemical properties.<sup>3</sup> Green composites, which are a combination of ordinary fibers and biopolymers, have emerged as an eco-friendly and more effective alternative to conventional composites. Figure 10.2 illustrates the pathway of green composites. Flax fabric (FF) process is very low-price and strongest (high tensile strength and low elongation) composites that are made from natural flax fibers of cellulose.<sup>4</sup> It possesses low density with low water absorption capacity (7%) compared with other natural fibers and effective vibration absorbing and ultraviolet ray blocking properties. Due to significant properties, fabric-based composites have been developed with good mechanical properties with marine and automotive use and in wind turbine blades. In recent years, flame-retardant composites have gained much importance. Biodegradable materials found on starch or FF are applicable in packaging technology (bottles and antistatic etc.) and agricultural sectors (mulch and controlled released devices).<sup>5</sup> An appropriate flame-retardant incorporation would essentially impart flame

retardant properties to the composites. Halogen-less fire retardants achieve the significance owing to a variety of ecological concerns.<sup>6</sup> Ammonium polyphosphate (APP) is one of the applications such as fire retardant and tumescent composite to facilitate in the group of the focused matter. In addition, the advantage of APP is that after disposal, the major ingredients of APP, nitrogen, and phosphorus mingle with top soil and take fertility on the way to the earth. Figure 10.3 represents the multifunctional applications of nanocomposites.

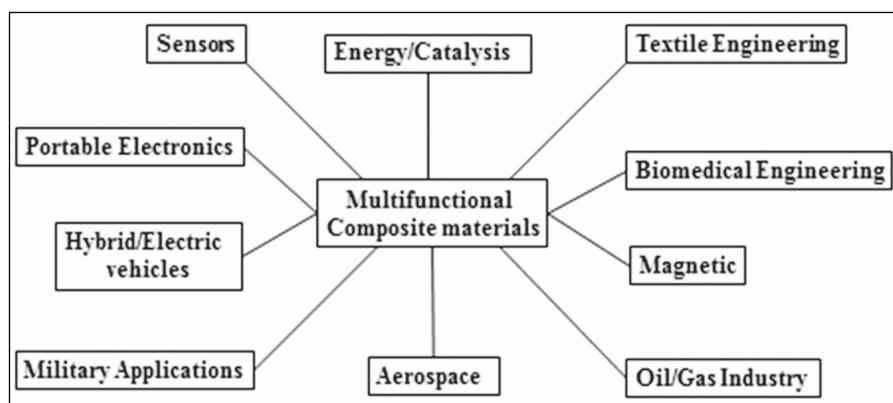


**FIGURE 10.3** Diagrammatic representation of applications of nanocomposites.

### 10.1.6 CURRENT STATUS OF WASTEWATER TECHNOLOGIES

Several technologies such as biological, thermal, and chemical treatment methods are available for the removal of industrial organic wastes. Conventional biological processes represent an environmental friendly way of treatment with reasonable costs. However, they are not adequate to treat nonbiodegradable wastewaters and usually require long residence time for micro-organisms to degrade the pollutants. Alternative pollutant destructive technologies are advanced oxidation processes (AOPs) which constitute a capable technology used for the management of wastewaters in the presence of organic complexes. They can be treated by different processes such as adsorption in waste materials, electrochemical oxidation, usage of membranes, coagulation, Fenton or photo-Fenton oxidation, foam floatation, adsorption using activated carbon, and combined coagulation/carbon adsorption. But these processes are nondestructive and generate secondary pollutants. One of the ways to destroy pollutants without the generation of

secondary toxic material is photocatalysis. In this method, the pollutants decompose to produce  $\text{CO}_2$ ,  $\text{H}_2\text{O}$ , and some inorganic acids.

The universal method for the photocatalytic degradation of organic pollutants involves the excitation of semiconductor by irradiation with photons of the supra-band gap energy and migration of the electron–hole pairs on active surface photocatalyst. The holes may be trapped by  $\text{H}_2\text{O}$  or  $\text{OH}^-$  adsorbed over surface, thus inducing extremely reactive hydroxyl radicals. Since oxidation is governed by free radical mechanism which is expected to control in an appropriate approach that barely varies between numerous pollutants, provided that these molecules are adsorbed on the photocatalyst's surface. Various methods have been suggested to handle the effluent removal from wastewaters. The methods are biodegradation, coagulation, adsorption, advanced oxidation process (AOP), and membrane process. All these methods have several advantages and disadvantages over the other methods. A balanced approach seems to be finding an appropriate technique which can be predominantly used for the destruction of the effluent in question. Among these techniques, the advanced oxidation processes appear to be a promising field of study, which have been reported as effective for the near ambient degradation of the soluble organic contaminants from wastewaters and soils. The steps involved are the following: photolysis (UV or VUV), hydrogen peroxide (this includes the  $\text{H}_2\text{O}_2 + \text{UV}$ , Fenton:  $\text{H}_2\text{O}_2 + \text{Fe}^{2+}/\text{Fe}^{3+}$ , Fenton-like reagents :  $\text{H}_2\text{O}_2 + \text{Fe}^{2+}$ -solid/ $\text{Fe}^{3+}$ -solid and photo-Fenton:  $\text{H}_2\text{O}_2 + \text{Fe}^{2+}/\text{Fe}^{3+} + \text{UV}$ ), Ozone (this includes ozonation, photo-ozonation, ozonation + catalysis and  $\text{O}_3 + \text{H}_2\text{O}_2$  and  $\text{O}_3 + \text{Fe}^{2+}/\text{Fe}^{3+}$ ), and photocatalysis (this includes heterogeneous catalysis, photocatalysis, and  $\text{TiO}_2 + \text{CdS}$  combinations).

### 10.1.7 BASIC PRINCIPLES OF PHOTOCATALYSIS

A significant body of literature reveal that the initial oxidation of a pollutant molecule occurs by indirect band via a surface OH radical and it is reacted directly by valence band hole prior to it is trapped either on the particle or even via hydroxyl radicals in solution. Photo-catalytic technique is a process of AOP, which is proved to be promising technology for eradicating the organic pollutants. This system is more efficient when compared to AOPs for the reason that semiconductors are economical and can simply mineralize different organic contaminants. The photocatalytic discoloration of a dye is most probably involved in the following mechanism and eqs 1.1–1.7. When a catalyst is open to light source, electrons are transferred from valence band into conduction band to enhance electron–hole pair.

Here,  $ecb$  and  $h+vb$  are electrons in conduction band and the electron vacancy in the valence band, respectively.  $h+vb$  can react easily with the surface-bound  $H_2O$  to produce  $OH$  radicals, whereas  $ecb$  can be directly attacked with  $O_2$  molecules to generate the superoxide radical. This will escape the combination of electron and hole created in the first step.

The  $OH$  and  $O_2$  produced in the above manner can be reacting with pollutants to form radical species and it is thus accountable for the degradation of the dyes.

A schematic presentation of photocatalytic study is shown in Figure 10.4.

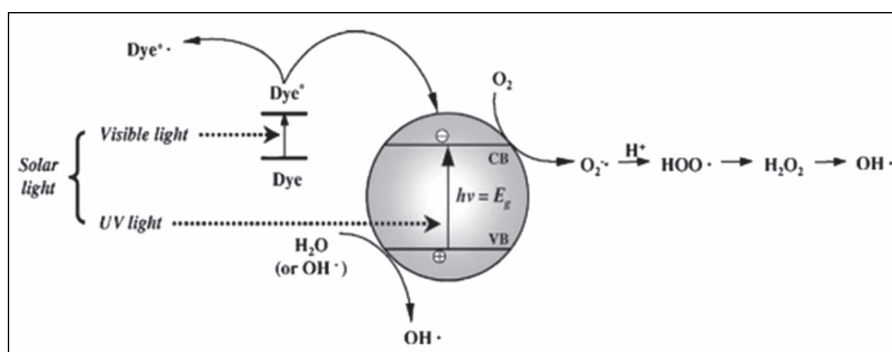


**FIGURE 10.4** Mechanism of photocatalytic process.

### 10.1.8 APPLICATIONS OF NANOCOMPOSITES IN PHOTOCATALYTIC DEGRADATION

There is an increasing interest in nanoscaled semiconductor material because of their vital roles in catalytic, magnetic, optical, and electrical applications. Also, the size-dependent property of the semiconductor nanoparticles is unique. It offers a typical opportunity to fabricate new exotic devices of unprecedented nature. In recent years, the application of nanoparticles is getting more generalized and covering different fields including optoelectronics, catalysis, medicine, sensor devices, etc. Wide band-gap semiconductor materials are the focus of material research owing to novel electric, catalytic, ultrafast optical nonlinear, photoelectric switch and piezoelectric properties. In recent times, researchers are mostly interested in the photophysical analysis, acoustic-optic, and catalytic properties of the ilmenite-type titanates such as  $CoTiO_3$ ,  $NiTiO_3$ , and  $ZnTiO_3$ . The utilization of combined photocatalysis and solar technologies may be developed to a useful process for the reduction of water pollutants



such as dyes and phenols. Combined semiconductor metal oxide photocatalysts enhance the photocatalytic process by the addition of charge carrier and extend the energy in the range of photo-excitation of the system. Recent studies showed that ZnO-TiO<sub>2</sub> nanocomposites because of possessing more efficient catalytic active sites degrade colored substances, pesticides, foam-producing chemicals, and toxic organic materials.<sup>7</sup> Dulin and Rnse (1960) reported that there are three nanocompounds existing in the ZnO-TiO<sub>2</sub> system, including Zn<sub>2</sub>TiO<sub>4</sub> (cubic), Zn<sub>2</sub>Ti<sub>3</sub>O<sub>8</sub> (cubic), and ZnTiO<sub>3</sub> (hexagonal). These composites have been predominantly used as a photocatalyst in decolorization of organic pollutants. Therefore, it has been performed to improve the photocatalytic effectiveness. Various investigations have been paying attention to the bimetal oxide semiconductor photocatalyst of ZnO-TiO<sub>2</sub> in the literature and some achievements are reported. Therefore, the composite particles made of nano ZnO with TiO<sub>2</sub> exhibit improved UV shielding ability.

ZnO and TiO<sub>2</sub> are exhibited the similar band-gap energy at around 3.2 eV and they are in the pure form. When they are in a composite form, they are semiconductor oxides which are widely used in photocatalytic reactions. The enhancement of lifetime to photo-induced pairs, due to electron and hole transfer between the TiO<sub>2</sub> and ZnO, is a promising candidate in many systems as playing the key role for the enhancement of the photocatalytic performance. Therefore, incorporating the two materials into an integrated structure would be of great significance because the resulting products may possess improved physicochemical properties, which should find applications in the variety of fields.

ZnTiO<sub>3</sub> with perovskite structure could be a useful candidate for the microwave resonator materials, gas sensors, and paint pigments which exhibits that its band gap is 3.06 eV. Some researchers used sol-gel method to synthesize zinc titanate nano-crystal powders due to its notable advantages such as high purity, good structural homogeneity, low-temperature preparation, and effortlessly controllable reaction condition. It has been found that calcination at 500°C for 2 h has not improved the crystalline nature of the composite. By increasing the annealing time from 2 to 5 h the composite was found to improve the crystalline nature to some extent which is proved by the effective photocatalytic demineralization studies.

## **10.2 PHOTOCATALYTIC DEGRADATION BY NANOCOMPOSITES**

The photocatalytic degradation of aqueous solution containing organic contaminants has been carried out using different reactor configurations

fabricated for laboratory experimental studies which include the batch reactor. The batch reactor consists of a suspended-particle vertical catalytic reactor with a UV lamp (6 W) for the kinetic and mechanistic studies.

### **10.2.1 BATCH REACTOR FOR UV-LIGHT MEDIATED PHOTOCATALYSIS**

The photodegradation study of dye solution has been carried out in vertical photo-catalytic reactor, as shown in Figure 10.5. Here, nano ZnO-TiO<sub>2</sub> composite particles are dispersed in solution and it is column throughout ventilation. The configuration and the working conditions for the photo-catalytic activity have been scrutinized by the trailer method. These are categorized into three parameters: (i) total capacity of the dye solution, (ii) stirring speed, and (iii) allowing time for adsorption–desorption equilibrium condition before the illumination of UV light. The experimental process consists of a mixture of 250 mL of dye or phenol solution of well-known concentration and in addition to that the photocatalyst allowed for 30 min to pre-adsorption then allowed by irradiation of UV light. The lamp produces 8 W of UV radiation with short wavelength at 254 nm. A sample of 3 mL was collected at constant increment of time intervals and catalyst was removed by centrifugation. The absorbance of solution concentration of dye is measured at 532 nm using UV-Vis spectrophotometer. After the investigation, the solutions come again to the batch reactor. In the presence of UV light at 30° C the pH of the solution has been modified to the pH range between 4 and 10 by using HCl or NaOH. The emission intensity of the UV light is used in the experimental study which is determined by ferrioxalate actinometry, which is found to be  $3.32 \times 10^{19}$  quanta s<sup>-1</sup>.

### **10.2.2 BATCH REACTOR FOR SUNLIGHT-MEDIATED PHOTOCATALYSIS**

The photodegradation study has been carried out in a batch reactor system. For this an open-type rectangular tray of 16 × 15 × 5 cm is made from borosilicate glass which is used as a reactor to maintain the dye solution. The slurry is stirred magnetically on the magnetic stirrer with medium rotation. The experimental procedure consists of irradiation of 250 mL of dye solution of known concentration mixed with known weight of the catalyst and the slurry has been stirred well using a magnetic stirrer and allowed for attaining the equilibration of adsorption–desorption process before irradiation of sunlight for 30 min. The residual concentration of dye solution is measured at 532 nm

using the UV-Vis spectrophotometer. The photodegradation study has been carried out under optimum condition. Solar light intensity is measured for every 30 min and the average sunlight intensity of the surroundings during the photocatalytic experiment is calculated. The light intensity is measured by a digital flux meter and the intensity of the sunlight was found in the range of  $808\text{--}1070\text{ Wm}^{-2}$ . The intensity is almost constant during the entire photocatalytic experiments.

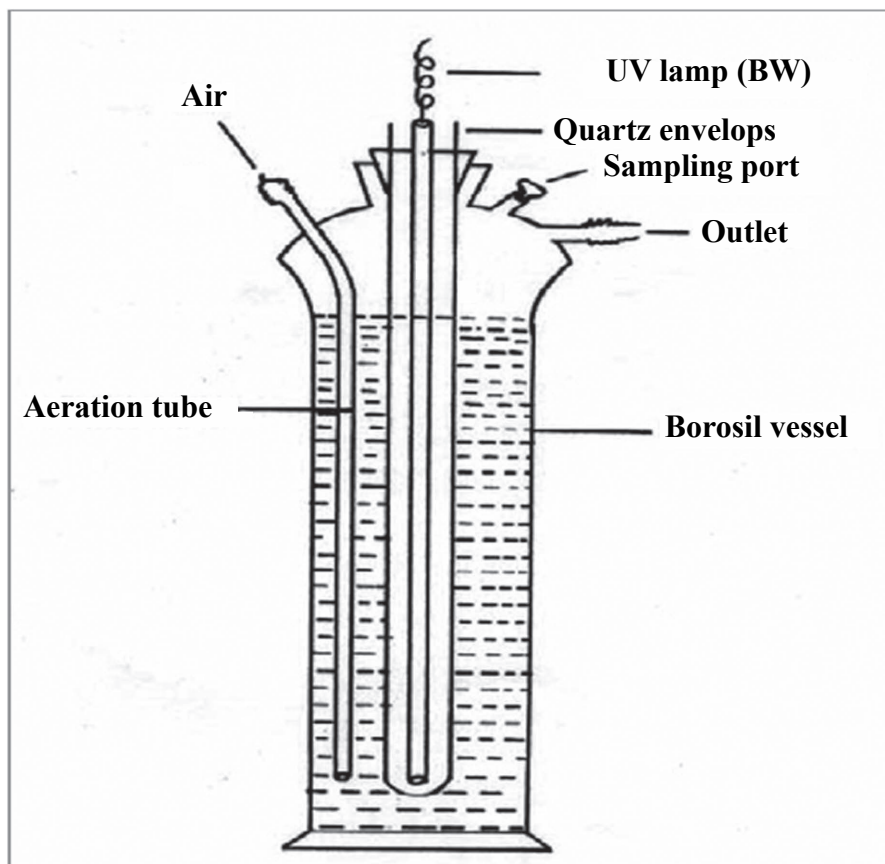


**FIGURE 10.5** Batch reactor system for photodegradation study.

### 10.2.3 PHOTODEGRADATION STUDIES

The reactive red 198 dye solution is kept constant with  $1\text{--}2\text{ g L}^{-1}$  of distilled water as a bulk solution for every degradation experiment. The

experimental procedure consists of irradiation of 250 mL of dye solution of known concentration with the known weight of the nanocatalyst and allows for equilibration of adsorption process before exposure to solar light. The dye solution is taken in the batch reactor and the catalyst is added and keeps on the stirrer with aeration for 30 min in dark conditions to attain equilibrium state to achieve highest adsorption of the dye solution onto the semiconductor surface. During the solar light irradiation no volatility of the solution is observed. Then the solution is collected separately at 5–60 min with continuous stirring and the samples of 3 mL are drawn at periodic intervals of irradiation time. Then the collected solution containing catalyst is centrifuged. The residual concentration of the dye solution is determined using UV–Vis spectrophotometer at 532 nm.

#### *10.2.3.1 PHOTODEGRADATION OF DYE USING ZnO-TiO<sub>2</sub> NANOCOMPOSITES*

ZnO-TiO<sub>2</sub> nanomaterials have been studied as outstanding photocatalyst in the field of photo electrochemical application. Recently, extensive investigations have been concentrated on the design, synthesis, and environmental applications of nanocomposite metal oxides such as ZnO-TiO<sub>2</sub> to improve the quantum efficiency of the photocatalysts for the applications in water purification. The ZnO-TiO<sub>2</sub> nanocomposite was synthesized by the sol-gel method and it has more advantages of higher surface activity due to the easy reclaim after reaction. Moreover, the sol-gel process for nanocomposite preparation is due to 100% without impure, uniformity of the film microstructure, low-temperature synthesis, and easily controlled reaction condition.

#### *10.2.3.2 PHOTODEGRADABILITY OF REACTIVE RED 198 DYE USING ZnO-TiO<sub>2</sub> NANOCOMPOSITES*

Photocatalytic degradation of reactive red 198 dye has been investigated in UV light in the presence of ZnO-TiO<sub>2</sub> nanocomposite particles. The photodegradability experiments were carried out using fixed amount of the ZnO-TiO<sub>2</sub> nanocomposite particles (1 g L<sup>-1</sup>) and concentration of the reactive red 198 as 100 µM at pH=7. The photo-catalytic activities of the dyes have been examined by exposing the dye solution to energy source in the absence and presence of nanophotocatalyst in a batch reactor. In the absence

of the nanophotocatalyst, the dye solution on irradiation with UV light of wavelength 254 nm, no photodegradation is observed and the solution is found to be in good stability even after 2 h of exposure. In the presence of the nanocatalyst (nano ZnO-TiO<sub>2</sub> composite particles) and in the absence of UV light, the dye solution again remains stable. However, the dye undergoes photodegradation on irradiation with UV light of 254 nm in the presence of catalysts such as nano ZnO-TiO<sub>2</sub> composite particles (with a band gap energy of 3.2 eV). The photocatalytic degradation study of ZnO nanoparticles is effective in the initial stage and it has undergone complete degradation within 165 min. Hence, the photodegradation efficiency increases with increasing weight of the nanophotocatalysts. The total active site of the catalyst surface area is increased with increasing catalyst weight. In the presence of both UV light and nano ZnO-TiO<sub>2</sub> composite particles, dye degradation is completed by the irradiation time of 210 min.

#### *10.2.3.3 EFFECT OF WAVELENGTH OF INCIDENT LIGHT IN PHOTOCATALYTIC DECOLORIZATION OF THE REACTIVE RED 198 DYE*

The photocatalytic degradation of the reactive red 198 dye has been investigated by exposing the dye solution to a light of wavelength 254 nm in the existence of ZnO-TiO<sub>2</sub> nanocomposite particles. A sample of 50  $\mu$ M of the dye solution on irradiation with 254 nm light has been found to undergo complete mineralization within 60 min. Underneath same conditions, with 375 nm light intensity, merely 40% of the decolorization has been achieved. The photocatalytic performance under short wavelength of 254 nm was found to be effective when compared to long 365-nm light because the shorter wavelength has more suitability by nanophotocatalyst than the longer wavelength light. The light penetration effect of distance of the photons on the particle is shorter and photoelectrons and holes are served to be very closer to the surface of the catalyst. Therefore, it reduces the time for migration to the surface of the catalyst, enhancing photocatalytic efficiency by slowing down the recombination process of electron-hole pairs over the catalyst's surface. There are several organic moieties that are excited by 254-nm light and are easily decolorized by direct action. However, the direct decolorization reaction rate is very low when compared than the presence of a photocatalyst. Therefore, the photocatalytic decolorization studies have been carried out using an incident UV short wavelength light at 254 nm.

#### 10.2.3.4 SYNTHESIS OF ZnO-TiO<sub>2</sub> NANOCOMPOSITE BY VARIOUS TYPES OF SOL-GEL METHOD

The following methods are some of the unique methods of sol-gel which are used to synthesize ZnO-TiO<sub>2</sub> nanocomposite particles.

1. Tetrabutyl titanate is used to synthesize the visible TiO<sub>2</sub> aerogel at R.T (room temperature). Initially, the TBT is dissolved in ethanol and is stirred for half an hour to get a starting solution. A beaker containing the mixture of DI water, acetic acid, and absolute ethanol is poured into the above precursor medium drop wise with constant stirring at R.T. Then the solution was constantly stirred for 1 h to attain a transparent yellow color TiO<sub>2</sub> sol gel. Zinc acetate is used as another starting material to synthesize ZnO aerogel. It is first dissolved in ethanol and is stirred for 5 min at 50°C under water bath in order to get a precursor solution. The diethanolamine and ethanol is then dropped into the precursor solution drop wise with continuous stirring for 30 min. Following that, the mixture of DI water and ethanol is added into the solution and is continuously stirred for 2 h to obtain transparent ZnO sol. After that, as-prepared ZnO sol is directly poured into the TiO<sub>2</sub> sol by 1:1 atomic molar ratio of Ti to Zn to get TiO<sub>2</sub>/ZnO composite aerogel. The composite aerogel is solid at room temperature and it dried at 70°C in air for 24 h. The completely dried gel was pulverized and then soaked in ammonium hydroxide aqueous solution. The soaking process is accomplished by doping of 1 g gel into a beaker containing 20 mL ammonia hydroxide solution. The beaker is preserved with aluminum foil sheet and it was kept at room temperature for 24 h. The NH<sub>3</sub> mass fraction of the ammonia aqueous solution is wished for 0%, 7%, and 28%, respectively. Herewith the ammonia mass activity fraction of 0% is considered for the process where the gel is not treated with ammonia hydroxide solution. After soaking, supernatant fluid was discarded and residue is dried at 70°C in an oven. The dried powder sample was annealed at 500, 600, and 700°C in air for 2 h.<sup>8</sup>
2. Zinc acetate is added to dehydrated isopropyl alcohol till a solution with a concentration of 0.5 mol L<sup>-1</sup> is prepared by the vigorous stirring. An equimolar quantity of diethanolamine as sol-stabilizer is introduced dropwise into the solution until the solution becomes transparent (sol A). 0.6 mL of titanium tetrachloride (Fluka 99.9%) is added slowly into 60 mL of 0.001 N solution of HCl (sol B). Sol

Bis, then, is added dropwise to sol A under vigorous stirring as well. Subsequently, the resulting solid is filtrated and washed with distilled water and then it is dried at 60°C. The obtained powder is denoted as TZ60. Later, TZ60 is calcined at 160, 220, 420, 620, 680, 750, 800, and 900°C, and the obtained samples are denoted as TZ160, TZ220, TZ420, TZ620, TZ680, TZ750, TZ800, and TZ900, respectively.<sup>9</sup>

3. The titanium (IV) isopropoxide is used as a precursor to synthesize transparent  $\text{TiO}_2$  solution at R.T as follows: Firstly, 4.32 mL of titanium (IV) isopropoxide was dissolved in 20 mL of absolute ethanol and is stirred for half an hour to get a titania precursor solution on the magnetic stirrer with medium rotation. A mixture of 0.26 mL of DI water, 3.4 mL of acetic acid, and 5 mL of absolute ethanol is added dropwise into the precursor solution by dropwise constant stirring condition on a magnetic stirrer. After that, the solution is continuously stirred for 1 h to achieve a yellow color transparent solution. The solution was then aged for a certain period of time. Herewith acetic acid is used as an inhibitor to ensure the slowdown of the hyderolysis process in titanium (IV) isopropoxide. In this study, the pH value of the system is determined to be  $\sim 5$  and the obtained sol is hereafter referred to as an acidic solution. Besides, another inhibitor diethanolamine is used and the pH value of the system is determined to be  $\sim 10$ . Then the prepared  $\text{TiO}_2$  solution is referred to as base solution. The synthesis of  $\text{ZnO-TiO}_2$  sol can be achieved via directly mixing the acidic two solution and the  $\text{ZnO}$  solution with strong stirring.<sup>10</sup>

#### **10.2.4 EFFECT OF pH USING NANO $\text{ZnO-TiO}_2$ COMPOSITE PARTICLES**

The photodegradation of dye solution (100  $\mu\text{M}$ ) in the presence of nano  $\text{ZnO-TiO}_2$  composite particles at a pH range of 3.0–10.0 at the temperature of  $30.0 \pm 0.1^\circ\text{C}$  on the catalyst surface has been investigated successfully. In the pH range from 3 to 10, the time significantly influences the degradation of pollutants, increasing from 120 to 195 min. This pH dependency may increase in the generation of OH radicals with the increase in pH (Shourong et al, 1997 & Lakshmi et al, 1995). In acid and neutral solutions, the reactions that occur may be represented as per eq. 4.1 in alkaline solution; increased adsorption of hydroxide ions may give rise to a greater concentration of OH radicals (eq 4.2).

At pH 5.6, the photodegradation reaction is completed within 135 min. A steady increase in the degradation of the dye solution is observed

from pH 3.0 to 5.7 which is followed by a slow decrease at neutral pHs. The degradation process is increased further at higher pH (pH = 10). The high pH value can give high concentration of OH ions to interact with the holes ( $h^+$ ) to form hydroxyl radicals (OH), and subsequently enhances the photodegradation rate of the dye solution. At the end of 10 min, the initial degradation rate value of nano ZnO-TiO<sub>2</sub> composite particles is in the range of 1.2–2.1  $\mu\text{M m}^{-1}$ .

#### **10.2.5 EFFECT OF CONCENTRATION USING ZnO-TiO<sub>2</sub> NANOCOMPOSITES**

The photocatalytic degradation of reactive red 198 pollutant has been carried out at different concentrations in the range of 50–120  $\mu\text{M}$ . Total mineralization of the dye has been found to occur at the end of 105 min for an initial concentration of 50  $\mu\text{M}$ . Increase in the concentration to 120  $\mu\text{M}$  increases the degradation time and it is found to be around 210 min. The photocatalytic behavior of the nano ZnO-TiO<sub>2</sub> composite particles can be well understood with taking into account the phase composition, particle surface area, and particle morphology.<sup>11</sup> The anatase phase with high crystallinity, more active sites, and numbers of substrates are adsorbed during the process. In this work, the crystallinity of nano ZnO-TiO<sub>2</sub> composite particles after thermal calcination at temperature of 500°C actually promotes the high crystallinity and to construct an anatase phase composition is evidently achieved. The ZnO-TiO<sub>2</sub> particle size of the powder was reduced by undergoing calcination process. As an end result, the photocatalytic performance of the nanocomposite particles is clearly enhanced. There was an increase in the rate constant of photodegradation of the dye with an increase in the concentration range of 50–75  $\mu\text{M}$  and further increase in the concentration to the range of 100–120  $\mu\text{M}$ , which leads to minimizing the rate of destruction. Maximum initial rate constant of degradation of 1.7 has been obtained under the conditions for a concentration of 75–90  $\mu\text{M}$ . Nano ZnO-TiO<sub>2</sub> composite particles show that the percentage degradation is 1.2–1.7  $\mu\text{M m}^{-1}$  at the end of 10 min of irradiation.

#### **10.2.6 ANALYSIS OF TOTAL ORGANIC CARBON (TOC)**

The investigated dye solution has undergone the determination of TOC using a batch photocatalytic reactor. The total organic carbon content (TOC) is an evaluation of the organic carbon present in the sample and indirectly implies



the oxidative power of the particular oxidation technique, when employed to samples treated by those techniques. Photocatalysis has already been proved to oxidize many organic compounds completely, giving rise to  $\text{CO}_2$ ,  $\text{H}_2\text{O}$ , and inorganic acids. In TOC estimations, 25 mL of the sample solution is filled up in an annular space between the UV lamp-quartz (6 W) assembly and the outer glass column of the tubular batch reactor with the inner wall of the glass column coated with the nanophotocatalyst. The inlet is connected to the aerator and the outlet tube is immersed into KOH solution of known concentration taken in a gas-washing bottle. After irradiating the samples for a specific duration, the KOH solution is titrated against standardized HCl by volumetry or conductometry. A blank is run with 25 mL water for the same irradiation time, to nullify the errors due to dissolved  $\text{CO}_2$  from aeration.

The amount of KOH is consumed by the liberated  $\text{CO}_2$  and the amount of the organic carbon present in the sample is calculated and compared with the values in theoretical calculation regarding this dye solution under photodegradation. The photocatalytic process in oxidizing the reactive red 198 dye has been analyzed through TOC determination and the experimental results revealed that the amount of  $\text{CO}_2$  evolved as 59.1 ppm, 117.8 ppm, and 233.2 ppm for 50, 100, and 200  $\mu\text{M}$ , respectively. And the theoretical value for this experiment is found to be 59.4 ppm, 118.8 ppm, and 237.6 ppm. It is indicated that almost all the organic carbon present in the reactive red 198 dye has been oxidized as confirmation from the quantitative analysis of  $\text{CO}_2$ . The destruction of pollutant has been confirmed by the complete removal of organic constituents from the aqueous solution of dye.

### **10.2.7 REUSABILITY**

The catalyst lifetime is an important parameter in the photocatalytic process because its use for a longer period of time leads to a significant cost reduction of the treatment. Reusability of catalysts for the decolorization of dye by photocatalysis is evaluated by using nano  $\text{ZnO-TiO}_2$  composite particles. The reusability experiment has been carried out using fixed amount of nano  $\text{ZnO-TiO}_2$  composite particles ( $1 \text{ g L}^{-1}$ ) and fixed concentration of the reactive red 198 dye as 50  $\mu\text{M}$  at  $\text{pH}=7$ . The solution ensuing from the photocatalytic activity of the dye is filtered, washed and the catalyst was dried at  $100^\circ\text{C}$  for reuse. The dried nanocatalyst is used for the degradation of dye, employing same photocatalytic conditions. The filtrate was analyzed to the AAS technique to determine the loss of  $\text{Zn}^{2+}$  or  $\text{Ti}^{2+}$  into solution as a result of suspension of the nano  $\text{ZnO-TiO}_2$  composite.

The dissolution of the composite is found to be insignificant (0.04% loss of catalyst was observed during 2 h of reaction time). Nanomaterials have shown effective photomineralized activity up to four cycles when used for the degradation of the dyes. It is because of the adsorption of the organic intermediates and the secondary by-products of photo-catalytic process in the voids and on the surface area of the photocatalyst which significantly influences the surface activity of the nanocatalysts. By the repetitive use of the composite, a loss has been occurred in the amount of the reused nano-photocatalyst. The study has shown effective evidence after four runs as 94, 86, 76, and 67% for the drying temperature of 10°C. The nano ZnO-TiO<sub>2</sub> composite particles have been exhibited remarkable photostability without any appreciable loss of photocatalytic activity after four cycles. Nanoparticles can be quite easily separated in a short time which shows that nano ZnO-TiO<sub>2</sub> composite particles can be easily recovered. After the reusability process, the utilized nanocatalysts have been separated from the processed solution by the easy separation/recovery step for further destruction processes. In this sense, one of the principal goals of these types of processes is the development of the stable heterogeneous catalysts with little usage of the weighed materials for the reaction processes. In this experimental study, catalysts have been reused and were giving reproducible and effective results.

### **10.2.8 CHALLENGES IN NANOSCIENCE AND TECHNOLOGY**

Nanotechnology may be the ultimate enabling technology, since it provides fundamental building blocks of living beings. Almost every field of industry will be deeply enhanced by the progress in nanotechnology. Presently, major challenges of nanotechnology are mainly due to the technology development challenge, common and ethical challenge, business-driven financial system, risk and improbability, safety, and armed applications. Main challenge is the material science required for local growth of nanostructures with desired solid-state or molecular properties, and for the control of local reactions. The novel components with electronic, mechanical, and chemical functionalities can be used for energy and information to autonomous nanosystems and it is expected that nanomechanics and nanochemistry will provide the original paths between physico-chemical processing and the real world of sensing actuation technologies. The development, characterization, and fictionalizations of nanoscale materials are the intimidating task to control the material property and make ideal functional materials with perceived properties.<sup>12</sup>

Public health and safety is probably the major concern associated with nanotechnology. The confidence of the public about the nanotechnology must be enhanced followed by the products of nanotechnology to be accepted by the society. Economic benefits are another one of the major challenges. Many new companies based on nanotechnology would be set up, and the prices will be appreciated at the cost of other companies. Nanotechnology products will earn revenues by taking the money from the revenues previously accorded to old products. Nanotechnology has been developed as an enhancement in army forces to improve the new systems. Some technologies have notified that nanotechnology would make it possible for terrorists to acquire nuclear weapons with very little fissionable material. Nanotechnology is a value-neutral tool. Depending on its usage, nanotechnology can be good or/and bad. If there is a new rule for the military to prevent conflict, nanotechnology offers great opportunities for a new and proactive approach to national security.

### **10.2.9 SUMMARY**

Overall, the results of this study contribute significant information on the development of safer and eco-friendly, bio-degradable, fire-resistant composites with superior mechanical assets. In this chapter, the photocatalytic degradation of azo dye like reactive red 198 has preceded in a batch reactor in the presence of UV light is discussed. In all the experiments, slurry of dye solution with a fixed amount of catalyst under constant stirring was illuminated with UV. The parameters such as photodegradability, effect of incident wavelength, and effect of concentration of the dye are studied. The photodegradation results show that the reactive red 198 dye has been undergone complete mineralization in the presence of nano ZnO-TiO<sub>2</sub> composite particles. The incident light of wavelength 254 nm is comparatively more effective than the 375-nm light for degradation. The initial rate constant of photo-catalytic degradation in dilute solution was initiated to boost with increase in the initial concentrations. The nanophotocatalyst ZnO-TiO<sub>2</sub> composite particles have been found to be stable under the present experimental conditions and undergo negligible photocorrosion. The total organic carbon (TOC) of the mineralized solutions has been determined experimentally by using a batch photocatalytic reactor. The TOC values determined have been found to tally exactly with the theoretical calculations. The dye has been completely mineralized to carbon dioxide, water, and other

unharmful inorganic ions such as sulfate, sulfite, nitrate, and nitrite. Hence, photocatalysis has been found to be an effective tool in the degradation of organics in water.

## KEYWORDS

- metal oxide nanocomposites
- photocatalytic degradation
- ZnO-TiO<sub>2</sub> nanocomposites
- dye degradation
- photocatalysis

## REFERENCES

1. Can Kurnaz, S. Production of Saffil Fibre Reinforced Zn-Al (ZA12) Based Metal Matrix Composites Using Infiltration Technique and Study of Their Properties. *Mater. Sci. Eng. A*. **2003**, 346 (1–2), 108–115.
2. Zhou, W.; Yamaguchi, T.; Kikuchi, K.; Nomura, N.; Kawasaki, A. Effectively Enhanced Load Transfer by Interfacial Reactions in Multi-Walled Carbon Nanotube Reinforced Al Matrix Composites. *Acta Mater.* **2017**, 125, 369–376.
3. Bledzki, A. K.; Franciszczak, P.; Osman, Z.; Elbadawi, M. Polypropylene Biocomposites Reinforced with Softwood, Abaca, Jute, and Kenaf Fibers. *Ind. Crops Prod.* **2015**, 70, 91–99.
4. Dittenber, D. B.; Ganga Rao, H. V. S. Critical Review of Recent Publications on Use of Natural Composites in Infrastructure. *Compos. Part.* **2012**, 43 (8), 1419–1429.
5. Lomeli-Ramirez, M. G.; Barrios-Guzman, A. J.; Garcia-Enriquez, S.; Rivera-Prado, J. J.; Manriquez-Gonzalez, R. Chemical and Mechanical Evaluation of Bio-Composites Based on Thermoplastic Starch and Wood Particles Prepared by Thermal Compression. *Bio Res.* **2014**, 9 (2), 2960–2974.
6. Chen, M. J.; Xu, Y. J.; Rao, W. H.; Huang, J. Q.; Wang, X. L.; Chen, L. et al. Influence of Valence and Structure of Phosphorus Containing Melamine Salts on the Decomposition and Fire Behaviours of Flexible Polyurethane Foams. *Ind. Eng. Chem. Res.* **2014**, 53, 8773–8783.
7. Fujishima, A.; Zhang, X.; Tryk, D.A. Heterogeneous Photocatalysis: From Water Photolysis to Applications in Environmental Cleanup. *Int. J. Hydrogen Energy*. **2007**, 32, 2664–2672.
8. Wang, J.; Mi, W.; Tian, J.; Dai, J.; Wang, X.; Liu, X. Effect of Calcinations of TiO<sub>2</sub>/ZnO Composite Powder at High Temperature on Photodegradation of Methyl Orange. *Compos. Part B.* **2013**, 45, 758–767.

9. Janitabar-Darzi, S.; Reza Mahjoub, A. Investigation of Phase Transformations and Photocatalytic Properties of Sol-Gel Prepared Nanostructured ZnO/TiO<sub>2</sub> Composites. *J. Alloys. Compd.* **2009**, *486*, 805–808.
10. Prabha, I.; Lathasree, S. Photodegradation of Phenol by Zinc Oxide Titania and Zinc Oxide-Titania Composites: Nanoparticle Synthesis, Characterization and Comparative Photocatalytic Efficiencies. *J. Mater. Semicond. Process.* **2014**, *26*, 603–613.
11. Cassiers, K.; Linssen, T.; Mathieu, M.; Bai, Y. Q.; Zhu, H. Y.; Cool, P.; Vansant E. F. Surfactant-Directed Synthesis of Mesoporous Titania with Nanocrystalline Anatase Walls and Remarkable Thermal Stability. *J. Phys. Chem. B.* **2004**, *108*, 3713–3721.
12. Baltes, H.; Brand, O.; Fedder, G. K.; Hierold, C.; Korvink, J. G.; Tabata, O. Enabling Technologies for MEMS and Nanodevices; Wiley-VCH: Weinheim, 2005.

## CHAPTER 11

---

# Recent Advances in the Biosynthesis of Noble Metal Nanoparticles Using Marine Macroalgae

K. F. PRINCY<sup>1</sup>, SREEJA E. S.<sup>2</sup>, and ANU GOPINATH<sup>3</sup>

<sup>1</sup>*Government College Kattappana, Idukki, Kerala, India*

<sup>2</sup>*Department of Marine Chemistry, Kerala University of Fisheries and Ocean Studies, Cochin, India*

<sup>3</sup>*Department of Aquatic Environment Management, Kerala University of Fisheries and Ocean Studies, Cochin, India*

---

### ABSTRACT

Conventional procedures for the fabrication of metal nanoparticles are costly and involve the use of various noxious chemicals. Consequently, there is a burgeoning interest associated with the development of facile, nontoxic, eco-friendly, and economical methods for nanoparticle production. In recent times, biosynthetic methods employing microbes and plant extracts have emerged as a feasible substitute for typically used physical and chemical procedures. However, plant-mediated synthesis is greener, facile, and more cost-effective. Nevertheless, in comparison with terrestrial plants, marine resources, especially marine macroalgae (seaweeds), are not much explored for nanobiosynthesis. The current chapter is intended to speculate on the significance of the utilization of marine macroalgae in the production of noble metal nanoparticles to overcome the drawbacks of traditional procedures. In addition, recent progress in algae-mediated synthesis of metal nanoparticles and their size, distribution, morphology, and important applications are briefly described, along with the future scope of research in this field.

---

Functional Nanocomposites and Their Applications. Dhanya K. R., Sanal P. S., Sabu Thomas, & Nandakumar Kalarikkal (Eds.)

© 2025 Apple Academic Press, Inc. Co-published with CRC Press (Taylor & Francis)

## 11.1 INTRODUCTION

Nanotechnology is emerging as a rapidly growing area of research due to its tremendous applications in diverse areas of science and technology. It deals with the production, characterization, and utility of materials with a dimension in the range of 1–100 nm.<sup>1</sup> The primary concept of nanotechnology was seeded by Richard P. Feynman, the Nobel laureate Physicist Professor, in his renowned lecture titled “There’s Plenty of Room at the Bottom” in 1959, and it was Professor Norio Taniguchi of Tokyo Science University who coined the term “Nanotechnology” in 1974 to explain the ultraprecision machining of materials at the nanometer scale. Dr. K. Eric Drexler is responsible for the current sense of nanotechnology. He explained nanotechnology in depth and popularized the topic through his speeches and books. The innovation of the atomic force microscope (AFM) and scanning tunneling microscope (STM) brought about a breakthrough in the field of nanotechnology, which facilitated the scientific community’s ability to observe features at the atomic or molecular level. This brings forth a new era of nanotechnological research that aims at the versatile applications of materials in the nanometer regime.

## 11.2 NANOPARTICLES: PROPERTIES AND THEIR SIGNIFICANCE

In the term nanotechnology, the prefix “**nano**” is derived from the Greek word “**nanos**,” synonymous with dwarf or extremely small. It refers to any engineered matter that is one billionth ( $10^{-9}$  m) in size and is regarded as a nanometer (nm). Nanoparticles are tiny clusters of atoms ranging in size from 1 to 100 nm and are considered the fundamental building blocks of nanotechnology.<sup>2</sup> According to the British Standards Institute (BSI) (2007), nanoparticles are particles with one or more dimensions at the nanoscale (1–100 nm).<sup>3</sup> As they bridge bulk materials with atomic or molecular structures, they are of great scientific interest.<sup>4</sup> The physical properties of a bulk material remain constant regardless of its size, but the phenomenon of miniaturization completely changes its properties. In the nanophase regime, particles exhibit unique and novel physical, chemical, and biological properties as compared to their bulk materials. This uniqueness of nanoparticles is primarily due to their extremely small size, which results in a large surface area to volume ratio, high surface energy, and spatial confinement, which do not exist in their bulk counterparts.<sup>5</sup>

In the nanometer range, there is a large proportion of atoms present on the surface, which leads to a high surface-to-volume fraction. Consequently, surface-dependent material properties became prominent. Also, as the size of the particle decreases, its energy levels become discrete due to the confinement of the spatial distribution of the electrons. This phenomenon called quantum confinement can bring about novel optical, electronic, and magnetic properties in nanomaterials that differ significantly from their bulk equivalents.<sup>6</sup> These unique characteristics enable nanoparticles to find numerous applications in diverse areas of life and industry.

Recently, a variety of nanoparticles made of various materials have been reported, including carbon-based nanoparticles (carbon nanotubes and fullerenes), noble metal nanoparticles (silver, gold, platinum, and palladium), magnetic nanoparticles (iron oxide), semiconductor nanoparticles (zinc oxide, titanium dioxide, and zinc sulfide), and their mixtures.<sup>7</sup> Among all these, noble metal nanoparticles have gained remarkable consideration due to their size- and shape-dependent properties, with tremendous applications in diverse fields such as catalysis, drug delivery, chemical sensing and imaging, optoelectronics, environmental remediation, biological labeling, biosensing, water purification, bioimaging, antimicrobials, and therapeutics.<sup>8</sup>

### **11.2.1 NOBLE METAL NANOPARTICLES**

Noble metal nanoparticles, particularly silver and gold nanoparticles, have piqued researchers' interest in recent decades due to their exceptional optical and electronic characteristics, which are not found in their bulk metal. The most remarkable feature of silver and gold nanoparticles is their surface plasmon resonance (SPR) property, which arises due to the collective oscillation of electrons on the surface of nanoparticles in resonance with the incident light.<sup>9</sup> Due to the SPR phenomenon, silver and gold nanoparticles exhibit characteristic absorption bands in the UV-visible absorption spectrum and varying colors in the reaction medium.<sup>10</sup> By altering the size or morphology of nanoparticles, the SPR characteristics, that is, both the color and position of bands, can be modified, resulting in particles with specific optical properties for multifaceted applications.<sup>11</sup> In the last 2 decades, research activities on the synthesis, characterization, and application of silver and gold nanoparticles have increased significantly.

Silver nanoparticles (AgNPs) are one of the most widely studied nanoparticles on account of their remarkable antimicrobial activity,<sup>12–14</sup> high



conductivity,<sup>15</sup> catalytic activity,<sup>16–18</sup> and optical properties.<sup>19</sup> They are being incorporated into numerous commercial products such as water filters,<sup>20</sup> cosmetics,<sup>21</sup> home appliances,<sup>22</sup> textiles,<sup>23</sup> and most significantly, medicinal devices such as wound dressings, pacemakers, catheters, and vascular prostheses.<sup>24</sup> Due to their catalytic activity and sensing efficacy, they have also been employed for environmental remediation.<sup>25</sup> A schematic representation of some of the applications of AgNPs is given in Figure 11.1.

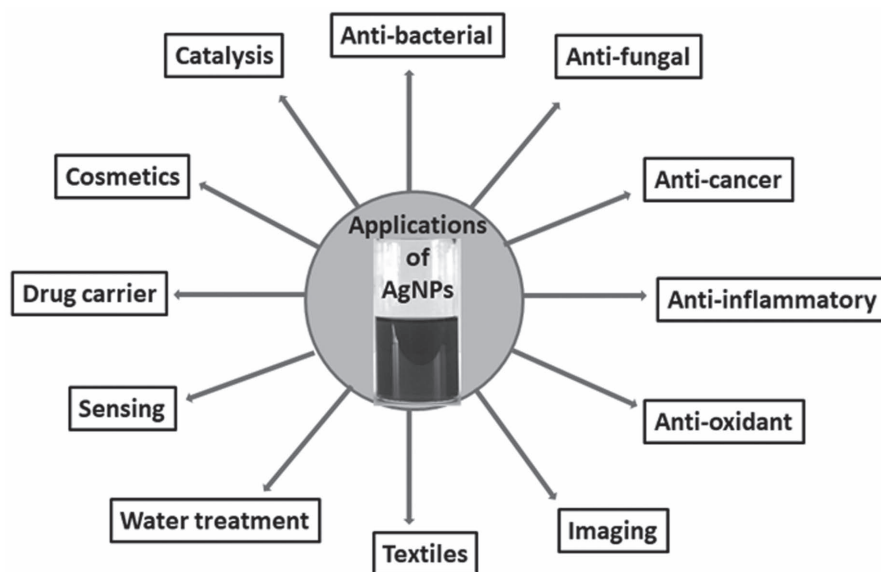


**FIGURE 11.1** Different applications of silver nanoparticles.

Gold nanoparticles (AuNPs) are also highly promising in the biomedical field due to their strong affinity toward biomolecules like proteins, antibodies, peptides, oligonucleotides, etc.<sup>26</sup> Therefore, functionalization of AuNPs with these biomolecules facilitates their use as biomarkers for disease diagnosis<sup>27</sup> and drug delivery.<sup>28</sup> Tunable size and functionality make them a proper scaffold for efficient recognition and delivery of biomolecules. Due to their high light scattering cross section and photostability, they are suitable for cellular imaging.<sup>29</sup> Their efficacy to absorb near-infrared energy and convert it to heat makes them very useful for photothermal therapy of cancer and other diseases.<sup>30</sup> They could also be used in catalysis, nanoelectronics, gene expression, chemical and biological sensors, and nonlinear optics.<sup>31</sup> Some of the important applications of AuNPs are represented in Figure 11.2.

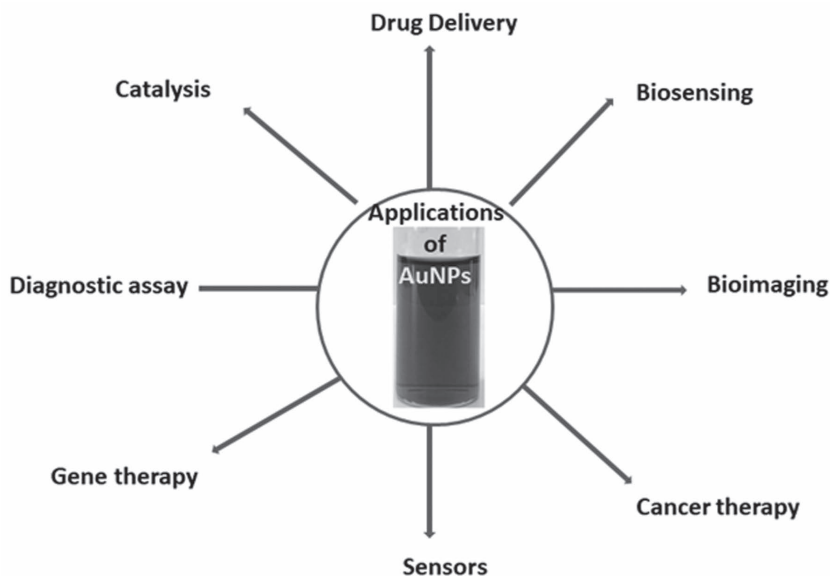


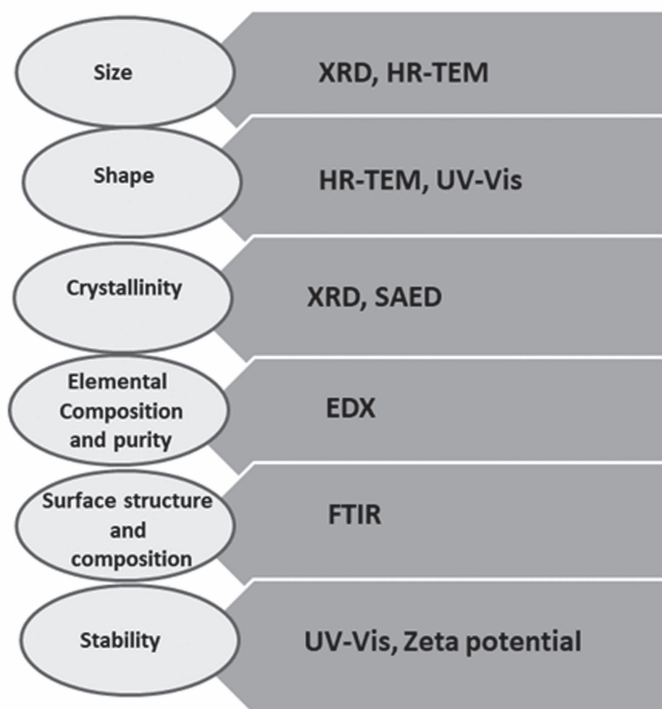
**FIGURE 11.2** Various applications of AuNPs.

### 11.3 CHARACTERIZATION TECHNIQUES FOR NOBLE METAL NANOPARTICLES

Metal nanoparticles are usually characterized by their shape, size, surface functional groups, elemental composition, and crystallinity.<sup>32</sup> There are several techniques available for the characterization of metal nanoparticles, such as UV-visible spectroscopy, high resolution transmission electron microscopy (HR-TEM), X-ray diffraction (XRD) technique, energy dispersive X-ray spectroscopy (EDX), Fourier transform infrared spectroscopy (FTIR), dynamic light scattering (DLS), field emission scanning electron microscopy (FE-SEM), X-ray photoelectron spectroscopy (XPS), thermogravimetric analysis (TGA), atomic force microscopy (AFM), zeta potential, etc. Of these, a concise description of the commonly used techniques (Scheme 11.1) is given below.

#### 11.3.1 UV-VISIBLE SPECTROSCOPY

UV-visible spectroscopy is typically the first technique used to elucidate the formation of metal nanoparticles in aqueous solutions. It is a potent,



**SCHEME 11.1** Important techniques for the characterization of nanoparticles.

nondestructive technique employed to explore the optical properties of nanoparticles. Noble metal nanoparticles, specifically silver and gold nanoparticles, are intensely colored and exhibit characteristic absorption in the visible region due to the phenomenon of SPR, which arises due to the collective oscillation of free electrons on their surface. The conduction electrons on the surface of metal nanoparticles oscillate when they are exposed to light excitation, and a resonance is achieved between the frequencies of surface electron oscillations and light photons. This is called surface plasmon resonance (SPR) and can be monitored through UV-visible spectral studies.<sup>33</sup> A light wavelength of 200–800 nm is normally used for characterizing various metal nanoparticles. For AgNPs, a characteristic absorption peak is obtained in the range of 400–450 nm, while AuNPs exhibit an absorbance peak within 500–550 nm. The SPR band is specific for each metal nanoparticle and is not observed in the spectra of their bulk-scale materials. The wavelength for maximum absorption ( $\lambda_{\text{max}}$ ) and band width provide a unique spectral fingerprint for a plasmonic nanoparticle with a precise size and shape. The

SPR characteristics are highly dependent on particle size and shape, nature of the capping agent, and dielectric constant of the surrounding media.<sup>34</sup>

UV-visible spectroscopy furnishes information about the size, shape, stability, and agglomeration of the nanoparticles. The position of the SPR band is directly correlated to the size of the nanoparticle. As particle size increases, a red shift in the position of the SPR band is observed, along with a variation in the color of the colloidal solution. The color of AuNPs varies from ruby red to purple and ultimately blue with an increase in particle size, whereas for AgNPs, it changes from light yellow to dark brown. When nanoparticles are very close to each other, that is, when the interparticle distances of nanoparticles become lower than their average diameter, the particles agglomerate so that the plasmon resonance of individual particle couples and their absorption peaks are shifted toward the longer wavelength region and broaden.<sup>35</sup> Aggregation of nanoparticles also causes a decrease in the intensity of the SPR peak. So absorption studies can provide valuable evidence regarding the stability of the nanoparticles. This size-dependent nature of the SPR band can also be used in various sensing applications.

In addition, the SPR band can give information regarding the dispersity of metal nanoparticles. Monodispersed spherical nanoparticles with a small size range are known to exhibit a single highly symmetrical and intense SPR band toward the lower wavelength.<sup>36</sup> Whereas, broad and red-shifted bands in the spectrum indicate the presence of anisotropic particles with an increased particle size. Therefore, UV-visible spectroscopic studies are important in the development of size and shape controlled synthesis of metal nanoparticles as well as tuning their optical properties by optimizing the reaction parameters.

A number of researchers have used UV-visible spectroscopy to monitor the absorption spectra of nanoparticles. In the coriander leaf extract-mediated biosynthesis of AuNPs, Narayanan and Sakthivel<sup>37</sup> confirmed the formation of AuNPs from the ruby-red color of the reaction medium and the SPR band at 525 nm. During *Allophylus cobbe* leaf extract-mediated biosynthesis of AgNPs, Gurunathan et al.<sup>38</sup> observed that the pale green color of the reaction medium turned to deep brown on exposure to AgNO<sub>3</sub>. Using a UV-visible spectrophotometer, they could notice a strong absorption band at about 420 nm, confirming the formation of AgNPs.

### **11.3.2 X-RAY DIFFRACTION (XRD) ANALYSIS**

The nondestructive X-ray diffraction (XRD) technique can be used to evaluate the crystalline nature, average crystallite size, phase purity, and preferential

crystal orientation of the metal nanoparticles. Due to the interaction between the incident X-rays and the atomic structure of a crystalline solid, a diffraction pattern is generated. Each crystalline solid has its distinctive atomic structure and XRD pattern. These patterns can be employed as fingerprints for the identification of the crystal structure of a solid.<sup>39</sup> The XRD spectra of metal nanoparticles exhibit characteristic diffraction peaks. So by comparing these diffraction peaks with the standard data in the Joint Committee on Power Diffraction Standards (JCPDS), it is possible to elucidate the structure of the metal nanoparticle.<sup>40</sup> The broadening of the peaks in the XRD pattern verifies the formation of particles in the nanoregime.<sup>41</sup> The mean crystallite size of the nanoparticle can also be calculated from the XRD data by means of the Debye–Scherrer equation (eq 11.1).

$$D = 0.94\lambda/\beta (\cos\theta) \quad (11.1)$$

where  $D$  is the average crystallite size, 0.94 is the value of the Scherrer constant,  $\lambda$  is the wavelength of X-ray (0.1542 nm),  $\beta$  is the full width at half maximum (FWHM), and  $\theta$  is the Bragg's angle.<sup>42</sup> This technique has been widely used by researchers to measure the size of both AgNPs and AuNPs. In the phytosynthesis of AgNPs using *Saraca indica* flower extract, Vidhu and Philip<sup>43</sup> observed the diffraction peaks of the synthesized AgNPs at 38.45°, 44.6°, 64.80°, 77.66°, and 81.65° relating to (111), (200), (220), (311), and (222) planes, which confirmed the formation of AgNPs with face centered cubic symmetry. Furthermore, the broad peaks with fair intensity reveal the nanocrystalline nature of AgNPs. From the XRD pattern, the size and crystalline nature of biosynthesized AuNPs were determined by Aromal et al.<sup>44</sup> The authors confirmed the crystalline nature of the synthesized AuNPs by observing strong and fine diffraction peaks and calculated their average crystallite size as 11 nm. Furthermore, based on the most intense diffraction peak in the XRD profile, the preferential crystal orientation of the metal nanoparticles is also assumed.

### **11.3.3 HIGH RESOLUTION TRANSMISSION ELECTRON MICROSCOPY (HR-TEM)**

HR-TEM is the most efficient method to analyze the morphological characteristics of metal nanoparticles. It can provide clear-cut information regarding particle size, shape, dispersity, crystallinity, and interparticle interaction. In transmission electron microscopic analysis, a beam of electrons from an electron gun is transmitted through an ultrathin sample to form an

image. Here, a thin film of the sample is first fixed on a copper grid coated with carbon, then a monochromatic beam of electrons penetrates the film and projects it onto a screen to create an image. HR-TEM can produce high-resolution images at the atomic-scale level so that the lattice fringes within the crystalline material can be visualized. It has the potential to directly image atoms in crystalline samples at resolutions close to 0.1 nm, smaller than the interatomic distance. Selected area electron diffraction (SAED) is a crystallographic technique equipped with an HR-TEM machine to recognize the crystallographic phases. The bright rings observed in the selected area of the electron diffraction pattern can confirm the crystallinity of the sample, and hence they can provide supporting evidence for XRD analysis. After bioreduction of Ag and Au ions by *Hibiscus rosa-sinensis* leaf extract, Philip<sup>45</sup> observed triangular, spherical, dodecahedral, and hexagonal Ag–Au nanoparticles with average sizes of 13–14 nm in TEM images. In a similar study, Dhayananthaprabhu et al.<sup>46</sup> used *Cassia auriculata* flower extract to synthesize AuNPs and observed spherical, hexagonal, and triangular shaped AuNPs with a size range of 10–55 nm through TEM analysis.

#### 11.3.4 ENERGY DISPERSIVE X-RAY (EDX) ANALYSIS

Energy dispersive X-ray (EDX or EDS) analysis helps to evaluate the elemental composition of metal nanoparticles. This simple X-ray spectroscopic analytical technique is usually incorporated with TEM or SEM. It records the number and energy of X-rays emitted from the specimen when it is bombarded with a high-energy electron beam. When a specimen is bombarded with an electron beam, the incident beam may eject a core electron (a K-shell electron) from the atoms at the sample surface and thus create an electron hole. This electron hole is filled by an outer, higher energy shell electron, and an X-ray is emitted corresponding to the difference in energy between the higher energy shell and the lower energy shell. The energy of the X-rays emitted is specific for each element. Therefore, by measuring the energy of the typical X-ray emitted, the elements present in a given sample can be identified. By observing a peak at 2 keV in the EDX spectrum, Sathishkumar et al.<sup>47</sup> confirmed the presence of AuNPs during their biosynthesis using *Illicium verum*. With the aid of the EDX spectrum, Dipankar and Murugan<sup>48</sup> confirmed the synthesis of AgNPs using *Iresine herbstii* leaf extract. Their analysis showed a sharp peak of Ag at around 3 keV, indicating the reduction of AgNO<sub>3</sub> to AgNPs.

### **11.3.5 ZETA POTENTIAL ANALYSIS**

Zeta potential analysis measures the stability and surface charge of the colloidal nanoparticles. Due to the presence of surface charge, nanoparticles attract a thin layer of oppositely charged ions to their surface. This double layer of ions moves with the nanoparticle as it diffuses throughout the solution. The electrical potential at the boundary of the double layer is known as the zeta potential of the particle, and its value usually ranges from +100 to −100 mV. The zeta potential measurement provides an indication of the stability of the colloidal dispersion. Nanoparticles with zeta potential values greater than +30 mV or less than −30 mV are normally stable, whereas colloids with low zeta potential values will tend to aggregate due to interparticle attraction.<sup>49</sup>

### **11.3.6 FOURIER TRANSFORM INFRARED (FTIR) SPECTROSCOPY**

FTIR spectroscopy is an eminent technique used to analyze the surface chemistry of nanoparticles. It enables the identification of various functional groups attached to the surface of the nanoparticles on behalf of their vibrational signatures in a precise, faster, and nondestructive way. The functional groups involved in bioreduction can be approximated using FTIR spectroscopy. It is associated with the vibrational motion of atoms within a molecule. In order to get the IR spectrum of a sample, infrared radiation of successively increasing wavelength is allowed to pass through the sample, and the percentage of transmittance is measured. The plot of percentage transmittance versus wave number is called an infrared spectrum. Each dip in the spectrum is called a peak, and it denotes the absorption of infrared radiation at that frequency. Every functional group requires a different frequency for absorption. Therefore, an IR spectrum can be considered the fingerprint of a molecule.

To investigate how functional groups contribute to bioreduction, the FTIR spectra of virgin plant biomass or extract will be compared with those of synthesized nanoparticles. A number of researchers have used FTIR to identify various plant biomolecules responsible for metal bioreduction.<sup>50–52</sup>

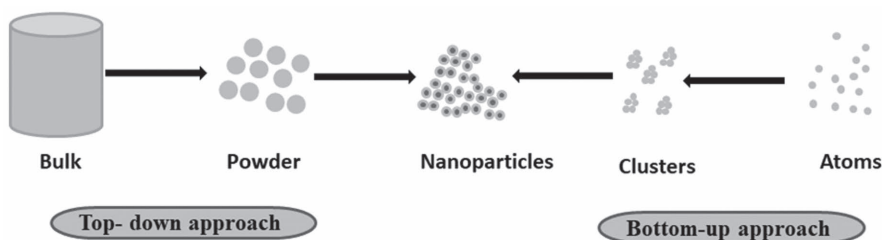
## **11.4 SYNTHESIS OF NOBLE METAL NANOPARTICLES**

The synthesis of metal nanoparticles is of great scientific interest due to their wide array of applications. Substantial efforts have been made toward

developing new and promising procedures for the synthesis of noble metal nanoparticles. In general, there are two synthetic strategies, namely the top-down approach and the bottom-up approach (Scheme 11.2), available for the fabrication of metal nanoparticles.

### 11.4.1 TOP-DOWN APPROACH

In the top-down approach, a bulk starting material is broken down into fine nanoparticles by means of various physical techniques like mechanical grinding, milling, etching, sputtering, arc discharge, laser ablation, thermal decomposition, etc., and the resulting nanosized particles are subsequently stabilized by adding a suitable colloidal protecting agent.<sup>53</sup> Using this approach, nanomaterials can be synthesized at bulk levels within a short span of time.<sup>54</sup> But it may introduce imperfections in the surface structure of the product. Such imperfections could have a significant impact on the surface chemistry and physical properties of nanomaterials owing to the increased surface-to-volume ratio.<sup>55</sup> Moreover, top-down approaches may bring about a relatively broad size distribution, varied particle shapes, and the presence of a considerable amount of impurities from the milling medium.<sup>56</sup> So, they are not fit for the synthesis of monodispersed particles.



**SCHEME 11.2** Various approaches for the synthesis of nanoparticles.

### 11.4.2 BOTTOM-UP APPROACH

In the bottom-up approach, nanoparticles are fabricated from the bottom, that is, by assembling atoms one after another, molecules one after another, or clusters one after another by using various chemical and biological procedures.<sup>57</sup> It involves the self-assembly of atoms into new nuclei, which then grow into particles of nanoscale dimension. The bottom-up methods



offer homogenous nanostructures with perfect crystallographic and surface configurations at a much cheaper cost.<sup>58</sup> So, they are preferred for the generation of uniform nanomaterials with definite size, shape, and morphology.

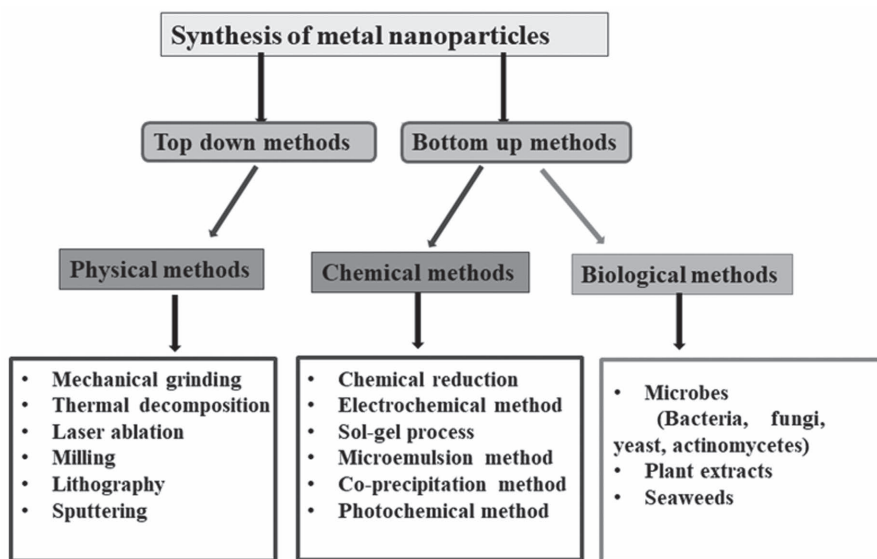
## **11.5 SIGNIFICANCE OF GREEN SYNTHESIS OF NANOPARTICLES**

The three common methods of nanoparticle synthesis are represented in Scheme 11.3. Among them, physical and chemical procedures are conventionally used for the synthesis of nanoparticles. Although these physico-chemical processes yield nanoparticles of well-defined dimensions, they are laborious, costly, often demand drastic conditions such as high temperature and pressure, and may also involve the use of nonpolar organic solvents, toxic reducing agents, and hazardous stabilizing agents in the synthetic procedures, which restrict their use in biomedical and clinical applications.<sup>59</sup> Moreover, the nanoparticles thus formed may also become hazardous due to the coating of the toxic moieties from the preparation media as ligands on their surface.<sup>60</sup> As a result, there is an essential need for an alternative, cost-effective, safe, and environmentally sound technique for nanoparticle fabrication.

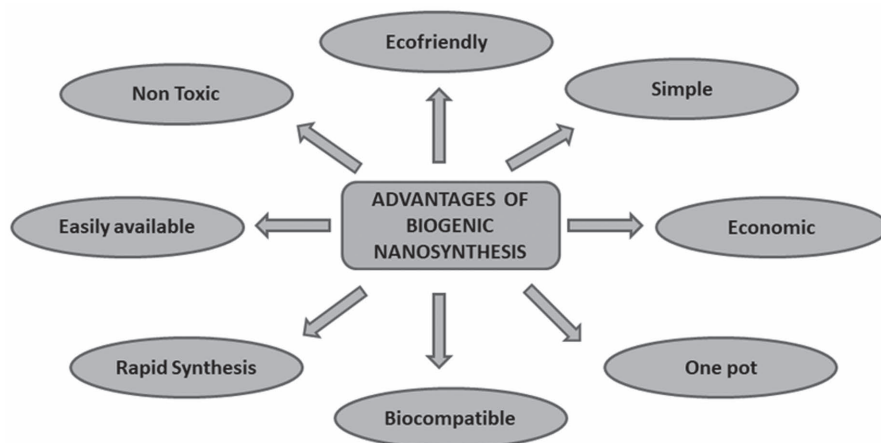
The necessity to develop cost-effective and eco-friendly methods for nanoparticle synthesis has attracted the interest of the scientific community in exploring the potential of biological entities. During the last decade, numerous research papers have been published regarding the biosynthesis of silver and gold nanoparticles by means of varied natural resources like microbes, terrestrial plants, and seaweeds.<sup>61–63</sup> The development of such biologically inspired nanosynthetic processes is evolving into an important branch of nanotechnology called green nanotechnology. It integrates the principles of green chemistry into nanotechnology and revolutionizes the nanosynthetic approach by using an environmentally benign solvent (water), nontoxic reducing agent, and a cost-effective and easily renewable stabilizing agent.

The biosynthetic strategies of metal nanoparticles are gaining more prominence due to their ease of use, rapid rate of synthesis, and economical and environmentally friendly nature. In most green nanosynthesis, the biological entities involved play a dual role as a metal ion reducing agent and also as a capping agent for the formed nanoparticle. Also, the biomolecules adsorbed on the surface of the particle make them biocompatible and offer very interesting applications in biomedicine and related fields. Since high

temperature and pressure are not prerequisites for this process, it is an energy-efficient methodology that can be easily adapted for large-scale synthesis.<sup>64</sup> Scheme 11.4 illustrates some of the advantages of green synthesis over traditional nanosynthesis.



**SCHEME 11.3** Various methods for the synthesis of nanoparticles.



**SCHEME 11.4** Advantages of bioassisted synthesis of nanoparticles.

Nature has an extensive variety of resources, such as microbes, plant extracts, marine algae, etc., as “biofactories” for the synthesis of nanoparticles. There are so many reports related to the usage of these natural sources for the fabrication of silver and gold nanoparticles using the green chemistry approach.

Several microorganisms, such as bacteria, fungi, actinomycetes, yeasts, viruses, etc., have emerged as environmentally sustainable precursors for the fabrication of silver and gold nanoparticles. Various microorganisms employ either extracellular or intracellular pathways for the biosynthesis of nanoparticles. In extracellular synthesis, metal ions are entrapped on the outer surface of the microbial cells and get reduced in the presence of enzymes or biomolecules, whereas intracellular synthesis takes place inside the microbial cells.<sup>65</sup> Researchers have suggested that extracellular synthesis of nanoparticles would be inexpensive, favor large-scale production, and necessitate simpler downstream processing.<sup>66</sup> Therefore, the extracellular pathway is more desirable than the intracellular method for the synthesis of nanoparticles. Several bacterial strains, such as *Klebsiella pneumoniae*,<sup>67</sup> *Bacillus licheniformis*,<sup>68</sup> *Pseudomonas fluorescens*,<sup>69</sup> and *Salmonella typhirium*,<sup>70</sup> have been successfully used in the biosynthesis of silver and gold nanoparticles. Some of the recent reports on the microbial-assisted synthesis of noble metal nanoparticles are given in Table 11.1.

Compared to microbe-assisted nanosynthesis, plant-mediated procedures are more advantageous in terms of ease, ready availability of resources, rapid rate of synthesis, and ecofriendliness. Furthermore, it eliminates the expensive and complex methodologies for maintaining microbial cultures and could also be extended to bulk-scale fabrication. Furthermore, the bioreduction efficacy of the plant extracts is found to be higher than that of microbial culture. Consequently, in recent years, researchers have started focusing on the utilization of various plant resources for the biosynthesis of metal nanoparticles. Various plant parts like leaves,<sup>87</sup> stems,<sup>88</sup> roots,<sup>89</sup> seeds,<sup>90</sup> fruits,<sup>91</sup> and flowers<sup>92</sup> have been exploited for the biosynthesis of metal nanoparticles. Plants are known to contain a large number of bioactive metabolites such as polyphenols, terpenoids, flavonoids, tannins, saponins, proteins, vitamins, ketones, aldehydes, amino acids, alkaloids, and polysaccharides, which play a crucial part in the reduction of metal ions as well as the stabilization of formed nanoparticles.<sup>93</sup> Terrestrial plants are extensively studied for their potential in the synthesis of metal nanoparticles.<sup>94–96</sup> Table 11.2 summarizes an overview of the green synthesis of silver and gold nanoparticles by plants.

**TABLE 11.1** Recent Reports on the Microbial-Assisted Synthesis of AgNPs and AuNPs.

Microorganism	Type of microorganism	Nanoparticle	Size (nm)	Shape	References
<i>Pseudomonas denitrificans</i>	Bacteria	AuNPs	25–30	Mostly spherical	[71]
<i>Klebsiella pneumoniae</i>	Bacteria	AuNPs	10–15	Spherical	[72]
<i>Bacillus cereus</i>	Bacteria	AgNPs	2–20	Spherical	[73]
<i>Aspergillus terreus</i>	Fungi	AgNPs and AuNPs	8–20 and 10–20	Spherical and anisotropic	[74]
<i>Fusarium oxysporum</i>	Fungi	AgNPs	1–50	Mostly spherical	[75]
<i>Bacillus clausii</i>	Bacteria	AgNPs	30–80	Nearly spherical	[76]
<i>Gordonia amarae</i>	Actinomycetes	AuNPs	5–15	Spherical	[77]
<i>Streptomyces microflavus</i>	Bacteria	AuNPs	20–50	Spherical	[78]
<i>Microbacterium</i> sp. NV4	Bacteria	AgNPs	17–26	Cubic	[79]
<i>Penicillium chrysogenum</i>	Fungi	AuNPs	1–3	Spherical	[80]
<i>Metarhizium anisopliae</i>	Fungi	AgNPs	28–38	Rod	[81]
<i>Magnusiomyces ingens</i> LH-F1	Yeast	AuNPs	10–80	Spherical, triangular, and hexagonal	[82]
<i>Guignardia mangiferae</i>	Fungi	AgNPs	5–30	Spherical	[83]
<i>Phomopsis liquidambaris</i>	Fungi	AgNPs	18.7	Spherical	[84]
<i>Staphylococcus epidermidis</i>	Bacteria	AuNPs	20–25	Spherical	[85]
<i>Pseudomonas fluorescens</i>	Bacteria	AuNPs	5–50	Spherical	[86]

**TABLE 11.2** Recent Reports on the Plant-Mediated Synthesis of AgNPs and AuNPs.

Plant	Nanoparticle	Size (nm)	Shape	References
<i>Ficus retusa</i>	AgNPs	15	Spherical	[97]
	AuNPs	10–25	Spherical	
<i>Garcinia mangostana</i>	AgNPs	23	Spherical	[98]
	AuNPs	20–40	Spherical	
<i>Enicostemma axillare</i>	AgNPs	15–20	Spherical	[99]
<i>Albizia procera</i>	AgNPs	6.18	Spherical	[100]
<i>Cleome viscosa</i>	AgNPs	20–50	Irregular	[101]
<i>Cinnamon</i>	AgNPs	20–30	Nearly spherical	[102]
<i>Carica papaya</i>	AgNPs	16–20	Spherical	[103]
<i>Elaeis guineensis</i>	AuNPs	35–75	Spherical	[104]
<i>Ginkgo biloba</i>	AuNPs	10–40	Spherical	[105]
<i>Citrullus lanatus</i>	AgNPs	17.96	Spherical	[106]
<i>Mimusops elengi</i>	AuNPs	9–14	Spherical	[107]
<i>Stevia rebaudiana</i>	AuNPs	17	Cubic	[108]
<i>Adathoda vasica</i>	AgNPs	10–50	Spherical	[109]
<i>Cymbopogon citratus</i>	AuNPs	20–50	Spherical, triangular, and rod	[110]
<i>Aloe vera</i>	AgNPs	35–55	Spherical and cubic	[111]
<i>Nerium oleander</i>	AuNPs	2–10	Spherical	[112]
<i>Ziziphora tenuior</i>	AgNPs	8–40	Spherical	[113]
<i>Abutilon indicum</i>	AgNPs	7–17	Spherical	[114]
<i>Beetroot</i>	AgNPs	10–15	Spherical	[115]

**TABLE 11.2** (Continued)

Plant	Nanoparticle	Size (nm)	Shape	References
<i>Calotropis gigantean</i>	AgNPs	5–30	Spherical	[116]
<i>Emblica officinalis</i>	AgNPs	10–20	Spherical	[117]
<i>Areca catechu</i> nut	AgNPs	18–24	Spherical	[118]
	AuNPs	13.7	Spherical	[119]
<i>Indigofera tinctoria</i>	AgNPs	9–26	Spherical	[120]
	AuNPs	6–29	Spherical, triangular, and hexagonal	
<i>Elephantopus scaber</i>	AgNPs	20–60	Spherical	[121]
<i>Cassia roxburghii</i>	AgNPs	15–20	Spherical	[122]
<i>Lawsonia inermis</i>	AgNPs	18–25	Spherical	[123]
<i>Ribes nigrum</i>	AuNPs	20	Hexagonal, triangular, and spherical	[124]
<i>Physalis angulate</i>	AgNPs	11–96	Nearly spherical	[125]
<i>Elettaria cardamomum</i>	AuNPs	15.2	Spherical	[126]

## **11.6 MARINE MACROALGAE OR SEaweEDS AS “NANOFactORIES”**

The marine ecosystem has acquired a major concern nowadays on the topic of the isolation and assessment of bioactive metabolites of pharmacological relevance. The phenomenal biodiversity encountered by the marine world values it as an abundant resource of numerous bioactive phytochemicals, including terpenoids, polyunsaturated fatty acids, xanthophylls, tocopherols, carotenoids, chlorophylls, polysaccharides, vitamins, phycocyanins, sterols, etc. These compounds are produced as a result of the exposure of marine organisms to complex habitats with harsh spatial, temporal, and seasonal variations.<sup>127</sup> Consequently, marine biological resources can be considered an expert candidate for nanotechnological applications.

Marine macroalgae, or seaweeds, exhibit intense diversity and have attracted potential attention. They normally flourish on rocks, corals, or any natural or man-made bedrock. They are consumed as sea vegetables in several southeast Asian countries, with the Japanese being the highest consumers. As an integral part of the marine environment, they offer a nourishing and breeding habitat for fish and invertebrates.<sup>128</sup>

Approximately 841 species of seaweeds were found in both intertidal and deepwater regions of the Indian coast, and they vary greatly in their color, quality, and biochemical constituents. Based on pigmentation, seaweeds are generally classified as Chlorophyceae (green algae), Rhodophyceae (red algae), and Phaeophyceae (brown algae).<sup>129</sup> Brown and red seaweeds are limited to marine ecosystems, while green algae are also found in freshwater and terrestrial environments. Seaweeds contain several nutrient-rich composites like proteins, lipids, dietary fibers, essential fatty acids, minerals, and vitamins. They are abundant sources of a wide array of bioactive substances like polysaccharides, proteins, sterols, polyphenols, flavonoids, terpenoids, etc. with potent therapeutic values.<sup>130</sup> They are the only source of phycocolloids such as alginates, carrageenans, carotenoids, and agars, which have a high commercial value. Algal sulfated polysaccharides are also found to have numerous biological activities, structural diversity, and pharmacological features. Owing to their nutritional value and availability of many bioactive properties, they are being considered functional foods and an important constituent of nutraceuticals.<sup>131</sup>

Due to the richness of phytochemicals having hydroxyl, amino, and carboxyl functional groups, the seaweed extract can function both as an efficient metal reducing agent and as a capping agent to provide excellent stability to the formed nanoparticles in a single step. However, these renewable

marine resources are the least explored for nanobiosynthesis. Only a limited number of reports exist on the marine macroalgae-assisted biosynthesis of nanoparticles.<sup>132</sup>

### 11.6.1 BIOSYNTHESIS OF NANOPARTICLES USING PHAEOPHYCEAE

The first report on the seaweed-mediated biosynthesis of nanoparticles was by Singaravelu et al. in 2007.<sup>133</sup> In this work, an aqueous extract of brown seaweed *Sargassum wightii* has been utilized for the bioreduction of  $\text{HAuCl}_4$  to form monodispersed AuNPs of the size range 8–12 nm. Govindaraju et al. also utilized *Sargassum wightii* for the extracellular synthesis of spherical AgNPs and studied their antibacterial potential against human pathogens.<sup>134</sup> Kumar et al. employed *Sargassum ilicifolium* for the biosynthesis of AgNPs, and their antibacterial and cytotoxic activities were studied.<sup>135</sup> Thangaraju et al. used another *Sargassum* species, *Sargassum polycystum*, for the biosynthesis of AgNPs with antibacterial and cytotoxic activity.<sup>136</sup> Dhas et al. synthesized spherical AuNPs of average size 35 nm using *Sargassum swartzii*, and their cytotoxic activity against human cervical carcinoma cells was reported.<sup>137</sup> Vijayan et al. could synthesize both silver and gold nanoparticles using an aqueous extract of brown seaweed, *Turbinaria conoides*, and investigated their antimicrofouling activity.<sup>138</sup> Arockiya Aarthi Rajathi et al. reported a rapid biological synthesis of antibacterial AuNPs using brown seaweed, *Stoechospermum marginatum*.<sup>139</sup> Brown algae *Padina pavonica*-mediated gold nanobiosynthesis and their antibacterial activity were described by Isaac et al.<sup>140</sup> Shiny et al. studied the antibacterial potential of AgNPs biosynthesized using the algae *Padina gymnospora*.<sup>141</sup> Princy et al. reported an eco-friendly synthesis of AuNPs using an aqueous extract of brown seaweed *Lobophora variegata* and its potential application in the reduction of hazardous nitrophenols to beneficial aminophenols.<sup>142</sup> *Sargassum muticum*-mediated biosynthesis of AgNPs and its antifungal, antiviral, antiplatelet, and antiangiogenesis activities were reported by Azizi et al.<sup>143</sup> In another work, *Sargassum cinereum*-mediated AgNPs showed excellent antibacterial activity against multidrug-resistant pathogens like *E. aerogenes*, *S. aureus*, *S. typhi*, and *P. vulgaris*.<sup>144</sup> In recent times, Ramakrishna et al. demonstrated the *Sargassum tenerrimum*-mediated green synthesis of AuNPs and its dose-dependent catalytic activity in the degradation kinetics of dyes like rhodamine B and sulforhodamine 101.<sup>145</sup> Table 11.3 summarizes the size and morphological characteristics of silver and gold nanoparticles biosynthesized using Phaeophyceae.



**TABLE 11.3** The Biosynthesis of AgNPs and AuNPs by Brown Seaweeds.

Marine macroalgae	Nanoparticle	Size (nm)	Morphology	References
<i>Sargassum wightii</i>	AgNPs	8–27	Spherical	[134]
	AuNPs	8–12	Spherical	[133]
<i>Sargassum ilicifolium</i>	AgNPs	23	Spherical	[135]
<i>Sargassum polycystum</i>	AgNPs	15–20	Spherical	[136]
<i>Sargassum swartzii</i>	AgNPs	6.18	Spherical	[137]
<i>Sargassum muticum</i>	AgNPs	20–50	Irregular	[143]
<i>Sargassum cinereum</i>	AgNPs	20–30	Nearly spherical	[144]
<i>Sargassum tenerimum</i>	AgNPs	20	Spherical	[146]
	AuNPs	5–45	Anisotropic and polydispersed	[145]
<i>Turbinaria conoides</i>	AgNPs	2–17	Spherical	[138]
	AuNPs	12–57	Anisotropic and polydispersed	
<i>Stoechospermum marginatum</i>	AuNPs	18–93	Spherical	[139]
<i>Padina pavonica</i>	AuNPs	10–72	Spherical	[140]
<i>Padina gymnospora</i>	AgNPs	25–40	Spherical	[141]
<i>Padina tetrastrum</i>	AgNPs	14	Spherical	[147]
	AuNPs	11.4	Spherical	[148]
<i>Lobophora variegata</i>	AuNPs	11.69	Spherical	[142]
<i>Dictyota bartayresiana</i>	AuNPs	23	Spherical	[149]
<i>Cystoseira baccata</i>	AuNPs	8.4 ± 2.2	Spherical	[150]

### 11.6.2 BIOSYNTHESIS OF NANOPARTICLES USING RHODOPHYCEAE

There are only a few reports available on the red algae-mediated synthesis of metal nanoparticles. Vivek et al. reported the biosynthesis of spherical AgNPs using the aqueous extract of red seaweed, *Gelidiella acerosa*.<sup>151</sup> In a similar study, an aqueous extract of *Galaxaura elongata*-mediated synthesis of AuNPs showed antibacterial activity against *E. coli* and *K. pneumoniae*.<sup>152</sup> Unlike the traditional green synthesis methods, a rapid and novel microwave-assisted protocol was devised by Priyadharshini et al. for the biosynthesis of AgNPs using the algae *Gracilaria edulis*.<sup>153</sup> The green synthesis of AgNPs using *Acanthophora spicifera* and its antimicrobial activity against biofilm forming bacteria *S. typhi* and *S. flexneri* were reported by Kumar et al.<sup>154</sup> A brief report on the Rhodophyceae-mediated biosynthesis of silver and gold nanoparticles is given in Table 11.4.

**TABLE 11.4** Red Seaweed-Mediated Biosynthesis of AgNPs and AuNPs.

Marine macroalgae	Nanoparticle	Size (nm)	Shape	References
<i>Gelidiella acerosa</i>	AgNPs	22	Spherical	[151]
<i>Gracilaria edulis</i>	AgNPs	12–100	Spherical	[153]
<i>Acanthophora spicifera</i>	AgNPs	48	Spherical	[154]
<i>Gracilaria dura</i>	AgNPs	6	Spherical	[155]
<i>Kappaphycus alverazii</i>	AgNPs AuNPs	73 10–40	Irregular	[156]
<i>Gracilaria corticata</i>	AgNPs	18–46	Nearly spherical	[157]
<i>Gracilaria birdiae</i>	AgNPs	20.3	Spherical	[158]
<i>Galaxaura elongata</i>	AuNPs	3.8–77	Rod, triangular, truncated, and hexagonal	[152]

### 11.6.3 BIOSYNTHESIS OF NANOPARTICLES USING CHLOROPHYCEAE

Using the marine green algae *Caulerpa racemosa*, Kathiraven et al. synthesized AgNPs with a size range of 5–25 nm and studied their antibacterial activity against human pathogens such as *Staphylococcus aureus* and *Proteus mirabilis*.<sup>159</sup> Kannan et al. synthesized AgNPs using both fresh and dried extracts of the green seaweed, *Codium capitatum*, and observed more bioreduction potential in the fresh seaweed extract.<sup>160</sup> In another study, Rajesh et al. synthesized AgNPs using green seaweed *Ulva fasciata* extract as a bioreductant.<sup>161</sup> AgNPs synthesized using the green seaweed *Ulva lactuca* efficiently degraded methyl orange and demonstrated to have photocatalytic activity.<sup>162</sup> Yousefzadi et al. employed *Enteromorpha flexuosa*, a green seaweed, for the eco-friendly biosynthesis of AgNPs, which showed excellent antibacterial activity.<sup>163</sup> Recently, Ramkumar et al. reported the biosynthesis of AgNPs using an aqueous extract of seaweed, *Enteromorpha compressa*, which performed as both a reductant and a stabilizing agent.<sup>164</sup> The biosynthesis of metal nanoparticles using green seaweed is summarized in Table 11.5.

Among several genres of bioreductants, seaweeds have distinct advantages, such as:

- High metal uptake capacity
- Ready availability
- Renewable marine resources
- Abundance of bioactive metabolites that may aid in bioreduction
- Safe to handle
- Highly economical
- One-step simple process

- Rapid rate of nanosynthesis
- Results in nanoparticles of high stability
- Better control over the size and shape of nanoparticles
- Appropriate for large-scale production

**TABLE 11.5** Green Seaweed-Mediated Biosynthesis of AgNPs and AuNPs.

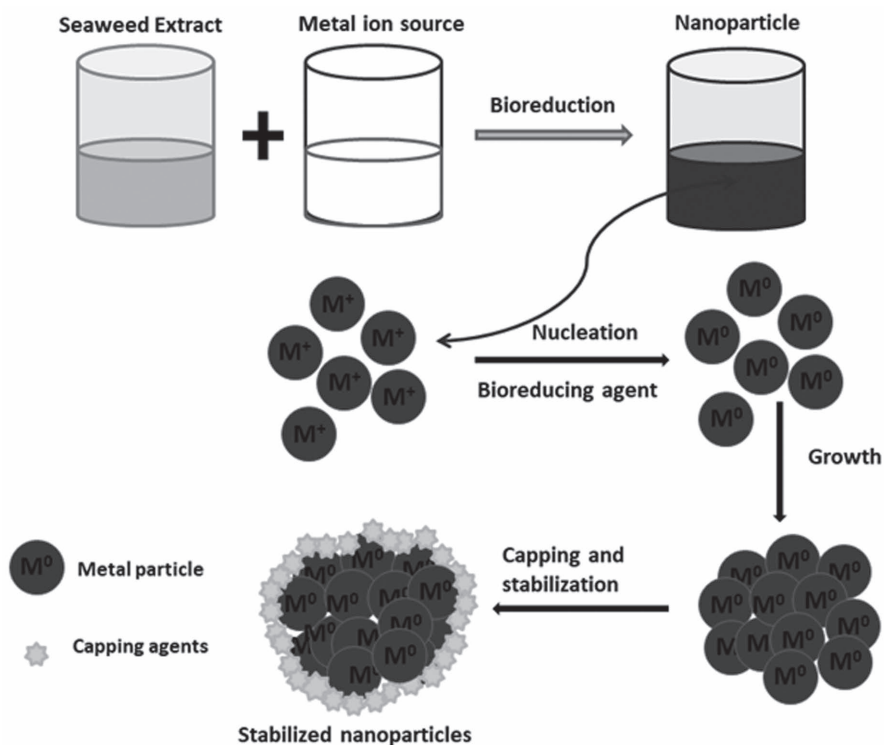
Marine macroalgae	Nanoparticle	Size (nm)	Shape	References
<i>Caulerpa racemose</i>	AgNPs	5–25	Spherical	[159]
<i>Codium capitatum</i>	AgNPs	3–44	Spherical	[160]
<i>Ulva fasciata</i>	AgNPs	28–41	Spherical	[161]
<i>Ulva lactuca</i>	AgNPs	20	Irregular	[162]
<i>Ulva reticulata</i>	AgNPs	40–50	Nearly spherical	[165]
<i>Enteromorpha flexuosa</i>	AgNPs	15	Circular	[163]
<i>Enteromorpha compressa</i>	AgNPs	40–50	Spherical	[164]
<i>Chaetomorpha linum</i>	AgNPs	3–44	Nearly spherical	[166]

## 11.7 PROBABLE MECHANISM OF SEAWEED-MEDIATED SYNTHESIS OF METAL NANOPARTICLES

Three components, namely, reducing agents, stabilizing agents, and solvent media, are needed for the biofabrication of metal nanoparticles.<sup>167</sup> During seaweed-mediated metallic nanoparticle synthesis, phytoconstituents of seaweed extracts play the dual role of reductant and stabilizer and utilize water as the solvent medium; hence, it is regarded as a green process. Nevertheless, the specific mechanism for the seaweed-mediated synthesis of nanoparticles has not yet been well understood. Due to the large variety of phytochemicals in the seaweed extract, it is a challenging task to identify a specific bioreducing and stabilizing agent responsible for the fabrication and stabilization of nanoparticles. However, it is very likely that for the bioreduction reaction of metallic ions, several phytoconstituents in plant extracts act synergistically.

Seaweed-mediated biosynthesis of nanoparticles is an eco-friendly and simple process. In ambient conditions (usually under 100°C), the precursor metal salt solution and the aqueous extract of seaweed are well mixed. On exposure to seaweed extract, bioreduction of the metal salt takes place immediately, and the formation of nanoparticles is typically revealed by a color change of the reaction mixture. The reaction is accomplished within a few minutes.

Seaweed-mediated biofabrication of metal nanoparticles involves three stages: activation, growth, and termination.<sup>168</sup> The first step is the activation phase, in which the metal ions are recovered from their precursor metal salt solution by the action of phytochemical metabolites in the seaweed extract, which have reduction potentials. As a result, the metal ions are converted from their higher oxidation states to zerovalent states, followed by the nucleation of atoms.<sup>169</sup> This is tailed by the growth period in which the segregated metal atoms associate to form metal nanoparticles, which can be further reduced by biological action to a variety of morphologies, including spheres, triangles, cubes, rods, hexagons, pentagons, and wires.<sup>170</sup> After the metal nanoparticles have been capped by seaweed extract metabolites, the termination phase in the biogenic nanosynthesis takes place, at which the metal nanoparticles acquire the most stable morphology.<sup>171</sup> The probable mechanism of seaweed-mediated green synthesis of nanoparticles is displayed in Scheme 11.5.



**SCHEME 11.5** Probable mechanism of seaweed-mediated nanobiosynthesis.

## **11.8 APPLICATIONS OF METALLIC NANOPARTICLES**

Metallic nanoparticles biofabricated from seaweeds can compete with conventional medicines and have been reported to have antibacterial,<sup>172</sup> anticancerous,<sup>173</sup> and antifungal activities.<sup>174</sup> Apart from medicinal applications, the metal NPs have extensive applicability in electronics, optics, cosmetics, coatings,<sup>175</sup> food packaging, sensing devices, space industries, therapeutics, bioremediation,<sup>176</sup> environmental health,<sup>177</sup> mechanics, light emitters, nonlinear optical devices, chemical industries,<sup>178</sup> and photoelectrochemical applications.<sup>179,180</sup>

## **11.9 CONCLUSION AND FUTURE ASPECTS**

The synthesis of noble metal nanoparticles using a biosynthetic pathway has significant potential and numerous substantial advantages when compared to the conventional method of nanoparticle synthesis. Increasing awareness toward a greener approach demands environment-friendly methods for synthesizing nontoxic nanomaterials that are also biocompatible. The waste products are relatively nontoxic and easy to dispose of because they are mostly composed of leftover natural plant extracts. Most of the studies related to metal nanoparticles are carried out by research laboratories on a small scale, and no reports are available on pilot plant or industrial-scale fabrication of nanomaterials using natural products. Hence, there must be efforts to establish industrial processes for the sustained production of biosynthesized metallic nanoparticles.

Though various biological entities have been exploited in the biosynthetic pathways of metal nanoparticles, the use of marine macroalgae or seaweed as nanofactories has been limited. The exact mechanism of how these plant metabolites carry out reduction and capping is still elusive and challenging. More detailed studies are also needed to uncover the reaction mechanism behind the formation of biosynthesized metallic nanoparticles. Plant-derived nanoparticles have a wide range of medical applications, such as fluorescent labeling, targeted therapeutic drug delivery, tumor destruction through hyperthermia, and can be used as antibacterial agents in bandages. Additionally, they could be used to deliver antimicrobial compounds to crops as pesticides.

Biofabrication of metal nanoparticles from marine resources, especially marine macroalgae, is a promising area in “greener” marine nanotechnology with enormous application in the fields of chemistry, electronics, medicine,

and agriculture. Marine renewable resources like seaweeds stand as a promising candidate for this eco-friendly and inexpensive synthetic process with significant advances in biomedical and environmental applications. In the future, functionalized biosynthesized metal nanoparticles are expected to offer a better platform in various fields of science, medicine, and agriculture.

## KEYWORDS

- **biosynthesis**
- **silver nanoparticles**
- **gold nanoparticles**
- **terrestrial plants**
- **microbes**
- **marine macroalgae**

## REFERENCES

1. Mohanpuria, P.; Rana, N. K.; Yadav, S. K. Biosynthesis of Nanoparticles: Technological Concept and Future Applications. *J. Nanopart. Res.* **2008**, *10*, 507–517.
2. Debjani, N.; Pratyusa, B. Green Nanotechnology—A New Hope for Medical Biology. *Environ Toxicol. Pharmacol.* **2013**, *36*, 997–1014.
3. BSI (British Standards Institute). Terminology for Nanomaterials Nanoparticles PAS **2007**, *136*, 1–16.
4. Suresh, A. K. Introduction to Nanocrystallites, Properties, Synthesis, Characterizations, and Potential Applications. *Metallic Nanocrystallites and Their Interaction with Microbial Systems*, Springer Briefs in Biometals; Barton, L. L., Ed.; 2012; pp 1–23.
5. Thakkar, K. N.; Mhatre, S. S.; Parikh, R. Y. Biological Synthesis of Metallic Nanoparticles. *Nanomed.: Nanotechnol. Biol. Med.* **2010**, *6*, 257–262.
6. Heiligt, F. J.; Niederberger, M. The Fascinating World of Nanoparticle Research. *Mater. Today* **2013**, *16*, 262–271.
7. Rafique, M.; Sadaf, I.; Rafique, M. S.; Tahir, M. B. A Review on Green Synthesis of Silver Nanoparticles and Their Applications. *Artif. Cells Nanomed. Biotechnol.* **2017**, *45*, 1272–1291.
8. Jain, P. K.; Huang, X.; El-Sayed, I. H.; El-Sayed, M. A. Noble Metals on the Nanoscale: Optical and Photothermal Properties and Some Applications in Imaging, Sensing, Biology, and Medicine. *Acc. Chem. Res.* **2008**, *41*, 1578–1586.
9. Garcia, M. A. Surface Plasmons in Metallic Nanoparticles: Fundamentals and Applications. *J. Phys. D Appl. Phys.* **2012**, *44*, 28.

10. Kreibitz, U.; Vollmer, M. *Optical Properties of Metal Clusters*, Vol. 25; Springer Science & Business Media: New York, 2013.
11. Hutter, E.; Fendler, J. H. Exploitation of Localized Surface Plasmon Resonance. *Adv. Mater.* **2004**, *16*, 1685–1706.
12. Kim, J. S.; Kuk, E.; Yu, K. N.; Kim, J. H.; Park, S. J.; Lee, H. J. Antimicrobial Effects of Silver Nanoparticles. *Nanomed. NBM* **2007**, *3*, 95–101.
13. Ahmed, S.; Ahmad, M.; Swami, B. L.; Ikram, S. A Review on Plants Extract Mediated Synthesis of Silver Nanoparticles for Antimicrobial Applications: A Green Expertise. *J. Adv. Res.* **2016**, *7*, 17–28.
14. Sudha, S. S.; Rajamanickam, K.; Rengaramanujam, J. Microalgae Mediated Synthesis of Silver Nanoparticles and Their Antibacterial Activity Against Pathogenic Bacteria. *Ind. J. Exp. Biol.* **2013**, *52*, 393–399.
15. Li, Y.; Wu, Y.; Ong, B. S. Facile Synthesis of Silver Nanoparticles Useful for Fabrication of High-Conductivity Elements for Printed Electronics. *J. Am. Chem. Soc.* **2005**, *127*, 3266–3267.
16. Vidhu, V. K.; Philip, D. Catalytic Degradation of Organic Dyes Using Biosynthesized Silver Nanoparticles. *Micron* **2014**, *56*, 54–62.
17. Verma, A.; D.; Jain, N.; Singha, S. K.; Quraishi, M. A.; Sinha, I. Green Synthesis and Catalytic Application of Curcumin Stabilized Silver Nanoparticles. *J. Chem. Sci.* **2016**, *128*, 1871–1878.
18. Dong, X. Y.; Gao, Z. W.; Yang, K. F.; Zhang, W. Q.; Xu, L. W. Nanosilver as a New Generation of Silver Catalysts in Organic Transformations for Efficient Synthesis of Fine Chemicals. *Catal. Sci. Technol.* **2015**, *5*, 2554–2574.
19. Mahmudin, L.; Suharyadi, E.; Utomo, A. B. S.; Abraha, K. Optical Properties of Silver Nanoparticles for Surface Plasmon Resonance (SPR)-Based Biosensor Applications. *J. Modern Phys.* **2015**, *6*, 1071–1076.
20. Monyatsi, L. M.; Mthombeni, N. H.; Onyango, M. S.; BMomba, M. N. Cost-Effective Filter Materials Coated with Silver Nanoparticles for the Removal of Pathogenic Bacteria in Groundwater. *Int. J. Environ. Res. Public Health* **2012**, *9*, 244–271.
21. Gajbhiye, S.; Sakharwad, S. Silver Nanoparticles in Cosmetics. *J. Cosmetics Dermatol. Sci. App.* **2016**, *6*, 48–53, 2016.
22. El-Nour, A.; Eftaiha, K. M. M.; Al-Warthan, A. A.; Ammar, R. A. A. Synthesis and Applications of Silver Nanoparticles. *Arab. J. Chem* **2010**, *3*, 135–140.
23. Dubas, S. T.; Kumlangdudsana, P.; Potiyaraj, P. Layer-by-Layer Deposition of Antimicrobial Silver Nanoparticles on Textile Fibers. *Colloids Surfaces A: Physicochem. Eng. Aspects* **2006**, *289*, 105–110.
24. Marassi, V.; Cristo, L. D.; Smith, S. G. J.; Ortelli, S.; Blosi, M.; Costa, A. L.; Mello, A. P. Silver Nanoparticles as a Medical Device in Healthcare Settings: A Five-Step Approach for Candidate Screening of Coating Agents. *R. Soc. Open Sci.* **2018**, *5*, 171113.
25. Guerra, F.; Attia, M.; Whitehead, D.; Alexis, F. Nanotechnology for Environmental Remediation: Materials and Applications. *Molecules* **2018**, *23*, 1760.
26. Cabuzu, D.; Cirja, A.; Puiu, R.; Grumezescu, A. M. Biomedical Applications of Gold Nanoparticles. *Curr. Top. Med. Chem.* **2015**, *15*, 1605–1613.
27. Mieszawska, A. J.; Mulder, W. J. M.; Fayad, Z. A.; Cormode, D. P. Multifunctional Gold Nanoparticles for Diagnosis and Therapy of Disease. *Mol. Pharm.* **2013**, *10*, 831–847.
28. Kong, F. Y.; Zhang, J. W.; Li, R. F.; Wang, Z. X.; Wang, W. J.; Wang, W. Unique Roles of Gold Nanoparticles in Drug Delivery, Targeting and Imaging Applications. *Molecules* **2017**, *22*, 1445.

29. Thurn, K. T.; Brown, E. M. B.; Wu, A.; Vogt, S.; Lai, B.; Maser, J.; Woloschak, G. E. Nanoparticles for Applications in Cellular Imaging. *Nanoscale Res. Lett.* **2007**, *2*, 430–441.
30. Riley, R. S.; Day, E. S. Gold Nanoparticle-Mediated Photothermal Therapy: Applications and Opportunities for Multimodal Cancer Treatment. *Wiley Interdiscip. Rev. Nanomed. Nanobiotechnol.* **2017**, *9*, 1449.
31. Priya Doss, C. G.; Debajyoti, C.; Debottam, S. The Impact of Gold Nanoparticles on hTERT Gene Expression Leading to Termination of Malignant Tumor. *Gene* **2012**, *493*, 140–141.
32. Vijay Kumar, P. P. N.; Pammi, S. V. N.; Kollu, P.; Satyanarayana, K. V. V.; Shameem, U. Green Synthesis and Characterization of Silver Nanoparticles Using Boerhaaviadiffusa Plant Extract and Their Antibacterial Activity. *Ind. Crop Prod.* **2014**, *52*, 562–566.
33. Noruzi, M. Biosynthesis of Gold Nanoparticles Using Plant Extracts. *Bioprocess Biosyst. Eng.* **2015**, *38*, 1–14.
34. Templeton, A. C.; Pietron, J. J.; Murray, R. W.; Mulvaney, P. Solvent Refractive Index and Core Charge Influences on the Surface Plasmonadsorbance of Alkanethiolate Monolayer Protected Gold Clusters. *J. Phys. Chem. B* **2000**, *104*, 564–570.
35. Das, R. K.; Gogoi, N.; Bora, U. Green Synthesis of Gold Nanoparticles Using *Nyctanthesarbortristis* Flower Extract. *Bioprocess Biosyst. Eng.* **2011**, *34*, 615–619.
36. Gade, A.; Gaikwad, S.; Duran, N.; Rai, M. Green Synthesis of Silver Nanoparticles by *Phoma glomerata*. *Micron* **2014**, *59*, 52–59.
37. Narayanan, K. B.; Sakthivel, N. Biological Synthesis of Metal Nanoparticles by Microbes. *Adv. Colloid Interface Sci.* **2010**, *156*, 1–13.
38. Gurunathan, S.; Han, J.; Kwon, D. N.; Kim, J. H. Enhanced Antibacterial and Anti-Biofilm Activities of Silver Nanoparticles Against Gram-Negative and Gram-Positive Bacteria. *Nanoscale Res. Lett.* **2014**, *9*, 373.
39. Huang, J.; Li, Q.; Sun, D.; Lu, Y.; Su, Y.; Yang, X. Biosynthesis of Silver and Gold Nanoparticles by Novel Sundried *Cinnamomumcamphora* Leaf. *Nanotechnology* **2007**, *18*, 105104–105114.
40. Prathna, T. C.; Chandrasekaran, N.; Raichur, A. M.; Mukherjee, A. Biomimetic Synthesis of Silver Nanoparticles by *Citrus limon* (Lemon) Aqueous Extract and Theoretical Prediction of Particle Size. *Coll. Surf. B: Bionterf.* **2011**, *82*, 152–159.
41. Venu, R.; Ramulu, T. S.; Anandakumar, S.; Rani, V. S.; Kim, C. G. Bio-directed Synthesis of Platinum Nanoparticles Using Aqueous Honey Solutions and Their Catalytic Applications. *Colloids Surfaces A: Physicochem. Eng. Aspects* **2011**, *384*, 733–738.
42. Alexander, L.; Klug, H. P. Determination of Crystalline Size with the X-ray Spectrometer. *J. Appl. Phys.* **1950**, *21*, 137–142.
43. Vidhu, V. K.; Philip, D. Spectroscopic, Microscopic and Catalytic Properties of Silver Nanoparticles Synthesized Using *Saraca indica* Flower. *Spectrochim. Acta A* **2014**, *117*, 102–108.
44. S. Aromal, A.; V. Vidhu, K.; Philip, D. Green Synthesis of Well-Dispersed Gold Nanoparticles Using *Macrotylomauniflorum*. *Spectrochim. Acta A* **2012**, *85*, 99–104, 2012.
45. Philip, D. Green Synthesis of Gold and Silver Nanoparticles Using *Hibiscus rosasinensis*. *Phys. E: Low-Dimensional Syst. Nanostruct.* **2010**, *42*, 1417–1424.
46. Dhayananthaprabhu, J.; Lakshmi Narayanan, R.; Thiyagarajan, K. Facile Synthesis of Gold (Au) Nanoparticles Using *Cassia auriculata* Flower Extract. *Adv. Mater. Res.* **2013**, *678*, 12–16.



47. Sathishkumar, M.; Pavagadhi, S.; Mahadevan, A.; Balasubramanian, R. Biosynthesis of Gold Nanoparticles and Related Cytotoxicity Evaluation Using A549 Cells. *Ecotoxicol. Environ. Saf.* **2015**, *114*, 232–240.
48. Dipankar, C.; Murugan, S. The Green Synthesis, Characterization and Evaluation of the Biological Activities of Silver Nanoparticles Synthesized from *Iresine herbstii* Leaf Aqueous Extracts. *Colloids Surf. B Biointerfaces* **2012**, *98*, 112–119.
49. Saeb, A. T. M.; Alshammari, A. S.; Al-Brahim, H.; Al-Rubeaan, K. A. Production of Silver Nanoparticles with Strong and Stable Antimicrobial Activity Against Highly Pathogenic and Multidrug Resistant Bacteria. *Sci. World J.* **2014**, *2014*, 1–9.
50. Singh, A.; Sharma, M. M.; Batra, A. Synthesis of Gold Nanoparticles Using *Chick Pea* Leaf Extract Using Green Chemistry. *J. Optoelectron. Biomed. Mater.* **2013**, *5*, 27–32.
51. Bhau, B. S.; Ghosh, S.; Puri, S.; Borah, B.; Sarmah, D. K.; Khan, R. Green Synthesis of Gold Nanoparticles from the Leaf Extract of *Nepenthes khasiana* and Antimicrobial Assay. *Adv. Mater. Lett.* **2015**, *6*, 55–58.
52. Aziz, N.; Faraz, M.; Pandey, R.; Shakir, M.; Fatma, T.; Verma, A.; Barman, I.; Prasad, R. Facile Algae-Derived Route to Biogenic Silver Nanoparticles: Synthesis, Antibacterial, and Photocatalytic Properties. *Langmuir* **2015**, *31*, 11605–11612.
53. Shanker, U.; Jassal, V.; Rani, M.; Kaith, B. S. Towards Green Synthesis of Nanoparticles: From Bio-assisted Sources to Benign Solvents: A Review. *Intern. J. Environ. Anal. Chem.* **2016**, *96*, 801–835.
54. Thakkar, K. N.; Mhatre, S. S.; Parikh, R. Y. Biological Synthesis of Metallic Nanoparticles. *Nanomed.: Nanotechnol. Biol. Med.* **2010**, *6*, 257–262.
55. Siddiqi, K. S.; Husen, A.; Rao, R. A. K. A Review on Biosynthesis of Silver Nanoparticles and Their Biocidal Properties. *J. Nanobiotechnol.* **2018**, *16*, 14.
56. A. Mittal, K.; Bhaumik, J.; Kumar, S.; U. Banerjee, C. Biosynthesis of Silver Nanoparticles: Elucidation of Prospective Mechanism and Therapeutic Potential. *J. Colloid Interface Sci.* **2014**, *415*, 39–47.
57. Baker, S.; B. Harini, P.; Rakshith, D.; Satish, S. Marine Microbes: Invisible Nanofactories. *J. Pharm. Res.* **2013**, *6*, 383–388.
58. Sharma, D.; Kanchi, S.; Bisetty, K. Biogenic Synthesis of Nanoparticles: A Review. *Arab. J. Chem.* **2015**.
59. Isaac, R. S. R.; Sakthivel, G.; Murthy, C. Green Synthesis of Gold and Silver Nanoparticles Using *Averrhoa bilimbi* Fruit Extract. **2013**, *2013*.
60. Kharisova, O. V.; Dias, H. V. R.; Kharisov, B. I.; Pérez, B. O.; Pérez, V. M. J. The Greener Synthesis of Nanoparticles. *Trends Biotechnol.* **2013**, *31*, 240–248.
61. Hulkoti, N. I.; Taranath, T. C. Biosynthesis of Nanoparticles Using Microbes—A Review. *Colloid Interface Sci.* **2014**, *12*, 1474–483.
62. Vijayaraghavan, K.; Ashokkumar, T. Plant-Mediated Biosynthesis of Metallic Nanoparticles: A Review of Literature, Factors Affecting Synthesis, Characterization Techniques and Applications. *J. Environ. Chem. Eng.* **2017**, *5*, 4866–4883.
63. Ponnuchamy, K.; Jacob, J. A. Metal Nanoparticles from Marine Seaweeds—A Review. *Nanotechnol. Rev.* **2016**, *5*. DOI: 10.1515/ntrev-2016-0010.
64. Dauthal, P.; Mukhopadhyay, M. Noble Metal Nanoparticles: Plant-Mediated Synthesis, Mechanistic Aspects of Synthesis, and Applications. *Ind. Eng. Chem. Res.* **2016**, *55*, 9557–9577.
65. Li, X.; Xu, H.; Chen, Z. S.; Chen, G. Biosynthesis of Nanoparticles by Microorganisms and Their Applications. *J. Nanomater.* **2011**, *2011*, 1–16.

66. Shivaji, S.; Madhu, S.; Singh, S. Extracellular Synthesis of Antibacterial Silver Nanoparticles Using Psychrophilic Bacteria. *Process Biochem.* **2011**, *46*, 1800–1807.
67. Malarkodi, C.; Rajeshkumar, S.; Vanaja, M. Eco-friendly Synthesis and Characterization of Gold Nanoparticles Using *Klebsiellapneumoniae*. *J. Nanostruct. Chem.* **2013**, *3*, 30.
68. Kalishwaralal, K.; Deepak, V.; Ramkumarpandian, S.; Nellaiah, H.; Sangiliyandi, G. Extracellular Biosynthesis of Silver Nanoparticles by the Culture Supernatant of *Bacillus licheniformis*. *Mater. Lett.* **2008**, *62*, 4411–4413.
69. Menon, S.; Rajeshkumar, S.; Kumar, S. V. A Review on Biogenic Synthesis of Gold Nanoparticles, Characterization, and Its Applications. *Resour. Efficient Technol.* **2017**, *3*, 516–527.
70. Ghorbani, H. R. Biosynthesis of Silver Nanoparticles Using *Salmonella typhirium*. *J. Nanostruct. Chem.* **2013**, *3*, 29.
71. Mewada, A.; Oza, G.; Pandey, S.; Sharon, M. Extracellular Synthesis of Gold Nanoparticles Using *Pseudomonas denitrificans* and Comprehending Its Stability. *J. Microbiol. Biotech. Res.* **2012**, *2*, 493–499.
72. Prema, P.; Iniya, P. A.; Immanuel, G. Microbial Mediated Synthesis, Characterization, Antibacterial and Synergistic Effect of Gold Nanoparticles Using *Klebsiella pneumoniae* (MTCC-4030). *RSC Adv.* **2016**, *6*, 4601–4607.
73. Gurunathan, S. Rapid Biological Synthesis of Silver Nanoparticles and Their Enhanced Antibacterial Effects Against *Escherichia fergusonii* and *Streptococcus mutans*. *Arab. J. Chem.* **2014**. DOI: 10.1016/j.arabjc.2014.11.014.
74. M. Balakumaran, D.; Ramachandran, R.; Balashanmugam, P.; Mukeshkumar, D. J.; P. Kalaichelvan, T. Mycosynthesis of Silver and Gold Nanoparticles: Optimization, Characterization and Antimicrobial Activity Against Human Pathogens. *Microbiol. Res.* **2016**, *182*, 8–20.
75. Shareefraza, J. U.; Ashraf, M.; Apoorva, B. U.; Gangadharan, M.; A. Pattiyeri, Yashawantha, K. M.; Patil, R.; Puthiyllam, P. Synthesis and Characterization of Silver Nanoparticles from *FusariumOxysporum* and Investigation of Their Antibacterial Activity. *Mater. Today Proceed.* **2019**, *9*, 506–514.
76. Mukherjee, K.; Gupta, R.; Kumar, G.; Kumari, S.; Biswas, S.; Padmanabhan, P. Synthesis of Silver Nanoparticles by *Bacillus clausii* and Computational Profiling of Nitrate Reductase Enzyme Involved in Production. *J. Genetic Eng. Biotechnol.* **2018**. DOI: 10.1016/j.jgeb.2018.04.004.
77. Bennur, T.; Khan, Z.; Kshirsagar, R.; Javdekar, V.; Zinjarde, S. Biogenic Gold Nanoparticles from the Actinomycete *Gordoniaaamarae*: Application in Rapid Sensing of Copper Ions. *Sens. Actuators B: Chem.* **2016**, *233*, 684–690.
78. Nejad, S.; Khatami, M.; Bonjar, G. H. Extracellular Synthesis Gold Nanotriangles Using Biomass of *Streptomyces microflavus*. *IET Nanobiotechnol.* **2016**, *10*, 33–38.
79. Krupa, A. N. D.; M.E Abigail, A.; Santhosh, C.; Grace, A. N.; Vimala, R. Optimization of Process Parameters for the Microbial Synthesis of Silver Nanoparticles Using 3-Level Box–Behnken Design. *Ecol. Eng.* **2016**, *87*, 168–174.
80. Magdi, H. M.; Bhushan, B. Extracellular Biosynthesis and Characterization of Gold Nanoparticles Using the Fungus *Penicilliumchrysogenum*. *Microsyst. Technol.* **2015**, *21*, 2279–2285.
81. Amerasan, D.; Nataraj, T.; Murugan, K.; Panneerselvam, C.; Madhiyazhagan, P.; Nicoletti, M.; Benelli, G. Myco-synthesis of Silver Nanoparticles Using *Metarhiziumanisopliae* against the Rural Malaria Vector *Anopheles culicifacies* Giles (Diptera: Culicidae). *J. Pest Sci.* **2015**, *89*, 249–256.

82. Zhang, X.; Qu, Y.; Shen, W.; Wang, J.; Li, H.; Zhang, Z.; Zhou, J. Biogenic Synthesis of Gold Nanoparticles by Yeast *Magnusiomycesingens LH-F1* for Catalytic Reduction of Nitrophenols. *Colloids Surfaces A: Physicochem. Eng. Aspects* **2016**, *497*, 280–285.
83. Balakumaran, M. D.; Ramachandran, R.; Kalaichelvan, P. T. Exploitation of Endophytic Fungus, *Guignardiamangiferae* for Extracellular Synthesis of Silver Nanoparticles and Their In Vitro Biological Activities. *Microbiol. Res.* **2015**, *178*, 9–17.
84. P. Seetharaman, K.; Chandrasekaran, R.; Gnanasekar, S.; Chandrakasan, G.; Gupta, M.; D. Manikandan, B.; Sivaperumal, S. Antimicrobial and Larvicidal Activity of Eco-Friendly Silver Nanoparticles Synthesized from Endophytic Fungi *Phomopsisliquidambaris*. *Biocatal. Agric. Biotechnol.* **2018**, *16*, 22–30.
85. Srinath, B. S.; Rai, V. R. Rapid Biosynthesis of Gold Nanoparticles by *Staphylococcus epidermidis*: Its Characterisation and Catalytic Activity. *Mater. Lett.* **2015**, *146*, 23–25.
86. Satisha, S.; Syed, B.; Prasad, N. N. Endogenic Mediated Synthesis of Gold Nanoparticles Bearing Bactericidal Activity. *J. Microsc. Ultrastruct.* **2016**, *4*, 162–166.
87. Elemike, E. E.; Fayemi, O. E.; Ekennia, A. C.; Onwudiwe, D. C.; Ebenso, E. Silver Nanoparticles Mediated by *Costusafer 2* Leaf Extract: Synthesis, Antibacterial, Antioxidant and Electrochemical Properties. *Molecules* **2017**, *22*, 701.
88. Karthiga, P. Preparation of Silver Nanoparticles by *Garcinia mangostana* Stem Extract and Investigation of the Antimicrobial Properties. *Biotechnology Research and Innovation* **2018**, *2*, 30–36.
89. Behravan, M.; Panahi, A. H.; Naghizadeh, A.; Ziaee, M.; Mahdavi, R.; Mirzapour, A. Facile Green Synthesis of Silver Nanoparticles Using *Berberis vulgaris* Leaf and Root Aqueous Extract and Its Antibacterial Activity. *Int. J. BiolMacromol.* **2019**, *124*, 148–154.
90. Jenkins, J. A.; Wax, T. J.; Zhao, J. Seed-Mediated Synthesis of Gold Nanoparticles of Controlled Sizes to Demonstrate the Impact of Size on Optical Properties. *J. Chem. Educ.* **2017**, *94*, 1090–1093.
91. Jayaprakash, N.; Vijaya, J. J.; Kaviyarasu, K.; Kombaiiah, K.; Kennedy, L. J.; Ramalingam, R. J.; Al-Lohedan, H. A. Green Synthesis of Ag Nanoparticles Using Tamarind Fruit Extract for the Antibacterial Studies. *J. Photochem. Photobiol. B: Biol.* **2017**, *169*, 178–185.
92. Khara, G.; Padalia, H.; Moteriya, P.; Chanda, S.; Peltophorumpterocarpum Flower-Mediated Synthesis, Characterization, Antimicrobial and Cytotoxic Activities of ZnO Nanoparticles. *Arab. J. Sci. Eng.* **2018**, *43*, 3393–3401.
93. Kumar, V.; Yadav, S. K. Plant-Mediated Synthesis of Silver and Gold Nanoparticles and Their Applications. *J. Chem. Technol. Biotechnol.* **2009**, *84*, 151–157.
94. Benelli, G. Plant-Mediated Biosynthesis of Nanoparticles as an Emerging Tool Against Mosquitoes of Medical and Veterinary Importance: A Review. *Parasitol. Res.* **2015**, *115*, 23–34.
95. Chung, I. M.; Park, I.; K. Seung-Hyun, Thiruvengadam, M.; Rajakumar, G.; Plant-Mediated Synthesis of Silver Nanoparticles: Their Characteristic Properties and Therapeutic Applications. *Nanoscale Res. Lett.* **2016**, *11*, 40.
96. Ahmed, S.; Ikram, S. Synthesis of Gold Nanoparticles Using Plant Extract: A Overview. *Nano Res. Appl.* **2015**, *1*, 1–14.
97. Zayed, M. F.; Eisa, W. H.; El-kousy, S. M.; Mleha, W. K.; Kamal, N. *Ficus retusa*-Stabilized Gold and Silver Nanoparticles: Controlled Synthesis, Spectroscopic Characterization, and Sensing Properties. *Spectrochim. Acta A* **2019**, *214*, 496–512.

98. Nishanthi, R.; Malathi, S.; John Paul, S.; Palani, P. Green synthesis and characterization of Bioinspired Silver, Gold and Platinum Nanoparticles and Evaluation of Their Synergistic Antibacterial Activity After Combining with Different Classes of Antibiotics. *Mater. Sci. Eng. C* **2019**, *96*, 693–707.
99. Raj, S.; S. Chand Mali, Trivedi, R. Green Synthesis and Characterization of Silver Nanoparticles Using *Enicostemma axillare* (Lam.) Leaf Extract. *Biochem. Biophys. Res. Commun.* **2018**, *503*, 2814–2819.
100. Rafique, M.; Sadaf, I.; M. Tahir, B.; M. Rafique, S.; Nabi, G.; Iqbal, T.; Sughra, K. Novel and Facile Synthesis of Silver Nanoparticles Using Albiziaprocera Leaf Extract for Dye Degradation and Antibacterial Applications. *Mater. Sci. Eng. C* **2019**, *99*, 1313–1324.
101. Lakshmanan Sathiyaseelan, G. A.; Kalaichelvan, P. T.; Murugesan, K. M. Plant-Mediated Synthesis of Silver Nanoparticles Using Fruit Extract of *Cleome viscosa* L.: Assessment of Their Antibacterial and Anticancer Activity. *Karbala Int. J. Mod.* **2018**, *4*, 61–68.
102. Premkumar, J.; Sudhakar, T.; Dhakal, A.; Shrestha, J. B.; Krishnakumar, S.; Balashanmugam, P. Synthesis of Silver Nanoparticles (AgNPs) from Cinnamon Against Bacterial Pathogens. *Biocataly. Agric. Biotechnol.* **2018**, *15*, 311–316.
103. Balavijayalakshmi, J.; Ramalakshmi, V. Carica Papaya Peel Mediated Synthesis of Silver Nanoparticles and Its Antibacterial Activity Against Human Pathogens. *J. Appl. Res. Technol.* **2017**, *15*, 413–422.
104. Ahmad, T.; Bustam, M. A.; Irfan, M.; Moniruzzaman, M.; AnwaarAsghar, H. M.; Bhattacharjee, S. Green Synthesis of Stabilized Spherical Shaped Gold Nanoparticles Using Novel Aqueous *Elaeisguineensis* (Oil Palm) Leaves Extract. *J. Mol. Struct.* **2018**, *1159*, 167–173.
105. Zha, J.; Dong, C.; Wang, X.; Zhang, X.; Xiao, X.; Yang, X. Green Synthesis and Characterization of Monodisperse Gold Nanoparticles Using *Ginkgo Biloba* Leaf Extract. *Optik* **2017**, *144*, 511–521.
106. Ndikau, M.; Noah, N. M.; Andala, D. M.; Masika, E. Green Synthesis and Characterization of Silver Nanoparticles Using *Citrulluslanatus* Fruit Rind Extract. *Int. J. Anal. Chem.* **2017**, *2017*, 1–9.
107. Majumdar, R.; Bag, B. G.; Ghosh, P. *Mimusopselengi* Bark Extract Mediated Green Synthesis of Gold Nanoparticles and Study of Its Catalytic Activity. *Appl. Nanosci.* **2015**, *6*, 521–528.
108. Sadeghi, B.; Mohammadzadeh, M.; Babakhani, B. Green Synthesis of Gold Nanoparticles Using *Stevia rebaudiana* Leaf Extracts: Characterization and Their Stability. *J. Photochem. Photobiol.* **2015**, *148*, 101–106.
109. Latha, M.; Priyanka, M.; Rajasekar, P.; Manikandan, R.; Prabhu, N. M. Biocompatibility and Antibacterial Activity of the *Adathodavasica* Linn Extract Mediated Silver Nanoparticles. *Microb. Pathogen.* **2016**, *93*, 88–94.
110. Murugan, K.; Benelli, G.; Panneerselvam, C.; Subramaniam, J.; Jeyalalitha, T.; Dinesh, D.; Madhiyazhagan, P. *Cymbopogoncitratu*s-Synthesized Gold Nanoparticles Boost the Predation Efficiency of copepod *Mesocyclopsaspercicornis* Against Malaria and Dengue Mosquitoes. *Exp. Parasitol.* **2015**, *153*, 129–138.
111. Tipayawat, P.; Phromviyo, N.; Boueroy, P.; Chompoosor, A. Green Synthesis of Silver Nanoparticles in Aloe Vera Plant Extract Prepared by a Hydrothermal Method and Their Synergistic Antibacterial Activity. *PeerJ* **2016**, *4*, DOI: 10.7717/peerj.2589.

112. Tahir, K.; Nazir, S.; Li, B.; Khan, A. U.; Khan, Z. U. H.; Gong, P. Y.; Ahmad, A. Nerium Oleander Leaves Extract Mediated Synthesis of Gold Nanoparticles and Its Antioxidant Activity. *Mater. Lett.* **2015**, *156*, 198–201.
113. Sadeghi, B.; Gholamhoseinpoor, F. A Study on the Stability and Green Synthesis of Silver Nanoparticles Using *Ziziphoratenuior* (Zt) Extract at Room Temperature. *Spectrochim. Acta A* **2015**, *134*, 310–315.
114. Mata, R.; Nakkala, J. R.; Sadras, S. R. Biogenic Silver Nanoparticles from *Abutilon indicum*: Their Antioxidant, Antibacterial and Cytotoxic Effects In Vitro. *Colloids Surfaces B: Biointerf.* **2015**, *128*, 276–286.
115. M. Bindhu, R.; Umadevi, M. Antibacterial and Catalytic Activities of Green Synthesized Silver Nanoparticles. *Spectrochim. Acta A* **2015**, *135*, 373–378.
116. Rajkuberan, C.; Sudha, K.; Sathishkumar, G.; Sivaramakrishnan, S. Antibacterial and Cytotoxic Potential of Silver Nanoparticles Synthesized Using Latex of *Calotropisgigantea* L. *Spectrochim. Acta A* **2015**, *136*, 924–930.
117. Ramesh, P. S.; Kokila, T.; Geetha, D. Plant Mediated Green Synthesis and Antibacterial Activity of Silver Nanoparticles Using *Emblicaofficinalis* Fruit Extract. *Spectrochim. Acta A* **2015**, *142*, 339–343.
118. Rajan, A.; Vilas, V.; Philip, D. Catalytic and Antioxidant Properties of Biogenic Silver Nanoparticles Synthesized Using *Areca catechu* Nut. *J. Mol. Liq.* **2015**, *207*, 231–236.
119. Rajan, A.; Vilas, V.; Philip, D. Studies on Catalytic, Antioxidant, Antibacterial and Anticancer Activities of Biogenic Gold Nanoparticles. *J. Mol. Liq.* **2015**, *212*, 331–339.
120. Vijayan, R.; Joseph, S.; Mathew, B. *Indigoferatinctoria* Leaf Extract Mediated Green Synthesis of Silver and Gold Nanoparticles and Assessment of Their Anticancer, Antimicrobial, Antioxidant and Catalytic Properties. *Artif. Cells Nanomed. Biotechnol.* **2017**, *46*, 861–871.
121. Francis, S.; Joseph, S.; Koshy, E. P.; Mathew, B. Microwave Assisted Green Synthesis of Silver Nanoparticles Using Leaf Extract of *elephantopusscaber* and Its Environmental and Biological Applications. *Artif. Cells Nanomed. Biotechnol.* **2017**, *46*, 795–804.
122. Muthukumaran, U.; Govindarajan, M.; Rajeswary, M. Green Synthesis of Silver Nanoparticles from *Cassia roxburghii*—A Most Potent Power for Mosquito Control. *Parasitol. Res.* **2015**, *114*, 4385–4395.
123. Ajitha, B.; Reddy, Y. A. K.; P. Reddy, S.; Suneetha, Y.; Jeon, H. J.; C. Ahn, W. Instant Biosynthesis of Silver Nanoparticles Using *Lawsoniainermis* Leaf Extract: Innate Catalytic, Antimicrobial and Antioxidant Activities. *J. Mol. Liq.* **2016**, *219*, 474–481.
124. Dobrucka, R.; Dlugaszewska, J.; Kaczmarek, M. Antimicrobial and Cytostatic Activity of Biosynthesized Nanogold Prepared Using Fruit Extract of *Ribesnigrum*. *Arab. J. Chem.* **2016**. DOI: 10.1016/j.arabjc.2016.02.009.
125. Kumar, V.; Singh, D. K.; Mohan, S.; Gundampati, R. K.; Hasan, S. H. Photo Induced Green Synthesis of Silver Nanoparticles Using Aqueous Extract of *Physalisangulata* and Its Antibacterial and Antioxidant Activity. *J. Environ. Chem. Eng.* **2017**, *5*, 744–756.
126. Rajan, A.; Rajan, A. R.; Philip, D. *Elettariacardamomum* Seed Mediated Rapid Synthesis of Gold Nanoparticles and Its Biological Activities. *OpenNano* **2017**, *2*, 1–8.
127. Manivasagan, P.; Kim, S. K. Biosynthesis of Nanoparticles Using Marine Algae: A Review. *Marine Algae Extracts* **2015**, 295–304.
128. Graham, L. E.; Graham, J. E.; Wilcox, L.; Algae, W. 2nd ed.; Benjamin-Cummings Publishing: Menlo Park, 2008; ISBN: 0321559657.

129. Holdt, S. L.; Kraan, S. Bioactive Compounds in Seaweed: Functional Food Applications and Legislation. *J. Appl. Phycol.* **2011**, *23*, 543–597.
130. Pereira, R. C.; Leticia, C. L. V. Bioprospecting for Bioactives from Seaweeds: Potential, Obstacles and Alternatives. *Rev. bras. farmacogn.* **2012**, *22*, 894–905.
131. Vijayan, S. R.; Santhiyagu, P.; Ramasamy, R.; Arivalagan, P.; Kumar, G.; Ethiraj, K.; Ramaswamy, B. R. Seaweeds: A Resource for Marine Bionanotechnology. *Enzyme Microb. Technol.* **2016**, *95*, 45–57.
132. Negi, S.; Singh, V. Algae: A Potential Source for Nanoparticle Synthesis. *J. Appl. Nat. Sci.* **2018**, *10*, 1134–1140.
133. Singaravelu, G.; Arockiamary, J. S.; Kumar, V. G.; Govindaraju, K. A Novel Extracellular Synthesis of Monodisperse Gold Nanoparticles Using Marine Alga, *Sargassum wightii* Greville. *Colloids Surf. B Biointerf.* **2007**, *57*, 97–101.
134. Govindaraju, K.; Kiruthiga, V.; Kumar, V. G.; Singaravelu, G. Extracellular Synthesis of Silver Nanoparticles by a Marine Alga, *Sargassum wightii* Grevilli and Their Antibacterial Effects. *J. Nanosci. Nanotechnol.* **2009**, *9*, 5497–5501.
135. Kumar, P.; Selvi, S. S.; Praba, A. L.; Selvaraj, M. Antibacterial Activity and In Vitro Cytotoxicity Assay Against Brine Shrimp Using Silver Nanoparticles Synthesized from *Sargassum ilicifolium*. *Dig. J. Nanomater. Biostruct.* **2012**, *7*, 1447–1455.
136. Thangaraju, N.; Venkatalakshmi, R. P.; Chinnasamy, A.; Kannaiyan, P. Synthesis of Silver Nanoparticles and the Antibacterial and Anticancer Activities of the Crude Extract of *Sargassum polycystum* Agardh. *C.; Nano Biomed. Eng.* **2012**, *4*, 89–94.
137. Dhas, T. S.; Kumar, V. G.; Karthick, V.; Govindaraju, K.; Shankara Narayana, T. Biosynthesis of Gold Nanoparticles Using *Sargassum swartzii* and Its Cytotoxicity Effect on HeLa Cells. *Spectrochim. Acta A* **2014**, *133*, 102–106.
138. Vijayan, S. R.; Santhiyagu, P.; Singamuthu, M.; Kumari Ahila, N.; R., Jayaraman, Ethiraj, K. Synthesis and Characterization of Silver and Gold Nanoparticles Using Aqueous Extract of Seaweed, *Turbinaria conoides* and Their Antimicrofouling Activity. *Sci. World J.* **2014**, *2014*, 1–10.
139. ArockiyaAarthiRajathi, F.; Parthiban, C.; GaneshKumar, V.; Anantharaman, P. Biosynthesis of Antibacterial Gold Nanoparticles Using Brown Alga, *Stoechospermummarginatum* (kützing). *Spectrochim. Acta A* **2012**, *99*, 166–173.
140. Sahayaraj, K.; Rajesh, S.; Rathi, J. M. Silver Nanoparticles Biosynthesis Using Marine Alga *Padinapavonica* (linn.) and Its Microbicidal Activity. *Dig. J. Nanomater. Biostruct.* **2012**, *7*, 1557–1567.
141. Shiny, P. J.; Mukherjee, A.; Chandrasekaran, N. Marine Algae Mediated Synthesis of the Silver Nanoparticles and Its Antibacterial Efficiency. *Int. J. Pharm. PharmSci.* **2013**, *5*, 239–241.
142. Princy, K. F.; Sreeja, S.; Anna, A.; Gopinath, A. A Novel Green Synthesis of Gold Nanoparticles Using Seaweed *Lobophora variegata* and Its Potential Application in the Reduction of Nitrophenols. *Particulate Sci. Technol.* **2019**. DOI: 10.1080/02726351.2018.1547340.
143. Azizi, S.; Namvar, F.; Mahdavi, M.; Ahmad, M.; Mohamad, R. Biosynthesis of Silver Nanoparticles Using Brown Marine Macroalga, *Sargassum Muticum* Aqueous Extract. *Materials* **2013**, *6*, 5942–5950.
144. Mohandass, C.; Vijayaraj, A. S.; Rajasabapathy, R.; Satheeshbabu, S.; S. Rao, V.; Shiva, C.; Demello, L. Biosynthesis of Silver Nanoparticles from Marine Seaweed *Sargassum cinereum* and Their Antibacterial Activity. *Indian J. Pharm Sci.* **2013**, *75*, 606–610.

145. Ramakrishna, M.; Rajesh Babu, D.; Gengan, R. M.; Chandra, S.; Nageswara Rao, G. Green Synthesis of Gold Nanoparticles Using Marine Algae and Evaluation of Their Catalytic Activity. *J. Nanostruct. Chem.* **2016**, 6, 1–13.
146. Kumar, P.; Selvi, S. S.; Govindaraju, M. Synthesis of Silver Nanoparticles from *Sargassum tenerrimum* and Screening Phytochemicals for Its Anti-Bacterial Activity. *Nano Biomed. Eng.* **2012**, 4, 12–16.
147. Rajeshkumar, S.; Kannan, C.; Annadurai, G. Synthesis and Characterization of Antimicrobial Silver Nanoparticles Using Marine Brown Seaweed *Padina tetrastrum*. *Drug Invent. Today* **2012**, 4, 511–513.
148. Princy, K. F.; Gopinath, A. Optimization of Physicochemical Parameters in the Biofabrication of Gold Nanoparticles Using Marine Macroalgae *Padina tetrastrum* and Its Catalytic Efficacy in the Degradation of Organic Dyes. *J. Nanostruct. Chem.* **2018**, 8, 333–342.
149. Varun, S.; Sudha, S.; Kumar, P. S. Biosynthesis of Gold Nanoparticles from Aqueous Extract of *Dictyota bartayresiana* and Their Antifungal Activity. *Indian J. Adv. Chem. Sci.* **2014**, 2, 190–193.
150. Gonzalez-Ballesteros, N.; Prado-Lopez, S.; Rodriguez-Gonzalez, J. B.; Lastra, M.; Rodriguez-Arguelles, M. C. Green Synthesis of Gold Nanoparticles Using Brown Algae *Cystoseira baccata*: Its Activity in Colon Cancer Cells. *Colloids Surf. B: Biointerfaces* **2017**, 153, 190–198.
151. Vivek, M.; Kumar, P. S.; Steffi, S.; Sudha, S. Biogenic Silver Nanoparticles by *Gelidium acerosa* Extract and Their Antifungal Effects. *Avicenna J. Med. Biotechnol.* **2011**, 3, 143–148.
152. Abdel-Raouf, N.; Al-Enazi, N. M.; Ibraheem, I. B. M. Green Biosynthesis of Gold Nanoparticles Using *Galaxaura elongata* and Characterization of Their Antibacterial Activity. *Arab. J. Chem.* **2017**, 10, S3029–S3039.
153. Priyadharshini, R. I.; Prasannaraj, G.; Geetha, N. Microwave-Mediated Extracellular Synthesis of Metallic Silver and Zinc Oxide Nanoparticles Using Macro-Algae (*Gracilariadulcis*) Extracts and Its Anticancer Activity Against Human PC3 Cell Lines. *Appl. Biochem. Biotechnol.* **2014**, 174, 2777–2790.
154. Kumar, P.; Senthamilselvi, S.; Lakshmi praba, A.; Premkumar, K.; Muthukumaran, R.; Visvanathan, P.; Ganeshkumar, R. S.; Govindaraju, M. Efficacy of Bio-Synthesized Silver Nanoparticles Using *Acanthopora spicifera* to Encumber Biofilm Formation. *Dig. J. Nanomater. Biostruct.* **2012**, 7, 511–522.
155. Shukla, M. K.; Singh, R. P.; Reddy, C. R. K.; Jha, B. Synthesis and Characterization of Agar-Based Silver Nanoparticles and Nanocomposite Film with Antibacterial Applications. *Bioresour. Technol.* **2012**, 107, 295–300.
156. Ganesan, V.; J. Aruna Devi, Astalakshmi, A.; Nima, P.; Thangaraja, A. Ecofriendly Synthesis of Silver Nanoparticles Using a Sea Weed, *Kappaphycus Alvarezii* (Doty) Doty ex P. C. Silva. *Int. J. Eng. Adv. Technol.* **2013**, 2, 559–563.
157. Kumar, P.; Selvi, S. S.; Govindaraju, M. Seaweed-Mediated Biosynthesis of Silver Nanoparticles Using *Gracilariacorticata* for Its Antifungal Activity Against *Candida* spp. *Appl. Nanosci.* **2013**, 3, 495–500.
158. de Aragao, A. P.; de Oliveira, T. M.; Quelemes, P. V.; Perfeito, M. L. G.; Araujo, M. C.; Santiago, J. D. A. S.; Cardoso, V. S.; Quaresma, P.; de Almeida, J. R. D. S.; da Silva, D. A. Green Synthesis of Silver Nanoparticles Using the Seaweed *Gracilariabirdiae* and Their Antibacterial Activity. *Arab. J. Chem.* **2016**. <https://doi.org/10.1016/j.arabjc.2016.04.014>.

159. Kathiraven, T.; Sundaramanickam, A.; Shanmugam, N.; Balasubramanian, T. Green Synthesis of Silver Nanoparticles Using Marine Algae *Caulerpa racemosa* and Their Antibacterial Activity Against Some Human Pathogens. *Appl. Nanosci.* **2014**, *5*, 499–504.
160. Kannan, R. R. R.; Stirk, W. A.; Van Staden, J. Synthesis of Silver Nanoparticles Using the Seaweed *Codium capitatum* P. C. Silva (Chlorophyceae). *South Afr. J. Bot.* **2013**, *86*, 1–4.
161. Rajesh, S.; Patric Raja, D.; Rath, J. M.; Sahayara, K. Biosynthesis of Silver Nanoparticles Using *Ulva fasciata* (Delile) Ethyl Acetate Extract and Its Activity Against *Xanthomonas campestris* pv. *Malvacearum*. *Biopest* **2012**, *5*, 119–128.
162. Kumar, P.; Govindaraju, M.; Senthamilselvi, S.; Premkumar, K. Photocatalytic Degradation of Methyl Orange Dye Using Silver(Ag) Nanoparticles Synthesized from *Ulva lactuca*. *Coll. Surf. B: Biointerf.* **2013**, *103*, 658–661.
163. Yousefzadi, M.; Rahimi, Z.; Ghafori, V. The Green Synthesis, Characterization and Antimicrobial Activities of Silver Nanoparticles Synthesized from Green Alga *Enteromorpha flexuosa* (wulfen) J. Agardh. *Mater. Lett.* **2014**, *137*, 1–4.
164. Ramkumar, V. S.; Pugazhendhi, A.; Gopalakrishnan, K.; Sivagurunathan, P.; Saratale, G. D.; Dung, T. N. B.; Kannapiran, E. Biofabrication and Characterization of Silver Nanoparticles Using Aqueous Extract of Seaweed *Enteromorpha compressa* and Its Biomedical Properties. *Biotechnol. Rep.* **2017**, *14*, 1–7.
165. Dhanalakshmi, P. K.; Azeez, R.; Rekha, R.; Poonkodi, S.; Nallamuthu, T. Synthesis of Silver Nanoparticles Using Green and Brown Seaweeds. *Phykos* **2012**, *42*, 39–45.
166. Kannan, R. R. R.; Arumugam, R.; Ramya, D.; Manivannan, K.; Anantharaman, P. Green Synthesis of Silver Nanoparticles Using Marine Macroalga *Chaetomorpha linum*. *Appl. Nanosci.* **2013**, *3*, 229–233.
167. Mohamad, N. A. N.; Arham, N. A.; Jai, J.; Hadi, A. Plant Extract as Reducing Agent in Synthesis of Metallic Nanoparticles: A Review. *Adv. Mater. Res.* **2014**, *832*, 350–355.
168. Velusamy, P.; Kumar, G. V.; Jeyanthi, V.; Das, J.; Pachaiappan, R. Bio-Inspired Green Nanoparticles: Synthesis, Mechanism, and Antibacterial Application. *Toxicol. Res.* **2016**, *32*, 95–102.
169. Malik, P.; Shankar, R.; Malik, V.; Sharma, N.; Mukherjee, T. K. Green Chemistry Based Benign Routes for Nanoparticle Synthesis. *J. Nano.* **2014**, *2014*, 302429.
170. Akhtar, M. S.; Panwar, J.; Yun, Y. S. Biogenic Synthesis of Metallic Nanoparticles by Plant Extracts. *ACS Sustain. Chem. Eng.* **2013**, *1*, 591–602.
171. Jha, A. K.; Prasad, K.; Prasad, K.; Kulkarni, A. R. Plant System: Nature's Nano Factory. *Colloids Surf. B Biointerfaces*. **2009**, *73*, 219–223.
172. Sharma, D.; Kanchi, S.; Bisetty, K. Biogenic Synthesis of Nanoparticles: A Review. *Arab. J. Chem.* **2015**. <https://doi.org/10.1016/j.arabjc.2015.11.002>.
173. Govindaraju, K.; Krishnamoorthy, K.; Alsagaby, S. A.; Singaravelu, G.; Premanathan, M. Green Synthesis of Silver Nanoparticles for Selective Toxicity Towards Cancer Cells. *IET Nanobiotechnol.* **2015**, *9*, 325–330.
174. Rajeshkumar, S.; Malarkodi, C.; Paulkumar, K.; Vanaja, M.; Gnanajobitha, G.; Annadurai, G. Algae Mediated Green Fabrication of Silver Nanoparticles and Examination of Its Antifungal Activity Against Clinical Pathogens. *Int. J. Met.* **2014**, *2014*, 1–8.
175. Singh, M.; Kumar, M.; Manikandan, S.; Chandrasekaran, N.; Mukherjee, A.; Kumaraguru, A. K. Drug Delivery System for Controlled Cancer Therapy Using Physicochemically Stabilized Bioconjugated Gold Nanoparticles Synthesized from Marine Macroalgae, *Padina Gymnospora*. *J. Nanomed. Nanotechnol.* **2014**, *5*, 1–7.



176. Iravani, S.; Korbekandi, H.; Mirmohammadi, S. V.; Zolfaghari, B. Synthesis of Silver Nanoparticles: Chemical, Physical and Biological Methods. *Res Pharm. Sci.* **2014**, *9*, 385–406.
177. Husain, S.; Afreen, S.; Yasin, D.; Afzal, B.; Fatma, T. Cyanobacteria as a Bioreactor for Synthesis of Silver Nanoparticles—An Effect of Different Reaction Conditions on the Size of Nanoparticles and Their Dye Decolorization Ability. *J. Microbiol. Methods* **2019**, *162*, 77–82.
178. Khan, I.; Saeed, K.; Khan, I. Nanoparticles: Properties, Applications and Toxicities. *Arab. J. Chem.* **2017**. <https://doi.org/10.1016/j.arabjc.2017.05.011>.
179. Mukherji, S.; Ruparelia, J.; Agnihotri, S. Antimicrobial Activity of Silver and Copper Nanoparticles: Variation in Sensitivity Across Various Strains of Bacteria and Fungi. *Nano-antimicrob.* **2012**, 225–251.
180. Makarov, V. V.; Love, A. J.; Sinitsyna, O. V. “Green” Nanotechnologies: Synthesis of Metal Nanoparticles Using Plants. *Acta Nat.* **2014**, *6*, 35–44.

# Computer Simulation of Structure and Mechanical Behavior of Polymer Nanocomposites

SHENGWEI DENG<sup>1</sup> and DHANYA K. R.<sup>2</sup>

*<sup>1</sup>College of Chemical Engineering, Zhejiang University of Technology, Hangzhou, People's Republic of China*

*<sup>2</sup>IUCNN, Mahatma Gandhi University, Kottayam, Kerala, India*

---

### ABSTRACT

The mechanical characteristics of polymers and their nanocomposites are directly correlated to their microstructures. Computer simulation is an important way to study the relationship between structures and their corresponding properties. Owing to the development of simulation techniques and computational capabilities in recent years, a variety of simulation methods at different scales are performed to study the mechanical characteristics of polymer nanocomposites. This chapter gives a brief introduction to different methods as well as applications, mainly discussing the mechanical properties of polymer nanocomposites. Typical simulation methods such as molecular dynamics simulation, MesoDyn, dissipative particle dynamics, the finite element method, and the lattice spring model are used in the study. Meanwhile, multiscale modeling, which focuses on complex heterogeneous polymer systems, shows great potential for predicting and guiding the design of advanced materials with novel mechanical properties.

## 12.1 INTRODUCTION

Polymer nanocomposites have considerable capability for the improvement of superior materials for various applications compared to neat polymers.<sup>1</sup> This new substance has benefited from the bonding of fillers and polymer chains that are in similar length scales. Generally, suitably formulated nanomaterials in a polymer matrix will enhance its properties as well as performance. Examples are depicted as large aspect ratio nanofillers that have well-dispersion or exfoliation in polymers show enormously high hardness.<sup>2,3</sup> However, these additives with homogeneous distribution in the polymer matrix may have adverse effects; for example, the final products are usually stiff but inextensible, such as ceramic class of particles, or larger but extremely softer particles, such as rubber.<sup>4</sup> Up until now, our fundamental knowledge of the enhancement effect in terms of polymer nanocomposite's mechanical behavior has not been fully developed. And it is still a hot research topic that is studied by numerous researchers. Various kinds of polymer nanocomposites have been synthesized by experiments in recent years and show novel properties. However, the development of such particles is still highly empirical with the method of trial and error, which results in the difficulty of fine control of properties. From the experimental point of view, it is a large crisis to analyze the arrangement and to work on the production of polymer nanocomposites, and the in situ observation of deformation and fracture processes<sup>5,6</sup> to get a wide-ranging picture of how the microstructure determines the macroscopic stress response is a challenge or time-consuming. Computer modeling and simulation have become a different method to analyze this type of problem and can be considered an ever-rising function that can be used to design and predict the properties of materials, which can be helpful for preparation, characterization, and experimental work.<sup>7</sup>

The main focus of this chapter is to explain the purpose of modeling and simulation techniques for the structure and mechanical behavior of polymer nanocomposites. The chapter covers methodologies at different parameters, such as length and time to analyze the problem. In Section 12.2, we briefly describe the typical computational methods used for polymer nanocomposites at the corresponding simulation scale. It is divided into three main categories: molecular and microscale methods (molecular dynamics), meso-scale methods (MesoDyn and dissipative particle dynamics), and macroscale methods (finite element method and lattice spring model). The present chapter focuses on a detailed description of each method and its important

aspects. In Section 12.3, we consider in detail the most important uses of these modeling techniques, some simulation methods, surface characteristics, and mechanical properties of polymer nanocomposites. Note that we mainly focus on polymer systems reinforced by inorganic nanoparticles (NPs). Section 12.4 denotes the importance of multistage methods of modeling and recreation to elucidate the hierarchical structure and characteristics that must be the combination of properties of polymers and NPs observed at various scales. And finally, we conclude the chapter by emphasizing the present crisis and future research scope.

## 12.2 MODELING AND SIMULATION TECHNIQUES

Different dimensions, such as length and time scales, are connected with dissimilar simulation methods to explain the crisis at an equivalent scale (Figure 12.1). The typical method at the smallest scale is quantum mechanics, with relevant lengths of angstroms and time scales of 10–15 s, while at the largest scale, for example, continuum mechanics and lengths can exceed meters scale and the times can approach years in some cases, for example, 109 s.

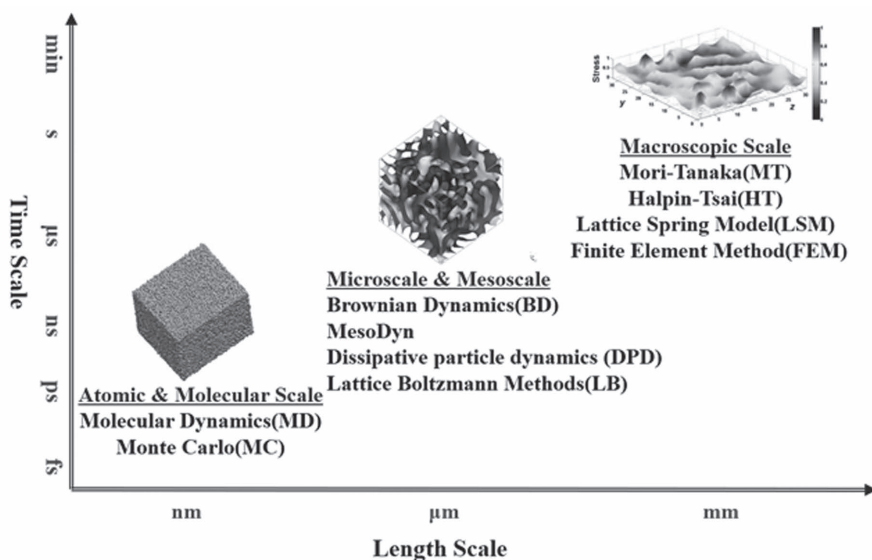


**FIGURE 12.1** Simulation and modeling methods at different length or time scales.

### 12.2.1 MOLECULAR AND MICROSCALE METHODS (MOLECULAR DYNAMICS)

Molecular Dynamics (MD) is known as the primary simulation method, considering its application in the dynamics of liquids. From this model and the mathematical derivation, two of the most important families of MD methods exist. The two main categories are classical mechanics-related MD simulations and quantum MD simulations. Quantum MD simulations are more advantageous than the classical approach, but require additional resources. However, current computer power is not adequate to study the mechanical properties of complex nanocomposites. In classical MD simulations, the influence of electrons is represented by one potential energy at the ground state.<sup>8</sup> At present, the conventional MD is useful for simulations of polymer nanocomposites comprising many thousands of atoms.

The time evolution can be calculated in MD simulations via the prediction of Newton's equations of motion:

$$\mathbf{F}_i = m_i \frac{d^2 \mathbf{r}_i(t)}{dt^2} \quad (12.1)$$

where  $\mathbf{r}_i(t)$  is considered as the  $i$ -th particle position vector and  $\mathbf{F}_i$  is the force acting upon the  $i$ -th particle at time  $t$ .  $m_i$  is known as the particle mass. "Particles" are generally represented as several monomers in polymer chains or a NP in the simulation of polymer nanocomposites. The MD trajectories are clarified by position vectors and velocity vectors, and this can be described by the time change in phase space of a system.

The scheme of the mathematical incorporation of equations of motion by Newton is to calculate an idea that explains positions  $\mathbf{r}_i(t + \Delta t)$  at time  $t + \Delta t$  under the conditions of the known positions at time  $t$ . The well-known algorithm Verlet is generally used in MD simulations. Velocities can be considered from the positions or propagated explicitly and can be used as an alternative to leapfrog or velocity Verlet methods.

On varying the positions as well as the velocities in the mathematical integration procedure, the forces present on the atoms have to be recomputed in each step. Statistical mechanics explains that physical quantities should be taken as averages and also represented as a statistical ensemble.

For example, considering a polymer chain in a polymer nanocomposite, a highly coarse-grained bead spring model<sup>9,10</sup> is adapted to confine the key physics of linear homopolymers in the matrix. All nonbonded beads act together through a truncated Lennard-Jones potential:

$$U_{LJ}(r) = 4\varepsilon \left[ (\sigma/r)^{12} - (\sigma/r)^6 - (\sigma/r_c)^{12} + (\sigma/r_c)^6 \right] \quad (12.2)$$

where  $\varepsilon$  is the binding energy,  $\sigma$  is the bead diameter,  $r$  is the distance between a pair of interacting beads, and  $r_c = 1.5\sigma$  is the cutoff radius.

For simplicity, parameters  $\varepsilon$  and  $\sigma$  were taken below as units. A cutoff length of  $1.5\sigma$  is used to study the mechanical properties of glassy polymers<sup>11</sup> in polymer nanocomposites. In a chain, covalent bonds will be in adjacent beads, and they must be molded by a large nonlinear elastic potential.

$$U(r) = -0.5KR_0^2 \ln \left[ 1 - (r/R_0)^2 \right] + 4\varepsilon \left[ (\sigma/r)^{12} - (\sigma/r)^6 \right] + \varepsilon \quad (12.3)$$

where  $R_0 = 1.5\sigma$  is the distance corresponding to the maximum possible extension of a bond and  $K = 30 \varepsilon/\sigma^2$ . The first term is attractive, and the second Lennard-Jones term is repulsive, and cutoff at the minimum of the potential, that is, Lennard-Jones potential,  $r_{\min}$  can be written as  $r_{\min} = 2^{1/6} \sigma$ .

Although this coarse-grained demonstration of a polymer sequence does not account for the chemical structure of a specific polymer, it can reproduce many of the mechanical characteristics of linear homopolymers.<sup>12,13</sup> Note that the chains considered here can also be unbreakable or semiflexible, depending on the individual system. Apart from the coarse-grained model, an all-atom or united-atom model is usually taken for the local stress allocation or functional group-related mechanical characteristics. Undoubtedly, the scope of application—for example, the length, size, and time scale of the systems that can be used—is strongly influenced by the interatomic potentials (force fields) in classic MD simulation. The final bonding forces that contain chemical bonds are considered experimental potential, and this will be connected with several factors like many types of bonds, corresponding bond angles, bond dihedrals, and nonbonded forces linked directly with weak forces of attraction like van der Waals forces and their electrostatic charge. Choosing a proper force field is crucial for the study of the arrangement and mechanical characteristics of each polymer nanocomposite.

## 12.2.2 MESOSCALE METHODS

### 12.2.2.1 MESODYN

The larger length and time nature of highly intricate fluid systems can be analyzed using MesoDyn. It is a dynamic simulation method, and this

includes polymer melts, blends, and block copolymers. Dynamic mean-field density functional theory is the basis of this method. Here, phase separation dynamics can be explained by Langevin, and there is a one-to-one relationship between the density distribution of the system and the potential field applied externally. Some distributions of bead positions are in coarse-grained time scale and they must be according to a function  $\Psi(R11, \dots, RnN)$ , where  $R_{\gamma s}$  is the bead position  $s$  from chain  $\gamma$ . Then the total bead concentration from all the chains is considered as the average value of a microscopic density operator, which can be considered as:

$$\rho_l[\Psi](\mathbf{r}) = \sum_{\gamma=1}^n \sum_{s=1}^N \delta_{ls}^K \text{Tr} \Psi \delta(\mathbf{r} - \mathbf{R}_{\gamma s}) \quad (12.4)$$

The interchain correlations are ignored, and the system is considered as a set of free Gaussian chains embedded in a mean field. The distribution functions of the free Gaussian chains factorize precisely, and the density function can be easily written as a single-chain density functional product. Here, the free energy function can be designated as:

$$F[\Psi] \equiv \text{Tr}(\Psi H^{id} + \beta^{-1} \Psi \ln \Psi) + F^{nid}[\rho^0] \quad (12.5)$$

where the first term represents the Hamiltonian equation's average rate and denotes internal Gaussian chain linkages that contain the Gaussian chain arrangement. Gibbs entropy of the distribution— $kB \text{Tr} \Psi \ln \Psi$  is the second term in the free energy functional, and the third term is known as the mean-field nonideal contribution.

The main origin of functional theory is well explained: the distribution function  $\psi$  is considered such that the free energy functional  $F[\Psi]$  is normally minimized. So  $\Psi$  is always free, and is completely categorized by the difficulties that it denotes the density distribution that will minimize the free energy functional. This limitation on the density fields is removed by an external potential  $U_r$ . The density functional of the free energy is denoted as:

$$F[\rho] = -\beta^{-1} n \ln \Phi + \beta^{-1} \ln n! - \sum_I \int U_I(\mathbf{r}) \rho_I(\mathbf{r}) d\mathbf{r} + F^{nid}[\rho] \quad (12.6)$$

where the term  $I$  stands for dissimilar types of monomers,  $\beta = 1/kT$ , and the total number of chains are denoted as “ $n$ .” Finally,  $\Phi$  is identified as the partition function of a single chain.

The chemical potentials can be derived by functional separation of the free energy,  $\mu_1(\mathbf{r}) = \delta F / \delta \rho_1(\mathbf{r})$ . On the basis of these equations, the well-known generalized time-dependent Ginzburg–Landau method can be recognized. The time dependence is explained by a diffusion-based equation.

The Langevin equations can be identified by the dynamics of the density fields:

$$\frac{\partial \rho_A}{\partial t} = M v_B \nabla \rho_A \rho_B \nabla [\mu_A - \mu_B] + \eta \quad (12.7)$$

$$\frac{\partial \rho_B}{\partial t} = M v_B \nabla \rho_A \rho_B \nabla [\mu_B - \mu_A] + \eta \quad (12.8)$$

where  $M$  is known as the bead mobility constant. The well-known Gaussian noise  $\eta$  satisfies the fluctuation-dissipation theorem. The kinetic coefficient  $M v_B \rho_A \rho_B$  model explains a local exchange method. The Langevin equations are represented for a noncompressible system with dynamic constraints:

$$(\rho_A(\mathbf{r}, t) + \rho_B(\mathbf{r}, t)) = \frac{1}{v_B} \quad (12.9)$$

where  $B$  is considered as an average bead volume.

#### 12.2.2.2 PARTICLE DYNAMIC DISSIPATIVE

Dissipative particle dynamics (DPD)<sup>14,15</sup> is recognized as the stochastic simulation method for enhancing the dynamic and rheological characteristics of very simple, structured, as well as difficult fluids. It is an off-lattice mesoscopic simulation method that contains a group of particles moving in a constant gap with a distinct time. Particles correspond to whole molecules or regions; relatively, they are single atoms or atomistic information not measured to speed up the entire simulation process. The main benefit of this system is that the time and length scales are normally larger than those of usual MD simulations. Nowadays, polymeric fluid simulations of 100 nm-sized linear dimensions for tens of microseconds are considered.

On analyzing the total nonbonded force present on a DPD particle  $i$ , which is written as the summation of all particles  $j$  that will be positioned within a permanent cut-off distance, it is considered as three pairwise-additive forces:

$$F_i = \sum_{i \neq j} F_{ij}^C + \sum_{i \neq j} F_{ij}^D + \sum_{i \neq j} F_{ij}^R \quad (12.10)$$

where the first term is known to be the conservative force. It can be performed next to the line between two particles' centers of mass. This cannot be detected as Lennard-Jones force,<sup>16</sup> and it will linearly decrease as the pair distance gradually increases,<sup>17</sup> as well as with the second term, dissipative force, and the third factor, random force. A thermostat is formed



when two forces combine, and it will keep the temperature of the entire system constant. The main property of all nonbonded forces is that they must preserve momentum locally. A single random force calculation is needed for each pair of interacting particles. The most significant use of DPD is to maintain volume and temperature constant; therefore, it takes place in the NVT group. On the other hand, the pressure will be kept constant when simulation is in the NPT ensemble. As for the polymer nanocomposites, the NPs can also be treated as beads in DPD to capture the overall structure evolution.<sup>17</sup>

### 12.2.3 MACROSCALE METHODS

#### 12.2.3.1 LSM

Born LSM is a geometric method for discrediting the linear elasticity assumption. Here, the material is shown by an arrangement of springs that engage the adjacent and next adjacent neighbor linkages occupied by a simple cubic lattice. The energy connected with a node “ $m$ ” can be written as follows:

$$G_m = \frac{1}{2} \sum_n (\mathbf{u}_m - \mathbf{u}_n)^T \cdot \mathbf{M}_{mn} \cdot (\mathbf{u}_m - \mathbf{u}_n) \quad (12.11)$$

where  $n$  is called the adjacent nodes linked to  $m$  by a spring and the vector  $\mathbf{u}_m$  is the dislocation of the  $m^{\text{th}}$  node from its initial point. Here  $\mathbf{M}_{nm}$  is the relation connected with numerous nodes of a central (k) and noncentral (c) force constant.

The elastic force distributed on the  $m$ th node with dislocation due to the harmonic type is shown in eq 12.11. The force substitute on the  $m$ th node, which represents the local dislocation of the energy between nodes  $m$  and all adjacent nodes  $n$ , is given by

$$\mathbf{F}_m = \sum_n \mathbf{M}_{nm} \cdot (\mathbf{u}_m - \mathbf{u}_n) \quad (12.12)$$

External forces represent the boundary nodes that also have spring constants; the limitations are linear forces, which make a steadiness on all nodes with stability, resulting in a series of thin linear equations. The resolution of these equations is the conjugate gradient method to find the equilibrium configuration equivalent to the situation without total energy at every node. Stress and strain factors are designed by means of various kinds of energy and dimensions. The average energy and the force incorporated are used to analyze the

Young's modulus, which is distinct as the ratio of pressure of a particle with strain.

A probabilistic LSM, formed based on the abovementioned model, is used to calculate the essential break strain. This is calculated by determining the extensibility of the material equivalent to the highest strain that the system can maintain before a tragic breakdown, that is, the arrangement of a main break. A probabilistic method is included in LSM to study the rupture procedure, wherein the break forms with a chance relative to the local stress. If it is resolving when the rupture surface is to be formed, a rate of failure  $p_s(t)$  can be denoted by the following equation:

$$p_s(t) = \left[ \frac{(\sigma_s(t) - e_s)}{e'_s} \right]^\beta \quad (12.13)$$

where " $\sigma_s(t)$ " is the local stress, " $e_s$ " is considered the least stress at which rupture can happen, and  $e'_s$  is an arbitrary scaling parameter (for simplification, here we choose  $e'_s = e_s$ ). The minimum stress for a break between two nodes is the average value of the smallest fracture strain of the two nodes (For more details, see Ref. [18]). Basically, the lattice spring formed permits determining micromechanical characteristics in a computationally well-organized method, particularly for complex systems.

### 12.2.3.2 THE FINITE ELEMENT METHOD

The finite element method (FEM) is valuable in engineering and can be considered a computational means for predicting engineering analysis,<sup>19</sup> which includes structural analysis of complicated heterogeneous systems. The analytical solution generally needs an explanation of border value problems for partial differential calculations. To explain the crisis, it is classified into slightly easier components that are known as finite elements. These types of easier equations that represent these finite elements are then calculated into a big system with various equations that denote the complete crisis. FEM clarifies variational types, and it is considered the calculus of variations to approximate a solution by reducing a connected error function.

A significant work out of the process contains (1) separating the area of complexity into a group of subdomains, with each one shown by a chain of element equations to the new idea, followed by (2) scientifically uniting all collections of this solution into an overall system of equations for the final prediction. The total system of equations is known as solution techniques,

which can be predicted from the first values of the unique problem to get a numerical answer. In the abovementioned primary method, the element equations are easy and are locally estimated from the original difficult equations, where the initial equations are known as partial differential equations (PDE). In the second step, an overall system of equations is formed from the element equations, and a complete change of coordinates from the subdomains' local nodes to the domain's overall nodes occurs. This spatial change contains suitable direction modifications as used in relation to the reference coordinate system. Usually, this process is performed with the help of commercial software,<sup>20</sup> for example, ANSYS structural analysis.

## **12.3 MODELING AND SIMULATION METHODS OF POLYMER NANOCOMPOSITES**

### **12.3.1 MORPHOLOGY**

It is well-known that the microstructure of polymer–nanoparticle mixtures has a great influence on the features of the final materials. MD simulation is an effective tool to investigate these structures.<sup>21</sup> Shen et al.<sup>22</sup> utilized coarse-grained MD simulations to analyze the influence of grafting chain length and grafted density on the structural characteristics of end-grafted NPs packed polymer nanocomposites. It is found that increasing the grafting density and grafted chain length enhances the spreading of NPs and improves the brush/matrix interface thickness, and an optimal grafting density is seen in this work (Figure 12.2). Karatasos et al.<sup>23</sup> explored the combination of graphene along with hyperbranched polyesters of two different pseudogenerations at various temperatures. The results explain that graphene platelets are generated by stacks that consist of two to three flakes. The properties of the spatial arrangement of the graphene planes and that of the produced clusters (including their relative orientation) strongly relate to the size as well as shape of the hyperbranched constituent and the temperature. An important slowing down is analyzed both in local and overall polymer dynamics in composite systems. Nigel Clarke et al.,<sup>24</sup> using MD simulations, investigated the effect of different spherical NPs on chain size with large NP loading. The results demonstrated that polymer chains can be disturbed by the existence of attractive NPs when the polymer radius of gyration is higher than the NP radius. Gao et al.<sup>25</sup> adopted a coarse-grained MD simulation to investigate the nanorod-filled polymer nanocomposites. The results showed that the characteristic relaxation time of the end-to-end vector correlation exhibits an Arrhenius-like temperature-dependent behavior.

Besides, both the rotational and translational diffusion coefficients have a linear relationship with temperature. Rissanou et al.<sup>26</sup> investigated the effect of graphene on the mobility of three common polymers, polyethylene, polystyrene, and poly(methyl-methacrylate). Results showed clear spatial dynamic heterogeneity for all model systems, with different dynamical behaviors of the adsorbed polymer segments. The segmental relaxation time of the polymer as a property of the distance from graphene shows an unexpected decrease beyond the first adsorption layer for polyethylene, which is close to graphene.

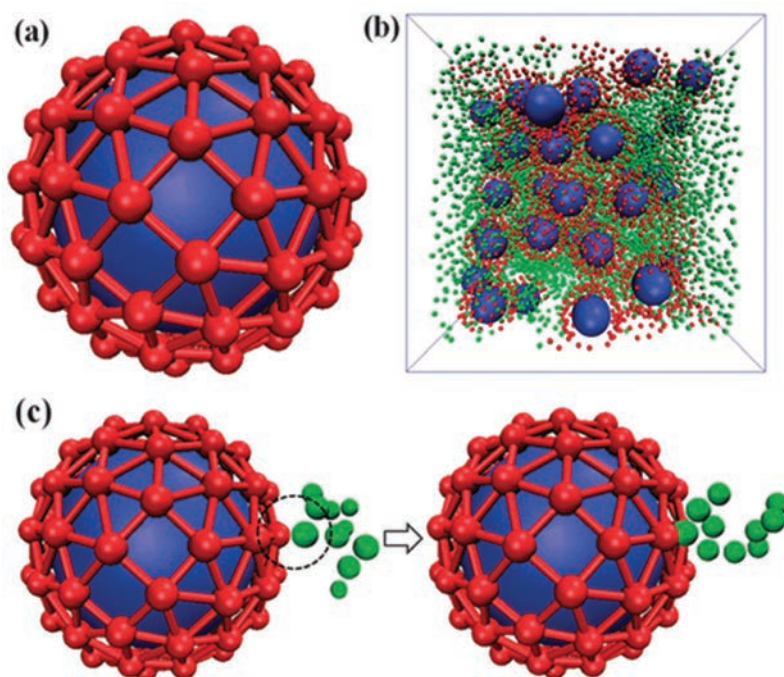


**FIGURE 12.2** (a) The snapshot of an isolated NP. The blue sphere is the solid NP core, and the bonded red spheres are the virtual surface points. (b) The snapshot of the simulated system. The green spheres indicate the grafted chains, and the matrix chains are not shown here. (c) The partial snapshot of the end-grafting process.<sup>22</sup>

*Source:* Reproduced from Ref. [22] with permission from the Royal Society of Chemistry.

To capture the mesoscale structure, mesoscale simulation methods could be applied in this field. These structures could serve as the input for a large-scale method for property analysis. Karatrantos et al.<sup>17</sup> investigated the chain linkage within polymer–nanorod nanocomposites in connection to polymer melts with model simulations in DPD polymer (Figure 12.3). The

nanorods have a radius less than the polymer radius of rotation and an aspect ratio of 7.5. A sudden enhancement in the number of entanglements in the nanocomposites, as shown by higher contour lengths of the initial route, is generally seen. Here, the end-to-end distance is fundamentally unaffected by the deviation of the nanorod volume fraction (0–11%). Yong et al.<sup>27</sup> developed a novel computational method to model FRP that combines the reaction kinetics for the polymerization process with the dynamics of the complex fluid using DPD. The results give a close look at the polymerization kinetics of the FRP as well as potential guidelines for tailoring experimental conditions to achieve the desired polymerization products. Ren et al.<sup>28</sup> constructed a 3-D computational multiscale micromechanics theory related to particular elemental investigations to calculate the valuable macroscale piezoresistive reaction of CNT-incorporated polymer nanocomposites. In this model, CNT piezoresistivity and mesoscale arrangement results are included on the basis of a 3-D multiscale mechanical–electrostatic coupled code. The

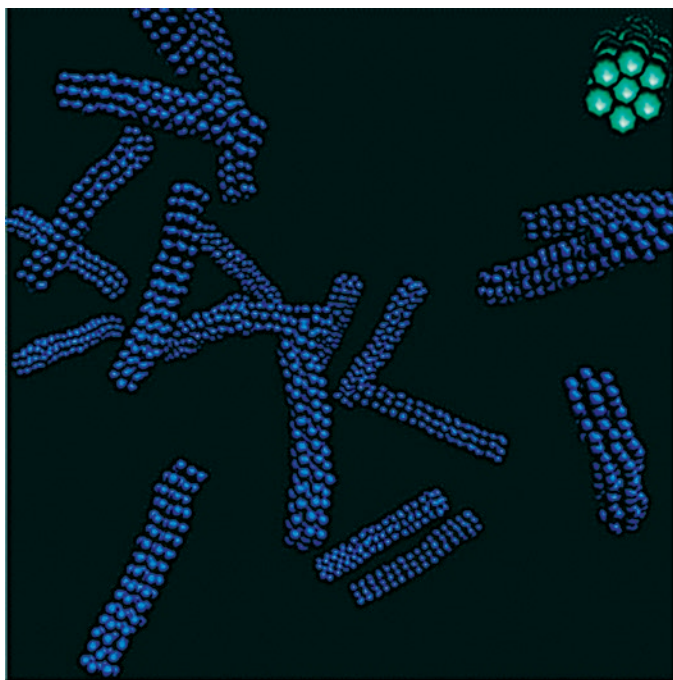


**FIGURE 12.3** Snapshot of hexagonal nanorods. Inset: a cross-section of the nanorod is taken on this analysis.<sup>17</sup>

*Source:* Reproduced from Ref. [17] with permission from the Royal Society of Chemistry.

experimental results not only describe how dissimilar nanoscale mechanisms affect the total macroscale piezoresistive reaction in a CNT structure but also suggest insight into how to manage the mesoscale CNT networks and how to modify the nanocomposite piezoresistive response.

### **12.3.2 MECHANICAL PROPERTIES**

MD simulations have been used to study the mechanical properties of nanocomposites of polymers. He et al.<sup>29</sup> developed a polymer composite molecular model, which is improved by adding nanoSiO<sub>2</sub> particles. The enhanced tribological characteristics of the polymer/nano-SiO<sub>2</sub> composites are analyzed by incorporating an upper iron layer that will slide on the polymer composites' surface. These results explain that an enhancement of about 190% in the Young's modulus is obtained by the introduction of nanoSiO<sub>2</sub> particles. Alian et al.<sup>30</sup> conducted comprehensive MD simulations of the nanoscale notching of graphene-toughened composites to analyze the properties of graphene as a strengthening and covering substance. The results exhibit that the notch resistance of a single-layer graphene-covered PE is 14-fold the notch resistance of pure PE. And the notch resistance of the multilayered fixed graphene arrangement can be efficiently maintained by suitably selecting the separation distance between the graphene layers. Wang et al.<sup>31</sup> calculated the glass transition nature and mechanical characteristics of nanocomposites of poly(ethylene terephthalate) (PET), PET/silica, and PET/hydroxylated silica. They showed that the accumulation of nanosilica would decrease the value of T<sub>g</sub> of PET in PET/silica nanocomposite. The use of hydroxylated silica enhanced the T<sub>g</sub> of PET in nanocomposites of PET/hydroxylated silica. Hagita et al.<sup>32</sup> analyzed MD simulations of spherical NPs of polymer nanocomposites to analyze the origin of the Kremer–Grest theory. The results explain that the linkage improves both the strain values and the NP aggregation. For large elongation ratios, the bond direction turns to the corresponding axis. For the “aggregated” NPs, this increase is important. Güryel et al.<sup>33</sup> considered the array and surface shapes of three polymer/graphene nanocomposites by using conventional MD simulations. Like the experimental findings, the results specify that graphene produces order in both the PE and PVDF systems by providing a nucleation site for crystallization and steering the progress of oligomer crystals on the basis of the direction of the graphene sheet, whereas the PS system remains disordered in the survival of graphene. Theodoros Davris et al.<sup>34</sup> found a linear dependence of the strengthening on the inverse radius of the NPs. Deformation simulations

that are related to a linearly rising strain gave a wide increase of 50% in the linear modulus when fillers were introduced into the polymer matrix, in spite of the use of direct interactions among the NPs (Figure 12.4).

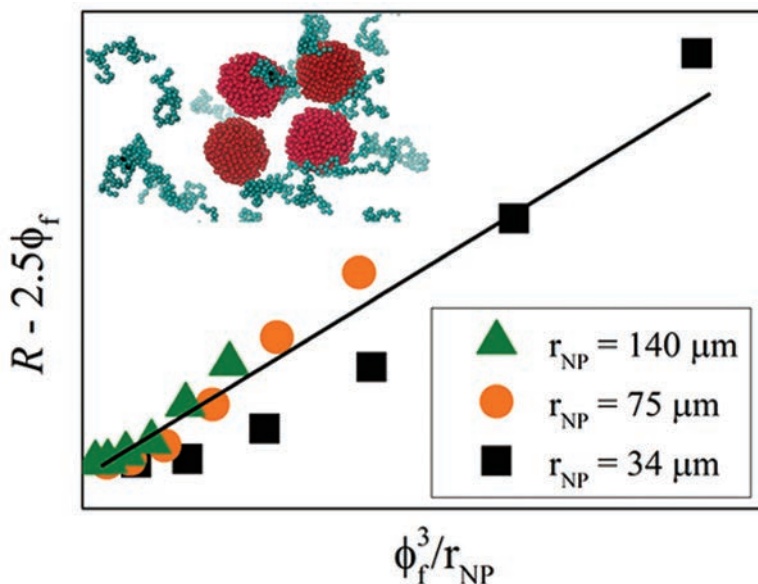


**FIGURE 12.4** Reinforcement of the simulated particulate systems arising from coupled hydrodynamic interactions and surface effects versus  $\phi_f^3/r_{NP}$ .<sup>34</sup>

Source: Reproduced from Ref. [34] with permission from the Royal Society of Chemistry.

Considering the material's excellent strength and stiffness, carbon nanotubes (CNTs) are used as additives to different structural materials, including polymer nanocomposites. Zheng et al.<sup>35</sup> investigated the effects and influence of several factors, such as grafting position, density, and the length and flexibility of the chains, on the allocation of graphene and CNTs. The results explain that when the location is positioned on the center surface of the graphene or the middle of the CNT, the distribution state is the top one, generating supreme stress–strain performance. Liu et al.<sup>36</sup> analyzed the important synergetic effect between graphene (GR) and CNT in raising the interfacial mechanical characteristics of polyethylene polymer composites. The arrangement of CNT has a slight influence on the interfacial mechanical characteristics of the  $\pi$ – $\pi$  stack hybrid GR–CNT. While for the covalent bond hybrid GR–CNT, the strengthening effect is larger and there is an increase

in the CNT's length and radius. Notably, simulation results show that multi-walled CNTs are more effective than single-walled CNTs. Quan Wang et al.<sup>37</sup> developed molecular cross-linked theories of virgin epoxy matrix and CNT-toughened composites with primary edged breaks. The results show mechanisms of the superior fracture behaviors and crack growth nature of the epoxy composites, which are better explained by an atomic study by analyzing the changes in the nonbond network energy and radius distribution function of epoxy matrix and CNTs.

Mesoscale simulation can also be applied to the study of the mechanical characteristics of polymer-based nanofillers. Didier R. Long et al.<sup>38</sup> explained and extended a model about the strengthening of nanofilled elastomers and also with thermoplastic behavior, and the model is solved by mesoscale numerical simulations. The results explained the dynamics of yield and rebirth of glassy bridges related to the nonlinear Payne and Mullins theories and allowed for semiquantitatively explaining the results obtained by Payne in 1963 (Figure 12.5).

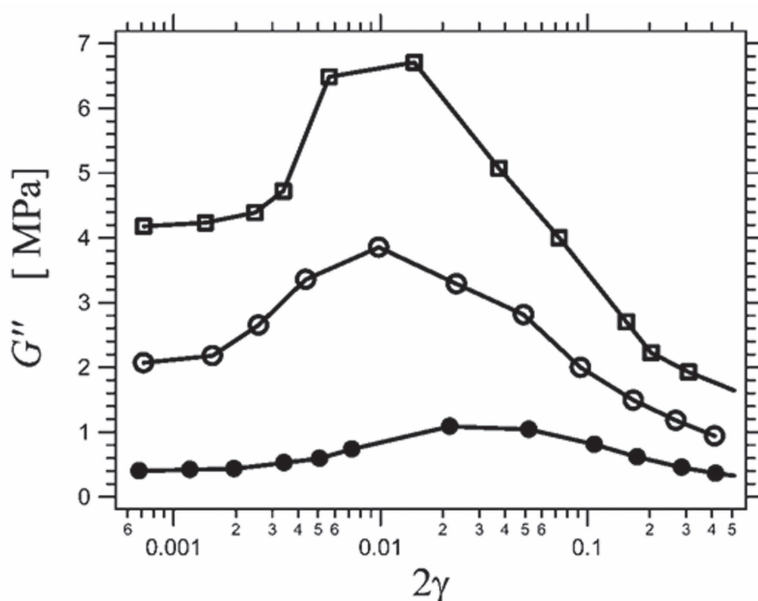


**FIGURE 12.5** Loss modulus  $G''$  (in MPa) measured in carbon black filled butyl rubbers as a function of the deformation amplitude and three different filler volume fractions:  $\square$ ,  $\Phi = 38.6\%$ ;  $\blacksquare$ ,  $\Phi = 33.6\%$ ;  $\bullet$ ,  $\Phi = 23.2\%$ .<sup>38</sup>

Source: Reproduced from Ref. [38] with permission from the Royal Society of Chemistry.



A continuum mechanics-based lattice spring model is also adopted to study the mechanical properties of nanocomposites. Buxton et al.<sup>39</sup> compared the mechanical properties of homopolymers containing either solid spheres, rods, or platelets. The effects of packing geometry on the mechanical properties of the composite are separated. Especially viscoelastic deformations are incorporated in the lattice spring model.<sup>40</sup> The results show that in the twice-as-percolating system, the strengthening effectiveness of the nanorods and the electrical conductivity of the particle are considerably improved relative to the properties in composites where the nanorods are arbitrarily dispersed in a homogeneous matrix (Figure 12.6). Deng et al.<sup>41</sup> found that the addition of NPs in polymer matrices shows a higher Young's modulus, and NPs distributed in the soft phase are more efficient at improving stiffness than those dispersed in the hard phase. In bicontinuous structures, the hard phase forms a stiff network and controls the stress, while in dispersed structures, the soft phase sustains the deformation, and stress is hard to transfer from the soft phase to the hard phase.

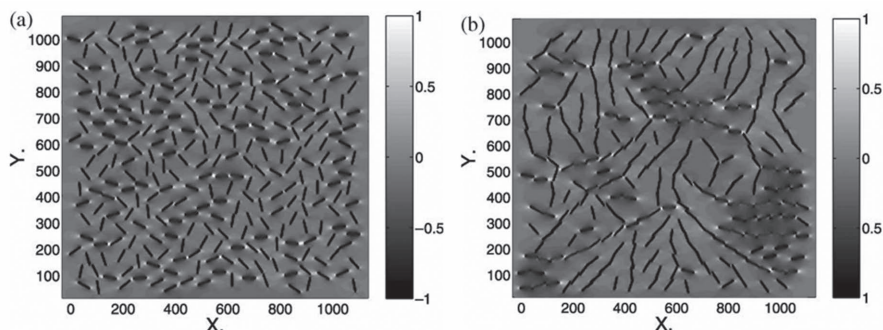


**FIGURE 12.6** Normal strain field contours for nanorods in a homogeneous system (a) or a phase-separating system (b).<sup>40</sup>

*Source:* Reproduced from Ref. [40] with permission from Taylor & Francis.

As for the finite element method, Stefano Cardea et al.<sup>42</sup> included two dissimilar parametric variational 3-D finite element (FE) models to analyze the mechanical behavior of cellulose acetate-graphene oxide nanocomposite membranes. The nanocomposite morphology, which is derived from electron scanning microscopy analysis, was used to make periodic representative volume elements. A numerical-experimental relationship was conducted comparing FE model results with the experimental ones received by compression tests, and a good calculation of the experimental method of Young modulus was received by FE simulations (Figure 12.7).

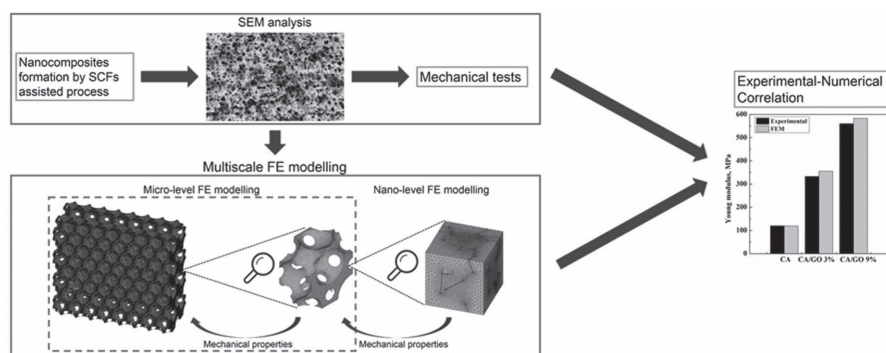


**FIGURE 12.7** The overview of numerical-experimental correlation with the help of FE modeling.<sup>42</sup>

*Source:* Reproduced with permission from Ref. [42]. © 2018 Elsevier.

## 12.4 CONCLUSIONS

A comprehensive understanding of the phenomena at different time and length scales is needed to study the arrangement and characteristics of polymer nanocomposites. Numerous conventional simulation methods have been employed in this area, such as MD at the microscale, MesoDyn at the mesoscale, and the lattice spring model at the macroscale. Combining with the experimental findings, the results have exposed success to various degrees in addressing many aspects of polymer nanocomposites. As for the simulation part, the simulation techniques introduced thus far have extremely dissimilar strengths as well as weaknesses. For example, atomic changes can be used to analyze molecular types of interactions and arrangements on a scale up to 10 nm. The resulting information is very useful in understanding the interaction strength at nanoparticle–polymer interfaces. However, molecular simulations are time-consuming for the study of the NP aggregation effect on mechanical properties. To explore the morphology and mechanical behavior at the mesoscale or macroscale, corresponding relatively large-scale methods are more effective. But these techniques may have restrictions when applied to polymer nanocomposites, and the reliability of the results may be decreased. Some crucial parameters in these methods need to be estimated using microscale or empirical methods.

Despite the progress over the past years, there are several difficulties in computer modeling and simulation.<sup>43</sup> Apart from the newly developed simulation methods, multiscale simulation would be a reasonable way to balance computing efficiency and accuracy for the simulation of polymer

nanocomposites. There are mainly two types of multiscale methods: sequential and concurrent multiscale approaches. In sequential conditions, computational recreation methods at one scale are used to describe the values of the model functioning on the neighboring, larger level. In similar methods and calculations, several computational methods are associated together in a collective model in which different scales of material properties are measured simultaneously and communicate using some kind of handshaking process. Multiscale simulation<sup>44</sup> helps us solve problems related to different lengths or time scales, for example, from the chemical structure to the final mechanical response of nanocomposites. How to effectively select and connect different simulation methods is still a problem in the application of multiscale simulation.

## ACKNOWLEDGMENTS

The author thanks Dr. Sanal Sebastian Payyappilly for helpful discussions.

## KEYWORDS

- **heterogeneous**
- **nanocomposites**
- **simulation**
- **mechanical properties**
- **molecular dynamics**

## REFERENCES

1. Ramanathan, T.; Abdala, A.; Stankovich, S.; Dikin, D.; Herrera-Alonso, M.; Piner, R.; Adamson, D.; Schniepp, H.; Chen, X.; Ruoff, R. Functionalized Graphene Sheets for Polymer Nanocomposites. *Nat. Nanotechnol.* **2008**, *3*, 327–331.
2. Stankovich, S.; Dikin, D. A.; Dommett, G. H.; Kohlhaas, K. M.; Zimney, E. J.; Stach, E. A.; Piner, R. D.; Nguyen, S. T.; Ruoff, R. S. Graphene-Based Composite Materials. *Nature* **2006**, *442*, 282–286.
3. He, F.; Lau, S.; Chan, H. L.; Fan, J. High Dielectric Permittivity and Low Percolation Threshold in Nanocomposites Based on Poly (Vinylidene Fluoride) and Exfoliated Graphite Nanoplates. *Adv. Mater.* **2009**, *21*, 710–715.

4. Moniruzzaman, M.; Winey, K. I. Polymer Nanocomposites Containing Carbon Nanotubes. *Macromolecules* **2006**, *39*, 5194–5205.
5. Stoclet, G.; Lefebvre, J.; Séguéla, R.; Vanmansart, C. In Situ SAXS Study of the Plastic Deformation Behavior of Polylactide Upon Cold-Drawing. *Polymer* **2014**, *55*, 1817–1828.
6. McCready, E. M.; Burghardt, W. R. In Situ SAXS Studies of Structural Relaxation of an Ordered Block Copolymer Melt Following Cessation of Uniaxial Extensional Flow. *Macromolecules* **2014**, *48*, 264–271.
7. Karatrantos, A.; Clarke, N.; Kröger, M. Modeling of Polymer Structure and Conformations in Polymer Nanocomposites from Atomistic to Mesoscale: A Review. *Polym. Rev.* **2016**, *56*, 385–428.
8. Datta, S.; Davim, J. P. *Computational Approaches to Materials Design: Theoretical and Practical Aspects: Theoretical and Practical Aspects*; IGI Global, 2016.
9. Auhl, R.; Everaers, R.; Grest, G. S.; Kremer, K.; Plimpton, S. J. Equilibration of Long Chain Polymer Melts in Computer Simulations. *J. Chem. Phys.* **2003**, *119*, 12718–12728.. DOI: 10.1063/1.1628670.
10. Ge, T.; Robbins, M. O. Anisotropic Plasticity and Chain Orientation in Polymer Glasses. *J. Polym. Sci. B Polym. Phys.* **2010**, *48*, 1473–1482. DOI: 10.1002/polb.22015.
11. Hoy, R. S.; Robbins, M. O. Strain Hardening of Polymer Glasses: Entanglements, Energetics, and Plasticity. *Phys. Rev. E* **2008**, *77*. DOI: 10.1103/PhysRevE.77.031801.
12. Ge, T.; Pierce, F.; Perahia, D.; Grest, G. S.; Robbins, M. O. Molecular Dynamics Simulations of Polymer Welding: Strength from Interfacial Entanglements. *Phys. Rev. Lett.* **2013**, *110*. DOI: 10.1103/PhysRevLett.110.098301.
13. Kalathi, J. T.; Kumar, S. K.; Rubinstein, M.; Grest, G. S. Rouse Mode Analysis of Chain Relaxation in Homopolymer Melts. *Macromolecules* **2014**, *47*, 6925–6931. DOI: 10.1021/ma500900b.
14. Groot, R. D.; Warren, P. B. Dissipative Particle Dynamics: Bridging the Gap Between Atomistic and Mesoscopic Simulation. *J. Chem. Phys.* **1997**, *107*, 4423–4435.
15. Espanol, P.; Warren, P. Statistical Mechanics of Dissipative Particle Dynamics. *EPL* **1995**, *30*, 191.
16. Frenkel, D.; Smit, B. Academic Press: San Diego, 1996.
17. Karatrantos, A.; Clarke, N.; Composto, R. J.; Winey, K. I. Topological Entanglement Length in Polymer Melts and Nanocomposites by a DPD Polymer Model. *Soft Matter* **2013**, *9*, 3877–3884.
18. Deng, S.; Zhao, X.; Huang, Y.; Han, X.; Liu, H.; Hu, Y. Deformation and Fracture of Polystyrene/Polypropylene Blends: A Simulation Study. *Polymer* **2011**, *52*, 5681–5694.
19. Reddy, J. N. An Introduction to the Finite Element Method. McGraw-Hill: New York, 1993.
20. Sun, W.; Vassilopoulos, A. P.; Keller, T. Finite Element Analysis of Initial Imperfection Effects on Kinking Failure of Unidirectional Glass Fiber-Reinforced Polymer Composites. *Compos. Struct.* **2018**, *203*, 50–59.
21. Karatrantos, A.; Composto, R. J.; Winey, K. I.; Clarke, N. Structure and Conformations of Polymer/SWCNT Nanocomposites. *Macromolecules* **2011**, *44*, 9830–9838.
22. Shen, J.; Liu, J.; Li, H.; Gao, Y.; Li, X.; Wu, Y.; Zhang, L. Molecular Dynamics Simulations of the Structural, Mechanical and Visco-Elastic Properties of Polymer Nanocomposites Filled with Grafted Nanoparticles. *Phys. Chem. Chem. Phys.* **2015**, *17*, 7196–7207.

23. Karatasos, K. Graphene/Hyperbranched Polymer Nanocomposites: Insight from Molecular Dynamics Simulations. *Macromolecules* **2014**, *47*, 8833–8845.
24. Karatrantos, A.; Clarke, N.; Composto, R. J.; Winey, K. I. Polymer Conformations in Polymer Nanocomposites Containing Spherical Nanoparticles. *Soft Matter* **2015**, *11*, 382–388.
25. Gao, Y.; Liu, J.; Shen, J.; Zhang, L.; Cao, D. Molecular Dynamics Simulation of Dispersion and Aggregation Kinetics of Nanorods in Polymer Nanocomposites. *Polymer* **2014**, *55*, 1273–1281.
26. Rissanou, A. N.; Harmandaris, V. Dynamics of Various Polymer–Graphene Interfacial Systems Through Atomistic Molecular Dynamics Simulations. *Soft Matter* **2014**, *10*, 2876–2888.
27. Yong, X.; Kuksenok, O.; Balazs, A. C. Modeling Free Radical Polymerization Using Dissipative Particle Dynamics. *Polymer* **2015**, *72*, 217–225.
28. Ren, X.; Chaurasia, A. K.; Oliva-Avilés, A. I.; Ku-Herrera, J. J.; Seidel, G. D.; Avilés, F. Modeling of Mesoscale Dispersion Effect on the Piezoresistivity of Carbon Nanotube-Polymer Nanocomposites via 3D Computational Multiscale Micromechanics Methods. *Smart Mater. Struct.* **2015**, *24*, 065031.
29. He, E.; Wang, S.; Li, Y.; Wang, Q. Enhanced Tribological Properties of Polymer Composites by Incorporation of Nano-SiO<sub>2</sub> Particles: A Molecular Dynamics Simulation Study. *Comput. Mater. Sci.* **2017**, *134*, 93–99.
30. Alian, A.; Dewapriya, M.; Meguid, S. Molecular Dynamics Study of the Reinforcement Effect of Graphene in Multilayered Polymer Nanocomposites. *Mater. Des.* **2017**, *124*, 47–57.
31. Wang, Y.-h.; Wang, W.-h.; Zhang, Z.; Xu, L.; Li, P. Study of the Glass Transition Temperature and the Mechanical Properties of PET/Modified Silica Nanocomposite by Molecular Dynamics Simulation. *Eur. Polym. J.* **2016**, *75*, 36–45.
32. Hagita, K.; Morita, H.; Doi, M.; Takano, H. Coarse-Grained Molecular Dynamics Simulation of Filled Polymer Nanocomposites Under Uniaxial Elongation. *Macromolecules* **2016**, *49*, 1972–1983.
33. Geerlings, P.; Güryel, S.; Walker, M.; De Proft, F.; Wilson, M. R. Molecular Dynamics Simulations of the Structure and the Morphology of Graphene/Polymer Nanocomposites. *Phys. Chem. Chem. Phys.* **2017**.
34. Davris, T.; Mermet-Guyennet, M. R.; Bonn, D.; Lyulin, A. V. Filler Size Effects on Reinforcement in Elastomer-Based Nanocomposites: Experimental and Simulation Insights into Physical Mechanisms. *Macromolecules* **2016**, *49*, 7077–7087.
35. Zheng, Z.; Wang, Z.; Wang, L.; Liu, J.; Wu, Y.; Zhang, L. Dispersion and Shear-Induced Orientation of Anisotropic Nanoparticle Filled Polymer Nanocomposites: Insights from Molecular Dynamics Simulation. *Nanotechnology* **2016**, *27*, 265704.
36. Liu, F.; Hu, N.; Ning, H.; Atobe, S.; Yan, C.; Liu, Y.; Wu, L.; Liu, X.; Fu, S.; Xu, C. Investigation on the Interfacial Mechanical Properties of Hybrid Graphene-Carbon Nanotube/Polymer Nanocomposites. *Carbon* **2017**, *115*, 694–700.
37. Li, Y.; Wang, S.; Wang, Q.; Xing, M. Enhancement of Fracture Properties of Polymer Composites Reinforced by Carbon Nanotubes: A Molecular Dynamics Study. *Carbon* **2018**, *129*, 504–509.
38. Merabia, S.; Sotta, P.; Long, D. R. A Microscopic Model for the Reinforcement and the Nonlinear Behavior of Filled Elastomers and Thermoplastic Elastomers (Payne and Mullins Effects). *Macromolecules* **2008**, *41*, 8252–8266.

39. Buxton, G. A.; Balazs, A. C. Lattice Spring Model of Filled Polymers and Nanocomposites. *J. Chem. Phys.* **2002**, *117*, 7649–7658.
40. Buxton, G. A.; Balazs, A. C. Predicting the Mechanical and Electrical Properties of Nanocomposites Formed from Polymer Blends and Nanorods. *Mol Simul.* **2004**, *30*, 249–257.
41. Deng, S.; Huang, Y.; Xu, S.; Lin, S.; Liu, H.; Hu, Y. Mechanical Properties of High-Performance Elastomeric Nanocomposites: A Sequential Mesoscale Simulation Approach. *RSC Adv.* **2014**, *4*, 63586–63595.
42. Naddeo, F.; Baldino, L.; Cardea, S.; Naddeo, A.; Reverchon, E. J. T. Finite Element Multiscale Modelling of Elastic Behavior of Cellulose Acetate—Graphene Oxide Nanocomposites, Produced Using a SC-CO<sub>2</sub> Assisted Technique. *J. Supercrit. Fluids*, **2018**, *140*, 248–257.
43. Zhao, J.; Wu, L.; Zhan, C.; Shao, Q.; Guo, Z.; Zhang, L. Overview of Polymer Nanocomposites: Computer Simulation Understanding of Physical Properties. *Polymer* **2017**, *133*, 272–287.
44. Guo, Z.; Song, L.; Boay, C. G.; Li, Z.; Li, Y.; Wang, Z. A New Multiscale Numerical Characterization of Mechanical Properties of Graphene-Reinforced Polymer-Matrix Composites. *Compos. Struct.* **2018**, *199*, 1–9.



# Index

---

## A

Acid dyes, 193  
Adsorption behavior, 189–190  
Ammonium polyphosphate (APP), 273  
Angle bending potential, 79  
ARC discharge method, 12  
Atom density, 97  
Atomistic models, 86–87  
Azoic dyes, 193

## B

Biogenic nanoparticles  
  amyloid fibrils, 224  
  DNA, 223  
  viral nanoparticles, 223–224  
Bionanomaterials  
  applications  
    biosensing, 229  
    drug delivery, 227–228  
    immunotherapy, 230–231  
    molecular imaging, 229–230  
    tissue engineering, 225–227  
  biogenic nanoparticles  
    amyloid fibrils, 224  
    DNA, 223  
    viral nanoparticles, 223–224  
  carbon-based nanoparticles, 224–225  
  classification  
    gold nanoparticles, 220  
    nanocomposites, 221–222  
    polymeric bionanoparticles, 221–222  
    silver nanoparticles, 221  
    titanium dioxide, 221  
  significance, 231–232  
Blending method, 140–141  
Bond stretching potential, 78  
Bottoms up approach (BUA), 219  
Brominated isobutyleneisoprene rubber (BIIR), 67  
Butyl rubber clay, 67–68

## C

Cadmium sulfide (CDS), 44  
Carbon nanotubes (CNT), 144–145, 269  
Chemical vapor deposition (CVD), 8  
Clay, 50  
  advantages, 53–54  
    barrier properties, 55–56  
    flammability, 55  
    mechanical properties, 55  
  minerals, 51  
  preparative methods  
    intercalation, 52  
    melt intercalation, 53  
    in situ intercalative polymerization method, 52–53  
  structure, 53  
  tire  
    bead, 58–59  
    breakers, 58  
    carcass or body ply, 57  
    chafers, 57  
    cushioning, 61  
    inner liner, 56–57  
    insulations, 58  
    load carrying capacity, 62  
    rolling resistance, 59–61  
    sidewall rubber, 58  
    traction, 61  
    transmits steering resistance, 62–63  
    tread, 58  
    wear and durability, 62  
COMPASS force, 116  
COMPASS force field, 89–90  
Computer simulation  
  macroscale methods  
    finite element method (FEM), 333–334  
    LSM, 332–333  
  mesoscale methods  
    dissipative particle dynamics (DPD), 331–332  
  MesoDyn, 329–331



modeling and simulation techniques, 327  
 molecular dynamics (MD), 328–329  
 polymer nanocomposites  
 mechanical properties, 337–340  
 morphology, 334–337

## D

Dissipative particle dynamics (DPD),  
 331–332  
 Drawing molecules, 86–87  
 Dysprosium oxide ( $\text{Dy}_2\text{O}_3$ ), 256–258

## E

Energy dispersive X-ray (EDX or EDS)  
 analysis, 297  
 Ethylenediaminetetra-acetic acid (EDTA),  
 260

## F

Field emission scanning electron  
 microscopy (FESEM), 203, 204  
 Flax fabric (FF) process, 272  
 Fourier transform infrared (FTIR)  
 spectroscopy, 298

## G

Gadolinium oxide ( $\text{Gd}_2\text{O}_3$ ), 253–255  
 Glass Fibre Reinforced Polymer (GFRP),  
 271  
 Grand intercalated Gr oxide (GrO), 83  
 Graphene, 2  
 synthesis and fabrication, 2  
 ARC discharge method, 12  
 carbon implantation, 12  
 chemical vapor deposition (CVD), 8  
 epitaxial growth, 7  
 high pressure high-temperature  
 (HPHT), 10  
 intercalation-aided exfoliation, 5–6  
 mechanical exfoliation, 3  
 molecular beam epitaxial method  
 (MBE), 7  
 molten salts, 6–7  
 pyrolysis of, 9–10  
 single-walled carbon nanotubes  
 (SWCNT), 12  
 solvent-aided sonication, 3–4

sputtering, 10–11  
 surfactant-assisted exfoliation, 4–5  
 Graphene-based thermoplastic polyurethane  
 (Gr/TPU)  
 analytical methods, 81  
 angle bending potential, 79  
 bond stretching potential, 78  
 boundary and constraint conditions,  
 123–124  
 COMPASS force field, 124–125  
 cross-terms, 80  
 cut-off distance, 130  
 electrostatic interactions, 80–81  
 energy increment, 127  
 experimental methods, 81  
 geometric parameter, 129–130  
 Gr/TPU nanocomposites, 99  
 boundary, 108  
 boundary and constraint conditions,  
 115–116  
 COMPASS force, 116  
 constraint conditions, 108  
 graphene concentration models, 106  
 Gr/PU nanocomposite, 114–115  
 Lamé coefficients, 120  
 MD simulations, 116  
 NPT-MD simulations, 119  
 NVT simulation, 118  
 prediction of properties, 113–114  
 simulations steps, 110–113  
 single layer Gr (SLGR), 100–101  
 stress–strain response, 114  
 thermoplastic polyurethane (TPU),  
 101–106  
 unit cell preparation, 106–107, 115  
 Young's modulus, 119  
 improper dihedral angle (four body)  
 potential energy, 80  
 MD-based modeling  
 corrosion properties, 85  
 grand intercalated Gr oxide (GrO), 83  
 mechanical properties, 84  
 parameters, 83–84  
 thermal properties, 85  
 thermoplastic polyurethanes (TPUs),  
 82  
 tribological properties, 85  
 modeling and simulation

advantages, 98  
assumptions for, 98  
atom density, 97  
atomistic models, 86–87  
bond order, 90  
COMPASS force field, 89–90  
concentration profile, 97–98  
connolly surface, 97  
cut-off distance, 91  
drawing molecules, 86–87  
empirical potentials, 88  
energy minimization, 87  
ensembles, 87–88  
fiber/polymer separation energies,  
96–97  
force-field, 88  
free volume, 97  
geometry optimization, 87  
hardness, 95  
interaction energy, 96  
limitations, 99  
mean square displacement (MSD), 97  
modulus, calculation, 95  
molecular energy, 97  
multi-body potentials, 90  
packing configurations, 97  
pair potentials, 88  
polarizable potentials, 91  
polymers, 91  
pressure control methods, 91–92  
properties in, 92–95  
radial distribution function (RDF), 97  
reactive potentials, 90  
semi-empirical potentials, 88  
temperature, 91–92  
time integration algorithm, 88  
toughness, 95–96  
normal and shear separation forces, 127  
numerical methods, 81  
potential energy (PE), 76  
simulation parameter, 130  
simulations, 125  
stress–strain response  
interfacial model, 120, 122  
normal displacement, 122  
shear displacement, 122–123  
unit cell preparation, 123  
torsional rotation potential, 79

van der Waals (vdW), 80  
velocities, 77  
Green synthesis  
biosynthetic strategies, 300  
microbe-assisted nanosynthesis, 302

## H

Halogen-less fire, 273  
High resolution transmission electron  
microscopy (HR-TEM), 296–297  
High pressure high-temperature (HPHT), 10

## L

Lamé coefficients, 120  
Lanthanide (Ln)  
absorption and emission, 245  
luminescence, 245  
phosphors, 246  
rare earths (RE) sesquioxides, 247  
properties, 244  
rare-earth oxide, 243  
bottom-up method, 249–250  
dysprosium oxide ( $\text{Dy}_2\text{O}_3$ ), 256–258  
ethylenediaminetetra-acetic acid  
(EDTA), 260  
gadolinium oxide ( $\text{Gd}_2\text{O}_3$ ), 253–255  
neodymium sesquioxide ( $\text{Nd}_2\text{O}_3$ ),  
250–253  
samarium oxide ( $\text{Sm}_2\text{O}_3$ ), 258–260  
synthesis, 247–248  
top-down method, 249  
Light-source  
composites in, 269  
advantages, 270  
ammonium polyphosphate (APP), 273  
applications, 270  
flax fabric (FF) process, 272  
Glass Fibre Reinforced Polymer  
(GFRP), 271  
green supported, 270–271  
halogen-less fire, 273  
metal, 270–271  
photocatalysis, 274–275  
photocatalytic degradation, 275–276  
polymer, 270–271  
wastewater technologies, 273–274  
photocatalytic degradation, 276

- challenges in, 285–286
- composite particles, 282–283
- concentration using, 283
- photodegradation studies, 278–279
- reactive red 198 dye, 279–280
- reusability, 284–285
- sol-gel method, 281–282
- sunlight-mediated photocatalysis, 277–278
- total organic carbon (TOC), 283–284
- UV-light mediated photocatalysis, 277
- wavelength, 280
- ZnO-TiO<sub>2</sub> nanomaterials, 279
- Zn-Al-based nanocomposites, 269
- Luminescence, 245
- phosphors, 246
- rare earths (RE) sesquioxides, 247

## M

- Macroscale methods
  - finite element method (FEM), 333–334
  - LSM, 332–333
- Magnetic multiwall carbon nanotube (MMWCNT), 204
- Magnetite/reduced graphene oxide (MRGO), 202
- Malachite green (MG), 201
- Manganese dioxide (MnO<sub>2</sub>), 166
  - nanostructures
    - co-precipitation, 172
    - electrospinning, 173
    - hierarchical hollow nanostructures, 175
    - hydrothermal synthesis, 170–172
    - low-temperature solid-phase synthesis, 173
    - microwave-assisted syntheses, 173, 175
    - sol-gel method, 169–170
    - template-assisted method, 167, 169
  - properties and applications, 176
    - batteries, 178–179
    - electrochemical biosensing, 180–181
    - heterogeneous catalysis, 181–182
    - supercapacitors, 177–178
    - water treatment, 179
- MD-based modeling
  - corrosion properties, 85
  - grand intercalated Gr oxide (GrO), 83

- mechanical properties, 84
- parameters, 83–84
- thermal properties, 85
- thermoplastic polyurethanes (TPUs), 82
- tribological properties, 85
- Mean square displacement (MSD), 97
- Mesoscale methods
  - dissipative particle dynamics (DPD), 331–332
  - MesoDyn, 329–331
- Metal matrix nanocomposites (MMNC), 199–200
- Molecular beam epitaxial method (MBE), 7
- Multi-walled carbon nanotubes (MWCNT), 269

## N

- Nanomaterials, 218
- Nanoparticles
  - characterization techniques
    - energy dispersive X-ray (EDX or EDS) analysis, 297
    - Fourier transform infrared (FTIR) spectroscopy, 298
    - high resolution transmission electron microscopy (HR-TEM), 296–297
    - UV-visible spectroscopy, 293–295
    - X-ray diffraction (XRD), 295–296
    - zeta potential analysis, 298
  - green synthesis
    - biosynthetic strategies, 300
    - microbe-assisted nanosynthesis, 302
  - marine macroalgae or seaweeds, 306
    - chlorophyceae, 309–310
    - phaeophyceae, 307
    - rhodophyceae, 308
    - seaweed-mediated biosynthesis, 310–311
  - metallic nanoparticles, 312
  - noble metal nanoparticles, 298
    - bottom-up approach, 299–300
    - top-down approach, 299
  - properties and significance
    - noble metal nanoparticles, 291–293
- Neodymium sesquioxide (Nd<sub>2</sub>O<sub>3</sub>), 250–253
- Normal and shear separation forces, 127
- NPT-MD simulations, 119
- Numerical methods, 81

**P**

- Photocatalytic degradation, 276
  - challenges in, 285–286
  - composite particles, 282–283
  - concentration using, 283
  - photodegradation studies, 278–279
  - reactive red 198 dye, 279–280
  - reusability, 284–285
  - sol-gel method, 281–282
  - sunlight-mediated photocatalysis, 277–278
  - total organic carbon (TOC), 283–284
  - UV-light mediated photocatalysis, 277
  - wavelength, 280
  - ZnO-TiO<sub>2</sub> nanomaterials, 279
- Poly (methyl methacrylate) (PMMA), 138
  - nanocomposites, synthesis
    - blending method, 140–141
    - carbon nanotubes (CNT), 144–145
    - chalcogenides, 145–146
    - electrical applications, 152–153
    - ex situ synthesis method, 140
    - gas sensors, 152
    - graphene, 144–145
    - metal nanoparticles, 141–143
    - metal oxide nanoparticles, 143–144
    - multi-components, 147
    - natural fibers, 147–148
    - optoelectronic applications, 153–155
    - polymer matrices, 140
    - polymers, 146
    - pyrene-functionalized, 148, 152
    - in situ polymerization, 141
    - sol-gel route, 139–140
- Polymer inorganic nanocomposites (PINC), 29
- Polymer nanocomposites, 326
- Polythiophene
  - applications, 44–46
  - metal matrix, 28
  - nanocomposites, 28, 29
    - cadmium sulfide (CDS), 44
    - CDSE nanocomposites, 43–44
    - CoO nanocomposites, 32
    - fullerene nanocomposite, 43
    - graphene nanocomposite, 42
    - MnO<sub>2</sub> nanocomposites, 36–37
    - montmorillonite nanocomposites, 38

- poly (3-alkylthiophenes), 30–32
- polythiophene, 39–42, 42, 43–44, 44
- polythiophene/multiwalled carbon nanotubes (PTh/MWCNT), 38–39
- single-walled carbon nanotubes (SWCN), 39–42
- TiO<sub>2</sub> nanocomposites, 35–36
- vanadium oxides, 33
- zinc oxide nanocomposites, 32
- polymer inorganic nanocomposites (PINC), 29
- reinforcement materials, 28
- Polythiophene/multiwalled carbon nanotubes (PTh/MWCNT), 38–39
- Potential energy (PE), 76

**R**

- Radial distribution function (RDF), 97
- Rare earths (RE) sesquioxides, 247
- Rare-earth oxide, 243
  - bottom-up method, 249–250
  - dysprosium oxide (Dy<sub>2</sub>O<sub>3</sub>), 256–258
  - ethylenediaminetetra-acetic acid (EDTA), 260
  - gadolinium oxide (Gd<sub>2</sub>O<sub>3</sub>), 253–255
  - neodymium sesquioxide (Nd<sub>2</sub>O<sub>3</sub>), 250–253
  - samarium oxide (Sm<sub>2</sub>O<sub>3</sub>), 258–260
  - synthesis, 247–248
  - top-down method, 249
- Reduced graphene oxide
  - determining
    - carbon-to-oxygen ratio, 17
    - electrical conductivity, 16
    - visual characteristics, 15–16
  - reduction strategies
    - chemical reagent reduction, 17–20
    - electrochemical removal, 21
    - graphite fluoride, 21
    - photocatalyst reduction, 21
    - thermal reduction, 20
  - synthesis and fabrication, 13–15
- Rubber clay
  - tire, 63
    - base compounds, 66–67
    - brominated isobutyleneisoprene rubber (BIIR), 67
    - butyl rubber clay, 67–68

EPDM/clay nanocomposites, 68–69  
inner liner, 64–66  
NR/SBR/organoclay nanocomposites,  
67  
SBR nanocomposites, 68  
tread, 63–64

## S

Samarium oxide ( $\text{Sm}_2\text{O}_3$ ), 258–260  
Single layer Gr (SLGR), 100–101  
Single-walled carbon nanotubes (SWCN),  
12, 39–42  
Sol-gel method, 281–282  
Solvent-aided sonication, 3–4  
Stress-strain response, 114  
interfacial model, 120, 122  
normal displacement, 122  
shear displacement, 122–123  
unit cell preparation, 123  
Sunlight-mediated photocatalysis, 277–278  
Surfactant-assisted exfoliation, 4–5

## T

Textile dyeing  
nanocomposites, 188  
acid dyes, 193  
adsorption behavior, 189–190  
applications, 190–191  
azoic dyes, 193  
basic dyes, 193  
catalyst, 189  
direct dyes, 192  
disperse dyes, 193  
dye removal, 191  
mordant dyes, 194, 199  
reactive dyes, 191  
sulfur dye, 194  
VAT dyes, 193  
removal  
ceramic–matrix nanocomposites,  
198–199  
electrostatic attraction, 204  
field emission scanning electron  
microscopy (FESEM), 203, 204  
hydrogel/clay nanocomposites, 208–209  
magnetic multiwall carbon nanotube  
(MMWCNT), 204

magnetite/reduced graphene oxide  
(MRGO), 202  
malachite green (MG), 201  
metal matrix nanocomposites  
(MMNC), 199–200  
photocatalytic degradation, 203  
polymer–matrix nanocomposites,  
205–208  
zinc oxide, 205  
types, 194–198  
Thermoplastic polyurethanes (TPUs), 82,  
101–106  
Time integration algorithm, 88  
Tire  
bead, 58–59  
breakers, 58  
carcass or body ply, 57  
chafers, 57  
cushioning, 61  
inner liner, 56–57  
insulations, 58  
load carrying capacity, 62  
rolling resistance, 59–61  
sidewall rubber, 58  
traction, 61  
transmits steering resistance, 62–63  
tread, 58  
wear and durability, 62  
Top-down approach (TDA), 219  
Torsional rotation potential, 79  
Total organic carbon (TOC), 283–284  
Toughness, 95–96  
Tribological properties, 85

## U

Unit cell preparation, 106–107, 115, 123  
UV-light mediated photocatalysis, 277  
UV-visible spectroscopy, 293–295

## V

Van der Waals (vdW), 80  
Vanadium oxides, 33  
Viral nanoparticles, 223–224

## W

Wastewater technologies, 273–274

**X**

X-ray diffraction (XRD), 241, 295–296

**Y**

Young's modulus, 119

**Z**

Zeta potential analysis, 298

Zinc oxide, 205

    nanocomposites, 32

Zn-Al-based nanocomposites, 269

ZnO-TiO<sub>2</sub> nanomaterials, 279